

OXFORD ENGINEERING SCIENCE SERIES • 42

Molecular Gas Dynamics and the Direct Simulation of Gas Flows

G. A. BIRD



OXFORD SCIENCE PUBLICATIONS

THE OXFORD ENGINEERING SCIENCE SERIES

7. K.H. HUNT: *Kinematic geometry of mechanism*
10. P. HAGEDORN: *Non-linear oscillations* (Second edition)
11. R. HILL: *Mathematical theory of plasticity*
13. N.W. MURRAY: *Introduction to the theory of thin-walled structures*
14. R.I. TANNER: *Engineering rheology*
15. M.F. KANNINEN and C.H. POPELAR: *Advanced fracture mechanics*
16. R.H.T. BATES and M.J. McDONNELL: *Image restoration and reconstruction*
19. R.N. BRACEWELL: *The Hartley transform*
20. J. WESSON: *Tokamaks*
22. C. SAMSON, M. LeBORGNE, and B. ESPIAU: *Robot control: the task function approach*
23. H.J. RAMM: *Fluid dynamics for the study of transonic flow*
24. R.R.A. SYMS: *Practical volume holography*
25. W.D. McCOMB: *The physics of fluid turbulence*
26. Z.P. BAZANT and L. CEDOLIN: *Stability of structures: elastic, inelastic, fracture, and damage theories*
27. J.D. THORNTON: *Science and practice of liquid-liquid extraction* (Two volumes)
28. J. VAN BLADEL: *Singular electromagnetic fields and sources*
29. M.O. TOKHI and R.R. LEITCH: *Active noise control*
30. I.V. LINDELL: *Methods for electromagnetic field analysis*
31. J.A.C. KENTFIELD: *Nonsteady, one-dimensional, internal, compressible flows*
32. W.F. HOSFORD: *Mechanics of crystals and polycrystals*
33. G.S.H. LOCK: *The tubular thermosyphon: variations on a theme*
34. A. LINÁN and F.A. WILLIAMS: *Fundamental aspects of combustion*
35. N. FACHE, D. DE ZUTTER, and F. OLYSLAGER: *Electromagnetic and circuit modelling of multiconductor transmission lines*
36. A.N. BERIS and B.J. EDWARDS: *Thermodynamics of flowing systems: with internal microstructure*
37. K. KANATANI: *Geometric computation for machine vision*
38. J.G. COLLIER and J.R. THOME: *Convective boiling and condensation* (Third edition)
39. I.I. GLASS and J.P. SISLIAN: *Nonstationary flows and shock waves*
40. D.S. JONES: *Methods in electromagnetic wave propagation* (Second edition)
41. M. KOJIC: *Computational algorithms in inelastic analysis of solids and structures*
42. G.A. BIRD: *Molecular gas dynamics and the direct simulation of gas flows*

MOLECULAR GAS DYNAMICS AND THE DIRECT SIMULATION OF GAS FLOWS

G. A. BIRD

*GAB Consulting Pty Ltd
Emeritus Professor, The University of Sydney*

CLARENDON PRESS • OXFORD
1994

Oxford University Press, Walton Street, Oxford OX2 6DP

Oxford New York Toronto

Delhi Bombay Calcutta Madras Karachi

Kuala Lumpur Singapore Hong Kong Tokyo

Nairobi Dar es Salaam Cape Town

Melbourne Auckland Madrid

and associated companies in

Berlin Ibadan

Oxford is a trade mark of Oxford University Press

*Published in the United States by
Oxford University Press Inc., New York*

© G. A. Bird, 1994

All rights reserved. No part of this publication may be reproduced, stored in a retrieval system, or transmitted, in any form or by any means, without the prior permission in writing of Oxford University Press. Within the UK, exceptions are allowed in respect of any fair dealing for the purpose of research or private study, or criticism or review, as permitted under the Copyright, Designs and Patents Act, 1988, or in the case of reprographic reproduction in accordance with the terms of licences issued by the Copyright Licensing Agency. Enquiries concerning reproduction outside these terms and in other countries should be sent to the Rights Department, Oxford University Press, at the address above.

This book is sold subject to the condition that it shall not, by way of trade or otherwise, be lent, re-sold, hired out or otherwise circulated without the publisher's prior consent in any form of binding or cover other than that in which it is published and without a similar condition including this condition being imposed on the subsequent purchaser.

A catalogue record for this book is available from the British Library

*Library of Congress Cataloging in Publication Data
(Data available)*

ISBN 0-19-856195-4

Typeset by the author

*Printed in Great Britain by
Bookcraft (Bath) Ltd
Midsomer Norton, Avon*

PREFACE

This book is a sequel to the monograph *Molecular gas dynamics* that was published in the Oxford Engineering Science Series in 1976. The preface to that book stated that it was intended for scientists and engineers who wished to analyse practical non-linear gas flows at the molecular level. The target readership is unchanged and the direct simulation Monte Carlo (or DSMC) method continues to be the tool that is advocated for this analysis. This is a computational tool and the intervening period has seen a two order of magnitude increase in computer speed and, more importantly, a three or four order of magnitude reduction in the effective cost of the computation. In addition, the molecular models and DSMC procedures that have been introduced since 1976 are incomparably superior to those that were available at that time.

The molecular models that had been employed in the DSMC method prior to 1976 were, with one exception, those handed down from the classical kinetic theory of gases. The Chapman-Enskog theory for the transport properties had been the main accomplishment of this theory and the traditional models had proved to be reasonably adequate for monoatomic gases. The classical models for diatomic and polyatomic molecules are less than adequate, and the above-mentioned exception was the introduction in 1974 of the phenomenological method of Larsen and Borgnakke. This has exerted such a strong influence on subsequent developments that it could well be regarded as a 'philosophy' rather than just a procedure. The phenomenological approach leads to models that mathematically mimic the physically significant aspects of real molecules and thereby bypass the limitations of the entirely physical analogues that had been employed in classical kinetic theory.

The phenomenological approach also led in 1981 to the introduction by the author of the variable hard sphere (or VHS) model that avoids many of the difficulties associated with the classical elastic models. The recent development of the variable soft sphere (or VSS) model by Koura and the generalized hard sphere (or GHS) model by Hash and Hassan have added optional features to this model that make it even more realistic in some situations. The Larsen-Borgnakke theory for the internal degrees of freedom has been extended to build upon these new models and, because it is phenomenological, it has also been extended to quantum versions for the vibrational and electronic modes. The 'DSMC models' are now well in advance of those developed in the context of classical kinetic theory and its application to the transport properties. The phenomenological approach also led to the CLL gas-surface interaction model that was introduced by Cercignani and Lampis in 1974. This has recently been reformulated by Lord for application to DSMC simulation.

Although many of the early chapters have the same titles as the corresponding chapters in *Molecular gas dynamics*, the introduction of the new models has led to massive changes in their content.

Chapter 6 on chemical reactions and thermal radiation is comprised almost entirely of new work. The dissociation model is integrated with the Larsen-Borgnakke model for vibrational excitation and, in addition to providing the background theory for the DSMC implementation, it contains a new theory for the dissociation and recombination reaction rates. This illustrates the usefulness of the new models for analytical as well as numerical studies.

The collisionless flow chapter is an update of that in *Molecular gas dynamics* and provides necessary background material for rarefied gas flow studies. Chapter 8 reviews the analytical methods that have been applied to transition regime flows. The detailed expositions have been restricted to cases that are required in later chapters for direct comparisons with DSMC results. The numerical methods are reviewed in Chapter 9, with particular emphasis on the points of distinction between the DSMC method, the molecular dynamics approach, and the lattice gas schemes. The period since 1976 has seen a greater level of understanding of the statistical aspects of direct simulations. This has led to significant changes in the recommended implementation strategy for the direct simulation method, and these are discussed in Chapter 10.

The first problem that is faced by a potential user of the DSMC method is the effort and time that is required to master all the tedious details in order to produce and to validate a new program. The final problem is that, once the results have been obtained, the recipient of the results has no way of verifying the work and, in the absence of physical inconsistencies, their acceptance depends on trust and, conversely, any rejection can only be based on prejudice. This is a problem that is shared by most methods of computational fluid dynamics (CFD), but has been more serious in the case of the DSMC method because it is a physically based probabilistic simulation rather than an application of standard numerical analysis to accepted mathematical equations. This book seeks to overcome these problems through the provision, on an included disk, of the FORTRAN source code of a set of thirteen demonstration programs. **Absolutely all the numerical results that are presented and discussed in this book have been obtained from these programs.** Moreover, any one of the results can be obtained from a run of less than 24 hours on a contemporary 'top of the line' personal computer.

The basic DSMC procedures and molecular models are presented and tested in the context of a homogeneous gas in Chapter 11. These are applied to steady one-dimensional flows in Chapter 12. These calculations are readily made for conditions under which the Navier-Stokes equations are also valid. The DSMC method, as well as the basic procedures, are validated through a careful study of the transport properties, both in simple gases and in gas mixtures. Comparisons are made with measured values as well as with the continuum theory.

The normal shock wave remains the most valuable single test case, both for comparisons with reliable experiments and as an illustration of the shortcomings of the conventional formulations of the Navier-Stokes equations. The landmark comparisons by Muntz et al of DSMC results for weak shock waves with experiment, with the Navier-Stokes solutions, and with a solution of the Burnett equations are reproduced as just some of the examples from a dedicated demonstration program for shock wave studies.

The procedures for the application of the DSMC method to flows with more than one independent variable are discussed in Chapters 13 to 16. The one-dimensional unsteady flow program merely required changes to the sampling routines of the steady flow program. It remains very general with options for cylindrical and spherical symmetry. The demonstration programs for two-dimensional, axially symmetric, and three-dimensional flows are limited to applications with straight or flat boundaries. In spite of this restriction, a representative set of test cases is presented. Most of these are similar to calculations that have already been published but some, such as the effect of Knudsen number on the formation of a vortex behind a vertical flat plate, cover new ground. The example that deals with the annular vortices in Taylor-Couette flow is based on recent work by Stefanov and Cercignani and is particularly interesting. This case also serves to draw attention to the fact that all DSMC calculations contain a physically realistic time parameter and provide meaningful information on the development of steady flows. The DSMC method has also been applied to the Taylor-Couette flow in recent work by Reichelmann and Nanbu. They made comparisons with experimental data for this flow and these demonstrate that the DSMC method correctly predicts the conditions under which vortices form in a rarefied gas.

The demonstration programs should give a feel for the operation of the DSMC method and promote an understanding of its capabilities. Most users will find that the complete absence of numerical instabilities more than compensates for the nuisance of the statistical scatter.

The DSMC method has been developed in an aerospace environment and, to date, most of the engineering applications of the method have been to aerospace problems. Many areas of potentially profitable application of the method have not yet been exploited. These include many aspects of semiconductor fabrication and almost any process that involves high vacuum, as well as in the development of the high-vacuum equipment itself. One reason for this is that the once high cost of DSMC computations gave it the reputation of an 'expensive' method. Given the recent reduction in the cost of computations, this reputation is no longer justified. Also, the inexpensive and easy application of the DSMC method means that experimenters can now make parallel simulations. The comparison of the measurements with the results from the simulations can enable values to be inferred for quantities that are not amenable to direct measurement.

It is hoped that this exposition of the DSMC method will enable many more workers to become involved in its application and to thereby share the pleasure that it has given the author over so many years.

Acknowledgements

Just as the early development of the DSMC method was supported by the Air Force Office of Scientific Research, the more recent developments by the author have been supported through the NASA Langley Research Center. These developments have benefited from discussions at Langley, particularly with Jim Moss, Frank Brock, Dick Wilmoth, Ann Carlson, Michael Woronowicz, Cevdet Celenligil, Rupe Gupta, and Didier Rault. This effort has also involved North Carolina State University and similar mention should be made of Hassan Hassan and David Hash.

The developments have also been influenced by discussions and correspondence with fellow DSMC developers and users in many parts of the world. Among others, thanks are due to Doug Auld in Australia, Don Baganoff, Tim Bartel, Iain Boyd, David Erwin, Brian Haas, Lyle Long, Dan McGregor, and Phil Muntz in the USA, John Harvey and Gordon Lord in England, Frank Bergemann in Germany, Carlo Cercignani in Italy, Malek Mansour in Belgium, and Kenichi Nanbu in Japan.

Several of the above, in particular Frank Brock, have also assisted with the checking of the manuscript. Valuable assistance in this task has also been received from Alan Fien and Bob Ash.

The author would also like to thank the editors at Oxford University Press for their helpful cooperation during the preparation of this book. It has been computer typeset by the author using WordPerfect 5.1.

*Sydney, Australia
November, 1993*

G.A.B.

CONTENTS

PREFACE	v
LIST OF SYMBOLS	xiii
1. THE MOLECULAR MODEL	
1.1 Introduction	1
1.2 The requirement for a molecular description	2
1.3 The simple dilute gas	4
1.4 Macroscopic properties in a simple gas	9
1.5 Extension to gas mixtures	16
1.6 Molecular magnitudes	19
1.7 Real gas effects	24
References	29
2. BINARY ELASTIC COLLISIONS	
2.1 Momentum and energy considerations	30
2.2 Impact parameters and collision cross-sections	33
2.3 Collision dynamics	34
2.4 The inverse power law model	37
2.5 The hard sphere model	39
2.6 The variable hard sphere (VHS) model	40
2.7 The variable soft sphere (VSS) model	41
2.8 The Maxwell model	43
2.9 Models that include the attractive potential	43
2.10 The generalized hard sphere (GHS) model	44
2.11 General comments	44
References	45
3. BASIC KINETIC THEORY	
3.1 The velocity distribution functions	46
3.2 The Boltzmann equation	50
3.3 The moment and conservation equations	55
3.4 The H -theorem and equilibrium	61
3.5 The Chapman–Enskog theory	64
References	76
4. EQUILIBRIUM GAS PROPERTIES	
4.1 Spatial properties	77
4.2 Fluxal properties	80
4.3 Collisional quantities in a simple gas	88
4.4 Collisional quantities in a gas mixture	96
4.5 Equilibrium with a solid surface	97
References	98

5.	INELASTIC COLLISIONS AND SURFACE INTERACTIONS	
5.1	Molecules with rotational energy	99
5.2	The rough-sphere molecular model	101
5.3	The Larsen–Borgnakke model in a simple gas	104
5.4	The Larsen–Borgnakke model in a gas mixture	108
5.5	The general Larsen–Borgnakke distribution	109
5.6	Vibrational and electronic energy	112
5.7	Relaxation rates	116
5.8	Gas–surface interactions	118
References		122
6.	CHEMICAL REACTIONS AND THERMAL RADIATION	
6.1	Introduction	123
6.2	Collision theory for bimolecular reactions	124
6.3	Reaction cross-sections for given reaction rates	126
6.4	Extension to termolecular reactions	128
6.5	Chemical equilibrium	130
6.6	The equilibrium collision theory	132
6.7	The dissociation–recombination reaction	133
6.8	The exchange and ionization reactions	140
6.9	Classical model for rotational radiation	144
6.10	Bound–bound thermal radiation	145
References		146
7.	COLLISIONLESS FLOWS	
7.1	Bimodal distributions	148
7.2	Molecular effusion and transpiration	151
7.3	One-dimensional steady flows	154
7.4	One-dimensional unsteady flows	156
7.5	Free-molecule aerodynamics	162
7.6	Thermophoresis	173
7.7	Flows with multiple reflection	175
References		182
8.	ANALYTICAL METHODS FOR TRANSITION REGIME FLOWS	
8.1	Classification of methods	183
8.2	Moment methods	185
8.3	Model equations	195
References		198
9.	NUMERICAL METHODS FOR TRANSITION REGIME FLOWS	
9.1	Classification of methods	199
9.2	Direct Boltzmann CFD	200
9.3	Deterministic simulations	201
9.4	Probabilistic simulation methods	203
9.5	Discretization methods	205
References		206

10. GENERAL ISSUES RELATED TO DIRECT SIMULATIONS	
10.1 Introduction	208
10.2 The relationship to the Boltzmann equation	208
10.3 Normalized or dimensioned variables	210
10.4 Statistical scatter and random walks	211
10.5 Computational approximations	214
References	216
11. DSMC PROCEDURES IN A HOMOGENEOUS GAS	
11.1 Collision sampling techniques	218
11.2 Collision test programs	220
11.3 Rotational relaxation and equilibrium	228
11.4 Vibrational excitation	238
11.5 Dissociation and recombination	245
11.6 Fluctuations and correlations	251
References	256
12. ONE-DIMENSIONAL STEADY FLOWS	
12.1 General program for one-dimensional flows	257
12.2 The viscosity coefficient of argon	262
12.3 The viscosity of an argon-helium mixture	269
12.4 The Prandtl number of nitrogen	271
12.5 The self-diffusion coefficient of argon	271
12.6 Mass diffusion in an argon-helium mixture	273
12.7 Thermal diffusion	275
12.8 The diffusion thermo-effect	278
12.9 Heat transfer in the transition regime	280
12.10 Breakdown of continuum flow in expansions	282
12.11 The normal shock wave	286
12.12 Stagnation streamline flow	306
12.13 Adiabatic atmosphere	311
12.14 Gas centrifuge	313
References	315
13. ONE-DIMENSIONAL UNSTEADY FLOWS	
13.1 General program for unsteady flows	316
13.2 The formation of a strong shock wave	317
13.3 The reflection of a strong shock wave	320
13.4 Formation of a weak shock wave	323
13.5 The complete rarefaction wave	325
13.6 Spherically imploding shock wave	328
13.7 Collapse of a cylindrical cavity	331
References	333

14. TWO-DIMENSIONAL FLOWS	
14.1 Grids for DSMC computations	334
14.2 DSMC program for two-dimensional flows	340
14.3 The supersonic leading-edge problem	340
14.4 Effect of cell size	346
14.5 The formation of vortices	348
14.6 The supersonic blunt-body problem	353
14.7 Diffusion in blunt-body flows	357
14.8 The flat plate at incidence	360
14.9 The Prandtl-Meyer expansion	367
References	369
15. AXIALLY SYMMETRIC FLOWS	
15.1 Procedures for axially symmetric flows	370
15.2 Radial weighting factors	372
15.3 Flow past a flat-nosed cylinder	374
15.4 The Taylor-Couette flow	378
15.5 Normal impact of a supersonic jet	384
15.6 The satellite contamination problem	387
References	388
16. THREE-DIMENSIONAL FLOWS	
16.1 General considerations	389
16.2 Supersonic corner flow	394
16.3 Finite span flat plate at incidence	401
16.4 Corner flow with normal jet plume	405
16.5 Concluding comments	407
References	407
APPENDIX A. Representative gas properties	408
APPENDIX B. Probability functions and related integrals	417
APPENDIX C. Sampling from a prescribed distribution	423
APPENDIX D. Listing of program FMF.FOR	429
APPENDIX E. Numerical artefacts	430
APPENDIX F. Summary of the DSMC demonstration programs	437
APPENDIX G. Listing of program DSMC0S.FOR	440
SUBJECT INDEX	453

LIST OF SYMBOLS

Notes: This list does not include the FORTRAN variables that appear in the demonstration programs. The values of the fundamental physical constants are based on the 1986 CODATA recommended values.

a	speed of sound; a constant
a_c	accommodation coefficient
A	a constant
A_{nm}	Einstein coefficient
b	miss-distance impact parameter; a constant
B	a constant
c	molecular speed; a constant; speed of light
c_f	skin friction coefficient, eqn (7.62)
c_p	specific heat at constant pressure
c_v	specific heat at constant volume
c_0	macroscopic flow speed
\mathbf{c}	molecular velocity vector
\mathbf{c}_0	macroscopic velocity vector
C	a constant; diffusion speed
C_h	heat transfer coefficient, eqn (7.64)
C_p	pressure coefficient, eqn (7.59)
C_D	drag coefficient
C_L	lift coefficient
C_N	normal force coefficient
C_P	parallel force coefficient
\mathbf{C}	diffusion velocity vector
d	molecular diameter; a constant; a distance
D	a constant
D_{12}	coefficient of diffusion
D_{11}	coefficient of self-diffusion
e	specific energy
e_p	photon energy
\mathbf{e}	unit normal vector
E_t	translational kinetic energy
E_a	activation energy
f	normalized velocity distribution function in velocity space, eqn (3.1); a function
f_0	Maxwellian or equilibrium velocity distribution function, eqn (3.47)
$F^{(N)}$	N particle distribution function, eqn (3.7)
$F_{(R)}$	reduced distribution function, eqn (3.8)
F	force; a fraction; cumulative distribution function
F_N	number of real molecules represented by a single DSMC molecule
\mathbf{F}	force vector

\mathcal{F}	single particle distribution function in phase space, eqn (3.5)
g	relative speed; quantum degeneracy; gravitational acceleration
\mathbf{g}	relative velocity vector
h	Planck constant, $h = 6.6260755 \times 10^{-34}$ J s; a height
H	Boltzmann's H -function
i	a quantum level
I	moment of inertia
j, k, l	vectors in a rough-sphere collision
j	an integer
k	Boltzmann constant, $k = \mathcal{R}/\mathcal{N} = mR = 1.380658 \times 10^{-23}$ J K ⁻¹
k_T	thermal diffusion ratio
k_f	rate coefficient for forward reaction
k_r	rate coefficient for reverse reactions
K	coefficient of heat conduction
K_{eq}	equilibrium constant
$K(0)$	mean square fluctuation
$K(t)$	temporal correlation function
$K(x)$	spatial correlation function
(Kn)	Knudsen number, $(Kn) = \lambda/L$
l	a linear dimension; direction cosine with x -axis
L	a linear dimension
m	molecular mass; direction cosine with y -axis; a number
m_r	reduced mass
m_u	atomic mass constant, $m_u = 1.6605402$ kg M^{24}
(Ma)	Mach number, $(Ma) = u/a$
$(Ma)_S$	shock Mach number
\mathcal{M}	molecular weight
n	number density; direction cosine with z -axis; a number
n_0	Loschmidt's number, $n_0 = 2.68666 \times 10^{25}$ m ⁻³
N	a number; a fraction
\dot{N}	a number flux
N_λ	number in a cubic mean free path
\mathcal{N}	Avogadro's number, $\mathcal{N} = 6.022137 \times 10^{23}$ mol ⁻¹
p	pressure
\mathbf{p}	pressure tensor
P	the continuum breakdown parameter, eqn (1.4); probability
(Pr)	Prandtl number, $(Pr) = \mu c_p/K$
q	energy flux
\mathbf{q}	heat flux vector
Q	a molecular quantity; partition function
Q_p	shape factor of a shock wave profile, eqn (12.33)
r	a distance; a radius; a multiplier
\mathbf{r}	position vector
R	gas constant, $R = \mathcal{R}/\mathcal{M}$
R_f	random fraction between 0 and 1
(Re)	Reynolds number, $(Re) = \rho v l / \mu$

\mathcal{R}	universal gas constant, $\mathcal{R}=8.314511 \text{ J mol}^{-1} \text{ K}^{-1}$
s	speed ratio, $s=u \beta$; number of square terms
s_d	trajectory fraction to a surface interaction
s_0	zero potential radius
S	surface area; parameter in Lennard-Jones model
(Sc)	Schmidt number, $(Sc)=\mu/(\rho D_{11})$
t	time
T	temperature
(Ta)	Taylor number, eqn (15.4)
u	velocity component in the x -direction; a velocity
U	potential energy; x -component of the diffusion velocity; a velocity
v	velocity component in the y -direction
V	a volume
V_C	cell volume
w	velocity component in the z direction
W	dimensionless coordinate
W_0	normalised dimensionless coordinate, eqn (2.24)
x	Cartesian axis in physical space; dummy argument
X	a position
y	Cartesian axis in physical space
z	Cartesian axis in physical space
Z	relaxation collision number
α	exponent in the VSS molecular model, eqn (2.36); accommodation coefficient; degree of dissociation; angle of incidence; a constant
α_T	thermal diffusion factor
β	reciprocal of the most probable molecular speed in an equilibrium gas, $\beta=(2RT)^{-\frac{1}{2}}$
γ	specific heat ratio, eqn (1.62)
δ	mean molecular spacing; Kronecker delta
ϵ	molecular energy; azimuthal impact parameter; the well-depth parameter; symmetry factor; fraction of specular reflection; 0, 1, or 2 for plane, cylindrical, or spherical flows
ϵ_0	free space dielectric constant
ζ	number of internal degrees of freedom
η	exponent in the inverse power law model; temperature exponent in the Arrhenius equation
θ	angle; elevation angle
θ_A	angle between apse line and relative velocity vector
Θ	characteristic temperature
κ	constant in the inverse power law model
λ	mean free path; wave length
Λ	the Larsen-Borgnakke inelastic fraction; the Arrhenius constant
μ	coefficient of viscosity
μ_e	electric dipole moment
ν	collision rate
ξ	total number of degrees of freedom

Ξ	sum of the average degrees of freedom
ρ	density
σ	cross-section
σ_T	total collision cross-section, eqn (2.14)
σ_μ	viscosity cross-section, eqn (2.28)
σ_M	momentum cross-section, eqn (2.29)
σ_R	reaction cross-section
τ	viscous stress, relaxation time
τ_a	local relaxation time
τ	viscous stress tensor
τ_{nm}	mean radiative lifetime
Γ	mass flux; gamma function
v	relative speed exponent of VHS model, $v = \omega - 1/2$
ϕ	intermolecular potential; azimuthal angle
Φ	dissipation function, eqn (3.37); perturbation of the equilibrium distribution function
χ	deflection angle
ψ	inverse power law for variation of cross-section with relative energy
ω	angular velocity; temperature exponent of the coefficient of viscosity
Ω	solid angle

Superscripts and subscripts

Note: The subscripts in the above list do not, in general, conform to the following meanings.

*	post-collision values; sonic conditions
,	thermal or peculiar component; a second value
"	single species thermal component in a mixture; another value
+-	moving in positive, negative directions
A,B	associated with particular species

a,b	to distinguish separate groups
A,B,C,D	separate species in chemical reactions; particular values
c	associated with collisions or cell; continuum value
coll	value based on a single collision
d	a reference value; dissociation value; direct
e	entering
el	associated with the electronic excitation
i,j,k	Cartesian tensor components
f	free-molecule value
i	inward or incident value; internal
int	based on or associated with internal modes
L	lower
m	centre of mass value; most probable value; reference value
max	maximum value
min	minimum value

n	radial component; normal component
ov	based on or associated with all modes
p	slip or jump value at a surface
p,q,s	particular molecular species
r	relative; reflected value
ref	reference value
rot	based on or associated with rotational modes
s	root mean square value; value adjacent to surface; selected value
S	sampled value
t	translational; total; transmitted
tr	based on or associated with the translational modes
T	third body in a ternary collision
u	unselected
U	upper
v	based on or associated with the vibrational modes
w	surface value
x,y,z	components in the x -, y -, and z -directions, respectively
0,1,2	particular values
∞	freestream value
—	
.	average value
<.>	average value
^	normalized value
[.]	truncated value

1

THE MOLECULAR MODEL

1.1 Introduction

A gas flow may be modelled at either the macroscopic or the microscopic level. The macroscopic model regards the gas as a continuous medium and the description is in terms of the spatial and temporal variations of the familiar flow properties such as the velocity, density, pressure, and temperature. The Navier–Stokes equations provide the conventional mathematical model of a gas as a continuum. The macroscopic properties are the dependant variables in these equations, while the independent variables are the spatial coordinates and time.

The microscopic or molecular model recognizes the particulate structure of the gas as a myriad of discrete molecules and ideally provides information on the position, velocity, and state of every molecule at all times. The mathematical model at this level is the Boltzmann equation. This has the fraction of molecules in a given location and state as its single dependent variable, but the independent variables are increased by the number of physical variables on which the state depends. In the simplest case of a monatomic gas with no internal degrees of freedom, the additional dimensions of this *phase space* are the three velocity components of the molecules. A one-dimensional steady flow of such a gas becomes a three-dimensional problem in phase space (the velocity distribution is axially symmetric about the velocity component in the flow direction), while a two-dimensional steady flow becomes five-dimensional. This means that the Boltzmann equation is not amenable to analytical solution for non-trivial problems, and it presents overwhelming difficulties to conventional numerical methods. However, the discrete structure of the gas at the molecular level enables these difficulties to be circumvented through direct physical, rather than mathematical, modelling.

This book is concerned with the analysis of gas flows at the microscopic or molecular level, with particular emphasis on computational methods that employ the physical or direct simulation approach. While this physical approach has some advantages over the traditional mathematical formulation for computational studies, notably the absence of numerical instabilities, the molecular model is generally more demanding of computer resources. It is therefore important to delineate the circumstances under which the continuum model loses its validity and must be replaced by the molecular model.

1.2 The requirement for a molecular description

The macroscopic properties may be identified with average values of the appropriate molecular quantities at any location in a flow. They may therefore be defined as long as there are a sufficient number of molecules within the smallest significant volume of a flow. This condition is almost always satisfied and the results from the molecular model can therefore be expressed in terms of the familiar continuum flow properties. Moreover, the equations that express the conservation of mass, momentum, and energy in a flow are common to, and can be derived from, either model. While this might suggest that neither of the approaches can provide information that is not also accessible to the other, it must be remembered that the conservation equations do not form a determinate set unless the shear stresses and heat flux can be expressed in terms of the lower-order macroscopic quantities. It is the failure to meet this condition, rather than the breakdown of the continuum description, which imposes a limit on the range of validity of the continuum equations. More specifically, the transport terms in the Navier–Stokes equations of continuum gas dynamics fail when gradients of the macroscopic variables become so steep that their scale length is of the same order as the average distance travelled by the molecules between collisions, or *mean free path*.

The degree of rarefaction of a gas is generally expressed through the *Knudsen number* (Kn) which is the ratio of the mean free path λ to the characteristic dimension L , i.e.

$$(Kn) = \lambda/L. \quad (1.1)$$

The traditional requirement for the Navier–Stokes equations to be valid is that the Knudsen number should be less than 0.1. This can be misleading if L is chosen to be some overall dimension of the flow in order to define a single *overall* Knudsen number for the complete flow. The limit can be specified precisely if a *local* Knudsen number is defined with L as the scale length of the macroscopic gradients; e.g.

$$L = \frac{\rho}{d\rho/dx}. \quad (1.2)$$

The error in the Navier–Stokes result is significant in the regions of the flow where the appropriately defined local number exceeds 0.1, and the upper limit on the local Knudsen number at which the continuum model must be replaced by the molecular model may be taken to be 0.2.

The transport terms vanish in the limit of zero Knudsen number and the Navier–Stokes equations then reduce to the inviscid Euler equations. The flow is then isentropic from the continuum viewpoint, while the equivalent molecular viewpoint is that the velocity distribution function is everywhere of the local equilibrium or Maxwellian form. The opposite limit of infinite Knudsen number is the *collisionless* or *free-molecule* flow regime. These Knudsen number limits on the conventional mathematical formulations are shown schematically in Fig. 1.1.

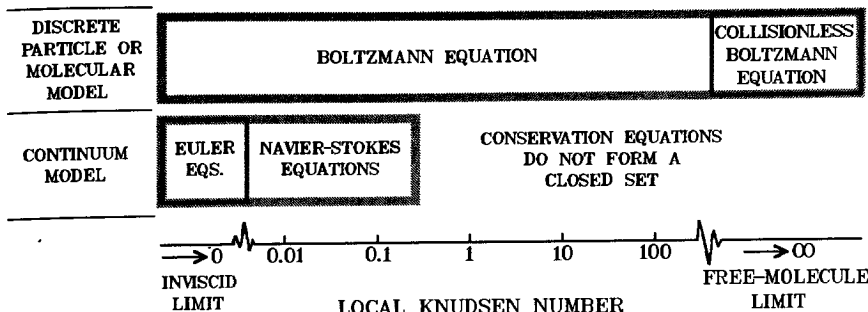


FIG. 1.1 The Knudsen number limits on the mathematical models.

A major achievement of classical kinetic theory, as described by Chapman and Cowling (1952), was the development of the Chapman-Enskog theory for the coefficients of viscosity, heat conduction, and diffusion. This theory authenticated the assumption, inherent in the Navier-Stokes formulation, that the shear stresses, heat fluxes, and diffusion velocities are linear functions of the gradients in velocity, temperature, and species concentration. The Chapman-Enskog theory also established the limits of validity of the formulation because it assumes that the velocity distribution function f is a small perturbation of the equilibrium or Maxwellian function f_0 . For example, it will be shown in Chapter 4 that, for the special case of a flow in the x -direction with gradients only in the y -direction, the Chapman-Enskog distribution function can be written

$$f = f_0 \left[1 - C \beta v' \left\{ 3 \left(\beta^2 c'^2 - \frac{5}{2} \right) \frac{\lambda}{T} \frac{\partial T}{\partial y} + 4 \beta u' s \frac{\lambda}{u_0} \frac{\partial u_0}{\partial y} \right\} \right], \quad (1.3)$$

where C is a numerical factor that depends on the gas. Note that the local Knudsen numbers based on the stream velocity and temperature appear explicitly in the terms that are attributable to the shear stress and the heat flux, respectively. Since the Chapman-Enskog result is the first term in a series expansion about these local Knudsen numbers, the theory is valid only when they are small in comparison with unity.

The transport properties are most significant within boundary layers and shock waves. The mean free path is inversely proportional to the gas density and, for a given shock strength, the width of the wave is also inversely proportional to the density. The local Knudsen numbers within the wave are therefore independent of the density and the validity of the Navier-Stokes equations depends only on the shock Mach number. It has been found that the restriction on the validity of the Navier-Stokes solutions for shock wave structure is that the shock Mach number should be significantly below two. In the case of a laminar boundary layer in a low-speed flow, the thickness of the layer is inversely proportional to the

square root of the density. The gradients therefore decrease less rapidly than the mean free path increases as the density falls, and the local Knudsen numbers become larger at low densities. The increase in the thickness of both these flow features means that, in a flow with shock waves and/or boundary layers, the proportion of the flow that is viscous increases as the flow becomes rarefied. At extremely low densities, the shock waves and boundary layers first merge and then lose their identity as free-molecule conditions are approached.

Outside boundary layers and shock waves, continuum flow is assumed to be isentropic and it might be thought that the Euler equations yield correct results at all Knudsen numbers. The gradients of the macroscopic properties in an isentropic flow depend only on the size of the flow. However, these changes in the macroscopic flow properties can occur only through intermolecular collisions and, as the density falls, the collision rate becomes too low for the maintenance of these gradients. The continuum model then breaks down, with the initial symptom being an anisotropic pressure tensor. The occurrence of this type of breakdown in gaseous expansions was studied by Bird (1970) and it was found to correlate with the 'breakdown parameter'

$$P = \frac{1}{v} \left| \frac{D(\ln \rho)}{Dt} \right|. \quad (1.4)$$

For a steady flow, this equation can be written

$$P = \frac{\pi^{1/2}}{2} s \frac{\lambda}{\rho} \left| \frac{dp}{dx} \right|, \quad (1.5)$$

and we recover a local Knudsen number similar to those in eqn (1.3). The initial breakdown in both steady and unsteady expansions has been found to correlate with a value of P of approximately 0.02.

A large Knudsen number may result from either a large mean free path or a small scale length of the macroscopic gradients. The former is usually the case and is a consequence of a very low gas density. This is why the title 'rarefied gas dynamics' is frequently applied to the subject matter of this book. However, it must be kept in mind that the alternative requirement of a small characteristic dimension can be met at any density. It has already been noted that the internal structure of a strong shock wave appears to require the molecular model at all densities. Similarly, the molecular approach is required for the study of the forces on a very small particle suspended or moving through the atmosphere, or for the propagation of sound at extremely high frequencies.

1.3 The simple dilute gas

The basic quantities associated with the molecular model are the number of molecules per unit volume and the mass, size, velocity, and internal state of each molecule. These quantities must be related to the mean free path and collision frequency in order to establish the distance and time

scales of the effects due to the collisional interactions among the molecules. Also, since the results from the molecular approach will generally be presented in terms of the macroscopic quantities, we must establish the formal relationships between the microscopic and macroscopic quantities. For reasons of simplicity and clarity, the discussion in this section will be restricted to a gas consisting of a single chemical species in which all molecules are assumed to have the same structure. Such a gas is called a *simple gas*.

The number of molecules in one mole of a gas is a fundamental physical constant called *Avogadro's number* N . Avogadro's law also states that the volume occupied by one mole of any gas at a particular temperature and pressure is the same for all gases. The number of molecules per unit volume, or *number density* n , of a gas depends on the temperature and pressure, but is independent of the composition of the gas. The mass m of a single molecule is obtained by dividing the *molecular weight* M of the gas by Avogadro's number, i.e.

$$m = M/N = M m_u, \quad (1.6)$$

where m_u is the atomic mass constant. The average volume available to a molecule is $1/n$, so the mean molecular spacing δ is given by

$$\delta = n^{-1/3}. \quad (1.7)$$

A hard elastic sphere of diameter d provides an over-simplified but useful model of a molecule. Then, as shown in Fig. 1.2, two molecules collide if their trajectories are such that the distance between their centres decreases to d . The *total collision cross-section* for these molecules is therefore

$$\sigma_T = \pi d^2. \quad (1.8)$$

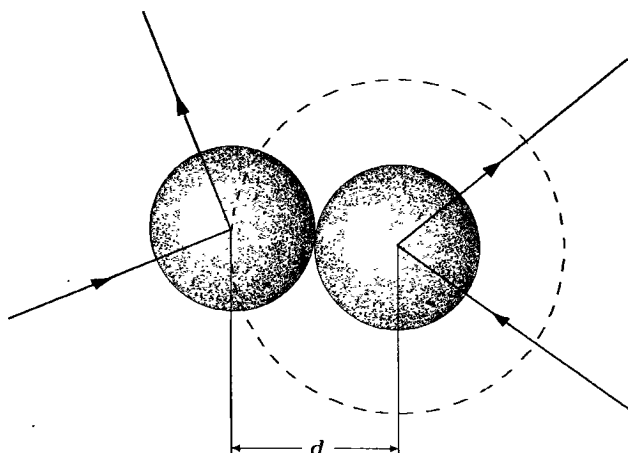


Fig. 1.2 Collision between two hard spheres of diameter d .

The word 'molecule' is used as a generic term and includes both monatomic molecules consisting of a single atom, diatomic molecules containing two atoms, and polyatomic molecules that contain more than two atoms. Each atom of a real molecule consists of a nucleus surrounded by orbiting electrons. Molecular size is a quantity that cannot be precisely and uniquely defined and it will be necessary to qualify the results from elementary kinetic theory that depend on the molecular 'diameter'.

Classical studies of the effects of intermolecular collisions are based on the force fields of the molecules. These fields are assumed to be spherically symmetric and the general form of the force between two neutral molecules is shown in Fig. 1.3 as a function of the distance between the nuclei. The force is effectively zero at large distances; it becomes weakly attractive when the molecules are sufficiently close for the interaction to commence, but then decreases again to become very strongly repulsive at short distances. The intermolecular forces in a diatomic or polyatomic gas are a function of the orientation of the molecules. However, in view of the random orientation in the extremely large number of collisions that occur in almost all cases, it is reasonable to assume spherically symmetric fields for these gases. Collision dynamics will be dealt with in detail in §2.2 where procedures for the calculation of collision cross-sections and molecular diameters will be discussed. The collision cross-section of realistic models is a function of the relative speed between the molecules and experience has shown that it is important to reproduce this behaviour. The form of the force field and the consequent distribution of scattering angles in the collisions is comparatively unimportant.

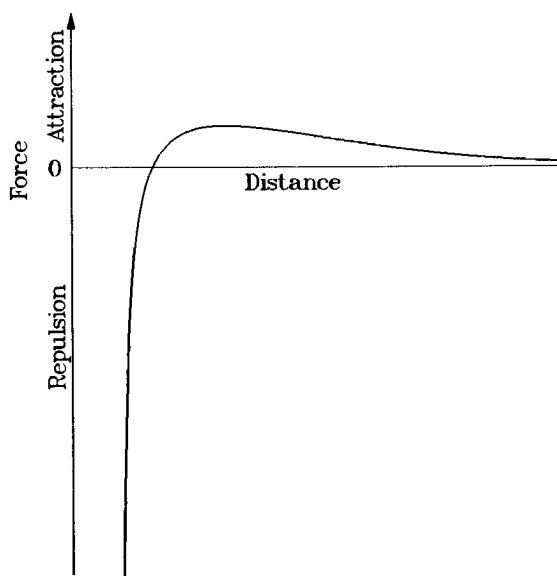


FIG. 1.3 Typical intermolecular force field.

The proportion of the space occupied by a gas that actually contains a molecule is of the order of $(d/\delta)^3$. Eqn (1.7) shows that, for sufficiently low densities, the molecular spacing δ is large compared with the effective molecular diameter d . Under these circumstances, only an extremely small proportion of space is occupied by molecules and each molecule will, for the most part, be moving outside the range of influence of other molecules. Moreover, when it does suffer a collision, it is overwhelmingly likely to be a *binary collision* involving only one other molecule. This situation may be characterized by the condition

$$\delta \gg d, \quad (1.9)$$

and defines a *dilute gas*. The time-scale of the macroscopic processes is set by the *mean collision time* which is, by definition, the mean time between the successive collisions suffered by any particular molecule. The reciprocal of this quantity is in more common use and is called the *mean collision rate* or *collision frequency* v per molecule. In the derivation of an expression for this quantity we will fix our attention on a particular molecule which will be referred to as the *test molecule*. The velocities of the other, or *field*, molecules are distributed in some unspecified manner. Consider those field molecules with velocity between c and $c + \Delta c$. These will be referred to as molecules of class c and their number density is denoted by Δn . If the velocity of the test molecule is c_t , the relative velocity between the test molecule and the field molecules of class c is $c_r = c_t - c$. Now choose a frame of reference in which the test molecule moves with velocity c_r while the field molecules of class c are stationary. Then, over a time interval Δt much shorter than the mean collision time, the test molecule would collide with any field molecule which has its centre within the cylinder of volume $\sigma_T c_r \Delta t$, as shown in Fig. 1.4.

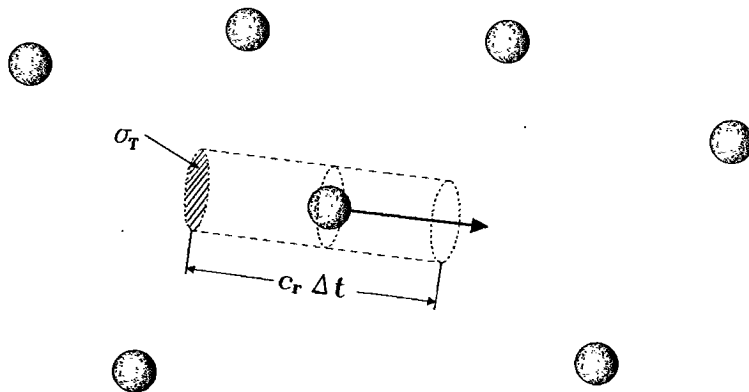


Fig. 1.4 Effective volume swept out by moving test molecule among stationary field molecules.

THE MOLECULAR MODEL

The probability of a collision between the test molecule and a molecule of class c in the time interval Δt is therefore $\Delta n \sigma_T c_r \Delta t$. When collisions do occur, the cylinder swept out by the collision cross-section along the trajectory becomes distorted. However, for a dilute gas in which only a very small proportion of the trajectory is affected by collisions, the restriction on Δt can be removed and the number of collisions per unit time with a class c molecule is $\Delta n \sigma_T c_r$. The mean collision rate is obtained by summing over all velocity classes and therefore over all values of c_r . That is,

$$v = \sum (\Delta n \sigma_T c_r) = n \sum [(\Delta n/n) \sigma_T c_r]$$

and, since $\Delta n/n$ is the fraction of molecules with cross-section σ_T and relative velocity c_r ,

$$v = n \overline{\sigma_T c_r}. \quad (1.10)$$

A bar over a quantity or expression denotes the average value over all molecules in the sample. For hard sphere molecules, this becomes

$$v = \sigma_T n \overline{c_r} = \pi d^2 n \overline{c_r}. \quad (1.10a)$$

The total number of collisions per unit time per unit volume of gas is therefore given by

$$N_c = \frac{1}{2} n v = \frac{1}{2} n^2 \overline{\sigma_T c_r}. \quad (1.11)$$

The symmetry factor of one half is introduced because each collision involves two molecules.

The *mean free path* is the average distance travelled by a molecule between collisions. It is defined in a frame of reference moving with the stream speed of the gas and is therefore equal to the mean thermal speed \overline{c} of the molecule divided by the collision frequency, i.e.

$$\lambda = c' / v = [n (\overline{\sigma_T c_r} / \overline{c'})]^{-1} \quad (1.12)$$

or, for the constant cross-section hard sphere case,

$$\lambda = [(\overline{c_r} / \overline{c'}) \pi d^2 n]^{-1}. \quad (1.12a)$$

Before moving on to discuss the formal relationships between the microscopic and macroscopic properties, we must elaborate on the concept of *equilibrium* as applied to gases. Consider a volume of gas that is completely isolated from any outside influence. If this gas remains undisturbed for a time that is sufficiently long in comparison with the mean collision time, it may be regarded as being in an equilibrium state. Then, if the number of molecules in the volume is sufficiently large that statistical fluctuations may be neglected, there are no gradients in the macroscopic properties with either distance or time. Also, the fraction of molecules in any velocity class remains constant with time, even though the velocity of an individual

molecule changes with each of its collisions. It is obvious that there can be no preferred direction in an equilibrium gas and the velocity distribution of the molecules must be isotropic. The form of the velocity distribution in an equilibrium gas will be derived in Chapter 3 and its properties will be discussed in Chapter 4. If the macroscopic gradients in a gas flow are sufficiently small and the collision rate is sufficiently high, the velocity distribution of each element of the gas adjusts to the equilibrium state appropriate to the local macroscopic properties as it moves through the gas. At the microscopic level, the flow can then be regarded as being in *local thermodynamic equilibrium* and, at the macroscopic or continuum level, this is equivalent to *isentropic* flow. As noted earlier, the continuum approach is valid only for flows in which the departure from equilibrium is small, but the definitions of the macroscopic flow properties that are presented in the following sections remain valid for any degree of non-equilibrium.

1.4 Macroscopic properties in a simple gas

The first of the macroscopic properties to be discussed is the *density* ρ . This is defined as the mass per unit volume of the gas, and is therefore equal to the product of the number of molecules per unit volume and the mass of an individual molecule, i.e.

$$\rho = n m . \quad (1.13)$$

In the continuum model, macroscopic quantities such as the density are associated with a 'point' in a flow. Values at a 'point' must, in fact, be based on the molecules within a small volume element that encloses the point. An element of volume V contains a number N of molecules and this number is subject to statistical fluctuations about the mean value nV . The probability $P(N)$ of a particular value of N is given by the Poisson distribution

$$P(N) = (nV)^N \exp(-nV)/N!. \quad (1.14)$$

For large values of nV , this distribution becomes indistinguishable from a normal or Gaussian distribution

$$P(N) \approx (2\pi nV)^{-1/2} \exp[-(N-nV)^2/(2nV)]. \quad (1.15)$$

The integration of this distribution shows that the probability of an individual sample falling within $A\sqrt{nV}$ from the average nV is $\text{erf}(A/\sqrt{2})$. The standard deviation of the fluctuations is therefore $1/\sqrt{nV}$. The expected magnitude of the fluctuations is shown in Fig. 1.5. Eqn (1.7) enables nV to be written V/δ^3 , where δ is the mean molecular spacing. Therefore, for a meaningful result, the establishment of a macroscopic quantity by averaging over the molecules in a small element of volume requires that the typical dimension $V^{1/3}$ of the element should satisfy the condition.

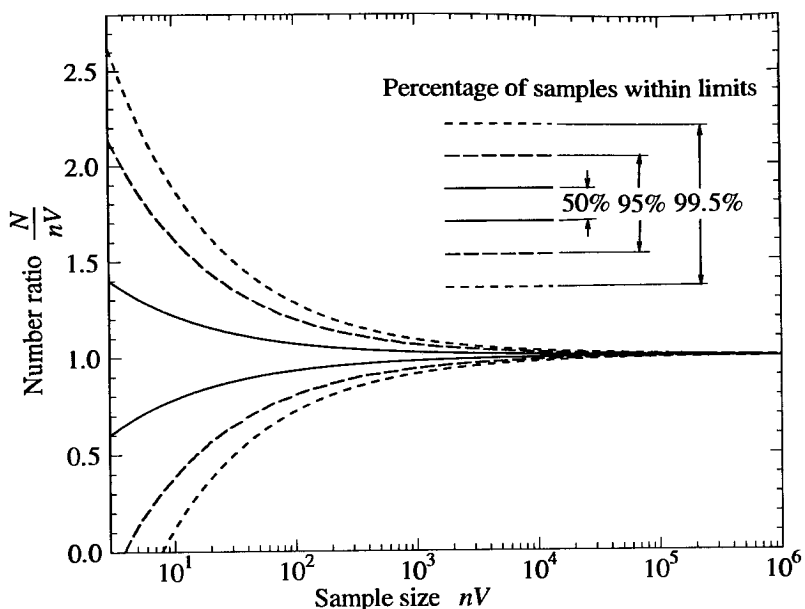


Fig. 1.5 Statistical fluctuations as a function of the sample size.

$$V^{1/3} \gg \delta . \quad (1.16)$$

Unless the dimensions of the volume element are small compared with the scale length L of the macroscopic gradients, the macroscopic properties based on the molecules in the element will depend on the size of the element. For a three-dimensional flow with gradients in all directions, this leads to the requirement that $V^{1/3}$ should be much smaller than L . However, for one-dimensional and two-dimensional flows, the volume element may be indefinitely elongated in the direction or directions with zero gradients. It is always possible in such flows to define an element with a dimension in the direction of a gradient small compared with the scale length L and the volume sufficiently large to define a meaningful average, even though $V^{1/3}$ may be larger than L .

The above discussion deals only with *instantaneous averages* in a single flow or system. Two additional types of average must be taken into account before conclusions can be made about the conditions that allow meaningful macroscopic quantities to be defined for a flow. The first is established by summing the appropriate properties of the molecules in the volume element over an extended time interval. This is called the *time average* and enables any steady flow to be described in terms of the macroscopic properties. The second average is an instantaneous average taken over the molecules in corresponding volume elements in an

indefinitely large number of similar systems. This *ensemble average* can be established whenever an experiment or calculation can be repeated indefinitely. Time or ensemble averages enable macroscopic properties to be established for almost any flow, although the description is essentially probabilistic and fluctuations may have to be taken into account. When both time and ensemble averages can be used to describe a flow, the two descriptions can be expected to be identical. The molecular motion is then said to be *ergodic*.

The remaining macroscopic properties of interest are related to the transport of mass, momentum, and energy in the flow as a result of the molecular motion. Before proceeding with the discussion of these quantities, we must establish an important general result for the flux of some quantity Q across a small element of area at some location in the gas. This relates the flux to averages taken over the molecules in a volume element at the same location. The element of area has the magnitude ΔS and unit normal vector e , as shown in Fig. 1.6. Consider the molecules of class c which have a velocity between c and $c + \Delta c$ and let their number density again be Δn . The molecules of this class that cross ΔS in a short time interval Δt are contained, at the beginning of Δt , within the cylinder projected from ΔS in the direction opposite to e with length $c \Delta t$. The height of this cylinder when measured in the direction of e , normal to ΔS , is $c.e \Delta t$, and its volume is $c.e \Delta t \Delta S$. The quantity Q is associated with each molecule and is either a constant or a function of c . The flux of Q across the element per unit area per unit time in the direction of e is, therefore, $\Delta n Q c.e$. The total flux is obtained by summing over all velocity classes and can be written

$$n \sum [(\Delta n / n) Q c.e]$$

or

$$n \overline{Q c.e}. \quad (1.17)$$

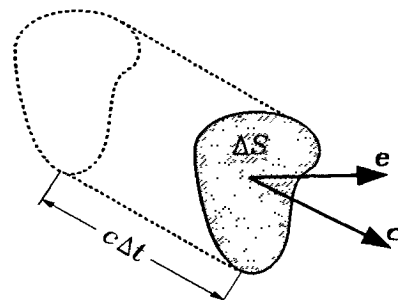


Fig. 1.6 Flux of molecules of class c across an element of area ΔS .

Note that the expression (1.17) is for the total flux and includes the contributions from molecules crossing the element of area in both the positive and negative e directions. We will sometimes require the flux in one direction only and, without loss of generality, this may be taken in the positive e direction. The required flux is then obtained by considering only those molecules with a positive value of $c \cdot e$. The flux in the positive e direction is, therefore,

$$n(\overline{Qc \cdot e})_{c \cdot e > 0}. \quad (1.18)$$

It has been assumed in the derivation of expressions (1.17) and (1.18) that the quantity Q is transferred across the element of area ΔS only when the molecule with which it is associated crosses the element. This is exact for the number flux and mass flux, but is not generally true when the momentum flux or energy flux is being considered. This is because the finite range of the intermolecular force field permits an interchange of momentum and energy between molecules that remain on opposite sides of the element. However, if the gas is dilute with $\delta \gg d$, these effects may be neglected.

The necessity for averages to be based on a sufficiently large sample, unless one resorts to time or ensemble averages, appears to impose a further restriction on expressions (1.17) and (1.18). The dimensions of the volume element in Fig. 1.6 should be large in comparison with the mean molecular spacing; i.e. $\bar{c} \Delta t$ should be much larger than δ . Also, the derivation of these expressions was based on the assumption that Δn is a constant. This is the case in an equilibrium gas but, in a non-equilibrium situation, the number of molecules scattered out of the class c by collisions may not equal the number scattered into the class. The analysis is therefore valid in a non-equilibrium gas only if Δt is much less than the mean collision time $1/\nu$. The gas must therefore be such that $\bar{c} \Delta t \gg \delta$.

Eqns (1.7) and (1.12) show that

$$\frac{\lambda}{\delta} = \frac{1}{\pi(\bar{c}_r \bar{c}')}\left(\frac{\delta}{d}\right)^2. \quad (1.19)$$

The ratio \bar{c}_r / \bar{c}' is of order unity and, consequently, $\lambda \gg \delta$ whenever the dilute gas condition ($\delta \gg d$) is satisfied. The ordering $\lambda \gg \delta \gg d$ is sometimes used as the definition of a dilute gas, but eqn (1.19) shows that eqn (1.9) is a sufficient condition.

Since e is a unit vector, the expression (1.17) can be written $(n \overline{Qc}) \cdot e$ and therefore defines the *flux vector* for the quantity Q as

$$n \overline{Qc}. \quad (1.20)$$

The flux vector related to the transport of mass is obtained by setting Q equal to the molecular mass, to give,

$$nm\bar{c} \quad \text{or} \quad \rho\bar{c}.$$

The mean molecular velocity \bar{c} defines the macroscopic *stream* or *mean* or *mass velocity* which is denoted by c_0 , i.e.

$$c_0 = \bar{c}. \quad (1.21)$$

The velocity of a molecule relative to the stream velocity is called the *thermal* or *peculiar* or *random velocity* and is denoted by c' , i.e.

$$c' = c - c_0. \quad (1.22)$$

Note that

$$\bar{c}' = \bar{c} - \bar{c} = 0,$$

so the mean thermal velocity is zero in a simple gas. The remaining macroscopic properties are defined by averages taken over the thermal velocities of the molecules. Therefore, in order to simplify the discussion of these quantities, we will now look at the element of gas from a frame of reference moving with the local stream velocity.

The flux vector for the thermal velocities is $n Q \bar{c}'$ and an expression for the momentum transport by the peculiar or thermal motion is obtained by setting Q equal to mc' . Since momentum is also a vector quantity, the resulting expression is a tensor with nine Cartesian components, called the *pressure tensor* p , i.e.

$$p = n m \bar{c}' \bar{c}' = \rho \bar{c}' \bar{c}' \quad (1.23)$$

and is best explained in terms of the separate components. Let u' , v' , and w' be the components of c' in the x -, y -, and z -directions and, as an example, consider the x -momentum flux in the y -direction. That is, set $Q = mu'$ and choose the element of area in the xz -plane so that its normal is in the y -direction. This component is

$$p_{xy} = \rho \overline{u' v'}$$

and the complete set is:

$$\begin{aligned} p_{xx} &= \rho \overline{u'^2}, & p_{xy} &= \rho \overline{u' v'}, & p_{xz} &= \rho \overline{u' w'}; \\ p_{yx} &= p_{xy}, & p_{yy} &= \rho \overline{v'^2}, & p_{yz} &= \rho \overline{v' w'}; \\ p_{zx} &= p_{xz}, & p_{zy} &= p_{yz}, \text{ and } & p_{zz} &= \rho \overline{w'^2}. \end{aligned} \quad (1.24)$$

A shorthand way of writing the nine equations (1.24) for the components of p is

$$p_{ij} = \rho \overline{c'_i c'_j}, \quad (1.24a)$$

where the subscripts i and j each range from 1 to 3. The values 1, 2, and 3 may be identified with the components along the x -, y -, and z -axes, respectively. That is,

$$c_1' \equiv u', \quad c_2' \equiv v', \quad c_3' \equiv w'.$$

The scalar *pressure* p is usually defined as the average of the three normal components of the pressure tensor; i.e.

$$p = \frac{1}{3} \rho \left(\overline{u'^2} + \overline{v'^2} + \overline{w'^2} \right) = \frac{1}{3} \rho \overline{c'^2}. \quad (1.25)$$

If the gas is in equilibrium, the three normal components are equal and the pressure is given by the product of the density and the mean value of the square of the thermal velocity components in any direction. Consider the case in which the gas is bounded by a solid surface and choose the reference direction normal to the surface. If the gas is also in equilibrium with the surface, the molecules reflected from the surface will be indistinguishable from the molecules that would come from an imaginary continuation of the gas on the other side of the surface. The scalar pressure p may then be identified with the normal force per unit area exerted by the gas on the surface. The latter quantity is usually of greater practical importance and, when there is an ambiguity, the term 'pressure' is applied to the normal force per unit area.

The *viscous stress tensor* τ is defined as the negative of the pressure tensor with the scalar pressure subtracted from the normal components. It is most conveniently represented in the component or subscript notation as

$$\tau = \tau_{ij} = -\left(\rho \overline{c'_i c'_j} - \delta_{ij} p\right), \quad (1.26)$$

where δ_{ij} is the Kronecker delta such that

$$\delta_{ij} = 1 \text{ if } i=j, \text{ and } \delta_{ij} = 0 \text{ if } i \neq j.$$

The average kinetic energy associated with the thermal or translational motion of a molecule is $\frac{1}{2} m \overline{c'^2}$, and the specific energy associated with this motion is

$$e_{tr} = \frac{1}{2} \overline{c'^2}. \quad (1.27)$$

This may be combined with eqn (1.25) to give

$$p = \frac{2}{3} \rho e_{tr},$$

which may be compared with the ideal gas equation of state

$$p = \rho R T = n k T. \quad (1.28)$$

Here k is the Boltzmann constant which is related to the universal gas constant R by $k = R/N$. Also $m = M/N$ and the ordinary gas constant $R = R/M$, so that $k = mR$. The *thermodynamic temperature* T is essentially an equilibrium gas property, but the above comparison shows that the ideal gas equation of state will apply to a dilute gas, even in a non-equilibrium situation, for a *translational kinetic temperature* T_{tr} defined by

$$\frac{3}{2} R T_{tr} = e_{tr} = \frac{1}{2} \overline{c'^2} \quad (1.29)$$

or

$$\frac{3}{2} k T_{tr} = \frac{1}{2} m \overline{c'^2} = \frac{1}{2} m \left(\overline{u'^2} + \overline{v'^2} + \overline{w'^2} \right).$$

If the temperature is calculated from the velocities of a set of molecules, it is preferable to have an expression in terms of averages over these velocities rather than over the thermal velocities. From eqn (1.22), $\overline{c'^2} = \overline{c^2} - 2\overline{cc'} + c_0^2$ and eqn (1.21) then enables eqn (1.29) to be written

$$\frac{3}{2}kT_{tr} = \frac{1}{2}m(\overline{c^2} - c_0^2) = \frac{1}{2}m(\overline{u^2} + \overline{v^2} + \overline{w^2} - u_0^2 - v_0^2 - w_0^2). \quad (1.29a)$$

The use of thermal velocities can also be avoided in the definition of the pressure tensor. For example,

$$p_{xy} = \rho(\overline{uv} - u_0v_0).$$

Note also that separate translational kinetic temperatures may be defined for each component. For example,

$$kT_{tr_x} = m\overline{u'^2} = p_{xx}/n \quad (1.30)$$

and the departure of these component temperatures from T_{tr} provides a measure of the degree of translational non-equilibrium in a gas.

Monatomic molecules may generally be assumed to possess translational energy only. Therefore, in a monatomic gas, the translational temperature may be regarded simply as the *temperature*. However, diatomic and polyatomic molecules also possess internal energy associated with the rotational and vibrational energy modes. Since three degrees of freedom are associated with the translational mode, a temperature T_{int} for the internal modes may be defined consistently with the translational temperature (see eqn (1.29)) by

$$\frac{1}{2}\zeta RT_{int} = e_{int}. \quad (1.31)$$

Here, ζ is the number of internal degrees of freedom and e_{int} is the specific energy associated with the internal modes. The principle of equipartition of energy means that the translational and internal temperatures must be equal in an equilibrium gas; the common value may then be identified with the thermodynamic temperature of the gas. An *overall kinetic temperature* T_{ov} may be defined for a non-equilibrium gas as the weighted mean of the translational and internal temperatures; i.e.

$$T_{ov} = (3T_{tr} + \zeta T_{int})/(3 + \zeta). \quad (1.32)$$

Note that the ideal gas equation of state does not apply to this temperature in a non-equilibrium situation.

Finally, the *heat flux vector* \mathbf{q} is obtained by setting Q equal to the molecular energy $\frac{1}{2}mc'^2 + \epsilon_{int}$, i.e.

$$\mathbf{q} = \frac{1}{2}\rho\overline{c'^2}\mathbf{c}' + n\overline{\epsilon_{int}}\mathbf{c}'. \quad (1.33)$$

ϵ_{int} is the internal energy of a single molecule and is related to e_{int} by

$$e_{int} = \overline{\epsilon_{int}}/m.$$

The component of heat flux in the x -direction can be written

$$q_x = \frac{1}{2} \rho \overline{c'^2 u'} + n \overline{\epsilon_{\text{int}} u'}. \quad (1.33a)$$

The use of thermal velocity components can again be avoided, to give

$$q_x = \frac{1}{2} \rho \left(\overline{c^2 u} - 2p_{xx}u_0 - 2p_{xy}v_0 - 2p_{xz}w_0 - \overline{c^2}u_0 \right) + n (\overline{\epsilon u} - \overline{\epsilon}u_0). \quad (1.33b)$$

1.5 Extension to gas mixtures

Consider a gas mixture consisting of a total of s separate chemical species. Values pertaining to a particular species will be denoted by the subscripts p or q each of which can range from 1 to s . The overall number density n is obviously equal to the sum of the number densities of all the individual species; i.e.

$$n = \sum_{p=1}^s n_p. \quad (1.34)$$

Consider a collision between a molecule of species p and one of species q . The effective diameters are d_p and d_q , and the requirement for a collision is that the distance between their centres decreases to $(d_p + d_q)/2$. The total collision cross-section is therefore

$$\sigma_{Tpq} = \pi (d_p + d_q)^2 / 4 = \pi d_{pq}^2, \quad (1.35)$$

where

$$d_{pq} = (d_p + d_q)/2.$$

A molecule of species p may be taken as a test molecule and the molecules of species q as the field molecules in the analysis leading to eqn (1.10). The mean collision rate for a species p molecule with a species q molecule is, therefore,

$$v_{pq} = n_q \overline{\sigma_{Tpq} c_{r_{pq}}}, \quad (1.36)$$

where $c_{r_{pq}}$ is the relative speed between the two molecules. If σ_{Tpq} is regarded as a constant, this becomes

$$v_{pq} = \pi d_{pq}^2 n_q \overline{c_{r_{pq}}}. \quad (1.36a)$$

The mean collision rate for species p molecules is obtained by summing over collision partners of all species; i.e.

$$v_p = \sum_{q=1}^s \left(n_q \overline{\sigma_{Tpq} c_{r_{pq}}} \right). \quad (1.37)$$

A mean collision rate per molecule for the mixture may be defined by averaging over test particles of all species to give

$$v = \sum_{p=1}^s \left\{ (n_p/n) v_p \right\}. \quad (1.38)$$

The number of collisions per unit time per unit volume between species p molecules and species q molecules is

$$n_p v_{pq}$$

or

$$n_p n_q \overline{\sigma_{T_{pq}} c_{rpq}}. \quad (1.39)$$

Note that, when $p = q$, this expression counts each collision twice over. Eqn (1.39) may be summed over all species q molecules to give the total number of collisions per unit volume per unit time that involve species p molecules as $n_p v_p$. This, in turn may be summed over all type p molecules to determine the total number of collisions N_c per unit time per unit volume. Since all collisions are then counted twice over, the symmetry factor of one half is introduced to give

$$N_c = \frac{1}{2} \sum_{p=1}^s (n_p v_p) = \frac{1}{2} n v$$

as would be expected from eqn (1.11).

The mean free path for a species p molecule is equal to its mean thermal speed divided by its collision frequency, i.e.

$$\lambda_p = \left(\sum_{q=1}^s (n_q \overline{\sigma_{T_{pq}} c_{rpq}} / c_p') \right)^{-1} \quad (1.40)$$

and the mean free path for the mixture is

$$\lambda = \bar{\lambda} = \sum_{p=1}^s \left\{ (n_p / n) \lambda_p \right\}. \quad (1.41)$$

The macroscopic density is equal to the sum of the individual species densities and can be written

$$\rho = \sum_{p=1}^s (m_p n_p) = n \bar{m}. \quad (1.42)$$

The stream velocity \mathbf{c}_0 has been defined for the simple gas such that $\rho \mathbf{c}_0$ is equal to the flux vector for the molecular mass. A similar procedure for the gas mixture yields

$$\mathbf{c}_0 = \frac{1}{\rho} \sum_{p=1}^s (m_p n_p \bar{\mathbf{c}}_p) = \bar{m} \mathbf{c} / \bar{m}. \quad (1.43)$$

For the mixture, \mathbf{c}_0 is called the *mass average velocity*. This is not the mean velocity, but a weighted mean with the weight of each molecule being proportional to its mass. The momentum of a gas is as if all the molecules move with \mathbf{c}_0 and it is this velocity that appears in the conservation equations.

The peculiar or thermal velocity \mathbf{c}' of each molecule is again measured relative to \mathbf{c}_0 , i.e.

$$\mathbf{c}' = \mathbf{c} - \mathbf{c}_0,$$

and the mean thermal velocity of species p is

$$\overline{\mathbf{c}'_p} = \overline{\mathbf{c}_p} - \mathbf{c}_0. \quad (1.44)$$

Therefore, the mean thermal velocity of a particular species is equal to its mean velocity relative to the mass average velocity. This quantity is called the *diffusion velocity* and is denoted by \mathbf{C}_p . Therefore,

$$\mathbf{C}_p \equiv \overline{\mathbf{c}'_p} = \overline{\mathbf{c}_p} - \mathbf{c}_0. \quad (1.45)$$

The definitions of the pressure tensor, the scalar pressure, the viscous stress tensor, the translational kinetic temperature, and the heat flux vector are rendered valid for the gas mixture simply by including the molecular mass within the averaging process. For example, the scalar pressure is

$$p = -\sum_{p=1}^s \frac{1}{3} m_p n_p \overline{c'^2_p} = -n \sum_{p=1}^s \frac{1}{3} (n_p/n) m_p \overline{c'^2_p},$$

or

$$p = \frac{1}{3} n m \overline{c'^2}. \quad (1.46)$$

The translational kinetic temperature is now defined by

$$\frac{3}{2} k T_{\text{tr}} = \frac{1}{2} \overline{m c'^2} \quad (1.47)$$

and, in an equilibrium monatomic gas, T_{tr} can again be regarded simply as the temperature with the mixture obeying the ideal gas equation of state.

In a non-equilibrium situation, it is convenient to define separate 'species temperatures' to serve as a quantitative measure of the degree of non-equilibrium between the species. Eqn (1.47) can be written

$$\frac{3}{2} k T_{\text{tr}} = \frac{1}{2} \sum_{p=1}^s \left\{ (n_p/n) m_p \overline{c'^2_p} \right\},$$

and the obvious definition of a species translational temperature is

$$\frac{3}{2} k T_{\text{tr}p} = \frac{1}{2} m_p \overline{c'^2_p}. \quad (1.48)$$

However, the thermal velocity \mathbf{c}'_p is measured relative to the mass average velocity \mathbf{c}_0 which involves all species. It is therefore desirable to relate the kinetic temperature defined by eqn (1.48) to one defined in a similar manner, but based on the *single species thermal velocity* \mathbf{c}''_p measured relative to the average velocity $\overline{\mathbf{c}_p}$ of the species, i.e.

$$\mathbf{c}''_p = \mathbf{c}_p - \overline{\mathbf{c}_p}. \quad (1.49)$$

This definition, together with eqn (1.45), enables eqn (1.48) to be written

$$\frac{3}{2} k T_{\text{tr}p} = \frac{1}{2} m_p \overline{c''_p} + \frac{1}{2} m_p C_p^2. \quad (1.50)$$

The kinetic temperature of species p , as defined by eqn (1.48), is therefore a measure of the sum of the 'single species thermal energy' and the 'kinetic energy of diffusion' of this species.

As in the simple gas case, rotational and vibrational kinetic temperatures may be defined for a gas containing diatomic or polyatomic molecules. Eqn (1.31) applies to the mixture as long as ζ is interpreted as the mean number of internal degrees of freedom. The single species translational temperature defined by eqn (1.48) may again be resolved into separate temperatures based on $\overline{u_p'^2}$, $\overline{v_p'^2}$, and $\overline{w_p'^2}$, but these must be assessed in conjunction with the component version of eqn (1.50) in order to determine the degree of translational non-equilibrium within each species. All the kinetic temperatures become equal and equivalent to the thermodynamic temperature when the gas is in equilibrium.

It is again possible to write the definitions of the second-order and third-order moments in terms of averages over the molecular velocities rather than the thermal velocities. The result for the temperature is

$$\frac{3}{2} k T_{\text{tr}} / 2 = \frac{1}{2} \left(\overline{mc^2} - \bar{m} c_0^2 \right). \quad (1.51)$$

Similar results apply for all the components of the stress tensor, for example,

$$\tau_{xy} = -n(\overline{muu} - \bar{m} u_0 v_0), \quad (1.52)$$

and the component of the heat flux vector in the x -direction is

$$q_x = n \left(\frac{1}{2} \overline{mc^2 u} - p_{xx} u_0 - p_{xy} v_0 - p_{xz} w_0 - \frac{1}{2} \overline{mc^2 u_0} + \overline{\epsilon u} - \bar{\epsilon} u_0 \right). \quad (1.53)$$

1.6 Molecular magnitudes

The accepted value of Avogadro's number for the number of molecules in one kmole[†] is 6.022137×10^{26} . The *standard number density* n_0 at a pressure of 1 atm (101,325 Pa) and a temperature of 0°C follows from eqn (1.28) as

$$n_0 = p/kT = 2.68666 \times 10^{25} \text{ m}^{-3}. \quad (1.54)$$

The standard number density can be regarded as a physical constant and the number 2.68684×10^{19} of molecules in a cubic centimetre is called *Loschmidt's number*. The volume of one kmole of an ideal gas under standard conditions is N/n_0 or 22.414 m^3 .

The discussion of the values of the other microscopic quantities will be based on air. For the purpose of this discussion, air will be assumed to be a simple gas of identical 'average air' molecules. The molecular weight of sea-level air is 28.96 kg kmole⁻¹ and eqn (1.6) then gives 4.81×10^{-26} kg as the mass of a single molecule.

[†] The SI system of units is inconsistent in that the 'SI mole' is a 'gram mole' and a numerical factor must be applied to expressions that contain it when the basic units are employed throughout. This book therefore employs the 'kilogram mole' which is abbreviated to 'kmole'.

A difficulty arises in the definition of the molecular diameter and mean free path in that the intermolecular force at moderate to high separation distances declines as some inverse power of this distance. An arbitrary collisional cut-off in either distance or deflection angle is necessary for realistic molecular models, and it is not then possible to unambiguously define the diameter and mean free path. The conventional solution to this problem is to deduce a molecular diameter from a comparison of the Chapman-Enskog result for the viscosity coefficient in a hard sphere gas with the measured coefficient of viscosity in the real gas. However, the hard sphere gas has a fixed cross-section and it will be shown in subsequent chapters that the accurate simulation of real gas flows requires a molecular model with a cross-section that varies with the relative velocity between the molecules. The cross-section change at the molecular level is related to the variation of the coefficient of viscosity with temperature at the continuum level. None of the molecular models of classical kinetic theory has both a bounded cross-section and the capability to reproduce the viscosity-temperature variation of a real gas. This difficulty has been overcome through the introduction (Bird, 1981) of the variable hard sphere or VHS model. This model incorporates the hard sphere scattering law for collisions, but its cross-section is a function of the relative translational energy in the collision. It will be shown in Chapter 4 that a viscosity coefficient proportional to temperature to the power ω is obtained if the average cross-section is proportional to temperature to the power $-(\omega - \frac{1}{2})$.

An average VHS molecular diameter may be obtained from a comparison of the measured coefficient of viscosity with the theoretical result (Bird 1981). For air, this gives $\bar{d} = 4.15 \times 10^{-10}$ m for the average diameter at 273 K and this is inversely proportional to the one-eighth power of temperature. The mean molecular spacing under standard conditions is obtained from n_0 through eqn (1.7) as $\delta_0 = 3.3 \times 10^{-9}$ m. Air under standard conditions therefore barely satisfies the dilute gas condition that $\delta \gg d$. The third distance of interest is the mean free path defined by eqn (1.12). It will be found that the mean free path in an equilibrium VHS gas is

$$\lambda = 1/(\sqrt{2} \pi \bar{d}^2 n). \quad (1.55)$$

The viscosity coefficient is very nearly proportional to temperature raised to the power $\frac{3}{4}$. The mean free path in equilibrium air under standard conditions is therefore 4.9×10^{-8} m and this is inversely proportional to number density and proportional to the $\frac{1}{4}$ power of the temperature. The mean free path is independent of temperature for the special case of a hard sphere gas which corresponds to $\omega = \frac{1}{2}$ and has a constant diameter.

The mean square molecular speed is given by eqns (1.28) and (1.29) as

$$\overline{c^2} = 3p/\rho = 3RT = 3kT/m. \quad (1.56)$$

The root mean square molecular speed $c'_s = (\overline{c^2})^{1/2}$ therefore differs from the speed of sound in the gas (which is given by $a^2 = \gamma RT$) only by a constant of order unity. Using the previously quoted value for the average mass of an air molecule, we obtain 485 m s^{-1} for the root mean square speed of the molecules in air at 0°C . For an equilibrium gas, we will find that the mean thermal speed \overline{c} is $(8/[3\pi])^{1/2}$ times c'_s , and the mean magnitude of the relative velocity of colliding molecules is $\sqrt{2}$ times the mean thermal speed. The mean collision rate of a molecule in equilibrium air under standard conditions is then given by eqn (1.10) as $7.3 \times 10^9 \text{ s}^{-1}$, and the total collision rate per unit volume follows from eqn (1.11) as $9.8 \times 10^{34} \text{ m}^{-3}\text{s}^{-1}$.

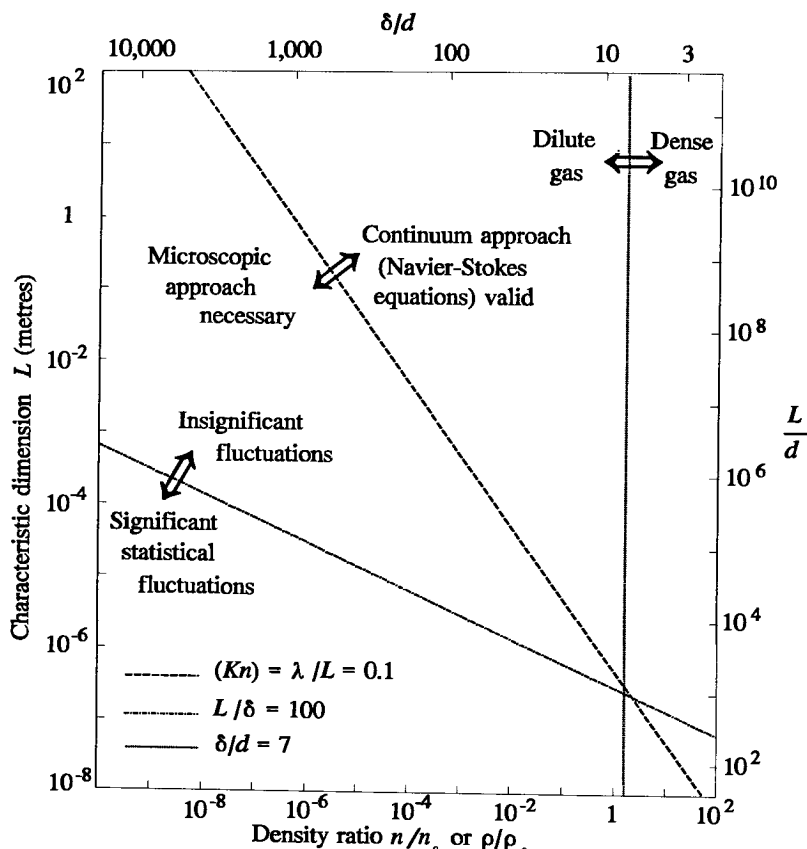


Fig. 1.7 Effective limits of major approximations.

We are now in a position to define the limits of validity of the dilute gas approximation, the continuum approach, and the neglect of statistical fluctuations. For the purposes of this study, the molecular diameter will be fixed at 4×10^{-10} m. The limits are conveniently expressed as functions of the gas density ρ and the characteristic dimension of the flow L . The density may be normalized by the density ρ_0 under standard conditions, but L is best retained as a dimensioned quantity. In the context of a double logarithmic plot of L versus ρ/ρ_0 , the three limits may be defined by straight lines, as shown in Fig. 1.7.

The dilute gas assumption requires that $\delta/d \gg 1$, and $\delta/d = 7$ has been chosen as the limit. Since both δ and d are independent of L , the line is vertical and a scale for δ/d has been set along the upper edge of Fig. 1.7.

The validity of the continuum approach has been identified with the validity of the Navier-Stokes equations. This requires that the Knudsen number ($Kn = \lambda/L$) should be small compared with unity, and ($Kn = 0.1$) has been chosen as the limit. This is a reasonable choice as long as L is chosen such that the Knudsen number is the local Knudsen number, as discussed in §1.2.

The macroscopic flow properties are subject to statistical fluctuations, as discussed in §1.4. The criterion for the onset of significant fluctuations has been chosen as $L/\delta = 100$. This corresponds to a value of L that is ten times as large as the side of a cubic element that contains 1,000 molecules. Figure 1.5 shows that the density in such an element would be subject to statistical fluctuations with a standard deviation of approximately three per cent.

A feature of Fig. 1.7 is that the lines describing the three limits very nearly intersect at a single point. This result would not be substantially altered by any reasonable changes in the typical dimensions and the criteria that define the limits. One consequence is that the continuum breakdown limit always lies between the dilute gas limit and the limit for significant fluctuations. Therefore as the density and/or the characteristic dimension are reduced in a dilute gas, the Navier-Stokes equations lose their validity before the level of statistical fluctuations becomes significant. The more rarefied the gas, the wider the margin between these limits. On the other hand, a significant level of fluctuation may be present in a dense gas even when the Navier-Stokes equations are valid. For example, the theory of Brownian motion is partially based on these equations although the phenomenon is, itself, a manifestation of significant statistical fluctuations.

The fact that fluctuations are more significant in dense gases indicates that, although the molecules become more closely packed as the density increases, the number of molecules that are involved in typical flows actually decreases as the density increases. There are several other functions of the density ratio that clarify this point.

Again using the hard sphere diameter of 4×10^{-10} m, the fraction of space that is occupied by molecules is

$$\pi d^3 n / 6 = 0.0009(n/n_0). \quad (1.57)$$

However, as the density changes, the flow gradients tend to scale with the mean free path and the number of molecules within one cubic mean free path is

$$n \lambda^3 = 3856(n/n_0)^{-2}. \quad (1.58)$$

This means that, for a given flow, the total number of molecules within the flowfield increases as the density decreases. The results from eqns (1.57) and (1.58), together with the ratio of molecular diameter to mean free path, are plotted against the density ratio in Fig. 1.8. This figure includes an upper scale that relates the density ratio to the altitude in the standard atmosphere.

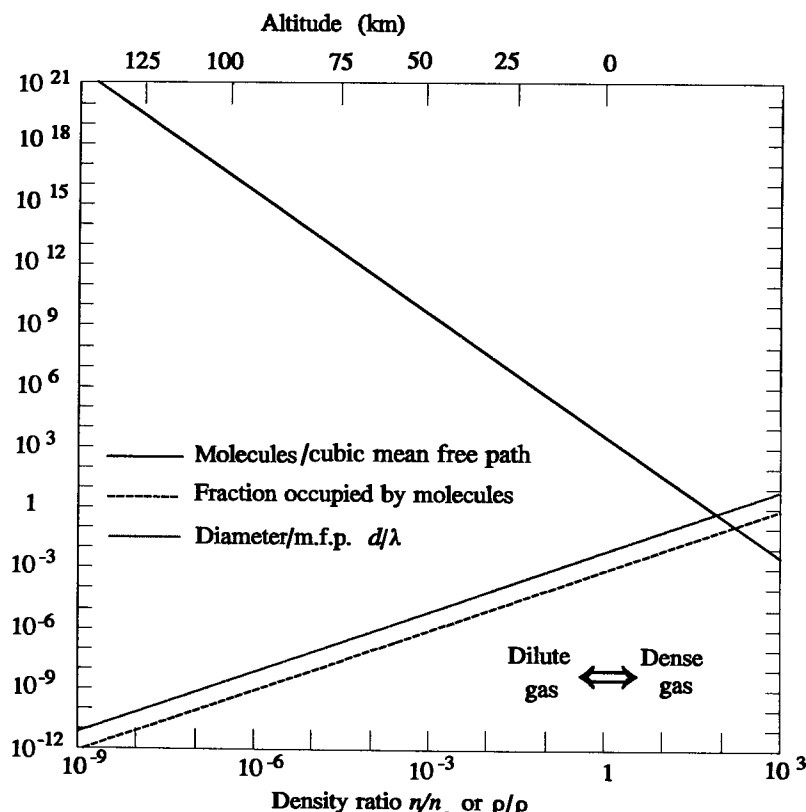


Fig. 1.8 Some consequences of molecular size.

1.7 Real gas effects

The discussion in the preceding sections has implicitly assumed that the molecules are adequately described by classical or Newtonian physics. Moreover, the possibility that molecules change their identities as a result of collisions has not been taken into account. Real gas models must include chemical reactions, and also the absorption and emission of radiation.

Quantum mechanics provides a more accurate description and shows that there is a limit on the precision with which the molecular positions and momenta may be specified. The Heisenberg uncertainty principle states that the product of the uncertainty $|\Delta r|$ in position and $|\Delta mc|$ in momentum is of the order of Planck's constant, i.e.

$$|\Delta r| |\Delta mc| \sim h. \quad (1.59)$$

For the classical model to be adequate, the uncertainties in position and momentum should be much smaller than the mean molecular spacing and the mean magnitude of the molecular momentum, respectively. This requires

$$\delta m\bar{c} \gg h \quad (1.60)$$

and means that δ should be much larger than the mean de Broglie wavelength ($h/m\bar{c}$) of the molecules. The condition for gross diffraction effects to be absent from collisions is that the molecular diameter d should be large compared with the de Broglie wavelength. The second condition is the more restrictive in a dilute gas, but, at this stage, our primary concern is with the general molecular description rather than the detail of the collision processes.

A measure of molecular speed may be obtained from eqn (1.56) and, using eqn (1.7), eqn (1.60) becomes

$$(3mkT)^{1/2}/(n^{1/3}h) \gg 1. \quad (1.61)$$

The substitution of the 'average air' mass at standard temperature and density into the expression on the left-hand side of this equation leads to a value of 117.4. Even at low temperatures, the dilute gas assumption would break down well before the density increased sufficiently to violate eqn (1.61). Representative data on gases other than air is presented in Appendix A. The only circumstance in which a quantum description becomes necessary for the general molecular model is when a light gas such as hydrogen or helium is at an extremely low temperature.

A further condition for the validity of the classical model is that the number of available quantum states should be very large in comparison with the number of molecules. The standard result for the ratio of the number of available translational states to the number of molecules is, to within a numerical factor of order unity, the cube of the expression on the left-hand side of eqn (1.61). The classical approximation is therefore

applicable to the translational motion which contributes three degrees of freedom to the gas. As discussed in §1.4, each fully excited degree of freedom contains a specific energy of $\frac{1}{2}kT$ in an equilibrium gas.

Quantum considerations must be taken into account when discussing the internal degrees of freedom associated with rotation and vibration of the molecules. The rotational mode has an angular momentum $I\omega$ and rotational energy $\frac{1}{2}I\omega^2$, where I is the moment of inertia about the axis of rotation and ω is the angular velocity. Rotation can be neglected for monatomic molecules and for diatomic molecules about the internuclear axis. This is because the moment of inertia is so small that the minimum quantum of angular momentum would involve rotational energy far higher than that associated with the temperatures of interest. Diatomic molecules have two degrees of freedom associated with the axes normal to the internuclear axis. The spacing of the rotational states is of the order of $k\Theta_{\text{rot}}$, where Θ_{rot} is the characteristic temperature of rotation. The rotational mode is not fully excited until the temperature is large compared with Θ_{rot} . Appendix A shows that the characteristic rotational temperatures of air molecules are between two and three degrees Kelvin, so that rotation is fully excited in air at normal temperatures. Triatomic and polyatomic molecules generally have three degrees of freedom of rotation.

Two degrees of freedom may be associated with the vibrational motion of diatomic molecules. However, the vibrational levels are widely spaced and the energy that would be assigned to a classical molecule with two degrees of freedom is truncated to that of the highest available level. The characteristic temperatures of vibration Θ_v for air molecules are between two and three thousand degrees Kelvin. Therefore, at normal temperatures, most air molecules are in the ground state, very few have vibrational energy equal to $k\theta_v$, and there are almost none in the higher levels. This means that vibration may be neglected at temperatures less than about 1000 K. A large number of vibrational modes are present in polyatomic gases, and some modes in gases such as carbon dioxide have characteristic temperatures that are comparable with the normal temperature.

The specific heat ratio γ is related to the number of excited degrees of freedom ξ by

$$\gamma = c_p/c_V = (\xi + 2)/\xi, \quad (1.62)$$

and γ must be treated as a variable when T is of the order of Θ_v . This applies to air at temperatures above 1,000 K and γ drops below the usual value of 7/5. If vibration was fully excited in air γ would be 9/7 but, before this is attained, a significant fraction of molecular oxygen and nitrogen is dissociated into atoms. The activation energy for the dissociation of oxygen is 5.12 ev and that for nitrogen is 9.76 ev. A characteristic temperature for dissociation Θ_d is defined by dividing the activation energy by the Boltzmann constant k . This gives 59,500 K for oxygen and 113,000 K for nitrogen. These large values are misleading in that there is significant dissociation at temperatures that are small compared with Θ_d . This is due, in part, to there being a significant number of collisions that involve

relative energies very much higher than kT . However, the main reason is that the reverse or recombination reaction cannot occur in a binary collision. It is an exothermic reaction and it is not possible to simultaneously satisfy the momentum and energy constraints if there is just one post-collision molecule. A third particle must participate in the collision, and three-body or ternary collisions are very rare events in a dilute gas. The dissociation-recombination reaction set is further complicated by the formation of a small amount of nitric oxide. This is important for the ionization reactions that become significant at temperatures of the order of 10,000 K. The ionization potential of NO is 9.34 ev and this is much less than the 12.3 ev for O₂, 15.7 ev for N₂, 13.7 ev for O, and 14.6 ev for N.

The electrons are negatively charged, are orders of magnitude lighter than the other particles, and interact with the positively charged ions through long-range Coulomb interactions. A number of the key approximations that are made for neutral gases cease to be valid when ionisation is present and additional modes of propagation of disturbances become possible. When there is a significant degree of ionization, the field of study changes from kinetic theory and gas dynamics to plasma physics. To the extent that this book deals at all with charged gases, it will be concerned only with very small degrees of ionization that allow simplified models of the plasma effects.

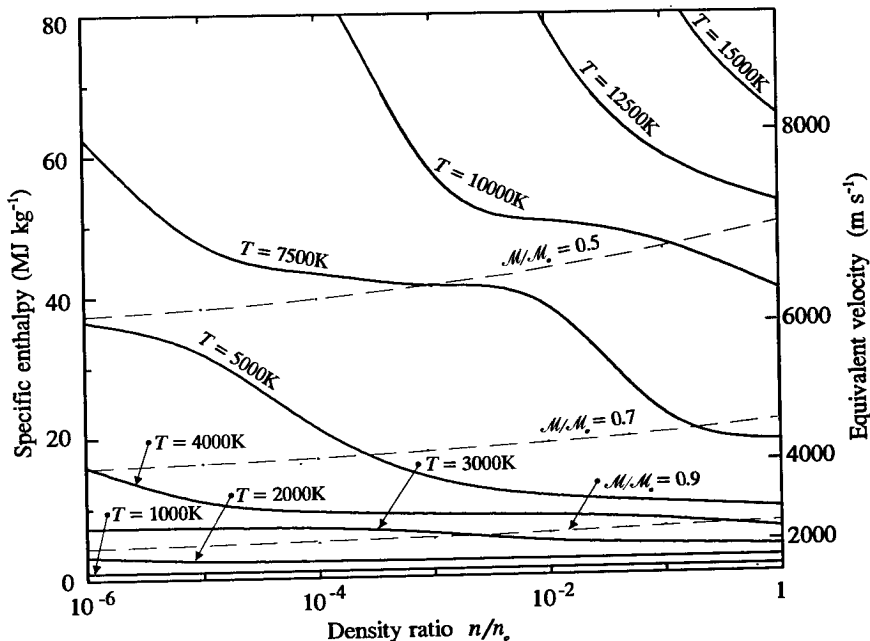


Fig. 1.9 Temperature and molecular weight as a function of enthalpy in equilibrium air.

The large amount of energy required by the dissociation reactions is made clear in Fig. 1.9 which shows the enthalpy of the gas that is required to reach various values of temperature in an equilibrium gas. The specific enthalpy $h = c_p T$ and, at temperatures of the order of the standard temperature, c_p is nearly constant with a value of 1002 J kg^{-1} . The numerical values of the specific enthalpy are unchanged when expressed in units of $\text{m}^2 \text{s}^{-2}$, and an equivalent velocity scale has been included in the figure. The energy of dissociation is primarily responsible for the order of magnitude increase in c_p in real air. The higher enthalpy for a given temperature at the lower densities is due to the ratio of ternary to binary collisions being proportional to density, and the consequent reduced rate of recombinations at low densities leads to a higher degree of equilibrium dissociation. A large number of reactions occur in high-temperature air, and this is responsible for the irregularity of the contours of constant temperature in Fig. 1.9. The number of particles increases in both dissociation and ionization reactions. This means that the molecular weight also changes, and some contours of constant molecular weight are shown in Fig. 1.9.

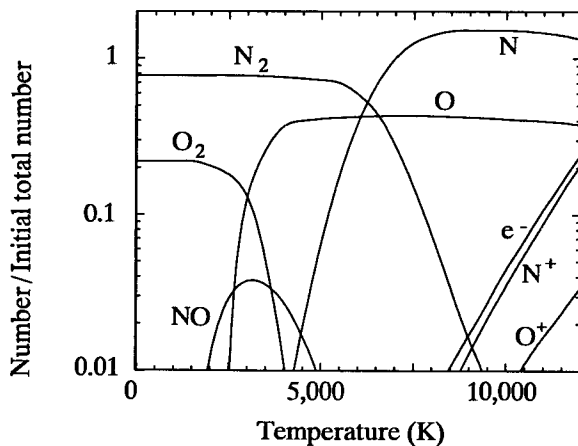


Fig. 1.10 Equilibrium composition of air at $n/n_0 = 10^{-2}$.

The equilibrium composition of air as a function of temperature is shown in Fig. 1.10 for a density ratio $n/n_0 = 10^{-2}$. Statistical mechanics enables these equilibrium properties to be readily calculated from the partition functions. However, when an equilibrium gas is subjected to a flow disturbance, a new equilibrium state can only be attained through inter-molecular collisions and these may not be sufficiently rapid for each gas element to remain in equilibrium as it passes through the flow. We are

then faced with a non-equilibrium flow in which the finite rates of the chemical reactions are coupled with the flow changes. The concept of local thermodynamic equilibrium was introduced in §1.3 in the context of the translational modes. Chemical non-equilibrium and the non-equilibrium between the translational and internal modes almost always accompany translational non-equilibrium, and frequently occur even when the translational modes are very close to equilibrium. The thermodynamic definition of temperature has no meaning in a non-equilibrium flow and, apart from the limiting case in which the internal modes and chemistry are *frozen*, such flows are non-isentropic. The analysis of non-equilibrium flows must be based on a knowledge of the details of the physical processes.

The time that is required for the gas to come to equilibrium is called the *relaxation time*. If there is a finite stream velocity, an element of gas moves a finite distance during this time and a relaxation distance is established. Relaxation times are generally proportional to the mean collision time and relaxation distances are generally proportional to the mean free path. The non-equilibrium regions of typical gas flows become more extensive as the Knudsen number increases and, in highly rarefied gases, the whole flowfield may be very far from equilibrium. The kinetic temperatures based on the various energy modes are then very different.

The translational modes are generally assumed to adjust to the new conditions within a few mean collision times, although it should be noted that relaxation times are based on the initial gradient of the change and a much longer time is needed for a full accommodation to the new conditions. In a region of translational non-equilibrium, the kinetic temperatures based on the separate components of the molecular velocities, as defined in eqn (1.30), will generally differ. For example, the kinetic temperature based on the velocity components in the direction of the flow within a strong normal shock wave may be double the kinetic temperature based on the velocity components normal to the flow direction. The relaxation times for the rotational modes are generally of the order of five to ten mean collision times, so that the adjustment is not much slower than that for the translation. On the other hand, the relaxation times for vibration are, at normal temperatures, at least two or three orders of magnitude slower than those for translation and rotation, and vibrational non-equilibrium is the rule rather than the exception.

Dissociation and recombination are chemical reactions and data for the speed of particular reactions is available in the form of rate coefficients at the continuum level and cross-sections for the reactions at the particle level. Alternatively, dissociation can be regarded as vibrational excitation to the level at which the atoms split apart, and the dissociation rate is set by the vibrational relaxation rate. Vibrational relaxation is much faster at very high temperatures and, together with the associated dissociation, it can then proceed more rapidly than the rotational relaxation. As noted earlier, recombination is an extremely slow process and the dissociation level in an expanding flow may often be regarded as frozen.

Thermal radiation is an additional mechanism for the transfer of energy in high-temperature gases and can occur even in collisionless flows. For equilibrium radiation, the energy absorbed at each frequency is equal to that radiated but, like the reactions, the radiation can be non-equilibrium. The most important mechanism for the emission of radiation is generally the *bound-bound* transitions between the quantum energy levels of the atoms and molecules. Since the energy associated with each level is fixed within narrow bounds, the energy in these transitions also falls within a narrow energy range and the radiation gives rise to distinct spectral lines. Radiation from rotational transitions has the lowest energy and is usually within the infrared band. This radiation is emitted only by molecules with dissimilar atoms and is almost absent from high-temperature air. Vibrational transitions are responsible for most of the radiation from high-temperature air and many of the lines fall within the visible region of the spectrum. The absorption of radiation can result in dissociation or recombination and this, together with emission from the reverse reactions, is called *bound-free* radiation. *Free-free* radiation is produced by changes in the energy of free electrons and is generally associated with problems in plasma physics that are outside the scope of this book.

Radiation theory may be based on a continuum or a particle approach. The continuum theory employs emission and absorption coefficients, and is concerned with the optical thickness of the gas. The particle approach to line radiation is based on the probabilities of the individual radiation events, and the Einstein coefficients are the fundamental quantities.

References

- BIRD, G.A. (1970). Breakdown of translational and rotational equilibrium in gaseous expansions. *Am. Inst. Aero. and Astro. J.* **8**, 1998–2003.
BIRD, G.A. (1981). Monte Carlo simulation in an engineering context. *Progress in Astro. and Aero.* **74**, 239–255.
CHAPMAN, S. and COWLING, T.G. (1952). *The mathematical theory of non-uniform gases* (2nd edn). Cambridge University Press.

2

BINARY ELASTIC COLLISIONS

2.1 Momentum and energy considerations

We have seen that intermolecular collisions in dilute gases are overwhelmingly likely to be binary collisions involving just two molecules. An elastic collision is defined as one in which there is no interchange of translational and internal energy. The pre-collision velocities of the two collision partners in a typical binary collision may be denoted by \mathbf{c}_1 and \mathbf{c}_2 . Given the physical properties of the molecules and the orientation of the trajectories, our task is to determine the post-collision velocities \mathbf{c}_1^* and \mathbf{c}_2^* .

Linear momentum and energy must be conserved in the collision. This requires

$$m_1\mathbf{c}_1 + m_2\mathbf{c}_2 = m_1\mathbf{c}_1^* + m_2\mathbf{c}_2^* = (m_1 + m_2)\mathbf{c}_m \quad (2.1)$$

and

$$m_1\mathbf{c}_1^2 + m_2\mathbf{c}_2^2 = m_1\mathbf{c}_1^{*2} + m_2\mathbf{c}_2^{*2}. \quad (2.2)$$

Here, m_1 and m_2 are the masses of the two molecules and \mathbf{c}_m is the velocity of the centre of mass of the pair of molecules. Eqn (2.1) shows that this centre of mass velocity is not affected by the collision. The pre-collision and post-collision values of the relative velocity between the molecules may be defined by

$$\mathbf{c}_r = \mathbf{c}_1 - \mathbf{c}_2 \quad (2.3)$$

and

$$\mathbf{c}_r^* = \mathbf{c}_1^* - \mathbf{c}_2^*.$$

Eqns (2.1) and (2.3) may be combined to give

$$\mathbf{c}_1 = \mathbf{c}_m + \frac{m_2}{m_1 + m_2} \mathbf{c}_r \quad (2.4)$$

and

$$\mathbf{c}_2 = \mathbf{c}_m - \frac{m_1}{m_1 + m_2} \mathbf{c}_r.$$

The pre-collision velocities relative to the centre of mass are $\mathbf{c}_1 - \mathbf{c}_m$ and $\mathbf{c}_2 - \mathbf{c}_m$. Eqn (2.4) shows that these velocities are antiparallel in this frame of reference and, if the molecules are point centres of force, the force

between them remains in the plane containing the two velocities. The collision is therefore planar in the centre of mass frame. The post-collision velocities may similarly be obtained from eqns (2.1) and (2.3) as

$$\mathbf{c}_1^* = \mathbf{c}_m + \frac{m_2}{m_1 + m_2} \mathbf{c}_r^* \quad (2.5)$$

and

$$\mathbf{c}_2^* = \mathbf{c}_m - \frac{m_1}{m_1 + m_2} \mathbf{c}_r^*.$$

This shows that the post-collision velocities are also antiparallel in the centre of mass frame. The conservation of angular momentum requires that the projected distance between the post-collision velocities be equal to the projected distance b between the pre-collision velocities.

Eqns (2.4) and (2.5) show that

$$m_1 c_1^2 + m_2 c_2^2 = (m_1 + m_2) c_m^2 + m_r c_r^2$$

and $m_1 c_1^{*2} + m_2 c_2^{*2} = (m_1 + m_2) c_m^2 + m_r c_r^{*2}, \quad (2.6)$

where

$$m_r = \frac{m_1 m_2}{m_1 + m_2} \quad (2.7)$$

is called the *reduced mass*. A comparison of eqn (2.6) with the energy equation (2.2) shows that the magnitude of the relative velocity is unchanged by the collision, i.e.

$$c_r^* = c_r. \quad (2.8)$$

Since both \mathbf{c}_m and \mathbf{c}_r may be calculated from the pre-collision velocities, the determination of the post-collision velocities reduces to the calculation of the change in direction χ of the relative velocity vector.

If \mathbf{F} is the force between two spherically symmetric point centre of force molecules and $\mathbf{r}_1, \mathbf{r}_2$ are their position vectors, the equations of motion of the molecules are

$$m_1 \ddot{\mathbf{r}}_1 = \mathbf{F}$$

and $m_2 \ddot{\mathbf{r}}_2 = -\mathbf{F}. \quad (2.9)$

$$m_2 \ddot{\mathbf{r}}_2 = -\mathbf{F}.$$

Hence

$$m_1 m_2 (\ddot{\mathbf{r}}_1 - \ddot{\mathbf{r}}_2) = (m_1 + m_2) \mathbf{F}$$

or, if the relative velocity vector is denoted by $\dot{\mathbf{r}}$,

$$m_r \ddot{\mathbf{r}} = \mathbf{F}. \quad (2.10)$$

The motion of the molecule of mass m_1 relative to the molecule of mass m_2 is therefore equivalent to the motion of a molecule of mass m_r relative to a fixed centre of force.

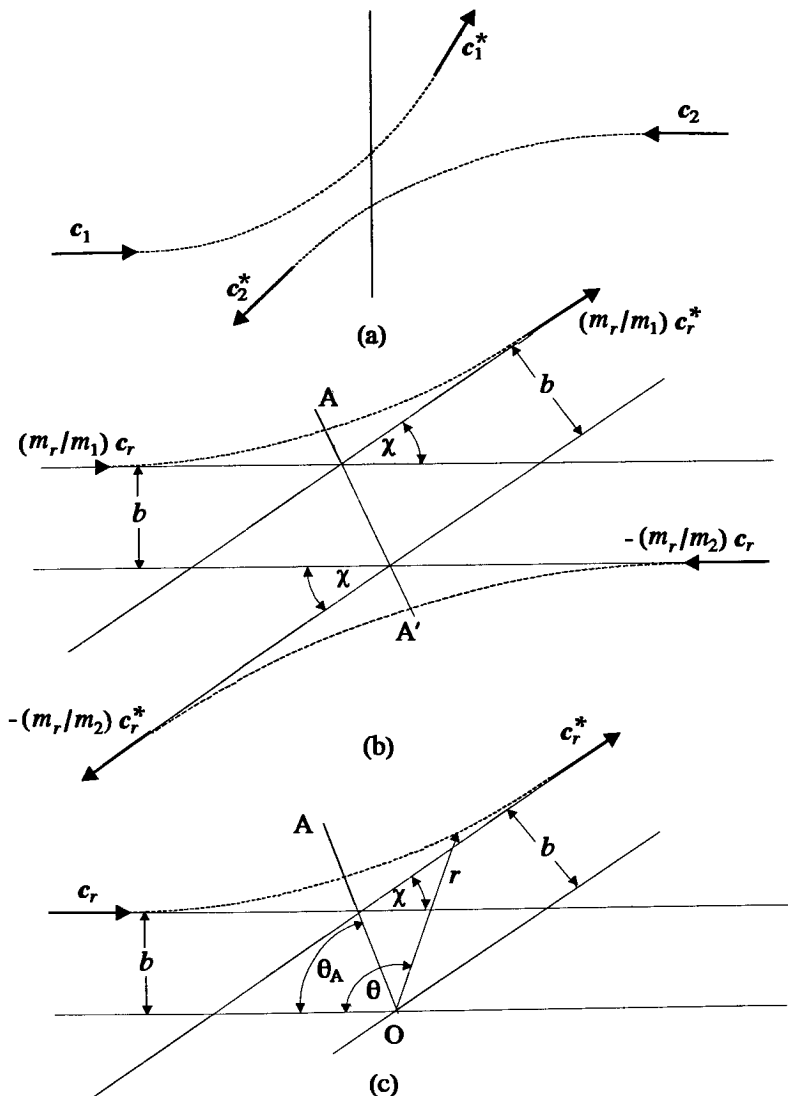


Fig. 2.1 Frames of reference for the analysis of binary collisions.
 (a) Planar representation of a collision in the laboratory frame of reference.
 (b) Binary collision in the centre of mass frame of reference.
 (c) Interaction of the reduced mass particle with a fixed scattering centre.

The above results are summarized in Fig. 2.1. The transformation from the laboratory to the centre of mass coordinate system transforms the three-dimensional trajectories into two-dimensional trajectories that are symmetrical about the *apse line AA'*. The two trajectories are reduced to one in the further transformation to the reduced mass frame of reference, and this trajectory remains symmetrical about the transformed apse line which passes through the scattering centre O. This symmetry reflects the symmetry of the equations with respect to the pre-collision and post-collision velocities. A further consequence of this symmetry becomes apparent if we consider a collision between two molecules of velocity c_1^* and c_2^* and such that the separation of their undisturbed trajectories in the centre of mass frame of reference is again equal to b . This collision results in post-collision velocities of c_1 and c_2 and is called the *inverse* of the original or *direct* collision. The trajectories of the direct and inverse collisions in the reduced mass frame of reference are shown in Fig. 2.2.

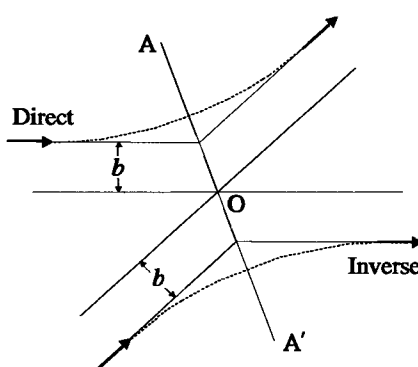


Fig. 2.2 Representation of the direct and inverse encounters of a reduced mass particle with a fixed scattering centre.

2.2 Impact parameters and collision cross-sections

Apart from the translational velocities of the two collision partners, just two *impact parameters* are required to completely specify a binary elastic collision between spherically symmetric molecules. The first is the distance of closest approach b of the undisturbed trajectories in the centre of mass frame of reference. The plane in which the trajectories lie in the centre of mass frame is called the collision plane, and the second impact parameter is chosen as the angle ϵ between the collision plane and some reference plane. As shown in Fig. 2.3, the line of intersection of the collision and reference plane is parallel to c_r . If we now consider the plane normal to c_r and containing O, the *differential cross-section* $\sigma d\Omega$ for the collision specified by the impact parameters b and ϵ is defined by

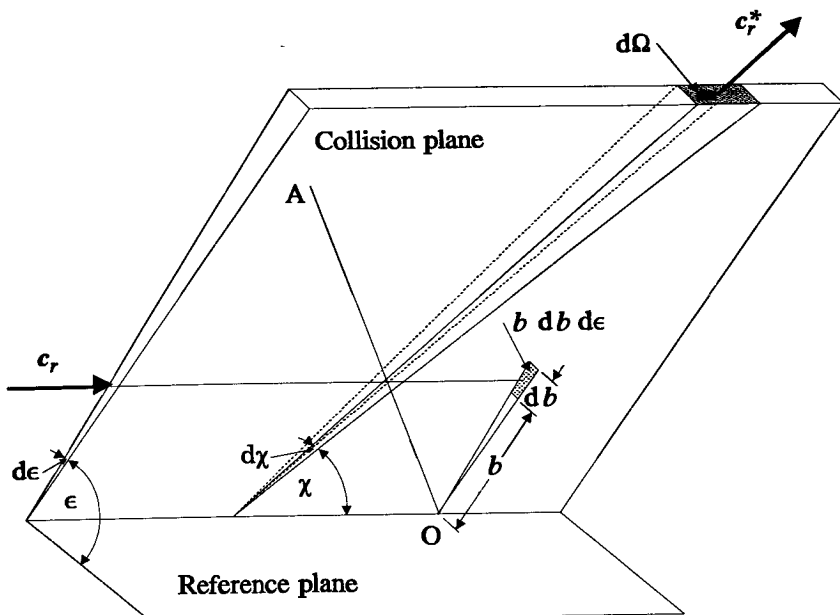


Fig. 2.3 Illustration of the impact parameters.

$$\sigma d\Omega = b db d\epsilon, \quad (2.11)$$

where $d\Omega$ is the unit solid angle about the vector c_r^* . From Fig. 2.3

$$d\Omega = \sin\chi d\chi d\epsilon \quad (2.12)$$

so that

$$\sigma = (b/\sin\chi) |db/d\chi|. \quad (2.13)$$

Finally, the total collision cross-section σ_T is defined by

$$\sigma_T = \int_0^{4\pi} \sigma d\Omega = 2\pi \int_0^\pi \sigma \sin\chi d\chi. \quad (2.14)$$

We will find that this integral diverges for some of the more realistic molecular models and it is then necessary to introduce effective or nominal cross-sections.

2.3 Collision dynamics

With reference to the polar coordinates r, θ defined in Fig. 2.1(c), the angular momentum and energy of the particle of reduced mass m_r within the force field about O may be equated to the limiting values of these quantities as $r \rightarrow \infty$. The equation for the angular momentum is simply

$$r^2\dot{\theta} = \text{const} = bc_r. \quad (2.15)$$

The energy within the force field is the sum of the kinetic and potential energies and, since the force tends to zero at large distances, this may be equated to the asymptotic kinetic energy, i.e.

$$\frac{1}{2}m_r(\dot{r}^2 + r^2\dot{\theta}^2) + \phi = \text{const} = \frac{1}{2}m_r c_r^2 = E_t. \quad (2.16)$$

Here, ϕ is the intermolecular potential which is related to the spherically symmetric force \mathbf{F} between the molecules by

$$\phi = \int_r^\infty F dr, \quad (2.17)$$

or

$$F = -d\phi/dr.$$

Time may be eliminated from eqns (2.15) and (2.16) to give the equation of the orbit as

$$\left(\frac{dr}{d\theta}\right)^2 = \frac{r^4}{b^2} - r^2 - \frac{\phi r^4}{\frac{1}{2}m_r c_r^2 b^2}.$$

Introducing the dimensionless coordinate

$$W = b/r, \quad (2.18)$$

this becomes

$$(dW/d\theta)^2 = 1 - W^2 - \phi/(\frac{1}{2}m_r c_r^2),$$

so that

$$\theta = \int_0^W (1 - W^2 - \phi/(\frac{1}{2}m_r c_r^2))^{-\frac{1}{2}} dW.$$

Now at the intersection of the orbit with the apse line OA,

$$\theta = \theta_A$$

and

$$dW/d\theta = 0.$$

Therefore

$$\theta_A = \int_0^{W_1} (1 - W^2 - \phi/(\frac{1}{2}m_r c_r^2))^{-\frac{1}{2}} dW, \quad (2.19)$$

where W_1 is the positive root of the equation

$$1 - W^2 - \phi/(\frac{1}{2}m_r c_r^2) = 0. \quad (2.20)$$

Finally, the deflection angle of the relative velocity is

$$\chi = \pi - 2\theta_A. \quad (2.21)$$

The above determination of an expression for the deflection angle χ constitutes the key step in the analysis of the dynamics of a binary elastic collision. However, as noted at the beginning of the chapter, the objective is to determine the post-collision velocities c_1^* and c_2^* . In a typical calculation, the components and magnitudes of c_m and c_r would be obtained from the pre-collision velocities of the collision partners through eqns (2.1) and (2.3). The specification of the impact parameter b then allows the deflection angle χ to be calculated from eqns (2.18)–(2.21). The components of c_r^* are then required so that the post-collision velocities can be calculated from eqn (2.5). To this end, a set of Cartesian coordinates x' , y' , and z' is introduced with x' in the direction of c_r . The components of c_r^* along these axes are

$$c_r \cos \chi, \quad c_r \sin \chi \cos \varepsilon, \quad \text{and} \quad c_r \sin \chi \sin \varepsilon.$$

The direction cosines of x' are

$$u_r/c_r, \quad v_r/c_r, \quad \text{and} \quad w_r/c_r$$

Since the orientation of the reference plane is arbitrary, the y' -axis may be chosen such that it is normal to the x -axis. The direction cosines of y' are then

$$0, \quad w_r(v_r^2 + w_r^2)^{-1/2}, \quad \text{and} \quad -v_r(v_r^2 + w_r^2)^{-1/2}$$

and those of z' follow as

$$(v_r^2 + w_r^2)^{1/2}/c_r, \quad -u_r v_r (v_r^2 + w_r^2)^{-1/2}/c_r, \quad \text{and} \quad -u_r v_r (v_r^2 + w_r^2)^{-1/2}/c_r.$$

The required expressions for the components of c_r^* in the original x -, y -, and z -coordinates are, therefore,

$$\begin{aligned} u_r^* &= \cos \chi u_r + \sin \chi \sin \varepsilon (v_r^2 + w_r^2)^{1/2}, \\ v_r^* &= \cos \chi v_r + \sin \chi (c_r w_r \cos \varepsilon - u_r v_r \sin \varepsilon) / (v_r^2 + w_r^2)^{1/2}, \end{aligned} \quad (2.22)$$

and

$$w_r^* = \cos \chi w_r - \sin \chi (c_r v_r \cos \varepsilon + u_r w_r \sin \varepsilon) / (v_r^2 + w_r^2)^{1/2}.$$

A *molecular model* is established through the definition of the force F or potential ϕ . As noted in Chapter 1, the force between real molecules is strongly repulsive at short distances and weakly attractive at larger distances. Models for analytical and numerical studies involve some degree of approximation. The simplest acceptable model is generally chosen, and most of these neglect the attractive component. A model may be said to be acceptable for a particular application if it leads to sufficiently accurate correlations between theory and experiment.

2.4 The inverse power law model

This model is sometimes called the point centre of repulsion model and is defined by

$$F = \kappa/r^n$$

or

$$\phi = \kappa/[(\eta-1)r^{n-1}]. \quad (2.23)$$

The ratio of the potential energy to the asymptotic kinetic energy may be written

$$\frac{\phi}{\frac{1}{2}m_r c_r^2} = \frac{2\kappa}{(\eta-1)r^{n-1}} m_r c_r^2 = \frac{2}{\eta-1} \left(\frac{W}{W_0} \right)^{n-1},$$

where W_0 is a second dimensionless impact parameter defined by

$$W_0 = b(m_r c_r^2/\kappa)^{1/(\eta-1)}. \quad (2.24)$$

Eqns (2.19) to (2.21) then show that the deflection angle is given by

$$\chi = \pi - 2 \int_0^{W_1} [1 - W^2 - \{2/(\eta-1)\}(W/W_0)^{n-1}]^{-1/2} dW \quad (2.25)$$

where W_1 is the positive root of the equation

$$1 - W^2 - \{2/(\eta-1)\}(W/W_0)^{n-1} = 0.$$

Note that, for a given η , χ is a function of the dimensionless impact parameter W_0 only. This single parameter dependence of the deflection angle is the basic reason for the usefulness of the inverse power law model. The differential cross-section is a function of c_r and, for a fixed value of c_r , eqn (2.24) and its derivative may be substituted into eqn (2.11), to give

$$\sigma d\Omega = W_0 \{ \kappa / (m c_r^2) \}^{2/(\eta-1)} dW_0 d\epsilon. \quad (2.26)$$

For any finite value of η , the force field extends to infinity and the integral in eqn (2.14) for the total-cross-section diverges.

The problem of an unbounded total collision cross-section σ_T is common to many classical models. Although σ_T is infinite, the vast majority of collisions are glancing collisions involving very slight deflections. It can be shown (Vincenti and Kruger 1965, Chap. IX, §8) that, when quantum effects are taken into account, the uncertainty principle does not allow these collisions to be properly defined. Therefore, when applying these models, a finite *cut-off* is a theoretical requirement as well as a practical necessity. Such a cut-off may be based either on the miss-distance b or the deflection angle χ . In most cases, the latter is to be preferred and, since χ is a function of W_0 for the inverse power law model, a deflection angle cut-off for this model may be applied through the specification of a maximum value $W_{0,m}$ of W_0 . Then, for a fixed value of c_r , the total cross-section σ_T

may be obtained by integrating eqn (2.26) over all possible values of the impact parameters A_0 and ϵ , i.e.

$$\psi_0 = \int_0^{2\pi} \int_0^{W_{0,m}} W_0 \{ \kappa / (m_r c_r^2) \}^{2/(\eta-1)} dW_0 d\epsilon.$$

or

$$\sigma_T = \pi W_{0,m}^2 \{ \kappa / (m_r c_r^2) \}^{2/(\eta-1)} = \pi W_{0,m}^2 \{ \frac{1}{2} \kappa / E_t \}^{2/(\eta-1)}. \quad (2.27)$$

However, since the value of $W_{0,m}$ is arbitrary, this expression is not suitable for setting the effective collision frequency or mean free path.

The calculation of the transport properties, such as the coefficient of viscosity, will be found to involve the differential rather than the total cross-section. A nominal total cross-section for a particular model may therefore be defined as the cross-section of the hard sphere model that matches the coefficient of viscosity for that model. This procedure effectively fixes the value of the constant κ . However, eqn (2.27) shows that the total cross-section of an inverse power law molecule is inversely proportional to $c_r^{4/(\eta-1)}$, and the hard sphere model is preferably replaced by either the VHS model (see §2.6) or the VSS model (see §2.7) with the same dependence on the relative speed.

The nominal cross-section established through the above procedure is not to be confused with the viscosity cross-section σ_μ . This is defined by

$$\sigma_\mu = \int_0^{4\pi} \sin^2 \chi \sigma d\Omega$$

or, from eqn (2.12),

$$\sigma_\mu = 2\pi \int_0^\pi \sigma \sin^3 \chi d\chi \quad (2.28)$$

and its name is derived from the fact that it is a convergent integral that is encountered in the Chapman-Enskog theory for the coefficient of viscosity. Also, it may be seen from Fig. 2.1(c) that the component of post-collision velocity in the direction of the pre-collision velocity is $(1 - \cos \chi) c_r$. This leads to the momentum transfer cross-section σ_M defined by

$$\sigma_M = \int_0^{4\pi} (1 - \cos \chi) \sigma d\Omega$$

or

$$\sigma_M = 2\pi \int_0^\pi \sigma (1 - \cos \chi) \sin \chi d\chi. \quad (2.29)$$

The momentum cross-section appears in the Chapman-Enskog theory for the diffusion coefficients, and may be referred to by the alternative name of *diffusion cross-section*.

2.5 The hard sphere model

The hard sphere model that was employed in much of the discussion in Chapter 1 may be regarded as the special case of the inverse power law model with $\eta = \infty$. As shown in Fig. 2.4, this force becomes effective at

$$r = \frac{1}{2}(d_1 + d_2) = d_{12}$$

and the apse line is the line through the centres of the spheres. Therefore,

$$b = d_{12} \sin \theta_A = d_{12} \cos(\frac{1}{2}\chi)$$

and

$$|db/d\chi| = \frac{1}{2}d_{12} \sin(\frac{1}{2}\chi)$$

so that eqn (2.13) gives

$$\sigma = d_{12}^2/4. \quad (2.30)$$

This equation shows that σ is independent of χ and that the scattering from hard sphere molecules is isotropic in the centre of mass frame of reference. That is, all directions are equally likely for c_r^* , as can be seen from purely geometric considerations. The total collision cross-section is, as expected,

$$\sigma_T = \int_0^{4\pi} \sigma d\Omega = \pi d_{12}^2. \quad (2.31)$$

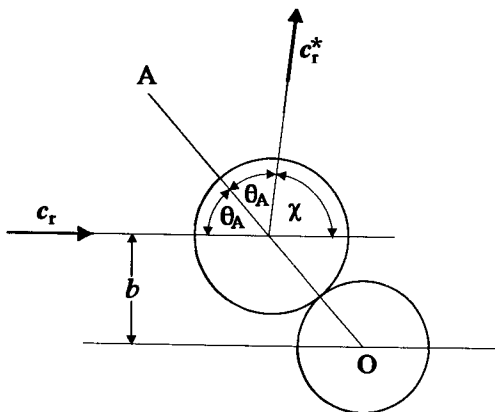


Fig. 2.4 Collision geometry of hard sphere molecules.

The viscosity cross-section is defined in eqn (2.28) and, for the hard sphere model, the constant cross-section may be taken outside the integral, to give

$$\sigma_{\mu} = \frac{2}{3} \sigma_T. \quad (2.32)$$

The momentum or diffusion coefficient that is defined in eqn (2.29) is given similarly as

$$\sigma_M = \sigma_T. \quad (2.33)$$

2.6 The variable hard sphere (VHS) model

In addition to the finite total cross-section, the hard sphere model has the advantage of easily calculated collision mechanics because of the isotropic scattering in the centre of mass frame of reference. Its disadvantages are that this scattering law is not realistic and that the cross-section is independent of the relative translational energy $E_t = \frac{1}{2}m_r c_r^2$ in the collision. Other than at extremely low temperatures, the effective cross-section of real molecules decreases as c_r and E_t increase. The rate of decrease is directly related to the change of the coefficient of viscosity with temperature. The viscosity coefficient of the hard sphere model is proportional to the temperature to the power of 0.5 and a variable cross-section is required to match the powers of the order of 0.75 that are characteristic of real gases. It has been found that the consequences of changes in the molecular model in analytical and numerical studies of gas flows correlate strongly with this change in the effective cross-section. By contrast, the observable consequences of changes in the scattering law are generally very small.

These observations led to the introduction (Bird 1981) of the variable hard sphere, or VHS, molecular model. This is a hard sphere molecule with a diameter d that is a function of c_r . The function is generally, but not necessarily, a simple inverse power law v , so that

$$d = d_{ref} (c_{r,ref}/c_r)^v, \quad (2.34)$$

where the subscript _{ref} denotes reference values. It will be shown in §3.5 that, if this power law follows eqn (2.27), the variation of the coefficient of viscosity with temperature is the same as that in the corresponding inverse power law model. The VHS model for a particular gas may be defined (§4.3) by the effective diameter at a particular reference temperature.

Because the VHS model combines a finite cross-section with a realistic temperature exponent of the coefficient of viscosity, it has permitted the definition (Bird 1983) of a mean free path and a Knudsen number that account for the real gas temperature exponent of the coefficient of viscosity. The deflection angle is given by the hard sphere result

$$\chi = 2 \cos^{-1}(b/d) \quad (2.35)$$

and, while d is a function of c_r , there is no coupling between c_r and χ . This means that σ may again be taken outside the integral in eqns (2.28) and (2.29), and the viscosity and momentum cross-sections are again given by eqns (2.32) and (2.33).

2.7 The variable soft sphere (VSS) model

As noted above, the cross-section in VHS model is determined from the viscosity coefficient, but the ratio of the momentum to the viscosity cross-section follows the hard sphere value. This is a deficiency in the model because the ratio varies with the power law in the case of the inverse power law model, and the effective real gas values are different from the hard sphere value. In response to this problem, Koura and Matsumoto (1991 and 1992) introduced the variable soft sphere (or VSS) model in which the diameter varies in the same way as in the VHS model, but the deflection angle is given by

$$\chi = 2 \cos^{-1} \{(b/d)^{1/\alpha}\}. \quad (2.36)$$

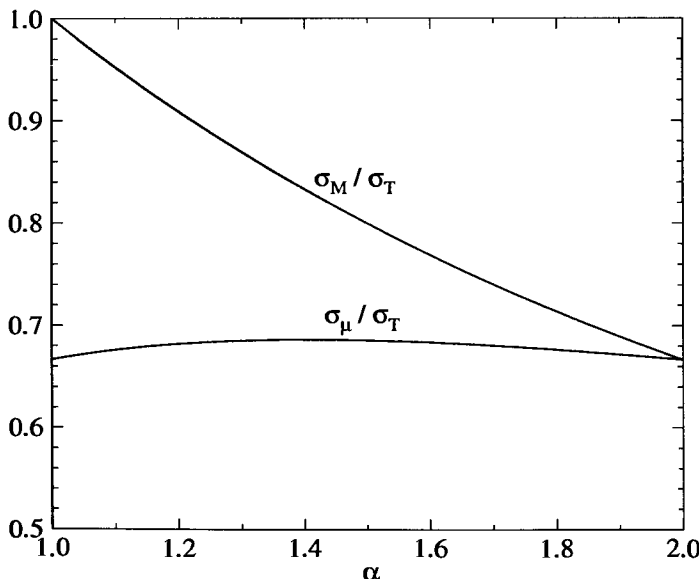


Fig. 2.5 The viscosity and momentum cross-sections as functions of the exponent in the VSS model.

The cross-section may again be taken outside the integral and it may be shown that the total cross-section σ_T remains equal to πd^2 . The viscosity and momentum cross-sections become

$$\sigma_{\mu} = \frac{4\alpha}{(\alpha + 1)(\alpha + 2)} \sigma_T. \quad (2.37)$$

and

$$\sigma_M = \frac{2}{(\alpha + 1)} \sigma_T. \quad (2.38)$$

Eqn (A2) shows that the Schmidt number, which is essentially the ratio of the viscosity to the diffusion, can be expressed as a function of the temperature exponent of the viscosity coefficient ω and α . The values of α generally lie between 1 and 2. Figure 2.5 shows that the viscosity cross-section is barely affected, while the momentum or diffusion coefficient depends strongly on α . A typical variation of the deflection angle with the impact parameter b is shown in Fig. 2.6 for the VHS, VSS and inverse ninth power law models. The normalization is such that all three models lead to the same coefficient of viscosity, but only the VSS and inverse power law models have the same diffusion coefficients. The VSS model leads to near 90° deflection angles over a wider range of impact parameters.

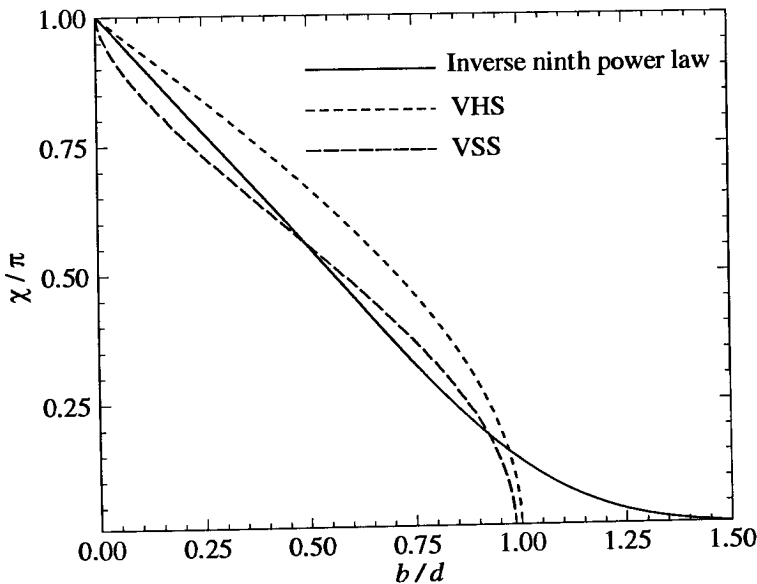


Fig. 2.6 The deflection angle in a collision as a function of the miss-distance impact parameter.

2.8 The Maxwell model

This is the special case of the inverse power law model with $\eta=5$. We then have

$$W_1 = W_0^2 [(1 + (2/W_0^4))^{1/4} - 1]^{1/4}$$

for the dimensionless distance of closest approach and eqn (2.25) may be integrated. The result is

$$\chi = \pi - [2/\{1 + (2/W_0^4)\}^{1/4}] K [\frac{1}{2} - \frac{1}{2}\{1 + (2/W_0^4)\}^{-1/4}], \quad (2.39)$$

where

$$K(\alpha) = \int_0^{\pi/2} (1 - \alpha \sin^2 y)^{-1/4} dy$$

is the complete elliptic integral of the first kind. Eqn (2.26) for the differential cross-section becomes

$$\sigma d\Omega = \frac{W_0}{c_r} \left(\frac{\kappa}{m_r} \right)^{1/2} dW_0 d\varepsilon. \quad (2.40)$$

We saw in §1.3 that the collision probability for a pair of molecules is proportional to the product of the cross-section and the relative speed. Eqn (2.40) therefore shows that the collision probability for a particular molecule in a Maxwellian gas is independent of velocity.

A gas of Maxwell molecules has a coefficient of viscosity that is linearly proportional to the temperature. This is unrealistic for real gases. The model is widely used for analytical studies but, in almost all cases, this is because all molecules have the same collision probability, and the analysis would not be possible if the collision probability was dependent on the relative speed. The model can be regarded as the limiting case of a ‘soft’ molecular model, while the hard sphere model may be regarded as the limiting case of a ‘hard’ molecular model.

2.9 Models that include the attractive potential

All the preceding models lead to a coefficient of viscosity that is either constant or is proportional to a *constant* power of the temperature. The addition of a long-range attractive potential to the inverse (repulsive) power law model leads to a better representation of the potential curve of real molecules. It also leads to a temperature-dependent power law for the variation of the coefficient of viscosity with temperature. The effect of the attractive potential is significant at temperatures well below the standard temperature, but is generally not significant at higher temperatures.

The *square-well model* adds a uniform attractive potential to the hard sphere model, while the *Sutherland model* adds an inverse power law attractive component to the hard sphere model. The more realistic models combine more general attractive and repulsive potentials. The best known of the attractive–repulsive models is the *Lennard–Jones potential* which

adds an inverse power law attractive component to the inverse power law model. The equation for the potential is

$$\phi = \frac{\kappa}{(\eta-1)r^{\eta-1}} - \frac{\kappa'}{(\eta'-1)r^{\eta'-1}}. \quad (2.41)$$

This model has four adjustable parameters and these allow the transport coefficients to be matched with the experimental values over a wide temperature range. The Lennard-Jones 12-6 model with $\eta=13$ and $\eta'=7$ has been widely used. The *Exp-6* model replaces the repulsive power law with a more complex exponential term. A detailed discussion and evaluation of these and other models can be found in Hirschfelder, Curtiss, and Bird (1954).

2.10 The generalized hard sphere (GHS) model

The GHS model (Hasssan and Hash 1993) is an extension of the VHS and VSS models. It bears the same relationship to the Lennard-Jones class of models as the conventional VHS or VSS models bear to the inverse power law model. The scattering distribution is that of the hard or soft sphere, but the variation of the total cross-section as a function of the relative translational energy mimics that of the corresponding attractive-repulsive potential. It is implemented through the parameters that describe the intermolecular potentials of the form of eqn (2.34), and can therefore make use of the existing database that has been built up from the measured transport properties of real gases.

2.11 General comments

It should be kept in mind that the justification for using any molecular model is that complete information on the differential cross-sections of the real molecules does not exist, would not affect the results, or renders the calculation intractable. The latter justification becomes more irrelevant as computer capability increases and more powerful numerical methods are introduced. Comprehensive theoretical and experimental information on cross-sections is available for some monatomic gases at low temperatures. Chatwani (1977) has used this data instead of a classical molecular model in studies of expansion flows of helium and neon. The cross-sections at very low temperatures are subject to significant quantum effects and can be complex functions of the relative velocity. The direct use of quantum information on the differential cross-sections is physically realistic, but the same results could well be obtained through the incorporation of the resulting total cross-section into the VHS model.

A model that reproduces the overall effects in a gas flow of some physical feature of real molecules, but does not explicitly incorporate that feature, is said to be a *phenomenological model*. The use of a VHS model, rather than one of the models with a more realistic scattering law, to produce the required temperature dependence of the transport properties is an example

of phenomenological modelling. The VHS model was empirically based on computational studies which showed that the variations in cross-section produce effects that are incomparably more important than those due to the scattering laws. Most phenomenological methods are, however, based on analytical studies, rather than observations of numerical studies.

Later chapters deal with the *inelastic collisions* of molecules with internal degrees of freedom. The models for these that were developed in the context of classical kinetic theory will be found to have restrictions that render them incapable of providing an adequate representation of real gases. Also, the number of impact parameters increases with the number of degrees of freedom, and the amount of information that would be required for a complete description of the differential cross-sections becomes prohibitively large. As the models are extended to deal with the inelastic aspects of real molecules, the practical models will be found to be increasingly phenomenological in nature.

References

- BIRD, G.A. (1981). Monte Carlo simulation in an engineering context. *Progr. Astro. Aero.* **74**, 239–255.
- BIRD, G.A. (1983). Definition of mean free path for real gases. *Phys. Fluids* **26**, 3222-3223.
- CHATWANI, A.U. (1977). Monte Carlo simulation of nozzle beam expansion. *Progr. Astro. Aero.* **51**, 461-475.
- HASSAN, H.A. and HASH, D.B. (1993). A generalized hard-sphere model for Monte Carlo simulations. *Phys. Fluids A* **5**, 738–744.
- HIRSCHFELDER, J.O., CURTISS, C.F., and BIRD, R.B. (1954). *The molecular theory of gases and liquids*. Wiley, New York.
- KOURA, K. and MATSUMOTO, H. (1991). Variable soft sphere molecular model for inverse-power-law or Lennard-Jones potential. *Phys. Fluids A* **3**, 2459-2465.
- KOURA, K. and MATSUMOTO, H. (1992). Variable soft sphere molecular model for air species, *Phys. Fluids A* **4**, 1083-1085.
- VINCENTI, W.G. and KRUGER, C.H. (1965). *Introduction to physical gas dynamics*. Wiley, New York.

3

BASIC KINETIC THEORY

3.1 The velocity distribution functions

A gas flow would be completely described, in a classical sense, by listings of the position, velocity, and internal state of every molecule at a particular instant. The number of molecules in a real gas is so large that such a description is unthinkable, and we must resort to a statistical description in terms of probability distributions. A number of distinct velocity distribution functions are employed in kinetic theory and possible confusion may be avoided by a general review of the relationships between them.

We will commence by defining the *single particle distribution function in velocity space*. Consider a sample of gas that is homogeneous in physical space and contains N identical molecules. A typical molecule has a velocity \mathbf{c} with components u , v , and w in the direction of the Cartesian axes x , y , and z . Just as x , y , and z define a space called physical space, u , v , and w define *velocity space*, as shown in Fig. 3.1. Each molecule can be represented in this space by the point defined by its velocity vector. The velocity distribution function $f(\mathbf{c})$ is then defined by

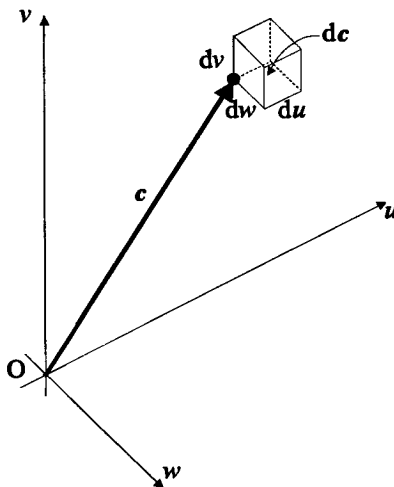


Fig. 3.1 Typical molecule and element in velocity space.

$$dN = Nf(\mathbf{c}) du dv dw, \quad (3.1)$$

where dN is the number of molecules in the sample with velocity components u to $u+du$, v to $v+dv$, and w to $w+dw$. The product $du dv dw$ may be identified as a volume element in velocity space and is denoted by $d\mathbf{c}$. An alternative form of eqn (3.1) is, therefore,

$$dN = Nf(\mathbf{c}) d\mathbf{c}, \quad (3.1a)$$

and this need not be restricted to Cartesian coordinates. The functional statement is usually omitted so that $f(\mathbf{c})$ becomes simply f . Also, since both dN and N refer to the molecules in the same volume of physical space, the number density may be used in place of the number. Therefore, the fraction of molecules within the velocity space element $d\mathbf{c}$ is

$$dn/n = f d\mathbf{c}. \quad (3.1b)$$

Since every molecule is represented by a point in velocity space,

$$\int_{-\infty}^{\infty} \int_{-\infty}^{\infty} \int_{-\infty}^{\infty} f du dv dw = \int_{-\infty}^{\infty} f d\mathbf{c} = N/N = 1. \quad (3.2)$$

This distribution function is therefore a normalized function such that its integration over all velocity space yields unity. Note that f can never be negative and must either have finite bounds in velocity space or tend to zero as \mathbf{c} tends to infinity.

The macroscopic quantities were defined in Chapter 1 in terms of averages over the molecular velocities. These averages may be established as instantaneous, time, or ensemble averages over the molecules in an element of physical space. These molecules may be regarded as constituting a homogeneous gas sample and the single particle distribution function in velocity space provides an appropriate description. In order to relate the macroscopic properties to this distribution function, we must determine the relationship between the function and the average value of any molecular quantity Q . This quantity is either a constant or a function of the molecular velocity. The mean value principle gives

$$\bar{Q} = \frac{1}{N} \int_N Q dN,$$

and substituting for dN from eqn (3.1a),

$$\bar{Q} = \frac{1}{N} \int_{-\infty}^{\infty} Q f(\mathbf{c}) N d\mathbf{c}.$$

Omitting the functional statements, we have the general result

$$\bar{Q} = \int_{-\infty}^{\infty} Q f d\mathbf{c}. \quad (3.3)$$

This process is often referred to as establishing a *moment* of the distribution function and the macroscopic properties are referred to as moments of the distribution function. For example, the stream velocity that was defined by eqn (1.21) as \bar{c} may be written

$$\bar{c} = \int_{-\infty}^{\infty} c f dc. \quad (3.4)$$

The macroscopic flow properties are generally functions of position and time, and it is sometimes desirable to express the explicit dependence of the distribution function on the position vector in velocity space r , and the time t . Just as dc has been used to denote a volume element in velocity space, a volume element in physical space may be denoted by dr . The product $dcdr$ then denotes a volume element in *phase space*, which is the multi-dimensional space formed by the combination of physical space and velocity space. The *single particle distribution function in phase space* $\mathcal{F}(c, r, t)$ is defined by

$$dN = \mathcal{F}(c, r, t) dc dr, \quad (3.5)$$

with dN now representing the number of molecules in the phase space element $dcdr$. In Cartesian coordinates, $dcdr$ becomes $du dv dw dx dy dz$ and dN is the number of molecules with velocity components ranging from u to $u+du$, v to $v+dv$, and w to $w+dw$ and spatial coordinates ranging from x to $x+dx$, y to $y+dy$, and z to $z+dz$. Note that \mathcal{F} defines the number rather than the fraction of molecules in the phase space element. It has not been normalized and an integration over the whole phase space yields the total number of molecules in the system N , rather than unity.

If the distribution function in velocity space $f(c)$ is applied to the physical space element dr , the number of molecules N in eqn (3.1) represents the total number of molecules in dr , while dN represents the number of molecules in the phase space element $dcdr$. We can then write

$$dN = N f(c) dc = \mathcal{F}(c, r, t) dc dr$$

and, since the number density in the phase space element is N/dr ,

$$n f(c) = \mathcal{F}(c, r, t).$$

Therefore, when $f(c)$ is used in a context in which it also depends on r and t , we have

$$n f \equiv \mathcal{F}. \quad (3.6)$$

We will take advantage of this identity to use f exclusively in the chapters that follow. Some authors (for example, Chapman and Cowling (1952) and Harris (1971)) have preferred \mathcal{F} , which they have denoted by f . Therefore, in common with a number of other authors (for example Kennard 1938 and Vincenti and Kruger 1965), our equations in nf will be equivalent to their equations in f .

The most specific distribution function is that for all N molecules in the system. At any instant, a complete system of monatomic molecules can be represented by a point in $6N$ dimensional phase space. If we consider a large number or ensemble of such systems, the probability of finding a system in the volume element $dc_1 dc_2 \dots dc_N dr_1 dr_2 \dots dr_N$ about the phase space point $c_1, r_1, c_2, r_2, \dots, c_N, r_N$ is

$$F^{(N)}(c_1, r_1, c_2, r_2, \dots, c_N, r_N, t) dc_1 dc_2 \dots dc_N dr_1 dr_2 \dots dr_N, \quad (3.7)$$

thus defining the N particle distribution function $F^{(N)}$. The subscript denotes the number of the molecule. A reduced distribution function $F^{(R)}$ for R of the N molecules is defined by

$$F^{(R)}(c_1, r_1, c_2, r_2, \dots, c_R, r_R, t) = \int_{-\infty}^{\infty} \int_{-\infty}^{\infty} F^{(N)} dc_{R+1} \dots dc_N dr_{R+1} \dots dr_N. \quad (3.8)$$

In particular, the single particle distribution function $F^{(1)}(c_1, r_1, t)$ is obtained by setting $R=1$. The probability of finding molecule number 1 in the phase space element $dc_1 dr_1$ at time t is $F^{(1)}(c_1, r_1, t)$ irrespective of the positions of the other $N-1$ molecules. Since the molecules are indistinguishable, the number of molecules in the phase space element at time t is $NF^{(1)}$. We therefore have

$$NF^{(1)} \equiv \mathcal{F} \quad (3.9)$$

and $F^{(1)}$ can be regarded as the normalized version of \mathcal{F} .

The two particle distribution function $F^{(2)}(c_1, r_1, c_2, r_2, t)$ is of particular importance when considering binary collisions. The definition of a dilute gas requires that only a very small fraction of the space occupied by the gas actually contains a molecule. Therefore, in such a gas, it is generally assumed that the probability of finding a pair of molecules in a particular two particle configuration is simply the product of the probabilities of finding the individual molecules in the two corresponding one particle configurations. This requires

$$F^{(2)}(c_1, r_1, c_2, r_2, t) = F^{(1)}(c_1, r_1, t) F^{(1)}(c_2, r_2, t) \quad (3.10)$$

and expresses the principle of *molecular chaos*. While the higher-order distribution functions are required for the study of dense gases, the single particle distribution function provides an adequate description of dilute gases.

If the molecules are diatomic or polyatomic, the dimensions of phase space are increased by the number of internal degrees of freedom. Also, if the molecules are not spherically symmetric, their orientations must be specified. In general, the dimensions of phase space are equal to the least number of scalar variables that are required to specify the position, velocity, orientation, and internal state of a molecule. Separate distribution functions are required for each species of a gas mixture. It is hardly surprising that most presentations of kinetic theory deal almost exclusively with gases consisting of a single species of monatomic molecules.

3.2 The Boltzmann equation

We have seen that the velocity distribution functions provide a statistical description of a gas on the molecular level. The next step is to establish the relationships between the distribution functions and the variables on which they depend. Ideally, the resulting equations would allow analytical solutions of problems in molecular gas dynamics.

The basic statistical mechanics equation for a gas is the Liouville equation which expresses the conservation of the N particle distribution function in $6N$ dimensional phase space. This equation is not directly useful, since the description of a real gas flow in terms of $F^{(N)}$ is completely out of the question. However, just as a hierarchy of reduced distribution functions $F^{(R)}$ was defined by eqn (3.8), a hierarchy of equations called the BBGKY equations may be obtained through the repeated integration of the Liouville equation. The final equation in the hierarchy is for the single particle distribution function $F^{(1)}$ and is the only one to hold out some hope of solution for flows of engineering interest. This equation also involves the two particle distribution function $F^{(2)}$, but becomes a closed equation for $F^{(1)}$ when molecular chaos (eqn (3.10)) is assumed. Then, through eqn (3.9), this becomes an equation for the single particle distribution in phase space, and is equivalent to the equation that was originally formulated by Boltzmann (1872). The mathematical limits that define the validity of the Boltzmann equation are most precisely established through the derivation from the Liouville equation (see, for example: Grad (1958); Cercignani (1969); or Harris (1971)). On the other hand, the physical significance of each term in the equation is more readily appreciated if the single particle distribution function is used throughout a derivation from first principles. The latter procedure will be followed here and, for clarity and simplicity, the derivation will be restricted to a simple gas.

At a particular instant, the number of molecules in the phase space element $d\mathbf{c}dr$ is given by eqn (3.5) as $\mathcal{F}d\mathbf{c}dr$. The identity (3.6) enables this to be written $nf d\mathbf{c}dr$. If the location and shape of the element does not vary with time, the rate of change of the number of molecules in the element is

$$\frac{\partial}{\partial t}(nf)d\mathbf{c}dr. \quad (3.11)$$

The processes that contribute to the change in the number of molecules within $d\mathbf{c}dr$ are illustrated in Fig. 3.2. They are:

- (i) The convection of molecules across the face of dr by the molecular velocity \mathbf{c} . The representation of the phase space element as separate volume elements in physical and velocity space emphasizes the fact that \mathbf{c} and r are treated as independent variables. \mathbf{c} is regarded as a constant within dr , and $d\mathbf{c}$ is regarded as being located at the point defined by r .

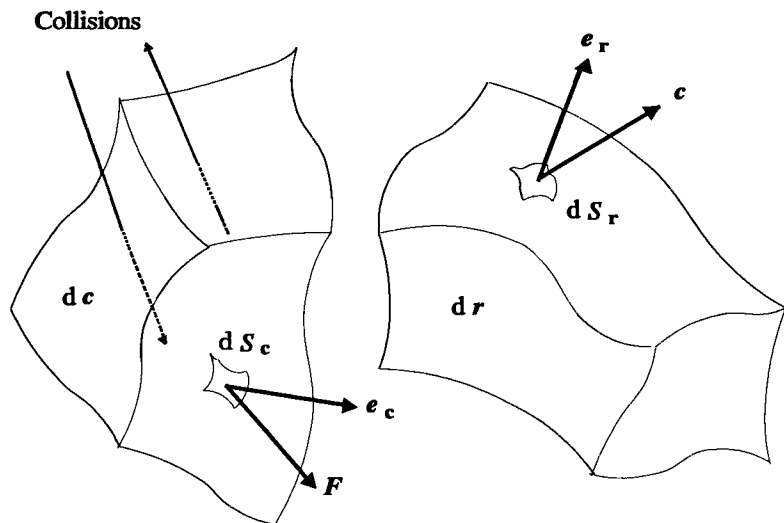


Fig. 3.2 Molecular flux to and from a phase space element $dcdv$.

(ii) The ‘convection’ of molecules across the surface of $dcdv$ as a result of the external force per unit mass F . The effect of the acceleration F on the molecules in $dcdv$ is analogous to the effect of the velocity c on the molecules in dr .

(iii) The scattering of molecules into and out of $dcdv$ as a result of intermolecular collisions. The gas is assumed to be dilute, as defined by eqn (1.9) and discussed in §1.3. One consequence of this assumption is that a collision may be assumed to be an instantaneous event at a fixed location in physical space. This means that a collision causes a molecule to jump from one point to another in velocity space, but it remains at the same point in physical space and time. Therefore, in Fig. 3.2, collisions are represented as affecting only the element $dcdv$. A second major consequence of the dilute gas assumption is that all collisions may be assumed to be binary collisions.

First consider process (i) which is a conservative process across the surface dr . The number of molecules in the phase space element is $nf dcdv$, so the number density of class c molecules within dr is $nfdc$. Eqns (1.17) and (3.3) then enable the net inflow of molecules of this class across the surface of dr to be written as

$$-\int_{S_r} nfc \cdot e_r dS_r dc.$$

Here, S_r is the total area of the surface of dr , dS_r is an element of this surface, and e_r is the unit normal vector of this element. Gauss' theorem enables the surface integral over S_r to be converted to a volume integral over dr . The expression then becomes

$$-\int_{dr} \nabla \cdot (nf\mathbf{c}) d(dr) dc$$

or, since nf and \mathbf{c} are constants within dr ,

$$-\nabla \cdot (nf\mathbf{c}) dr dc.$$

Also, since we are considering only molecules of class \mathbf{c} , the velocity \mathbf{c} may be taken outside the divergence in physical space. Therefore, the inflow of molecules of class \mathbf{c} across the surface of dr due to the velocity \mathbf{c} is

$$-\mathbf{c} \cdot \frac{\partial(nf)}{\partial r} dc dr. \quad (3.12)$$

We may take advantage of the analogy between process (ii) in velocity space and process (i) in physical space to write the inflow of molecules across the surface of dc , due to the external force per unit mass \mathbf{F} , as

$$-\mathbf{F} \cdot \frac{\partial(nf)}{\partial c} dc dr. \quad (3.13)$$

The total number of molecules scattered out of the element $dc dr$ as a result of collisions is readily obtained through an analysis similar to that which led to eqns (1.10) and (1.11) for the collision frequency and total number of collisions in the gas. However, in order to obtain a meaningful expression for the molecules scattered into the element, we must consider both the pre-collision and post-collision velocities of the molecules participating in the collisions. In particular, we are concerned with the collision of a molecule of class \mathbf{c} with one of class \mathbf{c}_1 such that their post-collision velocities are \mathbf{c}^* and \mathbf{c}_1^* , respectively. This is called a class $\mathbf{c}, \mathbf{c}_1 \rightarrow \mathbf{c}^*, \mathbf{c}_1^*$ collision, and we will now calculate the rate of scattering of molecules of class \mathbf{c} out of $dc dr$ as a result of collisions of this class. A molecule of class \mathbf{c} may be chosen as a test particle moving with speed c_r among stationary field molecules of class \mathbf{c}_1 . The volume swept out in physical space by the cross-section for this class of collision is $c_r \sigma d\Omega$ and the number of class \mathbf{c}_1 molecules per unit volume in physical space is $nf_1 dc_1$. The number of collisions of this class suffered by the test molecule per unit time is, therefore,

$$nf_1 c_r \sigma d\Omega dc_1.$$

Since the number of class \mathbf{c} molecules in the phase space element is $nfdcd\mathbf{r}$, the number of class $\mathbf{c}, \mathbf{c}_1 \rightarrow \mathbf{c}^*, \mathbf{c}_1^*$ collisions per unit time in the element is

$$n^2 f f_1 c_r \sigma d\Omega dc_1 dc dr. \quad (3.14)$$

Just as f denotes the value of the velocity distribution function f at \mathbf{c} , f_1 denotes the value of f at \mathbf{c}_1 . Similarly, f^* and f_1^* may be used to denote the values of f at \mathbf{c}^* and \mathbf{c}_1^* , respectively. Note also that the expression of a binary collision probability in terms of the product of two single particle distribution functions has implicitly invoked the principle of molecular chaos.

The existence of inverse collisions (Fig. 2.2) means that an analysis, exactly similar to that leading to eqn (3.14) may be made for the collisions of class $\mathbf{c}, \mathbf{c}_1 \leftrightarrow \mathbf{c}^*, \mathbf{c}_1^*$ that scatter molecules into class \mathbf{c} . This yields

$$n^2 f^* f_1^* c_r^* (\sigma d\Omega)^* d\mathbf{c}_1^* d\mathbf{c}^* dr \quad (3.15)$$

for the collision rate in the phase space element $d\mathbf{c}^* dr$. Eqn (2.8) shows that c_r^* is equal to c_r , while the symmetry between the direct and inverse collisions is such that there is a unit Jacobian for the transformation between the pre-collision and post-collision values of the product of the differential cross-section and velocity space elements. That is,

$$|(\sigma d\Omega) d\mathbf{c}_1 d\mathbf{c}| = |(\sigma d\Omega)^* d\mathbf{c}_1^* d\mathbf{c}^*| \quad (3.16)$$

and eqn (3.15) may be written

$$n^2 f^* f_1^* c_r \sigma d\Omega d\mathbf{c}_1 d\mathbf{c} dr. \quad (3.17)$$

The rate of increase of molecules of class \mathbf{c} in the phase space element $d\mathbf{c} dr$ as a result of the combined direct and inverse collisions of class $\mathbf{c}, \mathbf{c}_1 \leftrightarrow \mathbf{c}^*, \mathbf{c}_1^*$ is obtained by subtracting the loss rate (expression (3.14)) from the rate of gain (expression (3.17)). This gives

$$n^2 (f^* f_1^* - f f_1) c_r \sigma d\Omega d\mathbf{c}_1 d\mathbf{c} dr. \quad (3.18)$$

The total rate of increase of molecules of class \mathbf{c} in the element as a result of collisions is given by the integration of this expression over the complete cross-section for its collision with class \mathbf{c}_1 molecules, followed by the integration of the class \mathbf{c}_1 over all velocity space. The required expression for process (iii) is, therefore,

$$\int_{-\infty}^{\infty} \int_0^{4\pi} n^2 (f^* f_1^* - f f_1) c_r \sigma d\Omega d\mathbf{c}_1 d\mathbf{c} dr. \quad (3.19)$$

The expression (3.11) for the total rate of increase of molecules of class \mathbf{c} due to all three processes may be equated to the sum of expression (3.19) for process (iii) and expressions (3.12) and (3.13) for processes (i) and (ii), respectively. If the latter terms are transferred to the left-hand side and the complete equation is divided by $d\mathbf{c} dr$, we have the *Boltzmann equation* for a simple dilute gas. This is

$$\frac{\partial}{\partial t} (n f) + \mathbf{c} \cdot \frac{\partial}{\partial \mathbf{r}} (n f) + \mathbf{F} \cdot \frac{\partial}{\partial \mathbf{c}} (n f) = \int_{-\infty}^{\infty} \int_0^{4\pi} n^2 (f^* f_1^* - f f_1) c_r \sigma d\Omega d\mathbf{c}_1. \quad (3.20)$$

In a gas mixture consisting of a total of s separate species, a separate distribution function must be defined for each species. The Boltzmann equation then becomes a set of s simultaneous equations and, as in §1.5, particular species may be represented by the subscripts p or q . The Boltzmann equation for species p of the mixture can therefore be written

$$\begin{aligned} \frac{\partial}{\partial t}(n_p f_p) + c_p \cdot \frac{\partial}{\partial r}(n_p f_p) + \mathbf{F} \cdot \frac{\partial}{\partial \mathbf{c}}(n_p f_p) \\ = \sum_{q=1}^s \int_{-\infty}^{\infty} \int_0^{4\pi} n_p n_q (f_p^* f_{1q}^* - f_p f_{1q}) c_{rpq} \sigma_{pq} d\Omega dc_{1q}. \end{aligned} \quad (3.21)$$

It was noted in the preceding section that the presence of internal degrees of freedom requires the definition of extended distribution functions that allow for the additional dimensions of phase space. Also, the collision cross-sections of asymmetric molecules are a function of the molecular orientation and therefore change with time as the molecules rotate between collisions. Moreover inverse collisions do not exist for the classical models of polyatomic molecules. It is, however, possible to define cross-sections that are smoothed or averaged over the molecular rotations and vibrations. The Liouville theorem then leads to a unit Jacobean for the transformation corresponding to eqn (3.16), thus permitting a formulation similar to eqn (3.20). Chapman and Cowling (1970) have called the resulting equation the *generalized Boltzmann equation*.

The term on the right-hand side of the Boltzmann equation is called the *collision term*. Its integral form contrasts with the partial differential form of the terms expressing space and time dependence of nf , and is responsible for much of the mathematical difficulty associated with the Boltzmann equation. On the other hand, nf is the only dependent variable in the equation. This might be considered an advantage when comparing the Boltzmann equation with the Navier-Stokes equations of continuum gas dynamics, since these have the velocity components and, allowing for the equation of state, two of the thermodynamic properties as dependent variables. However, this advantage is far outweighed by the addition of the velocity space coordinates to the list of independent variables. A homogeneous gas problem becomes one-dimensional because the velocity distribution function is spherically symmetric in velocity space. This distribution becomes axially symmetric for a one-dimensional problem in physical space, so that a Boltzmann solution becomes a three-dimensional problem. For two- and three-dimensional flows there are no symmetries in velocity space and the problems become five- or six-dimensional. Time is an additional dimension if the problem is unsteady.

There is no possibility of obtaining analytical solutions of the Boltzmann equation for flows that involve complex geometries or large disturbances. Numerical solutions that require a computational mesh in phase space pose formidable problems because of the number of dimensions and the difficulties in setting the bounds of velocity space.

3.3 The moment and conservation equations

The quantity Q relates to a single molecule and is either a constant or a function of the molecular velocity. We have previously seen that the average value of this quantity may be obtained through the multiplication of the velocity distribution function by Q , followed by the integration of the product over all velocity space. These averages are referred to as moments of the distribution function. Similarly, a *moment of the Boltzmann equation* may be obtained by multiplying it by the quantity Q and then integrating the resulting equation over all velocity space. Since the moments of the distribution function include all the macroscopic properties of a monatomic gas, the moment equations may be expected to include the monatomic gas version of the conservation equations of continuum gas dynamics.

The multiplication of the Boltzmann equation (3.20) by Q yields

$$\begin{aligned} & Q \frac{\partial}{\partial t}(nf) + Q \mathbf{c} \cdot \frac{\partial}{\partial \mathbf{r}}(nf) + Q \mathbf{F} \cdot \frac{\partial}{\partial \mathbf{c}}(nf) \\ &= Q \int_{-\infty}^{\infty} \int_0^{4\pi} n^2 (f^* f_1^* - f f_1) c_r \sigma d\Omega d\mathbf{c}_1. \end{aligned} \quad (3.22)$$

Both f and Q refer to molecules of class \mathbf{c} and the moment equation is obtained by integrating over all classes of molecule. Since Q is either a constant or a function of \mathbf{c} only, it may be taken within the derivative in the first term. The required integral of this term is, therefore,

$$\int_{-\infty}^{\infty} \frac{\partial}{\partial t}(nQf) d\mathbf{c}$$

or, using eqn (3.3),

$$\frac{\partial}{\partial t}(n\bar{Q}). \quad (3.23)$$

Both \mathbf{c} and Q may be taken inside the derivative in the second term of eqn (3.22), the integral becoming

$$\int_{-\infty}^{\infty} \nabla \cdot (n \mathbf{c} Q f) d\mathbf{c}.$$

or

$$\nabla \cdot (n \overline{\mathbf{c} Q}). \quad (3.24)$$

The reason why \mathbf{c} may be taken inside the derivative in eqn (3.22) is that the dependent variable in the Boltzmann equation is the value of the distribution function for this particular class of molecule. Therefore, while f is a function of \mathbf{r} and t , \mathbf{c} and Q may be regarded as being independent of \mathbf{r} and t in eqn (3.22). However, the averages of \mathbf{c} and Q are established

through the distribution function f and must be treated as functions of \mathbf{r} and t . The integral in the third term in eqn (3.22) is

$$\int_{-\infty}^{\infty} \mathbf{Q} \cdot \mathbf{F} \cdot \frac{\partial}{\partial \mathbf{c}} (nf) d\mathbf{c},$$

which may be written

$$\int_{-\infty}^{\infty} \mathbf{F} \cdot \frac{\partial}{\partial \mathbf{c}} (n \mathbf{Q} f) d\mathbf{c} - \int_{-\infty}^{\infty} \mathbf{F} \frac{\partial \mathbf{Q}}{\partial \mathbf{c}} n f d\mathbf{c}.$$

It is assumed that \mathbf{F} is independent of \mathbf{c} and, since $f = 0$ or $f \rightarrow 0$ as $\mathbf{c} \rightarrow \infty$, the first integral vanishes and the second becomes

$$-n \mathbf{F} \cdot \frac{\partial \mathbf{Q}}{\partial \mathbf{c}}. \quad (3.25)$$

The integral of the term on the right-hand side of eqn (3.22) is called the *collision integral* and is denoted by $\Delta[\mathbf{Q}]$, i.e.

$$\Delta[\mathbf{Q}] = \int_{-\infty}^{\infty} \int_{-\infty}^{\infty} \int_0^{4\pi} n^2 \mathbf{Q} (f^* f_1^* - f f_1) c_r \sigma d\Omega d\mathbf{c}_1 d\mathbf{c}. \quad (3.26)$$

Eqns (3.23)–(3.26) may now be brought together to write the moment equation for \mathbf{Q} as

$$\frac{\partial}{\partial t} (n \bar{\mathbf{Q}}) + \nabla \cdot (n \bar{\mathbf{c}} \bar{\mathbf{Q}}) - n \mathbf{F} \cdot \frac{\partial \bar{\mathbf{Q}}}{\partial \mathbf{c}} = \Delta[\mathbf{Q}]. \quad (3.27)$$

This equation may also be called the *transfer equation* or the *equation of change*.

Two symmetries are associated with the collision term and they lead to several alternative forms of $\Delta[\mathbf{Q}]$. These clarify the physical meaning of this term and will be required for future applications. The first symmetry is between the collision partners and means that $\Delta[\mathbf{Q}]$ is unchanged if \mathbf{c} and \mathbf{c}_1 are interchanged and \mathbf{Q} , which represents the value of \mathbf{Q} at \mathbf{c} , is interchanged with the value \mathbf{Q}_1 at \mathbf{c}_1 . Similarly, \mathbf{c}^* and \mathbf{Q}^* may be interchanged with \mathbf{c}_1^* and \mathbf{Q}_1^* . The second symmetry is based in the existence of inverse collisions and is between the pre-collision and post-collision velocities. It enables \mathbf{Q} and \mathbf{Q}^* or \mathbf{Q}_1 and \mathbf{Q}_1^* to be interchanged, as long as \mathbf{c}_1 , \mathbf{c} , f_1 , and f are interchanged with \mathbf{c}_1^* , \mathbf{c}^* , f_1^* , and f^* . Advantage is taken of eqn (3.16) to avoid replacing $d\mathbf{c} d\mathbf{c}_1$ by $d\mathbf{c} d\mathbf{c}_1^*$. Application of the first symmetry to eqn (3.26) yields

$$\Delta[\mathbf{Q}] = \int_{-\infty}^{\infty} \int_{-\infty}^{\infty} \int_0^{4\pi} n^2 Q_1 (f_1^* f^* - f_1 f) c_r \sigma d\Omega d\mathbf{c} d\mathbf{c}_1. \quad (3.26a)$$

The second symmetry may then be applied to this equation to give

$$\Delta [Q] = \int_{-\infty}^{\infty} \int_{-\infty}^{\infty} \int_0^{4\pi} n^2 Q_1^* (f_1 f - f_1^* f^*) c_r \sigma d\Omega dc dc_1, \quad (3.26b)$$

and a second application of the first symmetry gives

$$\Delta [Q] = \int_{-\infty}^{\infty} \int_{-\infty}^{\infty} \int_0^{4\pi} n^2 Q^* (ff_1 - f^* f_1^*) c_r \sigma d\Omega dc dc_1. \quad (3.26c)$$

Eqns (3.26), (3.26a), (3.26b), and (3.26c) may then be summed and the resultant equation divided by four, to give

$$\Delta [Q] = \frac{1}{4} \int_{-\infty}^{\infty} \int_{-\infty}^{\infty} \int_0^{4\pi} n^2 (Q + Q_1 - Q^* - Q_1^*) (ff_1 - f^* f_1^*) c_r \sigma d\Omega dc dc_1 \quad (3.26d)$$

Also, eqn (3.26) may be written

$$\Delta [Q] = \int_{-\infty}^{\infty} \int_{-\infty}^{\infty} \int_0^{4\pi} n^2 Q f^* f_1^* c_r \sigma d\Omega dc_1 dc - \int_{-\infty}^{\infty} \int_{-\infty}^{\infty} \int_0^{4\pi} n^2 Q f f_1 c_r \sigma d\Omega dc_1 dc,$$

and application of the second symmetry to the first term on the right-hand side converts $Q f^* f_1^*$ to $Q^* f f_1$. Therefore,

$$\Delta [Q] = \int_{-\infty}^{\infty} \int_{-\infty}^{\infty} \int_0^{4\pi} n^2 (Q^* - Q) f f_1 c_r \sigma d\Omega dc dc_1 dc. \quad (3.26e)$$

A similar transformation of eqn (3.26) yields

$$\Delta [Q] = \int_{-\infty}^{\infty} \int_{-\infty}^{\infty} \int_0^{4\pi} n^2 (Q_1^* - Q_1) f_1 f c_r \sigma d\Omega dc dc_1 dc. \quad (3.26f)$$

Finally, eqns (3.26e) and (3.26f) may be summed and the resulting equation halved, to give

$$\Delta [Q] = \frac{1}{2} \int_{-\infty}^{\infty} \int_{-\infty}^{\infty} \int_0^{4\pi} n^2 (Q^* + Q_1^* - Q - Q_1) f_1 f c_r \sigma d\Omega dc dc_1. \quad (3.26g)$$

The physical meaning of $\Delta [Q]$ is most readily apparent from eqn (3.26g) since $(Q^* + Q_1^* - Q - Q_1)$ represents the change in the quantity Q as the result of a collision of class $c, c_1 \rightarrow c^*, c_1^*$. This change is summed over all classes of collision and halved to allow for the double counting of collisions in the integration. That the integration is equivalent to summing over all collisions is readily seen if we note that

$$\frac{1}{2} \int_{-\infty}^{\infty} \int_{-\infty}^{\infty} \int_0^{4\pi} n^2 f_1 f c_r \sigma d\Omega dc dc_1 = \frac{1}{2} \int_{-\infty}^{\infty} \int_{-\infty}^{\infty} \sigma_T c_r n^2 f_1 f dc dc_1 = \frac{1}{2} n^2 \overline{\sigma_T c_r},$$

which is in agreement with eqn (1.11) for the total number of collisions per unit time per unit volume of gas. The moment or transfer equation with the collision term in the form of eqn (3.26g) can therefore be derived independently of the Boltzmann equation and was, in fact, first derived by Maxwell (1867). The form of $\Delta[Q]$ in eqn (3.26d) is more closely allied to the Boltzmann formulation and states simply that the change in Q as a result of the inverse collisions is exactly equal to the change in Q as a result of the direct collisions.

If the quantity Q is either the mass m , momentum mc , or energy $\frac{1}{2}mc^2$ of a molecule, the conservation of these quantities in collisions requires that $Q+Q_1-Q^*-Q_1^*=0$. Eqns. (3.26d) and (3.26g) then show that the collision integral $\Delta[Q]$ is zero, as would be expected from the physical meaning of the integral. The quantities m , mc , and $\frac{1}{2}mc^2$ are called *collisional invariants*, while any that satisfy the condition $Q+Q_1-Q^*-Q_1^*=0$ are called *summational invariants*. It can be shown (e.g. Harris (1971) §4.2) that the collisional invariants, or linear combinations of them, are the only summational invariants. Therefore, if Q is a summational invariant, the collision integral $\Delta[Q]$ is 0 and Q can be written

$$Q = A \frac{1}{2}mc^2 + B.mc + C, \quad (3.28)$$

where A , B , and C are constants.

The collision integral is zero in the three equations for the collisional invariants and the averages on the left-hand side of the equations can be expressed in terms of the macroscopic gas properties. The three equations are the *conservation equations* of gas dynamics. First, the equation for the *conservation of mass* is obtained by setting $Q = m$ in eqn (3.27), to give

$$\frac{\partial}{\partial t} (nm) + \nabla \cdot (nm\bar{c}) = 0 \quad (3.29)$$

or, using eqns (1.13) and (1.21),

$$\frac{\partial \rho}{\partial t} + \nabla \cdot (\rho \mathbf{c}_0) = 0. \quad (3.30)$$

It is convenient to introduce the *substantial derivative*

$$\frac{D}{Dt} \equiv \frac{\partial}{\partial t} + \mathbf{c}_0 \cdot \nabla \equiv \frac{\partial}{\partial t} + u \frac{\partial}{\partial x} + v \frac{\partial}{\partial y} + w \frac{\partial}{\partial z} \quad (3.31)$$

to denote differentiation following the motion of the fluid element. The equation for the *conservation of mass*, or continuity equation, then becomes

$$\frac{D\rho}{Dt} = -\rho \nabla \cdot \mathbf{c}_0. \quad (3.32)$$

Next, the equation for the *conservation of momentum* or *equation of motion* is obtained by setting $Q = mc$ in eqn (3.27). This is the vector equation

$$\frac{\partial}{\partial t} (\rho\bar{c}) + \nabla \cdot (\rho\bar{c}\bar{c}) - \rho\mathbf{F} = 0. \quad (3.33)$$

But eqns (1.21) and (1.22) show that

$$\overline{\mathbf{c}\mathbf{c}} = \overline{(\mathbf{c}' + \mathbf{c}_0)(\mathbf{c}' + \mathbf{c}_0)} = \overline{\mathbf{c}'\mathbf{c}'} + \mathbf{c}_0\mathbf{c}_0$$

and eqn (3.33) may be written

$$\rho \frac{\partial \mathbf{c}_0}{\partial t} + \mathbf{c}_0 \frac{\partial \rho}{\partial t} + \mathbf{c}_0 \nabla \cdot (\rho \mathbf{c}_0) + \rho (\mathbf{c}_0 \cdot \nabla) \mathbf{c}_0 + \nabla \cdot (\rho \overline{\mathbf{c}'\mathbf{c}'}) - \rho \mathbf{F} = 0.$$

The continuity equation (3.30) enables the second and third terms to be removed, eqn (3.31) enables the first and fourth terms to be combined as a substantial derivative, and eqn (1.20) enables the fifth term to be written in terms of the pressure and the viscous stress tensor, i.e.

$$\rho \frac{D\mathbf{c}_0}{Dt} = -\nabla p + \nabla \cdot \boldsymbol{\tau} + \rho \mathbf{F}. \quad (3.34)$$

The vector and tensor quantities are clarified if we also write the momentum equation in the x -direction in Cartesian coordinates. This is

$$\rho \frac{Du_0}{Dt} = -\frac{\partial p}{\partial x} + \frac{\partial \tau_{xx}}{\partial x} + \frac{\partial \tau_{xy}}{\partial y} + \frac{\partial \tau_{xz}}{\partial z} + \rho F_x.$$

Finally, Q may be set equal to $\frac{1}{2}mc^2$ in eqn (3.27) to give the equation for the *conservation of energy* as

$$\frac{\partial}{\partial t} \left(\frac{1}{2} \rho \overline{c^2} \right) + \nabla \cdot \left(\frac{1}{2} \rho \overline{\mathbf{c}'\mathbf{c}'} \right) - \rho \mathbf{c}_0 \cdot \mathbf{F} = 0. \quad (3.35)$$

The averages over the molecular velocities may again be converted to averages over the peculiar and stream velocities, to give

$$\overline{c^2} = \overline{c'^2} + c_0^2$$

and

$$\overline{\mathbf{c}\mathbf{c}^2} = \overline{\mathbf{c}'\mathbf{c}'^2} + \mathbf{c}_0 \left(\overline{c'^2} + c_0^2 \right) + 2u_0 \overline{\mathbf{c}'u'} + 2v_0 \overline{\mathbf{c}'v'} + 2w_0 \overline{\mathbf{c}'w'}.$$

The macroscopic quantities may then be introduced and the final result is

$$\rho \frac{De}{Dt} = -p \nabla \cdot \mathbf{c}_0 + \Phi - \nabla \cdot \mathbf{q}. \quad (3.36)$$

The quantity Φ is called the *dissipation function* and may be written in Cartesian coordinates as

$$\begin{aligned} \Phi = & \tau_{xx} \frac{\partial u}{\partial x} + \tau_{yy} \frac{\partial v}{\partial y} + \tau_{zz} \frac{\partial w}{\partial z} + \tau_{xy} \left(\frac{\partial u}{\partial y} + \frac{\partial v}{\partial x} \right) \\ & + \tau_{yz} \left(\frac{\partial v}{\partial z} + \frac{\partial w}{\partial y} \right) + \tau_{zx} \left(\frac{\partial w}{\partial x} + \frac{\partial u}{\partial z} \right). \end{aligned} \quad (3.37)$$

Since the momentum equation (3.34) is a vector equation, the equations for the conservation of mass, momentum, and energy constitute five equations. The dependent variables include the three velocity components and, if the

equation of state is taken into account, two of the three thermodynamic properties p , ρ , and T . The viscous stress tensor τ contains nine components but, because of its symmetry and the relationship of the sum of the diagonal components to the pressure, it contributes only five dependent variables. Finally, the heat flux vector q contributes a further three dependent variables. The conservation equations therefore contain a total of thirteen dependent variables and do not form a determinate set. The *inviscid* case with τ and q both equal to zero does result in a determinate set, and these are called the *Euler equations*.

The application of moment equations other than the conservation equations generally requires the evaluation of the collision integral $\Delta[Q]$. This process may be illustrated by the special case of $Q = u^2$ for Maxwell molecules. The substitution of this value of Q into eqn (3.26e), together with eqn (2.40) for the cross-section of Maxwell molecules, yields

$$\Delta[u^2] = \int_{-\infty}^{\infty} \int_{-\infty}^{\infty} \int_0^{2\pi} \int_0^{\infty} n^2 (u^{*2} - u^2) f f_1 W_0 \left(\frac{2\kappa}{m} \right)^{1/2} dW_0 d\epsilon d\mathbf{c} d\mathbf{c}'.$$

The advantage of Maxwell molecules is that the molecular velocities appear only in the term $u^{*2} - u^2$, which may be written as $(u^* - u)^2 + 2u(u^* - u)$. Then with u and u_1 identified with u_r and u_1 in eqns (2.4) and (2.5), and using eqn (2.22),

$$u^* - u = \frac{1}{2}(u_r - u_r^*) = \frac{1}{2}\{(1 - \cos\chi)u_r - \sin\chi \sin\epsilon(v_r^2 + w_r^2)^{1/2}\}.$$

Therefore,

$$u^{*2} - u^2 = \frac{1}{4}\{(1 - \cos\chi)^2 u_r^2 - 2(1 - \cos\chi)u_r \sin\chi \sin\epsilon(v_r^2 + w_r^2)^{1/2} + \sin^2\chi \sin^2\epsilon(v_r^2 + w_r^2)\} + u\{(1 - \cos\chi)u_r - \sin\chi \sin\epsilon(v_r^2 + w_r^2)^{1/2}\}.$$

The integration over ϵ may be carried out first, to give,

$$\int_0^{2\pi} (u^{*2} - u^2) d\epsilon = \pi(u_r^2 + 2u u_r)(1 - \cos\chi) - \frac{1}{4}\pi(3u_r^2 - c_r^2)\sin^2\chi.$$

Eqn (2.3) shows that $u_r^2 + 2uu_r = u_1^2 - u^2$ and, since u and u_1 are described by the same distribution, this term disappears in the integration over velocity space. The remaining term contains only relative velocities, and the result is independent of whether these are expressed as differences between velocities or peculiar velocities and, therefore, $\Delta[u^2] = \Delta[u'^2]$. Eqns (2.3) and (1.22) give $u_r^2 = u_1^2 - 2u'_1 u' + u'^2$ and the double integration over velocity space yields $2\overline{u'^2}$. A similar result holds for c_r^2 , and the collision integral becomes

$$\Delta[u^2] = -\frac{3\pi}{2} \left(\frac{2\kappa}{m} \right)^{1/2} n^2 (\overline{u'^2} - \overline{c'^2}/3) \int_0^{\infty} \sin^2\chi W_0 dW_0.$$

Finally, from eqns (1.25) and (1.26),

$$\Delta[u^2] = -\frac{3\pi}{2} A_2(5) \left(\frac{2\kappa}{m}\right)^{1/2} \frac{n}{m} \tau_{xx}, \quad (3.38)$$

where

$$A_2(5) = \int_0^\infty \sin^2 \chi W_0 dW_0$$

for Maxwell molecules. $A_2(5)$ is a pure number and its value may be obtained through eqn (2.39) as 0.436.

The collision integral $\Delta[u^2]$ is also readily evaluated for the special case of the VHS model in which the diameter is inversely proportional to the square root of the relative speed, or $v = 1/2$. As with the Maxwell gas, all molecules in this gas have the same collision probability. Eqn (2.30) for the differential cross-section of hard sphere molecules may be combined with eqn (2.34) and substituted into eqn (3.26e). Then, if it is noted that $d\Omega = \sin \chi d\chi d\varepsilon d\epsilon d\epsilon'$, we have

$$\Delta[u^2] = \int_{-\infty}^{\infty} \int_{-\infty}^{\infty} \int_0^{\infty} \int_0^{\pi} n^2 (u^{*2} - u^2) f f_1 (c_{r,\text{ref}} d_{\text{ref}}^2 / 4) \sin \chi d\chi d\varepsilon d\epsilon d\epsilon'.$$

The integration over ε may be carried out in exactly the same manner as in the Maxwell gas case, so that

$$\Delta[u^2] = -\frac{3\pi}{2} n^2 (\overline{u'^2} - \overline{c'^2}/3) \frac{c_{r,\text{ref}} d_{\text{ref}}^2}{4} \int_0^\pi \sin^3 \chi d\chi,$$

and the final result is

$$\Delta[u^2] = \frac{1}{2} c_{r,\text{ref}} d_{\text{ref}}^2 (n/m) \tau_{xx}. \quad (3.39)$$

3.4 The H -theorem and equilibrium

Consider a spatially homogeneous volume of a simple dilute monatomic gas that is free of any external force. The Boltzmann equation (3.20) may be simplified for such a gas since the number density n is a constant, spatial derivatives $\partial/\partial r$ are zero, and the external force F is zero. The equation becomes

$$\frac{\partial f}{\partial t} = n \int_{-\infty}^{\infty} \int_0^{4\pi} (f^* f_1^* - f f_1) c_r \sigma d\Omega d\epsilon_1. \quad (3.40)$$

Over a small time interval, f changes to $f + \Delta f$ and the fractional change is $\Delta f/f$ or $\Delta(\ln f)$. Boltzmann's H -function is the mean value of $\ln(nf)$, i.e.

$$H = \overline{\ln(nf)}$$

or, using eqn(3.3),

$$H = \int_{-\infty}^{\infty} f \ln(nf) dc. \quad (3.41)$$

The quantity Q in the moment equation (3.27) may then be set equal to $\ln(nf)$ and, with the collision integral $\Delta[Q]$ in the form given by eqn (3.26d), we have

$$\begin{aligned} \frac{\partial H}{\partial t} &= \frac{n}{4} \int_{-\infty}^{\infty} \int_{-\infty}^{\infty} \int_0^{4\pi} (\ln f + \ln f_1 - \ln f^* - \ln f_1^*) (f^* f_1^* - ff_1) c_r \sigma d\Omega dc dc_1 \\ &= \frac{n}{4} \int_{-\infty}^{\infty} \int_{-\infty}^{\infty} \int_0^{4\pi} \ln(f f_1 / f^* f_1^*) (f^* f_1^* - ff_1) c_r \sigma d\Omega dc dc_1. \end{aligned} \quad (3.42)$$

If $\ln(f f_1 / f^* f_1^*)$ is positive, then $(f^* f_1^* - ff_1)$ must be negative and vice versa. The integral on the right hand side of eqn (3.42) is, therefore, either negative or zero and H can never increase, i.e.

$$\frac{\partial H}{\partial t} < 0. \quad (3.43)$$

This result is known as Boltzmann's H -theorem.

The question which now arises is whether H decreases without limit to $-\infty$, or tends to a finite value and thereafter remains constant. Now, as $c \rightarrow \infty$, $f \rightarrow 0$ and $\ln f \rightarrow -\infty$, and it appears that the integral for H in eqn (3.41) may diverge. However, since the energy of the gas is finite, the integral

$$\int_{-\infty}^{\infty} f c^2 dc$$

must converge. Therefore, for H to diverge, the approach of f to 0 would be more rapid than that of $\exp(-c^2)$ to 0 and, since $\exp(-x^2)x^n \rightarrow 0$ as $x \rightarrow \infty$ for all values of n , H must converge. Therefore, for any initial distribution of molecules in velocity space, the distribution will alter with time in such a way that H decreases monotonically to a finite lower bound. At subsequent times,

$$\frac{\partial H}{\partial t} = 0$$

and eqn (3.42) shows that this requires

$$f^* f_1^* - ff_1 = 0 \quad (3.44)$$

or, equivalently,

$$\ln f + \ln f_1 = \ln f^* + \ln f_1^*. \quad (3.45)$$

A comparison of eqns (3.45) and (3.40) shows that the stationary state for H is also a stationary state for f . We therefore have an *equilibrium state* in which the probable number of molecules in any element of velocity space remains constant with time.

Eqn (3.45) shows that, in the equilibrium state, $\ln f$ is a summational invariant. Therefore, from eqn (3.28), the necessary and sufficient condition for equilibrium is that

$$\ln f = A \frac{1}{2} m c^2 + \mathbf{B} \cdot \mathbf{m} \mathbf{c} + C. \quad (3.46)$$

This equation may be written in terms of the thermal velocity components as

$$\ln f = A \frac{1}{2} m c'^2 + m(\mathbf{A} \mathbf{c}_0 + \mathbf{B}) \cdot \mathbf{c}' + A \frac{1}{2} m c_0^2 + \mathbf{B} \cdot \mathbf{m} \mathbf{c}_0 + C.$$

Since there can be no preferred direction in the equilibrium gas, the distribution must be isotropic. This requires that the coefficient of \mathbf{c}' be zero, or

$$\mathbf{B} = -\mathbf{A} \mathbf{c}_0.$$

Therefore,

$$\ln f = \frac{1}{2} A m c'^2 - \frac{1}{2} A m c_0^2 + C,$$

or,

$$f = \exp(\frac{1}{2} A m c'^2 - \frac{1}{2} A m c_0^2 + C).$$

Since f is bounded, the coefficient of c'^2 must be negative and, for convenience, we introduce a new constant by setting $\frac{1}{2} A m = -\beta^2$. We therefore have

$$f = \exp(C + \beta^2 c_0^2) \exp(-\beta^2 c'^2).$$

The constant C may be eliminated through the normalization condition expressed in eqn (3.2). This requires that

$$\int_{-\infty}^{\infty} f d\mathbf{c} = \exp(C + \beta^2 c_0^2) \int_{-\infty}^{\infty} \exp(-\beta^2 c'^2) d\mathbf{c}' = 1.$$

But,

$$\int_{-\infty}^{\infty} \exp(-\beta^2 c'^2) d\mathbf{c}' = \int_{-\infty}^{\infty} \int_{-\infty}^{\infty} \int_{-\infty}^{\infty} \exp\{-\beta^2(u'^2 + v'^2 + w'^2)\} du' dv' dw'$$

$$= \int_{-\infty}^{\infty} \exp(-\beta^2 u'^2) du' \int_{-\infty}^{\infty} \exp(-\beta^2 v'^2) dv' \int_{-\infty}^{\infty} \exp(-\beta^2 w'^2) dw'.$$

The list of standard integrals in Appendix B shows that each component integral is $\pi^{1/2}/\beta$, so that

$$\exp(C + \beta^2 c_0^2) = \beta^3/\pi^{3/2}.$$

Therefore, the final result for the *equilibrium* or *Maxwellian distribution function* f_0 is

$$f_0 = (\beta^3/\pi^{3/2}) \exp(-\beta^2 c'^2). \quad (3.47)$$

The constant β may be related to the temperature of the gas. Eqns (1.29), (3.4), and (3.47) show that

$$3RT/2 = \frac{1}{2}\overline{c'^2} = \frac{\beta^3}{2\pi^{3/2}} \int_{-\infty}^{\infty} c'^2 \exp(-\beta^2 c'^2) dc$$

or again using the standard integrals of Appendix B,

$$\beta^2 = (2RT)^{-1} = m/(2kT). \quad (3.48)$$

Since we are dealing with an equilibrium gas, the translational temperature T_{tr} calculated through eqn (1.29) is equal to the thermodynamic temperature T and the subscript has been dropped. Substitution of eqn (3.48) into (3.47) gives

$$f_0 = \{m/(2\pi kT)\}^{3/2} \exp[-mc'^2/(2kT)] \quad (3.47a)$$

as an alternative definition of f_0 .

In the case of a gas mixture in equilibrium, it can be shown (Chapman and Cowling 1952, p. 84) that the distribution function of species p follows directly as

$$f_{0,p} = \{m_p/(2\pi kT)\}^{3/2} \exp[-m_p c_p'^2/(2kT)]. \quad (3.49)$$

The Maxwellian distribution applies also to the translational velocities of diatomic and polyatomic molecules. This result has been proven for the special case of rough-sphere molecules (Chapman and Cowling 1970, §11.4) using an extension of the method that has been applied here to monatomic molecules. The collision mechanics of more realistic models are sufficiently complex to rule out this approach. However, if it is assumed that, for each collision, a collision with the velocity components reversed is equally likely, the generalized Boltzmann equation leads to a derivation that is applicable to all molecular models (Chapman and Cowling 1970, §11.3). Moreover, for equilibrium situations, the methods of statistical mechanics are available and provide proofs that are more general than those from kinetic theory.

3.5 The Chapman-Enskog theory

The Chapman-Enskog method provides a solution of the Boltzmann equation for a restricted set of problems in which the distribution function f is perturbed by a small amount from the equilibrium Maxwellian form. It is assumed that the distribution function may be expressed in the form of the power series

$$f = f^{(0)} + \varepsilon_0 f^{(1)} + \varepsilon_0^2 f^{(2)} + \dots, \quad (3.50)$$

where ε_0 is a parameter which may be regarded as a measure of either the mean collision time or the Knudsen number. The first term $f^{(0)}$ is the Maxwellian distribution f_0 for an equilibrium gas, and an alternative form of the expression is

$$f = f_0 (1 + \Phi_1 + \Phi_2 + \dots). \quad (3.51)$$

The equilibrium distribution function constitutes the known first-order solution of this equation and the second-order solution requires the determination of the parameter Φ_1 .

Solutions of the Boltzmann equation for

$$f = f_0 (1 + \Phi_1) \quad (3.52)$$

were obtained independently by Enskog and Chapman, and these form the subject matter of the classical work by Chapman and Cowling (1952). For a simple gas, Φ_1 depends only on the density, stream velocity, and temperature of the gas so that the resulting solution constitutes a *normal solution* of the Boltzmann equation. Since f_0 satisfies the equations

$$\int_{-\infty}^{\infty} f \, dc = 1,$$

$$\int_{-\infty}^{\infty} c f \, dc = c_0,$$

and

$$\int_{-\infty}^{\infty} c^2 f \, dc = 3RT,$$

Φ_1 must be such that

$$\int_{-\infty}^{\infty} \Phi_1 f_0 \, dc = 0,$$

$$\int_{-\infty}^{\infty} c \Phi_1 f_0 \, dc = 0,$$

and

$$\int_{-\infty}^{\infty} c^2 \Phi_1 f_0 \, dc = 0. \quad (3.53)$$

It may further be shown that Φ_1 must have the form

$$\Phi_1 = -\frac{1}{n} A \mathbf{c}' \cdot \frac{\partial}{\partial r} (\ln T) + B \mathbf{c}'^0 \mathbf{c}' : \frac{\partial \mathbf{c}_0}{\partial r} \quad (3.54)$$

where A and B are functions of T and \mathbf{c}' . The superscript 0 above a tensor indicates that the sum of the diagonal components is zero. In the component or subscript notation of Chapter 1,

$$c'_i{}^0 c'_j = c'_i c'_j - c'^2 \delta_{ij}/3.$$

The double product of two tensors is a scalar quantity which may be written in the subscript notation as

$$c'_i{}^0 c'_j \frac{\partial c_{0i}}{\partial x_j},$$

or in full Cartesian component form as

$$(u'^2 - c'^2/3) \frac{\partial u_0}{\partial x} + u' v' \frac{\partial u_0}{\partial y} + u' w' \frac{\partial v_0}{\partial z} + v' u' \frac{\partial v_0}{\partial x} + (v'^2 - c'^2/3) \frac{\partial v_0}{\partial y} \\ + v' w' \frac{\partial v_0}{\partial z} + w' u' \frac{\partial w_0}{\partial x} + w' v' \frac{\partial w_0}{\partial y} + (w'^2 - c'^2/3) \frac{\partial w_0}{\partial z},$$

$$\text{where } c'^2 = u'^2 + v'^2 + w'^2.$$

Eqns (3.52) and (3.54) may be combined with eqns (1.26) and (1.33) to give expressions for the shear stress tensor and the heat flux vector as linear functions of the velocity and temperature gradients, respectively. The coefficients of the gradients may be identified with the familiar coefficients of viscosity and heat conduction. The coefficients A and B of eqn (3.54) are usually obtained as series of Sonine polynomials. Since the word 'order' has already been applied to the specification of the number of terms in eqn (3.51), the solution involving n terms of the Sonine polynomial series is usually referred to as the ' n th approximation'. The molecular model enters the analysis and it can be shown (Vincenti and Kruger 1965, Chap. X, §7) that the first approximation to the coefficient of viscosity μ for a monatomic gas is

$$\mu = \frac{(5/8)(\pi m k T)^{1/2}}{\int_0^\infty [m/(4kT)]^4 \int_{c_r}^7 \sigma_\mu \exp\{-mc_r^2/(4kT)\} dc_r}. \quad (3.55)$$

The first approximation to the coefficient of heat conduction K is related to the coefficient of viscosity by

$$K = (15/4)(k/m)\mu = (15/4)R\mu, \quad (3.56)$$

so that the Prandtl number in a monatomic gas, for which the specific heat at constant pressure c_p is equal to $5R/2$, is

$$(Pr) = \mu c_p / K = 2/3. \quad (3.57)$$

The viscosity cross-section σ_μ for a hard sphere gas is given by eqn (2.32). Eqn (3.55) is then readily evaluated to give the coefficient of viscosity in a hard sphere gas as

$$\mu = (5/16)(\pi m k T)^{1/2} / \sigma_T = (5/16)(R T / \pi)^{1/2} (m/d^2). \quad (3.58)$$

The diameter of a hard sphere gas that has a coefficient of viscosity μ_{ref} at temperature T_{ref} is therefore

$$d = \{(5/16)(m k T_{ref} / \pi)^{1/2} / \mu_{ref}\}^{1/2} \quad (3.59)$$

and is, of course, independent of the relative velocity and relative translational energy.

For VHS molecules, the cross-section is inversely proportional to a power of the relative speed. The definition can be extended to include the total cross-section and the relative translational energy, i.e.

$$\sigma_T / \sigma_{T,ref} = (d/d_{ref})^2 = (c_r/c_{r,ref})^{-2v} = (E_t/E_{t,ref})^{-v}, \quad (3.60)$$

where v is a constant and $\sigma_{T,ref}$ and d_{ref} are the total cross-section and diameter that apply when the relative speed is $c_{r,ref}$. As noted in §2.6, the viscosity cross-section is still given by eqn (2.32), and eqn (3.55) becomes

$$\mu = \frac{(15/8)(\pi m k)^{1/2} (4k/m)^v T^{1/2+v}}{\Gamma(4-v) \sigma_{T,ref} c_{r,ref}^{2v}}. \quad (3.61)$$

The VHS cross-section defined by eqn (3.60) therefore leads to a coefficient of viscosity proportional to a fixed power of the temperature.

The evaluation of eqn (3.55) for the inverse power law model of §2.4 gives

$$\mu = \frac{5m(R T / \pi)^{1/2} (2m R T / \kappa)^{2/(\eta-1)}}{8A_2(\eta) \Gamma\{4 - 2/(\eta-1)\}}. \quad (3.62)$$

$A_2(\eta)$ is a numerical factor defined by

$$A_2(\eta) \equiv \int_0^\infty \sin^2 \chi W_0 dW_0$$

and for which Chapman and Cowling (1952) give the following values

η	5	7	9	11	15	21	∞
$A_2(\eta)$	0.436	0.357	0.332	0.319	0.309	0.307	0.333

While the coefficients of viscosity and heat conduction can be regarded as continuum gas properties, it will be found that an essential feature of a successful molecular model for rarefied gas flow studies is that it should reproduce the viscosity coefficient of the real gas, and also the temperature dependence of this coefficient. This is essentially an empirical observation, but some analytical support may be obtained from a comparison of the collision integral $\Delta[u^2]$ for Maxwell molecules (eqn (3.38)) with the same collision integral for VHS molecules with $v = 1/2$ (eqn (3.39)), when both of

these are expressed in terms of the coefficient of viscosity. The coefficient of viscosity in a Maxwell gas is obtained by setting $\eta = 5$ in eqn (3.62), to give

$$\mu = \frac{2kT}{3\pi A_2(5)} \left(\frac{m}{2\kappa}\right)^{1/2}. \quad (3.63)$$

The coefficient of viscosity in a VHS gas with $\nu = 1/2$ is, from eqn (3.61)

$$\mu = \frac{2kT}{\sigma_{T,\text{ref}} c_{r,\text{ref}}}. \quad (3.64)$$

The substitution of eqn (3.63) into eqn (3.38) and the substitution of eqn (3.64) into eqn (3.39) both lead to exactly the same result for the collision integral. This is

$$\Delta[u^2] = \frac{p}{m} \frac{\tau_{xx}}{\mu}. \quad (3.65)$$

Therefore, as long as the viscosity coefficients are matched, the collision integrals are identical. The matching of the viscosity coefficient means that the two models give the same result in the continuum limit. The equality of the collision integrals mean that they also give the same result in approximate methods, such as the Mott-Smith theory (§8.2) for shock wave structure, that employ this collision integral and apply over the full range of Knudsen number.

The inverse power law model and the VHS model both lead to a power law temperature dependence of the coefficient of viscosity. That is,

$$\mu \propto T^\omega. \quad (3.66)$$

where

$$\omega = 1/2 + \nu = 1/2(\eta + 3)/(\eta - 1). \quad (3.67)$$

For a gas that has a coefficient of viscosity proportional to T^ω and with the value μ_{ref} at temperature T_{ref} , eqns (3.60), (3.61), and (3.67) show that the molecular diameter is related to the relative translational energy in the collision by

$$d = \left(\frac{(15/8)(m/\pi)^{1/2} (k T_{\text{ref}})^\omega}{\Gamma(9/2 - \omega) \mu_{\text{ref}} E_t^{\omega - 1/2}} \right)^{1/2}. \quad (3.68)$$

Alternatively, the formulation could have been for the total cross-section as a function of either the magnitude of the relative velocity or the relative translational energy.

In the case of a gas mixture, the diameter may be calculated for each of the molecules in the collision and the total cross-section can be calculated from mean diameter, as was done for eqn (2.31). However, it is desirable to define separate values of σ_T and ω for the collisions between unlike molecules and, for this purpose, the values obtained from the diffusion coefficient may be more appropriate than those obtained from the viscosity coefficient.

The Chapman-Enskog first approximation to the diffusion coefficient in a binary gas mixture of species 1 and species 2 molecules is

$$D_{12} = \frac{(3/16)(2\pi k T/m_r)^{1/2}}{\{m_r/(2kT)\}^3 \int_0^\infty c_r^5 \sigma_M \exp\{-m_r c_r^2/(2kT)\} dc_r}. \quad (3.69)$$

The momentum cross-section was defined in eqn (2.29) and, for both the hard sphere and VHS models, it was shown to be equal to the total cross-section. This allows the expression for the diffusion coefficient to be evaluated for the VHS model in terms of the reference cross-section ($\sigma_{T,\text{ref}}$)₁₂ at the temperature T_{ref} , to give

$$D_{12} = \frac{(3/8) \pi^{1/2} (2k T/m_r)^{\omega_{12}}}{\Gamma(7/2 - \omega_{12}) n (\sigma_{T,\text{ref}})_{12} c_{r,\text{ref}}^{2(\omega_{12}-1/2)}}. \quad (3.70)$$

For the special case of a hard sphere gas, this simplifies to

$$D_{12} = \frac{3(2\pi k T/m_r)^{1/2}}{16n(\sigma_T)_{12}}. \quad (3.71)$$

If the cross-collisions in a binary gas mixture are specified by the value (D_{12})_{ref} of the diffusion coefficient at the reference temperature T_{ref} , the collision diameter is related to the relative translational energy E_t in the collision by

$$d_{12} = \left(\frac{(3/8)(2k T_{\text{ref}})^{\omega_{12}}}{\Gamma(7/2 - \omega_{12})(\pi m_r)^{1/2} n (D_{12})_{\text{ref}} (2E_t)^{\omega_{12}-1/2}} \right)^{1/2}. \quad (3.72)$$

A typical difference between this diameter and that defined by substituting the viscosity-based diameters of the individual species into eqn (2.31) is shown in Fig. 3.3. This is for a mixture of argon and helium and it is based on the values of the transport properties that are quoted in Chapman and Cowling (1970). If the hard sphere model is used in place of the VHS model, the constant diameters for argon and helium atoms are 3.66×10^{-10} m and 2.19×10^{-10} m, respectively. The effective diameter of the argon-helium pair from eqn (2.31) is 2.93×10^{-10} m, while the diffusion-based diameter is 2.62×10^{-10} m. Part of the discrepancy may be due to the fact that the viscosity and diffusion coefficients are the first approximation to the exact analytical values, and the correction that is introduced by the second approximation is much higher for the diffusion coefficient than for the viscosity coefficient. However, it is almost certain that the difference between the viscosity- and diffusion-based diameters is largely due to the incorrect ratio of the momentum cross-section to the diffusion cross section. The VSS model was introduced in order to correct this ratio and the preceding VHS results may be reformulated for the VSS model.

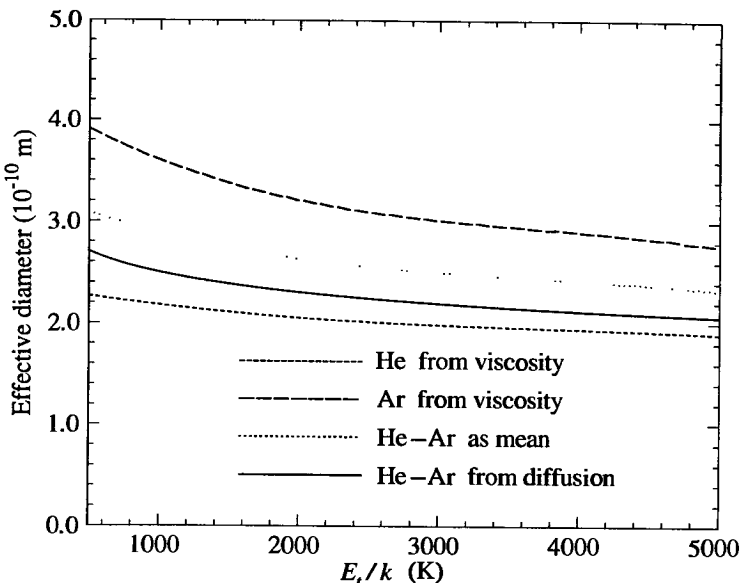


Fig. 3.3 Effective molecular diameters based on the VHS model for an argon-helium mixture.

When the variable soft sphere (or VSS) viscosity cross-section of eqn (2.37) is used in place of the VHS value in eqn (3.55), the coefficient of viscosity in a VSS gas becomes

$$\mu = \frac{5(\alpha+1)(\alpha+2)(\pi m k)^{1/2} (4k/m)^\omega T^{1/2+\omega}}{16\alpha\Gamma(4-\omega)\sigma_{T,\text{ref}} c_{r,\text{ref}}^{2\omega}}. \quad (3.73)$$

The viscosity-based diameter of a VSS molecule is, therefore,

$$d = \left(\frac{5(\alpha+1)(\alpha+2)(m/\pi)^{1/2} (k T_{\text{ref}})^\omega}{16\alpha\Gamma(9/2-\omega) \mu_{\text{ref}} E_t^{\omega-1/2}} \right)^{1/2}. \quad (3.74)$$

A similar procedure gives the diffusion coefficient in a VSS gas as

$$D_{12} = \frac{3(\alpha_{12}+1)\pi^{1/2}(2kT/m_r)^{\omega_{12}}}{16\Gamma(7/2-\omega_{12})n(\sigma_{T,\text{ref}})_{12} c_{r,\text{ref}}^{2(\omega_{12}-1/2)}}, \quad (3.75)$$

and the diffusion-based diameter becomes

$$d_{12} = \left(\frac{3(\alpha_{12}+1)(2kT_{\text{ref}})^{\omega_{12}}}{16\Gamma(7/2-\omega_{12})(\pi m_r)^{1/2} n(D_{12})_{\text{ref}} (2E_t)^{\omega_{12}-1/2}} \right)^{1/2}. \quad (3.76)$$

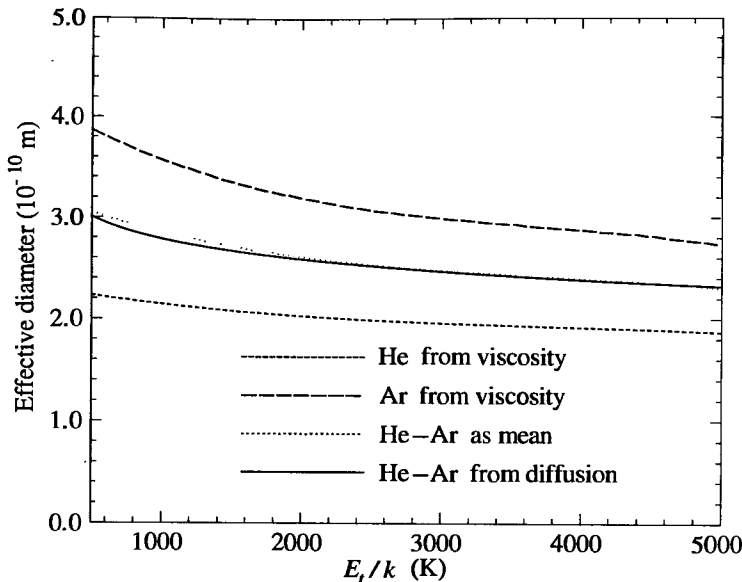


Fig. 3.4 Effective molecular diameters based on the VSS model for an argon–helium mixture.

Koura and Matsumoto (1992) have presented values of α for common gases, and their values for helium and argon are used in Fig. 3.4 to show the resulting VSS molecular diameters. The effective diameters based on the viscosity and diffusion coefficients are now consistent, and the VSS model is clearly superior to the VHS model.

Both the VHS and VSS models employ a power law relationship between the cross-section or diameter and the relative speed or collision energy. Alternative choices for the variation of cross-section with relative speed are available. A particularly interesting case due to Kušcer (private communication) is to set

$$\sigma_T = \sigma_{T,\infty} \{1 + 6kT_s/E_t\}, \quad (3.77)$$

where T_s is a reference temperature and $\sigma_{T,\infty}$ is the total cross-section in the limiting case of infinite c_r . The evaluation of eqn (3.55) for this cross-section gives

$$\mu = \frac{5}{16} \frac{(\pi mkT)^{1/2}}{\sigma_{T,\infty}} \frac{T}{T + T_s}. \quad (3.78)$$

This temperature dependence of the viscosity coefficient is identical to that in Sutherland's formula which reproduces (Chapman and Cowling 1970) the experimental data for many real gases over a considerable range of temperature. The Sutherland model is the combination of a hard sphere of diameter σ_∞ with a power law of attraction. The replacement of the hard

sphere component by the VHS model of eqn (3.60) leads to a VHS model that includes both attractive and repulsive power laws. The cross-section for this model is, therefore,

$$\sigma_T = \sigma_{T,\text{ref}} \left(\frac{E_{t,\text{ref}}}{E_t} \right)^{\omega-\frac{1}{2}} \left(1 + \frac{6kT_s}{E_t} \right), \quad (3.79)$$

However, while this model has two terms with separate exponents for E_t , the values of the exponents are restricted to $-(\omega - \frac{1}{2})$ and $-(\omega + \frac{1}{2})$. This combination cannot reproduce the behaviour of, for example, the Lennard-Jones model. It is preferable to employ the ‘generalized VHS’ (or GHS) model (Hassan and Hash, 1993) which has a cross-section defined by

$$\frac{\sigma_T}{s_0^2} = \alpha_1 \left(\frac{E_t}{\epsilon} \right)^{-\psi_1} + \alpha_2 \left(\frac{E_t}{\epsilon} \right)^{-\psi_2}. \quad (3.80)$$

Here, s_0 is the radius at which the potential is zero and ϵ is related to the maximum attractive force (or ‘well-depth’). These quantities may be visualized by reference to Fig. 1.3. ψ_1 and ψ_2 are, of course, the inverse power laws for the variation of the cross-section with the relative energy. These all have physical significance, while α_1 and α_2 are dimensionless numbers that are used to better fit the expression to the experimental database. While six parameters have been introduced, these could be reduced algebraically to four, and eqn (3.80) is essentially a four parameter model for the variation of collision cross-section with relative velocity. By contrast, the hard sphere model has zero parameters and the VHS model has one. Eqn (3.55) for the coefficient of viscosity may be evaluated for this model, to give

$$\mu = \frac{(5/8)(\pi m k T)^{\frac{1}{2}} / s_0^2}{(\alpha_1/3)\Gamma(4-\psi_1)(kT/\epsilon)^{-\psi_1} + (\alpha_2/3)\Gamma(4-\psi_2)(kT/\epsilon)^{-\psi_2}}. \quad (3.81)$$

It is not possible to define a reference cross-section or diameter for this model and, for it to be applied to a particular gas, numerical values must be supplied for all of the parameters in eqn (3.80). The existing database in the literature for the transport properties can be used for this purpose if the constants ψ_1 and ψ_2 in eqn (3.80) can be related to the power laws in a widely used model such as the Lennard-Jones model. The force between the molecules in the Lennard-Jones model is

$$F = \frac{\kappa}{r^\eta} - \frac{\kappa'}{r^{\eta'}}, \quad (3.82)$$

but the viscosity coefficient cannot be written in a closed form. However, it has been shown by Chapman and Cowling (1970, §10.41) that, if the power law of attraction is weak in comparison with that of repulsion (i.e. that η' is much less than η), an approximate expression for the coefficient of viscosity is

$$\mu = \mu_0 (1 + S/T^{(\eta-\eta')(\eta-1)})^{-1}. \quad (3.83)$$

Here, μ_0 is the coefficient of viscosity without the attractive component, and S is a function of the constants in the model. Eqn (3.81) can be written

$$\mu = \frac{15(\pi m k T)^{\psi_2} (k T / \epsilon)^{\psi_1}}{8\alpha_1 \Gamma(4-\psi_1) s_0^2} \left(1 + \frac{\alpha_2 \Gamma(4-\psi_2)}{\alpha_1 \Gamma(4-\psi_1)} (k T / \epsilon)^{\psi_1 - \psi_2} \right)^{-1}.$$

The power of T in the first part of this equation may be equated with that in eqn (3.66) and the power of T in the second part may be similarly equated with that in eqn (3.83). This gives two equations for ψ_1 and ψ_2 as functions of η and η' and these may be solved to give

$$\psi_1 = 2/(\eta - 1)$$

and

(3.84)

$$\psi_2 = (2 + \eta - \eta')/(\eta - 1).$$

Therefore, for the Lennard-Jones 6-12 potential with $\eta=13$ and $\eta'=7$, the power laws in the expression for the cross-section are $\psi_1=1/6$ and $\psi_2=2/3$. The parameters for a cross-collision in a gas mixture may be fitted to the diffusion coefficient. For the GHS model, this may be written

$$D_{12} = \frac{(3/8)(2\pi k T/m_r)^{1/2}/(s_0^2 n)}{\alpha_1 \Gamma(3-\psi_1) (k T / \epsilon)^{-\psi_1} + \alpha_2 \Gamma(3-\psi_2) (k T / \epsilon)^{-\psi_2}}. \quad (3.85)$$

The Chapman-Enskog distribution function is, itself, directly applicable to many problems in rarefied gas dynamics. The evaluation of the constants A and B in eqn (3.54) allows eqn (3.52) to be written

$$f = f_0 \left(1 - \frac{4K\beta^2}{5nk} (\beta^2 c'^2 - 5/2) \mathbf{c}' \cdot \frac{\partial(\ln T)}{\partial \mathbf{r}} - \frac{4\mu\beta^4}{\rho} \mathbf{c}'^0 \mathbf{c}' : \frac{\partial \mathbf{c}_0}{\partial \mathbf{r}} \right). \quad (3.86)$$

The physical implications of this equation are more readily appreciated if we consider the special case with the stream velocity in the x -direction and in which gradients exist only in the y -direction. Eqn (3.86) becomes

$$f = f_0 \left(1 - \frac{4K\beta^2 v'}{5nk} (\beta^2 c'^2 - 5/2) \frac{\partial(\ln T)}{\partial y} - \frac{4\mu s \beta^3 u' v'}{\rho} \frac{\partial(\ln u_0)}{\partial y} \right). \quad (3.87)$$

The Chapman-Enskog theory requires the two perturbation terms to be small compared with unity. This condition will be violated for sufficiently large thermal velocities, but the fraction of these falls as $\exp(-\beta^2 c'^2)$, and the overall validity of the distribution may be assessed on the assumption that the thermal speeds are of order $1/\beta$.

Additional terms in the Sonine polynomial expansions may be included to determine higher order approximations. Chapman and Cowling (1952) show that, in the second approximation, the coefficient of viscosity is increased by the factor $3(\eta-5)^2/\{2(\eta-1)(101\eta-113)\}$ and the coefficient of heat conduction by the factor $(\eta-5)^2/\{4(\eta-1)(11\eta-13)\}$. These are simple numerical constants that range from 0 in each case for Maxwell molecules to 0.0149 and 0.0227 for hard sphere molecules. However, additional terms are added in the second approximation to the distribution function and the numerical changes to this quantity are much greater. For example, consider a stationary gas with a temperature gradient in the y -direction. The first approximation is obtained by setting the final term in eqn (3.87) to zero. It may be shown that the second approximation is

$$f = f_0 \left(1 - \frac{4}{5} \frac{1}{45\eta^2 - 106\eta + 77} \{ -2(\eta-5)(\eta-1)\beta^4 c'^4 + (59\eta^2 - 190\eta + 147)\beta^2 c'^2 - 10(13\eta^2 - 37\eta + 28) \frac{K\beta^2 v'}{nk} \frac{\partial(\ln T)}{\partial y} \} \right), \quad (3.88)$$

where K now represents the second approximation including the above-mentioned numerical factor.

The viscous stress tensor and heat flux vector in a monatomic gas become, in the subscript notation,

$$\tau_{ij} = \mu \left(\frac{\partial u_i}{\partial x_j} + \frac{\partial u_j}{\partial x_i} \right) - \frac{2}{3} \delta_{ij} \mu \frac{\partial u_k}{\partial x_k}, \quad (3.89)$$

and

$$q_i = -K \frac{\partial T}{\partial x_i}, \quad (3.90)$$

respectively. The substitution of these relationships into the conservation equations makes them a determinate set and leads to the monatomic gas form of the *Navier–Stokes equations* of continuum gas dynamics.

Because the derivation of the above expressions for the transport properties has been based on only the first term in the Chapman–Enskog expansion of eqn (3.51), there are limits on the validity of the Navier–Stokes equations, as discussed in §1.2. The evaluation of the next term in this expansion (which should not be confused with the Sonine expansion) leads to a set of very complicated higher-order continuum equations, called the *Burnett equations*. There is now growing evidence (Fiscko and Chapman, 1989) that the use of the Burnett equations extends the validity of the continuum model to flows that are more rarefied than those for which the Navier–Stokes equations are valid. Moreover, it has been shown (Pham–Van-Diep et al. 1991) that, even when the local Knudsen number is such that the Navier–Stokes equations would be expected to lead to an ‘exact’ solution, the Burnett equations can provide a more accurate description of a gas flow.

The diffusion effects in a binary gas mixture are best explained through the diffusion equation. The diffusion velocity for a single component of the mixture was defined by eqn (1.45), and the *relative diffusion velocity* may be written (Chapman and Cowling 1970),

$$\mathbf{C}_1 - \mathbf{C}_2 = \frac{-n^2}{n_1 n_2} D_{12} \left(\nabla(n_1/n) + \frac{n_1 n_2 (m_2 - m_1)}{n \rho} \nabla(\ln p) - \frac{\rho_1 \rho_2}{\rho \rho} (\mathbf{F}_1 - \mathbf{F}_2) + k_T \nabla \ln T \right). \quad (3.91)$$

There are four terms within the large parentheses on the right-hand side of this equation. The first involves the *concentration gradient* in the gas and the diffusion acts to reduce this gradient. The other three terms are due to effects that act to set up concentration gradients. The second term is for *pressure diffusion* which causes heavy and light gases to move towards regions of high and low pressure, respectively. The third, or *forced diffusion*, term is present only when there is a force \mathbf{F} per unit mass that acts differentially on the molecules of the two species. The final term is due to *thermal diffusion* and introduces the thermal diffusion ratio k_T . Thermal diffusion is a subtle effect that depends on the differences in molecular size, and was discovered only in response to its prediction by the Chapman-Enskog theory. It causes the larger and (generally) heavier molecules to migrate towards the cooler regions of a flow. Pressure diffusion and thermal diffusion act in opposite directions in an expansion. However, they act in the same direction in the stagnation region of the hypersonic flow over a cold blunt body and the separation can be significant in the flow of a partly dissociated gas which necessarily involves large mass ratios. Forced diffusion can generally be neglected in neutral gases.

The Navier-Stokes equations are generally extended to include the concentration gradient effects that reduce concentration gradients when these are present as a result of boundary conditions or chemical reactions. However, the Navier-Stokes formulation almost always neglects the pressure and thermal diffusion effects that act to introduce concentration gradients. These are generated even when the boundaries involve a uniform composition and there are no chemical reactions. These separation effects can be significant in, for example, hypersonic gas flows and the omission of these terms can lead to significant errors.

As noted earlier, the correction to the first approximation to the diffusion coefficient due to the inclusion of extra terms in the Sonine polynomial expansion is much larger than the corresponding corrections to the viscosity and thermal conduction coefficients. As discussed by Chapman and Cowling (1970), the correction can be as high as 13%. Moreover, the corrections are not just numerical factors, but introduce the species number ratio or concentration as an additional parameter on which the diffusion coefficients depend. This latter point introduces additional difficulties to the continuum formulation through the Navier-Stokes equations.

References

- BOLTZMANN, L. (1872). *Sber. Akad. Wiss. Wien. Abt. II* **66**, 275.
- CHAPMAN, S. and COWLING, T.G. (1952). *The mathematical theory of non-uniform gases* (2nd edn). Cambridge University Press.
- CHAPMAN, S. and COWLING, T.G. (1970). *The mathematical theory of non-uniform gases* (3rd edn). Cambridge University Press.
- CERCIGNANI, C. (1969). *Mathematical methods in kinetic theory*, Plenum Press, New York.
- FISCKO, K.A. and CHAPMAN, D.R. (1989). Comparison of Burnett, Super-Burnett and Monte Carlo solutions for hypersonic shock structure. *Prog. in Aero. and Astro.* **118**, 374–395.
- GRAD, H. (1958). In *Encyclopaedia of Physics* (ed S. Flügge) vol. XII, p. 205. Springer-Verlag, Berlin.
- HARRIS, S. (1971). *An introduction to the theory of the Boltzmann equation*. Holt, Rinehart, and Winston, New York.
- HASSAN, H.A. and HASH, D.B. (1993). A generalized hard-sphere model for Monte Carlo simulation. *Phys. Fluids A* **5**, 738–744.
- KENNARD, E.H. (1938). *Kinetic theory of gases*. McGraw-Hill, New York.
- KOURA, K. and MATSUMOTO, H. (1992). Variable soft sphere molecular model for air species, *Phys. Fluids A* **4**, 1083–1085.
- MAXWELL, J.C. (1867) *Phil. Trans. Soc.* **157**, 49.
- PHAM-VAN-DIEP, G.C., ERWIN, D.A., and MUNTZ, E.P. (1991). Testing continuum descriptions of low Mach number shock structures. *J. Fluid Mech.* **232**, 403–413.
- VINCENTI, W.G. and KRUGER, C.H. (1965). *Introduction to physical gas dynamics*. Wiley, New York.

4

EQUILIBRIUM GAS PROPERTIES

4.1 Spatial properties

The results that were obtained in §3.4 for the equilibrium distribution function f_0 may be summarized as follows:

$$f_0 = (\beta^3 / \pi^{3/2}) \exp(-\beta^2 c'^2),$$

where

(4.1)

$$\beta = (2RT)^{-1/2} = \{m/(2kT)\}^{1/2}.$$

The fraction of the molecules that are located within a velocity space element of volume dc and located at c' follows from eqn (3.1) as

$$\frac{dN}{N} = \frac{dn}{n} = (\beta^3 / \pi^{3/2}) \exp(-\beta^2 c'^2) dc. \quad (4.2)$$

The peculiar or thermal velocity c' is equal to $c - c_0$ so that, in Cartesian coordinates (u, v, w) , the fraction of molecules with velocity components from u to $u + du$, v to $v + dv$, and w to $w + dw$ is

$$\frac{dn}{n} = (\beta^3 / \pi^{3/2}) \exp[-\beta^2 \{(u-u_0)^2 + (v-v_0)^2 + (w-w_0)^2\}] du dv dw. \quad (4.3)$$

For polar coordinates (c', θ, ϕ) in a frame of reference moving with the stream velocity, the volume of the velocity space element is

$$c'^2 \sin\theta d\theta d\phi dc'.$$

The fraction of molecules with speed between c' and $c' + dc'$, which make an angle between θ and $\theta + d\theta$ with the polar direction, and have an azimuth angle between ϕ and $\phi + d\phi$ is, therefore,

$$\frac{dn}{n} = (\beta^3 / \pi^{3/2}) c'^2 \exp(-\beta^2 c'^2) \sin\theta d\theta d\phi dc'. \quad (4.4)$$

The fraction of molecules with speeds between c' and $c' + dc'$, irrespective of direction, is obtained from eqn (4.4) by integrating ϕ between the limits 0 to 2π and θ from 0 to π , to give

$$(4/\pi^{1/2}) \beta^3 c'^2 \exp(-\beta^2 c'^2) dc'. \quad (4.5)$$

A distribution function f_c may be defined such that the fraction of molecules with speeds between c' and $c' + dc'$ is $f_c dc'$. Eqn (4.5) shows that

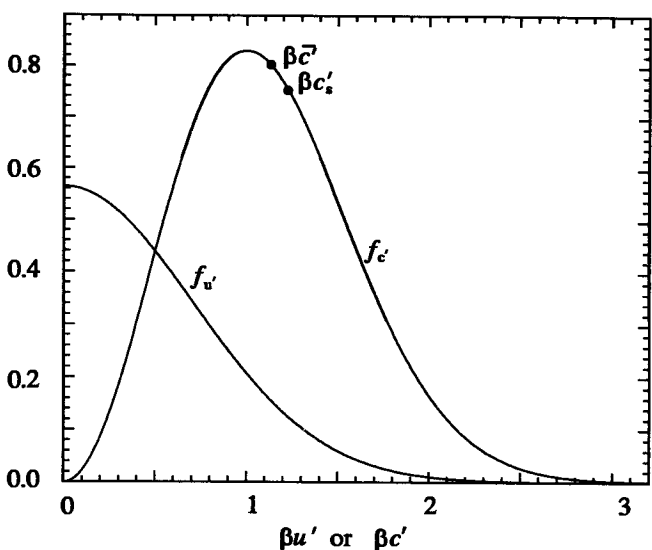


Fig. 4.1 Equilibrium distribution functions for the molecular speed and for a molecular velocity component.

$$f_{c'} = (4/\pi^{1/2}) \beta^3 c'^2 \exp(-\beta^2 c'^2). \quad (4.6)$$

The function $f_{c'}$ is plotted in Fig. 4.1. It is zero when c' is zero, increases to a maximum value when $\beta c'$ is unity, and then decreases as c' increases. The parameter β is, therefore, the reciprocal of the *most probable molecular thermal speed* c'_m , i.e.

$$c'_m = 1/\beta. \quad (4.7)$$

The average of any quantity that depends on the molecular speed may be obtained through the application of eqn (3.3) to the thermal speed distribution function $f_{c'}$. The *average thermal speed* \bar{c}' is

$$\bar{c}' = \int_0^\infty c' f_{c'} dc' = (4/\pi^{1/2}) \beta^3 \int_0^\infty c'^3 \exp(-\beta^2 c') dc',$$

or, referring to the standard integrals in Appendix B,

$$\bar{c}' = 2/(\pi^{1/2} \beta) = (2/\pi^{1/2}) c'_m. \quad (4.8)$$

The mean square thermal speed has already been determined in eqn (3.48) through the evaluation of β in terms of T . The root mean thermal speed c'_s follows as

$$c'_s = (3/2)^{1/2} (1/\beta) = (3/2)^{1/2} c'_m = (3\pi/8)^{1/2} \bar{c}'. \quad (4.9)$$

The ordering $c'_s > \bar{c}' > c'_m$ is a consequence of the high-speed tail of the distribution function. The fraction of molecules with thermal speed above some value c' is given by the integral of eqn (4.5) from c' to ∞ , i.e.

$$(4/\pi^{1/2})\beta^3 \int_{c'}^{\infty} c'^2 \exp(-\beta^2 c'^2) dc'.$$

Again using the standard integrals of Appendix B, this fraction becomes

$$1 + (2/\pi^{1/2})\beta c' \exp(-\beta^2 c'^2) - \text{erf}(\beta c'). \quad (4.10)$$

The *error function*

$$\text{erf}(a) = \frac{2}{\pi^{1/2}} \int_0^a \exp(-x^2) dx \quad (4.11)$$

will be encountered frequently. Appendix B presents tabulated values of this function, together with its limiting values, series representations, and a rational approximation.

The fraction of molecules with a velocity component within a given range, irrespective of the magnitude of the other components, is obtained by integrating eqn (4.2) over these other components. For example, the fraction of molecules with a thermal velocity component in the x -direction of between u' and $u' + du'$ is

$$(\beta/\pi^{1/2})^3 \int_{-\infty}^{\infty} \int_{-\infty}^{\infty} \int_{-\infty}^{\infty} \exp\{-\beta^2(u'^2 + v'^2 + w'^2)\} du' dv' dw',$$

or

$$(\beta/\pi^{1/2}) \exp(-\beta^2 u'^2) du'. \quad (4.12)$$

The distribution function for a thermal velocity component is, therefore,

$$f_{u'} = (\beta/\pi^{1/2}) \exp(-\beta^2 u'^2). \quad (4.13)$$

This function is also plotted in Fig. 4.1. Since the velocity distribution function f is spherically symmetric about the point representing the stream velocity, the most probable value of a particular thermal velocity component is zero. The average of the thermal velocity components in the x -direction averaged over only those molecules moving in the positive x -direction is

$$\begin{aligned} \int_0^{\infty} u' f_{u'} du' / \int_0^{\infty} f_{u'} du' &= 2(\beta/\pi^{1/2}) \int_0^{\infty} u' \exp(-\beta^2 u'^2) du' \\ &= 1/(\pi^{1/2} \beta) \end{aligned} \quad (4.14)$$

or, comparing this result with eqn (4.8), $\bar{c}'/2$.

Cylindrical coordinates in a frame of reference moving with the stream may be defined with a thermal velocity component c'_x in the axial direction, a component c'_n in the radial direction and an azimuth angle ϕ . The volume of the velocity space element is

$$c'_n d\phi dc'_n dc'_x$$

and the fraction of molecules with an azimuth angle between ϕ and $\phi+d\phi$, a radial velocity component between c'_n and $c'_n+dc'_n$, and an axial component between c'_x and $c'_x+dc'_x$ is

$$\frac{dn}{n} = (\beta^3/\pi^{3/2}) c'_n \exp\{-\beta^2(c'^2_x + c'^2_n)\} d\phi dc'_n dc'_x. \quad (4.15)$$

Therefore, the distribution function for the axial component of the thermal velocity is the same as that for the velocity component in any Cartesian direction, while the distribution for the radial component is

$$f_{c'_n} = 2\beta^2 c'_n \exp(-\beta^2 c'^2_n). \quad (4.16)$$

It is readily shown that the most probable radial velocity component is $1/(2^{1/2}\beta)$, while the average radial component is $\pi^{1/2}/(2\beta)$.

The high-speed 'tail' of the distribution functions is relevant to many practical problems. The fraction of molecules with thermal speeds greater than c_c is, from eqn (4.6),

$$\frac{dn}{n} = \frac{4\beta^3}{\pi^{1/2}} \int_{c_c}^{\infty} c'^2 \exp(-\beta^2 c'^2) dc',$$

or

$$\frac{dn}{n} = 1 - \text{erf}(\beta c_c) + \frac{2}{\pi^{1/2}} \beta c_c \exp(-\beta^2 c_c^2). \quad (4.17)$$

For large values of βc_c , the exponential term is dominant and, from eqn (C4),

$$\frac{dn}{n} = \frac{1}{\pi^{1/2}} \exp(-\beta^2 c_c^2) \left(2\beta c_c + \frac{1}{\beta c_c} - \frac{1}{2\beta^3 c_c^3} + \dots \right). \quad (4.18)$$

The fraction is approximately 0.046 for $\beta c_c=2$ and 0.00044 for $\beta c_c=3$, but declines to 8.0×10^{-11} at $\beta c_c=5$ and 4.2×10^{-43} at $\beta c_c=10$.

For a gas mixture in equilibrium, the equations of this section may be applied separately to each of the molecular species in the mixture.

4.2 Fluxal properties

We will now consider the flux of molecular quantities across a surface element in an equilibrium gas. The stream velocity \mathbf{c}_0 is inclined at the angle θ to the unit normal vector \mathbf{e} to the surface element, as shown in Fig. 4.2. Without loss of generality, we may choose Cartesian coordinates such that the stream velocity lies in the xy -plane and the surface element lies in the yz -plane, with the x -axis in the negative \mathbf{e} direction.

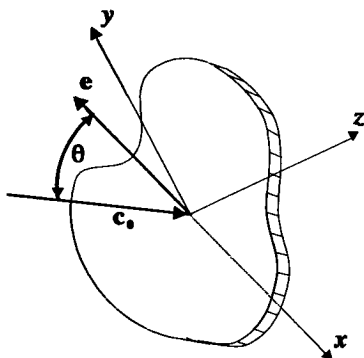


Fig. 4.2 Coordinate system for the analysis of molecular flux across a surface element.

Each molecule has velocity components

$$\begin{aligned} u &= u' + c_0 \cos \theta, \\ v &= v' + c_0 \sin \theta, \\ w &= w'. \end{aligned} \quad (4.19)$$

and

$$w = w'.$$

Therefore, from eqn (1.20), the *inward* (i.e. in the negative e or positive x -direction) flux of some quantity Q is

$$\overline{nQu},$$

or

$$n \int_{-\infty}^{\infty} \int_{-\infty}^{\infty} \int_0^{\infty} Qu f du dv dw, \quad (4.20)$$

where consideration has been limited to those molecules moving in the positive x -direction. For an equilibrium gas, the function f_0 may be substituted from eqn (4.1) to give the inward flux of the quantity Q across the element as

$$\frac{n\beta^3}{\pi^{3/2}} \int_{-\infty}^{\infty} \int_{-\infty}^{\infty} \int_0^{\infty} Qu \exp\{-\beta^2(u'^2 + v'^2 + w'^2)\} du dv dw$$

per unit area per unit time. Eqn (4.19) enables this result to be written in terms of the stream velocity and the thermal velocity components only, i.e.

$$\frac{n\beta^3}{\pi^{3/2}} \int_{-\infty}^{\infty} \int_{-\infty}^{\infty} \int_{-c_0 \cos \theta}^{\infty} Q(u' + c_0 \cos \theta) \exp\{-\beta^2(u'^2 + v'^2 + w'^2)\} du' dv' dw' \quad (4.21)$$

The *inward number flux* \dot{N}_i to the element is obtained by setting $Q=1$ in eqn (4.21). The variables in the integral may be separated to give

$$\begin{aligned}\dot{N}_i = & \frac{n\beta^3}{\pi^{3/2}} \int_{-\infty}^{\infty} \exp(-\beta^2 w'^2) dw' \int_{-\infty}^{\infty} \exp(-\beta^2 v'^2) dv' \\ & \times \int_{-c_0 \cos \theta}^{\infty} (u' + c_0 \cos \theta) \exp(-\beta^2 u'^2) du'.\end{aligned}$$

The standard integrals of Appendix B enable this to be written

$$\beta \dot{N}_i / n = [\exp(-s^2 \cos^2 \theta) + \pi^{1/2} s \cos \theta \{1 + \text{erf}(s \cos \theta)\}] / (2\pi^{1/2}), \quad (4.22)$$

where

$$s = c_0 \beta = c_0 / c'_m = c_0 / (2RT)^{1/2} \quad (4.23)$$

is called the *molecular speed ratio*.

For a stationary gas, both s and c_0 are zero and this reduces to

$$\beta \dot{N}_i / n = 1 / (2\pi^{1/2})$$

or, from eqn (4.8) and noting that $c=c'$,

$$\dot{N}_i = n \bar{c} / 4. \quad (4.24)$$

This result could have been deduced by physical reasoning from the stationary gas version of eqn (4.14). This states that the mean velocity component, taken over the molecules for which it is positive, is equal to half the mean molecular speed \bar{c} . Since half the molecules have a positive component in a particular direction, the number flux per unit area per unit volume in a particular direction must be $n \bar{c} / 4$.

The *inward normal momentum flux* p_i to the element is obtained by setting $Q=mu=m(u'+c_0 \cos \theta)$, i.e.

$$\begin{aligned}p_i = & \frac{nm\beta^3}{\pi^{3/2}} \int_{-\infty}^{\infty} \exp(-\beta^2 w'^2) dw' \int_{-\infty}^{\infty} \exp(-\beta^2 v'^2) dv' \\ & \times \int_{-c_0 \cos \theta}^{\infty} (u' + c_0 \cos \theta)^2 \exp(-\beta^2 u'^2) du'.\end{aligned}$$

or

$$\begin{aligned}\beta^2 p_i / \rho = & [s \cos \theta \exp(-s^2 \cos^2 \theta) + \pi^{1/2} \{1 + \text{erf}(s \cos \theta)\} \\ & \times (1/2 + s^2 \cos^2 \theta)] / (2\pi^{1/2}).\end{aligned} \quad (4.25)$$

For a stationary gas, this gives

$$p_i = \rho / (4\beta^2) = \rho RT / 2 = p / 2,$$

as would be expected in an equilibrium gas since the inward moving molecules contribute half the pressure. Similarly, the *inward parallel momentum flux* τ_i is obtained for $Q=mv=m(v'+c_0 \sin \theta)$. The integral is

$$\begin{aligned}\tau_i = & \frac{nm\beta^3}{\pi^{3/2}} \int_{-\infty}^{\infty} \exp(-\beta^2 w'^2) dw' \int_{-\infty}^{\infty} (v' + c_0 \sin \theta) \exp(-\beta^2 v'^2) dv' \\ & \times \int_{-c_0 \cos \theta}^{\infty} (u' + c_0 \cos \theta) \exp(-\beta^2 u'^2) du'\end{aligned}$$

and the final result follows as

$$\begin{aligned}\beta^2 \tau_i / \rho &= s \sin \theta [\exp(-s^2 \cos^2 \theta) + \pi^{1/2} s \cos \theta \{1 + \operatorname{erf}(s \cos \theta)\}] / (2\pi^{1/2}) \\ &= s \sin \theta (\beta N_i / n).\end{aligned}\quad (4.26)$$

The parallel momentum flux in a stationary equilibrium gas is, of course, zero as a consequence of the symmetry of the distribution function.

Finally, the *inward translational energy flux* $q_{i,tr}$ to the element is obtained by setting $Q = \frac{1}{2}mc^2 = \frac{1}{2}m(u^2 + v^2 + w^2)$ in eqn (4.21) to give

$$\begin{aligned}\tau_i = & \frac{nm\beta^3}{2\pi^{3/2}} \int_{-\infty}^{\infty} \int_{-\infty}^{\infty} \int_{-c_0 \cos \theta}^{\infty} \{(u' + c_0 \cos \theta)^2 + (v' + c_0 \sin \theta)^2 + w'^2\} \\ & \times (u' + c_0 \cos \theta) \exp\{-\beta^2(u'^2 + v'^2 + w'^2)\} du' dv' dw'\end{aligned}$$

or

$$\begin{aligned}\beta^2 q_{i,tr} / \rho &= [(s^2 + 2) \exp(-s^2 \cos^2 \theta) + \pi^{1/2} s \cos \theta (s^2 + 5/2) \\ &\quad \times \{1 + \operatorname{erf}(s \cos \theta)\}] / (4\pi^{1/2}).\end{aligned}\quad (4.27)$$

For a stationary gas, this becomes

$$\beta^3 q_{i,tr} / \rho = 1 / (2\pi^{1/2}). \quad (4.28)$$

Unlike the number and momentum flux, the energy flux is modified by the presence of internal energy. For an equilibrium non-reacting gas, the specific internal energy follows from eqn (1.31) as

$$e_{\text{int}} = \frac{1}{2} \zeta R T.$$

Here, ζ is the number of internal degrees of freedom and may be related to the specific heat ratio of the gas by

$$\gamma = (\zeta + 5) / (\zeta + 3),$$

so that

$$\zeta = (5 - 3\gamma) / (\gamma - 1). \quad (4.29)$$

The inward *internal energy flux* is equal to the product of the number flux N_i and the average internal energy per molecule. Therefore, from eqns (1.31), (4.22), and (4.29),

$$\begin{aligned}\beta^3 q_{i,int} / \rho &= \{(5 - 3\gamma) / (\gamma - 1)\} [\exp(-s^2 \cos^2 \theta) \\ &\quad + \pi^{1/2} s \cos \theta \{1 + \operatorname{erf}(s \cos \theta)\}] / (8\pi^{1/2}).\end{aligned}\quad (4.30)$$

The *total energy flux* to the element is obtained by summing eqn (4.27) for $q_{i,tr}$ and eqn (4.30) for $q_{i,int}$, to give

$$\beta^3 q_i / \rho = [\{2s^2 + (\gamma + 1)/(\gamma - 1)\}[\exp(-s^2 \cos^2 \theta) + 2\pi^{1/2} s \cos \theta \\ \times \{s^2 + \gamma/(\gamma - 1)\}\{1 + \text{erf}(s \cos \theta)\}]/(8\pi^{1/2}). \quad (4.31)$$

The version for a stationary gas is

$$\beta^3 q_i / \rho = \{(\gamma + 1)/(\gamma - 1)\}/(8\pi^{1/2}). \quad (4.32)$$

The average energy of the molecules crossing the surface element in a stationary monatomic gas is given by $q_i N_i$ for $s=0$, or m/β^2 . The average energy of a molecule in a spatial element is given by eqn (1.29) as $3mRT/2$ or $\frac{3}{4}m/\beta^2$. The average energy of the molecules crossing a surface element therefore exceeds that in a spatial element by the factor 4/3. The physical explanation for this is that the probability of a fast molecule crossing a surface element in a given time is greater than the corresponding probability for a slower molecule. This is the reason why the total energy flux of eqn (4.32) is exactly twice the translational energy flux of eqn (4.28) when the number of internal degrees of freedom $\zeta = 4$, rather than when $\zeta = 3$.

The above equation for N_i is usually derived in the context of molecular effusion in a free molecule gas. This problem is dealt with in detail in Chapter 5. The other equations for p_i , τ_i , and q_i are generally introduced in the context of free molecule aerodynamics. They then represent the pressure, shear stress, and heat flux incident on an element of solid surface. However, it must be emphasized that the equations apply to the flux quantities across an area element in an equilibrium gas *at any density* and represent important reference quantities.

The general behaviour of the molecular number flux in an equilibrium gas is illustrated in Fig. 4.3. If $s \cos \theta \rightarrow \infty$, then $\exp(-s^2 \cos^2 \theta) \rightarrow 0$ and $\text{erf}(s \cos \theta) \rightarrow 1$ so that the hypersonic form of eqn (4.22) is

$$\beta N_i / n = s \cos \theta,$$

or

$$n_i = n c_0 \cos \theta. \quad (4.33)$$

This is the equation that would be derived from first principles if one neglects the thermal velocity components and considers only the flux due to the stream speed. Eqn (4.26) shows that $\beta^2 \tau_i / (\rho s \sin \theta)$ is equal to $\beta N_i / n$, so that the behaviour of the parallel momentum flux is also covered by Fig. 4.3. The effect of the thermal velocity components is small at $s \cos \theta = 1$ where $\beta N_i / n = 1.02513$ and negligible at $s \cos \theta = 2$, where $\beta N_i / n = 2.00049$.

The opposite limit of large negative values of $s \cos \theta$ is also important and will be called the 'thermal backflow' limit. The numerical evaluation of eqn (4.22) can be difficult because the net flux is the small difference between two large terms, but this can be overcome by replacing the error function by the series expansion of eqn (B34). The leading term for the thermal backflow limit is

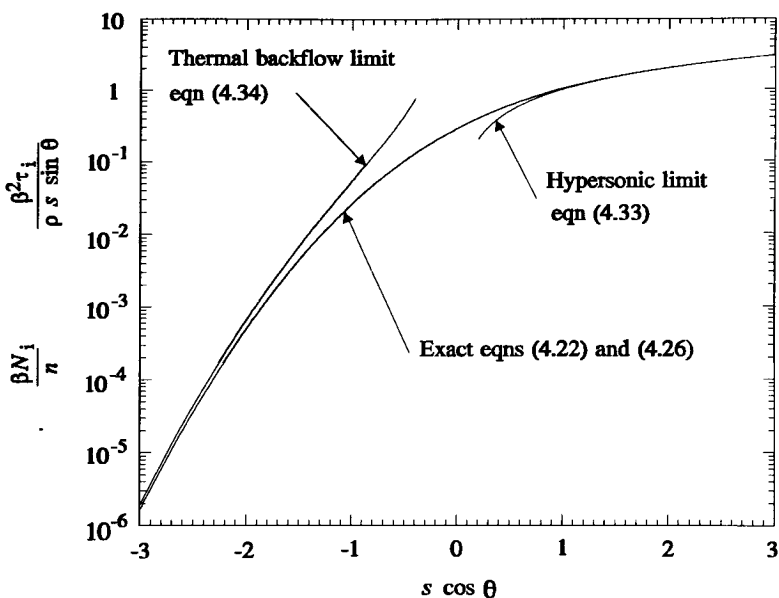


Fig. 4.3 Number and parallel momentum flux to a surface element.

$$\beta N_i/n = \beta^2 \tau_i / (\rho s \sin \theta) = \exp(-s^2 \cos^2 \theta) / (4\pi^{1/2} s^2 \cos^2 \theta). \quad (4.34)$$

This limit is also shown in Fig. 4.3 and it can be seen that the thermal backflow limit is approached much more gradually than the hypersonic limit.

Similar plots for the dimensionless normal momentum flux $\beta^2 p_i/\rho$ are presented in Fig. 4.4. Eqn (4.25) shows that the hypersonic limit for this quantity as the exponential and error function terms tend to zero and unity, respectively, is

$$\beta^2 p_i/\rho = \frac{1}{2} + s^2 \cos^2 \theta,$$

or

$$p_i / (\frac{1}{2} \rho c_0^2) = 1/s^2 + 2 \cos^2 \theta. \quad (4.35)$$

In the context of free-molecule aerodynamics, the incident pressure coefficient tends to a limiting value of $2 \cos^2 \theta$ as s becomes large in comparison with unity. The departure of the exact result from this is again very small for $s \cos \theta > 2$. The leading term for the incident normal momentum flux in the thermal backflow limit is

$$\beta^2 p_i/\rho = -\exp(s^2 \cos^2 \theta) / (4\pi^{1/2} s^3 \cos^3 \theta) \quad (4.36)$$

and Fig. 4.4 shows that this is again approached more gradually than the hypersonic limit.

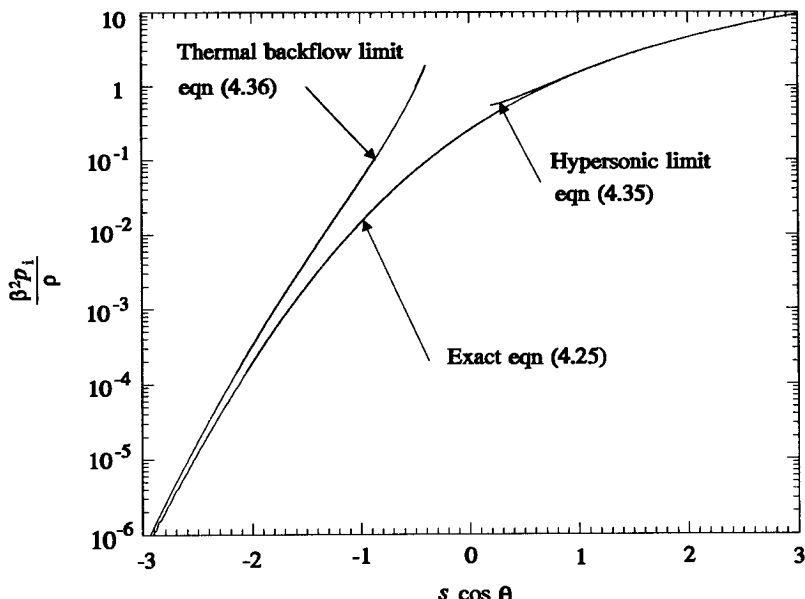


Fig. 4.4 Normal momentum flux to a surface element.

The energy flux is much more complex since it depends on s and θ independently, rather than on $s \cos \theta$, and also depends on the number of internal degrees of freedom. The internal energy flux can be written

$$\beta^3 q_{i,int} / \rho = (\zeta/4) \beta N_i / n \quad (4.37)$$

so that its behaviour is also covered by Fig. 4.3. The hypersonic limit of eqn (4.27) is

$$\beta^3 q_{i,tr} / \rho = \frac{1}{2} s \cos \theta (s^2 + 5/2)$$

or

$$q_{i,tr} / (\frac{1}{2} \rho c_0^3) = \cos \theta (1 + 5/(2s^2)). \quad (4.38)$$

The behaviour of the translational energy flux as a function of s and θ , separately, is shown in Fig. 4.5. Note that, when s is large compared with unity, the heat transfer depends strongly on the inclination of the element when it is almost aligned with the flow (i.e. when θ is near 90°).

The angular distribution of the molecules crossing a surface element is required for some problems. The integration of eqn (4.4) gives the number of molecules in a stationary gas that have speeds between c and $c+dc$ and an angle between θ and $\theta+d\theta$ with an axis normal to a surface element as

$$dn = 2\pi^{-1/2} \beta^3 c^2 \exp(-\beta^2 c^2) \sin \theta d\theta dc.$$

The flux of these molecules from the element is given by the product of this number with the velocity component $c \cos \theta$ normal to the element, i.e.

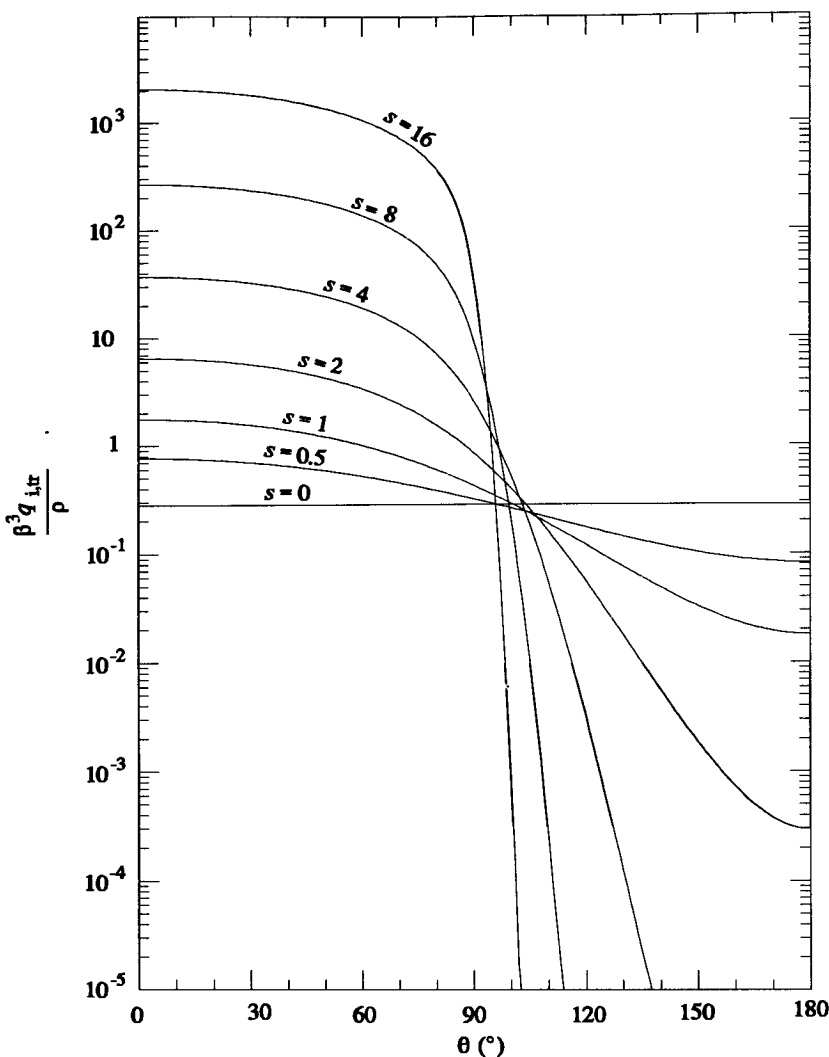


Fig. 4.5 Translational energy flux to a surface element.

$$d\dot{N} = 2\pi^{-1/2} n \beta^3 c^3 \exp(-\beta^2 c^2) \sin\theta \cos\theta d\theta dc. \quad (4.39)$$

The corresponding two-dimensional result may be obtained from eqn (4.15) by integrating over all values of the axial velocity. The flux of molecules with radial speed between c_n and $c_n + dc_n$ and which make an angle between ϕ and $\phi + d\phi$ with the plane normal to a two-dimensional element is

$$d\dot{N} = \pi^{-1} n \beta^2 c_n^2 \exp(-\beta^2 c_n^2) \cos\phi d\phi dc_n. \quad (4.40)$$

The equations of this section also apply to each species of a gas mixture.

4.3 Collisional quantities in a simple gas

General expressions were obtained in Chapter 1 for the mean collision rate and mean free path in a dilute gas. These involve the mean value of the product of the total collision cross-section and the magnitude of the relative velocity. The cross-section is generally a function of the relative velocity and the evaluation of these expressions requires the mean value of an arbitrary power j of the relative velocity.

The relative velocity in a binary collision is $\mathbf{c}_r = \mathbf{c}_1 - \mathbf{c}_2$, where the subscripts 1 and 2 denote the two molecules that are involved. Assuming molecular chaos, the two particle distribution function is equal to the product of the two single particle distribution functions f_1 and f_2 . The required mean value is then

$$\overline{c_r^j} = \int_{-\infty}^{\infty} \int_{-\infty}^{\infty} c_r^j f_1 f_2 d\mathbf{c}_1 d\mathbf{c}_2$$

and, from eqn (4.1) for an equilibrium gas,

$$\overline{c_r^j} = \frac{(m_1 m_2)^{3/2}}{(2\pi k T)^3} \int_{-\infty}^{\infty} \int_{-\infty}^{\infty} c_r^j \exp\left(-(m_1 c_1^2 + m_2 c_2^2)/(2kT)\right) d\mathbf{c}_1 d\mathbf{c}_2.$$

This integral is most easily evaluated if the variables are changed from \mathbf{c}_1 and \mathbf{c}_2 to \mathbf{c}_r and \mathbf{c}_m . The Jacobian of the transformation is

$$\frac{\partial(u_1, v_1, w_1, u_2, v_2, w_2)}{\partial(u_r, v_r, w_r, u_m, v_m, w_m)}$$

but, because of the symmetry of eqns (2.3) and (2.4), it is sufficient to evaluate the reduced one-dimensional Jacobian. This is, in the x -direction,

$$\frac{\partial(u_1, u_2)}{\partial(u_r, u_m)} = \begin{vmatrix} \frac{\partial u_1}{\partial u_r} & \frac{\partial u_1}{\partial u_m} \\ \frac{\partial u_2}{\partial u_r} & \frac{\partial u_2}{\partial u_m} \end{vmatrix}$$

or, using eqn (2.4),

$$\frac{\partial(u_1, u_2)}{\partial(u_r, u_m)} = \begin{vmatrix} \frac{m_2}{m_1 + m_2} & 1 \\ -\frac{m_1}{m_1 + m_2} & 1 \end{vmatrix} = \frac{m_2}{m_1 + m_2} + \frac{m_1}{m_1 + m_2} = 1.$$

The full Jacobian is therefore unity and $d\mathbf{c}_m d\mathbf{c}_r$ may be substituted for $d\mathbf{c}_1 d\mathbf{c}_2$ in the above integral. We also have, from eqn (2.6),

$$m_1 c_1^2 + m_2 c_2^2 = (m_1 + m_2) c_m^2 + m_r c_r^2,$$

where m_r is the reduced mass. Since the integrand is independent of the directions of \mathbf{c}_r and \mathbf{c}_m , the velocity space elements may be written in polar coordinates. An integration over all polar and azimuth angles then gives

$$d\mathbf{c}_r = 4\pi c_r^2 d\mathbf{c}_r \quad \text{and} \quad d\mathbf{c}_m = 4\pi c_m^2 d\mathbf{c}_m.$$

Therefore,

$$\overline{c_r^j} = \frac{2(m_1 m_2)^{3/2}}{\pi(kT)^3} \int_0^\infty \int_0^\infty c_r^{j+2} c_m^2 \exp[-\{(m_1 + m_2)c_m^2 + m_r c_r^2\}/(2kT)] d\mathbf{c}_m d\mathbf{c}_r,$$

or

$$\begin{aligned} \overline{c_r^j} &= \frac{2(m_1 m_2)^{3/2}}{\pi(kT)^3} \int_0^\infty c_m^2 \exp[-(m_1 + m_2)c_m^2/(2kT)] d\mathbf{c}_m \\ &\quad \times \int_0^\infty c_r^{j+2} \exp[-(m_r c_r^2)/(2kT)] d\mathbf{c}_r. \end{aligned} \quad (4.41)$$

Note that the distribution functions for c_m and c_r can be inferred from eqn (4.41) as

$$f_{c_m} = \frac{4(m_1 + m_2)^{3/2}}{\pi^{1/2}(2kT)^{3/2}} c_m^2 \exp[-(m_1 + m_2)c_m^2/(2kT)] \quad (4.42)$$

and

$$f_{c_r} = \frac{4m_r^{3/2}}{\pi^{1/2}(2kT)^{3/2}} c_r^2 \exp[-m_r c_r^2/(2kT)]. \quad (4.43)$$

The application of the standard integrals of Appendix B to eqn (4.43) gives

$$\overline{c_r^j} = (2/\pi^{1/2}) \Gamma((j+3)/2) (2kT/m_r)^{j/2}. \quad (4.44)$$

The mean value of the relative speed is obtained by setting $j=1$, i.e.

$$\overline{c_r} = (2/\pi^{1/2})(2kT/m_r)^{1/2}. \quad (4.45)$$

For a simple gas, $m_r = m/2$, and eqn (4.8) may be used to relate this value to the mean thermal speed of an individual molecule. The result is

$$\overline{c_r} = 2^{3/2}/(\pi^{1/2}\beta) = 2^{1/2}\overline{c}, \quad (4.46)$$

Note that this is also the mean value of the relative speed in *collisions* only for the special case of hard sphere molecules. The total cross-section of the other molecular models is a function of the relative speed and the mean value in collisions is affected by this function. The mean collision rate and mean free path in an equilibrium gas also depend on the molecular model.

Eqn (4.44) may be applied to the combination of eqn (1.10) for the collision rate and the definition in eqns (3.60) and (3.67) of the VHS model to give the mean collision rate per molecule in an equilibrium gas of VHS or VSS molecules as

$$v_0 = n \sigma_{T,\text{ref}} c_{r,\text{ref}}^{2\omega-1} \frac{2}{\pi^{\frac{1}{2}}} \Gamma(5/2 - \omega) \left(\frac{2kT}{m_r} \right)^{1-\omega}. \quad (4.47)$$

The preceding analysis does not apply to the GHS molecular model because its cross-section is not a power law of the relative speed. However, the mean value of the product of their relative speed and the cross-section can be written

$$\begin{aligned} \overline{\sigma_T c_r} &= \int_{-\infty}^{\infty} \int_{-\infty}^{\infty} \sigma_T c_r f_1 f_2 d\mathbf{c}_1 d\mathbf{c}_2 \\ &= \frac{(m_1 m_2)^{3/2}}{(2\pi k T)^3} \int_{-\infty}^{\infty} \int_{-\infty}^{\infty} \sigma_T c_r \exp\{-(m_1 c_1^2 + m_2 c_2^2)/(2kT)\} d\mathbf{c}_1 d\mathbf{c}_2. \end{aligned}$$

The variables may be transformed in exactly the same way as for the VHS and VSS molecules and the result can be written as

$$\overline{\sigma_T c_r} = (2/\pi)^{\frac{1}{2}} \{m_r/(kT)\} \int_0^{\infty} \sigma_T c_r^3 \exp\{-m_r c_r^2/(2kT)\} dc_r. \quad (4.48)$$

The GHS cross-section is given by eqn (3.80) and eqn (4.48) may then be integrated to give the collision rate in an equilibrium GHS gas as

$$v_0 = 2s_0^2 \left(\frac{2kT}{\pi m_r} \right)^{\frac{1}{2}} \left(\alpha_1 (kT/\epsilon)^{-\psi_1} \Gamma(2-\psi_1) + \alpha_2 (kT/\epsilon)^{-\psi_2} \Gamma(2-\psi_2) \right). \quad (4.49)$$

Eqn (3.73) enables the reference values in eqn (4.47) for the VSS molecules to be written in terms of the coefficient of viscosity. We then have

$$v_0 = \frac{5(\alpha+1)(\alpha+2)}{\alpha(5-2\omega)(7-2\omega)} \frac{p}{\mu}. \quad (4.50)$$

The number of collisions per unit time per unit volume follows from eqn (1.11) as

$$N_{c,0} = \frac{5(\alpha+1)(\alpha+2)}{2\alpha(5-2\omega)(7-2\omega)} \frac{np}{\mu}. \quad (4.51)$$

Eqns (1.12) and (4.8) then give the equilibrium mean free path as

$$\lambda_0 = \frac{4\alpha(5-2\omega)(7-2\omega)}{5(\alpha+1)(\alpha+2)} \left(\frac{m}{2\pi kT} \right)^{\frac{1}{2}} \frac{\mu}{\rho} = \frac{4\alpha(5-2\omega)(7-2\omega)}{5\pi^{\frac{1}{2}}(\alpha+1)(\alpha+2)} \frac{\beta\mu}{\rho}. \quad (4.52)$$

The simple hard sphere results are obtained if $\omega = \frac{1}{2}$ and $\alpha = 1$. Because the total cross-section is constant, the equilibrium collision rate can be written directly from eqns (4.45) and (1.10) as

$$v_0 = 2^{\frac{1}{2}} \sigma_T n \bar{c} = (4/\pi^{\frac{1}{2}}) \sigma_T n (kT/m)^{\frac{1}{2}}. \quad (4.53)$$

The number of collisions per unit time per unit volume again follows from eqn (1.11) as

$$N_{c,0} = 2^{-\frac{1}{2}} \sigma_T n^2 \bar{c}^2, \quad (4.54)$$

and the equilibrium mean free path follows from eqns (4.53) and (1.12) as

$$\lambda_0 = (2^{\frac{1}{2}} \sigma_T n)^{-1} = (2^{\frac{1}{2}} \pi d^2 n)^{-1}. \quad (4.55)$$

This can also be written from eqn (4.52) as

$$\lambda_0 = \frac{16}{5} \left(\frac{m}{2\pi k T} \right)^{\frac{1}{2}} \frac{\mu}{\rho}. \quad (4.56)$$

The hard sphere equations have been widely used to derive an effective diameter for real molecules and to define the mean free path in both numerical and analytical studies. These procedures are generally carried out at a single temperature and, if the results are then applied over a range of temperatures, errors will be introduced. Consistent correlations and accurate calculations require a molecular model that has a cross-section that changes with the relative collision velocity in a similar manner to the changes that occur in the real gas. As noted earlier, this is achieved if the model has a temperature dependence of the coefficient of viscosity that matches that in the real gas. The traditional hard sphere equations must therefore be replaced by those based on a more realistic model, and the VSS model is the obvious choice. This also permits the definition of a more realistic temperature-dependent diameter and Knudsen number.

The VSS result for the mean free path in eqn (4.52) differs from the conventional eqn (4.56) that employs the hard sphere model only by the numerical factor $\alpha(5-2\omega)(7-2\omega)/(4(\alpha+1)(\alpha+2))$. This factor is, of course, unity for hard sphere molecules which have $\omega = \frac{1}{2}$ and $\alpha = 1$, but decreases to 0.8244 for the more realistic $\omega = \frac{3}{4}$ and $\alpha = 1.5325$, and to 0.6173 for $\omega = 1$ and $\alpha = 2.1403$ which corresponds to the limiting case of Maxwell molecules.

This relationship between the mean free path and the coefficient of viscosity enables the Chapman-Enskog distribution function to be written in terms of the local Knudsen numbers. The substitution of eqn (4.52) into eqn (3.87), and using eqn (3.56), gives

$$f = f_0 \left[1 - \frac{5\pi^{\frac{1}{2}}(\alpha+1)(\alpha+2)\beta v'}{4\alpha(5-2\omega)(7-2\omega)} \right. \\ \left. \times \left(3(\beta^2 c'^2 - 5/2) \frac{\lambda}{T} \frac{\partial T}{\partial y} + 4\beta u' s \frac{\lambda}{u_0} \frac{\partial u_0}{\partial y} \right) \right]. \quad (4.57)$$

The implications of this equation for the range of validity of the Navier-Stokes equations were discussed in Chapter 1.

The mean value, over all collisions in a VHS or VSS gas, of any quantity Q that is a function of c_r alone, may be obtained by setting j to the value appropriate to the product of total cross-section and relative speed, and then including Q within the integral over c_r in eqn (4.41) and then dividing the resulting expression by eqn (4.44), i.e.

$$\bar{Q} = \{2/\Gamma(5/2-\omega)\} \{m_r/(2kT)\}^{5/2-\omega} \times \int_0^{\infty} Q c_r^{2(2-\omega)} \exp\{-m_r c_r^2/(2kT)\} dc_r. \quad (4.58)$$

In the case of the GHS gas, the mean value over all collisions of any quantity Q is given by

$$\bar{Q} = \frac{\int_0^{\infty} Q \sigma_T c_r^3 \exp\{-m_r c_r^2/(2kT)\} dc_r}{\int_0^{\infty} \sigma_T c_r^3 \exp\{-m_r c_r^2/(2kT)\} dc_r}$$

or, using eqn (4.48)

$$\bar{Q} = (2/\pi)^{1/2} \{m_r/(kT)\}^{3/2} \int_0^{\infty} Q \sigma_T c_r^3 \exp\{-m_r c_r^2/(2kT)\} dc_r / \overline{\sigma_T c_r}. \quad (4.59)$$

The collision cross-section in a VSS gas changes with the magnitude of the relative velocity in the collision, and eqns (3.60) and (3.74) show that it is inversely proportional to c_r to the power $2\omega-1$. A temperature-based effective or reference diameter d_{ref} is most conveniently defined as the diameter in a VSS gas in equilibrium at the mean value of $c_r^{2\omega-1}$. This diameter is related to the earlier reference cross-section of eqn (3.60) by

$$\sigma_{ref} = \pi d_{ref}^2 = \sigma_{T,ref} c_{r,ref}^{2\omega-1} / \overline{c_r^{2\omega-1}}. \quad (4.60)$$

Eqn (4.58) may be evaluated with $Q = c_r^{2\omega-1}$ to give

$$\overline{c_r^{2\omega-1}} = (2kT/m_r)^{\omega-1/2} / \Gamma(5/2-\omega). \quad (4.61)$$

Eqns (4.60) and (4.61) may then be combined with eqns (3.67) and (3.73) to give the reference diameter of a gas that has, at temperature T_{ref} , a coefficient of viscosity μ_{ref} with temperature exponent ω , i.e.

$$d_{ref} = \left(\frac{5(\alpha+1)(\alpha+2)(mkT_{ref}/\pi)^{1/2}}{4\alpha(5-2\omega)(7-2\omega)\mu_{ref}} \right)^{1/2}. \quad (4.62)$$

The average cross-section based on this relation is larger than the hard sphere cross-section that would be deduced from eqn (3.59) by the factor $4(\alpha+1)(\alpha+2)/[\alpha(5-2\omega)(7-2\omega)]$. This result is consistent with the earlier

finding for the mean free path and means that the hard sphere result of eqn (4.56) applies also to the VHS gas, as long as the cross-section is based on this reference diameter.

The VSS model may be implemented either through eqn (3.74), which makes no use of equilibrium gas results, or through this new reference diameter. The latter option has the advantage of avoiding the appearance of the viscosity coefficient in relations as a reference quantity, even when viscosity is physically irrelevant.

Eqn (4.60) can then be written

$$\pi d_{\text{ref}}^2 \overline{c_r^{2\omega-1}} = \sigma_{T,\text{ref}} c_{r,\text{ref}}^{2\omega-1} = \pi d^2 c_r^{2\omega-1},$$

where d is the diameter at relative speed c_r . Therefore, using eqn (4.61),

$$d = d_{\text{ref}} [\{2kT_{\text{ref}}/(m_r c_r^2)\}^{\omega-1/2}/\Gamma(5/2-\omega)]^{1/2}. \quad (4.63)$$

Some typical values of the reference diameter from eqn (4.62) at a reference temperature of 0°C, are presented in Appendix A. The equation that corresponds to eqn (4.63) and the reference diameters that appear in the original presentation of the VHS model (Bird 1981) differ from those defined here by a small numerical factor. This is because they were based on the mean value of c_r^2 raised to the power $\omega-1/2$, rather than the mean value of $c_r^{2\omega-1}$. The degree of arbitrary choice in the definition of a reference diameter is of no consequence because it can be eliminated from eqns (4.62) and (4.63). This recovers eqn (3.74) and shows that the model is independent of d_{ref} and does not require an equilibrium gas.

The introduction of the reference diameter and the combination of eqn (4.63) with eqn (1.10) and (4.44) enables the equilibrium collision rate per molecule in a VHS or VSS gas to be written

$$v_0 = 4d_{\text{ref}}^2 n (\pi k T_{\text{ref}}/m)^{1/2} (T/T_{\text{ref}})^{1-\omega}. \quad (4.64)$$

Similarly, the equilibrium mean free path may be written

$$\lambda_0 = \{2^{1/2} \pi d_{\text{ref}}^2 n (T_{\text{ref}}/T)^{\omega-1/2}\}^{-1}. \quad (4.65)$$

Note that the collision rate is independent of temperature in a Maxwell gas ($\omega=1$), while the mean free path is independent of temperature in a hard sphere gas ($\omega=1/2$). The value of ω in real gases is between these limits, and both the collision rate and mean free path depend on the temperature. The translational kinetic energy in the centre of mass frame of reference is $E_t = 1/2 m_r c_r^2$, and the substitution of $Q = 1/2 m_r c_r^2$ in eqn (4.59) gives

$$\overline{E_t} = (5/2-\omega)kT \quad (4.66)$$

for the mean translational kinetic energy in collisions. For the special case of hard sphere molecules, this reduces to

$$\overline{E_t} = 2kT. \quad (4.67)$$

The fraction of collisions in which $E_t = \frac{1}{2}m_r c_r^2$ exceeds some reference value E_m is important in the context of chemical reactions. The total number of collisions is proportional to the integral in eqn (4.43) and the number of these with $E_t > E_m$ is obtained by setting the lower limit for the integration over c_r to $(2E_m/m_r)^{\omega/2}$. The fraction then becomes

$$\frac{dN}{N} = \frac{2}{\Gamma(5/2-\omega)} \left(\frac{m_r}{2kT} \right)^{5/2-\omega} \int_{(2E_m/m_r)^{\omega/2}}^{\infty} c_r^{2(2-\omega)} \exp\left(-\frac{m_r c_r^2}{2kT}\right) dc_r \quad (4.68)$$

or, if the incomplete gamma function is introduced,

$$dN/N = \Gamma\{5/2-\omega, E_m/(kT)\}/\Gamma(5/2-\omega). \quad (4.69)$$

For hard sphere molecules, $\omega=1/2$ and the reduction formula of eqn (B6) enables this to be written

$$dN/N = \exp\{-E_m/(kT)\} \{E_m/(kT) + 1\}. \quad (4.70)$$

This fraction is higher than that for the more realistic molecules which have collision cross-sections that decrease as the relative translational energy increases. The fraction is shown in Fig. 4.6 as a function of the relative translational energy for the hard sphere model ($\omega=0.5$), the more realistic case with $\omega=0.75$, and the limiting 'soft molecule' case with $\omega=1$.

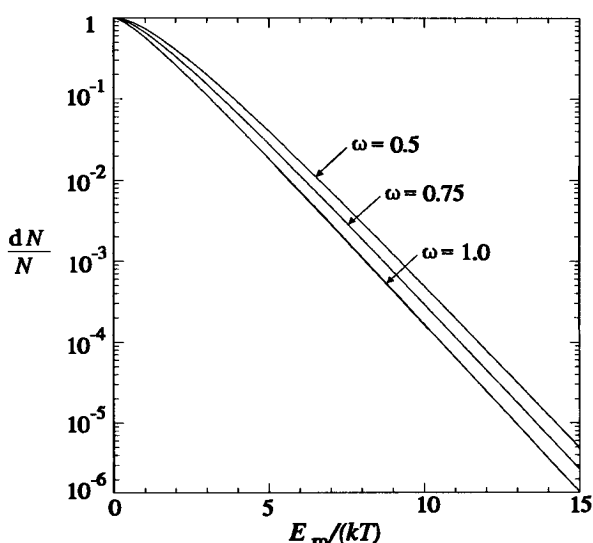


Fig. 4.6 The fraction of collisions with relative translational energy in excess of $E_m/(kT)$.

An important variation of this result occurs when one is interested only in the energy based on the component of the relative velocity along the apse line of the collision or, for hard sphere or VHS molecules, along the line of centres. This means that, for a given c_r , the angle θ_A must be between 0 and $\cos^{-1}\{(2E_m/m_r)^{1/2}/c_r\}$. The differential cross-section for VHS molecules is

$$\sigma d\Omega = \{\sigma_T/(4\pi)\} \sin \chi d\chi d\varepsilon,$$

and eqn (2.21) shows that

$$\sin \chi d\chi = -4 \sin \theta_A \cos \theta_A d\theta_A.$$

The effective total collision cross-section σ_E of the collisions with the required relative translational energy is, therefore,

$$\sigma_E = -2\sigma_T \int_0^{\cos^{-1}\{(2E_m/m_r)^{1/2}/c_r\}} \sin \theta_A \cos \theta_A d\theta_A,$$

or, since $\sin \theta_A d\theta_A = -d(\cos \theta_A)$,

$$\sigma_E = \sigma_T \left(1 - \frac{2E_m}{m_r c_r^2} \right). \quad (4.71)$$

The required fraction is therefore obtained by incorporating the factor in parentheses in eqn (4.71) into eqn (4.68), i.e.

$$\begin{aligned} \frac{dN}{N} &= \frac{2}{\Gamma(5/2-\omega)} \left(\frac{m_r}{2kT} \right)^{5/2-\omega} \\ &\times \int_{(2E_m/m_r)^{1/2}}^{\infty} c_r^{2(2-\omega)} \left(1 - \frac{2E_m}{m_r c_r^2} \right) \exp \left(-\frac{m_r c_r^2}{2kT} \right) dc_r, \end{aligned}$$

which may be evaluated to give

$$\frac{dN}{N} = \frac{1}{\Gamma(5/2-\omega)} \left[\Gamma\left(\frac{5}{2}-\omega, \frac{E_m}{kT}\right) - \frac{E_m}{kT} \Gamma\left(\frac{3}{2}-\omega, \frac{E_m}{kT}\right) \right]. \quad (4.72)$$

For the special case of a hard sphere gas, this reduces to give the strikingly simple result

$$dN/N = \exp\{-E_m/(kT)\} \quad (4.73)$$

for the fraction of collisions in which the relative translational energy along the line of centres exceeds the value E_m .

4.4 Collisional quantities in a gas mixture

Eqns (1.36)–(1.41) are the general results for the collision rates and the mean free path in a gas mixture. The preliminary equations in the preceding section allowed for collisions between molecules of different mass, and it was pointed out in §3.5 that it is desirable to define separate values of the collisional parameters for each combination of species. For a gas of VHS or VSS molecules, these parameters are the reference diameter, the reference temperature, and the temperature exponent ω .

Consider a mixture of s separate gas species of VHS molecules for which an s by s array of reference quantities is available. The analysis that led to the simple gas result of eqn (4.2) is readily modified to give the collision rate of a species p molecule with molecules of species q in an equilibrium gas. The reduced mass for this combination is used together with the appropriate reference parameters to give

$$(v_{pq})_0 = 2\pi^{1/2} (d_{\text{ref}})_{pq}^2 n_q \{T/(T_{\text{ref}})_{pq}\}^{1-\omega_{pq}} \{2k(T_{\text{ref}})_{pq}/m_r\}^{1/2}. \quad (4.74)$$

The mean collision rate for species p is obtained from eqn (1.37) as

$$(v_p)_0 = \sum_{q=1}^s \left(2\pi^{1/2} (d_{\text{ref}})_{pq}^2 n_q \{T/(T_{\text{ref}})_{pq}\}^{1-\omega_{pq}} \{2k(T_{\text{ref}})_{pq}/m_r\}^{1/2} \right). \quad (4.75)$$

The mean collision rate for the mixture follows from eqn (1.38), and the number of collisions per unit time per unit volume from eqn (1.11).

The mean free path of a species p molecule is equal to its mean thermal velocity divided by its collision rate. This quantity is obtained from eqns (4.8) and (4.75) as,

$$(\lambda_p)_0 = \left[\sum_{q=1}^s \left\{ \pi (d_{\text{ref}})_{pq}^2 n_q \left(\frac{(T_{\text{ref}})_{pq}}{T} \right)^{\omega_{pq}-1/2} \left(1 + \frac{m_p}{m_q} \right)^{1/2} \right\} \right]^{-1}. \quad (4.76)$$

Finally, the overall mean free path for this mixture is

$$\lambda_0 = \sum_{p=1}^s \frac{n_p}{n} \left[\sum_{q=1}^s \left\{ \pi (d_{\text{ref}})_{pq}^2 n_q \left(\frac{(T_{\text{ref}})_{pq}}{T} \right)^{\omega_{pq}-1/2} \left(1 + \frac{m_p}{m_q} \right)^{1/2} \right\} \right]^{-1}. \quad (4.77)$$

It is, therefore, not an easy matter to evaluate the exact Knudsen number for problems that involve the flow of gas mixtures.

A result that is required for future reference is the number of collisions per unit time per unit volume in an equilibrium gas between molecules of species p and molecules of species q . This result follows from eqn (4.74) as

$$(N_{pq})_0 = 2\pi^{1/2} (d_{\text{ref}})_{pq}^2 n_p n_q \{T/(T_{\text{ref}})_{pq}\}^{1-\omega_{pq}} \{2k(T_{\text{ref}})_{pq}/m_r\}^{1/2}. \quad (4.78)$$

Note that this expression counts all collisions twice over in the sense that a single collision event advances both N_{pq} and N_{qp} . A symmetry factor of $1/2$ must be applied to recover the result for the number of collision events in a simple gas.

The effective diameter that determines the collision cross-section at relative speed c_r follows from eqn (4.63) as

$$d_{pq} = (d_{\text{ref}})_{pq} [\{ 2k(T_{\text{ref}})_{pq} / (m_r c_r^2) \}^{\omega-1/2} / \Gamma(5/2 - \omega_{pq})]^{1/2}. \quad (4.79)$$

The average relative translational energy in collisions between VHS molecules follows from a similar extension of the simple gas theory. i.e.

$$\overline{(E_{\text{tr}})_{pq}} = (5/2 - \omega_{pq}) k(T_{\text{ref}})_{pq}. \quad (4.80)$$

To extend this result to the whole gas again requires a summation and averaging process that also involves the collision rate for each combination of molecules.

4.5 Equilibrium with a solid surface

Maxwell (1879) proposed two models for the interaction of a stationary equilibrium gas with a solid surface that maintain equilibrium. *Specular reflection* is perfectly elastic with the molecular velocity component normal to the surface being reversed, while those parallel to the surface remain unchanged. In *diffuse reflection*, the velocity of each molecule after reflection is independent of its initial velocity. However, the velocities of the reflected molecules as a whole are distributed in accordance with the half-range equilibrium or Maxwellian distribution for the molecules that are directed away from the surface. Equilibrium diffuse reflection requires that both the surface temperature and the temperature associated with the reflected gas Maxwellian be equal to the gas temperature. In the case of specular reflection, the gas may have a stream velocity parallel to the surface, and a specularly reflecting surface is functionally identical to a plane of symmetry.

The general requirement for equilibrium between a gas and solid surface at the molecular level is that the interaction should satisfy the *reciprocity condition*. This is a relationship between the probability of a gas-surface interaction with a particular set of incident and reflected velocities and the probability of the inverse interaction. It may be written (Cercignani 1969, Wenaas 1971, or Kuščer 1971) as

$$\begin{aligned} \mathbf{c}_r \cdot \mathbf{e} P(-\mathbf{c}_r, -\mathbf{c}_i) \exp\{-E_c/(k T_w)\} \\ = -\mathbf{c}_i \cdot \mathbf{e} P(\mathbf{c}_i, \mathbf{c}_r) \exp\{-E_c/(k T_w)\}. \end{aligned} \quad (4.81)$$

The unit vector \mathbf{e} has been taken normal to the surface, which is at temperature T_w . $P(\mathbf{c}_1, \mathbf{c}_2)$ is the probability that a molecule incident on the surface with velocity \mathbf{c}_1 leaves with velocity \mathbf{c}_2 , and E_c is the energy of the molecule. This condition is related to the principle of detailed balance, and is satisfied by both the diffuse and specular models for a gas in equilibrium with a surface.

References

- BIRD, G.A. (1981). Monte Carlo simulation in an engineering context. *Progr. Astro. Aero.* **74**, 239–255.
- CERCIGNANI, C. (1969). *Mathematical methods in kinetic theory*, Plenum Press, New York.
- KUŠČER, J. (1971). Reciprocity in scattering of gas molecules by surfaces. *Surface Sci.* **25**, 225–237.
- MAXWELL, J.C. (1879) *Phil. Trans. Roy. Soc.* **1**, Appendix.
- WENAAS, E.P. (1971), Scattering at gas-surface interface. *J. Chem. Phys.* **54**, 376–388.

5

INELASTIC COLLISIONS AND SURFACE INTERACTIONS

5.1 Molecules with rotational energy

As noted in Chapter 1, rotational energy is associated only with diatomic and polyatomic molecules that consist of two or more atoms. Furthermore, there is no rotation about axes with a small moment of inertia, such as the internuclear axis of diatomic molecules. The most realistic of the classical monatomic models is the point centre of force, and the obvious extension would be two or more point centres of force separated by fixed distances.

Lordi and Mates (1970) studied the *two centres of repulsion* model and found that a complex numerical solution was required for each set of impact parameters. The model does not yield closed form expressions for the transport properties and it is impractical for application to simulation studies that require the computation of many millions of typical collisions. The *sphero-cylinder* model consists of a smooth elastic cylinder with hemispherical ends and is a logical extension of the simple hard sphere model with apparent relevance to diatomic gases. The collision mechanics of sphero-cylinders has been developed by Curtiss and Muckenfuss (1958). The model requires additional variables for the specification of the spatial orientation as well as the angular velocity. A particular difficulty is that this orientation, and therefore the cross-section, changes with time. Whether or not two molecules collide depends not only on the miss distance, but also whether or not they 'mesh' or 'clash'. Moreover, there may be multiple 'chattering' impacts in a single collision event. The *weighted-sphere* model had already been suggested by Jeans (1904) and has been extensively developed by Dahler and Sather (1962) and Sandler and Dahler (1967). Although it is spherical in geometry, the molecule rotates about the offset centre of gravity rather than the geometric centre. It therefore suffers from essentially the same disadvantages as the sphero-cylinder model. The only exact physical model of a rotating molecule that has a cross-section that is not affected by its orientation is the *rough-sphere* model. The name of this model is based on its basic physical property which is that the velocities at the point of contact of the two molecules are reversed on impact. The model was first suggested by Bryan (1894) and the transport properties were analysed by Pidduck (1922). This is the most easily applied model and it is described in detail in §5.2. The transport properties have been presented and critically discussed by Chapman and

Cowling (1970). As with the hard sphere model for a monatomic gas, the coefficient of viscosity is proportional to the square root of the temperature. It is more unrealistic than the hard sphere model in that a glancing collision can result in a large deflection. Also, all collisions can result in a large interchange of rotational and translational energy and the rotational relaxation time is unrealistically short. This could be lengthened by specifying that some fraction of the collisions follow the hard sphere, rather than rough-sphere, mechanics. However, there does not seem to be any way around the main disadvantage of the model. This is that it possesses three internal degrees of freedom, while most applications call for the two degrees of freedom of the common diatomic gases. The limitations of the models based on exact dynamical systems are sufficient to justify recourse to a phenomenological approach.

One way of dealing with internal states is to set cross-sections for all the allowable transitions between the rotational energy levels. The number of levels is of the order of the ratio of the temperature to the characteristic temperature of rotation Θ_r , that is tabulated in Appendix A. Except in the case of hydrogen or deuterium, the number of rotational levels that must be considered is sufficiently large to make the approach based on the cross-sections for the individual transitions excessively cumbersome. It also means that the rotational modes are fully excited, and that a classical representation is valid. The phenomenological models superimpose the energy exchange between the internal and translational energy upon an otherwise monatomic model. The models are therefore spherically symmetric, but since real collisions tend to average over all molecular orientations, and there can be no preferred directions in an equilibrium gas, this should not be a serious limitation. The phenomenological processes must allow the specification of the requisite number of rotational degrees of freedom and lead to equipartition between these modes. There must also be exact equipartition between the rotational and translational modes and, when the gas is in equilibrium, the distribution function of each quantity must be the local Maxwellian. In practice, this means that the processes must satisfy the principle of reciprocity or detailed balancing. It must also allow the specification of the rotational relaxation time, including the temperature dependence of this time.

The most widely used phenomenological model is that of Borgnakke and Larsen (1975), and it is described in detail in §5.3. Detailed balance is ensured by the selection of the post-collision values directly from the Maxwellian distributions. The relaxation rate is controlled by regarding a fraction of the collisions as elastic. This method is quite unrealistic from the physical point of view, but satisfies all requirements for a successful phenomenological model. The 'energy sink' model (Bird 1976) is more realistic from the physical point of view and forces equipartition. However, it cannot be recommended because it leads to distortions of the equilibrium distribution function and does not satisfy detailed balancing. Pullin (1978) reviewed the phenomenological models and introduced a more realistic, but more cumbersome, development of the Larsen–Borgnakke approach.

5.2 The rough-sphere molecular model

As noted above, the essential feature of this model is that, in a collision, the relative velocity at the point of contact is reversed. Both the translational and rotational velocities contribute to this relative velocity and its reversal generally leads to an interchange of energy between the rotational and translational modes, as well as between the collision partners. The total energy is, of course, conserved.

The rough sphere is the simplest of the real physical models with rotation and is useful for comparative tests with phenomenological models. The phenomenological models may be set to have identical macroscopic properties, and the purpose of the tests is to determine whether there is then any difference in the results for typical flows. A simple gas generally suffices for such tests, and the analysis assumes that the molecules are identical. The objective is to determine the relationship between the pre-collision and post-collision values of the translational and rotational velocity components, as a function of the impact parameters.

The angular velocity of a molecule is denoted by ω and its components about the x -, y -, and z -axes are ω_x , ω_y , and ω_z , respectively. The rotational energy of a molecule is $\frac{1}{2}I\omega^2$, where I is the moment of inertia. The moment of inertia depends upon the radial mass distribution of the molecule and therefore allows a limited range of variability in the model. It is most convenient to take a uniform mass distribution, for which

$$I = md^2/10. \quad (5.1)$$

The combined distribution function is (Chapman and Cowling 1970)

$$f = \frac{(mI)^{3/2}}{(2\pi kT)^3} \exp\left(-\frac{mc'^2 + I\omega^2}{2kT}\right)$$

and this may be written

$$f = (\beta^3/\pi^{3/2}) \exp(-\beta^2 c'^2) \{1/(\pi^{3/2} \omega_m^{3/2})\} \exp(-\omega^2/\omega_m^2). \quad (5.2)$$

Here, ω_m is the most probable angular speed and is related to the temperature by

$$\omega_m = (2kT/I)^{1/2}, \quad (5.3)$$

or, using eqn (5.1) for the uniform mass distribution,

$$\omega_m = (20RT)^{1/2}/d. \quad (5.4)$$

The equilibrium distribution of the angular speed ω with respect to the most probable value is, therefore, completely analogous to the distribution of the thermal speed with respect to the most probable molecular speed. All directions are equally probable for the axis of rotation. A rotational temperature may be defined by

$$\frac{3}{2}kT_{\text{rot}} = \frac{1}{2}I\overline{\omega^2}. \quad (5.5)$$

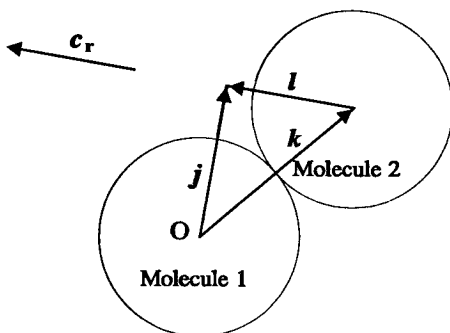


Fig. 5.1 The vectors j , k , and l in a rough-sphere collision.

The pre-collision values of the translational and rotational velocities of a collision pair are \mathbf{c}_1 , \mathbf{c}_2 , and $\boldsymbol{\omega}_1$, $\boldsymbol{\omega}_2$, respectively. These are regarded as known quantities and the objective is to determine the post-collision values \mathbf{c}_1^* , \mathbf{c}_2^* , $\boldsymbol{\omega}_1^*$, and $\boldsymbol{\omega}_2^*$.

The pre-collision relative velocity vector \mathbf{c}_r is defined here by

$$\mathbf{c}_r = \mathbf{c}_2 - \mathbf{c}_1.$$

Note that the sign convention is the opposite to that in eqn (2.3). The miss-distance impact parameter b is distributed between 0 and d , with probability proportional to d , while the azimuthal parameter ϵ is uniformly distributed between 0 and 2π . It is convenient to define three vectors j , k , and l in the collision plane, as shown in Fig. 5.1. The vector k is defined by the line joining the centre of molecule 1, which is taken as the origin O, to the centre of molecule 2. The vector l is in the direction of the relative velocity vector \mathbf{c}_r and joins the centre of molecule 2 to the plane through O normal to the direction of \mathbf{c}_r . Finally, the impact vector j is defined by $j = k + l$ and its magnitude is equal to the impact parameter b . Therefore, since the magnitude of k is equal to d and l is normal to j ,

$$l = (d^2 - b^2)^{1/2}. \quad (5.6)$$

Angles θ and ϕ are now defined such that θ is the angle between the x -axis and \mathbf{c}_r , and ϕ is the angle between the y -axis and the plane containing the x -axis and \mathbf{c}_r . Therefore

$$\cos \theta = u_r / c_r$$

and

$$\cos \phi = v_r / (c_r \sin \theta). \quad (5.7)$$

Then, with the azimuthal impact parameter measured from the plane $y = 0$, the components of the impact vector are

$$\begin{aligned} j_x &= b \cos \varepsilon \sin \theta, \\ j_y &= -b (\cos \varepsilon \cos \theta \cos \phi + \sin \varepsilon \sin \phi), \end{aligned} \quad (5.8)$$

and

$$j_z = b (\sin \varepsilon \cos \phi - \cos \varepsilon \cos \theta \sin \phi).$$

The magnitude of \mathbf{l} is given by eqn (5.6) and its components are

$$\begin{aligned} l_x &= lu_r/c_r, \\ l_y &= lv_r/c_r, \end{aligned}$$

and

$$l_z = lw_r/c_r. \quad (5.9)$$

The components k_x , k_y , and k_z of the vector \mathbf{k} along the line of centres follow from the relation $\mathbf{k} = \mathbf{j} - \mathbf{l}$. The components of the relative velocity of the point of contact are then given by

$$\begin{aligned} g_x &= u_r + \frac{1}{2}\{k_y(\omega_{z,1} + \omega_{z,2}) - k_z(\omega_{y,1} + \omega_{y,2})\}, \\ g_y &= v_r + \frac{1}{2}\{k_z(\omega_{x,1} + \omega_{x,2}) - k_x(\omega_{z,1} + \omega_{z,2})\}, \end{aligned} \quad (5.10)$$

and

$$g_z = w_r + \frac{1}{2}\{k_x(\omega_{y,1} + \omega_{y,2}) - k_y(\omega_{x,1} + \omega_{x,2})\}.$$

The scalar product of \mathbf{k} and \mathbf{c}_r is denoted by k_c , so that

$$k_c = \mathbf{k} \cdot \mathbf{c}_r = k_x u_r + k_y v_r + k_z w_r.$$

The post-collision values of the translational velocity components may now be related to the pre-collision values by

$$\begin{aligned} u_1^* - u_1 &= u_2 - u_2^* = \frac{2}{7}g_x + \frac{5}{7}k_c k_x / d^2, \\ v_1^* - v_1 &= v_2 - v_2^* = \frac{2}{7}g_y + \frac{5}{7}k_c k_y / d^2, \end{aligned} \quad (5.11)$$

and

$$w_1^* - w_1 = w_2 - w_2^* = \frac{2}{7}g_z + \frac{5}{7}k_c k_z / d^2,$$

Finally, the post-collision angular velocity components are given by

$$\begin{aligned} \omega_{x,1}^* - \omega_{x,1} &= \omega_{x,2}^* - \omega_{x,2} = \frac{10}{7}(k_y g_z - k_z g_y) / d^2, \\ \omega_{y,1}^* - \omega_{y,1} &= \omega_{y,2}^* - \omega_{y,2} = \frac{10}{7}(k_z g_x - k_x g_z) / d^2, \end{aligned} \quad (5.12)$$

and

$$\omega_{z,1}^* - \omega_{z,1} = \omega_{z,2}^* - \omega_{z,2} = \frac{10}{7}(k_x g_y - k_y g_x) / d^2.$$

5.3 The Larsen–Borgnakke model in a simple gas

If a collision is regarded as inelastic, the total energy is reassigned between the translational and internal modes by sampling from the equilibrium distributions of these modes that are appropriate to this total energy. The relaxation rate is controlled through the fraction of collisions that are regarded as inelastic. In fact, the inverse of this fraction provides a first approximation to the relaxation collision number. The elastic collisions are calculated as monatomic collisions. When this model is applied in simulation methods that require the computation of millions of collisions, it has near optimal computational efficiency.

In order to improve the physical realism of the model, Larsen and Borgnakke (1974) introduced the ‘restricted energy exchange’ modification. In this, all collisions are treated as inelastic, but the proportion of the energy of the collision pair that participates in the energy exchange is restricted. This is less efficient from the computational point of view and, more seriously, Pullin (1978) showed that it does not satisfy detailed balancing. We will be concerned only with the procedures for the completely inelastic collisions that are applied to some fraction Λ of the collisions. Real gases generally have a rotational relaxation time that varies with temperature. This may be simulated by variations in the fraction Λ but, if detailed balancing is to be satisfied, Λ may have to be a function of the macroscopic temperature, rather than of the energy of the collision pair. This point is investigated in §11.5.

For a gas with coefficient of viscosity proportional to temperature to the power ω , eqn (4.58) can be written in terms of the translational energy E_t in the collision as

$$\bar{Q} \propto \int_0^{\infty} Q E_t^{3/2-\omega} \exp\{-E_t/(kT)\} dE_t,$$

so that, by analogy with eqn (3.3), the distribution function for E_t is

$$f_{E_t} \propto E_t^{3/2-\omega} \exp\{-E_t/(kT)\}. \quad (5.13)$$

The internal energy E_i of a collision pair is the sum of the internal energies of the collision partners, i.e.

$$E_i = \epsilon_{i,1} + \epsilon_{i,2}. \quad (5.14)$$

The distribution function for the internal energy of a molecule with ζ internal degrees of freedom may be written (Hinshelwood 1940),

$$f_{\epsilon_i} \propto \epsilon_i^{\zeta/2-1} \exp\{-\epsilon_i/(kT)\}. \quad (5.15)$$

We now require the distribution function f_{E_i} for E_i . Consider the fraction of collision pairs with a particular value $\epsilon_{i,1}$ of internal energy in molecule 1, and therefore with $E_i - \epsilon_{i,1}$ in molecule 2. Using eqns (5.14) and (5.15), and noting that $dE_i = d\epsilon_{i,2}$ for fixed $\epsilon_{i,1}$, this fraction is proportional to

$$\epsilon_{i,1}^{\zeta/2-1} (E_i - \epsilon_{i,1})^{\zeta/2-1} \exp\{-E_i/(kT)\} d\epsilon_{i,1} dE_i. \quad (5.16)$$

The total fraction of collision pairs with internal energy in the range E_i to $E_i + dE_i$ is proportional to the expression obtained by integrating eqn (5.16) over all $\epsilon_{i,1}$ from 0 to E_i . Therefore,

$$f_{E_i} \propto E_i^{\zeta-1} \exp\{-E_i/(kT)\}. \quad (5.17)$$

The total energy E_c in the collision is the sum of the relative translational energy and the combined internal energy i.e.

$$E_c = E_t + E_i. \quad (5.18)$$

The probability density of E_t and E_i is proportional to the product of f_{E_t} and f_{E_i} i.e.

$$E_t^{3/2-\omega} E_i^{\zeta-1} \exp\{-(E_t + E_i)/(kT)\}$$

or, using eqn (5.18),

$$E_t^{3/2-\omega} (E_c - E_t)^{\zeta-1} \exp\{-E_c/(kT)\}.$$

The effective temperature T is defined by the total energy E_c in the collision, so that the exponential term may be regarded as a constant. The probability of a particular value of the translational energy is therefore

$$P = C E_t^{3/2-\omega} (E_c - E_t)^{\zeta-1}. \quad (5.19)$$

where C is a constant.

The maximum value of this probability is readily shown to occur for

$$\frac{E_t}{E_c} = \frac{3/2-\omega}{\zeta + 1/2-\omega} \quad (5.20)$$

and is

$$P_{\max} = C (3/2-\omega)^{3/2-\omega} (\zeta-1)^{\zeta-1} \{(\zeta + 1/2-\omega) E_c\}^{\zeta+1/2-\omega}.$$

The ratio of the probability to the maximum probability is, therefore,

$$\frac{P}{P_{\max}} = \left\{ \frac{\zeta + 1/2-\omega}{3/2-\omega} \left(\frac{E_t}{E_c} \right) \right\}^{3/2-\omega} \left\{ \frac{\zeta + 1/2-\omega}{\zeta-1} \left(1 - \frac{E_t}{E_c} \right) \right\}^{\zeta-1}. \quad (5.21)$$

A post-collision value of E_t^* is chosen at random from the range 0 to E_c . The ratio P/P_{\max} is evaluated by eqn (5.21) and is compared with a random fraction R_f that is generated from a uniform distribution between 0 and 1. This value of E_t^* is employed for the collision if the probability ratio is greater than R_f , but a new value is chosen and the process is repeated if the ratio is less than R_f . This is an application of the *acceptance-rejection method* for sampling from a prescribed distribution, that is discussed in Appendix C.

For a gas with $\omega = 1/2$ and two internal degrees of freedom, the equations take on a particularly simple form. The most probable value of E_t is $1/2 E_c$ and the probability ratio is

$$P/P_{\max} = 4(E_t/E_c)(1-E_t/E_c).$$

Note that the analysis applies equally to the VHS and VSS models and the inverse power law model, including the hard sphere and Maxwell cases.

The total energy in the collision is conserved and the post-collision internal energy and the post-collision value of the pair internal energy is, from eqn (5.18)

$$E_i^* = E_c - E_t^*. \quad (5.22)$$

This must now be divided between the two molecules. The post-collision total internal energy is a constant for this process, and eqn (5.16) shows that the probability that molecule 1 has a post-collision internal energy $\epsilon_{i,1}^*$ is

$$P = D (\epsilon_{i,1}^*)^{\zeta/2-1} (E_i^* - \epsilon_{i,1}^*)^{\zeta/2-1}, \quad (5.23)$$

where D is a constant.

The maximum probability occurs when the internal energy is equally divided between the two molecules, and the ratio of the probability to the maximum probability is

$$P/P_{\max} = 2^{\zeta-2} (\epsilon_{i,1}^* / E_i^*)^{\zeta/2-1} (1 - \epsilon_{i,1}^* / E_i^*)^{\zeta/2-1}. \quad (5.24)$$

The acceptance-rejection method may now be applied in a similar manner to the selection of the post-collision relative translational energy. The special case of two internal degrees of freedom is such that all values of the single molecule post-collision internal energy are equally possible.

The post-collision internal energy may be directly assigned to the two molecules. The post collision relative speed in the centre of mass frame of reference is

$$c_r^* = (2E_t^* / m_r) = 2(E_t^* / m)^{1/2}. \quad (5.25)$$

A new direction for this speed may be chosen at random for the VHS and hard sphere models, from eqn (2.35) for the VSS model, while, for the inverse power law model, eqn (2.22) for the post-collision velocity components is readily modified to allow for the energy change.

While the preceding equations are adequate for the application of the Larsen-Borgnakke model to numerical studies, its application to analytical studies requires explicit expressions for the distribution functions. Eqn (5.19) may written as the probability of E_t/E_c (E_c is regarded as a constant in this distribution), and the constant may then be determined from the condition that the integral of this probability with respect to E_t/E_c over the interval 0 to 1 must be unity. The modified constant is then

$$C E_c^{5/2-\omega+\zeta} = 1/B(5/2-\omega, \zeta) = \Gamma(5/2-\omega+\zeta)/(\Gamma(5/2-\omega)\Gamma(\zeta)),$$

and the distribution function for the fraction of translational energy in the collision is (Haas et al 1993)

$$f\left(\frac{E_t}{E_c}\right) = \frac{\Gamma(5/2-\omega+\zeta)}{\Gamma(5/2-\omega)\Gamma(\zeta)} \left(\frac{E_t}{E_c}\right)^{3/2-\omega} \left(1 - \frac{E_t}{E_c}\right)^{\zeta-1}. \quad (5.26)$$

The corresponding distribution function for the internal energy fraction is

$$f\left(\frac{E_i}{E_c}\right) = \frac{\Gamma(5/2-\omega+\zeta)}{\Gamma(5/2-\omega)\Gamma(\zeta)} \left(1 - \frac{E_i}{E_c}\right)^{3/2-\omega} \left(\frac{E_i}{E_c}\right)^{\zeta-1}. \quad (5.27)$$

A similar procedure can be applied to the probability expressed in eqn (5.23) to give the distribution function for the fraction of the post-collision internal energy in the species 1 molecule as

$$f\left(\frac{\varepsilon_{i,1}^*}{E_i^*}\right) = \frac{\Gamma(\zeta)}{\{\Gamma(\zeta/2)\}^2} \left(\frac{\varepsilon_{i,1}^*}{E_1^*}\right)^{\zeta/2-1} \left(1 - \frac{\varepsilon_{i,1}^*}{E_i^*}\right)^{\zeta/2-1}. \quad (5.28)$$

Note that the first distribution function becomes unity for the special case of two internal degrees of freedom. A similar distribution can be applied to any division of the internal energy of a single molecule into the energies of separate internal modes.

The preceding analysis has been essentially for the power-law models that include the VHS model, but Hassan and Hash (1993) have shown that it can be applied also to the GHS model. The distribution function for E_t can be written from eqn (4.59) as

$$f_{E_t} = \left(\frac{2}{\pi}\right)^{1/2} \frac{2}{m_r^2} \left(\frac{m_r}{kT}\right)^{3/2} \frac{1}{\sigma_T c_r} \sigma_T E_t \exp\left(-\frac{E_t}{kT}\right). \quad (5.29)$$

The product of f_{E_t} and f_{E_i} is now proportional to

$$\sigma_T E_t (E_c - E_t)^{\zeta-1} \exp\{-E_c/(kT)\}$$

and the probability of a particular value of the translational energy is now

$$P = C \sigma_T E_t (E_c - E_t)^{\zeta-1}, \quad (5.30)$$

where C is a constant (different from that in eqn (5.19)). This equation may be combined with the definition of the GHS model in eqn (3.80), to give

$$P = C' \{\alpha_1 (E_t/\varepsilon)^{1-\psi_1} + \alpha_2 (E_t/\varepsilon)^{1-\psi_2}\} \{(E_c/\varepsilon) - (E_t/\varepsilon)\}^{\zeta-1}, \quad (5.31)$$

where C' is another constant. The value of E_t at the maximum value of this probability is given by the solution of

$$\begin{aligned} & \alpha_1 (E_t/\varepsilon)^{-\psi_1} \{(\psi_1 - \zeta)(E_t/\varepsilon) + (1 - \psi_1)(E_c/\varepsilon)\} \\ & + \alpha_2 (E_t/\varepsilon)^{-\psi_2} \{(\psi_2 - \zeta)(E_t/\varepsilon) + (1 - \psi_2)(E_c/\varepsilon)\} = 0 \end{aligned} \quad (5.32)$$

and P_{\max} is found by substituting this value into eqn (5.31). An iterative solution is therefore required to determine P/P_{\max} in order to apply the acceptance-rejection method to the selection of a representative value of E_t . The remaining steps in the Larsen-Borgnakke method for the division of the internal energy between molecules and the division between modes within each molecule are unchanged from those for the power-law models.

5.4 The Larsen–Borgnakke model in a gas mixture

The two molecules in a collision may differ, not only in mass and diameter, but also in the number of internal degrees of freedom and the temperature exponent of the coefficient of viscosity. The latter difference can lead to mathematical difficulties but, if a separate exponent ω_{12} is determined for each combination of molecules in the collision, the simple gas theory is readily extended to the gas mixture. The distribution function for the relative translational energy is changed only by the replacement of ω by ω_{12} . Equation (5.15) applies if ζ is replaced by ζ_1 for the number of internal degrees of freedom of molecule 1. Eqn (5.16) then becomes

$$\varepsilon_{i,1}^{\zeta_1/2-1} (E_i - \varepsilon_{i,1})^{\zeta_2/2-1} \exp\{-E_i/(kT)\} d\varepsilon_{i,1} dE_i. \quad (5.33)$$

The integration of this equation over all values of the internal energy of molecule 1 now gives the following distribution function for E_i

$$f_{E_i} \propto E_i^{\bar{\zeta}-1} \exp\{-E_i/(kT)\}, \quad (5.34)$$

where $\bar{\zeta} = (\zeta_1 + \zeta_2)/2$ is the average number of internal degrees of freedom. The selection of the post-collision value of the translational energy is then unchanged from the simple gas case, as long as ζ is replaced by $\bar{\zeta}$ and ω is replaced by ω_{12} . However, the singularity at $\zeta=1$ must be taken into consideration in the case of a gas mixture. For example, the mean number of degrees of freedom is unity in the collision of a diatomic molecule with a monatomic molecule. Also, the rotational relaxation rate varies with the molecular species, and the collision between a diatomic molecule for which the rotational energy is to change with a similar molecule for which it is not to change can also lead to a value of unity for the mean number of effective degrees of freedom. The maximum probability then occurs when E_t is equal to E_c , and the probability ratio is

$$P/P_{\max} = (E_t/E_c)^{3/2-\omega_{12}}. \quad (5.35)$$

The distribution function for the ratio of the translational energy to the total energy in a collision between unlike molecules is

$$f\left(\frac{E_t}{E_c}\right) = \frac{\Gamma(5/2 - \omega_{12} + \bar{\zeta})}{\Gamma(5/2 - \omega_{12})\Gamma(\bar{\zeta})} \left(\frac{E_t}{E_c}\right)^{3/2-\omega_{12}} \left(1 - \frac{E_t}{E_c}\right)^{\bar{\zeta}-1}. \quad (5.36)$$

The equation simplifies when the mean number of participating internal degrees of freedom is unity.

The equations for the division of the internal energy between the two molecules are more strongly affected. The equation for the probability of internal energy in molecule 1 becomes

$$P = D (\varepsilon_{i,1}^*)^{\zeta_1/2-1} (E_i^* - \varepsilon_{i,1}^*)^{\zeta_2/2-1}.$$

The maximum probability is when the internal energy is

$$\varepsilon_{i,1}^* = \frac{1}{2} E_i^* (\zeta_1/2 - 1) / (\bar{\zeta}/2 - 1)$$

and the ratio of the probability to the maximum probability becomes

$$\frac{P}{P_{\max}} = \frac{(\bar{\zeta} - 2)^{\bar{\zeta}-2}}{(\zeta_1/2-1)^{\zeta_1/2-1}(\zeta_2/2-1)^{\zeta_2/2-1}} \left(\frac{\varepsilon_{i,1}^*}{E_i^*} \right)^{\zeta_1/2-1} \left(1 - \frac{\varepsilon_{i,1}^*}{E_i^*} \right)^{\zeta_2/2-1}. \quad (5.37)$$

If both ζ_1 and ζ_2 are equal to two, the internal energy is uniformly distributed, as for the simple gas case. The probability ratio for $\zeta_1 = 2$ is

$$P/P_{\max} = (1 - \varepsilon_{i,1}^*/E_i^*)^{\zeta_2/2-1}, \quad (5.38)$$

and that for $\zeta_2 = 2$ is

$$P/P_{\max} = (\varepsilon_{i,1}^*/E_i^*)^{\zeta_1/2-1}. \quad (5.39)$$

The singularity when ζ_1 and ζ_2 are unequal but have a mean value of two is more difficult. The probability equation for the energy in molecule 1 is

$$P = D \left(\frac{\varepsilon_{i,1}^*}{E_i^* - \varepsilon_{i,1}} \right)^{\zeta_1/2-1}, \quad (5.40)$$

and this is infinite when $\varepsilon_{i,1}^* = E_i^*$ and $\zeta_2/2-1$ is positive, or when $\varepsilon_{i,1}^* = 0$ and $\zeta_2/2-1$ is negative. The acceptance-rejection method can be applied if a cut-off value is applied to the energy before the singularity is reached.

The distribution function for the ratio of post-collision energy in the species 1 molecule is

$$f\left(\frac{\varepsilon_{i,1}^*}{E_i^*}\right) = \frac{\Gamma(\bar{\zeta})}{\Gamma(\zeta_1/2)\Gamma(\zeta_2/2)} \left(\frac{\varepsilon_{i,1}^*}{E_i^*} \right)^{\zeta_1/2-1} \left(1 - \frac{\varepsilon_{i,1}^*}{E_i^*} \right)^{\zeta_2/2-1}. \quad (5.41)$$

The preceding theory may be applied separately to each pair of species in a multiple mixture.

5.5 The general Larsen-Borgnakke distribution

A general Larsen-Borgnakke distribution function for the division of energy between the translational and internal modes, between molecules, and between internal modes in each molecule may be defined such that it includes all the distribution functions of the preceding sections as special cases. Consider a collision between a molecule of species 1 and a molecule of species 2. The parameter Ξ is defined as the sum of the *average* degrees of freedom. The translational modes contribute $5/2 - \omega_{12}$, so that

$$\Xi = (5/2 - \omega_{12}) + \zeta_{\text{rot},1}/2 + \zeta_{\text{rot},2}/2 + \sum \zeta_{\text{v},1}/2 + \sum \zeta_{\text{v},2}/2. \quad (5.42)$$

The subscripts 1 and 2 refer to the two molecules, while the subscripts r and v refer to the rotational and vibrational modes respectively. The vibrational modes require special treatment and this is presented in the following section. Let Ξ_a be one or more of the terms in eqn (5.42) and let Ξ_b be the *remaining* terms that are participating in the division of energy.

The energy to be assigned to the first group of modes is E_a and E_b is that to be assigned to the second group. The Larsen–Borgnakke result for the distribution of energy between the two groups is

$$f\left(\frac{E_a}{E_a + E_b}\right) = f\left(\frac{E_b}{E_a + E_b}\right) = \frac{\Gamma(\Xi_a + \Xi_b)}{\Gamma(\Xi_a)\Gamma(\Xi_b)} \left(\frac{E_a}{E_a + E_b}\right)^{\Xi_a-1} \left(\frac{E_b}{E_a + E_b}\right)^{\Xi_b-1}. \quad (5.43)$$

The sum $E_a + E_b$ of the energy in the two groups is a constant equal to the pre-collision value of the sum, so that the average energy in the first group is

$$\overline{E_a} = \frac{\Gamma(\Xi_a + \Xi_b)}{\Gamma(\Xi_a)\Gamma(\Xi_b)} \int_0^1 \left(\frac{E_a}{E_a + E_b}\right)^{\Xi_a} \left(1 - \frac{E_a}{E_a + E_b}\right)^{\Xi_b-1} d\left(\frac{E_a}{E_a + E_b}\right).$$

This may be evaluated through eqns (B4), (B37), and (B38), to give

$$\overline{E_a} = \frac{\Xi_a}{\Xi_a + \Xi_b} (E_a + E_b). \quad (5.44)$$

The average energy ratio is therefore equal to the ratio of the number of degrees of freedom, and this confirms that the Larsen–Borgnakke method leads to the equipartition of energy.

For the special case of the assignment of energy to a single internal mode with two degrees of freedom, $\Xi_a=1$, and eqn (5.43) reduces to

$$f\left(\frac{E_a}{E_a + E_b}\right) = \Xi_b \left(1 - \frac{E_a}{E_a + E_b}\right)^{\Xi_b-1}. \quad (5.45)$$

This distribution function is amenable to sampling from the inverse cumulative distribution function, and it is shown in Appendix C that the representative value corresponding to the random fraction R_f is

$$\frac{E_a}{E_a + E_b} = 1 - R_f^{1/\Xi_b}. \quad (5.46)$$

The probability that the energy E_a in the internal mode exceeds some reference value E_d is obtained by integrating eqn (5.45) with respect to $E_a/(E_a+E_b)$ from $E_d/(E_a+E_b)$ to 1, to give

$$P_{E_a > E_d} = \left(1 - \frac{E_d}{E_a + E_b}\right)^{\Xi_b}. \quad (5.47)$$

Note that these distributions for the partitioning of energy do not just sample from the local equilibrium distribution. The temperature of the Maxwellian that appears in the derivation of the Larsen–Borgnakke method is based on an ‘effective temperature’ of the *particular* collision.

The preceding analysis has implicitly assumed that the parameter Σ in eqn (5.42) includes all modes that are subject to Larsen-Borgnakke energy redistribution in the collision. It has generally been assumed that the total collision energy E_c must include the energy of all modes that are to be subject to redistribution in the collision. The following analysis shows that this is an unnecessary restriction.

Consider the selection of energy ε_1 into a single internal mode with ζ_1 degrees of freedom. The distribution functions are identical if the cumulative distributions are identical, and the analysis is facilitated if we represent the cumulative distribution by the probability $P_{\varepsilon_1 > E_a}$ that ε_1 exceeds some reference value E_a . The sum of the degrees of freedom of the other internal modes that are active for redistribution in the collision is $\Sigma \zeta$. If the collision energy includes that in all internal degrees of freedom, the distribution function for the energy in the mode being considered is, from eqn (5.43),

$$f\left(\frac{\varepsilon_1}{E_c}\right) = \frac{\Gamma(5/2 - \omega_{12} + \Sigma \zeta / 2 + \zeta_1 / 2)}{\Gamma(5/2 - \omega_{12} + \Sigma \zeta / 2) \Gamma(\zeta_1 / 2)} \left(1 - \frac{\varepsilon_1}{E_c}\right)^{3/2 - \omega_{12} + \Sigma \zeta / 2} \left(\frac{\varepsilon_1}{E_c}\right)^{\zeta_1 / 2 - 1}. \quad (5.48)$$

The probability that ε_1 exceeds E_a in this particular collision is, therefore,

$$P = \frac{\Gamma(5/2 - \omega_{12} + \Sigma \zeta / 2 + \zeta_1 / 2)}{\Gamma(5/2 - \omega_{12} + \Sigma \zeta / 2) \Gamma(\zeta_1 / 2)} \int_{E_a/E_c}^1 \left(1 - \frac{\varepsilon_1}{E_c}\right)^{3/2 - \omega_{12} + \Sigma \zeta / 2} \left(\frac{\varepsilon_1}{E_c}\right)^{\zeta_1 / 2 - 1} d\left(\frac{\varepsilon_1}{E_c}\right)$$

and eqns (B40) and (B41) enable this to be written

$$P = I_{1-E_a/E_c}(5/2 - \omega_{12} + \Sigma \zeta / 2, \zeta_1 / 2), \quad (5.49)$$

where I is the function defined by eqn (B40)

The required probability is obtained by integrating this probability over all collisions in which E_c exceeds E_a . E_c is the sum of the translational energy with the distribution function of eqn (5.13) and the internal energy with the distribution function of eqn (5.27). The distribution function for E_c is the product of the individual functions, and this may be normalized in the usual way. We then have

$$\begin{aligned} P_{\varepsilon_1 > E_a} &= \frac{1}{\Gamma(5/2 - \omega_{12} + \Sigma \zeta / 2 + \zeta_1 / 2)} \int_{E_a/kT}^{\infty} \left(\frac{E_c}{kT}\right)^{3/2 - \omega_{12} + \Sigma \zeta / 2 + \zeta_1 / 2} \\ &\quad \times I_{1-E_a/E_c}(5/2 - \omega_{12} + \Sigma \zeta / 2, \zeta_1 / 2) \exp\left(-\frac{E_c}{kT}\right) d\left(\frac{E_c}{kT}\right). \end{aligned} \quad (5.50)$$

If the redistribution is between the translational energy and the mode 1 internal energy only, the probability is given by eqn (5.50) with $\Sigma \zeta$ set to zero. Therefore, the necessary and sufficient condition for the serial redistribution to be valid is that the expression

$$\frac{1}{\Gamma(a+b)} \int_d^{\infty} c^{a+b-1} I_{1-d/c}(a,b) \exp(-c) dc \quad (5.51)$$

must be independent of a .

For the common case in which the redistribution is to an internal mode with two degrees of freedom, $b = 1$ and eqn (B43) eliminates the incomplete beta function. The expression then becomes

$$\frac{1}{\Gamma(a+1)} \int_d^{\infty} c^a (1-d/c)^a \exp(-c) dc,$$

and, if the integration variable is changed to $c-d$, this becomes

$$\frac{\exp(-d)}{\Gamma(a+1)} \int_0^{\infty} (c-d)^a \exp(-(c-d)) d(c-d).$$

The integral is now the gamma function of $a+1$ and the expression reduces to $\exp(-d)$, so that the condition is satisfied. Numerical integration is required for values of b other than 1. This was performed for a number of values of b , both less than 1 and greater than 1. In all cases, it was found that the expression was unaffected by the value of a .

The Larsen-Borgnakke process is therefore unaffected if there is a succession of redistributions, each of which involves only a single internal mode and the translational mode. Although the 'collision energy' in each of these 'serial' redistributions is less than that in a redistribution that involves all energy modes, this is exactly balanced by the greater fraction of the energy that goes into the single internal mode in the serial case. The parameter Ξ_b that appears in eqn (5.45) for the redistribution to a single internal mode with two degrees of freedom is obtained by excluding from Ξ the effective number of degrees of freedom of this mode. This will be shown to be valuable in the quantum vibration model because it removes the need to specify the effective number of degrees of freedom.

5.6 Vibrational and electronic energy

The reason for treating the vibrational energy modes separately from the rotational modes is that the vibrational levels are widely spaced and vibration can rarely be regarded as being fully excited. Advantage can be taken of the wide spacing to treat each level as a distinct species with specified cross-sections for the transitions between levels that occur as a result of intermolecular collisions. However, if a classical model were to be used, the obvious 'physical' model of a diatomic molecule would be two spheres connected by a spring. This would add a number of additional problems to those discussed in §5.1 for the spherocylinder model, and the model would almost certainly be inadequate as well as impractical. There seems to be no alternative to a phenomenological approach.

The Larsen–Borgnakke method can be applied to the vibrational modes through either a classical procedure that assigns a continuously distributed vibrational energy to each molecule, or through a quantum approach that assigns a discrete vibrational level to each molecule.

The classical version regards the degree of excitation and the effective number of vibrational degrees of freedom as variables. If it is assumed that the vibration follows the simple harmonic oscillator model, the specific vibrational energy associated with a mode having a characteristic vibrational temperature Θ_v is

$$e_v = \frac{R \Theta_v}{\exp(\Theta_v/T) - 1}. \quad (5.52)$$

Then, by analogy with eqn (1.31), the effective number of degrees of freedom at temperature T is

$$\zeta_v = \frac{2 \Theta_v / T}{\exp(\Theta_v / T) - 1}. \quad (5.53)$$

Note that, for small x , $\exp(x) = 1 + x$, so that the number of degrees of freedom tends to 2 as the temperature becomes large in comparison with the characteristic temperature. A number of vibrational modes may be associated with a molecule, and each of these will have a distinct characteristic temperature. The characteristic temperatures that are associated with typical diatomic and polyatomic molecules are listed in Appendix A. The total vibrational energy is obtained by summing over all modes.

In order to apply the harmonic oscillator model within the Larsen–Borgnakke method, an effective temperature must be determined from the energies in the collision. As noted earlier, the method involves an implicit temperature based on the total energy in the collision. Equipartition is achieved if the number of effective degrees of freedom is determined for each molecule from the total collision energy associated with that molecule. In a collision between a species p molecule with a species q molecule the effective temperature of the species p molecule is given by

$$T_p = \frac{(E_t + \epsilon_{i,p})/k}{5/2 - \omega_{pq} + \zeta_{\text{rot},p}/2 + \sum_{j=1}^{j_p} \frac{\Theta_{v,p,j}/T_p}{\exp(\Theta_{v,p,j}/T_p) - 1}} \quad (5.54)$$

where $\zeta_{\text{rot},p}$ is the number of rotational degrees of freedom and j_p the number of vibrational modes of this species. An iterative method must be used to solve this equation and the similar equation for species q for T_p and T_q , respectively. The number of vibrational degrees of freedom for each molecule is then obtained by substituting these temperatures into eqn (5.53) and summing over all modes.

It is also necessary to divide the internal energy ϵ_i of the individual molecules into the rotational energy ϵ_r and vibrational energy ϵ_v . Note that both the subscript to indicate the species and the asterisk superscript to indicate the post-collision values have been omitted because they each apply to all three energies. Each of ϵ_r and ϵ_v is distributed in accordance with the distribution function of eqn (5.15), and eqn (5.16) now shows that the probability of a particular value of ϵ_r is proportional to

$$(\epsilon_r)^{\zeta_r/2-1} (\epsilon_i - \epsilon_r)^{\zeta_v/2-1} \quad (5.55)$$

and

$$\epsilon_v = \epsilon_i - \epsilon_r. \quad (5.56)$$

These equations are similar to the equations that led to eqn (5.37), and the application of the acceptance-rejection procedure leads to similar problems with singularities when one or other of the exponents is zero or negative. These may be dealt with in a similar manner to that proposed in the discussion of eqn (5.37). Alternatively, the distribution between internal energies could have been avoided through the adoption of the serial mode of application of the Larsen-Borgnakke technique. In any case, this classical treatment of the vibrational modes has been effectively superseded by the quantum model.

The quantum versions of the Larsen-Borgnakke method restrict the values of the vibrational energy of a molecule to those that correspond to the discrete quantum levels. For level i of a particular mode, the harmonic oscillator model gives the vibrational energy of that mode as

$$\epsilon_i = i k \Theta_v. \quad (5.57)$$

Quantum models were introduced by Haas et al (1993) and by Bergemann and Boyd (1994). The following treatment is based largely on the latter model. The Boltzmann distribution of the energy levels i can be written

$$f_{\epsilon_v} \propto \exp\left(-\frac{\epsilon_v}{kT}\right) \delta(\epsilon_v - i k \Theta_v). \quad (5.58)$$

The Dirac delta function δ is defined such that

$$\int_a^b f(x) \delta(x - x_0) = \begin{cases} f(x_0) & \text{if } a < x_0 < b \\ 0 & \text{otherwise.} \end{cases} \quad (5.59)$$

The integer i ranges from 0 to ∞ , and the δ function effectively transforms an integration over a continuous distribution of energy into a summation over the discrete energy levels.

Consider the Larsen-Borgnakke distribution of energy into a particular vibrational mode of molecule 1. Advantage may be taken of the option that

allows the serial consideration of the internal modes, as discussed in the final paragraph of the preceding section. The parameter Ξ_b is then $5/2 - \omega_{12}$ and the 'collision energy' E_c is the sum of the pre-collision vibrational energy of molecule 1 and the relative translational energy. The energy in the modes other than that under selection is simply the relative translational energy E_t , and the distribution function for E_t is given by eqn (5.13). The distribution function for a particular combination of ϵ_v and E_t is given by the product of this distribution and that in eqn (5.58), or

$$(E_c - \epsilon_v)^{3/2 - \omega_{12}} \delta(\epsilon_v - i k \Theta_v) \exp\{-E_c/(kT)\}.$$

The energy E_c is a constant in this distribution, and the exponential term may again be regarded as a constant. The maximum probability is for the ground state at $\epsilon_v = 0$, and the ratio of the probability of a particular level to that of the ground state is

$$\frac{P}{P_{\max}} = \left(1 - \frac{\epsilon_v}{E_c}\right)^{3/2 - \omega_{12}} \delta(\epsilon_v - i^* k \Theta_v). \quad (5.60)$$

The analysis has followed the usual convention of regarding the ground state with $i^* = 0$ as being at zero energy. In fact, there is a finite zero-point energy of $1/2k\Theta_v$ in this state, and there is no difficulty associated with the setting of a negative lower limit in the definition of the Dirac delta for the ground state. The probability ratio may be written in a discrete form as

$$\frac{P}{P_{\max}} = \left(1 - \frac{i^* k \Theta_v}{E_c}\right)^{3/2 - \omega_{12}}. \quad (5.61)$$

The acceptance-rejection method is applied to this probability ratio in order to select the energy in the post-collision level i^* of molecule 1. This selection process is applied to potential levels that are chosen uniformly from the integers between 0 and the maximum level

$$i_{\max}^* = \lfloor E_c / (k \Theta_{v,1}) \rfloor, \quad (5.62)$$

where $\lfloor . \rfloor$ denotes truncation.

Note that the partial excitation of the gas as a whole comes entirely from the truncation of the vibrational energy to the discrete quantum levels during the selection process. The above analysis employs the equally spaced energy levels of the harmonic oscillator model. Alternatively, the method may be based on lists of the actual anharmonic vibrational levels for each molecular species. Dissociation of the molecule occurs if the selection process yields the vibrational level that corresponds to the dissociation energy. The resulting chemical rate coefficients are derived and discussed in §6.6.

The Boltzmann distribution for the electronic levels gives the following result for the fraction of molecules in level i

$$\frac{N_i}{N} = \frac{g_i \exp\{-\epsilon_{el,i}/(kT)\}}{\sum g_i \exp\{-\epsilon_{el,i}/(kT)\}}. \quad (5.63)$$

Here, $\epsilon_{el,i}$ is the energy of level i and g_i is the degeneracy (or number of states in the level), and the summation is over all electronic levels. The Dirac delta can again be used to write this discrete distribution as a continuous distribution function for ϵ_{el} . This is

$$f_{\epsilon_{el}} \propto g_i \exp\left(-\frac{\epsilon_{el}}{kT}\right) \delta(\epsilon_{el} - \epsilon_{el,i}). \quad (5.64)$$

The Larsen–Borgnakke method can then be applied in a similar manner to vibration. However, the effect of the degeneracy is best taken into account in the selection of the states prior to the application of the acceptance–rejection procedure. The selection is between the translational and the electronic mode, and the ‘collision energy’ E_c is the sum of the energies in these modes. The maximum possible level is determined by the truncation of E_c , and the degeneracies are taken into account when selecting a possible state uniformly from the total number of states in the allowed levels. The acceptance–rejection procedure is then applied to the selected state through the probability ratio

$$\frac{P}{P_{\max}} = \left(1 - \frac{\epsilon_{el,i}}{E_c}\right)^{3/2-\omega_{12}}. \quad (5.65)$$

5.7 Relaxation rates

Consider a gas in which the temperature T_i of a particular internal mode is different from that of the gas as a whole. Intermolecular collisions cause T_i to relax towards the final equilibrium temperature. From eqn (5.44), the average value of the energy that is selected by the Larsen–Borgnakke method into a fully excited internal mode is

$$\bar{\epsilon} = E_c / (5/2 - \omega + \bar{\zeta}), \quad (5.66)$$

where E_c is the total collision energy and $\bar{\zeta}$ is the mean number of internal degrees of freedom that contribute to E_c . While E_c is a constant for the selection process that is described by eqn (5.66), it varies from collision to collision and the mean value of E_c may be approximated by

$$\overline{E_c} = (5/2 - \omega_{12} + \bar{\zeta}) k T_e,$$

where T_e is the *final equilibrium* temperature of the gas. Therefore, if the (non-equilibrium) collision rate is v and the fraction of inelastic collisions is Λ , the overall rate at which energy is transferred to the internal mode is

$$d\epsilon_i/dt = v \Lambda k T_e.$$

The rate at which energy is transferred from this mode is

$$\frac{d\epsilon_i}{dt} = -v \Lambda k T_i,$$

so that the net rate of change of the internal temperature is

$$\frac{dT_i}{dt} = v \Lambda (T_e - T_i). \quad (5.67)$$

Both v and Λ may be functions of temperature, and the integration of this equation must be with respect to $v\Lambda t$. This gives

$$T_i = T_e - (T_e - T_{i,0}) \exp(-v\Lambda t), \quad (5.68)$$

where $T_{i,0}$ is the value of the internal temperature at zero time.

The *relaxation time* is defined (Chapman and Cowling 1970) as the time in which a disturbance to the equilibrium state decays to $1/e$ of its original value. This time is $1/(v\Lambda)$, and the relaxation collision number on the 'collision rate time-scale' is given approximately by

$$Z_i = 1/\Lambda. \quad (5.69)$$

A more precise result for the rotational mode (Haas et al 1994) is

$$Z_i = \frac{3\zeta_{\text{rot}}(5-2\omega + \zeta_{\text{rot}})}{(3+\zeta_{\text{rot}})(5/2-\omega)(5/2-\omega + \zeta_{\text{rot}})[1 - \{1 - \zeta_{\text{rot}}\Lambda/(5/2-\omega + \zeta_{\text{rot}})\}^2]}. \quad (5.70)$$

This is illustrated in Fig. 5.2 for $\zeta_{\text{rot}} = 2$. The departure of the product ΛZ_i from the approximate value of unity is relatively small for realistic cases.

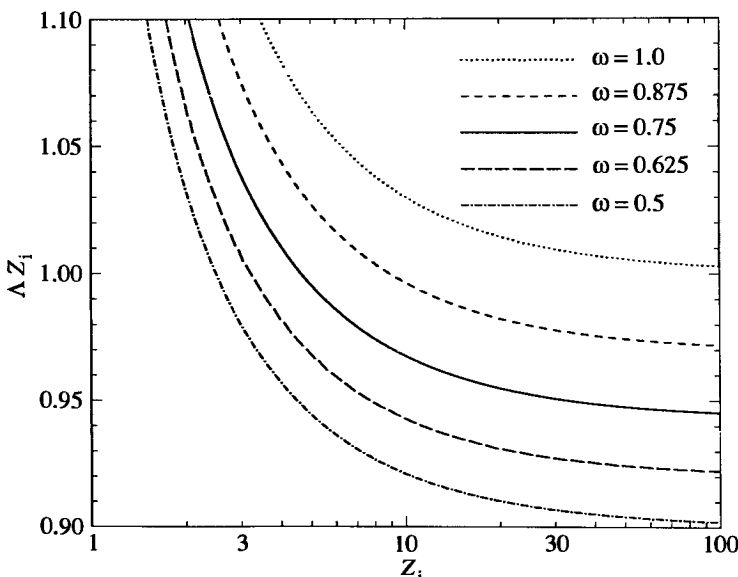


Fig. 5.2 The relationship of the inelastic fraction to the relaxation rate.

5.8 Gas-surface interactions

The majority of problems involve the interaction of gas molecules with solid surfaces. The gas generally has a stream velocity relative to the surface, and this means that the stagnation temperature of the gas differs from its static temperature. In addition, the surface temperature must differ from at least one of these, and the distribution function of the incident molecules will be different from that for the reflected molecules. Therefore, the distribution function of the gas near the surface will not be an equilibrium distribution. Also, the energy of a molecule relative to the surface before it strikes the surface will generally be different from the corresponding energy after it has been reflected from the surface, so that the process is inelastic. The current models for gas-surface interactions are largely phenomenological in nature and their adequacy varies with the nature of the surface and the magnitude of the impact energy of the molecule relative to the surface. The most widely used models are based on generalizations of the diffuse and specular models that were discussed in §4.5 in the context of a gas and surface in equilibrium.

The most common generalization of the diffuse model is to allow the incident and reflected molecules to have different temperatures. For example, it may be assumed that the molecules that are incident on the surface are characteristic of those in an equilibrium gas at temperature T_i , and that those reflected from the surface are characteristic of those in an equilibrium gas at temperature T_r . Note that the temperature T_r may differ from the temperature T_w of the surface. An indication of the extent to which the reflected molecules have their temperature adjusted toward that of the surface is given by the thermal *accommodation coefficient*

$$\alpha_c = (q_i - q_r) / (q_i - q_w). \quad (5.71)$$

Here, q_i and q_r are respectively the incident and reflected energy fluxes, while q_w is the energy flux that would be carried away in diffuse reflection with $T_r = T_w$. The range of α_c is from zero for no accommodation to unity for complete thermal accommodation. Accommodation coefficients may also be defined for the normal and tangential components of momentum. However, the accommodation coefficients may be written as functions of the macroscopic pressure, shear stress, and heat flux and, in general, it is preferable to describe the interaction directly in terms of these quantities.

Experiments with 'engineering' surfaces in contact with gases at normal temperatures indicate that the reflection process approximates diffuse reflection with complete thermal accommodation. This behaviour may be a consequence of such surfaces being microscopically rough with the incident molecules suffering multiple scattering, or of the molecules being momentarily trapped or adsorbed on the surface. Most analytical and numerical studies are based on the assumption of diffuse reflection, and it is fortunate that this appears to be adequate for the vast majority of practical gas flows. The diffuse assumption should be critically reviewed whenever one or more of the following factors are present:

- (i) a smooth metal surface that has been outgassed through exposure to high vacuum and high temperatures;
- (ii) the ratio of the molecular weight of the gas to that of the surface molecules is small in comparison with unity;
- (iii) the translational energy of the molecules relative to the surface is larger than several electron volts.

Measurements of the heat transfer to static gases from heated wires with carefully prepared and thoroughly outgassed surfaces indicate that thermal accommodation coefficients can be significantly less than one. In fact, the thermal accommodation coefficient for light gases on heavy metals surfaces may be very small in comparison with unity (Thomas 1967). Other experiments, using molecular beams directed at similarly prepared surfaces, have shown that the reflected molecules can, on the average, retain some momentum parallel to the surface. These results have been reinforced by measurements in supersonic wind tunnels that employ highly rarefied gases. These indicate that the drag coefficients of bodies such as cones can be significantly lower than the values that would be expected for diffuse reflection. Finally, a measurement of the angular distribution of atomic oxygen from a carbon surface on orbit (Gregory and Peters 1986) found that there was a peak in the reflected number flux in the specular direction. The problem is particularly serious for high-speed flows. As the translational energy of the incident molecules relative to the surface becomes large in comparison with the value corresponding to the surface temperature, complete thermal accommodation is less easily achieved. In addition, for very-high-impact speeds, some of the relative translational energy may be transferred to the internal modes of the incident molecule rather than to the surface. There is also the possibility of chemical reactions, either with surface molecules or with adsorbed gas molecules.

A practical problem that is seriously affected by the above uncertainties is the prediction of the orbital drag of satellites. The translational energy of the atmospheric molecules relative to the surface is approximately 5 eV, compared with a typical 0.025 eV for a molecule of a stationary gas at standard temperature. In addition, the satellite surface is cleaned by outgassing during its long exposure to an ultra high vacuum. The satellite drag coefficient is uncertain and, since this is required in order for the atmospheric density to be inferred from observations of the orbital decay, the atmospheric density is also uncertain.

Any physical model for the interaction of a molecule with a surface would have to be far more complex than the models that have been presented for intermolecular collisions in the gas phase. This applies even to the ideal case of a macroscopically flat surface with no adsorbed gas layer. There is no model of gas surface interactions that is adequate for quantitative studies over a wide range of parameters for all combinations of gases and surfaces, and it is unlikely that one will be forthcoming. If sufficient experimental data were to become available for a particular

application, it could be used to determine the adjustable parameters in an empirical model that satisfies the physical constraints. In the absence of such a model, non-diffuse reflection has most frequently been represented by assuming that some fraction ϵ of the molecules are reflected specularly, while the remainder are reflected diffusely. However, this model cannot reproduce the molecular beam data that has been obtained for particular cases and there is no justification for the implicit assumption that the result should lie between the limits set by complete diffuse and complete specular reflection. There is, therefore, a need for a more general empirical model.

It is generally accepted that any such model should satisfy the *reciprocity* condition that was defined in eqn (4.81). However, its proof (Wenaas 1971) for the non-equilibrium situation is based on a model of the surface as a phase space array of a large number of identical components. On the assumption that each of these components interacts only once with a gas molecule, the reciprocity condition follows as a consequence of the time reversal invariance of the laws of quantum mechanics. There may be some reservations about the validity of the reciprocity principle when the impact energy of the incident molecule is sufficient to produce a collective reaction among the atoms of the surface lattice. Miller and Subbarao (1971) have verified the reciprocity principle experimentally, but their molecular beam experiments were restricted to a narrow energy range and to cases in which the reflected energy was not very different from the incident energy. Cercignani and Lampis (1971) produced a gas-surface interaction model that satisfies reciprocity. This model has been further developed by Lord (1991a,b), and his results are summarized in the following paragraphs.

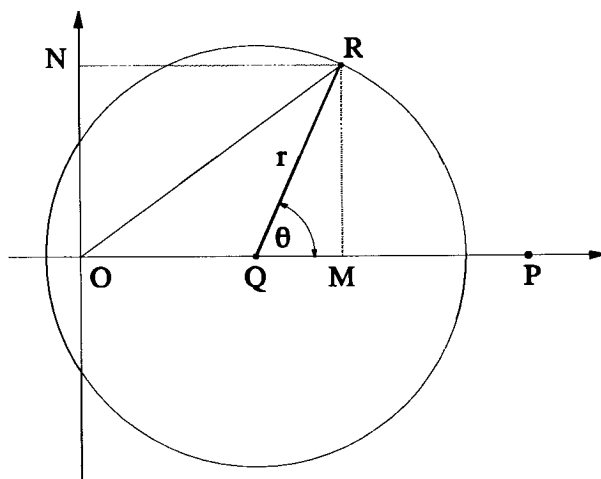


Fig. 5.3 Geometrical representation of the Cercignani–Lampis model.

The model assumes that there is no coupling between the normal and tangential components of the velocity during the reflection process. Set u to be the normal component of the molecular velocity normalized to the most probable molecular speed at the surface temperature, and v and w to be the similarly normalized tangential components.

The probability that an incident molecule with a normalized tangential component v_i is reflected with v_r is

$$P(v_i, v_r) = \{\pi a_t(2-a_t)\}^{-\frac{1}{2}} \exp[-(v_r - (1-a_t)v_i)^2 / \{a_t(2-a_t)\}]. \quad (5.72)$$

Here, a_t is an accommodation coefficient for this component of velocity and $\alpha_t = a_t(2-a_t)$ can be regarded as the accommodation coefficient for the energy of this component normalized to kT . These equations satisfy the reciprocity equation (4.81) and also the normalization condition

$$\int_{-\infty}^{\infty} P(v_i, v_r) dv = 1. \quad (5.73)$$

The integral in the normalization condition for the normal component of velocity extends only from 0 to ∞ , and the corresponding probability or 'scattering kernel' is

$$P(u_i, u_r) = (2u_r/\alpha_n) I_0[2(1-\alpha_n)^{\frac{1}{2}} u_i u_r / \alpha_n] \exp[(u_r^2 + (1-\alpha_n)u_i^2) / \alpha_n]. \quad (5.74)$$

It can be shown that the probability function for the magnitude $(v^2 + w^2)^{\frac{1}{2}}$ of the two tangential components also satisfies this equation, as does the function for two components of the angular velocity. Lord introduced the graphical construction of Fig. 5.3 to illustrate this general probability function. The state of the incident molecule may be represented by the point P on the x -axis, and its distance OP from the origin can represent the magnitude of either u_i , $(v_i^2 + w_i^2)^{\frac{1}{2}}$, or ω_i . The point Q represents the average state of the reflected molecules and is situated on OP such that $OQ/OP = (1-\alpha)^{\frac{1}{2}}$, where the energy accommodation coefficient is either α_n or a_t , as appropriate. The actual state of the reflected molecule is represented by the point R and the probability distribution of this state is given by a two-dimensional Gaussian distribution centred on Q. This shows that the probability of the state lying in the element $r dr d\theta$ at r, θ is

$$(\pi\alpha)^{-1} \exp(-r^2/\alpha) r dr d\theta, \quad (5.75)$$

where r is the distance QR and θ is the angle PQR. Note that all values of θ are equally probable. The distance OR represents u_r , $(v_r^2 + w_r^2)^{\frac{1}{2}}$, or ω_r , while the projections OM and ON onto the axes represent either v_r and w_r or the two components of the angular velocity of a reflected diatomic molecule.

A disadvantage of this version of the model is that the accommodation coefficients for the velocity components are directly linked to those for the energies based on these components. This means that it does not include the case of diffuse reflection with incomplete thermal accommodation. Lord (1991) has further extended the model to include this case.

References

- BERGEMANN, F. and BOYD, I.D. (1994). New discrete vibrational energy model for the direct simulation Monte Carlo method. *Prog. in Aero. and Astro.* **157**, in press.
- BIRD, G.A. (1976). *Molecular gas dynamics*, Oxford University Press.
- BORGNAKKE, C. and LARSEN, P.S. (1975). Statistical collision model for Monte Carlo simulation of polyatomic gas mixture, *J. Comput. Phys.* **18**, 405–420.
- BRYAN, G.H. (1894). *Rep. Br. Ass. Advanc. Sci.*, p. 83.
- CERCIGNANI, C. and LAMPIS, M. (1974). In *Rarefied gas dynamics*, (ed. K. Karamcheti), p. 361, Academic Press, New York.
- CHAPMAN, S. and COWLING, T.G. (1970). *The mathematical theory of non-uniform gases* (3rd edn), Cambridge University Press.
- CURTISS, C.F. and MUCKENFUSS, C. (1958). Kinetic theory of nonspherical molecules. *J. Chem. Phys.* **29**, 1257–1272.
- DAHLER, J.S. and SATHER, N.F. (1962). Kinetic theory of loaded spheres I. *J. Chem. Phys.* **38**, 2363–2382.
- GREGORY, S.J. AND PETERS, R.N. (1986). In *Rarefied gas dynamics*, (ed. V. Boffi and C. Cercignani), 1, pp 641–656, B.G. Tuebner, Stuttgart.
- HAAS, B.L., McDONALD, J.D., and DAGUM, L. (1993). Models of thermal relaxation mechanics for particle simulation methods, *J. Comput. Phys.* **107**, 348–358.
- HAAS, B.L., HASH, D., BIRD, G.A., LUMPKIN, F.E., and HASSAN, H. (1994) Rates of thermal relaxation in direct simulation Monte Carlo methods, *Phys. Fluids*, to be published.
- HASSAN, H.A. and HASH, D.B. (1993). A generalized hard-sphere model for Monte Carlo simulation. *Phys. Fluids A* **5**, 738–744.
- HINSHELWOOD, C.N. (1940). *The kinetics of chemical change*, p. 39. Clarendon Press, Oxford.
- JEANS, J.H. (1904). *Q. Jl. Pure Appl. Math.* **25**, 224.
- LARSEN, P.S. and BORGNAKKE, C. (1974). In *Rarefied gas dynamics* (ed. M. Becker and M. Fiebig), 1, Paper A7, DFVLR Press, Porz-Wahn, Germany.
- LORD, R.G. (1991a). In *Rarefied gas dynamics* (ed. A.E. Beylich), p. 1427, VCH Verlagsgesellschaft mbH, Weinheim, Germany.
- LORD, R.G. (1991b). Some extensions to the Cercignani-Lampis gas scattering kernel, *Phys. Fluids A* **3**, 706–710.
- LORDI, J.A. and MATES, R.E. (1970). Rotational relaxation in nonpolar diatomic molecules. *Phys. Fluids* **13**, 291–308.
- MILLER, D.R. and SUBBARAO, R.B. (1971). Direct experimental verification of the reciprocity principle for scattering at the gas–surface interface, *J. Chem. Phys.*, **55**, 1478–1479.
- PIDDUCK, F.B. (1922). *Proc. R. Soc. A.* **101**, 101.
- PULLIN, D.I. (1978). Kinetic models for polyatomic molecules with phenomenological energy exchange, *Phys. Fluids* **21**, 209–216.
- SANDLER, S.I. and DAHLER, J.S. (1967). Kinetic theory of loaded spheres IV. *J. Chem. Phys.* **47**, 2621–2630.
- THOMAS, L.B. (1967). In *Fundamentals of gas-surface interactions*, p. 346, Academic Press, New York.
- WENAAS, E.P. (1971). Equilibrium cosine law and scattering symmetry at the gas–surface interface, *J. Chem. Phys.* **54**, 376–388.

6

CHEMICAL REACTIONS AND THERMAL RADIATION

6.1 Introduction

The molecular model is ideally suited to the study of chemically reacting gas flows in that the basic theory of gas phase chemical reactions is primarily concerned with processes at the molecular level (e.g. Levine and Bernstein 1987). The theory is supported by studies in experimental chemistry that are becoming increasingly concerned with measurements at the molecular level. In addition, computational methods are now being applied to the interactions between reactive molecules, but these can involve extensive calculations for each set of impact parameters. It is impossible to make such a calculation for each of the billions of collisions in a flow simulation, but it might eventually be possible to build up a database of outcomes for all ~~impact~~ parameters in the collisions of interest. Such a database could be accessed at each collision and would not only provide a practical approach to the chemical reaction problem, but would remove the need for the approximate molecular models that have been developed in the preceding chapters. However, the available microscopic data is fragmentary and the existing computer simulations of reacting gas flows have necessarily been based on approximate models.

The simulation models are related to the well-known collision theory for chemical reactions that is outlined in §6.2. Given the paucity of the microscopic data, the initial simulations of reacting flows (Bird 1979) employed kinetic theory to deduce the microscopic data from the continuum rate constants. This theory is presented in §6.3, while the following section deals with the extension of collision theory to termolecular collisions. This leads in §6.6 to the derivation of the ratio of forward and reverse cross-sections that produce chemical equilibrium. The combined theory is applied in §6.7 to the dissociation-recombination reaction. This section also presents a new method for these reactions that employs the Larsen-Borgnakke model for vibrational excitation in order to treat dissociation as vibrational excitation to the energy level that corresponds to dissociation.

The new method requires data only for the vibrational relaxation rate and obviates the need for explicit data on the dissociation rate. This is consistent with the basic physics of the vibration-dissociation process. The method is extended in §6.8 to the exchange reactions and again predicts rates that are consistent with the measured rates.

With regard to the application of the generalized Larsen–Borgnakke distributions of §5.5 to chemical reactions, it should be noted that the Maxwell gas versions (i.e. with $\omega = 1$) of these distributions are identical to the ‘prior distributions’ that are employed in theoretical chemistry (e.g. Levine and Bernstein 1987, §5.5.4). The molecular model enters into the differentiation of the set of molecules that suffer collisions from the set that constitutes the gas. The introduction of the more general results from §5.5 brings the actual distributions for inelastic collisions (the post-reaction distributions may still differ) into agreement with the prior distributions. Information theory is then largely superfluous and ‘entropy maximization’ procedures are no longer required for the establishment of equilibrium.

6.2 Collision theory for bimolecular reactions

Most gas phase chemical reactions may be treated as collision processes. We have seen that the VHS molecular model provides an adequate representation of real monatomic gases and that phenomenological models lead to acceptable results for gases with internal degrees of freedom. We will now investigate the extent to which a classical phenomenological approach can deal with flows that include chemical reactions and thermal radiation. A logical starting point is provided by the classical collision theory that has long been established as the simplest theory for chemical reaction rates.

The dilute gas model deals exclusively with binary collisions and is most readily extended to *bimolecular* reactions. A typical bimolecular reaction may be written schematically as



where A, B, C, and D represent separate molecular species. Note that the word ‘molecule’ is used in this book as a generic term and includes atoms, ions, electrons, and photons, as well as molecules. As long as the reaction takes place in a single step with no species other than the reactants present, as is implied by eqn (6.1), it has been found that the *rate equation* for the change of concentration of species A may be written

$$-\frac{dn_A}{dt} = k_f(T)n_A n_B - k_r(T)n_C n_D. \quad (6.2)$$

The number density has been used as the measure of concentration in place of the more usual moles per unit volume, which is generally denoted by $[N_A]$. The two are related by $n_A = N[N_A]$, where N is Avogadro’s number. The *rate coefficients* or ‘constants’ $k_f(T)$ and $k_r(T)$ relate to the forward and reverse reactions, respectively. The rate coefficients are functions of temperature and are independent of the number densities and time. A further result that originally had an empirical basis is that the rate coefficients are of the form

$$k(T) = \Lambda T^\eta \exp(-E_a/kT), \quad (6.3)$$

where Λ and η are constants, and E_a is called the *activation energy* of the

reaction. For the special case of $\eta = 0$, this equation is called the Arrhenius equation. The formulation is essentially macroscopic, and the use of the thermodynamic temperature means that there is an implied assumption that the process does not involve a high degree of thermal non-equilibrium. This requires that the time-scale of the reaction process should be large compared with the mean collision time, thus enabling the translational and rotational velocities of the molecules to remain essentially Maxwellian.

Although the total cross-section σ_T was originally defined for elastic collisions, it did not require any modification for application to collisions that involve energy interchange between translational and fully excited internal modes. However, for chemical reactions or for the excitation of the discrete vibrational energy levels, a separate *reaction cross-section* σ_R is introduced. This is a total cross-section, but a more complete knowledge of a reaction would enable a differential cross-section to be specified as a function of the impact parameters. The ratio σ_R/σ_T of the reaction cross-section to the elastic cross-section may be regarded as the probability that an elastic collision will result in a chemical reaction. It may then be identified with the *steric factor*. However, the use of a steric factor implies that the reaction cross-section must be smaller than the elastic cross-section and, while this is generally the case, it is desirable to leave open the possibility that the reaction cross-section may exceed the elastic cross-section. If the bimolecular reaction between A and B has an activation energy E_a , it is reasonable to assume that it cannot take place unless the translational energy in the centre of mass frame of reference, together with any internal energy that is available, exceeds the activation energy. If the reaction is endothermic (i.e. it requires an energy input) the activation energy will be equal to or greater than this reaction energy. It should be noted that exothermic reactions that release energy may have a finite activation energy.

A simple but unrealistic case is to take hard sphere molecules and to assume that the reaction cross-section is zero if the translational energy along the line of centres is less than E_a and is equal to σ_R if this energy exceeds E_a . Assuming a quasi-equilibrium gas, the rate of reactive collisions of a species A molecule is given by the product of the elastic collision rate of eqn (4.75), the fraction given by eqn (4.73), and the ratio σ_R/σ_T . The forward reaction rate for the type A molecules then follows from eqn (1.39) as

$$\frac{dn_A}{dt} = -\frac{\sigma_R n_A n_B}{\epsilon} \left(\frac{8kT}{\pi m_r} \right)^{1/2} \exp\left(-\frac{E_a}{kT}\right), \quad (6.4)$$

where ϵ is a symmetry factor that is equal to unity if $A \neq B$ and two if $A = B$.

A comparison of this equation with eqns (6.2) and (6.3) show that the collision theory result is of the expected form. However, the hard sphere model is not adequate for real gases, the reaction cross-section may not be a constant, and the internal degrees of freedom may contribute to the collision energy. The conventional collision theory result will therefore be extended to deal with a more realistic molecular model.

6.3 Reaction cross-sections for given reaction rates

Consider the case in which the collision energy E_c includes the energy in ζ_A internal degrees of freedom of the class A molecules and ζ_B internal degrees of freedom of the class B molecules. If the sum of the internal energy contributions is denoted by E_i , eqn (5.27) shows that

$$f_{E_i} \propto E_i^{\bar{\zeta}-1} \exp\{-E_i/(kT)\},$$

where $\bar{\zeta} = (\zeta_A + \zeta_B)/2$ is the average number of internal degrees of freedom that contribute to the collision energy. The distribution function for the relative translational energy E_t associated with collisions in a gas of power-law VHS molecules is given by eqn (5.13) as

$$f_{E_t} \propto E_t^{3/2-\omega_{AB}} \exp\{-E_t/(kT)\},$$

where ω_{AB} is the viscosity-temperature exponent that is specified for collisions between molecules of species A with those of species B. In this case, the full translational energy is included and the reduction that occurs when it is restricted to the energy along the line of centres will be allowed for through the energy dependence of the reaction cross-section. The distribution function for $E_c = E_t + E_i$ is given by the product of the distributions for E_i and E_t . For a fixed value of E_i , this may be written

$$f_{E_c} \propto (E_c - E_i)^{3/2-\omega_{AB}} E_i^{\bar{\zeta}-1} \exp\{-E_c/(kT)\},$$

and this distribution may be integrated over all values of E_i to give the averaged distribution function for the collision energy. The constant may be evaluated from the condition that the integrated distribution over all values of the collision energy must be unity. The final result for the distribution of E_c normalized to kT is

$$f\left(\frac{E_c}{kT}\right) = \frac{1}{\Gamma(\bar{\zeta} + 5/2 - \omega_{AB})} \left(\frac{E_c}{kT}\right)^{\bar{\zeta} + 3/2 - \omega_{AB}} \exp\left(-\frac{E_c}{kT}\right). \quad (6.5)$$

The fraction of collisions with E_c greater than E_a is obtained by integrating eqn (6.5), with respect to E_c/kT , from E_a/kT to ∞ . The result is

$$\frac{dN}{N} = \frac{\Gamma(\bar{\zeta} + 5/2 - \omega_{AB}, E_a/(kT))}{\Gamma(\bar{\zeta} + 5/2 - \omega_{AB})} \equiv Q(\bar{\zeta} + 5/2 - \omega_{AB}, E_a/(kT)). \quad (6.6)$$

The incomplete gamma function in this equation may be reduced through eqn (B6) and this leads to particularly simple results when the first argument is an integer. For hard sphere molecules and an integer number of internal degrees of freedom, eqn (6.6) reduces to

$$\frac{dN}{N} = \exp\left(-\frac{E_a}{kT}\right) \left\{ 1 + \frac{E_a}{kT} + \frac{1}{2} \left(\frac{E_a}{kT}\right)^2 + \dots + \frac{1}{(n+1)!} \left(\frac{E_a}{kT}\right)^{\bar{\zeta}+1} \right\}. \quad (6.7)$$

For reactions in which $E_a >> kT$, the final term in the series is dominant and $s = \bar{\zeta} + 2$ is often (see, for example, Vincenti and Kruger, 1965, Chap. VII, §5) referred to as defining the number of 'square terms' that contribute energy to the reaction.

A rate coefficient of the form of eqn (6.3) is obtained (Bird 1979, 1981) if the reaction cross-section is assumed to have the form

$$\sigma_R = 0 \quad \text{if } E_c < E_a \quad (6.8)$$

and

$$\sigma_R = \sigma_T C_1 (E_c - E_a)^{C_2} (1 - E_a/E_c)^{\bar{\zeta} + 3/2 - \omega_{AB}} \quad \text{if } E_c > E_a,$$

where C_1 and C_2 are constants. The forward reaction rate for molecules of species A is given by the combination of eqns (1.39), (4.75), (6.5), and (6.8), to give

$$\frac{dn_A}{dt} = \frac{2}{\pi^{\nu/2} \epsilon} n_A n_B \sigma_{\text{ref}} \left(\frac{2kT_{\text{ref}}}{m_r} \right)^{\nu/2} \left(\frac{T}{T_{\text{ref}}} \right)^{1-\omega_{AB}} \frac{C_1}{\Gamma(\bar{\zeta} + 5/2 - \omega_{AB})}$$

$$\times \int_{\frac{E_a}{kT}}^{\infty} (E_c - E_a)^{C_2} (1 - E_a/E_c)^{\bar{\zeta} + 3/2 - \omega_{AB}} \left(\frac{E_c}{kT} \right)^{\bar{\zeta} + 3/2 - \omega_{AB}} \exp \left(-\frac{E_c}{kT} \right) d \left(\frac{E_c}{kT} \right).$$

If the variable in the integration is changed to $E_c - E_a$, the integral is transformed to a gamma function and the rate coefficient is

$$k(T) = \frac{2C_1 \sigma_{\text{ref}}}{\pi^{\nu/2} \epsilon} \left(\frac{2kT_{\text{ref}}}{m_r} \right)^{\nu/2} \frac{\Gamma(\bar{\zeta} + C_2 + 5/2 - \omega_{AB})}{\Gamma(\bar{\zeta} + 5/2 - \omega_{AB})} \frac{k^{C_2 T_{\text{ref}}^{C_2 + 1 - \omega_{AB}}}}{T_{\text{ref}}^{1 - \omega_{AB}}} \exp \left(-\frac{E_a}{kT} \right). \quad (6.9)$$

A comparison of eqn (6.9) with eqn (6.3) shows that the constants in eqn (6.8) can be written

$$C_1 = \frac{\pi^{\nu/2} \epsilon \Lambda}{2 \sigma_{\text{ref}}} \frac{\Gamma(\bar{\zeta} + 5/2 - \omega_{AB})}{\Gamma(\bar{\zeta} + \eta + 3/2)} \left(\frac{m_r}{2kT_{\text{ref}}} \right)^{\nu/2} \frac{T_{\text{ref}}^{1 - \omega_{AB}}}{k^{\eta - 1 + \omega_{AB}}},$$

and

$$C_2 = \eta - 1 + \omega_{AB}.$$

The probability of reaction (or steric factor) at each collision with $E_c > E_a$ between power-law VHS molecules is, therefore,

$$\frac{\sigma_R}{\sigma_T} = \frac{\pi^{\nu/2} \epsilon \Lambda T_{\text{ref}}^{\eta}}{2 \sigma_{\text{ref}} (kT_{\text{ref}})^{\eta - 1 + \omega_{AB}}} \frac{\Gamma(\bar{\zeta} + 5/2 - \omega_{AB})}{\Gamma(\bar{\zeta} + \eta + 3/2)} \left(\frac{m_r}{2kT_{\text{ref}}} \right)^{\nu/2} \frac{(E_c - E_a)^{\eta + \bar{\zeta} + 1/2}}{E_c^{\bar{\zeta} + 3/2 - \omega_{AB}}}. \quad (6.10)$$

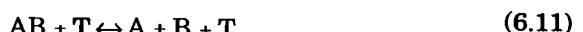
This probability tends to zero as E_c tends to E_a if $\eta + \bar{\zeta} + \frac{1}{2}$ is greater than zero, but tends to infinity if this quantity is less than zero. The latter case is not physically realistic, and η should not be less than $-\frac{1}{2} - \bar{\zeta}$. Large negative values are indicative of reactions in which the internal modes contribute to the collision energy. Note also that the reaction probability tends to zero as E_c tends to infinity if η is less than $-1 + \omega_{AB}$. Dissociation reactions in air generally have values of η of the order of -1 and the reaction probability given by eqn (6.10) then has a maximum value at some value of E_c . This is the type of cross-section versus energy curve that is supported by the available evidence from molecular beam experiments (Gardiner 1969).

The contribution of the internal modes to the collision energy is an arbitrary parameter, in that the desired rate can usually be matched by a range of values of $\bar{\zeta}$, but when the above considerations are combined with the limit on the available internal energy, this range can be seen to be very limited. The resulting reaction cross-sections are generally very small in comparison with the elastic cross-sections but, for very fast reactions, they approach, but hardly ever exceed, the elastic cross-section.

The above theory for the reaction probability provides a microscopic reaction model that can reproduce the conventional rate equation in the continuum limit. However, the form of eqn (6.8) is based largely on considerations of mathematical tractability, and the model is essentially phenomenological in nature. As noted in §6.1, the ideal microscopic model would consist of complete tabulations of the differential reaction cross-sections as functions of the energy states and impact parameters. These would have to come from extensive quantum theory computations that were supported by experiment. Some microscopic data is available for particular reactions, but very little is available for reactions of engineering interest. Where comparisons can be made, the reaction cross-sections from the phenomenological theory are of the correct order. This agreement provides grounds for optimism about the validity of the results that are obtained from the application of the phenomenological model under the highly non-equilibrium conditions that are generally encountered in rarefied gas flows.

6.4 Extension to termolecular reactions

A termolecular reaction involves three molecules and is related to ternary or three-body collisions. This is an important reaction in high-temperature air in that it is the reverse or recombination reaction in the dissociation of molecular oxygen and nitrogen. A typical dissociation–recombination reaction can be represented as



Here, AB represents the dissociating molecule, A and B are atoms (or at least one molecule if AB is polyatomic), and T is the 'third body' atom or molecule. There is an energy E_d required for the dissociation which is an *endothermic* reaction. A similar amount of energy is associated with the *exothermic* recombination, and it might appear that the reverse reaction in eqn (6.13) could be a bimolecular reaction rather than a *termolecular* reaction involving three molecules. However, it is easily seen that eqn (2.1) for the momentum and eqn (2.2) for the energy in a binary collision cannot be simultaneously satisfied in the presence of heat release. Three-body or ternary collisions are therefore required for recombination. The rate of formation of either species A or species B in the forward reaction can be written

$$\frac{dn_A}{dt} = k_f n_{AB} n_T, \quad (6.12)$$

while the loss of species A in the reverse reaction is

$$\frac{dn_A}{dt} = k_r n_A n_B n_T. \quad (6.13)$$

Note that the product of the rate constant for a termolecular reaction and a number density has the same dimensions as the rate constant in a bimolecular reaction.

The collision theory can be extended to ternary reactions by assigning a 'lifetime' to a binary collision between two molecules, and then considering triple collisions as a second binary collision between the combination of the first two molecules with a third molecule. Alternatively, the recombination can be regarded as the combination of two binary collisions. The first of these forms an orbiting pair that is stabilized by the second collision with the third body, as long as the second collision occurs within a sufficiently small elapsed time. The two approaches are effectively equivalent and, whatever the dependence of the lifetime on the relative speed and on the translational energy in the first binary collision, the probability of the recombination will be directly proportional to the number density n_T of the third body species. If the recombination rate corresponding to the reverse reaction in eqn (6.1) is specified by a rate equation of the form of eqn (6.3), the recombination probability at each binary collision between a species A molecule and a species B molecule can be obtained in a similar manner to eqn (6.10). If the activation energy is taken as zero, the contribution from the internal degrees of freedom is also zero, and the recombination probability that is associated with the binary collision is

$$\frac{\sigma_R}{\sigma_T} = \frac{\pi^{1/2} n_T \epsilon \Lambda T_{ref}^\eta}{2 \sigma_{ref}} \frac{\Gamma(5/2 - \omega_{AB})}{\Gamma(\eta + 3/2)} \left(\frac{m_r}{2k T_{ref}} \right)^{1/2} \left(\frac{E_c}{k T_{ref}} \right)^{\eta-1+\omega_{AB}}. \quad (6.14)$$

This probability tends to infinity as E_c tends to zero unless $\eta - 1 + \omega_{AB}$ is equal to or greater than zero. The value of ω_{AB} is close to 0.75, so that ω should not be less than about 0.25. This is more restrictive in practice than the corresponding constraint for the bimolecular reaction.

6.5 Chemical equilibrium

Chemical equilibrium requires a balance between the forward and reverse reactions such that the concentrations of all species remain constant with time. Therefore, from eqn (6.2) for a bimolecular reaction,

$$K_{\text{eq}} \equiv \frac{k_f}{k_r} = \frac{n_C n_D}{n_A n_B} \quad (6.15)$$

where K_{eq} is the *equilibrium constant*. Similarly, the equilibrium constant for the termolecular dissociation–recombination reaction of eqn (6.11) follows from eqns (6.12) and (6.13) as

$$K_{\text{eq}} \equiv \frac{k_f}{k_r} = \frac{n_A n_B}{n_{AB}}. \quad (6.16)$$

For the dissociation of *symmetrical* or *homonuclear* diatomic molecules in which species A is the same as species B, this becomes

$$K_{\text{eq}} = \frac{k_f}{k_r} = \frac{n_A^2}{n_{AA}}. \quad (6.17)$$

The *degree of dissociation* α may now be defined as the mass fraction of dissociated gas. Therefore,

$$\alpha = \frac{n_A m_A}{\rho} = \frac{n_A}{n_A + 2n_{AA}}. \quad (6.18)$$

The combination of eqns (6.17) and (6.18) shows that

$$\frac{\alpha^2}{1 - \alpha} = \frac{m_A k_f}{2\rho k_r}. \quad (6.19)$$

Equilibrium statistical mechanics relates the numbers of the various species in a system to the *partition functions*. For the bimolecular reaction,

$$\frac{N_C N_D}{N_A N_B} = \frac{Q^C Q^D}{Q^A Q^B} \exp\left(-\frac{E_a}{kT}\right), \quad (6.20)$$

where Q is the partition function for the species that is indicated by the superscript, and E_a should be interpreted here as the difference between the forward and backward activation energies. The number N is related to the volume V of the system by

$$N = nV,$$

and the combination of eqns (6.15) and (6.20) enables the law of mass action for this reaction to be written

$$K_{\text{eq}} \equiv \frac{k_f}{k_r} = \frac{n_C n_D}{n_A n_B} = \frac{Q^C Q^D}{Q^A Q^B} \exp\left(-\frac{E_a}{kT}\right). \quad (6.21)$$

In the case of the termolecular dissociation–recombination reaction, the system volume does not cancel and the corresponding equation is

$$K_{\text{eq}} \equiv \frac{k_f}{k_r} = \frac{n_A n_B}{n_{AB}} = \frac{Q^A Q^B}{V Q^{AB}} \exp\left(-\frac{E_a}{kT}\right). \quad (6.22)$$

Equation (6.19) for the symmetrical molecule can then be written

$$\frac{\alpha^2}{1-\alpha} = \frac{m_A}{2\rho V} \frac{(Q^A)^2}{Q^{AA}} \exp\left(-\frac{E_d}{kT}\right). \quad (6.23)$$

Each partition function may be written as the product of the separate translational, rotational, vibrational, and electronic partition functions for that species, i.e.

$$Q = Q_{\text{tr}} Q_{\text{rot}} Q_v Q_{\text{el}}. \quad (6.24)$$

For the reactions that are encountered in high-temperature air and over the temperature range of interest, approximate expressions are available for the partition functions. First, the translational partition function is

$$Q_{\text{tr}} = V(2\pi mkT/h^2)^{3/2}. \quad (6.25)$$

Note that the equilibrium constants are independent of the system volume when this function is applied to either bimolecular or termolecular reactions. The rotational partition function is generally written

$$Q_{\text{rot}} = T/(\epsilon' \Theta_r) \quad (6.26)$$

where ϵ' is a symmetry factor equal to 2 for homonuclear molecules and 1 for heteronuclear molecules. The harmonic oscillator model leads to a vibrational partition function of the form

$$Q_v = 1/\{1 - \exp(-\Theta_v/T)\}. \quad (6.27)$$

Finally, the electronic partition function is summed over the j levels, i.e.

$$Q_{\text{el}} = \sum_{i=0}^j g_i \exp(-\Theta_{\text{el},i}/T), \quad (6.28)$$

where g_i are the degeneracies (i.e. the number of states in the level), and the ground state energy $\Theta_{\text{el},0}$ is set to zero.

The partition functions have been used to calculate the equilibrium composition of reacting gases, and some results from their application to high-temperature air are shown in Figs 1.9 and 1.10. They can also be used to calculate the backward rate coefficient from the forward coefficient, or to test the consistency of listed forward and backward coefficients.

Reaction cross-section data at the microscopic level should be consistent with the principle of detailed balancing. Because chemical reactions involve the internal as well as the translational states, the formulation of the reciprocity principle for a reacting gas would be a formidable task, but the data can be employed in a way that leads to chemical equilibrium.

6.6 The equilibrium collision theory

Continuum studies of flows that involve chemical reactions almost always employ rate equations in the form of eqn (6.3) for both the forward and reverse reactions. However, the simple form of eqn (6.3) does not match the mathematical complexity of the partition functions, and each set of rate equations is consistent with chemical equilibrium only over a narrow range of temperature. This temperature range will, in general, be different for each reaction and, for a complex gas with many simultaneous reactions, the correct equilibrium state will not be attained at any temperature. The same error arises also in particle based calculations if the theory of §6.3 and §6.4 is used to determine the reaction cross-sections from both the forward and reverse rate equations.

The above difficulty can be overcome if the theory is used to calculate the reaction cross-sections only for the forward reaction, and the reaction cross-sections for the reverse reactions are related to those for the forward reactions through the partition functions. The temperature in the partition functions must be the local macroscopic temperature.

The reactions almost invariably require an activation energy in only one direction, and the reaction in this direction is chosen to be the forward reaction. The cross-section for the reverse reaction can then be set to a fraction F of the elastic cross-section and, for a bimolecular collision, this fraction is a function only of the macroscopic temperature. In the case of a termolecular reverse reaction, it is also proportional to the number density of the molecules that constitute the third bodies in the collisions. In both cases the fraction is independent of the collision energy, i.e.

$$\sigma_R / \sigma_T = F \quad (6.29)$$

for the bimolecular reaction, and

$$\sigma_R / \sigma_T = n_T F \quad (6.30)$$

for the termolecular reaction.

The change with time of the number density of species C in the reverse bimolecular reaction is

$$dn_C/dt = n_C v_{CD} F.$$

The equilibrium collision rate of eqn (4.75) may be used for v_{CD} and the resulting equation combined with eqns (1.39) and (6.2) to give

$$k_r = (2/\epsilon) \pi^{-1/2} \sigma_{ref} (T/T_{ref})^{1-\omega} (2kT_{ref}/m_r)^{1/2} F, \quad (6.31)$$

where the values of σ_{ref} , T_{ref} , and ω are the values appropriate to the collision pair for the reverse reaction, and ϵ . It is easily seen that this equation applies also to the termolecular reverse reaction as long as F is defined by eqn (6.30), rather than (6.29). The forward reaction rate is in the form of eqn (6.3) and may be written

$$k_f = \Lambda_f T^{\eta_f} \exp\{-E_a/(kT)\}. \quad (6.32)$$

Equations (6.31) and (6.32) for the rate coefficients may be substituted into eqn (6.21) to give, for the bimolecular reaction,

$$\frac{\Lambda_f T^{\eta_f} \exp\{-E_a/(kT)\}}{(2/\epsilon)\pi^{-1/2}\sigma_{ref}(T/T_{ref})^{1-\omega}(2kT_{ref}/m_r)^{1/2}F} = \frac{Q^C Q^D}{Q^A Q^B} \exp\left(-\frac{E_a}{kT}\right). \quad (6.33)$$

The exponential term disappears and, using eqn (6.29),

$$\frac{\sigma_R}{\sigma_T} = \frac{\Lambda_f T^{\eta_f}}{(2/\epsilon)\pi^{-1/2}\sigma_{ref}(T/T_{ref})^{1-\omega}(2kT_{ref}/m_r)^{1/2}} \frac{Q^A Q^B}{Q^C Q^D}. \quad (6.34)$$

A similar procedure for the termolecular reverse reaction gives

$$\frac{\sigma_R}{\sigma_T} = \frac{\Lambda_f T^{\eta_f}}{(2/\epsilon)\pi^{-1/2}\sigma_{ref}(T/T_{ref})^{1-\omega}(2kT_{ref}/m_r)^{1/2}} \frac{n_T V Q^{AB}}{Q^A Q^B}. \quad (6.35)$$

As expected, the reaction probabilities are functions of the macroscopic temperature. While this is less physically realistic than the dependence on E_c for the forward reactions, the probabilities lead to exact equilibrium.

The theory may be extended to cover the comparatively rare reactions that have a finite activation energy $E_{a,r}$ for the reverse reaction. The energy in the exponential term on the right-hand side of eqn (6.33) becomes the difference between the forward and reverse activation energies. In addition, the collision rate must be reduced by multiplying it by the fraction of collisions that have energies in excess of $E_{a,r}$. This fraction in an equilibrium gas at temperature T is given by eqn (6.6), and the modified expression for the bimolecular reaction is

$$\frac{\sigma_R}{\sigma_T} = \frac{\pi^{1/2} \Lambda_f T^{\eta_f} \Gamma(\bar{\zeta} + 5/2 - \omega) \exp(-E_{a,r}/(kT)) (Q^A Q^B)/(Q^C Q^D)}{(2/\epsilon)\sigma_{ref}(T/T_{ref})^{1-\omega}(2kT_{ref}/m_r)^{1/2} \Gamma(\bar{\zeta} + 5/2 - \omega, E_{a,r}/(kT))} \quad (6.36)$$

where $\bar{\zeta}$ is now the average number of internal degrees of freedom that contribute to $E_{a,r}$. This reaction probability is applied only to those reactions that have energy greater than $E_{a,r}$. The same factors can be applied to eqn (6.35) for the termolecular reactions.

6.7 The dissociation–recombination reaction

The preceding theory may be illustrated through its application to the dissociation and recombination reaction. For example, for oxygen



Typical rates for the reaction that can be applied for all collision partners or ‘third bodies’ are given by Gupta et al. (1990) as

$$k_f = 6.0 \times 10^{-12} T^{-1} \exp\{-8.2 \times 10^{-19}/(kT)\}$$

and

$$k_r = 8.3 \times 10^{-45} T^{-1/2}. \quad (6.38)$$

The units are such that the rate coefficient is in $\text{m}^3\text{molecule}^{-1}\text{s}^{-1}$ for the binary reaction and $\text{m}^6\text{molecule}^{-2}\text{s}^{-1}$ for the ternary reaction.

The application of the rates of eqn (6.38) implicitly assumes that the equilibrium constant is

$$K_{\text{eq}} = 7.23 \times 10^{32} T^{-1/2} \exp(-59400/T). \quad (6.39)$$

On the other hand, the equilibrium constant from statistical mechanics is given by eqn (6.22) as

$$K_{\text{eq}} = \frac{(Q^0)^2}{V Q^{O_2}} \exp\left(-\frac{E_a}{kT}\right).$$

The substitution into this equation of the approximate partition functions of eqns (6.25) to (6.28), and the incorporation of the appropriate data for oxygen from Appendix A gives

$$\begin{aligned} K_{\text{eq}} = & 1.785 \times 10^{28} T^{1/2} \{1 - \exp(-2270/T)\} \exp(-59400/T) \\ & \times \{5 + 3 \exp(-228.9/T) + \exp(-325.9/T) + 5 \exp(-22830/T) \\ & + \exp(-48621/T)\}^2 / \{3 + 2 \exp(-11393/T) + \exp(-18985/T)\}. \end{aligned} \quad (6.40)$$

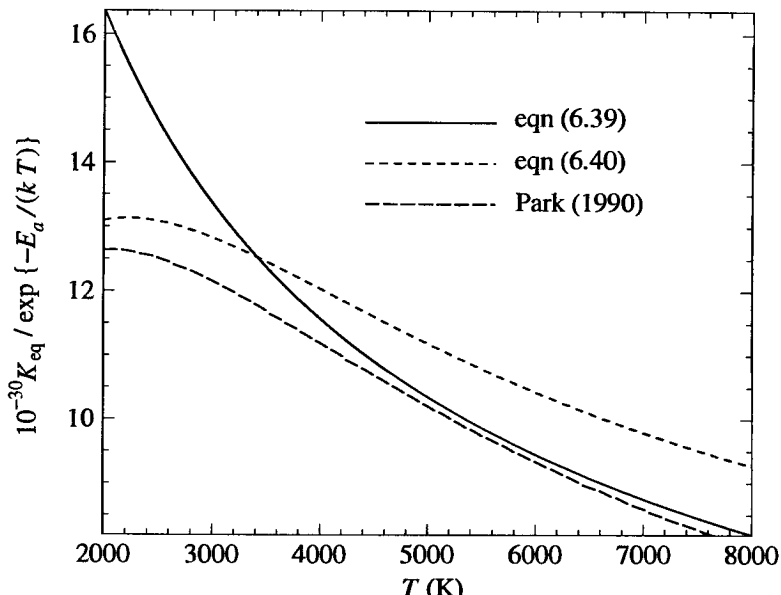


Fig. 6.1 A comparison of the equilibrium constant from typical reaction rates with that from statistical mechanics.

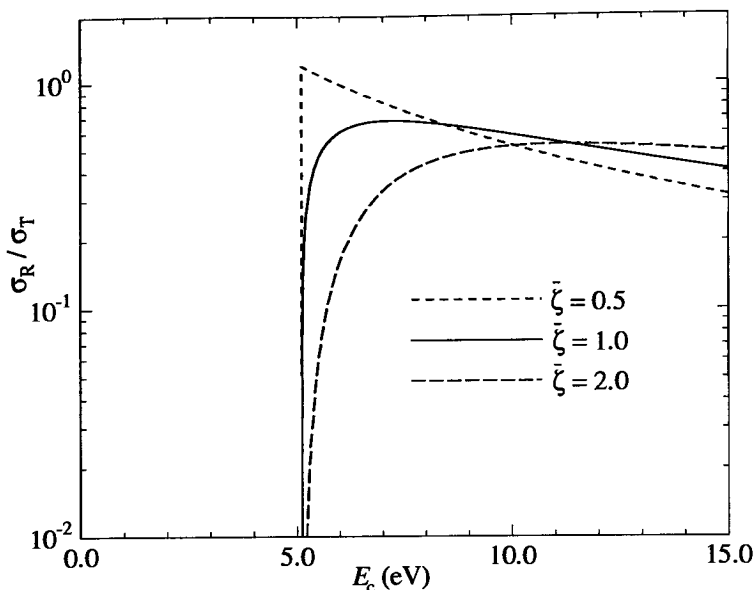


Fig. 6.2 Reaction probabilities for the dissociation of oxygen.

The number of electronic states has been truncated through the omission of those that make only small contributions at the temperatures of interest. In addition, the vibrational function is based on the harmonic oscillator model and neglects rotational-vibrational coupling. These effects have been included in a study by Jaffe (1987) and the resulting partition functions and equilibrium constants have been tabulated by Park (1990).

The comparison in Fig. 6.1 of the equilibrium constants from eqns (6.39) and (6.40) demonstrates that they are in agreement only at a temperature of 3500 K. However, the more accurate equilibrium constant of Park (1990) shows that the rates of eqn (6.38) lead very nearly to equilibrium at higher temperatures. The errors in the approximate partition functions are less serious for nitrogen.

The forward rate of eqn (6.38) may be converted to collision energy dependent steric factors by eqn (6.10). In order to avoid the singularity in this equation when $E_c = E_a$, the average number of internal degrees of freedom that contribute to E_c must not be less than 0.5. Figure 6.2 shows the reaction probabilities as a function of the collision energies for this value, and for several higher values. The reaction cross-section can exceed the elastic cross-section for $\bar{\zeta} = 0.5$. However, a larger contribution from the internal degrees of freedom is to be expected and these lead to steric factors that are more realistic from the physical point of view.

The incorporation of the reverse reaction rate of eqn (6.38) into eqn (6.14) leads to an infinite reaction probability as $E_c \rightarrow 0$. This may be avoided by setting the temperature index η to $1 - \omega_{AB}$, so that the power of E_c is zero and the ratio of the reaction cross-section to the elastic cross-section is a constant. The change in η should be compensated for by changing the constant Λ so that k_r is unchanged at the temperature of interest. When this is done for a temperature of 3500 K, and noting that the third-body number density is here equal to the overall number density, the result is

$$\sigma_R / \sigma_T = 0.9 \times 10^{-4} n / n_0, \quad (6.41)$$

where n_0 is the number density under standard conditions. This procedure is consistent with the 'equilibrium collision theory' that was presented in the preceding section. If $\eta = 1 - \omega_{AB}$ in eqn (6.14) and the reverse rate equation that appears in this equation is replaced by the forward rate equation through eqn (6.22), eqn (6.14) becomes identical with eqn (6.35). However, the cross-section ratio or steric factor of eqn (6.41) leads only approximately to equilibrium and it is preferable to dispense completely with the reverse rate equation and to base the reaction cross-sections for the reverse reactions on the equilibrium collision theory. This theory applies to bimolecular as well as termolecular reverse reactions and can also deal with reverse reactions that have a finite activation energy.

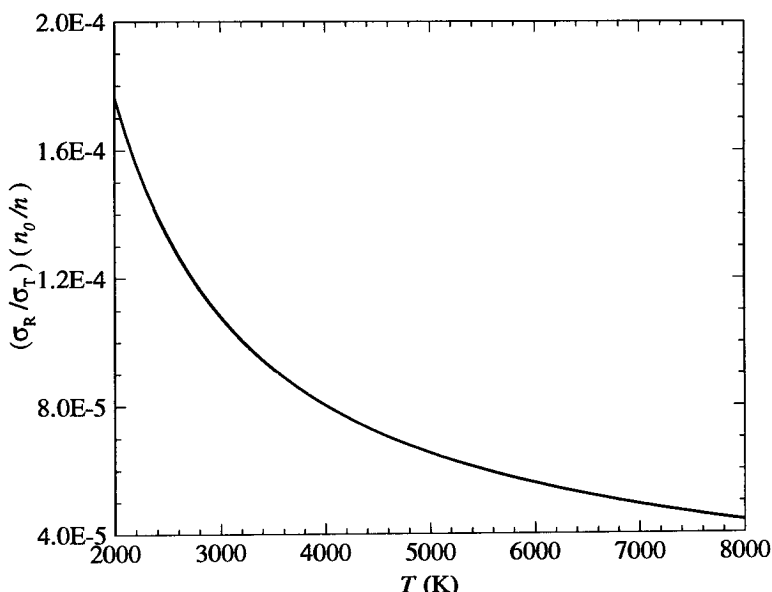


Fig. 6.3 The reaction cross-section for the recombination of oxygen.

The evaluation of eqn (6.35) for the recombination of oxygen using the forward reaction rate of eqn (6.38) and the approximate partition functions of eqns (6.25)–(6.28) leads to the results shown in Fig. 6.3. The ratio σ_R/σ_T is the probability of recombination in any binary collision between two O atoms. This is independent of the collision energy, but depends on the gas temperature. The accuracy could be improved through the use of the tabulated values (Park 1990) of the partition functions. The dependence on the number density reflects the fact that the recombination reaction is termolecular.

Although it can match the experimentally determined reaction rates and can lead to equilibrium at all temperatures, the preceding theory is essentially phenomenological in nature and it would be preferable to have a theory that is more closely related to the physics. Dissociation occurs when the vibrational energy of the molecule reaches the value that corresponds to the dissociation energy. It is therefore desirable to combine the theories for dissociation and vibrational excitation. The rate at which the individual molecules in an equilibrium gas attain the dissociation energy E_d in the vibrational mode may be calculated from the Larsen–Borgnakke theory. While this theory is also phenomenological, its parameters are inferred from the measured vibrational relaxation rate.

Consider a collision that is inelastic with respect to the vibrational excitation of the diatomic molecule that is subject to dissociation. The probability that the vibrational energy exceeds the dissociation energy may be written down directly from eqn (5.47). Ξ_b is set equal to the sum of the translational contribution and the total number of post-collision internal modes, so that the energy $E_a + E_b$ is equal to the total collision energy E_c . If molecule 1 dissociates in the collision, there are no rotational or vibrational degrees of freedom associated with the resulting atoms, so that all the internal energy in this molecule goes into breaking the interatomic bond. First consider the case in which the third body molecule (subscript 2) is also diatomic. The collision energy is sufficiently high that the vibrational mode as well as the rotational mode must be included in Ξ_b , which becomes $9/2 - \omega$. The required probability is, therefore,

$$P' = (1 - E_d/E_c)^{9/2-\omega}. \quad (6.42)$$

This probability applies only to collisions in which E_c exceeds E_d , and the probability of this is given by the integration of eqn (6.5). The overall probability that $\epsilon_{v,1}$ exceeds E_d is obtained by including the probability of eqn (6.48) in this integration, i.e.

$$P_{\epsilon_{v,1}>E_d} = \frac{1}{\Gamma(\bar{\zeta} + 5/2 - \omega)} \int_{E_d/(kT)}^{\infty} \left(\frac{E_c}{kT} \right)^{\bar{\zeta} + 3/2 - \omega} \exp\left(-\frac{E_c}{kT}\right) P' d\left(\frac{E_c}{kT}\right). \quad (6.43)$$

The average number of internal degrees of freedom in eqn (6.49) refers to the pre-collision state of the two molecules. If it is assumed that the vibrational modes are fully excited, the average number is four, and eqn (6.49) becomes

$$P_{\epsilon_{v,i} > E_d} = \frac{1}{\Gamma(13/2-\omega)} \int_{E_d/(kT)}^{\infty} \left(\frac{E_c}{kT}\right) \left(\frac{E_c - E_d}{kT}\right)^{9/2-\omega} \exp\left(-\frac{E_c}{kT}\right) d\left(\frac{E_c}{kT}\right).$$

This may be evaluated through a simple change of variable to give

$$P_{\epsilon_{v,i} > E_d} = \left(1 + \frac{E_d}{(11/2-\omega)kT}\right) \exp\left(-\frac{E_d}{kT}\right). \quad (6.44)$$

In the application of the Larsen-Borgnakke theory, the sampling from the distributions is applied to only a fraction of the collisions. A separate fraction is applied to each mode, and the inverses of these fractions define the rotational and vibrational relaxation collision numbers. The Landau-Teller theory for vibrational relaxation predicts vibrational collision numbers of the order of unity at temperatures of the order of 20,000 K, and it is reasonable to assume that energy redistribution occurs in all collisions that are sufficiently energetic to be included in the integration of eqn (6.43). This essentially assumes a steric factor of unity in the collisions that meet the energy criterion, and the expression on the right-hand side of eqn (6.44) becomes the fraction of collisions that lead to dissociation.

The number of dissociations per unit volume per unit time is then given by the product of this fraction with the number of collisions between the relevant molecular species per unit volume per unit time in the gas. The equilibrium collision rate given by eqns (4.74) and (1.39) as

$$N_{12} = 2\pi^{-1/2} \sigma_{\text{ref}} n_1 n_2 (T/T_{\text{ref}})^{1-\omega} (2kT_{\text{ref}}/m_r)^{1/2}.$$

The symmetry factor has been omitted from this rate because, when both molecule 1 and molecule 2 are of the same species, either molecule could meet the requirement for dissociation. This can be combined with eqns (6.12) and (6.44) to give the following expression for the rate coefficient

$$k_f = \frac{2\sigma_{\text{ref}}}{\pi^{1/2}} \left(\frac{T}{T_{\text{ref}}}\right)^{1-\omega} \left(\frac{2kT_{\text{ref}}}{m_r}\right)^{1/2} \left(1 + \frac{E_d}{(11/2-\omega)kT}\right) \exp\left(-\frac{E_d}{kT}\right). \quad (6.45)$$

Most reactions are sufficiently slow that the use of the equilibrium collision rate does not lead to significant error. A correction may be required for very fast reactions, and this point has been discussed by Baras and Nicolis (1990).

In the case of the dissociation of a diatomic molecule in a collision with an atom, all the internal energy must be in molecule 1 and Ξ_b is $5/2-\omega$. Also, the mean number of degrees of freedom of the pre-collision molecules is two, and the final result is

$$k_f = \frac{2\sigma_{\text{ref}}}{\pi^{1/2}} \left(\frac{T}{T_{\text{ref}}}\right)^{1-\omega} \left(\frac{2kT_{\text{ref}}}{m_r}\right)^{1/2} \left(1 + \frac{E_d}{(7/2-\omega)kT}\right) \exp\left(-\frac{E_d}{kT}\right). \quad (6.46)$$

This theory is essentially an improvement on the ‘available energy’ theory for dissociation that was proposed by Fowler and Guggenheim (1952), and applied by Hansen (1965). While the original theory required an arbitrary choice for the number of internal degrees of freedom that contribute to the required dissociation energy, the division of energy is now defined by the Larsen–Borgnakke distribution function and there are no disposable parameters. However, it should be noted that these equations assume a vibrational collision number of unity at the temperature that corresponds to dissociation. They could be made more general through the inclusion of a finite Z_v in the denominator.

The prediction of eqn (6.45) for the oxygen rate coefficient is compared in Fig. 6.4 with the forward coefficient from eqn (6.38). The corresponding rate given by Gupta et al. (1990) for the dissociation of nitrogen is

$$k_f = 3.2 \times 10^{-13} T^{-1/2} \exp\{-1.56 \times 10^{-18}/(kT)\}, \quad (6.47)$$

and this is also compared with the prediction of eqn (6.45). The rate coefficients of eqns (6.38) and (6.47) are based on curve fits of eqn (6.3) to experimental data. It is generally accepted that the data for the forward dissociation rates is subject to at least a factor of three uncertainty and it is clear that the predicted dissociation rate is of the correct magnitude.

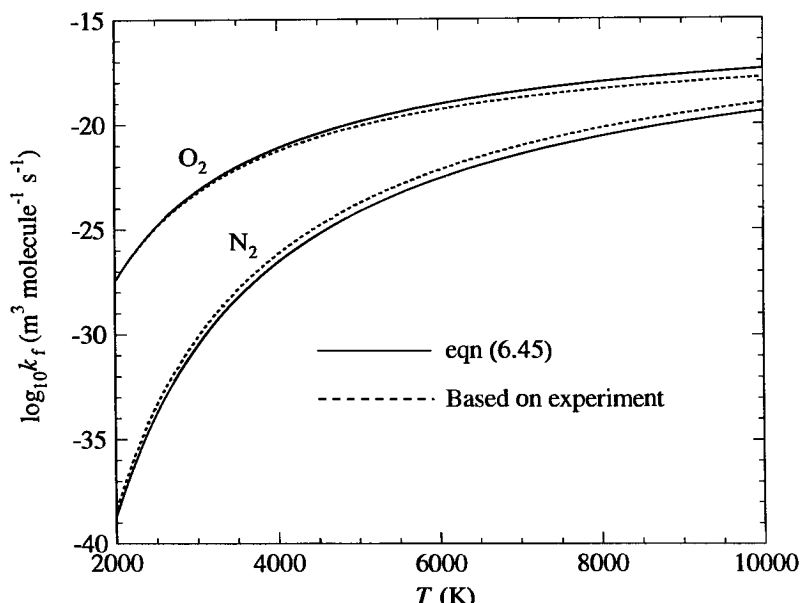


Fig. 6.4 Rate coefficients for the dissociation of oxygen and nitrogen.

Bird (1994) compares the theoretical rate coefficients from eqns (6.45) and (6.46) with a range of measured coefficients for the dissociation of oxygen and nitrogen. The theoretical values generally lie within, or just below, the range of experimental results. The agreement tends to be better at temperatures above 10,000 K, and the variation with temperature is in close agreement with experimentally based coefficients that have $\eta = -\frac{1}{2}$. The experimental rate coefficients for dissociation by an atom are generally higher than those for dissociation by a molecule, but the factor is generally larger than that predicted by the theory.

It must be kept in mind that a completely classical theory such as this cannot account for the quantum effects that exist in real gases. While it is not surprising that these effects appear to be relatively small for the dissociation of moderately heavy molecules such as oxygen and nitrogen, light gases and ionization reactions should be approached with caution.

This 'exact available energy' theory for dissociation is compatible with the 'equilibrium collision' theory for recombination that was developed in §6.5. If the mean number of internal degrees per molecule in the pre-collision pair $\bar{\zeta}$ is retained explicitly, eqns (6.45) and (6.46) can be written in a form that applies to all third-body molecules. This is

$$k_f = \frac{2\sigma_{\text{ref}}}{\pi^{\frac{1}{2}}} \left(\frac{T}{T_{\text{ref}}} \right)^{1-\omega} \left(\frac{2kT_{\text{ref}}}{m_r} \right)^{\frac{1}{2}} \left(1 + \frac{E_d}{(\bar{\zeta} + 3/2 - \omega)kT} \right) \exp\left(-\frac{E_d}{kT}\right). \quad (6.48)$$

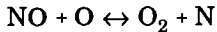
and it may be combined with the version of eqn (6.35) for like molecules, to give the probability of recombination as

$$\frac{\sigma_R}{\sigma_T} = 2C \left(1 + \frac{E_d}{(\bar{\zeta} + 3/2 - \omega)kT} \right) \frac{n_T V Q^{A_2}}{(Q^A)^2}. \quad (6.49)$$

The constant C , which is close to unity, is the ratio of the mean product of relative velocity and collision cross-section in the dissociating collisions to the same quantity in the recombining collisions.

6.8 The exchange and ionization reactions

There are several reactions that change the identity of the dissociated atoms in air under high-temperature conditions. These are



with a suggested (Gupta et al. 1990) rate coefficient

$$k_f = 5.3 \times 10^{-21} T \exp\{-2.72 \times 10^{-19}/(kT)\},$$

and



with a suggested forward rate coefficient

$$k_f = 1.12 \times 10^{-16} \exp\{-5.17 \times 10^{-19}/(kT)\}.$$

The general Larsen-Borgnakke result of eqn (5.47) may also be applied to these reactions. If the rotational mode of the diatomic molecule is included in the second group, the parameter Ξ_b is $7/2-\omega$, so that

$$P' = (1 - E_a/E_c)^{7/2-\omega}.$$

Note that E_a in this equation is the activation energy of the exchange reaction, rather than the energy in the first group of modes, as in eqn (5.47). The mean pre-collision number of internal degrees of freedom is two and the integration of eqn (6.49) leads to the remarkably simple result

$$P_{\epsilon_v > E_a} = \exp\{-E_a/(kT)\}. \quad (6.51)$$

Because the activation energy is now much smaller than the dissociation energies, a finite vibrational relaxation number Z_v must be included in the denominator, i.e.

$$k_f = \frac{2\sigma_{\text{ref}}}{\pi^{1/2} Z_v} \left(\frac{T}{T_{\text{ref}}}\right)^{1-\omega} \left(\frac{2kT_{\text{ref}}}{m_r}\right)^{1/2} \exp\left(-\frac{E_a}{kT}\right). \quad (6.52)$$

The vibrational relaxation collision number τ_v is the product of the collision rate and the relaxation time. The Landau-Teller theory predicts that the relaxation time is related to temperature raised to the power of minus one third. Experimental data is available for the relaxation time in common gases at temperatures of the order of 5,000 K, and this confirms the Landau-Teller prediction. Millikan and White (1963) have shown that the measured data can be fitted to an expression of the form

$$p\tau_v = C \exp(C_2 T^{-1/3}),$$

where C and C_2 are constants. This equation can be combined with eqn (1.28) for the pressure and with either eqn (4.64) or eqn (4.74) for the collision rate to obtain an expression for the vibrational collision number as a function of the temperature. This is, with C_1 as another constant,

$$Z_v = (C_1/T^\omega) \exp(C_2 T^{-1/3}). \quad (6.53)$$

The rate coefficients predicted by eqn (6.52), with the vibrational collision number of eqn (6.53) evaluated at the temperature corresponding to the activation energy of the forward reaction, is compared in Fig. 6.5 with the experimentally based coefficients of eqn (6.56). In the absence of specific data for NO, the data for N₂ in Table A6 is applied to both gases. Given the uncertainty in the vibrational collision number, the agreement with the continuum rate data is again satisfactory.

It is not clear that the rotational energy should play any part in the exchange reactions, and the possible consequences of this uncertainty can be investigated by ignoring the rotational mode. The parameter Ξ_b in the general Larsen-Borgnakke distribution is then $5/2-\omega$ and

$$P' = (1 - E_a/E_c)^{5/2-\omega}.$$

The mean precollision number of internal degrees of freedom is now one and the integration of eqn (6.43) again leads to

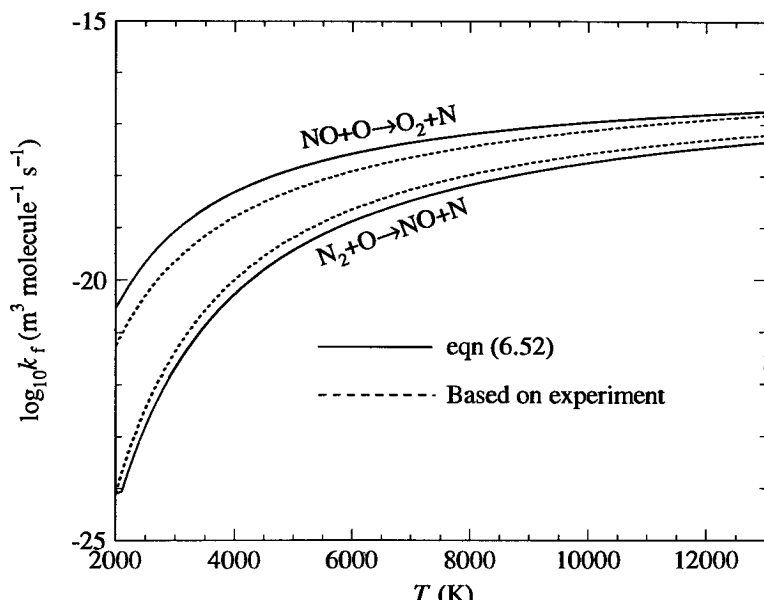


Fig. 6.5 Rate coefficients for the exchange reactions.

$$P_{\epsilon_{v,i} > E_a} = \exp \left\{ -E_a / (kT) \right\}. \quad (6.54)$$

The increased probability of energy going into the vibrational mode due to the neglect of the post-collision rotation is therefore exactly balanced by the omission of the pre-collision rotation from the calculation of the probability that E_c exceeds E_a . This is consistent with the analytical justification of the serial application of the Larsen–Borgnakke method in §5.5.

Eqn (6.54) is therefore a general result for collisions in which the number of internal modes does not change. It defines the fraction of collisions in which the post-collision energy in a single mode will exceed the energy E_a . This fraction is compared in Fig. 6.6 with the fraction of collisions in which the total energy E_c exceeds E_a . The latter fraction is given by eqn (6.6) and this function has been plotted for $\omega = 0.75$ and a range of values for the mean number of internal degrees of freedom that contribute to E_c . The effect of ω on this function has already been shown in Fig. 4.6.

Ionization reactions involve the electronic states and, not only are the electronic levels widely and unevenly spaced, but the transitions between them are subject to restrictive selection rules. This means that simple classical theories are unlikely to be successful in predicting the rate coefficients of ionization reactions. Nevertheless, the available energy theory should provide an upper limit for these rates.

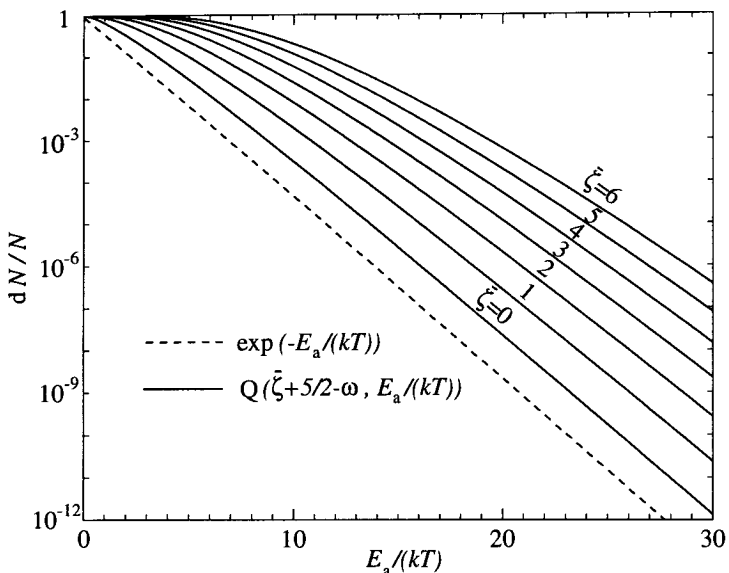


Fig. 6.6 The functions that determine the fraction of collisions that satisfy the various energy constraints.

Consider the ionization of molecular nitrogen in an impact with another nitrogen molecule, i.e.



for which a typical rate constant is

$$k_f = 2.5 \times 10^{-22} T^{1/2} \exp\{2.5 \times 10^{-18}/(kT)\}. \quad (6.55)$$

The average molecular energy associated with the electronic excitation is

$$\varepsilon_{el} = (k \sum_{i=0}^j g_i \Theta_{el,i} \exp(-\Theta_{el,i}/T)) / Q_{el}, \quad (6.56)$$

and the contribution from each level is kT when $T = \Theta_{el}$ for that level. The probability that the ionization energy is attained in the electronic mode of one molecule is approximately that given by eqn (6.51) with the activation energy set to the ionization energy E_i . The rate coefficient is then similar to eqn (6.52), or

$$k_f = \frac{2\sigma_{ref}}{\pi^{1/2} Z_i} \left(\frac{T}{T_{ref}}\right)^{1-\omega} \left(\frac{2kT_{ref}}{m_r}\right)^{1/2} \exp\left(-\frac{E_i}{kT}\right).$$

A comparison of this equation with eqn (6.55) leads to a steric factor of approximately 0.0001. This is essentially the ratio of the ionization to the elastic cross-section.

The important reaction in the initial ionization in air is the associative-ionization reaction, rather than the direct impact ionization. This is



with a typical rate constant of

$$k_f = 1.5 \times 10^{-20} T^{1/2} \exp\{4.5 \times 10^{-19}/(kT)\}. \quad (6.57)$$

The application of the general Larsen-Borgnakke distribution to this case requires a numerical integration of eqn (6.49), and the fraction of 'available energy' collisions that leads to reactions is less than one in a hundred.

6.9 Classical model for rotational radiation

Bound-bound radiation may be emitted as a consequence of transitions between rotational states. This is significant only for heteronuclear molecules that have a permanent electric dipole moment, and this type of radiation need not be considered when dealing with symmetric diatomic molecules such as oxygen and nitrogen. Rieger (1974) has compared the quantum and classical models for rotational emission and has shown that the classical model can produce useful results.

The classical model regards the molecule as a rotating dipole and the radiated power is matched by a reduction in the rotational energy of the molecule. The magnitude of the angular velocity is related to the rotational energy E_r by

$$\omega = (2E_r/I)^{1/2}, \quad (6.58)$$

where I is the moment of inertia. The wavelength of the radiation is

$$\lambda = 2\pi c/\omega = (2\pi^2 c^2 I/E_r)^{1/2} \quad (6.59)$$

where c is the speed of light. After a time interval Δt , the angular velocity decays to

$$\omega' = \omega/(1 + \delta\omega^2 \Delta t)^{1/2},$$

where

$$\delta = \frac{\mu_e^2}{3\pi c^3 I \epsilon_0}. \quad (6.60)$$

Here μ_e is the electric dipole moment and ϵ_0 is the free space dielectric constant.

The corresponding change in the wavelength of the radiation is

$$\lambda' = \lambda(1 + \kappa \Delta T / \lambda^2)^{1/2},$$

where

$$\kappa = \frac{4\pi\mu_e^2}{3\epsilon_0 c I}. \quad (6.61)$$

The radiation energy emitted over this time interval is

$$\begin{aligned} E_{\text{rad}} &= \frac{1}{2} I (\omega^2 - \omega'^2) \\ &= 2\pi^2 c^2 I (1/\lambda^2 - 1/\lambda'^2). \end{aligned} \quad (6.62)$$

The HF molecule may be used to illustrate the magnitudes of the quantities in these equations. The moment of inertia is 1.34×10^{-47} kg m² and the electric dipole moment is 6.07×10^{-30} C m. A typical angular velocity at temperature T is $(kT/I)^{1/2}$ and, at a temperature of 2,000 K, this is 4.5×10^{13} s⁻¹. The wavelength associated with this frequency 4.2×10^{-5} m. This indicates that rotational radiation generally falls in the infra-red region of the electromagnetic spectrum.

6.10 Bound-bound thermal radiation

Bound-bound radiation occurs as a result of radiative transitions between the quantized energy levels of atoms and molecules. These radiative events occur spontaneously and are not associated directly with intermolecular collisions. The transitions in atoms are between the electronic levels but, in the case of molecules, radiative transitions involve the rotational, vibrational, and electronic levels. Because the levels designate the energy in the particular mode, a transition between a particular pair of levels involves a fixed energy e_p of the photon. This energy is related to the frequency ν

$$e_p = h\nu, \quad (6.63)$$

so that bound-bound transitions give rise to emission and absorption *lines*.

The probability of the spontaneous emission is expressed through the *Einstein coefficient* A_{nm} which is defined such that the probability per unit time that a particle at energy state n will undergo a radiative transition to state m , with the radiant energy in the element of solid angle $d\Omega$, is

$$A_{nm} d\Omega.$$

The number of $n \rightarrow m$ transitions per unit time per unit volume is therefore

$$-(dn/dt)_{n \rightarrow m} = 4\pi n_n A_{nm} = n_n / \tau_{nm}, \quad (6.64)$$

where τ_{nm} is the *mean radiative lifetime* for the transition. Einstein coefficients are also defined for the absorption and for the induced emission of radiation. However, it may be shown (e.g. Vincenti and Kruger 1965) that the coefficients are related by equilibrium constraints, and only one of the three is independent.

Typical magnitudes of the mean radiative lifetime and the wavelength of the radiation are shown in Table 6.1. The mean radiative lifetimes are several orders of magnitude greater than the mean collision time at standard density, but become comparable with this time at low densities.

Table 6.1 Molecular band systems in air.

Band	Transition	τ (s)	λ (m)
N ₂ ,1+	3 → 2	1.1×10 ⁻⁵	1.06×10 ⁻⁶
N ₂ ,2+	5 → 3	2.7×10 ⁻⁸	0.34×10 ⁻⁶
O ₂ ,S-R	5 → 1	8.2×10 ⁻⁹	0.20×10 ⁻⁶
NO, β	3 → 1	6.7×10 ⁻⁷	0.22×10 ⁻⁶
NO, γ	2 → 1	1.2×10 ⁻⁷	0.23×10 ⁻⁶

There are then insufficient collisions to maintain the equilibrium fraction of molecules at the higher electronic levels, and the radiation is said to be 'collision limited'.

In an equilibrium gas, the fraction of molecules with electronic states in level i is given by the Boltzmann distribution of eqn (5.63). If this equation applies, the gas is said to be in 'local thermal equilibrium'. For the non-equilibrium case, the Larsen-Borgnakke method can be used to select the electronic states, as described in §5.6. This requires data on the ratio of the excitation to the elastic cross-section.

In the cases of the inelastic collisions and chemical reactions, it was possible to formulate a phenomenological model at the particle level such that the description becomes identical with that given by the continuum model when the density is sufficiently high for this model to be valid. This does not appear to be possible for thermal radiation.

References

- BARAS, F and NICOLIS, G. (1990). Microscopic simulations of exothermic chemical systems, In *Microscopic simulations of complex flows*, (ed. M. Mareschal), pp 339–352, Plenum Press, New York.
- BIRD, G.A. (1979). Simulation of multi-dimensional and chemically reacting flows, In *Rarefied gas dynamics*, (ed. R. Campargue), pp 365–388, CEA, Paris.
- BIRD, G.A. (1981). Monte Carlo simulation in an engineering context, *Prog. Astro. Aero.*, **74**: Part I, 239–255.
- BIRD, G.A. (1994). A new chemical reaction model for DSMC calculations, *Prog. in Astro. and Aero.* **158**, in press.
- FOWLER, R.H. and GUGGENHEIM, E.A. (1952). *Statistical thermodynamics*, Cambridge University Press.
- GARDINER, W.C. (1969). *Rates and mechanisms of chemical reactions*, Benjamin, New York.
- GUPTA, R.N., YOS, J.M., THOMPSON, R.A., and LEE, K-P (1990). A review of reaction rates and thermodynamic and transport properties for an 11-species air model for chemical and thermal nonequilibrium calculations to 30 000 K, NASA Reference Publication 1232.
- JAFFE, R.L. (1987). The calculation of high-temperature equilibrium and non-equilibrium specific heat data for N₂, O₂, and NO, Am. Inst. Aero. and Astro. Paper AIAA-87-1633.

- HANSEN, C.F. (1965). Estimates for collision-induced dissociation rates. *AIAA J.* **3**, 61-66.
- LEVINE, R.D. and BERNSTEIN, R.B. (1987). *Molecular reaction dynamics and chemical reactivity*, Oxford University Press.
- MILLIKAN, R.C. and WHITE, D.R. (1963). Systematics of vibrational relaxation. *J. Chem. Phys.* **39**, 3209-3213.
- PARK, CHUL (1990). *Nonequilibrium hypersonic aerothermodynamics*, Wiley, New York.
- REIGER, T.J. (1974). Pure rotational emission from diatomic molecules in the quantum and classical limits, *J. Quant. Spectrosc. Radiat. Transfer*, **14**, 59-67.
- VINCENTI, W.G. and KRUGER, C.H. (1965). *Introduction to physical gas dynamics*, Wiley, New York.

COLLISIONLESS FLOWS

7.1 Bimodal distributions

As discussed in Chapter 1, collisionless or free-molecule flows are the limiting case in which an appropriately defined Knudsen number tends to infinity, i.e.,

$$(Kn) \equiv \lambda/L \rightarrow \infty. \quad (7.1)$$

Collisionless flows are associated either with very low densities, and therefore with very high mean free paths, or with very small typical dimensions.

In the absence of intermolecular collisions, collisionless flowfields are formed by the superimposition of several classes of molecule. These classes could be separate streams with different temperatures and with a relative velocity between them, or a freestream and the reflected molecules from a surface. In most cases, these separate classes will each conform to an equilibrium or Maxwellian distribution. The superimposition may be such that the whole or only part of the distributions contribute to the region of interest in the collisionless flow.

First consider the case in which two *full-range* distributions contribute to the flow. These will be denoted by the subscripts 1 and 2. They are at separate temperatures and, without loss of generality, the relative velocity of magnitude c_r may be chosen to be along the x -axis of gas 2. The gas then comprises a number density n_1 of stationary gas defined by

$$f_1 = (\beta_1^3/\pi^{3/2}) \exp(-\beta_1^2(u^2 + v^2 + w^2)) \quad (7.2)$$

and n_2 of gas with a stream speed c_r and a distribution function

$$f_2 = (\beta_2^3/\pi^{3/2}) \exp(-\beta_2^2([u - c_r]^2 + v^2 + w^2)). \quad (7.3)$$

The combined distribution function is

$$nf = n_1 f_1 + n_2 f_2,$$

and the macroscopic properties or moments of the distribution function are given by eqn (3.3) as

$$\bar{Q} = \frac{1}{n} \int_{-\infty}^{\infty} \int_{-\infty}^{\infty} \int_{-\infty}^{\infty} (n_1 Q_1 f_1 + n_2 Q_2 f_2) du dv dw. \quad (7.4)$$

The mean molecular mass is obtained by setting $Q = m$, to give

$$\bar{m} = (n_1 m_1 + n_2 m_2)/n. \quad (7.5)$$

The stream speed of the mixture is defined by eqn (1.43) and is obtained by setting $Q = mu$ and then using eqn (7.5), to give

$$c_0 = \frac{n_2 m_2}{n_1 m_1 + n_2 m_2} c_r. \quad (7.6)$$

The translational temperature is best obtained through the alternative definition of eqn (1.51) by setting $Q = mc^2$ and then using eqns (7.5) and (7.6), to give

$$T = \frac{1}{n} \left(n_1 T_1 + n_2 T_2 + \frac{n_1 m_1 n_2 m_2}{m_1 n_1 + m_2 n_2} \frac{c_r^2}{3k} \right). \quad (7.7)$$

This is most instructively written as

$$T = \bar{T} \left(1 + \frac{2n_1 n_2}{3n^2} \bar{s}^2 \right), \quad (7.8)$$

where

$$\bar{T} = (n_1 T_1 + n_2 T_2)/n$$

and

$$\bar{s} = c_r / (2k \bar{T} / \bar{m})^{1/2} = c_r \bar{\beta}.$$

The superimposition of two cool gas streams with a high relative velocity can therefore lead to high kinetic temperatures, even though there are no collisions between the molecules of the two streams. This is because the combination of two equilibrium velocity distributions with a significant relative velocity between them leads to a highly non-equilibrium velocity distribution function. The kinetic temperature is properly defined for all distribution functions, whereas the thermodynamic temperature has no meaning in other than an equilibrium situation (when it is equal to the kinetic temperature). Kinetic temperatures in collisionless flows must not be interpreted as, or confused with, thermodynamic temperatures.

In most cases, the geometry is such that only part of each distribution function applies at a particular location. For example, consider the case in which a stream of density n_∞ , speed c_∞ , and temperature T_∞ is directed at an angle θ to the normal to a solid surface. The coordinate system is the same as that adopted for the molecular flux calculations in §4.2, and was illustrated in Fig. 4.2. The distribution function for the stream is

$$f_\infty = (\beta_\infty^3 / \pi^{3/2}) \exp(-\beta_\infty^2 \{(u - c_\infty \cos\theta)^2 + (v - c_\infty \sin\theta)^2 + w^2\}), \quad (7.9)$$

and, if it is assumed that the surface interaction is diffuse with complete accommodation to the surface temperature T_w , the distribution function for the reflected molecules is

$$f_r = (\beta_w^3 / \pi^{3/2}) \exp(-\beta_w^2 \{u^2 + v^2 + w^2\}). \quad (7.10)$$

The number density n_r that is associated with the reflected molecules is given by the condition that, in a steady state, the flux of molecules from the surface must be equal to that to the surface. Therefore, from eqns (4.22) and (4.24)

$$\frac{n_r}{2\pi^{1/2}\beta_w} = \frac{n_\infty}{2\pi^{1/2}\beta_\infty} (\exp\{-s^2 \cos^2\theta\} + \pi^{1/2}s \cos\theta \{1 + \text{erf}[s \cos\theta]\}),$$

so that

$$n_r = n_\infty (T_\infty/T_w)^{1/2} (\exp\{-s^2 \cos^2\theta\} + \pi^{1/2}s \cos\theta \{1 + \text{erf}[s \cos\theta]\}), \quad (7.11)$$

where

$$s = c_\infty \beta_\infty = c_\infty / (2k T_\infty/m)^{1/2}.$$

The gas is homogeneous in composition and m applies to both the incident and reflected molecules. The moment equation must now be based on two *half-range* distributions and may be written

$$\bar{Q} = \frac{1}{n} \int_{-\infty}^{\infty} \int_0^{\infty} \left(\int_0^{\infty} n_\infty Q_\infty f_\infty du + \int_{-\infty}^0 n_r Q_r f_r du \right) dv dw. \quad (7.12)$$

The number density n above the surface may be obtained by evaluating this equation with the Q 's set equal to unity. This gives

$$n = \{1 + \text{erf}(s \cos\theta)\} n_\infty/2 + n_r/2,$$

or, using eqn (7.11),

$$n = \frac{n_\infty}{2} \left(1 + \text{erf}(s \cos\theta) + (T_\infty/T_w)^{1/2} (\exp\{-s^2 \cos^2\theta\} + \pi^{1/2}s \cos\theta \{1 + \text{erf}[s \cos\theta]\}) \right), \quad (7.13)$$

This density applies at the surface and as far above the surface as the flow remains macroscopically uniform. When $s \cos\theta$ is above about 3, the exponential term becomes negligible and the error function is very close to unity. The density can then be written

$$n = n_\infty \{1 + (T_\infty/T_w)^{1/2} \pi^{1/2} s \cos\theta\}. \quad (7.14)$$

The components of the stream velocity can be evaluated by setting Q to the corresponding molecular velocity components. The velocity component in the x -direction is normal to the surface and, as expected, it is zero for the combined distribution. The velocity component of the combined distributions parallel to the surface in the y -direction is

$$v_c = \frac{1}{2} (n_\infty/n_r) c_0 \sin\theta (1 + \text{erf}[s \sin\theta]). \quad (7.15)$$

Eqn (7.11) can again be substituted for n_r , but the origins of the *slip velocity* are clearer if this is not done. The *temperature jump* can also be calculated from eqn (7.12), but the expression is excessively complicated.

7.2 Molecular effusion and transpiration

Molecular effusion is the term that is applied to the flow that occurs when an equilibrium gas is separated from a vacuum by a thin wall in which there is a small hole. If the dimensions of the hole are sufficiently small in comparison with the mean free path, each molecule that passes through the hole is subject to a negligibly small probability of being affected by the flow of other molecules towards or through the hole. The flux through the hole is then the same as that across any small surface element in an equilibrium gas, as analysed in § 4.2. The number flux is given by eqn (4.24) and, multiplying this by m , the free-molecule mass flux per unit area is

$$\Gamma_f = \frac{nm}{2\pi^{\frac{1}{2}}\beta} = \rho \left(\frac{RT}{2\pi} \right)^{\frac{1}{2}}. \quad (7.16)$$

The free-molecule flux may be compared with the result from continuum theory which is valid when the mean free path is extremely small in comparison with the dimensions of the hole. The inviscid continuum model is a choked flow with sonic velocity in the plane of the hole. The continuum mass flux is, therefore,

$$\Gamma_c = \rho^* a^*$$

with the asterisk representing sonic conditions. The macroscopic quantities in the free-molecule result are the stagnation conditions and, using the standard one-dimensional steady continuum flow relationships between the sonic and stagnation conditions,

$$\Gamma_c = \left(\frac{2}{\gamma+1} \right)^{\frac{\gamma+1}{2(\gamma-1)}} \rho (\gamma RT)^{\frac{1}{2}}. \quad (7.17)$$

Here, γ is the specific heat ratio of the gas so that the continuum and free-molecule results differ only by a numerical factor.

A comparison of eqns (7.16) and (7.17) shows that the ratio of the free-molecule to the continuum mass flux is

$$\begin{aligned} \frac{\Gamma_f}{\Gamma_c} &= \frac{1}{(2\pi\gamma)^{\frac{1}{2}}} \left(\frac{\gamma+1}{2} \right)^{\frac{\gamma+1}{2(\gamma-1)}} \\ &= 0.5494 \quad \text{for } \gamma = 5/3. \end{aligned} \quad (7.18)$$

Assuming a circular hole, the obvious choice of Knudsen number is the ratio of the mean free path in the undisturbed gas to the diameter of the hole. For a problem with a very simple geometry, such as this, it would be expected that the transition between the two limits would be monotonic with the major change occurring between Knudsen numbers of 0.1 and 10. Liepmann (1961) has discussed the effusion flow in depth and reports experiments that generally confirm these expectations.

The interaction of separate molecular streams and molecular species in gas flows takes place through intermolecular collisions and, since these are absent in collisionless flows, a relatively complex flow may be built up by the superimposition of simpler flows. Several important examples of this involve combinations of effusion flows.

First, consider the case in which there is an equilibrium gas on both sides of the thin wall containing the small orifice. For sufficiently high Knudsen number, effusion will occur in both directions with each stream of gas being quite independent of the other. If the gas on one side of the orifice is contained in a vessel that is maintained at temperature T_A , and that on the other side is in a vessel maintained at temperature T_B , there must be an equal flux of gas in each direction. If there is a similar simple gas in both vessels, eqn (7.16) gives

$$\rho_A (RT_A)^{1/2} = \rho_B (RT_B)^{1/2},$$

and, using eqn (1.28),

$$\frac{p_A}{p_B} = \left(\frac{T_A}{T_B} \right)^{1/2}, \quad (7.19)$$

so that a pressure difference is established between the two vessels. This phenomenon is called *thermal transpiration*.

Next consider the case in which a mixture of species 1 and species 2 molecules is separated from a vacuum by a membrane that contains a number of free-molecule orifices. After passing through the membrane, the gas is collected. The number density ratio in the collected gas will be proportional to the number flux ratio and, again using eqn (7.16) and noting that $R = k/m$,

$$\frac{n_1'}{n_2'} = \frac{n_1}{n_2} \left(\frac{m_2}{m_1} \right)^{1/2}. \quad (7.20)$$

The prime denotes the collected gas, and eqn (7.20) shows that there is an enhancement in the number density of the light gas.

The spatial distribution of the gas in the effusion flowfield is also of interest. The number density of the gas upstream of the orifice will now be denoted by n_0 to distinguish it from the number density n in the effusing gas. The number of molecules per unit time effusing from an orifice of area S that have a speed between c and $c + dc$, and that also make an angle between θ and $\theta + d\theta$ with the normal to the plane of the orifice, is given by eqn (4.39) as

$$2\pi^{-1/2} n_0 S \beta^3 c^3 \exp(-\beta^2 c^2) \sin \theta \cos \theta d\theta dc.$$

When these molecules have moved a distance r (that is large in comparison with the radius of the orifice) they cross an annulus of area $2\pi r^2 \cos \theta d\theta$, so that the number per unit time is also given by

$$2\pi dncr^2 \cos \theta d\theta.$$

The number density dn due the class c molecules is therefore

$$dn = \frac{n_0 S \cos\theta}{r^2} \frac{\beta^3}{\pi^{3/2}} c^2 \exp(-\beta^2 c^2) dc$$

and, integrating over all speeds from 0 to ∞ ,

$$n = \frac{n_0 S \cos\theta}{4\pi r^2}. \quad (7.21)$$

There is therefore a 'cosine distribution' superimposed on an 'inverse square' decay of the number density in the effusing molecules. While eqn (7.21) requires that r should be large compared with the radius r_0 of the orifice, it may be used to obtain an exact expression for the number density along the normal from the centre (i.e. the axis or centreline of the effusing flow). Consider an annular element of width dx at a radius x in the plane of the orifice. With respect to this element, the axis is such that $\cos\theta = r/(r^2+x^2)^{1/2}$ and the number density along the axis is

$$n = \frac{n_0 r}{2} \int_0^{r_0} \frac{x dx}{(x^2+r^2)^{1/2}}$$

or

$$n = (n_0/2) [1 - \{1 + (r_0/r)^2\}^{-1/2}]. \quad (7.22)$$

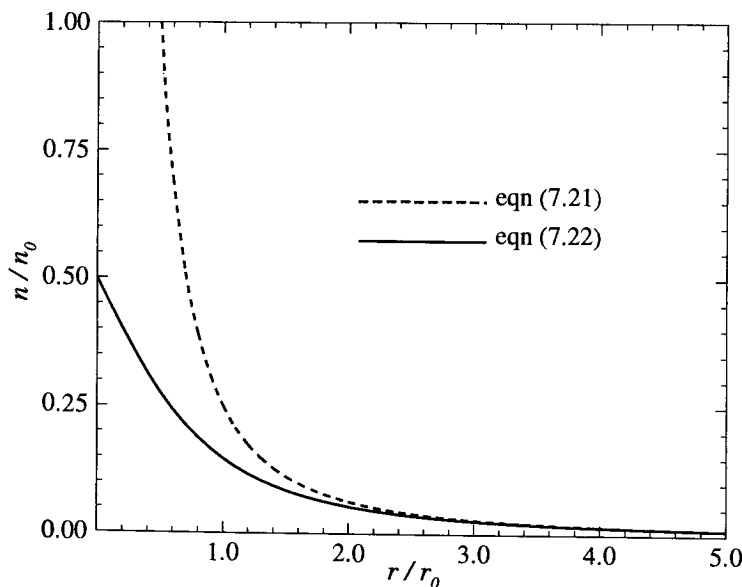


Fig. 7.1 Number density along the normal from the centre of an orifice.

7.3 One-dimensional steady flows

A flow may be regarded as one-dimensional if it can be solved through the application of the molecular flux equations in one direction. The mass flux aspect of the molecular effusion problem qualifies as one-dimensional, even though the flowfield is two or three-dimensional. This is the simplest class of flows and the free-molecule limits of the classical Couette flow and the parallel plate heat transfer problem may be compared with the corresponding continuum flows.

Consider the *one-dimensional heat transfer* between two infinite plane parallel plates separated by a distance h that is very small in comparison with the mean free path λ of the gas between the plates. Assume diffuse reflection with complete thermal accommodation to the temperature T_U at the upper plate, and T_L at the lower plate. The monatomic gas of number density n between the plates then consists of an upward moving stream of density n_L and temperature T_L emitted from the lower plate, together with a downward moving stream of density n_U and temperature T_U emitted from the upper plate.

The flux of diffusely reflected molecules from a surface is identical with the effusion of molecules from a fictitious equilibrium gas on the reverse side of the surface. The number density of the reflected molecules is half that of the fictitious gas, since half of these are moving in the direction normal to the surface. Therefore, from eqns (4.23) and (4.24),

$$n_U T_U^{1/2} = n_L T_L^{1/2}$$

and, since

$$n = n_U + n_L,$$

$$n_L = \frac{n T_U^{1/2}}{T_U^{1/2} + T_L^{1/2}}, \quad n_U = \frac{n T_L^{1/2}}{T_U^{1/2} + T_L^{1/2}}. \quad (7.23)$$

The energy flux q_L from the lower plate is obtained by setting $\beta = (2RT_L)^{-1/2}$ and $\rho = 2n_L m$ in eqn (4.27), to give

$$q_L = mn_L \pi^{-1/2} (2RT_L)^{3/2}.$$

Similarly, the downward energy flux from the upper plate is

$$q_U = mn_U \pi^{-1/2} (2RT_U)^{3/2}.$$

The net upward heat flux is obtained by combining these equations with eqn (7.23), to give

$$q_f = -2^{3/2} \rho \pi^{-1/2} R^{3/2} T_U^{1/2} T_L^{1/2} (T_U^{1/2} - T_L^{1/2}). \quad (7.24)$$

The continuum heat transfer between the plates is

$$q_c = -K(dT/dy),$$

with the y -axis normal to the lower plate. If we assume that $K = CT^\omega$ with C and ω constant, this becomes

$$q_c = - \frac{C}{\omega + 1} \frac{dT^{\omega+1}}{dy}.$$

The continuum energy equation in a static gas requires that q_c be a constant, so that

$$T^{\omega+1} = - \frac{(\omega+1)q_c}{C} y + \text{const.}$$

Since $T = T_L$ at $y = 0$, the constant of integration is $T_L^{\omega+1}$. The continuum solution is then obtained by setting $y = h$, i.e.

$$q_c = - \frac{C(T_U^{\omega+1} - T_L^{\omega+1})}{(\omega+1)h}. \quad (7.25)$$

For this flow, the free molecule and continuum solutions differ in their functional relationships as well as in the numerical constant. The free molecule heat transfer is proportional to the gas density and is independent of the plate spacing, whereas the continuum heat transfer is inversely proportional to the plate spacing and independent of the density. Therefore,

$$\frac{q_c}{q_f} \propto \frac{1}{\rho h} \propto \frac{\lambda}{h} \propto (Kn), \quad (7.26)$$

so that the ratio of the continuum to the free molecule heat transfer is proportional to the Knudsen number of the flow.

The free molecule heat transfer problem is readily extended to *Couette flow* by giving the upper plate a velocity U in the x -direction (which lies in the plane of the plate), while the lower plate remains stationary. The number fluxes and the normal momentum flux are not affected by this velocity. The shear stress on the lower plate τ_L due to the molecules from the upper plate having a mean velocity U in the x -direction is obtained by setting $s = U\beta$, $\beta = (2RT_U)^{-1/2}$, $\rho = 2n_U m$, and $\theta = \rho/2$ in eqn (4.26). This gives

$$\tau_L = mn_U U(2RT_U/\pi)^{1/2}$$

or, using eqn (7.23),

$$\tau_L = \frac{\rho U}{T_U^{1/2} + T_L^{1/2}} \left(\frac{2RT_UT_L}{\pi} \right)^{1/2}. \quad (7.27)$$

The factor of 2 in the definition of the density was included because the flux equations are applied to the fictitious gas on the opposite side of the upper plate, and this has the number density $2n_U$. The reflected molecules from the lower plate do not contribute to the shear stress so that τ_U is the net value. There will be an equal and opposite shear stress on the upper plate. The energy flux q_U from the upper plate is obtained by making a similar substitution into eqn (4.27), to give

$$q_U = mn_U (2RT_U/\pi)^{1/2} (U^2/2 + 2RT_U). \quad (7.28)$$

In both the above cases, the gas between the two plates is macroscopically uniform. The combination of the two equilibrium distributions gives the following non-equilibrium bimodal distribution function for this gas;

$$f = \frac{1}{\pi^{1/2} n} \left(n_U \beta_U^3 \exp \left[-\beta_U^2 \{ (u-U)^2 + v^2 + w^2 \} \right] + n_L \beta_L^3 \exp \left[-\beta_L^2 (u^2 + v^2 + w^2) \right] \right). \quad (7.29)$$

The macroscopic properties of the gas are obtained by evaluating the appropriate moments of this distribution function. The stream velocity is in the x -direction with magnitude

$$u_0 = (n_U/n)U, \quad (7.30)$$

and the temperature is

$$T = \{ T_L^{1/2} (T_U + \frac{1}{3} U^2 / R) + T_U^{1/2} T_L \} / (T_U^{1/2} + T_L^{1/2}). \quad (7.31)$$

There is, therefore, a discontinuity in temperature and velocity between the surfaces of the plates and the adjacent gas. Such discontinuities are generally present at surfaces in free molecule flows.

7.4 One-dimensional unsteady flows

The determination of the properties of unsteady flows is best done through the *collisionless Boltzmann equation* using a transformation that was introduced by Narasimha (1962). Since intermolecular collisions are absent, the collision terms on the right-hand side of eqn (3.20) drop out. Then, in the absence of force fields, the collisionless Boltzmann equation is

$$\frac{\partial}{\partial t} (nf) + \mathbf{c} \cdot \frac{\partial}{\partial \mathbf{r}} (nf) = 0. \quad (7.32)$$

We have seen from eqn (3.6) that nf is identical with the distribution function in phase space \mathcal{F} , so that the functional relationship is $nf(\mathbf{c}, \mathbf{r}, t)$. We will be concerned with the application of eqn (7.32) to initial value problems, for which

$$nf(\mathbf{c}, \mathbf{r}, t=0) = n_i f_i(\mathbf{c}, \mathbf{r}). \quad (7.33)$$

Eqn (7.32) has the form of the Liouville equation and the solution is that nf remains constant along the molecular paths which are the characteristics of the equation, i.e.

$$nf(\mathbf{c}, \mathbf{r}, t) = n_i f_i(\mathbf{c}, \mathbf{r} - \mathbf{c}t). \quad (7.34)$$

Eqn (7.34) may be multiplied by a molecular quantity Q and integrated over velocity space, to give,

$$n \bar{Q}(\mathbf{r}, t) = \int_{-\infty}^{\infty} Q n_i f_i(\mathbf{c}, \mathbf{r} - \mathbf{c}t) d\mathbf{c}.$$

Now make the transformation from \mathbf{c} to

$$\mathbf{r}' = \mathbf{r} - \mathbf{c}t, \quad (7.35)$$

for which the Jacobian is

$$\frac{\partial(x', y', z')}{\partial(u, v, w)} = -t^3.$$

Therefore,

$$n \bar{Q}(r, t) = \frac{1}{t^3} \int Q n_i f_i \left(\frac{\mathbf{r} - \mathbf{r}'}{t}, \mathbf{r}' \right) d\mathbf{r}' . \quad (7.36)$$

with the limits of the integration being the extent of the gas at time $t=0$.

As an example, consider a semi-infinite stationary uniform gas on the negative side of the plane $x=0$ and separated by a thin wall from a vacuum on the positive side of the plane. At time $t=0$, the wall is removed and the gas expands freely into the vacuum. Given that the gas is monatomic and originally at the temperature T_1 and number density n_1 , the problem is to determine the number density, velocity, and temperature of the gas as a function of x and t , for values of x and t that are very small in comparison with the mean free path and mean collision time, respectively, in the flow. This is called the *free expansion* problem and is probably the simplest one-dimensional unsteady collisionless flow.

The one-dimensional form of eqn (7.36) is

$$n \bar{Q}(x, t) = \frac{1}{t} \int Q n_i f_{u_i} \left(\frac{x-x'}{t}, x' \right) dx' ,$$

where

$$(7.37)$$

$$x' = x - ut .$$

Eqn (4.13) gives the distribution function as a function of $\beta_1 = (2RT_1)^{-1/2}$ and, setting $n_i = n_1$ and $Q = 1$, the density is

$$\begin{aligned} n(x, t) &= \frac{1}{t} \int_{-\infty}^0 n_1 (\beta_1 / \pi^{1/2}) \exp(-\beta_1^2 u'^2) dx' \\ &= \frac{n_1}{\pi^{1/2}} \int_{\beta_1 x/t}^{\infty} \exp\left(-\frac{\beta_1^2 (x-x')^2}{t^2}\right) d\left(\frac{\beta_1 (x-x')}{t}\right). \end{aligned}$$

Therefore, using the standard integrals of Appendix B,

$$\frac{n}{n_1} = \frac{1}{2} \operatorname{erfc}\left(\frac{\beta_1 x}{t}\right). \quad (7.38)$$

Similarly, the stream velocity is obtained by setting $Q=u$, to give

$$nu_0 = (\frac{1}{2}\pi^{-1/2}n_1/\beta_1) \exp\{-(\beta_1 x/t)^2\}$$

or

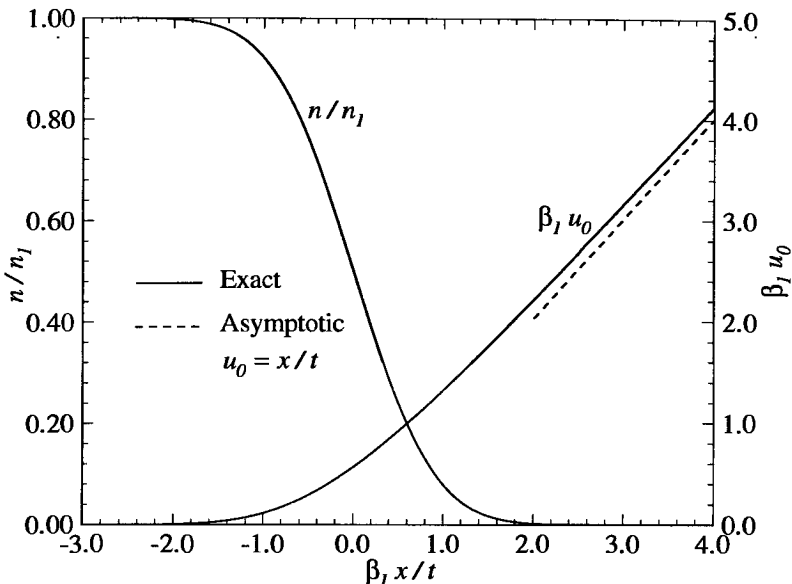


Fig. 7.2 Number density and stream velocity in a free expansion.

$$\beta_1 u_0 = \pi^{-\frac{1}{2}} \exp\{-(\beta_1 x/t)^2\} / \operatorname{erfc}(\beta_1 x/t). \quad (7.39)$$

Note that eqns (7.38) and (7.39) are functions of $\beta_1 x/t$ alone and, at $x=0$, $n/n_1 = \frac{1}{2}$ and $\beta_1 u_0 = \pi^{-\frac{1}{2}}$. The number flux across the plane $x=0$ is therefore constant and equal to $n_1/(2\pi^{\frac{1}{2}}\beta_1)$. A comparison with eqn (7.16) shows that this is identical with the number flux in the steady effusion problem. The behaviour of n/n_1 and $\beta_1 u_0$ as functions of $\beta_1 x/t$ is shown in Fig. 7.2. The density profile is symmetric about the origin, with the perturbation from the undisturbed densities falling as $\exp\{-(\beta_1 x/t)^2\}$.

The analysis is not restricted to the determination of flow fields. For example, consider the extension of the above problem to include a specularly reflecting wall in the plane $x=x_w$. The problem is to determine the pressure p_w on the wall in the free-molecule case in which $(Kn)=\lambda_1/x_w \rightarrow \infty$. The pressure on the wall is equal to twice the normal momentum flux at the location $x=x_w$. Therefore, setting $x=x_w$ and $Q=mu^2$ in eqn (7.37),

$$\begin{aligned} p_w &= \left(2/t\right) \int_{-\infty}^0 \pi^{-\frac{1}{2}} \beta_1 n_1 m u^2 \exp(-\beta_1^2 u^2) dx' \\ &= \frac{2\rho_1 \beta_1}{\pi^{\frac{1}{2}}} \int_{\beta_1 x_w/t}^{\infty} \left(\frac{x_w - x'}{t}\right)^2 \exp\left(-\frac{\beta_1^2 (x_w - x')^2}{t^2}\right) d\left(\frac{x_w - x'}{t}\right), \end{aligned}$$

and, again using the standard integrals,

$$\frac{p_w}{p_1} = 1 - \operatorname{erf}\left(\frac{\beta_1 x_w}{t}\right) + \frac{2}{\pi^{1/2}} \left(\frac{\beta_1 x_w}{t}\right) \exp\left(-\frac{\beta_1^2 x_w^2}{t^2}\right). \quad (7.40)$$

The analysis of the free expansion problem may also be extended to cover the expansion of a gas cloud of finite width. If this width is sufficiently small in comparison with the undisturbed mean free path, collisionless analysis is applicable at all locations and at all times. If the gas is initially distributed uniformly between the planes $x = -l$ and $x = +l$, the density and velocity are obtained similarly to eqns (7.38) and (7.39), but with the limits over x' from $-l$ to $+l$, rather than from $-\infty$ to 0. The results for the density and stream velocity are

$$n/n_1 = [\operatorname{erf}\{\beta_1(x+l)/t\} - \operatorname{erf}\{\beta_1(x-l)/t\}]/2 \quad (7.41)$$

and

$$\beta_1 u_0 = \frac{\exp\{-\beta_1^2(x-l)^2/t^2\} - \exp\{-\beta_1^2(x+l)^2/t^2\}}{\pi^{1/2} [\operatorname{erf}\{\beta_1(x+l)/t\} - \operatorname{erf}\{\beta_1(x-l)/t\}]} \quad (7.42)$$

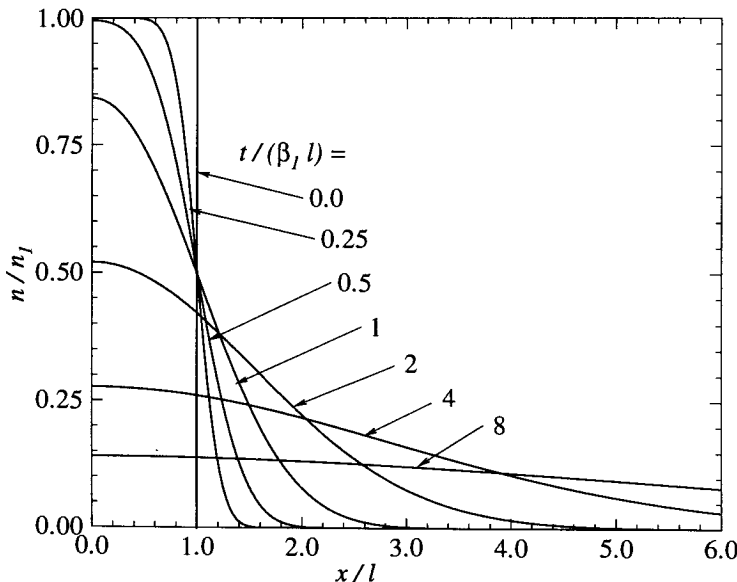


Fig. 7.3 Number density profiles in the expansion of a gas cloud.

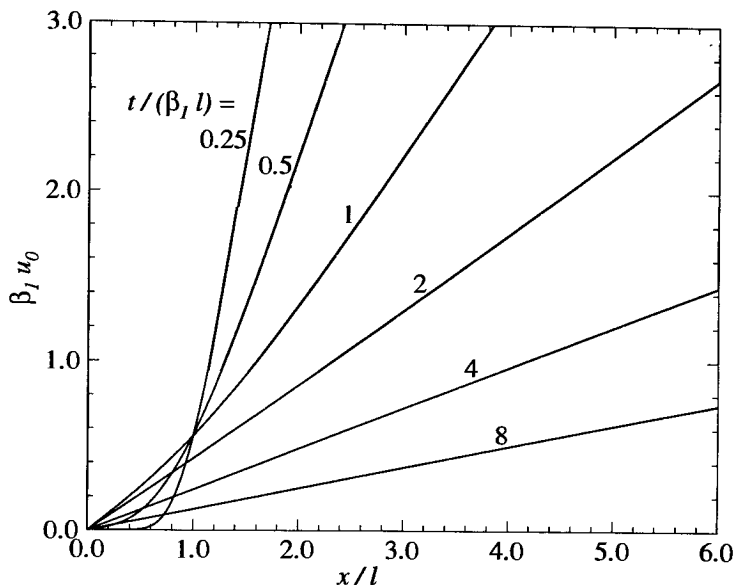


Fig. 7.4 Stream velocity profiles in the unsteady expansion of a gas cloud.

The character of these solutions is shown in Fig. 7.3 for the number density and Fig. 7.4 for the flow velocity. The gas cloud is symmetrical about $x=0$ at all times. For points within the initial extent of the gas cloud from $x=-l$ to $x=+l$, the density falls continuously, while the velocity increases to a maximum and then decreases. On the other hand, for points that are initially outside the cloud, the maximum velocity is at the leading edge of the cloud, while the density increases to a maximum and then decreases. Narasimha (1962) deals also with the corresponding cylindrically and spherically symmetric flows.

The *one-dimensional piston problem* is another basic flow for which results are required for future reference. A specularly reflecting plane piston impulsively acquires a velocity $\pm U$ at time $t=0$ and moves either into or away from an initially uniform stationary gas of number density n_1 and temperature T_1 . This problem may appear to be quite distinct from the free expansion problem. However, if the problem is viewed from a frame of reference moving with the piston face, the piston may be regarded as a fixed plane at $x=0$ with the gas on the positive side acquiring the velocity $-U$ towards the plane at time $t=0$. Similarly, the gas on the negative side of the plane may be regarded as impulsively acquiring a velocity away from the plane. The collisionless Boltzmann equation (7.37) may now be applied to the problem.

The number density becomes

$$n = \frac{1}{t} \int_0^\infty n_1 \frac{\beta_1}{\pi^{-1/2}} \exp\{-\beta_1^2(u+U)^2\} dx' + \frac{1}{t} \int_{-\infty}^0 n_1 \frac{\beta_1}{\pi^{-1/2}} \exp\{-\beta_1^2(u-U)^2\} dx',$$

the first term corresponding to the gas initially on the positive side of $x=0$ and the second term to that initially on the negative side. In terms of the standard integrals, this becomes

$$\begin{aligned} n/n_1 &= \pi^{-1/2} \left(\int_{-\beta_1(x/t-U)}^{\infty} \exp[-\beta_1^2((x-x')/t+U)^2] d[\beta_1((x-x')/t+U)] \right. \\ &\quad \left. + \int_{\beta_1(x/t-U)}^{\infty} \exp[-\beta_1^2((x-x')/t-U)^2] d[\beta_1((x-x')/t-U)] \right) \end{aligned}$$

and may be evaluated to give

$$n/n_1 = 1 + \frac{1}{2} \{ \operatorname{erf}(\beta_1 x/t + s) - \operatorname{erf}(\beta_1 x/t - s) \}. \quad (7.43)$$

where $s = U\beta$ is the speed ratio of the piston.

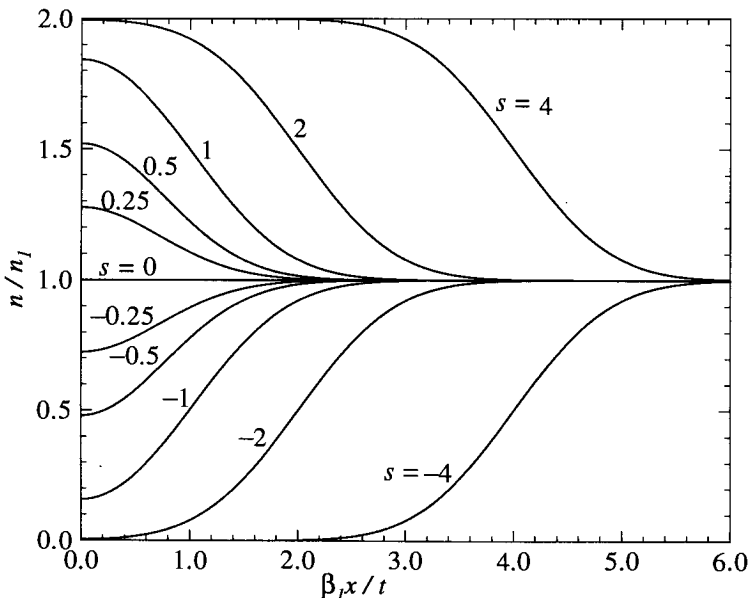


Fig. 7.5 Number density profiles for the one-dimensional piston problem.

The solution for the density is illustrated in Fig 7.5. The sign convention for U has been chosen such that a positive s corresponds to a piston moving into the gas and a negative s to the piston moving away from the gas. For positive values of s , the gas is doubled back with speed $x/t = U$ relative to the piston or plane of symmetry, or $x/t = 2U$ in the frame of reference fixed in the stationary gas into which the piston moves. Superimposed on this, there is a progressive spreading of the front due to the thermal motion of the molecules. The latter effect is dominant at small speed ratios, the number density at the piston face being

$$n/n_1 = 1 + \text{erf}(s). \quad (7.44)$$

For negative values of s , the profiles of n/n_1 lie between 1 and 0 and are symmetrical with those for positive values of s which lie between 1 and 2.

Solutions for the other flowfield properties, such as the stream velocity, may be obtained by substituting the appropriate value of Q into eqn (7.37). The pressure on the piston face could be obtained by a similar calculation to that leading to eqn (7.40) for the free expansion impingement problem. It should be remembered that the pressure tensor is generally anisotropic in a collisionless flow.

7.5 Free-molecule aerodynamics

This is concerned with the pressure, shear stress, and heat transfer at the surfaces of aerodynamic bodies in steady flight. The surface pressure and shear stress may be integrated over the complete body to determine the overall aerodynamic forces on the body. The properties of the flowfield around the body may also be required in some applications. The Knudsen number is generally defined as the ratio of the mean free path in the undisturbed atmosphere to the characteristic dimension of the body, the free-molecule solution being assumed to apply when the Knudsen number is sufficiently high. The justification for this assumption is that, under these circumstances, the molecules reflected from the body generally travel a very large distance before colliding with another molecule. There is then a negligible chance that the products of such collisions will collide with the body, so that the incident molecules are those of the equilibrium freestream. Note that the most significant collisions in the determination of the validity of the free-molecule assumption are those between the reflected and freestream molecules, and the mean free path for these may be much smaller than the freestream mean free path. This point is particularly important when the speed ratio, and therefore the Mach number, is large and the surface temperature is of the order of the stream temperature.

The surface properties follow from the application of the flux equations of §4.2 to the incident and reflected molecules. The subscripts i and r will be used to denote the incident and reflected molecular streams; a flux being regarded as positive if it is directed towards the surface. In the absence of adsorption or emission effects at the surface, the incident number flux to a surface element must be balanced by the reflected number flux. Therefore,

$$\dot{N} = \dot{N}_i + \dot{N}_r = 0; \quad (7.45)$$

$$p = p_i + p_r; \quad (7.46)$$

$$\tau = \tau_i + \tau_r; \quad (7.47)$$

and

$$q = q_i + q_r. \quad (7.48)$$

The results are obviously dependent on the nature of the gas-surface interaction and, in the absence of a general theory for such interactions, calculations will be made for a combination of the classical models of diffuse and specular reflection. From the discussion of these models in §4.5 it can be seen that, for specular reflection,

$$p_r = p_i \quad \text{or} \quad p = 2p_i, \quad (7.49)$$

$$\tau_r = -\tau_i \quad \text{or} \quad \tau = 0, \quad (7.50)$$

and

$$q_r = -q_i \quad \text{or} \quad q = 0. \quad (7.51)$$

The only simplification to eqns (7.45)–(7.48) for diffuse reflection is

$$\tau_r = 0 \quad \text{or} \quad \tau = \tau_i. \quad (7.52)$$

The values of p_i , τ_i , and q_i for small surface elements are given directly by eqns (4.25), (4.26), and (4.31), respectively. These equations provide p_i , τ_i , and q_i as functions of the angle θ between the unit normal vector to the surface and the direction of the freestream velocity U_∞ . The angle of incidence α of the element is equal to $\pi/2 - \theta$, and is the more appropriate angle for aerodynamic studies. The other parameters that are relevant to this study are the freestream density $\rho_\infty = n_\infty m$, the parameter $\beta_\infty = (2RT_\infty)^{-1/2}$ which is a function of the freestream temperature T_∞ , and the speed ratio of the freestream $s = U_\infty \beta_\infty$. Eqns (7.49)–(7.52) show that these results provide a complete solution for the specular reflection case.

In diffuse reflection, the molecules are bought to rest relative to the surface and are re-emitted with the equilibrium distribution corresponding to a temperature T_r . The quantities p_r and q_r are therefore given by the flux equations for a stationary gas. From eqn (4.25)

$$p_r = \frac{n_r m}{4\beta_r^2} \quad (7.53)$$

and, from eqn (4.32),

$$q_r = \left(\frac{\gamma+1}{\gamma-1} \right) \frac{n_r m}{8\pi^{1/2}\beta_r^3}. \quad (7.54)$$

The parameter n_r may be regarded as the number density of a fictitious gas

within the surface that is effusing across the surface. The value of n_r is found in §7.1 from the condition, expressed in eqn (7.45), that the net number flux to the surface element is zero. From eqn (7.11)

$$n_r = n_\infty (T_\infty/T_r)^{1/2} [\exp(-s^2 \sin^2 \alpha) + \pi^{1/2} s \sin \alpha \{1 + \text{erf}(s \sin \alpha)\}]. \quad (7.55)$$

This fictitious internal number density should not be confused with the number density n_s of the gas just above the surface. Eqn (7.13) gives this as the sum of the fraction of the stream number density that is directed to the surface and the half of n_r that is directed away from the surface, i.e.

$$n_s = \frac{1}{2} [\{1 + \text{erf}(s \sin \alpha)\} n_\infty + n_r]. \quad (7.56)$$

The number flux to the surface may be written non-dimensionally as

$$\frac{\dot{N}_i}{n_\infty u_\infty} = \frac{1}{2\pi^{1/2} s} [\exp(-s^2 \sin^2 \alpha) + \pi^{1/2} s \sin \alpha \{1 + \text{erf}(s \sin \alpha)\}], \quad (7.57)$$

and this is illustrated in Fig. 7.6. When s is small in comparison with unity, the number flux ratio is large in comparison with unity. This is because there is a flux to the surface due to the thermal motion of the molecules even when the speed ratio is zero. The number flux is unity to the front of surfaces that are nearly normal to a stream with a high speed ratio. The flux to the rear of such surfaces is extremely small.

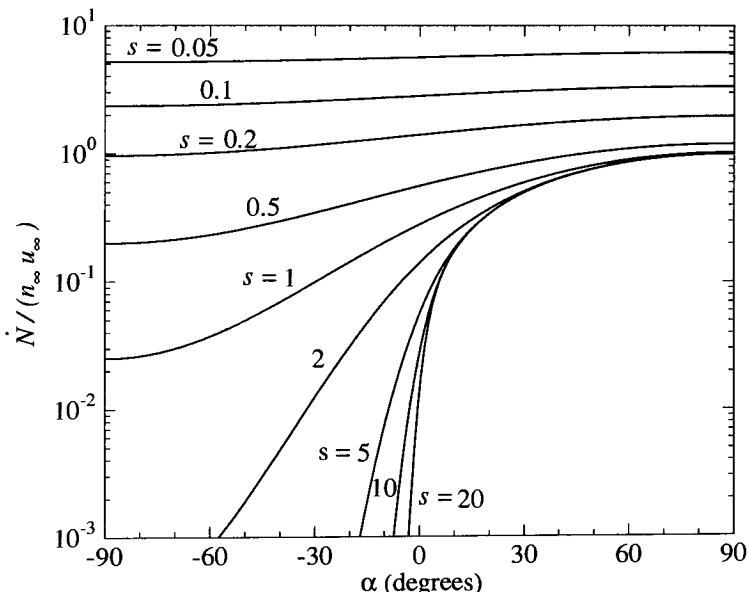


Fig. 7.6 The number flux to a surface element at incidence α .

If a fraction ϵ of the molecules is reflected specularly and the remaining fraction $1-\epsilon$ is reflected diffusely, the above results may be combined to obtain general expressions for the pressure, shear stress, and heat transfer. That for the pressure is

$$\begin{aligned} p/p_{\infty} = (2\beta_{\infty}^2 p/\rho_{\infty}) &= [(1+\epsilon)\pi^{-1/2}s \sin \alpha + \frac{1}{2}(1-\epsilon)(T_r/T_{\infty})^{1/2}] \\ &\times \exp(-s^2 \sin^2 \alpha) + [(1+\epsilon)(\frac{1}{2}+s^2 \sin^2 \alpha) \\ &+ \frac{1}{2}(1-\epsilon)(T_r/T_{\infty})^{-1/2}\pi^{1/2}s \sin \alpha][1 + \operatorname{erf}(ss \sin \alpha)]. \end{aligned} \quad (7.58)$$

The terms that include the temperature ratio are due to the diffusely reflected molecules. The specularly reflected molecules contribute the same pressure as that due to their incidence on the element. The *pressure coefficient* is related to this pressure ratio by

$$C_p = \frac{p - p_{\infty}}{\frac{1}{2}\rho_{\infty} U^2} = \frac{(p/p_{\infty}) - 1}{\frac{1}{2}\gamma(Ma)^2} = \frac{(p/p_{\infty}) - 1}{s^2}, \quad (7.59)$$

where the *Mach number* (Ma) is the ratio of the stream speed to the speed of sound. The pressure coefficients can be large in comparison with unity at small speed ratios because the pressure perturbations in collisionless flows are directly proportional to the speed ratio, rather than to the square of the speed ratio as in continuum flows. It is desirable to avoid negative coefficients and, for collisionless flows, it is preferable to define a modified pressure coefficient as

$$C_p' = \frac{p/p_{\infty}}{s^2}. \quad (7.60)$$

The collisionless pressure is best illustrated by separate plots for the modified pressure coefficients (C_p')_i due to the incident molecules and (C_p')_r due to the reflected molecules. These are shown in Figs 7.7 and 7.8, respectively. The reflected molecule results are for diffuse reflection and the modified pressure coefficient is multiplied by the square root of the ratio of the freestream to the reflected gas temperature. The pressure coefficient due to the incident molecules on a near normal surface in a flow with a very high speed ratio is 2. The pressure due to the reflected molecules is relatively small in high-speed flows unless the surface temperature is very large in comparison with the temperature of the undisturbed freestream. The pressure on surfaces at negative incidences is very small unless the speed ratio is of order unity or less. For fully specular reflection, the pressure due to the reflected molecules would be exactly equal to that due to the incident molecules. The general result for the shear stress is

$$\begin{aligned} \tau/p_{\infty} = (2\beta_{\infty}^2 p)/\rho_{\infty} &= \pi^{-1/2}(1-\epsilon)s \cos \alpha [\exp(-s^2 \sin^2 \alpha) \\ &+ \pi^{1/2}s \sin \alpha \{1 + \operatorname{erf}(ss \sin \alpha)\}]. \end{aligned} \quad (7.61)$$

The *local skin friction coefficient* is defined by

$$c_f = \frac{\tau}{\frac{1}{2}\rho_{\infty} U_{\infty}^2} = \frac{\tau/p_{\infty}}{\frac{1}{2}\gamma(Ma)^2} = \frac{\tau/p_{\infty}}{s^2}. \quad (7.62)$$

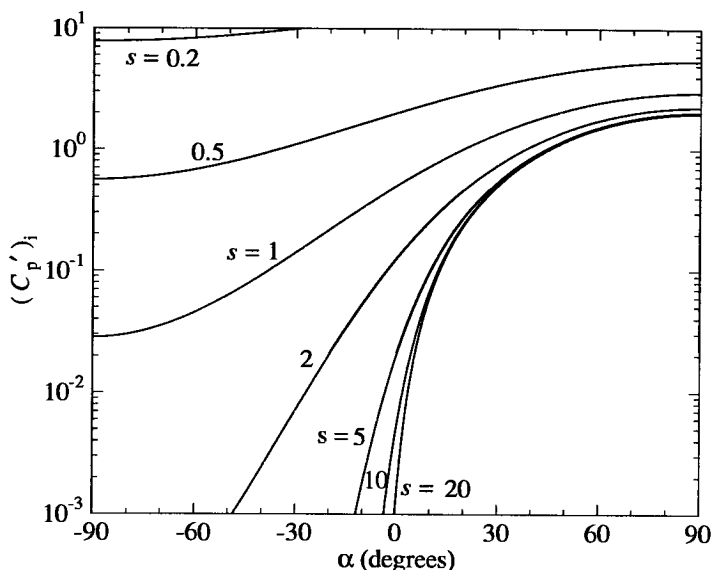


Fig. 7.7 Modified pressure coefficient due to the incident molecules.

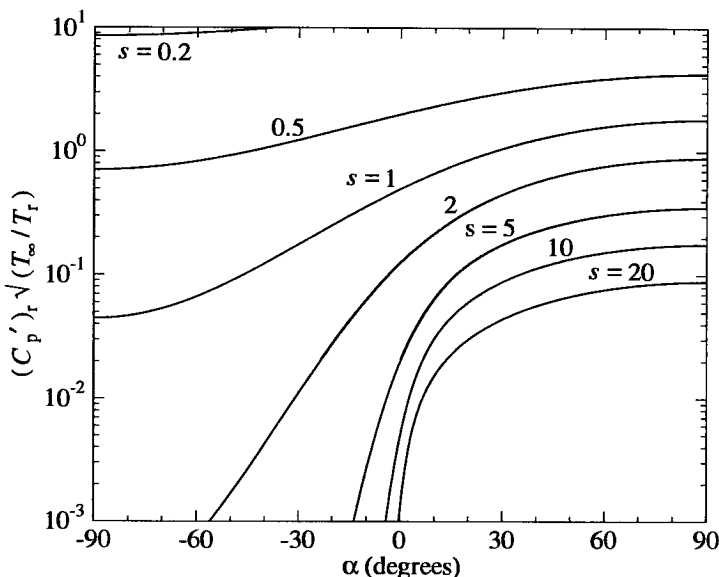


Fig. 7.8 Modified pressure coefficient due to the reflected molecules.

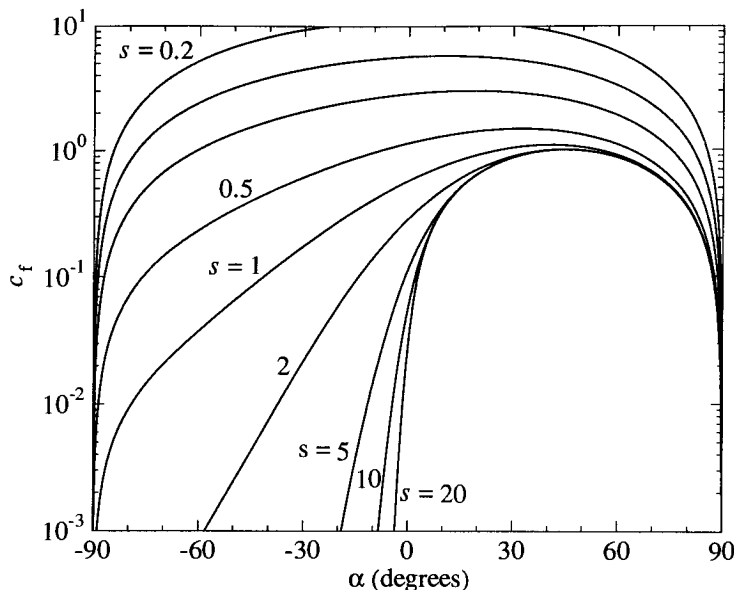


Fig. 7.9 The local skin friction coefficient on a surface element.

The overall shear stress is zero for fully specular reflection and is entirely due to the incident molecules when the reflection is fully diffuse. Figure 7.9 shows that the maximum skin friction coefficient occurs at zero incidence when the speed ratio is extremely small, but is near 45° at very high speed ratios.

The general result for the heat transfer to the surface is

$$2\beta_{\infty}^3 q/\rho_{\infty} = (1-\varepsilon)/(2\pi^{1/2}) \left[[s^2 + \gamma/(\gamma-1) - \{1/2(\gamma+1)/(\gamma-1)\}(T_r/T_{\infty})] \right. \\ \times [\exp(-s^2 \sin^2 \alpha) + \pi^{1/2} s \sin \alpha \{1 + \text{erf}(s \sin \alpha)\}] \\ \left. - \frac{1}{2} \exp(-s^2 \sin^2 \alpha)\right], \quad (7.63)$$

and a *heat transfer coefficient* may be defined by

$$C_h = \frac{q}{\frac{1}{2}\rho_{\infty} U^3} = \frac{2\beta_{\infty}^3 q/\rho_{\infty}}{s^3}. \quad (7.64)$$

The term that includes the temperature ratio represents the heat that is carried away by the diffusely reflected molecules. Figures 7.10 and 7.11 illustrate the heat transfer, for $\gamma = 5/3$, through the separate contributions from the incident and reflected molecules. The incident contribution applies also to any fraction of specularly reflected molecules, but this fraction would make a zero contribution to the net heat transfer. For high-speed flows, it can be seen that the reflected heat transfer can equal the incident heat transfer only if the temperature ratio is approximately s^2 .

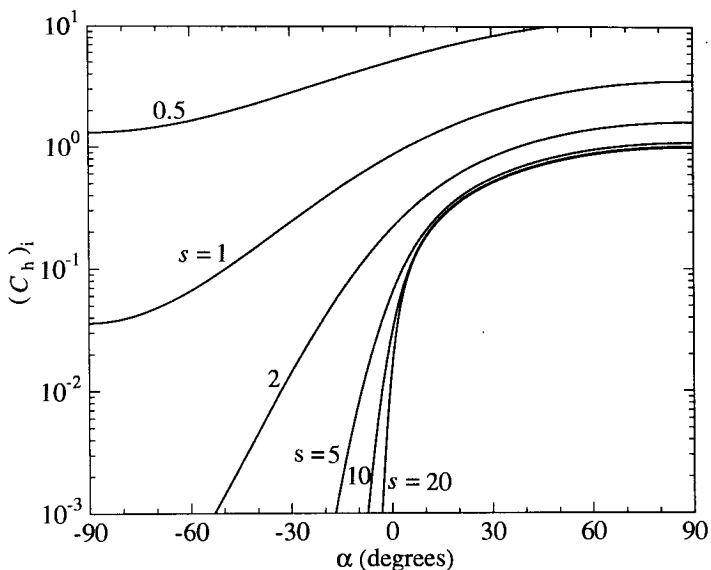


Fig. 7.10 Heat transfer coefficient due to the incident molecules.

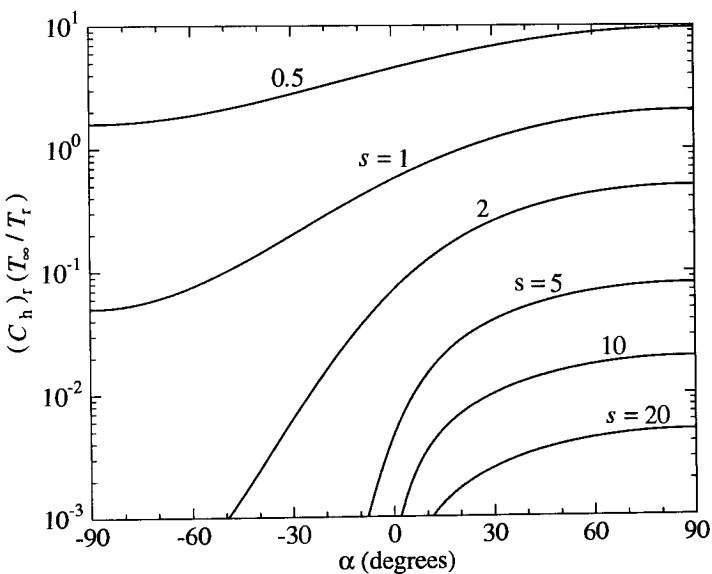


Fig. 7.11 Heat transfer coefficient due to the reflected molecules.

Note that, with the sign convention that has been used in this chapter, the energy accommodation coefficient of eqn (5.54) becomes

$$\alpha_c = \frac{q_i + q_r}{q_i + q_w} = \frac{q}{q_i + q_w}.$$

Therefore, the reflected gas temperature T_r may be replaced by the surface temperature T_w in eqn (7.63) if the right-hand side is multiplied by the accommodation coefficient α_c . For complete thermal accommodation, T_r may be replaced by T_w in all the equations.

The 'adiabatic surface temperature' T_a of an insulated surface element at which $q=0$ then follows from eqn (7.63) as,

$$\frac{T_a}{T_\infty} = \frac{2(\gamma-1)}{\gamma+1} \left(\frac{\gamma}{\gamma-1} + s^2 - \frac{\frac{1}{2} \exp(-s^2 \sin^2 \alpha)}{\exp(-s^2 \sin^2 \alpha) + \pi^{1/2} s \sin \alpha \{1 + \operatorname{erf}(s \sin \alpha)\}} \right). \quad (7.65)$$

It is instructive to compare the temperature T_a with the continuum stagnation temperature T_0 which is defined by

$$\frac{T_0}{T_\infty} = 1 + \frac{\gamma-1}{2} (Ma)^2 = 1 + \frac{\gamma-1}{\gamma} s^2. \quad (7.66)$$

It can be seen from eqns (7.65) and (7.66) that, for surfaces at positive incidence in a high speed ratio flow, the ratio of the collisionless adiabatic temperature to the continuum stagnation temperature tends to $2\gamma/(\gamma+1)$. This ratio is $5/4$ for a monatomic gas, $7/6$ for a diatomic gas, and so on. The general behaviour of this temperature ratio is shown in Fig. 7.12. The ratio falls below unity for surfaces at negative incidence and actually tends to zero at the rear of a vertical plate in a hypersonic flow. This is because the molecules that reach such a surface have a very small velocity relative to the surface. However, the number flux under these conditions is so minute that the result has little significance.

The above equations may be applied directly to determine the aerodynamic forces on a thin flat plate at incidence α in a stream of speed ratio s . The equations apply to the lower surface for positive values of α and to the upper surface for negative values of α . The upper surface pressure may be subtracted from the lower surface pressure to obtain the net force per unit area, and the normal force coefficient can be written from eqn (7.58) as

$$C_N = [2(1+\varepsilon)\pi^{-1/2} s \sin \alpha \exp(-s^2 \sin^2 \alpha) + (1-\varepsilon)(T_r/T_\infty)^{1/2} \pi^{1/2} s \sin \alpha + (1+\varepsilon)(1+2s^2 \sin^2 \alpha) \operatorname{erf}(s \sin \alpha)]/s^2. \quad (7.67)$$

The parallel force coefficient can be obtained similarly from the shear stress eqn (7.61) as

$$C_P = 2(1-\varepsilon)\pi^{-1/2} s \cos \alpha \{ \exp(-s^2 \sin^2 \alpha) + \pi^{1/2} s \sin \alpha \operatorname{erf}(s \sin \alpha) \}/s^2. \quad (7.68)$$

The normal and parallel force coefficients may now be resolved into the directions normal to and parallel to the stream direction in order to obtain the lift and drag coefficients for the flat plate. The reference area is again based on the planform area, and the results are

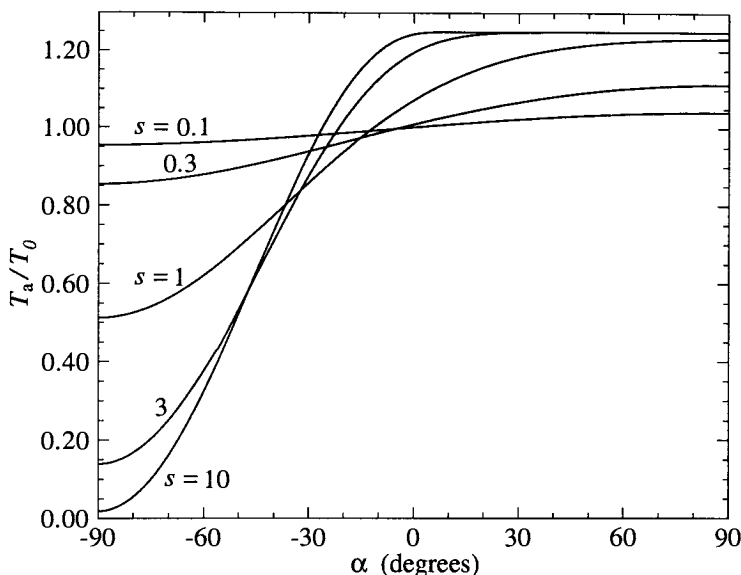


Fig. 7.12 The ratio of the collisionless adiabatic surface temperature to the continuum stagnation temperature in a monatomic gas.

$$C_L = \frac{4\epsilon}{\pi^{1/2}s} \sin\alpha \cos\alpha \exp(-s^2 \sin^2\alpha) + \frac{\cos\alpha}{s^2} [1 + \epsilon(1 + 4s^2 \sin^2\alpha)] \\ \times \operatorname{erf}(s \sin\alpha) + \frac{(1-\epsilon)}{s} \pi^{1/2} \sin\alpha \cos\alpha \left(\frac{T_r}{T_\infty}\right)^{1/2} \quad (7.69)$$

and

$$C_D = 2 \frac{\{1 - \epsilon \cos(2\alpha)\}}{\pi^{1/2}s} \exp(-s^2 \sin^2\alpha) \\ + \frac{\sin\alpha}{s^2} [1 + 2s^2 + \epsilon\{1 - 2s^2 \cos(2\alpha)\}] \operatorname{erf}(s \sin\alpha) \\ + \frac{(1-\epsilon)}{s} \pi^{1/2} \sin^2\alpha \left(\frac{T_r}{T_\infty}\right)^{1/2}. \quad (7.70)$$

The lift coefficient and lift-drag ratio of a flat plate at a speed ratio of 10 and with the surface temperature equal to the freestream temperature are shown in Figs 7.13 and 7.14, respectively. These conditions are representative of orbital conditions, and show that lifting performance in free-molecule flow is poor for fully diffuse flow. Good lifting performance requires the assumption of an unrealistic degree of specular reflection. Lifting performance is slightly better at lower speed ratios.

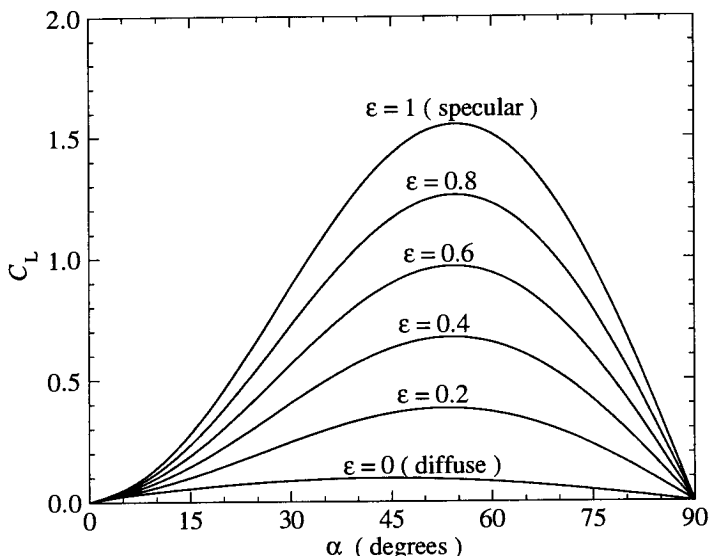


Fig. 7.13 Lift of a flat plate at $s = 10$ and $T_r = T_\infty$.

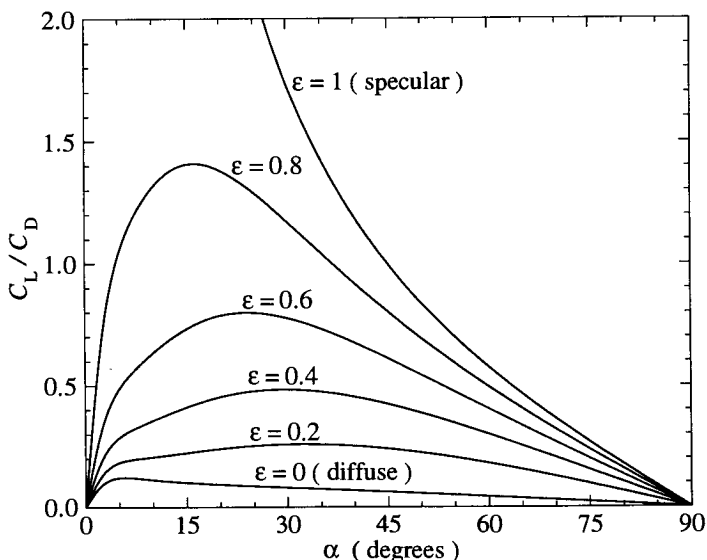


Fig. 7.14 Lift-drag ratio of a flat plate at $s = 10$ and $T_r = T_\infty$.

For bodies other than flat plates, eqns (7.58), (7.61), and (7.63) must be integrated over the surface. This has been done for many simple geometries and a list of the then available solutions was given by Schaaf and Chambre (1961). The chances of obtaining a closed form analytical solution depend on the geometrical complexity of the problem.

The procedure may be illustrated through the calculation of the drag coefficient of a sphere of radius r . Polar coordinates are chosen such that the pole points in the opposite direction to the stream. The polar angle θ is then identical to the angle θ in the flux equations of §4.2 and, in terms of the angle of incidence α that has been used in this section, it is equal to $\pi/2 - \alpha$. The drag coefficient based on the frontal area of the sphere is

$$C_D = \frac{D}{\frac{1}{2}\rho_\infty U^2 \pi r^2} = \frac{\int_0^\pi (p \cos \theta + \tau \sin \theta) 2\pi r^2 \sin \theta d\theta}{\frac{1}{2}\rho_\infty U^2 \pi r^2}.$$

Eqn (7.58) for the pressure and eqn (7.61) for the shear stress may be substituted into this equation and the integral evaluated to give,

$$C_D = \frac{2s^2 + 1}{\pi^{1/2} s^3} \exp(-s^2) + \frac{4s^4 + 4s^2 - 1}{2s^4} \operatorname{erf}(s) + \frac{2(1-\varepsilon)\pi^{1/2}}{3s} \left(\frac{T_w}{T_\infty}\right)^{1/2}. \quad (7.71)$$

A remarkable feature of eqn (7.71) is that the fraction of specular reflection disappears from all terms except the term including the temperature ratio that is due to the reflected molecules. Therefore, for a cold sphere, the drag coefficient is the same for both diffuse and specular reflection, with the common value tending to two as the speed ratio becomes large. This is an accident of geometry in that the high pressure near the stagnation point under specular conditions is matched by the high shear stress near the maximum radius under diffuse conditions. This result should not be interpreted as meaning that the drag coefficient of a sphere is independent of the gas-surface interaction model. It was pointed out in §5.6 that a combination of specular and diffuse reflection is only an approximation to the real scattering law, and some models lead to a limiting drag coefficient quite different from two.

The drag of some shapes can be highly dependent on the model for the gas-surface interaction. For example, eqn (7.70) shows that the drag coefficient of a cold vertical flat plate at a high speed ratio is

$$C_D = 2 + 2\varepsilon. \quad (7.72)$$

The factor of two difference between the diffuse and specular limits occurs in this case because there is no contribution from the shear stress, the drag being due entirely to the pressure. For a flat plate at zero incidence, there is a finite drag due to the shear stress in the diffuse reflection case, but the drag is zero for the unrealistic case of completely specular reflection.

In the case of a gas mixture, all of the above equations may be applied separately to each molecular species, and the results may then be superimposed.

7.6 Thermophoresis

A thermal force acts on a small suspended particle in a gas with a temperature gradient, even though the temperature of the particle may be uniform and equal to the local gas temperature. The force is essentially due to the asymmetry of the Chapman–Enskog distribution function and the phenomenon is called *thermophoresis*. At sufficiently low densities or for sufficiently small particles, intermolecular collisions may be neglected and the magnitude of the effect is predicted by a free-molecule analysis. In addition to the non-equilibrium boundary conditions, this example differs from the earlier collisionless flows in that the corresponding continuum flow is not well defined.

Consider a spherical particle of radius r and, as shown in Fig. 7.15, take the origin at the centre of the sphere and choose the x -axis in the direction of the temperature gradient. The first approximation to the Chapman–Enskog distribution is then given by eqn (3.85) as

$$f = f_0 \left\{ 1 - \frac{4}{5} \frac{\beta^2 K}{RT} \left(\beta^2 c^2 - \frac{5}{2} \right) u \frac{d T}{d x} \right\}. \quad (7.73)$$

Now consider the small surface element at point P on the sphere defined by the polar angle θ and azimuth angle ϕ . Axes x' , y' , z' are taken with x' normal to and directed towards the surface element and y' along the line of intersection of the plane defined by OPx and the plane of the surface element. Eqns (1.18) and (3.3) may then be applied in the x' , y' , z' frame of reference, with f from eqn (7.73), to give the flux of the quantity Q to the surface element as

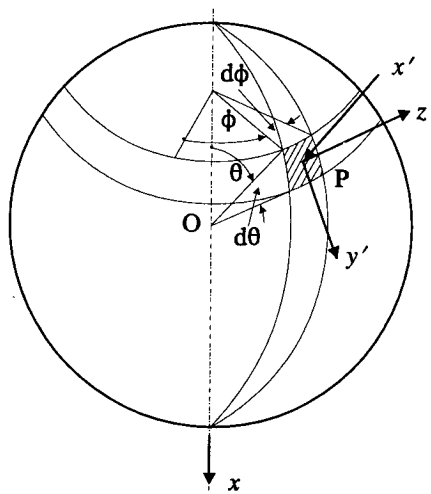


Fig. 7.15 Coordinate system for the analysis of the thermophoretic force on a sphere.

$$\frac{n\beta^3}{\pi^{3/2}} \int_{-\infty}^{\infty} \int_0^{\infty} \int_0^{\infty} Q U \exp(-\beta^2(U^2 + V^2 + W^2)) \\ \times \left\{ 1 - \frac{4}{5} \frac{\beta^2 K}{\rho R T} \left(\beta^2(U^2 + V^2 + W^2) - \frac{5}{2} \right) (U \cos \theta + V \sin \theta) \frac{dT}{dx} \right\} dU dV dW,$$

where U , V , and W are the velocity components in the x' , y' , and z' directions, respectively. By putting $Q = mU$ and $Q = mV$ we obtain, respectively, the pressure p_i and shear stress τ_i due to the impact of the incident molecules. The results are

$$p_i = \frac{\rho}{4\beta^2} - \frac{2\beta K}{5\pi^{1/2}} \cos \theta \frac{dT}{dx}, \quad (7.74)$$

and

$$\tau_i = \frac{\beta K}{5\pi^{1/2}} \sin \theta \frac{dT}{dx}. \quad (7.75)$$

A term, such as the first one on the right-hand side of eqn (7.74), that is uniform around the sphere obviously makes no contribution to the net force on the sphere. A property of the Chapman-Enskog distribution is that the number flux is isotropic so that, if the surface temperature is uniform, the force exerted by diffusely reflected molecules is also uniform and makes no net contribution to the force. The pressure due to the specularly reflected molecules is equal to p_i . The shear stress due to diffusely reflected molecules is zero and that due to any specularly reflected molecules is equal to $-\tau_i$. The net force is therefore given by

$$F = -\frac{\beta K}{5\pi^{1/2}} \frac{dT}{dx} \int_0^{\pi} \{2(1+\varepsilon)\cos^2 \theta + (1-\varepsilon)\sin^2 \theta\} 2\pi r^2 \sin \theta d\theta,$$

where ε is the fraction of specularly reflected molecules. Therefore,

$$F = -\frac{16\pi^{1/2}}{15} \beta r^2 K \frac{dT}{dx}. \quad (7.76)$$

This result was first obtained by Waldmann (1959). Note that the disappearance of the fraction ε of specular reflection from the final result is due to the spherical geometry and would not occur for particles which have a different shape. This case with a uniform temperature over the surface is appropriate to a particle with a very high thermal conductivity. A temperature gradient would be induced in a particle that has a low thermal conductivity, and this would increase the force. A force due to the unbalance in the pressure due to diffusely reflected molecules acts on any particle that has a non-uniform temperature, even if the surrounding gas has a uniform temperature. The non-uniform surface temperature is most commonly caused by thermal radiation, and the phenomenon in an equilibrium background gas is called *photophoresis*.

7.7 Flows with multiple reflection

The analysis of collisionless flows becomes much more difficult if the molecules that are reflected from a surface may re-impinge on the surface instead of escaping completely. Flows that involve multiple interactions have practical application to internal flows and also to external flows past bodies of complex geometry.

Consider a surface exposed to a gas under free-molecule conditions. The number of molecules incident per unit time on a surface element dS at the location S directly from the external gas may be denoted by $\dot{N}_1(S)dS$. Now let $P(S', S)$ be the probability that a molecule reflected from an element dS' at location S' strikes location S . The number of molecules per second which strikes dS as their second collision with the surface is, therefore,

$$\dot{N}_2(S)dS = \int_S P(S', S) \dot{N}_1(S') dS' dS.$$

Similarly, the number striking dS as their third collision is

$$\dot{N}_3(S)dS = \int_S P(S', S) \dot{N}_2(S') dS' dS.$$

Therefore, if $\dot{N}(S)$ is the total number flux at location S ,

$$\begin{aligned} \dot{N}(S) &= \dot{N}_1(S) + \dot{N}_2(S) + \dot{N}_3(S) + \dots \\ &= \dot{N}_1(S) + \int_S P(S', S) \{\dot{N}_1(S') + \dot{N}_2(S') + \dot{N}_3(S') + \dots\} dS', \end{aligned}$$

or

$$\dot{N}(S) = \dot{N}_1(S) + \int_S P(S', S) \dot{N}(S') dS'. \quad (7.77)$$

This is a Fredholm integral equation of the second kind and its solution must form part of the analysis of collisionless flows that involve multiple reflections.

As an example, consider the free-molecular flow through a circular tube of length b and radius r . The centreline of the tube lies along the x -axis and the origin is at the entrance to the tube. The molecules that pass through the tube will be made up of those that pass directly through it without any collision with the inside surface, plus a fraction of those emitted from each element of the inside surface. The total flux \dot{N}_t through the tube may therefore be written

$$\dot{N}_t = \dot{N}_d + \int_0^b \dot{N}(x) P_e(x) dx, \quad (7.78)$$

where \dot{N}_d is the direct number flux, $P_e(x)$ is the probability that a molecule reflected from the element of length dx at x passes through the tube, and $\dot{N}(x)$ follows from the axially symmetric version of eqn (7.77), i.e.

$$\dot{N}(x) = \dot{N}_1(x) + \int_0^b P(x', x) \dot{N}(x') dx'. \quad (7.79)$$

Solutions of this problem were first obtained by Clausing (1932) and have been discussed in detail by Patterson (1971). The functions \dot{N}_d , $P_e(x)$, $\dot{N}_1(x)$, and $P(x', x)$ may be found for this simple geometry by straightforward but tedious analysis. However, the solution of the integral equation for $\dot{N}(x)$ must be carried out numerically. The final integration of eqn (7.78) requires the assumption that $\dot{N}(x)$ is a linear function of x , with the coefficients provided by the numerical solution of eqn (7.79).

The above problem is of comparatively simple geometry and the predominantly analytical approach through the integral equation becomes quite unworkable for more complex problems. On the other hand, this class of problem is ideally suited to a probabilistic numerical method called the *test-particle Monte Carlo method* (Davis 1960). A digital computer is used to calculate a very large number of typical molecular trajectories, and these collectively predict the behaviour of the real system. Since intermolecular collisions may be neglected, these trajectories are independent of one-another and they may be generated serially. The method will now be illustrated through its application to the circular tube flux problem to calculate the numbers N_t and N_d that are associated with the fluxes.

The flow chart for the simulation program is shown in Fig. 7.16. The additional notation that is used in this chart is as follows: $L = b/r$ is the length-radius ratio of the tube, N_e is the total number of test particles that enter the tube, r_1 is the initial radius of the particle at $x=0$, l_1 , m_1 , and n_1 are the direction cosines of the initial trajectory with the x -, y -, and z -axes, x_c is the x -coordinate of the intersection point either with the inside of the cylinder or its imaginary projections outside $x=0$ to b , and l_c , m_c , and n_c are the direction cosines of the particle trajectory after diffuse reflection from the inside surface of the cylinder.

The distribution function for the initial radius is one of those dealt with in Appendix C, and the required expression follows directly from eqn (C6) as

$$r_1 = (R_f)^{1/2} r. \quad (7.80)$$

This chooses the initial radii at random from a uniform distribution over the entry plane. However, the number of trajectories is extremely small in comparison with the number of molecules that would be expected to enter the tube in a real gas, and the variance due to the scatter in the initial state may be avoided by setting a uniform distribution. The equation for the initial radius of the N th trajectory is then

$$r_1 = \{(N - 0.5)/N_1\}^{1/2} r. \quad (7.81)$$

The number flux of molecules effusing across the entry plane of the tube is given by eqn (4.20) with $Q = 1$. The external gas is in equilibrium and the distribution function may be put into the polar coordinate form of eqn (4.4)

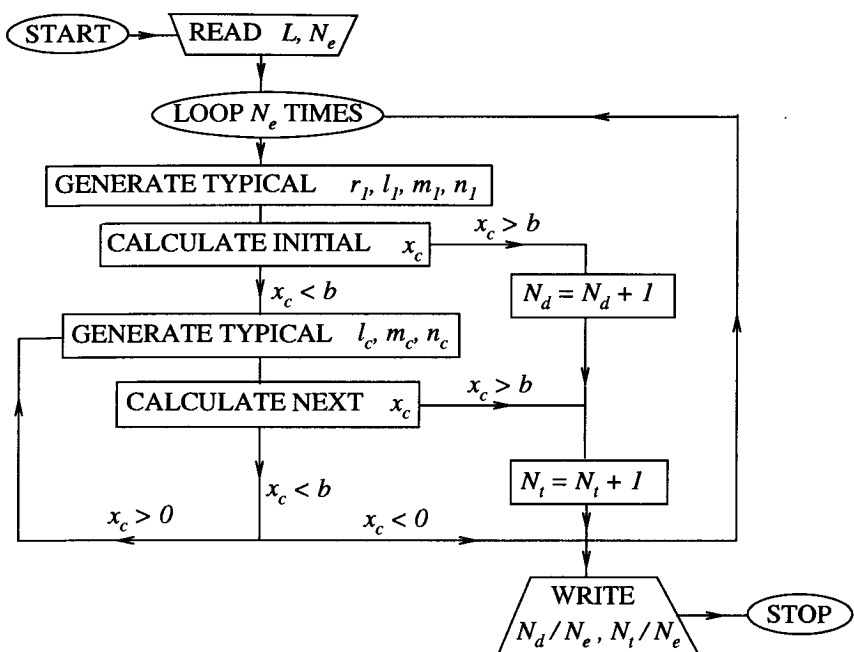


Fig. 7.16 Flow chart of the test-particle Monte Carlo program for the cylindrical tube flux program.

with the polar direction along the axis of the tube. The u velocity component may then be written $c' \cos \theta$ and the number flux of molecules is

$$\dot{N}_i = \frac{n \beta^3}{\pi^{3/2}} \int_0^{\infty} \int_0^{2\pi} \int_{-\pi/2}^{\pi/2} c'^3 \exp(\beta^2 c'^2) \sin \theta \cos \theta d\theta d\phi d\mathbf{c}' . \quad (7.82)$$

The probability that a molecule passes through the tube depends on its initial direction at the entry plane and on the direction in which it is reflected at any intersections with the inside of the tube. In particular, this probability is independent of the molecular speed c' and there is no need to consider the distribution of this quantity.

The azimuth angle ϕ is uniformly distributed between 0 and 2π and a typical value is, from eqn (C5),

$$\phi = 2\pi R_f . \quad (7.83)$$

The distribution of the polar angle θ is best dealt with through the distribution of $\cos \theta$ because

$$\sin \theta \cos \theta d\theta = \cos \theta d(\cos \theta) .$$

The distribution function for $\cos \theta$ is therefore identical with that for the radius r which led, through eqn (C6), to eqn (7.79). The limits on $\cos \theta$ are from 0 to 1 and we can write

$$\cos\theta = (R_f)^{1/2}. \quad (7.84)$$

The direction cosines l_1 , m_1 , and n_1 are given by

$$l_1 = \cos\theta,$$

$$m_1 = \sin\theta \cos\phi,$$

and

$$n_1 = \sin\theta \sin\phi. \quad (7.85)$$

The x -coordinate of the intersection of the particle trajectory with the cylinder, or its projections outside $x=0$ to b , is readily obtained from elementary three-dimensional coordinate geometry. A general theorem with wide application to simulation studies is that the intersection of the line

$$x = x_i + l_1 s$$

$$y = y_i + m_1 s \quad (7.86)$$

$$z = z_i + n_1 s$$

and the quadric surface

$$f(x, y, z) \equiv a_{11}x^2 + a_{22}y^2 + a_{33}z^2 + 2a_{23}yz + 2a_{31}zx + 2a_{12}xy + 2a_{14}x + 2a_{24}y + 2a_{34}z + a_{44} = 0 \quad (7.87)$$

is given by the roots of

$$A_1 s^2 + 2A_2 s + A_3 = 0, \quad (7.88)$$

where

$$A_1 = a_{11}l_1^2 + a_{22}m_1^2 + a_{33}n_1^2 + 2a_{23}m_1n_1 + 2a_{31}n_1l_1 + 2a_{12}l_1m_1,$$

$$A_2 = l_1(a_{11}x_i + a_{12}y_i + a_{13}z_i + a_{14}) + m_1(a_{21}x_i + a_{22}y_i + a_{23}z_i + a_{24}) + n_1(a_{31}x_i + a_{32}y_i + a_{33}z_i + a_{34}),$$

and

$$A_3 = f(x_i, y_i, z_i).$$

Real roots of eqn (7.88) may be substituted into eqn (7.86) to determine the points of intersection. Since the present case is axially symmetric, we may choose $y_i = -r_1$ and $z_i = 0$. The coefficients a_{22} and a_{33} are equal to unity, $a_{44} = -r^2$, and all the other coefficients are zero. Eqns (7.86)–(7.88) then give the following equation for the x -coordinate of the intersection of the particle trajectory with the cylinder

$$x_c = l_1[r_1m_1 + \{r^2(m_1^2 + n_1^2) - r_1^2n_1^2\}^{1/2}] / (m_1^2 + n_1^2). \quad (7.89)$$

Because of the axial symmetry, the y -and z -coordinates of the point of intersection may be set to $-r$ and 0, respectively. If the point of intersection lies within the cylinder, the assumption of diffuse reflection means that the selection of the direction cosines l_c , m_c , and n_c is similar to the above selection of m_1 , l_1 , and n_1 , respectively. Note that the flux direction is now along the y -, rather than the x -, axis. The x -coordinate of the subsequent point of intersection with the cylinder is, again using eqns (7.86)–(7.89),

$$x = x - c + 2l_c r m_c / (m_c^2 + n_c^2). \quad (7.90)$$

This value of x becomes the next value of x_c .

A FORTRAN 77 implementation of this method is listed in Appendix D. This is a very simple program that contains only about 30 executable statements. The value of the ratio N_t/N_e that was calculated by Clausing (1932) for $L = 1$ was 0.672. A personal computer with a 33 MHz i486 CPU calculates 10,000 trajectories per second for this case. The results from 10^7 typical trajectories were $N_t/N_e = 0.6720$, while $N_d/N_e = 0.3820$. The expected statistical scatter for a sample of 10^7 is much less than one part in 1000, so that this level of agreement is to be expected. The scatter is more clearly demonstrated by calculating the 10^7 trajectories as 10,000 runs, each with a sample of 1000. The results are shown in Fig. 7.17.

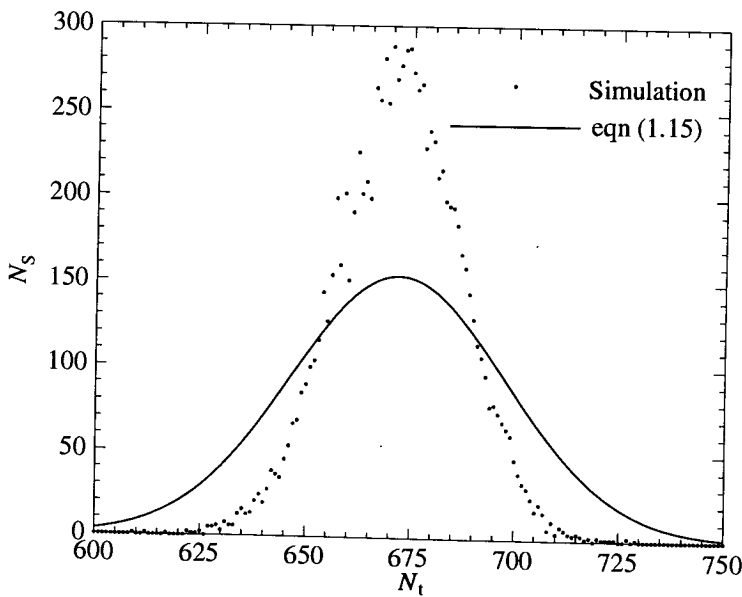


Fig. 7.17 A comparison of the scatter associated with 10,000 separate Monte Carlo simulations with the normal distribution of eqn (1.15).

Simulations

N_S is the number of trajectories that have a particular value of N_t . The calculated distribution is compared with the normal distribution that is defined by eqn (1.15). For a total sample of 1000, the normally distributed value of N_S may be written as a function of N_t , i.e.

$$N_S = 10000(2\pi\bar{N}_t)^{-\frac{1}{2}} \exp\{-(N_t - \bar{N}_t)^2/(2\bar{N}_t)\}, \quad (7.91)$$

where the mean value \bar{N}_t is here equal to 672. This has a standard deviation equal to the square root of the mean value, or approximately 26. The actual scatter is less than that predicted by the normal distribution, and almost all the results lie within 26 of the mean value. If the results are fitted to a normal distribution, the actual standard deviation is approximately 14. A useful way of estimating the expected magnitude of the scatter is to divide the result by the square root of the sample size. For this case, the estimate of the standard deviation is approximately 21.

As noted earlier, the number of molecules that are involved in a real flow is generally many orders of magnitude larger than the sample size in the simulation, and it is desirable to minimize the scatter. The scatter in the initial radius of the molecule at the entry plane may be reduced by using eqn (7.81), but this leads to an almost imperceptible reduction in the scatter. However, the direction cosines of the entry molecules may also

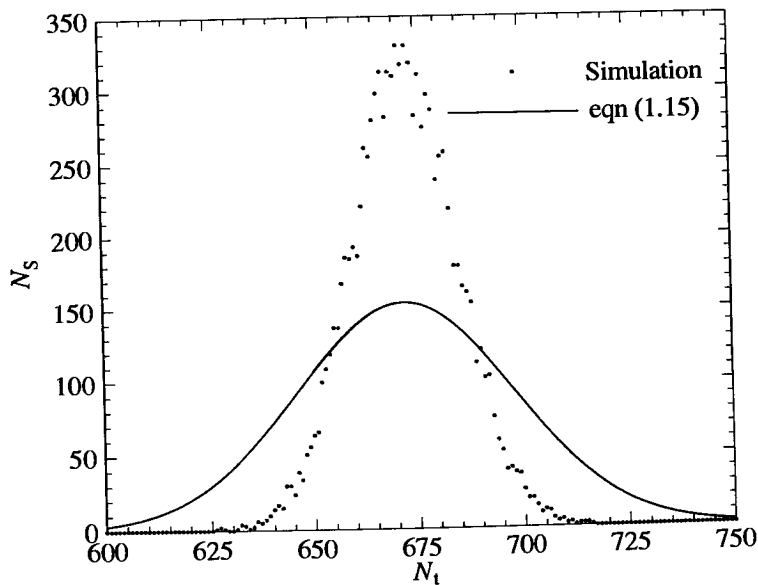


Fig. 7.18 Similar to Fig. 7.17, but with variance reduction applied to the initial values.

be distributed more uniformly. The program requires three random fractions while setting the initial conditions of each trajectory, so that the initial distribution is three-dimensional. The loop of N over NTR in program FMF (Appendix D) may be replaced by three nested loops of $N1$, $N2$, and $N3$ over the cube root of NTR , say NTC . The first random fraction can be replaced, for the $N1$ th trajectory, by

$$(N1 - R_f)/NTC, \quad (7.92)$$

with similar expressions involving $N2$ and $N3$ for the other random fractions. This ensures that the initial states of the trajectories are distributed more uniformly over the three-dimensional space. This is a form of *variance reduction* and the resulting scatter is shown in Fig. 7.18. The standard deviation of a normal distribution fitted to the actual scatter is approximately 12. The scatter is inversely proportional to the square root of the sample size, so that a similar reduction in the scatter could be obtained by an increase in the sample of one third. If the molecular speed had been required for the simulation, the initial distribution would have been four-dimensional, and the variance reduction procedure would be barely practical for a sample of 1000 in each run.

Similar agreement with the (largely) analytical solution of Clausing has been obtained for other values of the length-radius ratio. The implementation of the test-particle Monte Carlo method is much easier than the implementation of the more analytical method based on the Fredholm integral equation. The cost of the computation of 10^7 or 10^8 trajectories is negligible, so that four figure accuracy is readily obtained with the Monte Carlo method. However, the major advantage of the Monte Carlo method is the ease with which it is able to deal with more complex flow geometries. Changes that would make the integral equation approach quite impractical can generally be made through alterations to several statements in the simulation program. A number of configurations of engineering interest were dealt with by Davis (1961).

The above example required only the determination of the ratio of the exit to the entry number fluxes. When applying the Monte Carlo approach to problems such as the determination of the drag coefficient of complex shapes, it becomes necessary to relate the momentum transfer to the gas density. The simplest procedure for steady flows is to assume that each simulated trajectory represents a much larger number of real trajectories such that the computed trajectories represent those occurring in the real gas over unit time. The sum of the momentum and energy transfer over all trajectories then gives the momentum and energy fluxes, and the pressure, shear stress, and heat transfer follow.

The test-particle Monte Carlo method is not suited to the computation of unsteady flows. For these it is preferable to adopt a collisionless version of the direct simulation Monte Carlo (or DSMC) method that is described in Chapter 10. In this method, a large number of trajectories are computed simultaneously, and there is a computational time parameter that corresponds to physical time in the real gas.

References

- CLAUSING, P. (1932). *Annln. Phys.* **12**, 961.
- DAVIS, D.H. (1961). Monte Carlo calculation of molecular flow rates through a cylindrical elbow and pipes of other shapes. *J. Appl. Phys.* **31**, 1169-1176.
- LIEPMANN, H.W. (1961). Gaskinetics and gasdynamics of orifice flow. *J. Fluid Mech.* **10**, 65-79.
- NARASIMHA, R. (1962). Collisionless expansion of gases into vacuum. *J. Fluid Mech.* **12**, 294-308.
- PATTERSON, G.N. (1971). *Introduction to the kinetic theory of gas flows*, University of Toronto Press, Toronto.
- SCHAAF, S.A. and CHAMBRE, P.L. (1961). *Flow of rarefied gases*, Princeton University Press.
- WALDMANN, L.Z. (1959). *Z. Naturforsch.* **A14**, 589.

ANALYTICAL METHODS FOR TRANSITION REGIME FLOWS

8.1 Classification of methods

A *transition regime flow*[†] is defined here as one in which the mean free path is neither very small nor very large in comparison with a typical linear dimension of the flow. The mathematical difficulties associated with the full Boltzmann equation generally preclude direct approaches that would lead to exact closed-form solutions. Moreover, for flows that involve chemical reactions and thermal radiation, there is difficulty even in the formulation of a Boltzmann equation that includes these effects. This has meant that a large number of indirect approaches have been investigated, and many of the resulting methods involve a degree of approximation that would not be accepted for less difficult equations. It is therefore necessary to distinguish between and to assess the results from a wide variety of competing methods. The answers to the following questions assist with the evaluation process:

- 1 (i) Does the method depend on arbitrary assumptions about the functional form of certain parameters, or even on arbitrary modifications of the equations?
- 1 (ii) Does the method lead to expressions for the dependent variables, or does it merely transform the equations into forms that are claimed to be more amenable to solution (either analytical or numerical) than the original equations?
- 2 (iii) Is the method capable of handling all values of all parameters, or is it restricted to limiting cases in which one of the parameters is either very large or very small?
- 3 (iv) What is the degree of complexity in terms of real gas effects, boundary conditions, and number of flowfield dimensions that can be handled by the method?
- 4 (v) Does the method require an initial approximation to the complete flowfield and depend on the convergence of a subsequent iteration process?

[†] This should not be confused with the 'transition' between laminar and turbulent flow and, to avoid this possibility, some authors refer instead to 'transitional' regime flows.

When any degree of approximation is involved, careful comparisons must be made with the results from other analytical and numerical methods, and with experiment. This is particularly important when the answer to question (i) is affirmative. General conclusions should not be based on comparisons for a single case, or even for a single problem. Also, comparative tests should, as far as possible, be based on the full range of flow quantities over the complete flowfield, rather than on the variation of a single integrated quantity with Knudsen number. The fact that solutions are available for the two limiting cases of collisionless and continuum flows means that superficially good results may be obtained from physically unreal methods that happen to provide a fortuitously good curve fit between these known limits. Particular scrutiny should be given to solutions that are based on approximations which introduce adjustable parameters.

With reference to the second question, it should be noted that some analytical methods provide 'solutions' that may require extensive numerical work in order to produce a result for a specific flow. In some cases, this numerical effort may exceed that which would be required for a direct numerical solution of the problem. These methods should then be regarded as providing alternative and perhaps less exact formulations rather than solutions.

Problems which involve large disturbances are invariably non-linear and there is then no analytical method that does not incorporate assumptions or approximations. The small-perturbation approach may be based on the smallness of the Knudsen number or its reciprocal, in order to obtain approximate solutions for the near continuum and near collisionless regimes, respectively. Some methods may also require that the speed ratio be small or large, or that the flow disturbance itself be small. In particular, if the disturbance is sufficiently small that the velocity distribution function is perturbed only slightly from the equilibrium or Maxwellian form, the small-perturbation approach leads to the linearized Boltzmann equation. The theory of this equation has been dealt with in detail by Cercignani (1969, 1988). The small-perturbation solutions provide important reference values, especially when they are obtained without resort to arbitrary assumptions about parameters or modifications to the equations. However, solutions are available only for a restricted set of problems with comparatively simple boundary conditions. These have limited application to problems that are encountered in practice.

A number of methods depend on essentially arbitrary assumptions about the form of the velocity distribution function. Most of these can be classed as *moment methods* and are discussed in §8.2. The other area of major approximation is to alter the form of the Boltzmann equation itself. It is indicative of the difficulties that have been posed by the Boltzmann equation that such a radical approach was adopted by a sufficient number of workers for it to have gained a measure of respectability that lasted for a considerable period. This *model equation* approach is discussed in §8.3.

8.2 Moment methods

This approach employs the moment equations that are obtained by first multiplying the Boltzmann equation by a molecular quantity Q , and then integrating it over velocity space. The moment equation for Q was derived as eqn (3.27) in the form

$$\frac{\partial}{\partial t}(n \bar{Q}) + \nabla \cdot (n \bar{cQ}) - nF \cdot \overline{\frac{\partial Q}{\partial c}} = \Delta [Q]. \quad (8.1)$$

The macroscopic gas quantities were defined in §1.4 in terms of the averages of the microscopic molecular quantities Q . The substitution of the various values of Q into eqn (8.1) leads to a series of equations in the macroscopic quantities, as described in §3.3. However, the presence of $\bar{c}Q$ in the second term means that, as Q progresses to successively higher orders of c , each equation involves a moment of still higher order. We therefore have an infinite number of equations and moments. Eqn (3.3) enables a typical moment to be written

$$\bar{Q} = \int_{-\infty}^{\infty} Q f dc$$

and the basis of the moment method is that f is assumed to conform to some expression that contains a finite set of macroscopic quantities or moments. The equation based on the moment that is of the highest order in c contains an even higher order moment, but this can now be written in terms of the lower-order moments, thus closing the series of equations and forming a determinate set.

The Chapman-Enskog solution of the Boltzmann equation has already been discussed in §3.5. It is the second-order solution based on a series expansion of the velocity distribution function f . This series may be written schematically as

$$f = f_0 \{ 1 + a_1(Kn) + a_2(Kn)^2 + \dots \}, \quad (8.2)$$

where the coefficients a_n are functions of ρ , \mathbf{c}_0 , and T only. The Knudsen number is defined here as the ratio of the scale length of the flow gradients to the mean free path. The first-order[†] solution is the local equilibrium or Maxwellian distribution function f_0 , with the gas being fully described by ρ , \mathbf{c}_0 , and T . The viscous stress tensor τ and the heat flux vector q vanish in an equilibrium gas and the conservation equations (3.33)–(3.35) reduce to the Euler equations of inviscid fluid flow. The conservation equations are the five moment equations formed by setting Q equal to m , $m\mathbf{c}$, and $\frac{1}{2}mc^2$ and, since these quantities are conserved in collisions, the collision term $\Delta[Q]$ vanishes.

[†] As far as the powers of (Kn) are concerned, this is the zero-order solution. However, in §3.5, the ‘order’ of the solution was based on the number of terms in the series and this convention is continued here.

The second-order Chapman-Enskog solution leads to the velocity distribution function of eqn (3.80) which also involves only the moments ρ , c_0 , and T . This distribution function enables τ and q to be written as products of the coefficients μ and K with the velocity and temperature gradients, respectively, thus reducing the conservation equations to the Navier-Stokes equations of continuum gas dynamics.

The above considerations show that, from the kinetic theory point of view, both the Euler and Navier-Stokes equations may be regarded as 'five moment' solutions of the Boltzmann equation, the former being valid for the $(Kn) \rightarrow 0$ limit and the latter for $(Kn) \ll 1$. In the context of continuum gas dynamics, the Euler equations describe reversible adiabatic (isentropic) flows, while the Navier-Stokes equations provide the standard description of viscous flows. This means that the first- and second-order Chapman-Enskog solutions merely reconcile the molecular and continuum approaches for small Knudsen number flows. It is obvious that the expansion for f in eqn (8.2) must break down as the Knudsen number approaches unity, but there remains the possibility that the use of more than two terms may extend the range of applicability of the continuum approach to higher Knudsen numbers. The third-order solution of Eqn (8.2) leads to the Burnett equations. These were discussed in §3.5 and it was pointed out that there is evidence that they not only extend the range of validity of the Navier-Stokes equations, but can provide a more accurate description at all Knudsen numbers. They are, however, extremely complex and closed form solutions are not available even for the simple flows that are readily solved at the Navier-Stokes level of approximation. Moreover, at the higher Knudsen numbers, the numerical effort in solving the Burnett equations is far greater than that involved in obtaining accurate solutions from the direct simulation methods that are described in the later chapters.

Grad (1949) put forward an alternative expansion for f as a series of Hermite tensor polynomials with the first-order solution again being the local Maxwellian. The third-order solution leads to an expression for f as the local Maxwellian multiplied by an expression involving τ and q as well as ρ , c_0 , and T . This means that the total number of moment equations that are required for a determinate set is equal to the total number of dependent variables in the conservation equations. This number is readily seen to be thirteen, thus leading to Grad's Thirteen Moment equations. While these represented a logical and important development in kinetic theory, the results from their application to specific problems in the transition regime have proved to be disappointing (Schaaf and Chambre 1961).

The failure of the systematic expansion methods to produce equations that significantly extend the upper Knudsen number limits of the Navier-Stokes equations indicates that more radical steps must be taken if workable approximations are to be found for the distribution function in the transition regime. For one-dimensional steady flow problems with two-point boundary conditions, the procedure has been to choose f as a combination of the two Maxwellian distributions that apply at the boundaries.

As the first example, consider the 'four moment solution' of Liu and Lees (1961) for the steady one-dimensional heat flux between infinite flat plates. The lower plate in the plane $y=0$ is at the temperature T_L and the upper plate in the plane $y=h$ is at the temperature T_U . The assumption that is made about the form of the distribution function is that it is a combination of two half-range Maxwellians, each with a different temperature. This may be expressed as

$$nf = N_1 f_1 + N_2 f_2, \quad (8.3)$$

where f_1 and f_2 are the distribution functions of the molecules moving in the positive and negative y -directions, respectively. The temperatures T_1 and T_2 of these Maxwellian distributions as well as the parameters N_1 and N_2 are functions of y .

The average of any molecular quantity Q is given by eqns (8.3), (3.3), and (4.1) as

$$\bar{Q} = (1/n) \{ N_1 \beta_1^3 \pi^{-3/2} \int_{-\infty}^{\infty} \int_0^{\infty} \int_{-\infty}^{\infty} Q \exp(-\beta_1^2 c'^2) du dv dw \\ + N_2 \beta_2^3 \pi^{-3/2} \int_{-\infty}^{\infty} \int_0^{\infty} \int_{-\infty}^{\infty} Q \exp(-\beta_2^2 c'^2) du dv dw \}. \quad (8.4)$$

The boundary conditions are such that the stream velocity must be zero and $c'=c$. Setting Q equal to m , v , c^2 , and $\frac{1}{2}mc^2$ yields the following expressions for the important macroscopic quantities in terms of the four unknown quantities N_1 , N_2 , β_1 , and β_2 :

$$\rho = nm = \frac{1}{2}(N_1 + N_2)m, \quad (8.5)$$

$$v_0 = \bar{v} = (N_1/\beta_1 - N_2/\beta_2)/(2n\pi^{1/2}), \quad (8.6)$$

$$T = \overline{c^2}/(3R) = (N_1/\beta_1^2 + N_2/\beta_2^2)/(4nR), \quad (8.7)$$

and

$$q_y = \frac{1}{2}nmvc^2 = m(N_1/\beta_1^3 - N_2/\beta_2^3)/(2\pi^{1/2}). \quad (8.8)$$

The moment equation for this problem is, from eqn (3.27)

$$\frac{d}{dy} \left(n \int_{-\infty}^{\infty} Q v f d\mathbf{c} \right) = \Delta[Q]. \quad (8.9)$$

The conserved quantities m , mv , and $\frac{1}{2}mc^2$ provide obvious choices for Q in three of the four moment equations that are required. The collision integral vanishes for these equations and eqn (8.9) becomes

$$n \int_{-\infty}^{\infty} Q v f d\mathbf{c} = \text{const.} \quad (8.10)$$

Setting $Q = m$, we obtain

$$N_1/\beta_1 - N_2/\beta_2 = 0. \quad (8.11)$$

The constant is zero in eqn (8.11) because the left-hand side may be directly related through eqn (8.6) to the stream velocity normal to the plates, and the boundary conditions require this to vanish at the plates. For $Q = v$, eqn (8.10) yields

$$N/\beta_1^2 + N_2/\beta_2^2 = \text{const}$$

and, using eqn (8.7),

$$N_1/\beta_1^2 + N_2/\beta_2^2 = 4p/m \quad (8.12)$$

with the pressure $p = nmRT$ a constant for this flow. Similarly, with $Q = \frac{1}{2}mc^2$, and using eqn (8.8)

$$N_1/\beta_1^3 - N_2/\beta_2^3 = 2\pi^{\frac{1}{2}}q_y/m. \quad (8.13)$$

Because the problem essentially involves heat transfer in the y -direction, Lees and Liu chose $Q = \frac{1}{2}mvc^2$ for the fourth moment. Eqn (8.9) then becomes

$$\frac{5m}{16} \frac{d}{dy} \left(\frac{N_1}{\beta_1^4} + \frac{N_2}{\beta_2^4} \right) = \Delta[\frac{1}{2}mvc^2].$$

The collision integral for $\frac{1}{2}mvc^2$ may be evaluated in a similar manner to that for u^2 in §3.3 and, for the special case of Maxwell molecules the result is (Vincenti and Kruger 1965, p. 364)

$$\Delta[\frac{1}{2}mvc^2] = -\pi A_2(5)(2\kappa/m)nq_y.$$

The constant $A_2(5)$ and the parameter κ may be eliminated by eqns (3.56) and (3.64) for the coefficient of heat conduction in a gas of Maxwell molecules. The fourth moment equation then becomes

$$\frac{d}{dy} \left(\frac{N_1}{\beta_1^4} + \frac{N_2}{\beta_2^4} \right) = -\frac{8Rpq_y}{mK}. \quad (8.14)$$

Now, from eqns (8.5), (8.7), and (8.11)

$$T = p/(nmR) = (2R\beta_1\beta_2)^{-1} = (T_1 T_2)^{\frac{1}{2}} \quad (8.15)$$

which, with eqns (8.8), (8.11), and (8.12), gives

$$\frac{1}{\beta_1} - \frac{1}{\beta_2} = \frac{\pi^{\frac{1}{2}}q_y}{2p} \quad (8.16)$$

and

$$\frac{N_1}{\beta_1^4} + \frac{N_2}{\beta_2^4} = \frac{4p}{m} \left(\frac{\pi q_y^2}{4p^2} + 2RT \right).$$

Eqn (8.14) can therefore be written

$$q_y = -K \frac{dT}{dy} \quad (8.17)$$

which is, of course, the standard continuum result. The four moment solution departs from the continuum solution only through the boundary conditions which are

$$T_1 = T_L \quad \text{at } y = 0$$

and

$$T_2 = T_U \quad \text{at } y = h. \quad (8.18)$$

Eqns (8.15) and (8.16) then give

$$T_0 = T_L - \frac{1}{2} (\frac{1}{2} \pi T_L / R)^{1/2} q_y / p$$

and

$$T_h = T_U + \frac{1}{2} (\frac{1}{2} \pi T_U / R)^{1/2} q_y / p \quad (8.19)$$

for the temperature T_0 at $y = 0$ and T_h at $y = h$.

For a gas of Maxwell molecules, $K = CT$ and the solution of eqn (8.17) that was given in eqn (7.25) becomes

$$q_y = -\frac{1}{2} C (T_h^2 - T_0^2) / h. \quad (8.20)$$

Eqns (8.19) and (8.20) form a determinate set for the solution of q_y , T_0 , and T_h . The result for the heat flux is best expressed as the ratio of q_y to the free-molecule flux q_f as a function of the overall Knudsen number based on the average value of the mean free path and the plate spacing. Eqns (4.52) and (3.56) enable the mean free path to be written

$$\lambda = \frac{8}{15} \left(\frac{1}{2\pi RT} \right)^{1/2} \frac{K}{R\rho} = \frac{8}{15} \left(\frac{1}{2\pi RT} \right)^{1/2} \frac{CT}{R\rho}. \quad (8.21)$$

Then, noting that the pressure is constant in this flow, the Knudsen number based on the average mean free path in the gas between the plates is

$$(Kn) = \frac{\bar{\lambda}}{h} = \frac{8CT^{3/2}}{15h(2\pi R)^{1/2}p}. \quad (8.22)$$

The equations may be solved numerically and the results for $T_U/T_L = 4$ are shown in Fig. 8.1. The transition from continuum to free-molecule flow is, in this case, centred on an overall Knudsen number of 0.2 and spans more than a thousandfold change in this number. There is a 1% departure from the continuum solution at $(Kn) = 0.0018$, and the heat flux reaches 99% of the free-molecule value at $(Kn) = 140$. The empirical ‘bridging formula’ approach to transition regime flows generally constructs a smooth curve between the continuum solution at a Knudsen number of 0.1 and the free-molecule solution at a Knudsen number of 10. This approach is not supported by the four moment solution for this problem.

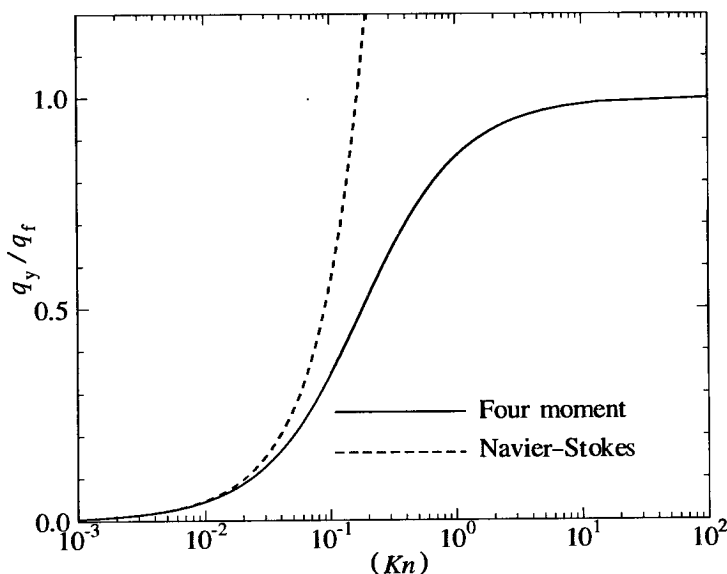


Fig. 8.1 The four moment solution for the one-dimensional heat transfer between parallel plates with a temperature ratio of four.

The temperature jump or 'slip' at a surface at temperature T_p can be written in terms of the *local* Knudsen number (Kn') which is defined as the ratio of the local mean free path to the scale length of the temperature gradient. The resulting temperature jump is

$$T - T_p = \pm \frac{15\pi}{16} (T_p T)^{1/2} \frac{\lambda}{T} \frac{dT}{dy} = \pm \frac{15\pi}{16} (T_p T)^{1/2} (Kn'), \quad (8.23)$$

with the positive and negative signs applying at the lower and upper plates, respectively. The difference between the temperatures of the upward and downward moving molecules can be written

$$T_1 - T_2 = - \frac{15\pi}{16} \left\{ (T_1 T)^{1/2} + (T_2 T)^{1/2} \right\} \frac{\lambda}{T} \frac{dT}{dy}, \quad (8.24)$$

and is consistent with the result for the temperature jump.

Eqn (8.23) shows that the temperature jump tends to zero with the Knudsen number, and the heat transfer tends to the continuum value. However, the assumed distribution function of eqn (8.3) does not tend to the Chapman-Enskog distribution function. This can be illustrated through the calculation of the difference between the separate temperatures of the upward and downward moving molecules in the Chapman-Enskog gas. The temperature T^* of the upward moving molecules in this

gas is obtained by setting the stream velocity in eqn (4.57) to zero, setting this expression into eqns (3.3) and (1.29), and performing the integration over v from 0 to ∞ . The temperature of the downward moving molecules is obtained similarly, and the temperature difference between the upward and downward moving molecules is

$$\frac{T^+ - T^-}{T} = - \frac{5(\alpha+1)(\alpha+2)}{\alpha(5-2\omega)(7-2\omega)} \frac{\lambda}{T} \frac{dT}{dy}. \quad (8.25)$$

The Maxwell gas case is given by $\omega = 1$, and a comparison of eqns (8.24) and (8.25) shows that they then differ by more than a factor of two. It is, therefore, incorrect to say that the four moment solution is in agreement with the Navier-Stokes solution at small values of the overall Knudsen number. The Chapman-Enskog result would obviously be more accurate well away from the surface, but the moment solution employs the correct distribution for molecules that are diffusely reflected from the wall. However, it can be safely concluded that the temperature jump ratio is of the order of the local Knudsen number. If the u_0 stream velocity component varies in the y -direction, there is also a difference in the stream velocity of the upward and downward moving molecules. This is obtained in a similar manner to eqn (8.25) as

$$\frac{u^+ - u^-}{u} = - \frac{5(\alpha+1)(\alpha+2)}{2\alpha(5-2\omega)(7-2\omega)} \frac{\lambda}{u} \frac{du}{dy}. \quad (8.26)$$

This shows that the *velocity slip* ratio at the surface is of the order of the local Knudsen number based on the scale length of the gradient in the stream velocity. Continuum flow solutions that are based on Navier-Stokes equations are improved if the usual 'no-slip' boundary conditions are modified to allow for the slips in velocity and temperature that occur at solid surfaces. The Chapman-Enskog distribution adjusts to the surface distribution in a region, called the *Knudsen layer*, that has a thickness of the order of the mean free path.

Probably the best-known moment method is that of Mott-Smith (1951) for shock wave structure. This is also a one-dimensional flow and it is assumed that the distribution function within the wave may be represented as a linear combination of the distribution functions that apply in the uniform upstream and downstream flows. This is a bimodal distribution and can be written

$$nf = N_1 f_1 + N_2 f_2, \quad (8.27)$$

where the subscripts ₁ and ₂ denote the uniform upstream and downstream conditions, respectively. This equation is identical to eqn (8.3) for the four moment distribution function but, in that case, f_1 and f_2 were variables rather than constants, and the distribution could not be described as bimodal. The x -axis may be taken normal to the wave and eqn (4.1) gives

$$f_1 = (\beta_1^2/\pi^{3/2}) \exp[-\beta_1^2 \{(u - u_{01})^2 + v^2 + w^2\}]$$

and

$$(8.28)$$

$$f_2 = (\beta_2^2/\pi^{3/2}) \exp[-\beta_2^2 \{(u - u_{01})^2 + v^2 + w^2\}] .$$

The weighting factors N_1 and N_2 must be such that $N_1 = n_1$ and $N_2 = 0$ upstream of the wave, while $N_1 = 0$ and $N_2 = n_2$ downstream of the wave. Eqn (8.27) may be integrated over velocity space and the normalization condition of eqn (3.2) then requires

$$n = N_1 + N_2 . \quad (8.29)$$

The application of the conservation equations between the upstream and downstream conditions leads to the Rankine-Hugoniot 'jump' equations for n_2 , u_{02} , and β_2 as functions of n_1 , u_{01} , and β_1 . The evaluation of all the flow quantities within the wave as the appropriate moments of the bimodal distribution function of eqn (8.27) requires a solution for n , N_1 , and N_2 as functions of position within the wave. One relation between these quantities has already been provided by eqn (8.29). A second is obtained by applying the mass conservation equations between the upstream state and a point within the wave. Eqn (3.30) gives

$$n_1 u_{01} = n u_0 \quad (8.30)$$

and, evaluating $u_0 = \int_{-\infty}^{\infty} u f \, dc$ for the distribution defined by eqn (8.27),

$$n_1 u_{01} = N_1 u_{01} + N_2 u_{02} . \quad (8.31)$$

The third relation is supplied by an additional moment equation. The choice of the quantity Q in this equation is arbitrary; Mott-Smith used both u^2 and u^3 . With $Q = u^2$, eqn (3.27) for a steady one-dimensional flow is

$$\frac{d}{dx} (n \overline{u^3}) = \Delta [u^2]$$

and, using eqn (3.66) for the collision integral in a gas of either Maxwell molecules or VHS molecules with $v = 1/2$,

$$\frac{d}{dx} (n \overline{u^3}) = \frac{p}{m} \frac{\tau_{xx}}{\mu} . \quad (8.32)$$

Eqns (3.64) and (3.65) show that the viscosity coefficient for these gas models can be written CT where C is a constant. Eqn (4.52) for the mean free path[†] enables C to be written in terms of the upstream conditions, i.e.

$$C = \frac{\rho_1 \lambda_1}{2} \left(\frac{2\pi k}{m T_1} \right)^{1/2} .$$

This may be substituted into eqn (8.32), to give

[†] This book employs the mean free path of eqn (4.52) that takes into account the change in collision cross-section with relative velocity. This causes the results to differ from earlier treatments that employ the hard sphere value by the factor $(5-2\omega)(7-2\omega)/24$, or $5/8$ for Maxwell model that is employed here.

$$\frac{d}{dx} (\bar{n u^3}) = \frac{(2RT_1/\pi)^{1/2}}{n_1 \lambda_1} \frac{n}{m} \tau_{xx}. \quad (8.33)$$

Now,

$$\bar{n u^3} = N_1 \int_{-\infty}^{\infty} u^3 f_1 d\epsilon + N_2 \int_{-\infty}^{\infty} u^3 f_2 d\epsilon$$

and

$$\begin{aligned} \int_{-\infty}^{\infty} u^3 f_1 d\epsilon &= \frac{\beta_1^3}{\pi^{3/2}} \int_{-\infty}^{\infty} \int_{-\infty}^{\infty} \int_{-\infty}^{\infty} \{u_{01} + (u - u_{01})\}^3 \exp[-\beta_1^2((u - u_{01})^2 \\ &\quad + v^2 + w^2)] du dv dw \\ &= u_{01} (u_{01}^2 + 3RT). \end{aligned}$$

A similar expression may be obtained for the second term and, using eqn (8.30)

$$\bar{n u^3} = N_1 u_{01} (u_{01}^2 + 3RT_1 - u_{02}^2 - 3RT_2) + N_2 u_{02} (u_{02}^2 + 3RT_2).$$

Conservation of energy between the upstream and downstream states requires

$$u_{01}^2 + 5RT_1 = u_{02}^2 + 5RT_2,$$

so that

$$\frac{d}{dx} (\bar{n u^3}) = \frac{2}{5} u_{01} (u_{01}^2 - u_{02}^2) \frac{dN_1}{dx}. \quad (8.34)$$

Also, from eqn (1.26) and noting that τ_{xx} is symmetrical about the x -axis,

$$(n/m) \tau_{xx} = n^2 (\bar{c'^2}/3 - \bar{u'^2}) = 2n^2 (\bar{v'^2} - \bar{u'^2})/3.$$

Then, similarly to the derivation of eqn (1.29a) from (1.29),

$$\bar{u'^2} = \bar{u^2} - u_0^2$$

and the mean value of u^2 may be evaluated in a similar manner to the above treatment of the mean value of u^3 . This gives,

$$(n/m) \tau_{xx} = 2n(nu_0^2 - N_1 u_{01}^2 - N_2 u_{02}^2)/3$$

and, using eqns (8.29), (8.30), and (8.31),

$$\begin{aligned} (n/m) \tau_{xx} &= 2\{(N_1 u_{01} + N_2 u_{02})^2 - N_1(N_1 + N_2)u_{01}^2 - N_2(N_1 + N_2)u_{02}^2\}/3 \\ &= -2N_1 N_2 (u_{01} - u_{02})^2/3. \end{aligned}$$

N_2 may again be eliminated through eqn (8.31) to give

$$\frac{n}{m} \tau_{xx} = -\frac{2}{3} N_1 (n_1 - N_1) \frac{u_{01}}{u_{02}} (u_{01} - u_{02})^2. \quad (8.35)$$

The substitution of eqns (8.34) and (8.35) into (8.33) leads to the following differential equation for N_1/n_1 as a function of x/λ_1

$$\frac{d}{d(x/\lambda_1)} \left(\frac{N_1}{n_1} \right) = -\alpha \frac{N_1}{n_1} \left(1 - \frac{N_1}{n_1} \right), \quad (8.36)$$

where

$$\alpha = \frac{5}{3\pi^{1/2}} \frac{(2RT_1)^{1/2}}{u_{02}} \frac{u_{01} - u_{02}}{u_{01} + u_{02}}. \quad (8.37)$$

The solution of eqn (8.36) is

$$N_1 = \frac{n_1}{1 + \exp\{\alpha(x/\lambda_1)\}} \quad (8.38)$$

and the substitution of this and eqn (8.31) into eqn (8.27) provides an expression for the distribution function within the wave as a function of x/λ_1 . The density profile follows directly from eqn (8.28) as

$$\frac{n - n_2}{n_1 - n_2} = \frac{N_1}{n_1} = \frac{1}{1 + \exp\{\alpha(x/\lambda_1)\}}. \quad (8.39)$$

The profiles of the other macroscopic flow quantities may be obtained as the appropriate moment of the bimodal distribution function.

The Mott-Smith solution has been found to be inadequate for the weaker (shock Mach numbers less than about 1.6) shock waves that are adequately described by the Navier-Stokes equations. However, it will be shown in §12.11 that the bimodal distribution function is qualitatively correct for very strong shock waves, and the Mott-Smith method is reasonably successful in predicting the structure of such waves. The shock thickness L is well predicted when the molecular model is chosen to match the coefficient of viscosity, but the profiles of real waves are not symmetrical as is predicted by the theory. It must also be remembered that the good result for the thickness of strong waves is based on the choice of u^2 as the quantity Q in the fourth moment equation. This is the usual choice, but there is no rigorous justification for it, and Rode and Tanenbaum (1967) and Sather (1973) have shown that the result is highly sensitive to it. It may be noted that, concurrently with the experimental justification of the result with $Q = u^2$, an argument was presented (Desphande and Narasimha 1969) to the effect that the u^3 result should be superior to the u^2 result.

The method was extended to the other inverse power law molecular models by Muckenfuss (1962). This made it possible to match the real gas temperature exponent, as well as the actual value, of the coefficient of viscosity and improved the agreement with measured values. The shock thickness was found to be related to the exponent η in the inverse power law model and the shock Mach number (Ma)_S by

$$L/\lambda_1 \propto (Ma)_S^{4/(\eta-1)}. \quad (8.40)$$

The justification for the VHS molecular model is that the observable effects of molecular model can be fully related to the change in the collision cross-section with the relative speed. The significant collisions in the shock structure problem are those that occur with relative speeds that are characteristic of the downstream temperature T_2 . The temperature ratio across the shock is proportional to $(Ma)_S^2$ so that, from eqns (3.61) and (3.68),

$$\frac{(\sigma_T)_2}{(\sigma_T)_1} \propto \left(\frac{T_2}{T_1} \right)^{-\nu} \propto (Ma)_S^{-4/(\eta-1)}. \quad (8.41)$$

The increase in shock thickness with shock Mach number therefore correlates exactly with the reduction in the relevant collision cross-section.

The moment method has been applied successfully to other steady one-dimensional problems such as condensation and evaporation (Ytrehus 1994). While the results from some applications of the method are in remarkably good agreement with experiment, the solutions are not unique because the method is based on several arbitrary choices. One of these is associated with the form of the assumed distribution function, and the other with the choice of the non-conserved quantities for the additional moment equations. The best choices for one set of parameters is not necessarily the best for another set, even for the same problem. Also, the use of a more complicated distribution function, with a consequent increase in the number of moments, does not necessarily lead to more consistent results. The moment methods have not been applied to two-dimensional or axially symmetric problems such as the steady transition regime flow past a sphere. The major problem is that the form of the distribution function varies greatly with from one location to another in such a flow. The difficulty in formulating a suitable expression for the distribution function is further complicated by the fact that, for these flows, it is three-dimensional rather than axially symmetric in velocity space. Finally, even if it were possible to find a workable approximation to the distribution function, the resulting equations would be more difficult to solve than the Navier-Stokes equations for the corresponding viscous continuum flow.

8.3 Model equations

The model equation approach involves an approximation to the form of the Boltzmann equation itself. It is the collision term on the right hand side of the Boltzmann equation that poses the greatest mathematical difficulties, and it is this term that is modified. The best known model equation is called the BGK equation after Bhatnagar, Gross, and Krook (1954). This may be written

$$\frac{\partial}{\partial t}(nf) + \mathbf{c} \cdot \frac{\partial}{\partial \mathbf{r}}(nf) + \mathbf{F} \cdot \frac{\partial}{\partial \mathbf{c}}(nf) = n\nu(f_0 - f). \quad (8.42)$$

While the parameter ν is generally regarded as a collision frequency, it has a restricted functional dependence in that it is proportional to density and

may depend on temperature, but is assumed to be independent of the molecular velocity \mathbf{c} . The appearance of the local Maxwellian f_0 means that the equation remains a non-linear integro-differential equation. This is because f_0 is a function of the stream velocity \mathbf{c}_0 and the temperature T , and these must be obtained as integrals over f . The integration over both f_0 and f must result in identical values of \mathbf{c}_0 and T so that the collision term vanishes when moments are taken over the conserved quantities. This condition ensures that the BGK equation is consistent with the conservation equations.

The BGK equation for a stationary homogeneous gas without an external force field follows from eqn (8.42) as

$$\frac{\partial f}{\partial t} = v(f_0 - f)$$

and clearly has the correct solution $f=f_0$ at equilibrium. The Chapman-Enskog method may be applied to the equation (Vincenti and Kruger 1965, p. 379). This converts the conservation equations to the form of the Navier-Stokes equations, although the numerical constants in the transport properties do not correspond to any of the recognised molecular models. The BGK equation obviously provides the correct collisionless or free-molecule solution, since the form of the collision term is then immaterial. An exact solution would therefore span the complete range of Knudsen number and would be at or close to the correct limits at the extremes of this range. The approximate collision term would, however, lead to an indeterminate error in the transition regime.

A comparison of eqns (8.42) and (3.20) shows that the depletion component of the collision term in the Boltzmann equation

$$-\int_{-\infty}^{\infty} \int_0^{4\pi} n^2 f f_1 c_r \sigma d\Omega dc_1$$

is replaced in the BGK equation by

$$-n v f.$$

The correct velocity dependent collision frequency $v(\mathbf{c})$ follows directly from the Boltzmann term as

$$v(\mathbf{c}) = n \int_{-\infty}^{\infty} \int_0^{4\pi} f_1 c_1 \sigma d\Omega dc_1. \quad (8.43)$$

This is independent of molecular velocity only for the physically unreal Maxwell molecules, or for VHS molecules with $\omega=1$. The use of a velocity independent v in the BGK equation is generally an unjustified approximation, but at least the form of the depletion term is correct. The same cannot be said for the component of the collision term that represents the replenishing collisions. This is written

$$n v f_0$$

and assumes that, irrespective of the form of f , the number of molecules scattered by collisions into class c is equal to the number that would be scattered out of this class in an equilibrium gas having the assumed velocity independent collision frequency.

Liepmann et al. (1962) applied the BGK equation to the shock structure problem. For one-dimensional steady flow, eqn (8.42) becomes

$$u \frac{d}{dx} (nf) = nv(f_0 - f). \quad (8.44)$$

This may be integrated to give the following integral equation

$$nf = \int_{-\infty}^x \frac{n v f_0(x')}{u} \exp\left(-\int_{x'}^x \frac{v dx''}{u}\right) dx', \quad (8.45)$$

where x' and x'' are dummy variables and the negative and positive signs on the lower limit apply for positive and negative u , respectively. Eqn (8.45) was solved numerically by Liepmann et al. using an iterative scheme that required an initial guess for f_0 . The results are in good agreement with the Navier-Stokes solution, and therefore with experiment, for shock Mach numbers significantly less than two. For very strong shock waves, the method leads to highly asymmetric velocity and density profiles in which the upstream region is far more extended than in the measured profiles. The probable reason for the failure of the BGK model in the upstream region of a very strong shock wave lies in the use of a collision frequency that is independent of f . This collision frequency is related to T through the BGK result for the coefficient of viscosity but, since this relationship is based on near-equilibrium theory, it is not adequate in the region of extreme non-equilibrium near the leading edge of the wave.

The assumptions inherent in the BGK equation are least likely to have deleterious effects in problems that involve small perturbations and have their boundary conditions prescribed in terms of equilibrium distributions. The distribution function then departs only very slightly from the Maxwellian form, irrespective of the value of the Knudsen number. This leads to linearized forms of the Boltzmann and BGK equations and, for these, the comparative mathematical simplicity of the model equations is particularly significant. In addition, the temperature variations and therefore the changes in the collision cross-sections are small, and the accuracy of the molecular model is not of critical importance. Most of the results in Cercignani (1969 and 1988) are for the BGK equation rather than for the full Boltzmann equation. There are a number of problems of practical importance that involve small perturbations. As noted by Cercignani (1991), these generally involve low Mach numbers and include a number of environmental problems. However, for non-linear problems that involve large perturbations and complex physical effects, analytical solutions are out of the question and recourse must be had to numerical methods.

References

- BHATNAGAR, P.L., GROSS, E.P. and KROOK, M. (1954). Model for collision processes in gases, I. Small amplitude processes in charged and neutral one-component systems. *Phys. Rev.* **94**, 511–524.
- CERCIGNANI, C. (1969). *Mathematical methods in kinetic theory*. Plenum Press, New York.
- CERCIGNANI, C. (1988). *The Boltzmann equation and its applications*. Springer, New York.
- CERCIGNANI, C. (1991). *Mathematics and the Boltzmann equation*, In *Rarefied Gas Dynamics* (ed. A.E. Beylich), pp 3–13. VCH, Weinheim.
- DESHPANDE, S.M. and NARASIMHA, R. (1969). The Boltzmann collision integrals for a combination of Maxwellians. *J. Fluid Mech.* **36**, 545–554.
- GRAD, H. (1949). On the kinetic theory of rarefied gases. *Commun. pure appl. Math.* **2**, 331–407.
- SCHAAF, S.A. and CHAMBRE, P.L. (1961). *Flow of rarefied gases*, Princeton University Press.
- LIEPMANN, H.W., NARASIMHA, R., and CHAHINE, M.T. (1962). Structure of a plane shock layer. *Phys. Fluids* **5**, 1313–1344.
- LIU, C.Y. and LEES, L. (1961). Kinetic theory description of plane compressible Couette flow. In *Rarefied gas dynamics* (ed. L. Talbot), pp 391–428. Academic Press, New York.
- MOTT-SMITH, H.M. (1951). The solution of the Boltzmann equation for a shock wave. *Phys. Rev.* **82**, 885–892.
- MUCKENFUSS, C. (1962). Some aspects of shock structure according to the bimodal model. *Phys. Fluids* **5**, 1325–1336.
- RODE, D.L. and TANENBAUM, B.S. (1967). Mott-Smith shock thickness using the v_x^P method. *Phys. Fluids* **10**, 1352–1354.
- SATHER, N.F. (1973). Approximate solutions of the Boltzmann equation for shock waves. *Phys. Fluids* **16**, 2106–2109.
- VINCENTI, W.G. and KRUGER, C.H. (1965). *Introduction to physical gas dynamics*, Wiley, New York.
- YTREHUS, T. (1994). Moment solutions in the kinetic theory of strong evaporation and condensation: Application in cometary dust–gas dynamics. *Prog. in Astro. and Aero.* **158**, in press.

9

NUMERICAL METHODS FOR TRANSITION REGIME FLOWS

9.1 Classification of methods

As was noted in the preceding chapter, very few of the 'analytical' methods lead to closed form solutions and most depend on numerical procedures for the production of the final results. On the other hand, the 'numerical' methods rely on computation from the outset. While the analytical methods are almost invariably based on the Boltzmann equation which is the accepted mathematical model of a gas flow at the molecular level, a large fraction of the numerical methods are based directly on the simulation of the physics of the flow and do not depend on a mathematical model. This difference in approach can be used to define two classes of methods, but the situation is complicated by the efforts that have been made to link some of the simulation methods to the Boltzmann equation with sufficient rigour that they can be claimed to be 'solutions' of that equation. All methods that employ simulated particles or molecules will be classed here as simulation methods.

A general difficulty with simulation methods is that they are not unique and there may be many variants of a particular method. Furthermore, modifications to a method, or to the computational procedures through which it is implemented, may alter the relative advantages, or even the validity of that method. Successive applications of a method by the same person may use quite different procedures, even though the description of the method is not changed. Conversely, changes to the procedures that are well within the usual variations between implementations may be claimed to define a 'new' method which is given a different name. This can lead to confusion and to difficulties with 'quality control'. While all numerical methods are subject to these problems, physical simulation methods suffer from the fact that they are not as clearly defined as the conventional numerical methods for the solution of equations. The problem has been compounded by the restrictions on the length and content of scientific papers, in that these do not allow a full exposition of the theory behind the procedures, let alone the actual coding of the computer programs. Also, as the simulation becomes more exact through the inclusion of additional physical effects, the programs become more substantial and a large number of test cases are required for code verification prior to 'production runs' being made.

9.2 Direct Boltzmann CFD

The most direct numerical approach to the Boltzmann equation would be to apply the conventional methods of computational fluid dynamics (or CFD). The velocity distribution function is the only dependent variable for a simple gas and this may be represented in a finite difference or finite element form by its numerical value over a network of points or elements in phase space.

A major problem is posed by the sheer number of points or elements that must be employed for this representation. For a steady one-dimensional problem with gradients in only one spatial dimension, the distribution function is axially symmetric in velocity space and a three-dimensional array is required in phase space. In addition, the velocity space domain is of infinite extent. Finite bounds must therefore be chosen such that only a negligible fraction of molecules lie outside them, but it is difficult to predict the proper placement of these bounds. This problem is particularly severe in the case of hypersonic or high-temperature flows because a minute fraction of molecules with very high velocities relative to the bulk of the gas can have a significant effect on the macroscopic flow properties. The velocity distribution function becomes three-dimensional for two-dimensional flows, thus requiring a five-dimensional array in phase space. If the flow is unsteady, time must be added as a further independent variable. If 100 grid intervals were employed for each dimension, the finite difference or element solution of the Boltzmann equation for a three-dimensional unsteady flow would require 10^{14} grid points. Suitably coupled simultaneous equations must be solved for each of the molecular species in a gas mixture. Also, each of the internal modes that are associated with these species add further to the effective dimensions of phase space. Physical effects such as chemical reactions and thermal radiation pose almost insurmountable problems for the Boltzmann formulation, if only because of the difficulty in defining inverse collisions.

In view of these difficulties, it is no surprise that direct solutions of the Boltzmann equation have been restricted to simple flow geometries, monatomic gases, and low to moderate Mach numbers. Even so, there are problems due to the very large number of operations that are required to evaluate the collision term. The integrals are replaced by summations in the discrete approximation. At each point in phase space, a sum must be taken over all other velocity space points with each term in the sum representing, itself, a summation over the impact parameters of the collision. The direct solutions have employed summation procedures that reduce the computational effort associated with the collision term.

The first successful method for the direct numerical solution of the Boltzmann equation was introduced in a series of papers by Nordsieck, Hicks, and Yen (for example: Nordsieck and Hicks 1967, and Yen 1970). They dealt with one-dimensional steady flow problems and employed a conventional finite difference technique for the 'fluid-like' terms on the left-hand side of the equation. A Monte Carlo sampling technique was used to

reduce the computing effort required by the summations associated with the collision term. The steady flow equation was employed and this necessitated an initial estimate of the distribution function over the whole flowfield, with the final solution being approached through an iterative procedure. The number of points in the computational grid was minimal and, since collisions were represented by transitions between points in the velocity space grid, there was an effective rounding off of the velocities in collisions. This led to a systematic error which tended to build up from step to step in the iteration. A least squares procedure was used to keep the error in check by ensuring that the conservation laws were satisfied. In addition to these new problems associated with the collision term, the finite difference method for the remaining terms posed the usual problems with regard to grid dependence and stability. Despite these difficulties, satisfactory results were obtained for a number of problems; most notably the structure of normal shock waves (Hicks et al. 1972).

The Boltzmann CFD approach was extended to two-dimensional steady flows by Tcheremissine (1973). Alternatives to the Monte Carlo procedure for the evaluation of the collision integral have been proposed and tested by Tcheremissine (1991) and Tan et al. (1989). These methods attempt to reduce the computational load associated with the collision term by concentrating on the more non-equilibrium portion of the velocity distribution function. The basic disadvantage of the Boltzmann CFD methods is the necessity to specify a bounded grid in velocity space. This causes problems with regard to the overall computational load and with the ease of use of the method. Any attempt to ease the computational load by applying location dependent procedures to velocity space tends to make the method even more difficult to apply.

9.3 Deterministic simulations

While the particulate nature of a gas is responsible for the mathematical difficulties that are associated with the Boltzmann equation, it also permits the circumvention of these problems through the development of physically based simulation methods. Direct simulation methods model the real gas by a large number of simulated molecules in a computer. This number has ranged from the order of hundreds in early calculations, to millions in some contemporary simulations. The position coordinates, velocity components, and internal state of each of the simulated molecules are stored in the computer and are modified with time as the molecules are simultaneously followed through representative collisions and boundary interactions in simulated physical space. The time parameter in the simulation may be identified with physical time in the real flow and all calculations are unsteady, although steady flow may be attained as the large-time state of the unsteady flow. Because a steady flow develops through a physically real unsteady flow, there are minimal problems with boundary conditions. There is no need for an initial estimate of the flowfield and there is no artificial iteration process.

The *molecular dynamics (or MD) method* (Alder and Wainwright 1957) was the first physical simulation method. While this method may employ probabilistic procedures when setting the initial configuration of the molecules, the calculation of the subsequent molecular motion, including the collisions and boundary interactions, is deterministic. Collisions occur when the cross-sections overlap, and the computation time for a straightforward application of the method is proportional to the square of the number of simulated molecules. A major difficulty with this method is that, for a given molecular size, flow geometry, and gas density, the number of simulated molecules is not a free parameter.

The parameter that best expresses the number of molecules that are involved in a flow is the number of molecules within one cubic mean free path. For a nominal molecular diameter of 4×10^{-10} m, eqn (1.58) gives this number as

$$N_\lambda = n \lambda^3 = 3856(n_0/n)^2, \quad (9.1)$$

where n_0 is the standard number density. If we consider the MD simulation of a problem that requires a three-dimensional flow field that extends over 30 mean free paths in each direction, approximately 10^8 simulated molecules would be required at standard density. However, for the same calculation at a density of the order of 100 times standard density, the required number is reduced to the easily attained 10^4 . MD calculations with a realistic molecular diameter are therefore restricted to dense gases, and the overwhelming number of MD applications fall into this category. Note that the Boltzmann equation is restricted to dilute gases, and this requires the density to be no greater than about twice the standard density.

At the other extreme, problems in rarefied gas dynamics typically involve a density ratio of the order of 10^{-6} , and eqn (9.1) then shows that the required number of simulated molecules would be 10^{20} . If the MD method is to be applied to low-density problems, the correct mean free path can be obtained only through the device of replacing the large number of small molecules by a small number of large molecules. This leads to errors due to an incorrect equation of state, biased impact parameters and, in some cases, the clustering or trapping of molecules in acute corners and small openings. The best-known such application is that of Meiburg (1986) to the two-dimensional unsteady flow past an inclined flat plate with a chord length of 75 mean free paths. The required molecular diameter was 0.75 times the mean free path, or 1% of the chord of the plate. MD calculations must be three-dimensional and Meiburg's calculation employed a thin 'slice' with specularly reflecting boundaries. This procedure would not be possible for axially symmetric flows which would appear to require a full three-dimensional calculation. It may be noted that many two-dimensional MD calculations employ cylindrical rather than spherical molecules, and this leads to non-physical macroscopic properties. The MD method has proved to be valuable for the simulation of dense gases and liquids (Allen and Tildesley 1987), but it is inappropriate for dilute gases.

9.4 Probabilistic simulation methods

The first probabilistic simulation method was introduced by Haviland and Lavin (1962) and is best termed the *test particle Monte Carlo method*. The test particle method for collisionless flows was presented in §7.7 as the logical method for dealing with complex flows that involve multiple surface reflections. In the transition regime, it becomes necessary to compute typical intermolecular collisions in addition to the molecule-surface interactions. This can only be done if there is already a representation of the complete flowfield. The distribution function is chosen for this representation and, as in the finite difference method, it is stored at a number of locations in phase space. The method therefore shares a major disadvantage of the finite difference method in that an initial estimate must be made of the distribution function over the whole flowfield. A large number of 'test particle' trajectories are computed with the assumed distribution serving as the 'target' gas for the computation of typical intermolecular collisions. An updated target distribution is then constructed from the history of the test or incident molecules. The process is continued until there is no difference between the target and incident distributions.

The alternative to the test particle approach is to introduce a time variable and to follow the trajectories of a very large number of simulated molecules simultaneously within a computer. The first paragraph in the preceding section applies equally well to this method, called the *direct simulation Monte Carlo (or DSMC) method*, but the probabilistic procedures depend on the dilute gas assumption. Therefore, while the MD method is strictly applicable only to dense gas flows, the DSMC method can be applied only to dilute gas flows. The DSMC method was first applied to the homogeneous gas relaxation problem (Bird 1963), and the first application to a flow was to the shock structure problem (Bird 1965). Hammersley and Handscomb (1964) state that 'Monte Carlo methods comprise that branch of experimental mathematics which is concerned with experiments on random numbers'. They also applied the term 'direct simulation' to the modelling of probabilistic problems, which is the simplest form of the Monte Carlo method. The term 'direct simulation Monte Carlo' is therefore a generic term that more than covers the many variants of the method that have been introduced over the years.

The essential DSMC approximation is the uncoupling, over a small time interval or 'step', of the molecular motion and the intermolecular collisions. All the molecules are moved (including the computation of the resulting boundary interactions) over the distances appropriate to this time step, followed by the calculation of a representative set of intermolecular collisions that are appropriate to this interval. The time step should be small in comparison with the mean collision time and, as long as this condition is met, experience has shown that the results are independent of its actual value. The molecule movement routines are trivial, and a simple indexing of the molecules to sub-cells as well as cells causes all collisions to be between near-neighbours. The procedures for the probabilistic

selection of a representative set of collisions are based directly on the relations that have formed the basis of kinetic theory for more than a century. Because of this, the method has the same limitations as classical kinetic theory, which includes the Boltzmann equation. The principal limitations are the assumption of molecular chaos and the requirement of a dilute gas. The DSMC method cannot be applied to dense gases or to highly ionized plasmas that are dominated by long-range interactions.

The cell or spatial element network is required only in physical space, with the velocity space information being contained in the positions and velocities of the simulated molecules. The physical space network is used to facilitate the choice of the molecules for collisions and for the sampling of the macroscopic flow properties. Advantage may be taken of symmetries in physical space to reduce the number of dimensions of the cell network, and also the number of position coordinates that need to be stored for each molecule, but the collisions are always treated as three-dimensional phenomena. Note that the positions and velocities of the simulated molecules are continuously distributed, velocity space is unlimited, and the conservation of mass, momentum, and energy is imposed to within the round-off error of the computer.

The microscopic boundary conditions are specified by the behaviour of the individual molecules, rather than in terms of the distribution function. This facilitates the incorporation of complex physical effects, such as chemical reactions, into the simulation. The DSMC method employs simulated molecules of the correct physical size and their number is reduced to a manageable level by regarding each simulated molecule as representing a fixed number F_N of real molecules. This is typically a very large number and advantage can sometimes be taken of its size to specify some properties through a distribution of values instead of a single value for each simulated molecule. The macroscopic boundary conditions are usually specified as a uniform gas at zero time. The flow develops from this initial state with time in a physically realistic manner, rather than by iteration from an initial approximation to the flow. All procedures may be specified such that the computational time is directly proportional to the number of simulated molecules. The computational efficiency of the DSMC method is far higher than that of the MD method.

The DSMC method can be applied to weakly ionized gases as long as the electric field is obtained from theoretical considerations or calculations that are external to the DSMC procedures. The field cannot be obtained directly from the simulation because the spurious fields due to statistical fluctuations in the electron and ion number densities would generally be large in comparison with the real fields. The problem may be avoided when the Debye distance is very small through the enforcement of charge neutrality by moving the electrons with the ions. Finite electric fields can be calculated by a simultaneous solution of the Poisson equation, as in the study by Sugimura and Vogenitz (1975). Alternatively, the field in a shock front may be estimated (Bird 1986) from an approximate theory for ambipolar diffusion.

9.5 Discretization methods

The *lattice gas* cellular automata (Boon 1990) and similar methods have a computational efficiency that is even higher than that of the DSMC method, but this is achieved at the expense of physical reality. In fact, these methods are more accurately described as providing gas analogues, rather than gas models.

The lattice gas takes its name from the regular array of points or nodes into which physical space is discretized. Time is also discretized to uniform steps, the particle speeds are restricted either to one or to just a few values, and their directions are restricted to those of the lines that join adjacent nodes. The symmetry requirements for a fluid simulation require that a plane or two-dimensional lattice should be triangular rather than square. The information on the state of each node is contained in a word with a length of the order of one byte. The velocities and time step are such that the particles move exactly to another node, generally to a neighbouring node. The interactions between the nodes are performed through operations on the individual bits of these words. Rules for the interactions have been developed such that the continuity and momentum equations are satisfied and the system as a whole exhibits a fluid-like behaviour. However, there are difficulties in establishing the temperature, the energy equation is not properly defined, and the gas properties do not resemble those of any real gas. A quantitative comparison of the results from the triangular lattice model[†] with experimental data and analytical results has been made by Long et al. (1987).

Nadiga et al (1989) investigated a nine-velocity model based on a square lattice that included the diagonals. There were three speeds such that the particles were either stationary or moved to an adjacent node at each time step. They were able to define a Knudsen number, showed that the Boltzmann H function indicated an approach to equilibrium, and demonstrated the production of shock waves. Also, while the system was found to be reversible, it was very sensitive to random perturbations when moving in the reverse direction. However, the system exhibited a number of unphysical features, and it was not possible to define the thermodynamics with sufficient precision to allow the behaviour of the model to be used to predict that of a real gas.

The use of a plane lattice means that the *gas* as well as the *flow* is two-dimensional. Three-dimensional lattices have been developed, and these require a word length of the order of three bytes to describe each node. The fact that vacant as well as occupied nodes add to the storage requirement is a disadvantage of the lattice gas model. This becomes particularly serious in the case of three-dimensional calculations and can negate the storage savings of the approximate lattice models as compared with the more realistic DSMC molecular models.

[†] This is sometimes called a hexagonal lattice because the bisectors of the lines joining the nodes define a hexagon.

Cellular automata are a field of study in their own right and they provide insight to phenomena that involve the collective behaviour of a very large number of particles. However, when applied to gas flows, the level of physical realism is such that they are of little use for engineering studies.

The *discrete ordinate or discrete velocity method* was introduced by Broadwell (1964) and generalized by Gatignol (1970). The discretization of velocity space allows the Boltzmann equation to be replaced by a set of non-linear hyperbolic differential equations. The number of equations in this set is equal to the number of discrete velocities, and the collision term involves a double summation over the velocity points. The solution of this set is a formidable task and applications have been limited to simple geometries and simple molecular models.

The number of discrete velocities in some applications of the discrete ordinate method is so small that the method resembles an analytical form of the lattice gas model. On the other hand, some versions of the DSMC method have employed a very large number of discrete velocities (e.g. Goldstein et al. 1989). Gropengiesser et al. (1991) introduced a method called the 'Finite Pointset Method' that employs discretization in both physical and phase space. The relative advantages and disadvantages of continuously distributed and discrete molecular locations and velocities in direct simulation methods will be discussed in the following chapter.

References

- ALLEN, M.P. and TILDESLEY, D.J. (1987). *Computer simulation of liquids*, Oxford University Press.
- ALDER, B.J. and WAINWRIGHT, T.E. (1957). Studies in molecular dynamics, *J. Chem. Phys.* **27**, 1208–1209.
- BIRD, G.A. (1963). Approach to translational equilibrium in a rigid sphere gas, *Phys. Fluids* **6**, 1518–1519.
- BIRD, G.A. (1965). Shock wave structure in a rigid sphere gas, In *Rarefied gas dynamics* (ed. J.H. de Leeuw), Vol. 1, pp. 216–222, Academic Press, New York.
- BIRD, G.A. (1989). Computation of electron density in high altitude re-entry flows, Am. Inst. Aero. And Astro. Paper 89-1882.
- BOON, J.P. (1980). Lattice gas automata: a new approach to the simulation of complex flows, In *Microscopic simulations of complex flows* (ed. M. Mareschal), pp. 25–45, Plenum Press, New York.
- BROADWELL, J.E. (1964). Study of rarefied flow by the discrete velocity method, *J. Fluid Mech.* **19**, 401–414.
- GATIGNOL, R. (1970). Théorie cinétique d'un gaz à répartition discrète de vitesses, *Z. Flugwissenschaften* **18**, 93–97.
- GOLDSTEIN, D., STURTEVANT, B., and BROADWELL, J.E. (1989). Investigation of the motion of discrete-velocity gases, *Prog. in Astro. and Aero.* **118**, 100–117.
- GRO彭GIESSER, F., NEUNZERT, H., STRUCKMEIER, J., and WIESEN, B. (1991). Rarefied gas flow around a disc with different angles of attack, In *Rarefied gas dynamics*, (ed. A.E. Beylich), pp 546–553, VCH, Weinheim.

- HAMMERSLEY, J.M. and HANDSCOMB, D.C. (1964). *Monte Carlo methods*, Wiley, New York.
- HAVILAND, J.K. and LAVIN, M.L. (1962). Applications of the Monte Carlo method to heat transfer in a rarefied gas, *Phys. Fluids* **5**, 1399-1405.
- HICKS, B.L., YEN, S-M, and REILLY, B.J. (1972). The internal structure of shock waves, *J. Fluid Mech.* **53**, 85-112.
- LONG, L.N., COOPERSMITH, R.M., and MCLACHLAN, B.G. (1987). Cellular automatons applied to gas dynamics problems, Am. Inst. of Aero. And Astro., Paper 87-1384.
- MEIBURG, E. (1986). Comparison of the molecular dynamics method and the direct simulation technique for flows around simple geometries, *Phys. Fluids* **29**, 3107-3113.
- NADIGA, B.T., BROADWELL, J.E., and STURTEVANT, B. (1989). Study of a multispeed cellular automaton, *Prog. in Astro. and Aero.* **118**, 155-170.
- NORDSIECK, A. and HICKS, B.L. (1967). Monte Carlo evaluation of the Boltzmann collision integral, In *Rarefied gas dynamics*, (ed. C.L. Brundin), pp. 675-710, Academic Press, New York.
- SUGIMURA, T. and VOGENITZ, F.W. (1975). Monte Carlo simulation of ion collection by rocket-borne mass spectrometer, *J. Geophys. Res.* **80**, 673-684.
- TAN, Z., CHEN, Y-K, VARGHESE, P.L., and HOWELL, J.R. (1989). New numerical strategy to evaluate the collision integral of the Boltzmann equation, *Prog. in Astro. and Aero.* **118**, 359-373.
- TCHEREMISSINE, F.G. (1973). *Dokl. Akad. Nauk SSSR* **209**, 811-814.
- TCHEREMISSINE, F.G. (1991). Fast solutions of the Boltzmann equation, In *Rarefied gas dynamics*, (ed. A.E. Beylich), pp 273-284, VCH, Weinheim.
- YEN, S-M., (1970). Monte Carlo solutions of nonlinear Boltzmann equation for problems of heat transfer in rarefied gases. *Int. J. Heat Mass Transfer* **14**, 1865-69.

10

GENERAL ISSUES RELATED TO DIRECT SIMULATIONS

10.1 Introduction

The remaining chapters of this book are concerned with the detailed procedures of the DSMC method, the implementation of these procedures through demonstration programs, and the verification and illustration of the method through the results from these programs. The recommended DSMC procedures have evolved over a considerable period of time and this developmental process will continue. Alternative procedures are available for most aspects of the simulation, and there may be some argument over the best choice for particular applications. The issues that relate directly to the procedures will be dealt with as they arise in the chapters that follow. However, there are a number of general issues that are relevant to all direct simulation methods, and these are best discussed prior to the presentation and implementation of the DSMC algorithms.

10.2 The relationship to the Boltzmann equation

The Boltzmann equation dates from 1872 and, for the first ninety years from that date, theoretical advances in all regimes of fluid mechanics were based on the mathematical analysis of the relevant equations. Digital computers became generally available around 1960, and this introduced the capability for making direct physical simulations of gas flows without any recourse to the conventional mathematical models of the flow. However, the mathematical tradition in fluid mechanics was such that there were difficulties in gaining acceptance for the simulation methods. Tradition remains strong in some quarters and, in these, a numerical solution of the approximate mathematical model that is provided by the Boltzmann equation would be valued more highly than the results from a physical simulation that did not make the approximations that are inherent to the Boltzmann model. While progress has been made in methods for the direct numerical solution of the Boltzmann equation, it is clear that solutions are more readily obtained through direct simulation. The relative advantage of the simulation methods increases with the complexity of the flow and, for most cases of engineering interest, there is no practical alternative to direct simulation. Nevertheless, the simulation methods continue to suffer criticism for having a physical rather than a mathematical foundation.

In reply to this criticism, it can be pointed out that the Boltzmann equation was not 'handed down carved in stone'. It was derived through physical reasoning that is very close to that behind the DSMC procedures. As noted earlier, the assumptions of molecular chaos and a dilute gas are required by both the Boltzmann formulation and the DSMC method, and the major difference between them is that the DSMC method does not depend on the existence of inverse collisions. It has been shown (Bird 1970) that the Boltzmann equation can be derived through the DSMC procedures. While this derivation was based on the now obsolete 'time-counter' procedure for collision sampling, the new procedures (see §11.1) are even closer to classic kinetic theory. The DSMC method is, therefore, as soundly based as the Boltzmann equation itself. Moreover, because it does not rely on inverse collisions, it can be applied to complex phenomena such as ternary chemical reactions that are inaccessible to the Boltzmann formulation.

Just as there are computational approximations associated with direct numerical solutions of the Boltzmann equation, there are computational approximations inherent in the DSMC. These are discussed in §10.5 and relate primarily to the number of simulated molecules and the finite intervals in space and time. It is these computational approximations, rather than the actual simulation procedures, that introduce the need for test cases to verify the method. While these test cases deal with particular flow configurations, the DSMC procedures are general. In addition, there are physical approximations associated with the molecular models and boundary interactions. With regard to these, it is much easier to introduce more complex and accurate models into the direct simulation environment than into the formal Boltzmann solutions.

The MD method is most appropriately used to study dense gas effects near the critical point. The Boltzmann equation is not valid for dense gases, and there is no equation that can be put in its place. To limit direct simulation objectives to a solution of the Boltzmann equation is unduly restrictive. The MD method was more readily accepted than the DSMC method, and it is probable that this was partly due to the absence of an accepted mathematical model at the particle level for dense gases and liquids. Another probable reason for this more ready acceptance is that the MD method is largely deterministic.

Given the physical basis of the DSMC method, the existence, uniqueness, and convergence issues that are important in the traditional mathematical analysis of equations, are largely irrelevant. At the same time, some people would obviously find it comforting if it was possible to construct an analytical representation of all of the procedures of the method, such that this representation did allow formal proofs of existence, uniqueness, and convergence. Unfortunately, the attempts to do this have generally proved to be inimical to the quality of the simulation. A problem that is common to all of these attempts is that many of the important practical details, such as the use of sub-cells, are extremely difficult to incorporate into an analytical model. Conditional steps, such as the action that is taken with

regard to collisions when there are just one or two molecules in a cell, pose even greater difficulties. In addition, some of the probabilistic aspects of the DSMC method, such as the undesirable introduction of random walk effects, appear to have posed insuperable difficulties and, while they may be present in the simulation, they are absent from the analytical representations. Finally, the procedures for physical effects such as chemical reactions and thermal radiation are sufficiently complex to be beyond any possible analytical representation. Any requirement for such a representation is an avoidable constraint that tends to inhibit the development of optimal simulation procedures.

Nanbu (1980) introduced a variation of the DSMC method that was derived directly from the Boltzmann equation, and a convergence proof for it has been presented by Babovsky and Illner (1989). Since the dependent variable in the Boltzmann equation is the velocity distribution function for a single molecule, the Nanbu procedures alter the velocity for only one of the two molecules that are involved in each collision. This is clearly physically inconsistent with a real gas, and has the obvious disadvantage that twice as many collisions must be calculated. More seriously, there is no longer exact momentum and energy conservation in each collision and, while they are conserved on the average, there will be random walks in these quantities at each collision. Random walks, which are discussed more fully in §10.4, degrade the results for large perturbation problems and can render useless the results for flows with small perturbations. The 'Finite Pointset Method' (Gropengiesser et al. 1991) is another variant of the DSMC method that is claimed to be directly related to the Boltzmann equation. Both the location and velocity of the simulated molecules appear to be rounded to a finite number of points at predetermined locations in phase space. The scatter in the results seems higher than would normally be expected for DSMC calculations of similar magnitude, and the most probable explanation for this is that the rounding procedure also leads to random walks.

10.3 Normalized or dimensioned variables

Basic physical data is always presented in a dimensioned form, but the results from experiments are generally expressed in a dimensionless form. The latter is particularly desirable when the dimensionless parameters are those that can be used to correlate the data from many different experiments. In analytical work, the basic equations are often transformed into a dimensionless form so that the results are automatically in the most general form. The early applications of the DSMC method were to basic flows and employed the unrealistic hard sphere molecular model. This meant that the results could not be compared directly with experimental values, but could be readily expressed in terms of the dimensionless parameters. The desired comparison with experiment could then be made by matching the dimensionless parameters. The Knudsen number is the most important parameter for rarefied gas flows, and this was specified as

one of the data items. There was then a strong case for expressing the rest of the data in a dimensionless or normalized form.

The programs in the earlier exposition (Bird 1976a) of the DSMC method employed normalised variables, but a number of problems became apparent over the years. One was that some readers had more difficulty in understanding the normalization procedures than they had with the other DSMC procedures. More seriously, some of the normalization procedures gave a misleading impression of the basis of the method. In particular, the specified mean free path was obtained through the setting of a 'cross-section' variable that was proportional to the number of simulated molecules. Like the diameter in the MD method, the diameter based on this variable was almost always many orders of magnitude larger than the real molecular diameter. This apparent size was of no significance in the DSMC method, because it was used only to allow for the comparatively small number of the simulated molecules when setting the collision rate. It is preferable to specify the number of molecules that are represented by each simulated molecule as a distinct parameter, and to employ the real gas cross-section when setting the collision rate. A further problem is that it is not possible to obtain a closed form expression for the mean free path in a mixture of VHS or VSS molecules and normalization is then extremely difficult. Also, complex flows may include chemical reactions and normalization then becomes almost impossible.

An additional factor is that most DSMC calculations are now made in an engineering context or in parallel with experiments. The molecular models are now sufficiently realistic for the simulation results to be compared directly with the measured values. It is therefore desirable for all the variables in the programs to be in a dimensioned form. If dimensionless results are required, the normalization is best applied to the results. This simplifies many of the procedures in that the physical constants, such as the Boltzmann constant, appear explicitly in the programs. The demonstration programs in the following chapters employ dimensioned variables, with SI units used throughout.

10.4 Statistical scatter and random walks

The representation of the extremely large number of real molecules by a relatively small number of simulated molecules means that the DSMC results are subject to a level of statistical scatter that is, in most applications, many orders of magnitude greater than the scatter that is present in the real gas. This scatter can generally be assumed to follow the Poisson distribution, and the standard deviation is of the order of the inverse square root of the sample size. The total number of simulated molecules is generally such that the level of scatter associated with an instantaneous sample is unacceptably large, and a cumulative sample is required. The results are generally based on a time average for a steady flow or an ensemble average for an unsteady flow.

An important point is that the volume of physical space is completely specified only when the flow is three-dimensional. The width of the 'slice' of flow in a two-dimensional flow, or the 'cross-sectional area' of a one-dimensional flow may be assigned in an arbitrary manner. They are usually set to unit value for convenience, and this generally leads to an extremely large value for the number of real molecules that are represented by each simulated molecule. However, the width or cross-section can be set to the extremely small values that correspond to a one-to-one correspondence between the real and simulated molecules. The scatter should then have real physical significance, and this situation has been studied and reported in a number of papers that have been reviewed by Garcia (1990). The initial results (Garcia 1986) showed that the DSMC method exactly reproduced the equilibrium fluctuations and, in a non-equilibrium system, the peak of the measured density-velocity static correlation function was linearly proportional to the temperature gradient, in agreement with theory and light scattering experiments. Later studies (Malek Mansour et al. 1987) showed that the static correlation of the temperature fluctuations was in excellent agreement with the numerical solution of the correlation equations. Comparison was also made (Garcia et al. 1987) of the fluctuations in a Couette flow simulation with the predictions of fluctuating hydrodynamic theory, and the agreement was again very good.

Advantage can be taken of the fact that the simulated molecules almost always represent a much larger number of real molecules to impose uniform rather than random spacing in physical and velocity space between variables in the situations in which it is physically appropriate. DSMC implementations have generally taken advantage of this with regard to the initial locations of the molecules. A so-called 'low discrepancy' variation of the DSMC method was introduced (Babovsky et al. 1989) in which known uniformities were applied to the distributions in all procedures. For example, in the case of VHS molecules, the post-collision direction of the relative velocity in the centre-of-mass frame of reference is uniformly distributed in space. Therefore, for all the collisions in a cell during a particular time step, these directions could be spread out as evenly as possible in space. One option for doing this is through the replacement of completely random sequences by quasi-random or low discrepancy sequences (Kuipers and Niederreiter 1976). Morokoff and Caflisch (1991) have shown that the gains from these procedures are very small unless the instantaneous sample population of the distribution is sufficiently large to provide a reasonable representation of that distribution. Unfortunately, most of the distributions that involve molecular velocities are multi-dimensional in velocity space and deal with a small sample population at each time step. Systematic variance reduction has not been demonstrated for the DSMC method. However, it was shown in §7.7 that some degree of variance reduction can be obtained when this principle is applied to the much larger samples that can be employed in the test particle Monte Carlo method for collisionless flows.

As noted above, the statistical fluctuations decline with the square root of the sample size and it should be possible to achieve any desired level of accuracy by continuing or repeating the simulation to build up the size of the sample to the required magnitude. The gradual approach of a sampled quantity to its correct value is sometimes referred to as 'convergence'. This is undesirable because the progressive reduction in statistical scatter is a completely different process to that commonly referred to as 'convergence' in the conventional CFD methods.

Some implementations have produced results in which the scatter fails to decline beyond a certain level, or may even increase with time. This behaviour has been found to be due to simulation procedures that allow a random walk in one or more of the variables. One characteristic of a random walk is that the displacement from the mean position or value *increases* with the square root of time. This displacement may cause an output variable to either increase or decrease, and the mean time between zero crossings also increases with the square root of time.

Random walks can arise whenever one of the molecular quantities are conserved only on the average, rather than exactly, in any of the simulation procedures. The molecular quantities are the position coordinates, the velocity components, and the internal energies. The random walk due to the 'Nanbu procedure' has already been discussed in §10.2. The application of species based *weighting factors* leads to similar random walks. Such weighting factors have been used when dealing with trace species, because these would be represented by a very small sample if the number of real molecules represented by each simulated molecule was the same for each species. The sample of the trace species is increased if each of the simulated molecules of this species represents fewer real molecules than those of the dominant species, and this difference is termed a weighting factor. However, in a collision between molecules with different weights, the properties of the molecules of the species with the higher weight must be changed in only some of the collisions. Momentum and energy are then not conserved exactly in each collision, but only in the average, and each departure from exact conservation is effectively a random walk in that quantity. The deviation due to the random walk can more than outweigh the reduced scatter in the trace gas properties due to the increased sample, and the use of species based weighting factors is no longer recommended.

Random walks also arise when the position coordinates or the velocity components are rounded-off in order to be stored as discrete values rather than as exact numbers. The motivation for this can be to reduce the memory storage requirements by 'packing' the coordinates and velocity components into integers. The discrete ordinate methods generally avoid this problem with regard to the velocity components by restricting the collisions to a discrete and pre-determined number that exactly conserve momentum and energy. This ceases to be possible when the internal energy modes are included. There does not appear to be any way of avoiding random walks when position coordinates are rounded to discrete values, even when there are an extremely large number of available sites.

Because of the limited precision with which variables are manipulated and stored in computers, some degree of rounding is unavoidable. This means that are always random walks, albeit with a very small step length, even when the logic is 'exact'. This effect was investigated by monitoring the total energy in a DSMC simulation of a uniform gas with a fixed sample of 1,000 molecules. After 50,000,000 collisions (or 100,000 per molecule) with a 32 bit word length, the total energy was found to change by no more than three parts in a thousand. This indicates that the unavoidable random walks are of acceptable magnitude.

The unavoidable statistical scatter, and the fact that it declines only as the square root of the sample size, has been a major problem for the DSMC method. The magnitude of the computational task meant that, for many years, the method was thought to be applicable only to problems that involve large perturbations. For example, the scatter applies to the molecular velocity components so that, in a problem that involves low subsonic stream velocities, the statistical 'noise' could be at least an order of magnitude greater than the required 'signal'. The reduction in the cost of computing has meant that it is now possible, at least for one-dimensional flows, to deal with time or ensemble averages in the millions, and the scatter is then reduced to less than one part in a thousand. A weak disturbance can be completely lost in the scatter in an instantaneous sample or during the earlier stages of a simulation but, as long as the procedures are such that random walks are precluded, it emerges correctly as the average builds up.

10.5 Computational approximations

The computational approximations associated with the DSMC method are the ratio of the number of simulated molecules to the number of real molecules, the time step over which the molecular motion and collisions are uncoupled, and the finite cell and sub-cell sizes in physical space.

The first approximation leads to the statistical scatter, as discussed in the preceding section, but there does not seem to be any value of this ratio at which the fluctuations change their nature or become unstable. It is possible to argue qualitatively that fluctuations may become unstable in some flow configurations. For example, consider a region within the bow wave in a low-density hypersonic shock layer. A positive fluctuation in density would lead to more collisions with the oncoming freestream molecules in this region, and the positive fluctuation would be expected to be reinforced. However, there have been many simulations of this class of flow and these have shown that the fluctuations are stable. This is an empirical result and it would be desirable to have an analytical proof of this stability. The fact that the scatter, when it does have physical significance, is consistent with the analytical predictions provides some reassurance.

The most serious statistical problem is when a significant effect in the real gas is a consequence of the few molecules towards the extremes of the

distribution. The number of simulated molecules may be so small in comparison with the real molecules that the important part of the distribution may not be adequately populated. This problem generally arises in connection with chemical reactions or thermal radiation. A solution in the latter case is to take advantage of the large number of real molecules represented by each simulated molecule and assign a distribution of electronic states, rather than a single state, to each simulated molecule. Of all the flows that have been simulated, the only non-reacting flow that has proved (Bird 1976b) to be sensitive to the number of simulated molecules is the hypersonic flow within a conical molecular beam skimmer. This is because a single molecule that has a sufficiently high velocity normal to the axis to strike the inside of the cone can produce such a large number of similar molecules when reflected back into the beam, that the hypersonic beam breaks down to a subsonic flow. The time to breakdown is much longer in the simulated flow than in the real flow. Note that this is essentially a physical effect, albeit a spurious one, that is predictable from the statistics.

The DSMC simulation becomes more exact as the time step and cell size tend to zero. It should be noted that disturbances can propagate at the sound or shock wave speed even though the ratio of the cell size to the time step may be much smaller than this ratio. There is, therefore, no stability criterion that is analogous to the Courant condition for finite difference methods in continuum CFD. During the early stages of the development of the method, some concern was expressed (Bird 1976a) about large values of this ratio. This was because the relative locations of the molecules in the cell were disregarded when choosing potential collision pairs. It was feared that coincidental collisions between molecules at opposite sides of the cells, coupled with the immediate migration of these molecules to the next cell, might cause false disturbances to propagate with speed equal to the ratio of the cell size to the time step. In practice this ratio has been set to many times the speed of the sound or shock waves and there has been no sign of false disturbances. This is presumably because the predicted disturbances relied on continuance of unlikely coincidences. In any case, the recent adoption of sub-cells, as described below, has significantly reduced the scope for any such effects.

The DSMC method originally regarded the molecules in a cell as a representative sample of those in the real gas at the location of the cell. Then, as noted above, the relative positions of the molecules within the cell were disregarded when choosing potential collision pairs. Meiburg (1986) pointed out that if there is a velocity gradient across a cell, the choice of a collision pair from opposite sides of the cell can, when coupled with an adverse set of randomly selected impact parameters, actually reverse the portion of the systematic gradient that is represented by the pre-collision velocities of that pair. This particularly adverse case is unlikely, and it would have been more accurate to say that the collisions tend to reduce the vorticity within the cell. One could reply that most CFD methods do not allow vorticity *within* a cell and the vorticity can only be represented by

the velocity gradients *between* cells. To the extent that the DSMC method retains any vorticity in a cell, it is an improvement on most CFD methods. Fortunately, it is possible to do very much better through the introduction of sub-cells that cause all collisions to be between near neighbours. The DSMC procedures include an optimally efficient indexing scheme to allow pairs within a particular cell to be selected from an unsorted array of molecules. This has been extended to allow the choice to be from sub-cells that are formed by very small subdivisions of the cells. The use of sub-cells involves a negligible computational overhead, and the DSMC method has now been shown to provide an excellent representation of vortical flows. In fact, the original version is capable of providing good results for such flows, and Meiburg's contrary conclusions were based on a calculation with a cell size that was an order of magnitude larger than the recommended size.

The linear dimensions of the cells should be small in comparison with the scale length of the macroscopic flow gradients in the direction in which the dimension is measured. In regions with large macroscopic gradients, this generally means that the cell dimension should be of the order of one third the local mean free path. The time step should be much less than the local mean collision time. These guidelines will be subject to critical review in some of the examples in the following chapters.

In addition, both obvious and subtle errors can arise from the inescapable imperfections of computer arithmetic. These 'numerical artefacts' are discussed in Appendix E.

References

- BABOVSKY, H., GROPENGIESSER, F., NEUNZERT, H., STRUCKMEIER, J. and WIESEN, B. (1989). Low-discrepancy method for the Boltzmann equation, *Prog. in Astro. and Aero.* **118**, 85–99.
- BABOVSKY, H. and ILLNER, R. (1989). A convergence proof for Nanbu's simulation method for the full Boltzmann equation, *SIAM J. Num. Anal.* **26**, 45–65.
- BIRD, G.A. (1976a). *Molecular gas dynamics*, Oxford University Press.
- BIRD, G.A. (1976b). Transition regime behaviour of supersonic beam skimmers, *Phys. Fluids* **19**, 1486–1491.
- BIRD, G.A. (1970). Direct Simulation of the Boltzmann Equation, *Phys. Fluids* **13**, 2676–2681.
- GARCIA, A.L. (1990). Hydrodynamic fluctuations and the direct simulation Monte Carlo method. In *Microscopic simulations of complex flows*, (ed. M. Mareschal), pp 177–188, Plenum Press, New York.
- GARCIA, A. (1986). Nonequilibrium fluctuations studied by a rarefied-gas simulation. *Phys. Rev. A* **34**, 1454–1457.
- GARCIA, A.L., MALEK MANSOUR, M., LIE, G.C., MARESCHAL, M., and CLEMENTI, E. (1987). Hydrodynamic fluctuations in a dilute gas under shear, *Phys. Rev. A* **36**, 4348–4355.
- GROPENGIESSER, F., NEUNZERT, H., STRUCKMEIER, J., and WIESEN, B. (1991). Rarefied gas flow around a disc with different angles of attack, In *Rarefied gas dynamics*, (ed. A.E. Beylich), pp 546–553, VCH, Weinheim.

- KUIPERS, L. and NIEDERREITER, H. (1976). *Uniform distribution of sequences*, Wiley, New York.
- MALEK MANSOUR, M., GARCIA, A.L., LIE, G.C., and CLEMENTI, E. (1987). Fluctuating hydrodynamics in a dilute gas, *Phys. Rev. Letters* **58**, 874-877.
- MEIBURG, E. (1986). Comparison of the Molecular Dynamics method and the direct simulation technique for flows around simple geometries, *Phys. Fluids* **29**, 3107-3113.
- MOROKOFF, W.J. and CAFLISCH, R.E. (1991) A quasi-Monte Carlo approach to particle simulation of the heat equation, UCLA Computational and Applied Mathematics Report 91-13.
- NANBU, K. (1980). Direct simulation scheme derived from the Boltzmann equation. I. Multicomponent gases, *J. Phys. Soc. of Japan* **45**, 2042-2049.

11

DSMC PROCEDURES IN A HOMOGENEOUS GAS

11.1 Collision sampling techniques

The DSMC procedures for the simulation of a representative set of inter-molecular collisions are best derived and demonstrated in the context of a homogeneous or 'zero-dimensional' gas. However, in order to make the procedures directly useful as subroutines in the later programs, the homogeneous gas is divided into a one-dimensional structure of cells and sub-cells. This also permits the testing of the procedures for any effects due to the number of molecules per cell or sub-cell. The procedures for the establishment of the correct collision rate are based on the cells, while individual collision pairs are chosen from the sub-cells.

The probability of a collision between two molecules in a homogeneous gas is proportional to the product of their relative speed c_r and total collision cross-section σ_T . Eqn (1.11) for the non-equilibrium collision rate in a homogeneous gas could be used to establish the number $N_c \Delta t$ of collisions in each cell at each time step of duration Δt , and this number could then be computed. The mean value of the product of c_r and σ_T is calculated for each cell, and the maximum value could also be recorded. The collision pairs could then be chosen by the acceptance-rejection method, with the probability of a particular pair being given by the ratio of their product of c_r and σ_T to the maximum product. However, this procedure would have a computation time proportional to the square of the total number of molecules in the cell.

The so-called 'time-counter' or TC method was therefore introduced (see, for example, Bird 1976) in order to obtain a computation time directly proportional to the number of molecules. This involved the calculation of representative collisions and, at each collision, a time parameter in each cell was advanced by the amount appropriate to that collision. The process was repeated until the cell time caught up with the flow time. This process had the optimal computational efficiency, and it was shown analytically that it led to the correct non-equilibrium collision rate. However, in extreme non-equilibrium situations such as the leading edge of extremely strong shock waves, there were problems due to correlations between the probability and the spacing of the collisions in time. The occasional acceptance of a collision pair with a small collision probability could result in the cell time being advanced by such a large interval that no other collisions could be computed for a number of time steps. A number of

alternative schemes have been proposed and some of these (for example, Koura 1986) involve only a small time penalty. However, the programs in this book employ a scheme called the NTC method (Bird 1989) which completely avoids the problems with the TC method without any loss of computational efficiency. It has the further advantage that the number of pair selections is determined in advance of the entry to the collision coding, rather than within this coding when the cell time reaches the flow time. This allows easy vectorization of the collision procedure.

Consider a DSMC cell of volume V_C in which each simulated molecule represents F_N real molecules. The probability P of collision between two simulated molecules over the time interval Δt is equal to the ratio of the volume swept out by their total cross-section moving at the relative speed between them to the volume of the cell, i.e.

$$P = F_N \sigma_T c_r \Delta t / V_C. \quad (11.1)$$

The relative speed varies with the choice of the collision pair and the total cross-section is generally a function of the relative speed, but the other quantities in eqn (11.1) are independent of this choice. The average number of real molecules in the cell is nV_C and the average number of simulated molecules is $N = nV_C/F_N$, where n is the number density in the real gas. The full set of collisions could be calculated by selecting, in turn, all $N(N-1)/2$ pairs in the cell and by computing the collisions with probability P . This method has been used in DSMC simulations, but is inefficient because P is generally a very small quantity and the number of choices is very nearly proportional to the square of the number of molecules. Also, since F_N is an extremely large number, the number of choices should be $N^2/2$, and this error becomes significant for small values of N . The procedure can be made more efficient and the second difficulty removed if only a fraction of the pairs are included and the resultant probability increased by dividing eqn (11.1) by this fraction. Maximum efficiency is achieved if the fraction is such that the maximum probability becomes unity. The fraction is then given by

$$P_{\max} = F_N (\sigma_T c_r)_{\max} \Delta t / V_C, \quad (11.2)$$

and the number of pair selections per time step is obtained by multiplying this equation by $N^2/2$. However, in most cases, N is a fluctuating quantity and, because the mean of the square differs from the square of the mean, N^2 should be replaced by the product of the instantaneous value and a time or ensemble averaged value. Therefore, the NTC method is that

$$\frac{1}{2} N \bar{N} F_N (\sigma_T c_r)_{\max} \Delta t / V_C \quad (11.3)$$

pairs are *selected* from the cell at the time step, and the collision is computed with probability

$$\frac{\sigma_T c_r}{(\sigma_T c_r)_{\max}}. \quad (11.4)$$

Note that, if N is doubled through halving F_N , the number of pair selections also doubles, so that the computing time is linear with N . The parameter $(\sigma_T c_r)_{\max}$ should be stored for each cell and is best set initially to a reasonably large value, but with provision for it to be automatically updated if a larger value is encountered during the sampling. Note that this parameter occurs in the numerator of eqn (11.3) and the denominator of eqn (11.4), so that the rate is not affected by its exact value. Within the statistical scatter, the NTC method yields the exact collision rate in both simple gases and gas mixtures, and under either equilibrium or non-equilibrium conditions.

In the case of a gas mixture, the procedures are species independent and the NTC method is best applied to all the molecules as a single group. However, a practical problem arises when there is a very large variation in the molecular masses. This is because the collisions that involve the light molecules will have high values of the relative speed and, since these will set the value of $(\sigma_T c_r)_{\max}$, the acceptance rate for the heavy molecules will be low, and the overall selection process will be inefficient. The method can be applied separately to the species and, for a collision between a species p and a species q molecule, eqns (11.3) and (11.4) can be written

$$\frac{1}{2} N_p \bar{N}_q F_N \{(\sigma_T c_r)_{\max}\}_{pq} \Delta t / V_C \quad (11.5)$$

and

$$\frac{\sigma_T c_r}{\{(\sigma_T c_r)_{\max}\}_{pq}}, \quad (11.6)$$

respectively. This causes a storage problem when there are a large number of species in that two variables, that are doubly subscripted with respect to the total number of species, must be defined for each sub-cell. The solution is to split the molecules into several groups and to regard p and q as defining groups of species rather than a single species.

11.2 Collision test programs

A FORTRAN 77 program, called DSMC0.FOR, has been written to test the NTC procedure in a homogeneous gas mixture. The number of simulated molecules per cell is an important factor in assessing the performance of a collision scheme so that, although the gas is uniform, it is divided into a set of cells and sub-cells. The geometry is a one-dimensional gas of unit cross-section between two plane specularly reflecting walls that are normal to the x -axis. The overall structure of the demonstration programs is illustrated by the listing of program DSMC0S.FOR in Appendix G.

The only variables that are at the disposal of the user are those in the PARAMETER statement that set the dimensions of the subscripted variables, and those in subroutine DATA0 that set the data for a particular run of the program. The subroutine that sets the data will always be listed as the final subroutine in a program. The main program contains an inner

loop over the number NIS of time steps between flow samples and a second loop over the number NSP of samples between the updating of the restart file DSMC0.RES and the output file DSMC0.OUT. The program stops after NPT update cycles have been completed. Apart from these loops, the main program calls subroutines that are, as far as possible, standardized for inclusion in other programs.

The first subroutine is named INIT0, and is called whenever a new run is started by entering '1' when the program requests a code for a continuing or new calculation. This subroutine sets the physical constants and then calls the data subroutine. The data is limited, in this case, to information on the individual species, and this is converted to the fuller information on all classes of collision. The flowfield is divided into MNC cells of uniform width CW, and each of these is divided into NSC equal width sub-cells. Finally, the required random locations and velocity components of the initial state of the gas are set. Because the flow is one-dimensional, only the x -coordinate is stored for each molecule. All positions are equally likely on the plane normal to the x -axis. Note that all three velocity components are stored, and the collisions are computed as three-dimensional events. The second subroutine SAMPIO initialises the sampling variables.

Subroutine MOVE0 moves the molecules through distances appropriate to the time interval DTM. Apart from the specular reflections from the end walls at $x = XF$ and $x = XR$, the procedures are trivial. Specular reflection reverses the velocity component normal to the surface, while those parallel to the surface are unchanged. The final position of a molecule that strikes a surface normal to the x -axis at x_c and would have moved to x' beyond it is given by

$$x_c - x = x' - x_c,$$

or

$$x = 2x_c - x'. \quad (11.7)$$

Subroutine INDEX sorts the molecule numbers in the one-dimensional array IR into the order of the groups and, within a group into the order of the cells. Finally, within the cell, it arranges them in the order of the sub-cells. This sorting procedure employs multi-level linked lists and the computation time is directly proportional to the total number of molecules. The cross-reference array permits the efficient selection of pairs of molecules from the same group of species and from the same, or the nearest possible, sub-cell as potential collision pairs.

The NTC method is employed in subroutine COLLM to determine the appropriate set of collisions. This includes subroutines SELECT for the selection of representative collision pairs and ELASTIC for the computation of the collision. The comment statements refer to the equations on which the coding is based. The selection of the post-collision components of the relative velocity in the centre of mass frame of reference in subroutine ELASTIC requires further discussion. The deflection angle of c_r for the VSS model in this frame of reference is given by eqn (2.36), i.e.

$$\cos(\chi/2) = (b/d)^{1/\alpha},$$

where the diameter d is the effective diameter for collisions between the two molecules. Therefore,

$$\cos\chi = 2\{(b/d)^2\}^{1/\alpha} - 1,$$

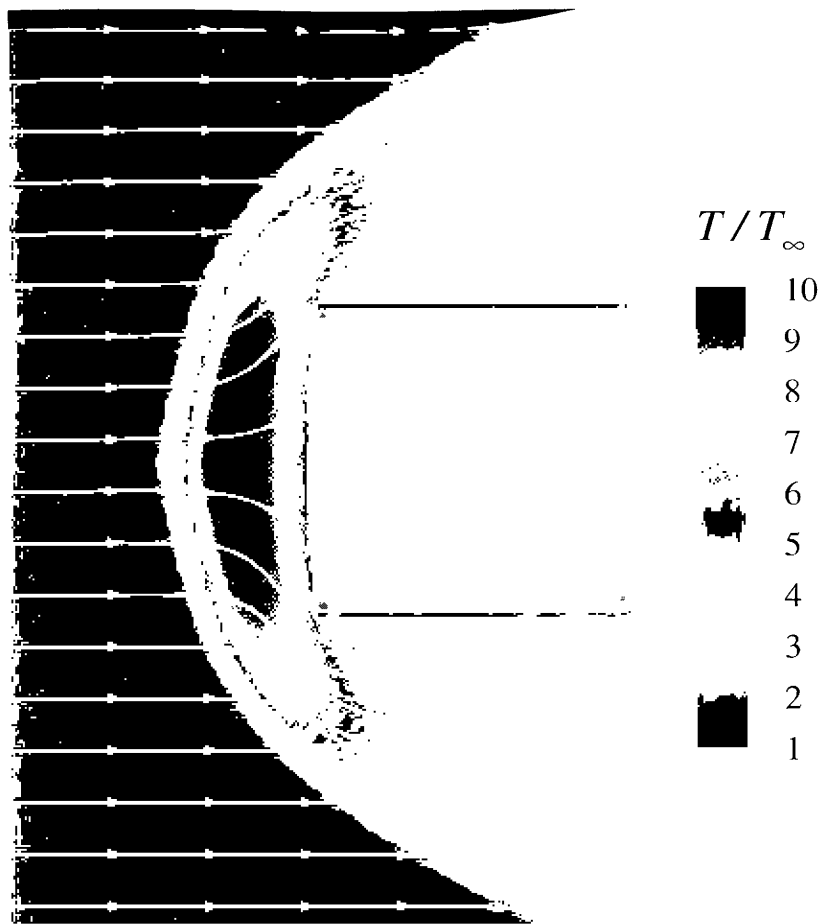
and the square of the ratio of the impact parameter b to d is uniformly distributed between 0 and 1. This distribution is that of the random fraction itself, so that the selection rule can be written

$$\cos\chi = 2R_f^{1/\alpha} - 1. \quad (11.8)$$

For the VHS model, $\alpha=1$, and all directions are equally probable for the post-collision direction of the relative velocity. Advantage may be taken of this to replace χ in eqn (11.6) by an elevation angle θ , and an azimuth angle ϕ may be chosen from a uniform distribution between 0 and 2π . The three post-collision components of the relative velocity are then given by multiplying the relative speed by $\cos\theta$, $\sin\theta\cos\phi$, and $\sin\theta\sin\phi$. The VSS model requires the computation of the post-collision relative velocity components through the far more complex relations of eqn (2.22). Should the scattering parameter α be very close to unity, the VHS logic is applied in place of the VSS logic.

Both the indexing subroutine INDEX and the collision subroutine COLLM have been greatly complicated by the inclusion of the molecular groups that are, as explained above, required only in the case of gas mixtures with large mass differences. As well as making the programs more difficult to read, this complication involves a computational overhead of several percent. However, while this program is only for the testing of the collision procedures, the aim is to develop general subroutines that are capable of handling all applications of the DSMC method. The simpler procedures for a simple gas are illustrated in the program DSMC0S.FOR.

The flow properties in each cell are sampled within the subroutine SAMPLE, and the output file DSMC1.OUT is updated in the subroutine OUT0. The latter subroutine employs the definitions of the macroscopic properties that have been given in the earlier chapters, and the equations are identified in the comments. Double precision is used for variables such as the total number of collisions that are expected to be advanced beyond the limit of single precision arithmetic (see Appendix E). The operation of the indexing and collision selection procedures was tested through sampling the mean separation of the molecules in collisions. With an average of 2.5 molecules in each sub-cell and with all the molecular species in a single group, the mean spacing was found to be just under 40% of the sub-cell width. This means that the sampled collisions are close to the ideal of all collisions being between nearest neighbours. In addition, the acceptance rate of the collision pairs in eqn (11.4) was sampled. The maximum value of the product of the relative speed and cross-section was initially set to the product of the reference cross-section of the most prevalent combination of



late 1 Stream ines and temperature contours in the flow of argon at a
ac number of 5.37 past a flat-nosed cylinder. The Knudsen number
sed on the d'ameter of the cylinder is 0.016 and the calcu ation is
herw'se s'milar to the case discussed in §15.3.

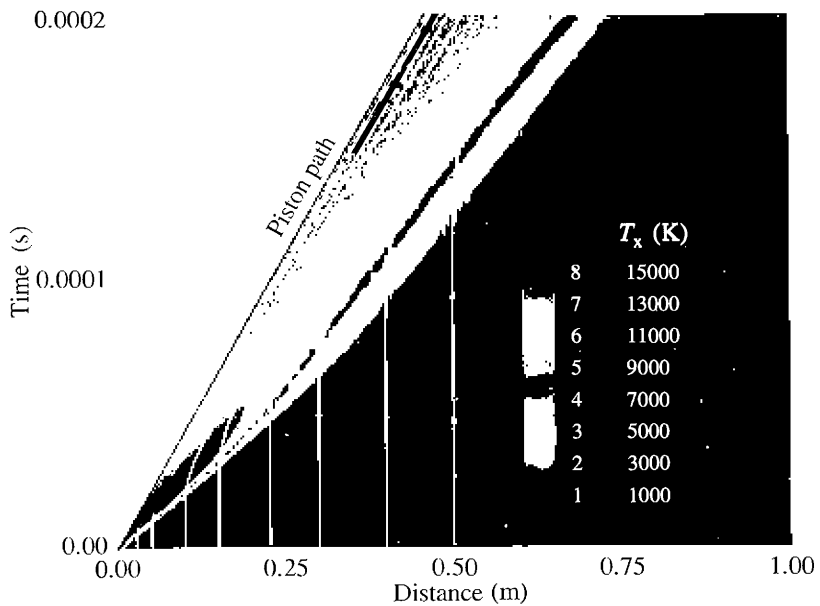


Plate 2 Particle paths and contours of parallel temperature in the formation of a shock of $(Ma)_S = 10$ in a monatomic gas with a undisturbed mean free path of 0.0129 m. Further details are presented in §13.2.

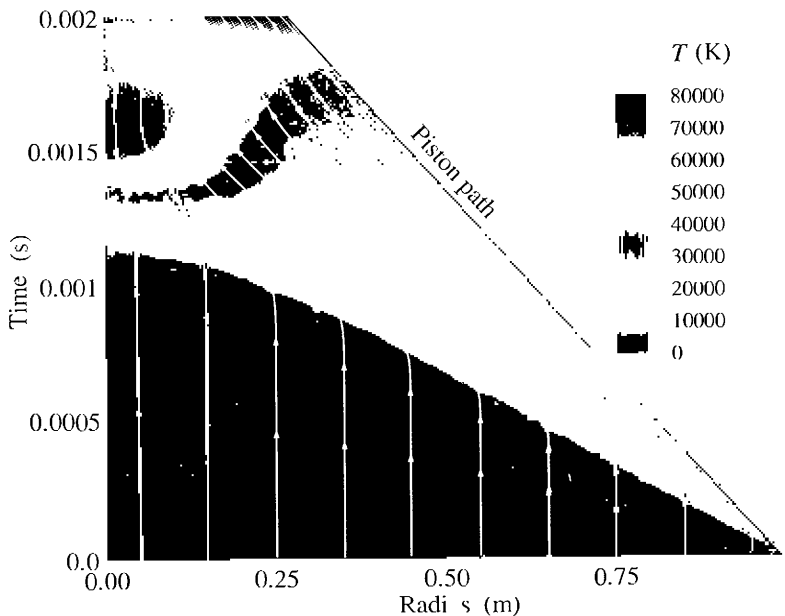


Plate 3 Particle paths and temperature contours in the spherically imploding shock wave from a spherical piston moving at 2285.5 ms^{-1} into argon at 273 K. The undisturbed mean free path is 0.0258 m. See §13.5.

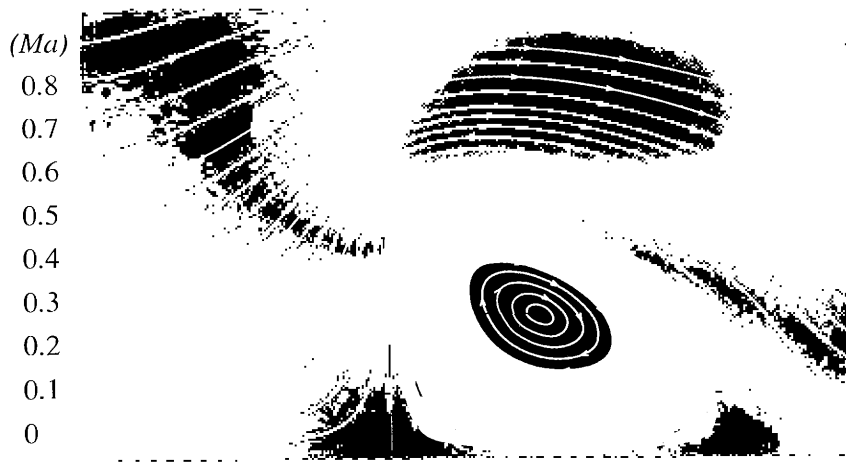


Plate 4 Streamlines and Mach number contours in the flow past a vertical flat plate. This case is for $(Ma) = 0.53$ and $(Kn) = 0.044$. See §14.5.

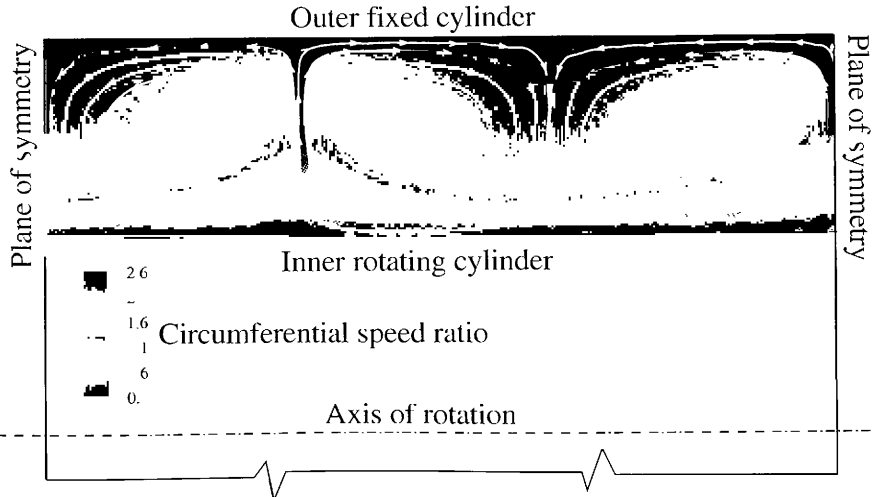


Plate 5 Contours of circumferential speed ratio and streamlines in the 'normal' plane of the Taylor-Couette flow that is discussed in §15.4

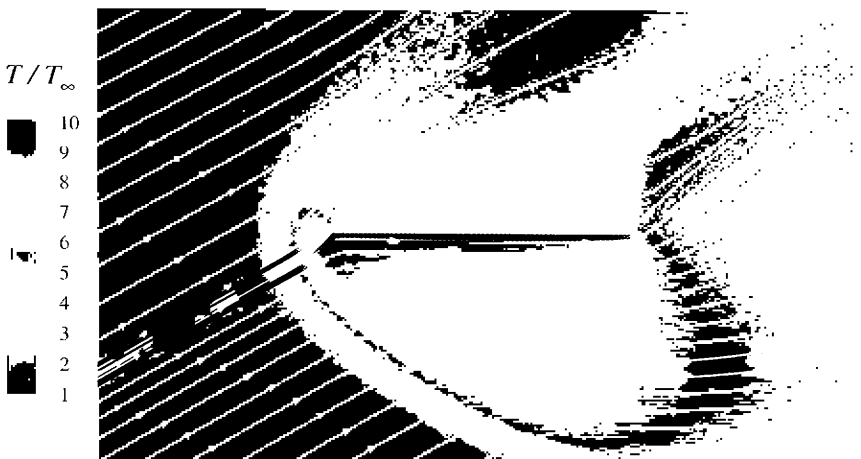


Plate 6 Streamlines and contours of constant temperature in a flow at a Mach number of 5 past a flat plate at an incidence of 30° . The Knudsen number is 0.0324 and the surface reflection is diffuse. See §14.8.



Plate 7 Contours of constant pressure coefficient on the surfaces in a supersonic corner flow with a normal jet from the horizontal surface. Further details are given in §16.4.

these species and 300 ms^{-1} , which approximates to the most probable speed of these molecules at the initial temperature. For the test case data that is described in the following paragraph, the initial acceptance rate was approximately 55%, and this declined to around 45% as the maximum value increased with the occurrence of unlikely collisions with very fast relative speeds. As explained in the preceding section, the collision rate is correct as long as the maximum value is reasonably high, and it is not affected by the gradual growth of the maximum value.

As noted earlier, the data that affects the dimensions of the arrays is set in the PARAMETER statement. The test case employs 1000 molecules (MNM=1000), 50 cells (MNC=50) with eight sub-cells per cell (MNSC=400), and five species (MNSP=5) in a single group (MNSG=1). The remaining variables are set in the DATA0 subroutine. The initial gas has a number density of 10^{20} m^{-3} at a temperature of 300 K. The number fractions of the molecular species range from 0.6 for the most prevalent species to 0.02 for the least prevalent. The flowfield extends in the x -direction from the origin to $x = 1 \text{ m}$, and its cross-section is assumed to be 1 m^2 . Therefore, in order to obtain 1000 molecules, the number of real molecules that are represented by each simulated molecule is set to 10^{17} . The cell width is then 0.02 m and, while this is of the order of the equilibrium mean free path, there are no gradients in the flow and the sub-cell width is small in comparison with the mean free path. A typical molecular velocity component is 200 ms^{-1} , so that a time step of 0.000025 s leads to a typical displacement in the x -direction of 0.005 m. This is 25% of the cell width and this value has been chosen as the time step. The flow is sampled after each fourth time step (this should lead to only a small degree of correlation between successive samples) and the files are updated at intervals of 40 samples. The program stops after 500 file updates. Because this is simply a test of the procedures, the molecular masses and diameters have been set to nominal values that are of the order of those in real gases. In addition, many of the molecular properties that would normally be set to separate values in the data subroutine have been set to common values in the initialization subroutine. The viscosity coefficient is set to 0.75 for all interactions, and the VHS model has been selected through the setting of the scattering parameter to unity.

Because of the relatively small sample of 1000 simulated molecules in this test case, and the fact that the initial velocity components of each molecule are set independently, the overall gas temperature differs from the nominal value. The overall temperature was found to vary by one or two degrees from the nominal value of 300 K. Also, although the gas is nominally at rest, there is a finite velocity due to the scatter. For this sample, the individual velocity components were found to be of the order of five to 10 ms^{-1} .

The total number of collision events counted by the variable NCOL was 17,214,867 and, for each of these, the appropriate values of the doubly subscripted variable COL were advanced by one. The final state of NCOL from a run of DSMC0.FOR with the listed data is shown in Table 11.1.

Table 11.1 Sample size of collisions

Species	1	2	3	4	5
1	17,590,774	6,923,654	3,101,569	2,679,354	712,407
2	6,923,654	2,683,570	1,222,127	1,053,081	277,859
3	3,101,569	1,222,127	504,620	430,004	125,206
4	2,679,354	1,053,081	430,004	357,630	107,509
5	712,407	277,859	125,206	107,509	27,600

Table 11.2 Ratio of the calculated to theoretical collision rates.

Species	1	2	3	4	5
1	0.999384	1.000546	1.001161	1.000897	0.997228
2	1.000546	0.996645	1.002060	1.001812	1.001123
3	1.001161	1.002060	0.993330	0.997551	1.004428
4	1.000897	1.001812	0.997551	0.983847	1.003631
5	0.997228	1.001123	1.004428	1.003631	0.966407

This sampled collision rate is compared in Table 11.2 with the exact analytical result of eqn (4.78) for an equilibrium gas mixture. Apart from the rate for collisions between the trace species (number 5), the collision rates are in excellent agreement with the theoretical values. That for the 5-5 collision is low by about five standard deviations, so that the discrepancy is significant. The average number of molecules per sub-cell is 2.5 so that, if we consider a sub-cell containing a species 5 molecule, the probability that there is another type 5 molecule in the sub-cell is less than one in thirty. Given the adverse statistics for the trace molecules, and the fact that the molecular species was ignored in the selection of potential collision pairs, the results are surprisingly good.

The run was repeated with each species specified as a separate group. Each of the 25 classes of collision was then treated separately with regard to the selection of collision pairs and the establishment of the collision rate. The result for the collision rate is shown in Table 11.3, and the rate for the class 5-5 collisions is now in agreement with the theory. However, since the species of the collision pair is now specified, the selection is generally forced beyond the sub-cell, and the mean spacing between collision pairs (averaged over all species) increased from 0.00098 to 0.00247, which approximates the width of the sub-cell. This increase is undesirable and, in general, it would be preferable to accept the slightly low collision rate for self collisions between the trace species.

Table 11.3 The ratio of collision rate to the theoretical value when each species forms a separate group.

Species	1	2	3	4	5
1	1.001099	1.000952	1.000459	1.001607	1.001462
2	1.000952	1.002584	0.999471	0.999052	0.997745
3	1.000459	0.999471	1.004441	0.998531	0.996351
4	1.001607	0.999052	0.998531	1.002897	0.993467
5	1.001462	0.997745	0.996351	0.993467	1.004225

The specification of separate collision groups for each species also leads to an increase in the computation time, even though the acceptance ratio for collision pairs is higher. The greatest concern with this acceptance ratio is that the maximum value of the product $(\sigma_T c_r)_{\max}$ of the relative speed and collision cross-section may increase during a very long run to such an extent that the selection process becomes unduly inefficient. Therefore, for the case with all molecules in a single group, the mean value of this product over all cells was sampled. The minimum and maximum values in any cell were also recorded and the results are shown in Fig. 11.1. The initial value of the product was set to the excessively low value of $1.155 \times 10^{-16} \text{ m}^3 \text{s}^{-1}$, but it increased during the first few collisions to values that allowed the correct collision rate to be established. The important conclusion from this test is that, even in a long run, the rare very fast collisions do not increase $(\sigma_T c_r)_{\max}$ to the stage where the selection procedure becomes excessively inefficient. The collision rate would be unaffected and the program would be slightly more efficient if the values of $(\sigma_T c_r)_{\max}$ were reset in steady flows to their value at (say) one million collisions at each successive million collisions. This is not done in the demonstration programs, but it is recommended that the collision pair acceptance ratio should be included in the output and be monitored.

In addition to checking that the procedures produce satisfactory results when the computational parameters, such as the number of molecules per cell, have their recommended values, the way in which the simulation breaks down for unreasonable values of these parameters should be investigated. The earlier test cases were therefore rerun with the variable FNUM increased by a factor of ten, so that the number of simulated molecules was reduced to 100. The average number of molecules per cell was then only two, and there was only one molecule to every four sub-cells. Table 11.4, for the case in which all species are in one group, shows that the error in the rate for the 5-5 collisions between trace molecules is now very significant, and there are discrepancies in the rates for the other collisions between the less prevalent species. The mean separation between collision pairs increased to 0.00474 m which is five times worse than the case with an adequate number of molecules per cell.

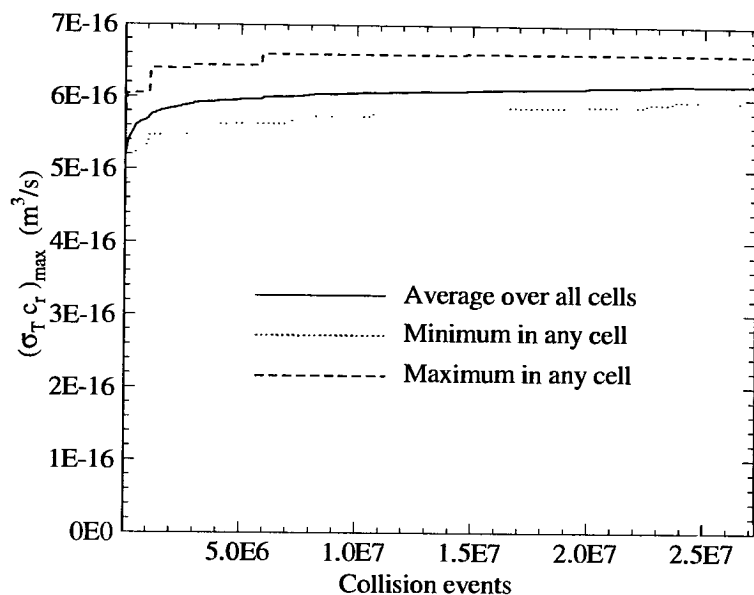


Fig. 11.1 The sampled values of the maximum value of the product of the relative speed and the collision cross-section.

When all species were placed in separate groups, Table 11.5 shows that all collision rates were about two to three percent higher than the theoretical rates. The mean spacing between collision pairs increased to 0.00614 m. Molecular groups can be used to obtain more accurate rates for collisions between trace species, but this is at the cost of increased separations between collision pairs, and is not necessary if the average number of molecules per cell and sub-cell meet the recommended minimum values.

Table 11.4 Comparison with theoretical collision rates with only two molecules per cell and all species in a single group.

Species	1	2	3	4	5
1	0.997301	1.016905	1.036046	1.043018	1.019806
2	1.016905	0.968886	1.033997	1.046500	1.021853
3	1.036046	1.033997	0.952629	1.062859	1.053322
4	1.043018	1.046500	1.062859	0.936944	1.071641
5	1.019806	1.021853	1.053322	1.071641	0.503295

Table 11.5 Comparison with theoretical collision rate with only two molecules per cell and all molecular species in separate groups.

Species	1	2	3	4	5
1	1.025179	1.025466	1.025064	1.025147	1.028721
2	1.025466	1.034196	1.022251	1.022558	1.029195
3	1.025064	1.022251	1.030747	1.021415	1.022737
4	1.025147	1.022558	1.021415	1.025757	1.022754
5	1.028721	1.029195	1.022737	1.022754	1.018747

To illustrate the circumstances in which molecular groups should be used, a calculation was made for a mixture of 10% helium and 90% xenon, by number. The overall number density, the temperature, the number of simulated molecules, and the numbers of cells and sub-cells were the same as in the test case. With a single molecular group, the overall acceptance rate of collision pairs was 26%, but this increased to 46% when each species was regarded as a single group. This led to a 25% reduction in the computing time, but the mean spacing between collision pairs increased by 60%. A large mass ratio such as this is comparatively rare and, even though the reduction in computing time is significant, the case for the inclusion of molecular groups in the standard DSMC routines is marginal. The case for their inclusion does become overwhelming when electrons are present, and this was the critical consideration.

As noted earlier, it is debatable whether there should be alternative routines and programs when dealing with simple gases rather than gas mixtures. A simple gas version of DSMC0.FOR was therefore produced in order to assess the penalty due to the redundant code when the mixture code is applied to a simple gas. This program is listed in Appendix G as DSMC0S.FOR. For the data in subroutine DATA0S, the simple gas program was only 11% faster than the mixture program running the corresponding data. Comparisons of computer time can be compiler dependent, particularly in cases such as this where the redundant loops over molecular species could be removed by an optimizing compiler, but this result indicates that it is not worth maintaining separate programs for simple gases and gas mixtures. The remaining programs will be for the more general case.

The value of the VSS scattering index data in DSMC0S was changed from 1.0 to 1.5 in order to utilize the VSS logic rather than the VHS logic. The increase in the computation time was 12%, which is slightly greater than that due to running the data with the more general mixture program. The acceptance rate of collision pairs in the NTC collision routine was approximately 55% for this simple gas case.

The DSMC procedures are more readily understood at the level of the source code in the simple gas implementation DSMC0S.FOR, rather than in the more general DSMC0.FOR for the gas mixture.

11.3 Rotational relaxation and equilibrium

The program DSMC0R.FOR is an extension of program DSMC0.FOR and introduces an implementation of the Larsen-Borgnakke model for the selection of the appropriate rotational energies of diatomic or polyatomic molecules.

The rotational energy of molecule N is stored as PR(N), and this variable constitutes the named COMMON/MOLSR/. The named COMMON/GASR/ contains the information on the number of rotational degrees of freedom of each gas species and on the relaxation time. There is no reliable and universal theory for the variation of the rotational relaxation rate with relative speed in the collision or with the macroscopic temperature, and provision has been made for the rotational collision number to be specified as a second-order polynomial in the temperature.

The main test case data in subroutine DATA0R is for a simple diatomic gas with a constant rotational relaxation collision number of 5.0. The number of simulated molecules is 100,000 and these are in a single cell and sub-cell. Initially, the translational temperature of the gas is set to 500. and the rotational temperature to zero. The time step is set to about half the mean collision time, and the flow is sampled and the results are output at each step. The gas is assumed to come to equilibrium after 100 time steps or about 50 collisions per molecule. During this relaxation stage, the samples are set to zero at each time step, so that the macroscopic properties represent an instantaneous sample, and a time history of the temperatures is sent to the file RELAX.OUT. After the establishment of steady or equilibrium state, the sample of the macroscopic properties is time averaged.

The Larsen-Borgnakke calculation is in the subroutine INELR which is called in the collision subroutine between the SELECT and ELASTIC subroutines. The first step is to determine whether the rotational energy of either or both of the molecules is to be adjusted. The probability with which the rotational energy of a molecule is to be changed is equal to the reciprocal of the relaxation collision number Λ . This is used to set the indicator IRL to 0 if the rotational energy of molecule L is regarded as 'inelastic' and subject to change, or to 1 if it is 'elastic' and is not to be changed. The indicator IRM for molecule M is set in a similar manner. The variable ECC is set to the total energy that is to be divided, and this will be referred to as the 'available energy' for the Larsen-Borgnakke redistribution of energy. This loop over the two molecules also sets XIB as the total number of modes (translational and rotational) that participate in this redistribution (this corresponds to the parameter Ξ in §5.5).

The rotational energy of molecule L is first selected as long as IRL is equal to 1, and, secondly, that of molecule M is selected if IRM is equal to 1. At each selection, the mode that corresponds to that under selection is subtracted from XIB, so that this parameter corresponds to Ξ_b in the general Larsen-Borgnakke method. The ratio of the new rotational energy

to ECC is set as the variable ERM either through eqn (5.46) for two internal degrees of freedom, or the subroutine LBS for three degrees of freedom. The selection in the subroutine LBS is based on the general Larsen–Borgnakke distribution of eqn (5.43). The sum of E_a and E_b can be set to the available energy and is designated by E_c . The ratio of the probability of a particular value of E_a to the maximum probability can then be written

$$\frac{P}{P_{\max}} = \left\{ \frac{\Xi_a + \Xi_b - 2}{\Xi_a - 1} \left(\frac{E_a}{E_c} \right) \right\}^{\Xi_a - 1} \left\{ \frac{\Xi_a + \Xi_b - 2}{\Xi_b - 1} \left(1 - \frac{E_a}{E_c} \right) \right\}^{\Xi_b - 1}. \quad (11.9)$$

The variables XIA and XIB represent Ξ_a and Ξ_b , respectively. The selection is based on the acceptance-rejection method, and the subroutine distinguishes between the general expression and the simplified expressions when either or both of Ξ_a and Ξ_b are unity.

In the case that both molecules are subject to selection, the available energy is reduced by the new rotational energy of molecule L, after the selection of that quantity. However, the initial or total available energy is accessible equally to molecules L and M. This is because the new rotational energy in molecule L could well be zero, and its initial rotational energy had been included in ECC. The end result is the same as if the total available energy was first divided between the translational and internal energies, and the internal energy was then divided between the molecules. The initial selection to a single internal mode has been employed because this procedure must be adopted for the quantized vibration procedure that will be developed in the following section.

The sampling routine is extended to cover the rotational energies, and the output includes the rotational temperatures of the mixture and the individual molecular species. The rotational temperature of species p is, from eqn (1.31),

$$T_{\text{rot},p} = (2/k)(\overline{\epsilon_{\text{rot},p}}/\zeta_p), \quad (11.10)$$

where ϵ_{rot} is the rotational energy of an individual molecule. The rotational temperature of the gas mixture is defined by

$$T_{\text{rot}} = (2/k)(\overline{\epsilon_{\text{rot}}}/\bar{\zeta}), \quad (11.11)$$

while the overall temperature is, from eqn (1.32),

$$T = (3T_{\text{tr}} + \bar{\zeta}T_{\text{rot}})/(3 + \bar{\zeta}). \quad (11.12)$$

The distribution functions of both the molecular speed and the rotational energies are also sampled and are output to the file DSMC0R.OUT.

The application of eqn (11.12) to the main test case data gives a nominal overall temperature of 300 K. Given the finite sample of 100,000, the actual overall temperature was 299.736 K. The time-averaged sampling of the temperatures at intervals of approximately half a mean molecular collision time, from 50 to 500 mean collision times, leads to a sampled

rotational temperature of 299.700 K and a translational temperature of 299.760 K. The sample size is 90,000,000 and the discrepancy is one part in 10,000. This corresponds to approximately one standard deviation, so that the procedures have been shown to lead to equipartition. Sample sizes of this magnitude require double precision arithmetic on 32 bit machines.

The approximate relaxation equation (5.68) was derived in §5.7 from an essentially macroscopic viewpoint that employed the internal and equilibrium (or overall) temperatures of the gas and did not take into account the finite sample of simulated molecules. When a molecule is accepted for rotational energy selection, the energy is chosen from the total collision energy, the average value of which is related to the overall temperature throughout the calculation. The overall temperature is a constant in this adiabatic relaxation process in a stationary gas, and another approximation to the relaxation equation can be derived from the Larsen-Borgnakke selection procedures. From the microscopic point of view, the relaxation can be regarded as a step process with the transition to equilibrium being completed when all molecules have been selected for rotational adjustment. The average energy of the fraction F_s of molecules that have been accepted for selection *one or more* times is directly proportional to the overall or equilibrium temperature T , while that of the fraction F_u that have not been selected is directly proportional to the initial rotational temperature $T_{\text{rot},0}$. The rotational temperature can therefore be written

$$T_{\text{rot}} = F_s T + F_u T_{\text{rot},0}. \quad (11.13)$$

The number of selections from a total of N molecules after time t is equal to $Nv\Lambda t$, where v is the collision rate per molecule and Λ is the fraction of inelastic collisions for rotation. Therefore, using the standard result from probability theory for the unselected fraction and noting that the sum of the fractions is unity, eqn (11.13) can be written

$$T_{\text{rot}} = T - (T - T_{\text{rot},0})(1 - 1/N)^{Nv\Lambda t}. \quad (11.14)$$

For $N \gg 1$ and $Nv\Lambda t \gg 1$, eqn (11.14) can be approximated by

$$T_{\text{rot}} = T - (T - T_{\text{rot},0}) \exp(-v\Lambda t). \quad (11.15)$$

in agreement with eqn (5.64).

For the main test case, $T = 300$, $\Lambda = 1/5$ and $T_{\text{rot},0} = 0$, so that the prediction for the rotational temperature is

$$T_{\text{rot}} = 300(1 - \exp(-vt/5)). \quad (11.16)$$

The translational temperature is given similarly by

$$T_{\text{tr}} = 300 + 200 \exp(-vt/5). \quad (11.17)$$

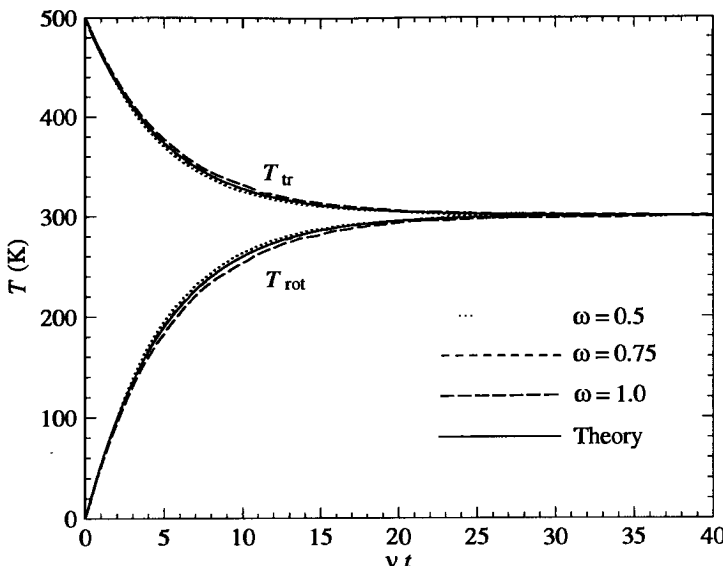


Fig. 11.2 Rotational relaxation in a homogeneous simple gas.

The DSMC results for the relaxation process are compared with the predictions of eqns (11.16) and (11.17) in Fig. 11.2. The theory is approximate and the dependence of the relaxation process on the viscosity-temperature index ω is in agreement with the more exact equation (5.70). It is fortuitous that the DSMC results for the realistic values of $\omega=0.75$ and $Z_r=5$ agree almost exactly with the simple approximate result. Figure 11.2 verifies that the Larsen-Borgnakke relaxation as programmed in subroutine INELR is an exponential process when it is expressed on the 'collision time-scale'. Moreover, the relaxation collision number is given approximately by the reciprocal of the fraction of inelastic collisions in the Larsen-Borgnakke model. It should be noted that the abscissa in Fig. 11.2 is based on the sampled collision rate *per molecule* of the molecules. It is linear with time only in the 'Maxwell' case with $\omega=1$, because the collision rate is then independent of the relative speed between the colliding molecules. Also, there will be a difference in the collision rate between the $\omega=0.75$ case and the hard sphere cases. This creates problems in the application of measured relaxation times to the simulation of real gases. If the measured or 'handbook' values are quoted as 'collision numbers', it is essential to determine how the collision rate was established. There is a possibility of a factor-of-two error simply because the quoted relaxation collision number may be based on the rate of *collision events*, rather than *collisions per molecule*. In any case, the quoted rates will almost certainly be based on the unrealistic hard sphere model. A correction can be made

but, in the case of a temperature dependent relaxation rate, the temperature dependence of this rate must be reconciled with the temperature dependence of the collision rate that is present for any model other than the unrealistic Maxwell model. The VHS and VSS models have a definite cross-section, and the problem would be much more severe for models, such as the inverse power law model, that involve arbitrary cut-offs.

The situation is further complicated by the existence of alternative definitions of the relaxation rate. The preceding discussions have employed the conventional definition of eqn (5.67) that is based on the departure of the temperatures from the equilibrium value T_e . In this, the internal temperature is given by

$$\frac{dT_i}{dt} = (T_e - T_i)/\tau, \quad (11.18)$$

where τ is the relaxation time. Lumpkin et al. (1991) employed a similar definition, but with the translational temperature in place of the equilibrium temperature, i.e.

$$\frac{dT_i}{dt} = (T_{tr} - T_i)/\tau_a, \quad (11.19)$$

where τ_a is an alternative relaxation time. This definition is frequently expressed in terms of the energy rather than the temperature, and is employed in continuum flow studies when the equilibrium conditions are not known. The translational energy is then characteristic of a heat bath and the relaxation time is a function of pressure as well as temperature. Vincenti and Kruger (1965) note that this is not a relaxation process in the strict sense and call τ_a a *local* relaxation time. When eqn (11.19) is applicable and T_i is based on two internal degrees of freedom, the solutions of eqns (11.18) and (11.19) are similar and the alternative relaxation time is related to the conventional relaxation time by

$$\tau = 3\tau_a/5. \quad (11.20)$$

In addition to the difference in the definition of relaxation time, the results of Lumpkin et al. differ from those obtained from program DSMC0R as a consequence of a programming detail that may not, at first sight, be considered significant. In subroutine INELR, the Larsen–Borgnakke model is applied on a ‘single molecule’ basis in that each molecule is considered in turn for energy redistribution with probability Λ in each case. On the other hand, Lumpkin et al. apply this probability to the collision pair and, if a pair is accepted, the energy redistribution is applied to both molecules. The reason for the consequent difference in the relaxation rate can be seen from the theory that led to eqn (11.17). As long as most of the collisions that involve redistribution between the translational and rotational modes make the redistribution to only one of the molecules, a high proportion of the redistributions involve a molecule that has not previously been involved in a redistribution. The transfer is less effective if both of the molecules in a collision pair are always chosen for redistribution, and the program was temporarily modified to implement the ‘collision pair’ option.

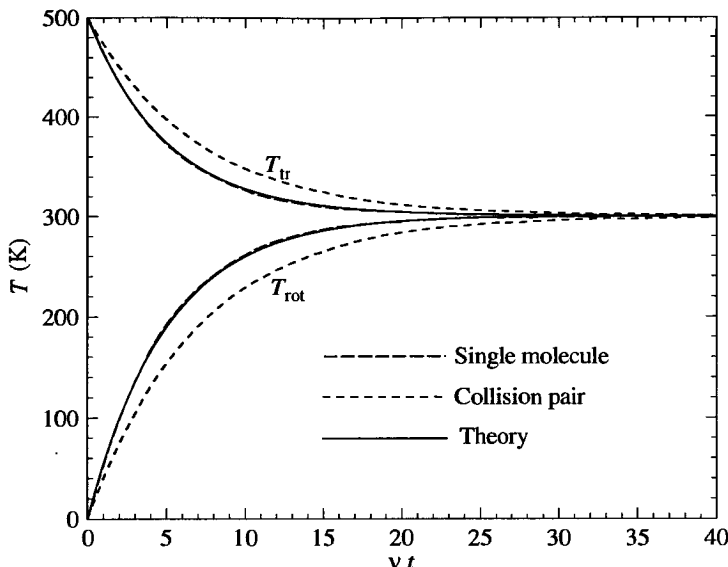


Fig. 11.3 The effect of the alternative selection procedures on the relaxation rate.

Either procedure can be used to model a given relaxation rate, but Fig. 11.3 shows that different values of Λ would be required. The program DSMC0R makes provision through the array SPR for the rotational relaxation probability of each species to vary with the species of the collision partner, and this can be implemented only when the 'single molecule' option is adopted. This example shows that the details of a procedure, at a level that would generally not be described in a journal publication, can lead to significant differences in the results and to consequent confusion. This case provides a salutary warning on the difficulties that can be caused by an inadequate description of DSMC procedures. Neither party may be aware that an alternative procedure can exist, let alone has been used.

Both the above discussion and the theory in Chapter 5 have reflected a preference for the relaxation collision number to be based on the relaxation time τ . However, the measured data for Z is usually based on the local relaxation time τ_a , and it must be adjusted before the Larsen–Borgnakke inelastic fraction can be set to $1/Z$ as a convenient approximation.

The subroutine INELR implements the Larsen–Borgnakke procedure in a hierarchical manner in that the energy is first divided between the translational and rotational components and, should both the molecules be chosen for redistribution, the rotational energy is then divided between the molecules. The 'single molecule' result in Fig. 11.3 has been obtained from the alternative subroutine INELRS that is also included in DSMC0R. This

implements the serial redistribution that was described in §5.5. Each molecule is considered for redistribution in turn and, should both be accepted, the redistribution to the second is with the translational energy that has already been modified by the first redistribution. It was shown in §5.5 that this leads to equipartition, and the result in Fig. 11.3 verifies that it does not affect the relaxation rate. The theoretical result is again based on eqns (11.16) and (11.17).

The molecular speed and rotational energy distribution functions are output to file DSMC0R.OUT at 400 points. The results for the speed distribution are compared in Fig. 11.4 with the theoretical distribution of eqn (4.6). While there is some scatter in the high-speed tail due to the small sample, it is clear that the collision procedures do not lead to any distortion of the Maxwellian distribution. In order to compare the rotational energy distribution with the equilibrium distribution, the constant in eqn (5.15) must be evaluated from the normalization condition that its integration from 0 to ∞ should be unity. The result is

$$f_{\epsilon_r} = \frac{1}{\Gamma(\frac{1}{2}\zeta_r) kT} \left(\frac{\epsilon_r}{kT} \right)^{\frac{1}{2}\zeta_r - 1} \exp\left(-\frac{\epsilon_r}{kT}\right). \quad (11.21)$$

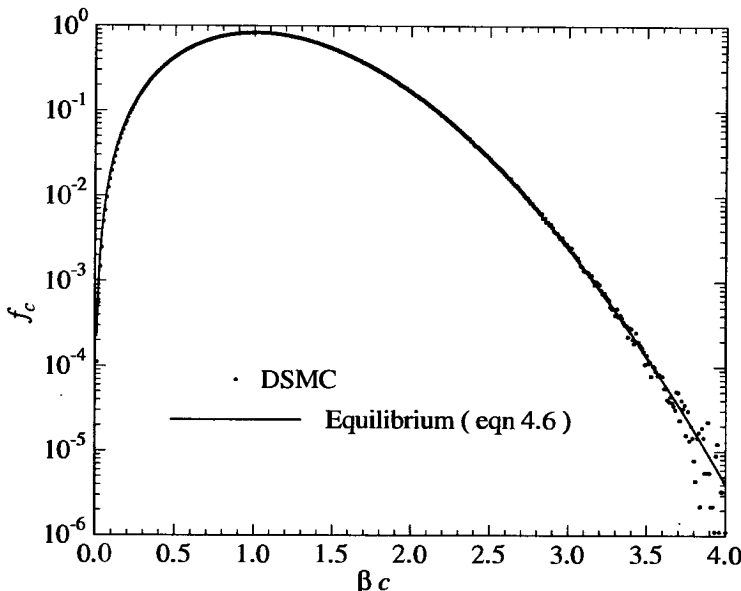


Fig. 11.4 The sampled distribution function for the molecular speed.

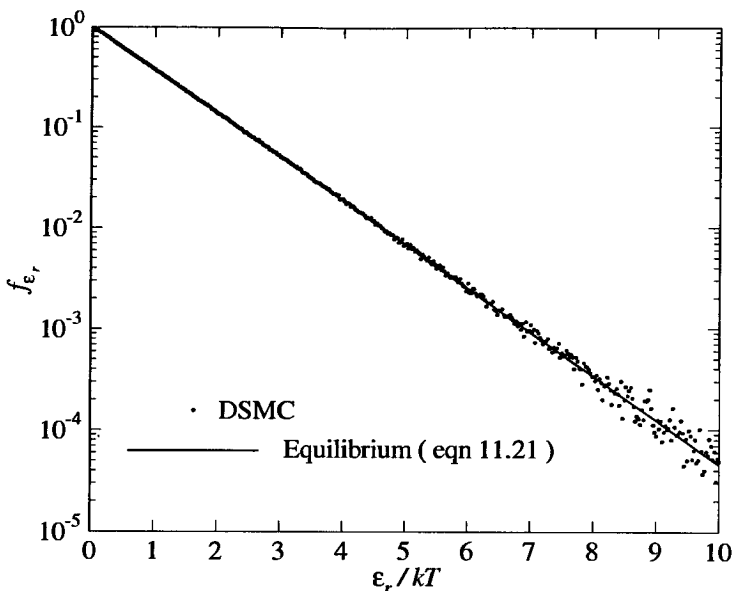


Fig. 11.5 Distribution function for the rotational energy of a diatomic gas.

For the special case of two rotational degrees of freedom, the maximum probability is for zero rotational energy and the probability decays as a simple exponential. This result is consistent with the Boltzmann distribution for the energy levels of a single internal mode. The main test case involves a gas with two degrees of freedom of rotation, and the sampled distribution is compared in Fig. 11.5 with the prediction of eqn (11.21). The two are in excellent agreement.

A similar rotational relaxation calculation was made for a gas mixture. The composition by number was 50% polyatomic molecules with three rotational degrees of freedom, 25% diatomic molecules with two rotational degrees of freedom, and 25% monatomic molecules with no internal degrees of freedom. The relaxation collision number was five for the dominant species and ten for the diatomic gas. The molecular masses were again set to nominal values.

The average number of internal degrees of freedom in this gas is two so that, for an initial translational temperature of 500 K, the final equilibrium temperature should again be 300 K. The computed temperatures of the mixture, based on a time average that was made after the establishment of equilibrium, were 299.74 K for the overall, 299.81 K for the translational, and 299.63 K for the rotational temperature. The translational and rotational temperatures for the polyatomic component were 299.77 K and 299.73 K, respectively. The similar values for the diatomic component

were 300.14 K and 299.32 K, while the translational temperature of the monatomic component was 299.55 K. This verifies that the definitions of the temperatures of both the gas mixture and the separate species, that were presented in eqns (11.10)–(11.12), lead to consistent values.

The relaxation behaviour was similar to that in the simple gas, but the collision rate per molecule is different for each species and, while the relaxation curves on the ‘collision time-scale’ conform to eqn (11.15), the absolute time-scale (i.e. in seconds) for the polyatomic gas differs from that in the diatomic gas.

The distribution of rotational energy in the polyatomic molecules is of interest. The most probable rotational energy of a molecule with ζ_r internal degrees of freedom is $(\frac{1}{2}\zeta_r - 1)kT$. This is zero for the diatomic gas, but is $\frac{1}{2}kT$ for the polyatomic gas. The distribution function from the DSMC computation is compared with the theoretical distribution function in Fig. 11.6. Note that these comparisons are to validate the coding in DSMC0R.FOR, rather than the Larsen–Borgnakke method itself. The method is based on the selection of the translational and internal energies from the relevant equilibrium distributions, so that any discrepancy would indicate an error in its implementation.

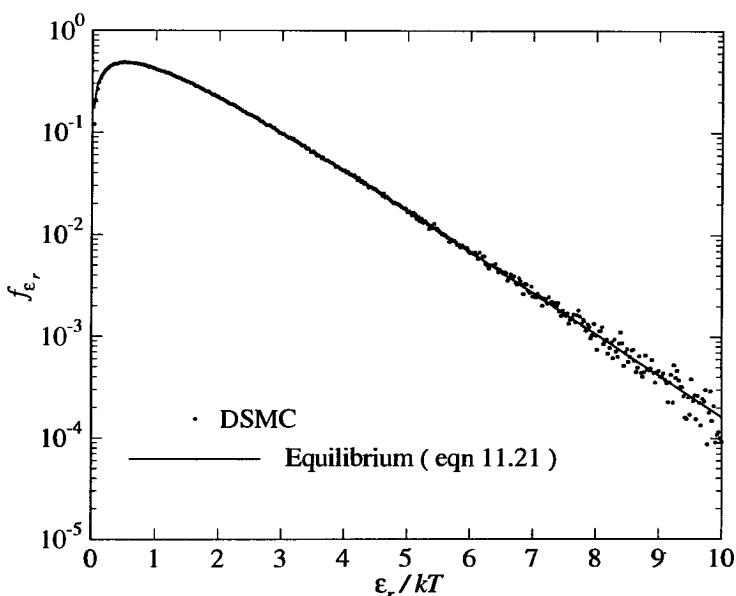


Fig. 11.6 Distribution function of the rotational energy in a polyatomic gas.

The Larsen-Borgnakke method is physically unreal in that only a fraction of the collisions are regarded as inelastic. Further criticism has been based on the selection of the post-collision values from an equilibrium distribution. This has led to claims that the method may be inadequate for highly non-equilibrium situations. However, it should be noted that the 'temperature' of the distribution changes from collision to collision, and does reflect the degree of non-equilibrium.

It was noted in §5.3 that a modified form of the Larsen-Borgnakke method had been introduced in response to the first criticism. This has been implemented in the alternative subroutine INELRA in program DSMC0R. This regards all collisions as inelastic, but transfers only the fraction Λ of the calculated change in rotational energy at each collision. This did not affect the relaxation rate but, as had been predicted, the procedure does not satisfy detailed balance. The steady state rotational and translational temperatures were 297.83 K and 301.58 K, respectively. More seriously, the equilibrium distribution function of the rotational energy is drastically affected. Fig. 11.5 shows that the rotational energies are grouped in a narrow band around the mean rotational energy and that both high and low energies are under-represented. The modified model could therefore lead to errors in chemical reactions that depend on the rotational energy.

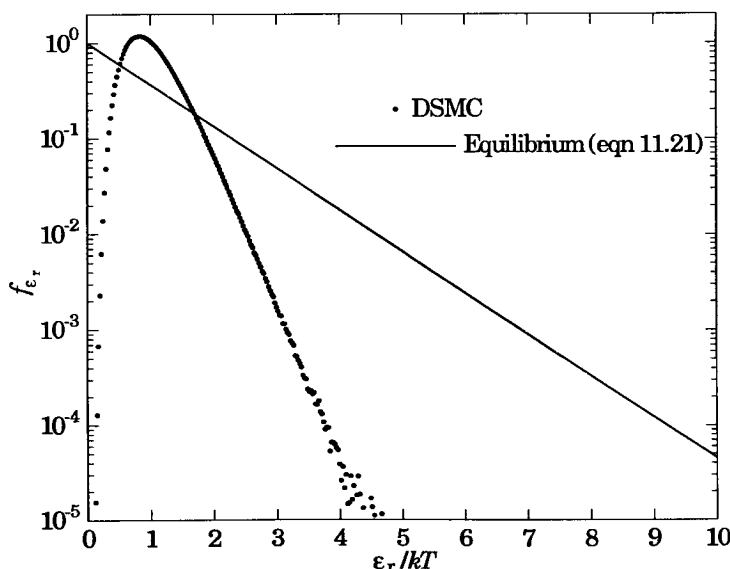


Fig. 11.7 The rotational distribution function for the modified Larsen-Borgnakke method.

11.4 Vibrational excitation

The program DSMC0V.FOR is concerned with the modelling of vibrational excitation. This program employs the harmonic oscillator model, and implements the quantum version of the Larsen–Borgnakke model that was outlined in §5.6. Not only is this more realistic than the classical version, but is more easily implemented and leads to a much faster execution time. The stored vibrational information on each molecule is the energy level of the vibrational mode. This program assumes that there is only one vibrational mode associated with each molecule, and separate levels would be required for polyatomic molecules that generally have more than one mode. The levels are relatively small integers and would be preferable to employ the short integers that are available with most compilers, but the program has been restricted to the FORTRAN 77 standard.

The data for the main test case is set in the subroutine DATA0V. It checks that a single vibrational mode in a simple diatomic gas remains in equilibrium with the translational and rotational modes and also samples the distribution of the levels. The initial temperature of the rotational mode in DSMC0R.FOR is always zero, but those of the rotational and vibrational modes in DSMC0V.FOR can be set to either zero or to the initial translational temperature FTMP. In the latter case, routines are required in subroutine INIT0V for the selection of representative rotational energies and vibrational levels that are appropriate to the temperature T .

First consider the selection of the rotational energy. For a diatomic molecule with two degrees of freedom, eqn (C16) allows the value to be directly related to a single random fraction R_f , i.e.

$$\varepsilon_r = -\ln(R_f)kT. \quad (11.22)$$

For ζ_r not equal to 2, the acceptance–rejection procedure may be used to find a typical value of ε_r/kT . The distribution function for this quantity is given by eqn (C13), and the ratio of the probability to the maximum probability is

$$\frac{P}{P_{\max}} = \left(\frac{1}{\zeta/2-1} \frac{\varepsilon}{kT} \right)^{\zeta/2-1} \exp\left(\zeta/2-1-\frac{\varepsilon}{kT}\right). \quad (11.23)$$

The acceptance–rejection procedure for this ratio is implemented in the subroutine SIE.

Now consider the selection of a representative vibrational level of a molecule in a gas at temperature T . The harmonic oscillator model may be applied to a mode with characteristic vibrational temperature Θ_v . From eqn (5.57), the vibrational energy ε_v is limited to the discrete values given by $ik\Theta_v$, where the level i ranges from zero to infinity. There are two degrees of freedom associated with a vibrational mode, and the level may be determined from the truncation of the energy selected by eqn (11.22), i.e.

$$i = \lfloor -\ln(R_f)T/\Theta_v \rfloor. \quad (11.24)$$

The cumulative distribution function that led to eqn (11.19) can be written from eqn (C15) as

$$F_{\epsilon_v/(kT)} = 1 - \exp \{-\epsilon_v/(kT)\}. \quad (11.25)$$

The range of sampled energy $\epsilon_v/(kT)$ that leads, after the truncation, to level i is from $i\Theta_v/T$ to $(i+1)\Theta_v/T$, and eqn (11.25) shows that the fraction of samples within this range is

$$\exp \{-i\Theta_v/T\} - \exp \{-(i+1)\Theta_v/T\}.$$

Therefore, the average value of the vibrational energy of a single molecule can be written

$$\begin{aligned} \bar{\epsilon}_v &= k\Theta_v \{ \exp(-\Theta_v/T) - \exp(-2\Theta_v/T) \\ &\quad + 2k\Theta_v \{ \exp(-2\Theta_v/T) - \exp(-3\Theta_v/T) \} \\ &\quad + 3k\Theta_v \{ \exp(-3\Theta_v/T) - \exp(-4\Theta_v/T) \} + \dots \} \end{aligned}$$

or

$$\bar{\epsilon}_v = k\Theta_v \exp(-\Theta_v/T) \{ 1 + \exp(-\Theta_v/T) + \exp(-\Theta_v/T)^2 + \exp(-\Theta_v/T)^3 + \dots \}$$

This involves an infinite geometrical series with a multiplier less than unity, and the final result is

$$\bar{\epsilon}_v = \frac{k\Theta_v}{\exp(\Theta_v/T) - 1}, \quad (11.26)$$

in exact agreement with the harmonic oscillator result of eqn (5.52). This result proves that the truncation to the quantum levels of the values selected from the continuous distribution for a fully excited mode properly accounts for the partial vibrational excitation of the gas.

The procedures for the vibrational excitation are integrated with those for the rotational excitation in the subroutine INELV. This program implements the serial application of the Larsen-Borgnakke method that was introduced in the final paragraph of §5.5 and on which the analysis of §5.6 was based. The molecules are considered in turn and the vibrational mode is considered before the rotational mode. The vibrational procedures are a direct implementation of the equations in §5.6, and the coding is related to the relevant equation numbers by comment statements.

The vibrational temperature is usually defined as the temperature in the harmonic oscillator result of eqn (5.52) that corresponds to the sampled value of the average vibrational energy. This can require an iterative process in the case of a gas mixture, and this definition cannot be applied to the more realistic anharmonic case. An alternative measure of the temperature is provided by the Boltzmann distribution of states. It can be seen from eqn (5.63) that, given the energy spacing between any two levels, the ratio of the number of molecules in the two levels can be used to define a vibrational temperature. In equilibrium, the temperatures based on all combinations of levels are equal and, for the harmonic oscillator model, the common temperature is equal to the temperature based on eqn (5.63).

Ideally, the temperature would be based on the slope of the line through all levels in a logarithmic plot of the level densities. However, to sample the number of molecules in a large number of levels in all cells would require excessive storage, and only two levels are sampled in this program.

The initialization and sampling routines include the array CSV which is a progressive count of the vibrational energy of each mode in each cell. This array is used in the output subroutine OUT0V to determine the average vibrational energy per molecule in each mode. The array CSVS is a progressive count of the number N_0 of molecules of each species in the ground state and the number N_1 in the first vibrational level. The vibrational temperature of species m can then be written

$$T_{v,m} = \Theta_{v,m} / \ln(N_{0,m}/N_{1,m}). \quad (11.27)$$

The effective number of degrees of freedom in this mode is then

$$\zeta_{v,m} = 2 \bar{\epsilon}_{v,m} / (k T_{v,m}). \quad (11.28)$$

Although this program employs equally spaced vibrational levels, these two equations do not depend in any way on the harmonic oscillator model.

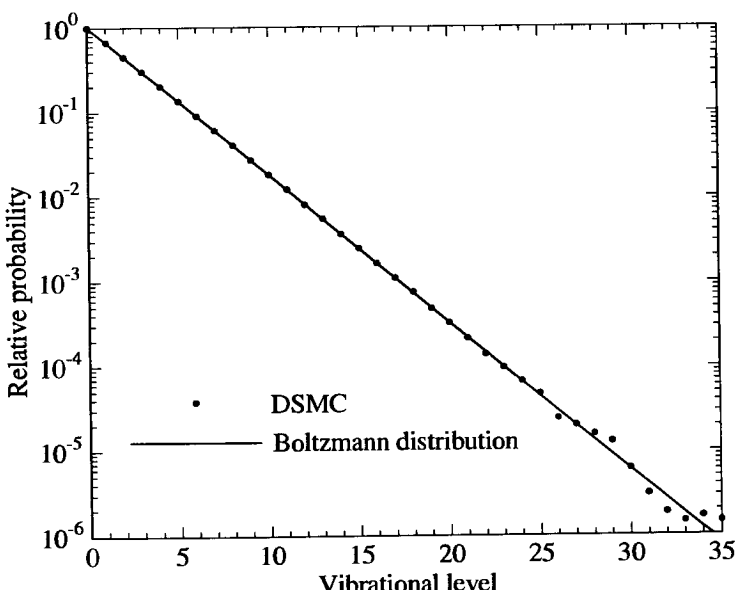


Fig. 11.8 The distribution function of the vibrational states in a gas with $\Theta_v = 2000$ K at a temperature of 5000 K.

The overall vibrational temperature is given by

$$T_v = \sum_{m=1}^j (\zeta_{v,m} T_{v,m}) / \sum_{m=1}^j (\zeta_{v,m}). \quad (11.29)$$

The summation is over the modes for the temperature of a single species and over all modes of all species for the overall vibrational temperature. The overall temperature now becomes

$$T = (3 T_{tr} + \bar{\zeta}_{rot} T_{rot} + \bar{\zeta}_v T_v) / (3 + \bar{\zeta}_{rot} + \bar{\zeta}_v). \quad (11.30)$$

The data in the listing of DSMC0V.FOR is for a diatomic gas which has a single vibrational mode with characteristic temperature 2000 K. The initial translational temperature was set to 5000 K and the 'run options' were chosen such that the rotational and vibrational temperatures were also set to this value. This run verified that the temperatures remained in equilibrium, and the time-averaged values for the overall, translational, rotational, and vibrational temperatures were 5006 K, 5007 K, 5009 K, and 5002 K, respectively. As shown in Fig. 11.8, the sampled vibrational distribution function is in excellent agreement with the Boltzmann distribution. This figure also shows that the temperature based on the first two levels is consistent with that based on the overall distribution.

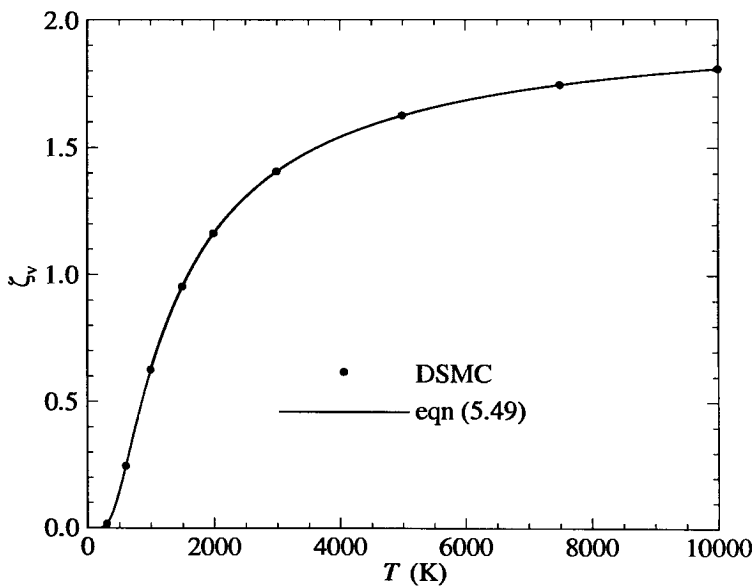


Fig. 11.9 Degree of excitation in a gas with $\Theta_v = 2,000$ K.

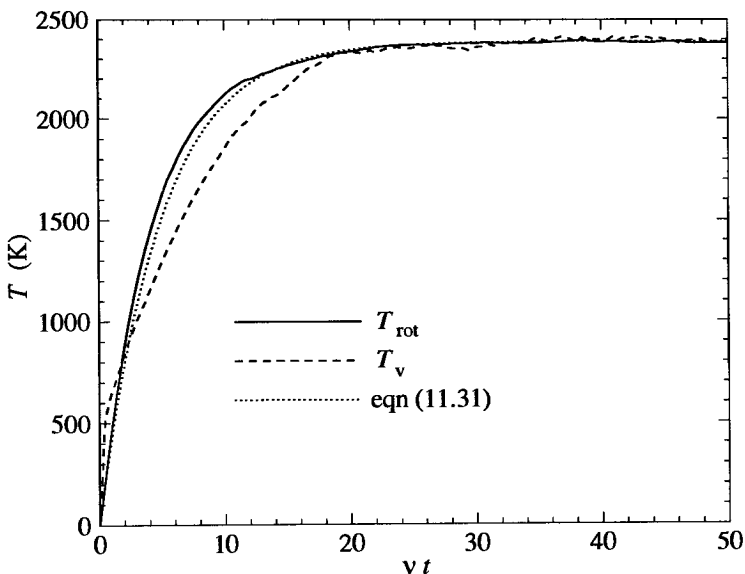


Fig. 11.10 Rotational and vibrational relaxation for $Z_{\text{rot}}=5$ and $Z_{\text{v}}=5$.

The effective number of degrees of freedom of vibration in the test case was found to be 1.630, and this is also in excellent agreement with the theoretical value of 1.627 from eqn (5.53). Similar runs were made for a number of other temperatures, and the degree of vibrational excitation as a function of temperature is compared in Fig. 11.9 with the prediction of the harmonic oscillator model. Again, the agreement is within the expected statistical scatter.

The listed test case was repeated with the initial rotational and vibrational temperatures set to zero and the initial translational temperature set to 5000 K. The final equilibrium temperature was then 2388 K and, if the quantum procedures were to have no effect on the relaxation process, the theoretical relaxation equation would be

$$T_{\text{v}} = T_{\text{rot}} = 2388 \{1 - \exp(-vt/5)\}. \quad (11.31)$$

The data on the relaxation process is written to the file RELAX.OUT, and the results for this case are shown in Fig. 11.10. The calculation employed 100,000 simulated molecules so that the expected level of statistical scatter is about 1%. The scatter in the rotational temperature is consistent with this, but, since the vibrational temperature is based on the number of molecules at the first level, the scatter is significantly higher. Allowing for the higher scatter, the relaxation behaviour of the vibrational temperature, as defined by eqn (11.27), is very satisfactory.

However, this definition cannot be used in situations where the degree of non-equilibrium is such that the distribution of molecules in the vibrational levels departs markedly from the Boltzmann form. For example, if there is a population inversion between the ground state and the first level, eqn (11.27) would lead to a negative temperature. In less extreme situations, such as the vibrational relaxation behind a very strong shock wave, the population of the upper levels increases more rapidly than that of the lower levels, and this leads to an unrealistically low vibrational temperature from eqn (11.27). More seriously, eqn (11.28) combines this low temperature with the actual mean value of the vibrational temperature and this can lead to values of the 'effective number of degrees of freedom' of a single vibrational mode well in excess of two. This is physically incorrect and, when substituted into eqns (11.29) and (11.30), it also leads to errors in the overall temperature. An alternative definition (Vincenti and Kruger 1965) may be based on the harmonic oscillator model of eqn (5.52). This is

$$T_{v,m} = \Theta_{v,m} / \ln(1 + k \Theta_{v,m} / \bar{\epsilon}_{v,m}). \quad (11.32)$$

If the quantum vibrational model is used, eqn (5.54) may be used to base this definition on the average level: i.e.

$$T_{v,m} = \Theta_{v,m} / \ln(1 + 1/\bar{i}). \quad (11.33)$$

The effective number of degrees of freedom is then given directly from eqn (5.53) and eqns (11.29) and (11.30), for the overall vibrational temperature and temperature are still applicable.

The test case data employs constant rotational and vibrational relaxation collision numbers, but the program makes provision for these numbers to be functions of the temperature. The use of the macroscopic temperature ensures that the principle of detailed balance is satisfied, as noted in the discussion of the Larsen-Borgnakke model in §5.3, but the model is improved if the probability of energy redistribution is a function of a 'collision temperature' based in the energy in the collision. The Larsen-Borgnakke model contains an implicit temperature equal to the energy E_c that is being redistributed divided by the product of the effective number of energy modes that contribute to E_c and the Boltzmann constant. This temperature can be written

$$T_{\text{coll}} = E_c / (\Xi k), \quad (11.34)$$

where Ξ is given by eqn (5.42). The program DSMC0V.FOR employs the serial application option, and the Larsen-Borgnakke redistribution is always between the translational mode and a single internal mode. The parameter Ξ is therefore equal to $5/2 + \omega_{12}$ plus either two for the rotational mode, or the equilibrium number of vibrational degrees of freedom for the vibrational mode. In order to test whether detailed balance can be satisfied with a collision temperature dependent relaxation rate, the option for a temperature dependent vibrational rate in DSMC0V.FOR employs the temperature T_{coll} that is defined in eqn (11.34). The contribution of ζ_v to Ξ is based on the variable SVIB that samples ζ directly from eqn (11.28).

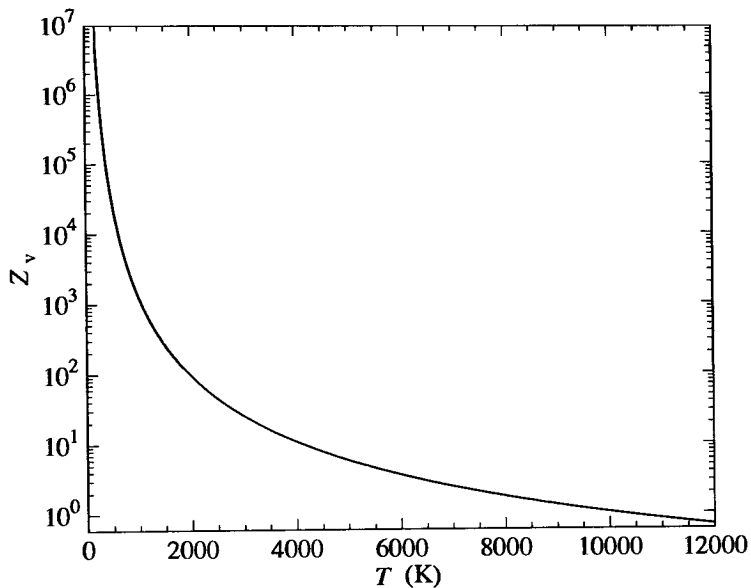


Fig. 11.11 Temperature dependence of vibrational relaxation rate.

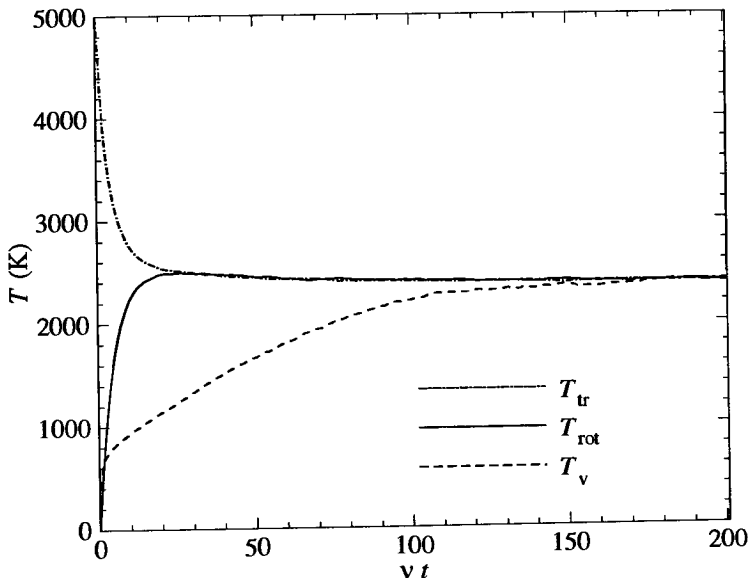


Fig. 11.12 Vibrational relaxation with temperature dependent rate.

The two test cases were repeated for a temperature dependent vibrational relaxation collision number with the constants C_1 and C_2 in eqn (6.53) equal to 10 and 100, respectively. The resulting vibrational relaxation collision number is shown as a function of temperature in Fig. 11.12. This is typical behaviour in that the collision number is extremely high at low temperatures, but drops below unity at high temperatures. The test case with all modes set to 5000 K confirmed that the ‘collision temperature’ dependent vibration rate is consistent with detailed balance. Both the average temperatures of the separate modes and the vibrational distribution function were indistinguishable from those for the corresponding case with a constant vibrational relaxation collision number. The results from the relaxation test case are shown in Fig. 11.12, and are more representative of a real gas. The rotational mode quickly comes to equilibrium with the translational mode, while the vibrational relaxation slows as the temperature drops. The time-averaged overall equilibrium temperature was 2387 K, while the translational, rotational, and vibrational temperatures were 2387 K, 2385 K, and 2386 K, respectively. More importantly, the distribution function for the vibrational energy was again in excellent agreement with the Boltzmann distribution.

11.5 Dissociation and recombination

The DSMC procedures for the modelling of real gases are extended to the dissociation and recombination reactions in the program DSMC0D.FOR. This program is limited to the dissociation of a single homonuclear diatomic gas, and nitrogen has been chosen for the test case. Dissociation is closely linked to vibrational excitation and the program employs the quantum model for vibration that was developed in §5.6. The vibrational procedure in this program is for the realistic anharmonic (or unequally spaced) levels.

The energy in vibrational level i of nitrogen is given by the following empirical equation (Herzberg 1950),

$$\begin{aligned}\varepsilon_{v,i} = k [3395\{(i + \frac{1}{2}) - 0.006126(i + \frac{1}{2})^2 \\ + 0.00000318(i + \frac{1}{2})^3\} - 1692.3].\end{aligned}\quad (11.35)$$

The zero-point energy has been subtracted in order to set the energy of the ground state ($i=0$) to zero. The characteristic temperature of dissociation is 113,200 K and this falls between levels 46 and 47. By contrast, the maximum level for the harmonic oscillator model would be 33. The amplitudes of the vibrational oscillations are often represented by the Morse potential which writes the potential energy of the oscillation as

$$U = E_d \{1 - \exp(-\beta(r - r_e))\}^2. \quad (11.36)$$

This energy is zero when the internuclear distance r is equal to the distance r_e , and $r \rightarrow \infty$ as the potential energy approaches the dissociation energy E_d . For nitrogen, r_e is 1.094×10^{-10} m and the parameter β is 2.67×10^{10} m⁻¹. The Morse potential with these values has been used to construct Fig. 11.13. For a harmonic oscillator, the mean interatomic spacing is equal to r_e for all vibrational levels but, in the anharmonic case, Fig. 11.13 shows that it increases by up to 60% for molecules in the higher vibrational levels. This increase could be used to make an estimate of the increase in the collision cross-section for these molecules.

The energy in the levels is entered in the array ELEV as part of the data in the subroutine DATA0D. The characteristic vibrational temperature is set in the array SPD, as in DSMC0V.FOR, and the maximum level (just below the dissociation limit, is set in the array MLEV. Other data that relates directly to the dissociation–recombination reaction is the characteristic temperature of dissociation in SPD, and the information on the species codes in IDISS, IRECC, and IRSC.

A molecule dissociates when the Larsen–Borgnakke selection of energy into the vibrational mode leads to a level above the maximum level, and the dissociation rate should be consistent with the theory of §6.6. The ‘equilibrium collision’ theory for recombination is employed, and the ratio of the recombination cross-section to the elastic cross-section in an atom–atom collision is given by eqn (6.49).

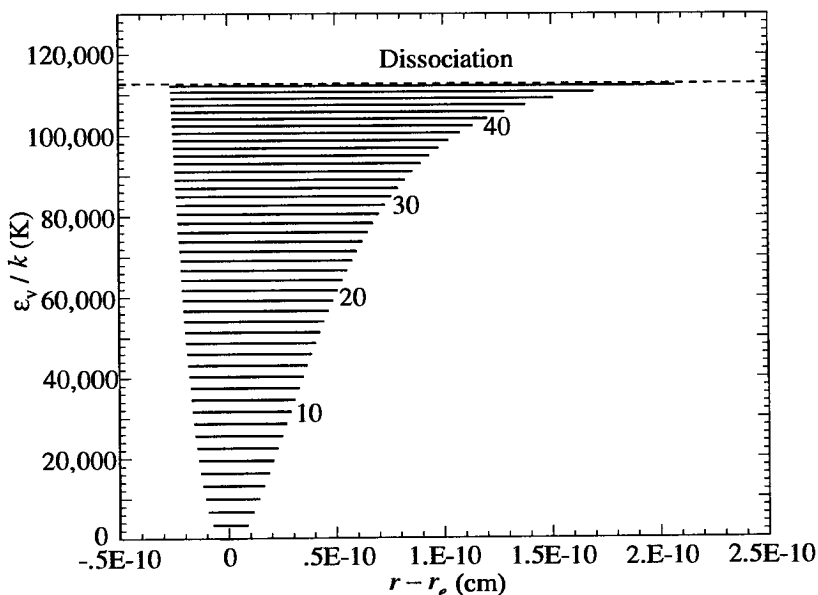


Fig. 11.13 The vibrational energy level diagram for nitrogen.

The Larsen–Borgnakke redistribution of energy in the collisions follows program DSMC0V.FOR and employs the ‘serial’ procedure in which each active internal mode interacts separately with the translational mode. This is modified for the consideration of dissociation in that the pre-collision rotational as well as the vibrational and translational energy is distributed between the vibrational and translational modes. Should the collision energy exceed the dissociation energy, a redistribution is made in order to determine whether dissociation occurs. The selection of possible levels for the acceptance–rejection scheme must extend beyond the dissociation energy and, for this purpose, notional levels are assumed with an energy spacing equal to that between the levels that span the dissociation energy. If the selected level is beyond the dissociation limit, the molecule is marked for dissociation by setting its species code to the negative of its proper value. The dissociation energy is subtracted from the collision energy, but a small amount of energy is stored as rotational energy and is subsequently converted to relative translational energy between the atoms. If the molecule was changed immediately into two atoms, the number of molecules would change and the indexing of the molecules would be upset. The marked molecule remains available for further collisions, but no further changes to its internal energies are allowed. The coding for the dissociation is in the subroutine DISSOC which is called after all collisions have been completed. The subroutine ELASTIC is used to compute a ‘collision’ between the newly formed atoms. The centre of mass velocity in this collision is equal to the velocity of the molecule, while the post-collision relative velocity is such that the translational energy is equal to the energy that had been assigned to the rotational energy of the molecule. This procedure leads to the exact conservation of mass, momentum, and energy in the overall computation of the dissociation.

The serial application of the Larsen–Borgnakke method means that the DSMC procedure corresponds to the derivation of eqn (6.52) for the dissociation rate coefficient due to collisions with atoms. The differing results for the molecule and atom as collision partners might appear to conflict with the logic behind the serial option for the application of the Larsen–Borgnakke method. However, the difference occurs only for dissociating collisions and comes about because of the disappearance of the rotational mode of the molecule in these collisions. The test case data in the listing of the program DSMC0D.FOR is for pure nitrogen, initially with the translational, rotational, and vibrational modes in equilibrium at a temperature of 30,000 K. The initial number density n_i of the gas is equal to the standard number density, and dissociations and recombinations proceed as the gas comes to chemical equilibrium. The rate coefficient of eqn (6.52) can be combined with eqn (6.2) to give a theoretical result for the initial rate of creation of atomic nitrogen. This result is compared in Fig. 11.14 with the results from DSMC0D.FOR.

The computed initial rate of formation of atomic nitrogen is about 25% higher than the theoretical rate. This is in spite of the theory being based

on the assumption that the vibrational collision number is unity, while the actual values of Z_v in the collisions with sufficient energy for dissociation in the simulation reduce the reaction rate by about one third. The theory differs from the simulation in that it employs a continuously distributed vibrational energy that necessitates the use of the harmonic oscillator model. The possible effects of the anharmonic model were tested by altering the data on the energy levels in DSMC0D.FOR to the uniformly spaced levels that correspond to the harmonic oscillator model. The initial rate of formation of atomic nitrogen was then 60% of the value for the anharmonic model. This resolves the discrepancy between the theory and the computation.

The reason for the higher reaction rate for the anharmonic model lies in the *uniform* choice of the possible levels prior to the application of the acceptance-rejection routine to eqn (5.61). Because the anharmonic levels are concentrated at the higher energy levels, this increases the probability of dissociation. It may be questioned whether the uniform choice of levels is correct. The effect may be avoided if the vibrational energy is chosen from the continuous distribution of eqn (C16) and then truncated to a level. However, if this is done, the equilibrium vibrational temperature is the order of 10% too low. The increased rate for the anharmonic model is therefore a real effect, and it brings the reaction rates from the 'exact available energy theory' of §6.6 into even closer agreement with the measured rates.

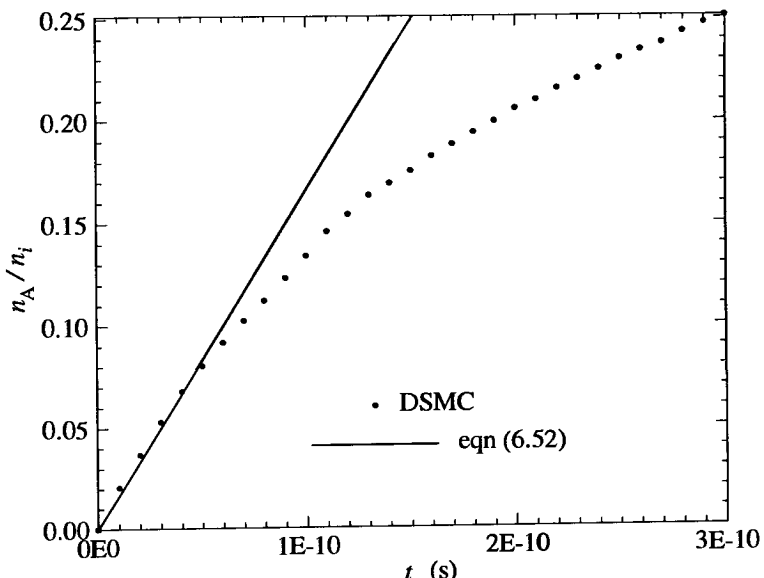


Fig. 11.14 Initial rate of formation of atomic nitrogen.

The recombination procedures in the program DSMC0D.FOR are based on the 'equilibrium collision theory' that led to eqn (6.35). The ratio of the partition functions that appears in this equation, and also in eqn (6.23) for the equilibrium degree of dissociation, can be written for a symmetrical diatomic gas as

$$\frac{(Q^A)^2}{VQ^{A_2}} = \left(\frac{\pi m_A k}{h^2} \right)^{3/2} \Theta_r T^{1/2} \{1 - \exp(-\Theta_v/T)\} \frac{(Q_{el}^A)^2}{Q_{el}^{A_2}}. \quad (11.37)$$

The values for nitrogen may be substituted into this equation and the result substituted into eqn (6.35), to give

$$\frac{\sigma_R}{\sigma_T} = \frac{9.907 \times 10^{-29} (1 + 41000/T) n}{T^{1/2} \{1 - \exp(-3395/T)\} \{4 + 10 \exp(-27658/T) + 6 \exp(-41495/T)\}^2}.$$

This is an excessively complex equation to evaluate at each collision and, to an accuracy of several percent over the temperature range of interest, it may be approximated by

$$\sigma_R / \sigma_T = 8 \times 10^{-27} n T^{-1}. \quad (11.38)$$

The program assumes that the probability of recombination at each elastic collision is given by an equation of the form of (11.38), and the numerical coefficient and the temperature exponent are set in the array RECC. The factor C in eqn (6.49) has been set to unity and, because the forward rate is 25% higher than the theoretical rate on which the equation is based, the numerical factor was increased to 1.0×10^{26} .

At each collision between two atoms, the probability of recombination is calculated within the subroutine COLLMC and the cumulative probability PRC is increased accordingly. Each time that PRC exceeds unity, the two atoms are marked for recombination, PRC is reduced by unity, and the recombination switch IRECOM is changed from zero to unity. The marking in this case is by multiplying the species code by the parameter which denotes the maximum number of molecules and adding the address code of the atom with which it is to be recombined. Both the species code and the address of the recombination partner can be decoded from this integer. The actual recombination is coded in the subroutine RECOMB which, like DISSOC, is called after all the collisions for the time step have been calculated, and the indexing arrays are not required until they are reset at the next time step. Should IRECOM be unity, the molecules are scanned to determine a marked atom and the address of the recombination partner is decoded. The relative energy of these atoms is calculated, they are then combined to a molecule, and its velocity is set to the centre of mass velocity of the pair. The third-body molecule is then chosen by the subroutine SELECT, and the subroutine ELASTIC is then used to calculate an elastic collision between it and the new molecule. The energy in this collision is supplemented by the pre-recombination relative energy of the atoms and the dissociation energy. The Larsen-Borgnakke method is then applied to

redistribute this energy between the translational energy of the new molecule and third-body molecule, the rotational mode of the new molecule, and the vibrational energy of this molecule.

The gas composition in a run of DSMC0D.FOR changes until the rate of recombination equals the rate of dissociation. The gas is then in a state of chemical equilibrium. Eqns (11.37) and (6.23) may be combined with the physical data for nitrogen to give the following expression for the equilibrium degree of dissociation as a function of the initial number density n_i and the equilibrium temperature T .

$$\alpha^2/(1-\alpha) = (0.5047 \times 10^{28}/n_i) T^{1/2} \{1 - \exp(-3395/T)\} \{4 + 10 \exp(-27658/T) + 6 \exp(-41495/T)\}^2 \exp(-113200/T). \quad (11.39)$$

The electronic partition functions are included in eqn (11.37), even though electronic excitation is not included in the simulation. This does not lead to any inconsistency because the functions contribute equally to eqns (11.38) and (11.39), and the additional partition functions merely change the equilibrium state. The equilibrium degree of dissociation as a function of temperature is shown in Fig. 11.15 for the initial number density equal to the standard number density, and also for an initial number density of one tenth this value. Because three-body collisions are rare events in a dilute gas, the dissociation occurs at temperatures that are small in comparison with the characteristic temperature of dissociation.

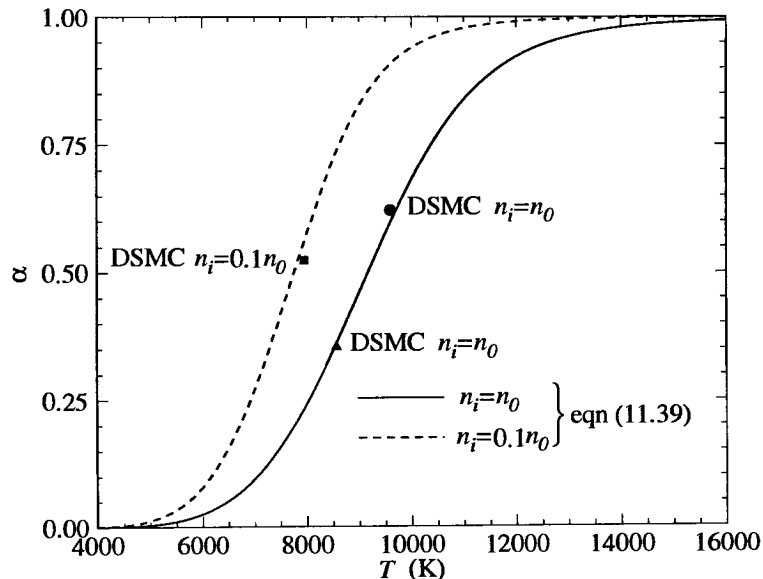


Fig. 11.15 Equilibrium degree of dissociation in nitrogen.

The listed test case with an initial temperature of 30,000 K relaxes to the temperature and degree of dissociation indicated by the circular symbol in Fig. 11.14. The effective number of vibrational degrees of freedom of the molecular nitrogen at equilibrium is 1.69, and this may be compared with the corresponding harmonic oscillator value of 1.67. The anharmonic effect on the overall energy in the vibrational mode is therefore very much smaller than the anharmonic effect on the dissociation rate.

If the initial temperature is reduced to 20,000 K, the gas relaxes to the conditions indicated by the triangular symbol in Fig. 11.14. The final test case was for an initial temperature of 25,000 K at a number density of one tenth the standard number density. The equilibrium state is indicated by the square symbol and, again, there is good agreement between the calculated and theoretical equilibrium states. In equilibrium at this lower density, there is approximately one recombination (and one dissociation) reaction for every million collisions. The fraction of recombinations decreases linearly with the gas density and, under rarefied conditions, recombinations are so rare that they can generally be ignored.

The integration of the dissociation model with that for the vibrational excitation has been shown to lead to satisfactory results for both the dissociation rate and the equilibrium state. As shown in §6.6, the exchange reactions can also be based on the vibrational relaxation rate. Carlson (private communication) has shown that the DSMC method can be used for five species real air calculations without there being any need for experimentally based data on the reaction rates.

11.6 Fluctuations and correlations

The effects of the statistical fluctuations are apparent in all results from the DSMC method. As discussed in §10.4, these fluctuations can be related to those in a real gas and, since they exist in an equilibrium gas that is macroscopically at rest, they are clearly non-dissipative. There are computational procedures that can cause the fluctuations to be enhanced or reduced as a result of numerical effects. Also, there are circumstances in which macroscopic fluctuations arise in a real gas, and these may be associated with changes in the nature of the microscopic fluctuations. It is therefore desirable to have a quantitative description of the fluctuations that occur in the DSMC simulation of a homogeneous gas.

The characteristics of the fluctuations have been determined by the program DSMC0F, which is based on the simple gas program DSMC0. The program samples the size distribution of the number fluctuations, the mean square number fluctuations of the macroscopic quantities, and the temporal and spatial correlation functions. The first step is to verify the assumption of §1.4 that the number fluctuations are consistent with the Poisson distribution of eqns (1.14) and (1.15). The data in the listed test case of DSMC0F is for an average nV of 100 molecules per cell. Fig. 11.16 shows that the sampled probability $P(N)$ of the number N during the run of DSMC0F is consistent with the prediction of eqn (1.15).

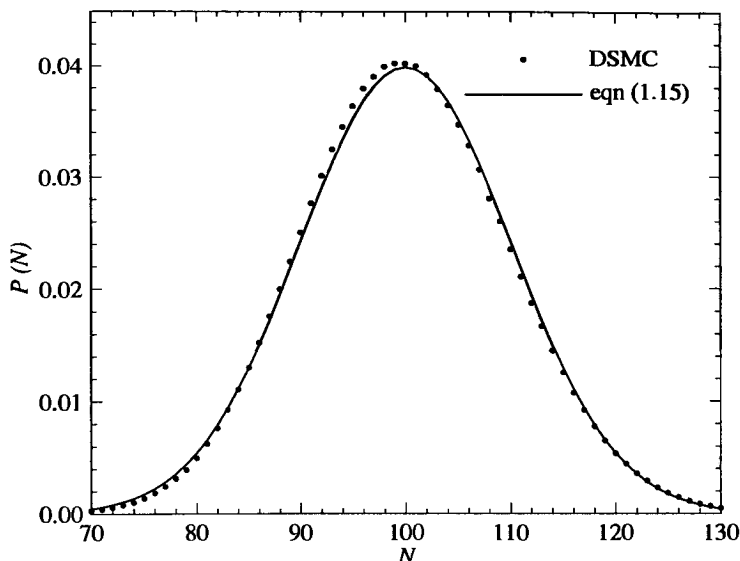


Fig. 11.16 The number distribution of simulated molecules in a cell.

The departure of the instantaneous number N from the average number nV is associated with a fluctuation δn in the number density. If the averages of macroscopic quantities are denoted by $\langle \cdot \rangle$, the *mean square fluctuation* of the number density at a given location is defined by

$$K(0) \equiv \langle \delta n \delta n \rangle. \quad (11.40)$$

As long as the mean fluctuation is zero, the mean square fluctuation can be related to the mean and the mean square of the quantity. Again using the number density as an example,

$$\langle \delta n \delta n \rangle = \langle n n \rangle - \langle n \rangle \langle n \rangle. \quad (11.41)$$

This expression is employed in DSMC0F to calculate the mean square fluctuations of the number density and the velocity components in each cell. It cannot be applied to the temperature because, as can be seen from eqn (1.29), the fluctuations lead to spurious velocities in a stationary gas. These cause a systematic lowering of the temperature and, if this effect is regarded as contributing to the temperature fluctuation, the mean of this fluctuation is not zero.

The fractional fluctuation is of the order of the square root of the sample size, so that a normalized mean square fluctuation of the number density that would be expected to be of order unity is

$$\hat{K}(0) = (\langle \delta n \delta n \rangle / n^2) \langle N \rangle = \langle \delta N \delta N \rangle / \langle N \rangle. \quad (11.42)$$

The most probable molecular speed c'_m may be used to define the normalized mean square fluctuation of a velocity component, for example u , as

$$\hat{K}(0) = (\langle \delta u \delta u \rangle / c'^2_m) \langle N \rangle. \quad (11.43)$$

The sampled values of these normalized mean square fluctuations are shown in Fig. 11.17. There is considerable scatter in the mean square fluctuation of the number density, but the mean value across the flow is very close to unity. There is remarkably little scatter in the corresponding values for the velocity components, and these are all close to 0.5. Note that $c'^2_m = 2kT/m$, so that, if the normalization had been with regard to kT/m , the normalized values for the velocity components would also have been close to unity.

If the average is taken over the product of the fluctuations at two points that are separated in either distance or time we have the spatial and temporal correlation functions, respectively. For example, the normalized temporal correlation function of the number density is

$$\hat{K}(t) = (\langle \delta n_0 \delta n_t \rangle / n^2) \langle N \rangle = \langle \delta N_0 \delta N_t \rangle / \langle N \rangle. \quad (11.44)$$

The subscript $_0$ indicates the local fluctuation that was unsubscripted in the previous equations and the subscript t indicates the fluctuation at the same location, but separated by the time interval t . Note that the mean values that are employed in the normalization are not functions of time.

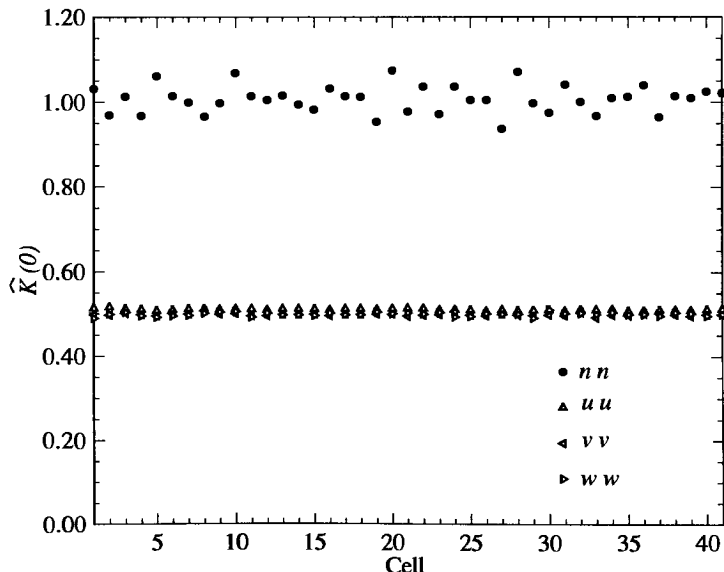


Fig. 11.17 The normalized mean square fluctuations in each cell.

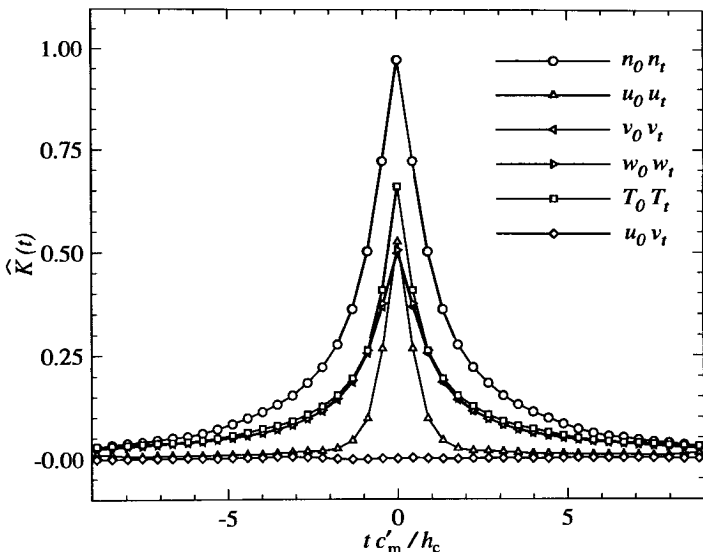


Fig. 11.18 The normalized temporal correlation functions.

The sampled time correlation functions for the cell midway between the boundaries in the flow of DSMC0F are shown in Fig. 11.18. This includes the temperature correlation function which is normalized in a similar manner to the velocity components, but with the mean temperature in place of the most probable molecular speed. The correlation function reduces to the mean square fluctuation as the time interval tends to zero. The u and v velocity components are uncorrelated even in this limit. The correlation function of the velocity component normal to the surfaces declines significantly faster than the other functions.

The time interval has been normalized by the cell height h_c divided by the most probable molecular speed. This is the time that a molecule moving with this speed normal to the cell boundary requires to cross the cell and this normalization takes no account of the mean free path and collision rate. The listed data in program DSMC0F is for a cell height equal to the one tenth the mean free path. The calculation was repeated with the collision routine disabled in order to obtain the collisionless or free-molecule result. It was also repeated for the density increased by a factor of five so that the cell height was half the mean free path. The three density correlation functions are compared in Fig. 11.19. A similar result is obtained for the other functions so that the density, and therefore the mean free path and collision rate, has very little effect on the decay of the correlation function. This is a somewhat surprising result in that the average diffusion rate of the molecules through the gas is strongly affected by the collision rate (Bird 1986).

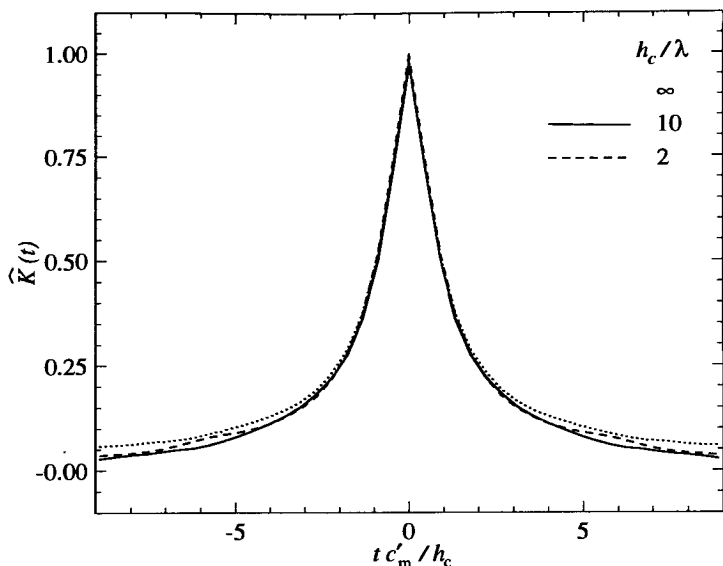


Fig. 11.19 The effect of density on the temporal correlation function.

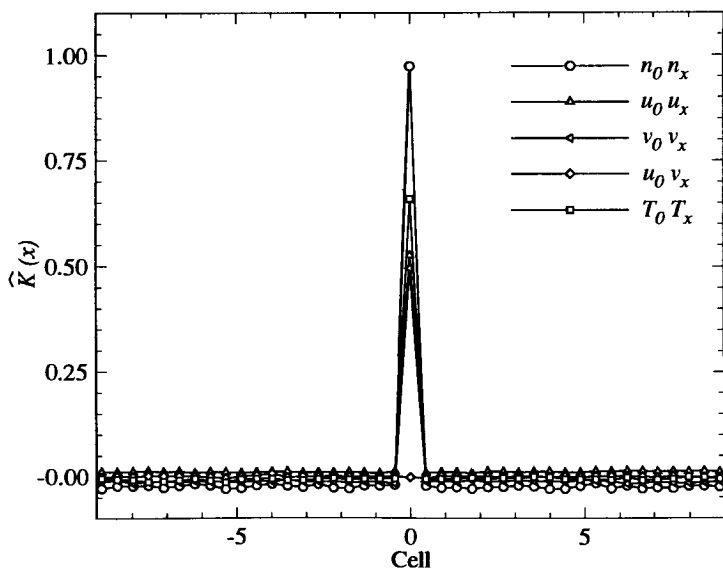


Fig. 11.20 The spatial correlation functions.

The normalized spatial correlation function of the number density in a macroscopically uniform gas is

$$\hat{K}(x) = (\langle \delta n_0 \delta n_x \rangle / n^2) \langle N \rangle = \langle \delta N_0 \delta N_x \rangle / \langle N \rangle. \quad (11.45)$$

This function is again sampled in the central cell and this location is denoted by the subscript $_0$. The correlation function is plotted against the cell number, so that the spatial displacement x is effectively normalized by the cell height. The correlation function is again equal to the mean square fluctuation when the displacement is zero, but Fig. 11.20 shows that there is no sign of any correlation between the fluctuations in separate cells.

References

- BIRD, G.A. (1976). *Molecular gas dynamics*, Oxford University Press.
- BIRD, G.A. (1986). The diffusion of individual molecules within a gas. In *Rarefied gas dynamics* (ed V. Boffi and C. Cercignani), vol. 1, pp 400–409, B.G. Teubner, Stuttgart.
- BIRD, G.A. (1989). Perception of numerical methods in rarefied gas dynamics. *Progr. Astro. and Aero.* **118**, 211–226.
- HERZBERG, G. (1950). *Spectra of diatomic molecules*, Van Nostrand, New York.
- KOURA, K. (1986). Null-collision technique in the direct simulation Monte Carlo technique, *Phys. Fluids* **29**, 3509–3511.
- LUMPKIN, K., HAAS, B. and BOYD, I. (1991). Resolution of differences between collision number definitions in particle and continuum simulations, *Phys. Fluids* **3**, 2282–2284.
- VINCENTI, W.G. and KRUGER, C.H. (1965). *Introduction to physical gas dynamics*, Wiley, New York.

12

ONE-DIMENSIONAL STEADY FLOWS

12.1 General program for one-dimensional flows

All calculations in this chapter are made with either the ‘general one-dimensional’ program DSMC1.FOR, or with several variants of this program that have special adaptions for the study of shock waves. The term ‘one-dimensional’ is taken here to mean that there can be macroscopic flow gradients in only one direction. There can be finite flow velocity components in more than one direction and, in addition to the plane flow geometry, the program can be applied to flows with cylindrical or spherical symmetry. The geometry is specified by setting the parameter IFX to 0 for plane flows, to 1 for cylindrical flows, or to 2 for spherical flows. All DSMC calculations are unsteady but, since this chapter deals only with steady flows, the sampling is concerned primarily with the steady flow that is established at large times. The gas is a simple gas or a gas mixture of monatomic or diatomic gases, and the DSMC collision procedures follow those of program DSMC0R.FOR.

The macroscopic flow gradients must be in the x -direction and, for cylindrical and spherical flows, the axis or centre must be at $x=0$ so that x becomes the radius. There is an ‘inner’ and an ‘outer’ boundary at the fixed values of x that are set by the variables XB(1) and XB(2). Each of these flow boundaries is specified through the variables IB(1) and IB(2) as one of:

- (i) The axis of a cylindrical flow or the centre of a spherical flow.
- (ii) A plane of symmetry for IFX=0, or a specularly reflecting cylinder or sphere for IFX=1 or 2, respectively.
- (iii) A solid diffusely reflecting surface with complete accommodation to a specified temperature. For plane or cylindrical flows, this surface may have a velocity in the y -direction. The axis of the cylindrical flow is along the z -axis, so that this is a circumferential velocity.
- (iv) A boundary with an external stream of specified composition, density, and temperature. The stream may also have a velocity component in the x -direction.
- (v) An interface with a vacuum.

The initial state of the flowfield may be either a vacuum or a uniform and macroscopically stationary gas of specified composition, density, and temperature. A number of the subroutines are common to the earlier programs and the full program is listed on the enclosed disk.

The flowfield is divided into $n_c \equiv \text{MNC}$ cells, and each of the cells is divided into NSC sub-cells. The cells of uniform width that were used in the programs for homogeneous gas studies become inefficient for problems that involve large changes in density. Should cells of non-uniform width be used, it is important that there should be an efficient procedure for determining the appropriate cell for a molecule at a given location x . An analytical expression for the cell number as a function of x is available if the cell widths are in arithmetic or geometric progression. The geometric progression is generally better suited to the density variations that occur in real flows and is defined by

$$a + ar + ar^2 + \dots + ar^{n_c-1} = a(1 - r^{n_c})/(1 - r).$$

The molecule location is normalized to lie between 0 and 1 by setting

$$\hat{x} = (x - x_1)/(x_2 - x_1),$$

where x_1 and x_2 are the boundaries of the region. The variation in cell width is defined by the ratio $c_w \equiv \text{CWR}$ of the width of the cell adjacent to the boundary at x_2 to the width of the cell adjacent to x_1 . The multiplier r is therefore given by

$$r = c_w^{1/(n_c-1)}.$$

Also, since the normalized width of the flow region is unity, the sum of the series must also be unity, and the width of the first cell is

$$a = (1 - r)/(1 - r^{n_c}).$$

The normalized coordinate of the lower valued boundary of cell m is

$$a(1 - r^{m-1})/(1 - r),$$

and the cell number is given by equating the normalized coordinate to this expression, solving for m , and truncating the solution to the nearest integer. The final result is, therefore,

$$m = \lfloor 1 + \ln\{1 - (1 - r)\hat{x}/a\}/\ln(r) \rfloor. \quad (12.1)$$

Each time a molecule is moved, the boundaries of the original cell are checked to determine whether the cell has changed and, if it has, eqn (12.1) is used to determine the number of the new cell. The sub-cells in a given cell are of uniform width.

The flow can have a uniform 'gravitational' acceleration g along the x -axis. This is applied through the elementary equations

$$\Delta x = u \Delta T + \frac{1}{2} g (\Delta t)^2$$

and

$$\Delta u = g \Delta t.$$

The logic for the interaction of molecules with solid boundaries has not been extended to include the effects of this acceleration and the option should be used only with type (iv) and type (v) boundaries in plane flows.

The more general boundaries that are employed in this program require a number of new procedures. The first is for the generation of typical molecules that are diffusely reflected from a surface. The distribution function for these molecules is identical to that for the molecules crossing a boundary from an external stationary equilibrium gas. For a surface or boundary normal to the x -axis, the distribution function for the velocity component normal to the boundary follows from eqns (4.20) and (4.1) as

$$f_u \propto u \exp(-\beta^2 u^2).$$

The normalization condition is that the integration of this distribution with respect to u from 0 to ∞ must be equal to unity. Therefore,

$$f_u = 2\beta^2 u \exp(-\beta^2 u^2), \quad (12.2)$$

and the distribution function for $\beta^2 u^2$ follows as

$$f_{\beta^2 u^2} = \exp(-\beta^2 u^2).$$

This distribution is identical with that of eqn (C11) so that, from eqn (C12), a typical value of u is given by

$$u = \{-\ln(R_f)\}^{1/2}/\beta. \quad (12.3)$$

Eqn (12.3) is implemented for the reflected molecules in the subroutine REFLECT1. The distribution function for a velocity component parallel to the boundary is the same as that for a velocity component within a stationary gas. Both parallel components of a diffusely reflected molecule are generated by a single call of the subroutine RVELC.

Should there be a stream velocity component u_0 , the thermal velocity component is $u' = u - u_0$, and the distribution function for the ratio of the thermal velocity component to the most probable thermal speed is

$$f_{\beta u'} \propto (\beta u' + s_n) \exp(-\beta^2 u'^2), \quad (12.4)$$

where $s_n = \beta u_0$ is the speed ratio based on the normal component of the stream velocity. The acceptance-rejection method is required for the generation of typical velocity components from this distribution. The maximum of this distribution occurs at

$$\beta u' = \{(s_n^2 + 2)^{1/2} - s_n\}/2$$

and the ratio of the probability to the maximum probability is

$$\frac{P}{P_{\max}} = \frac{2(\beta u' + s_n)}{s_n + (s_n^2 + 2)^{1/2}} \exp\left(\frac{1}{2} + \frac{s_n}{2}\{s_n - (s_n^2 + 2)^{1/2}\} - \beta^2 u'^2\right). \quad (12.5)$$

The procedure generates a value of $\beta u'$ that is uniformly distributed over a range that extends well into the tails of the distribution and covers virtually all entering molecules, but is subject to the condition that $\beta u' + s_n$ must be directed into the flow. The value of P/P_{\max} is then evaluated and is compared with the next random fraction R_f . β is the inverse of the most probable molecular speed in the entering gas.

The parallel components of velocity of the entering molecules are again generated by a call of the subroutine RVELC. The rotational energy of the stream, reflected, and entering molecules are generated by calls of the subroutine SROT. This subroutine includes the procedure that was the subject of subroutine SIE in DSMC0V.FOR and DSMC0D.FOR. The number flux of the entering molecules is calculated directly from eqn (4.22). This involves the error function, and the function subroutine ERF has been included. The cross-sectional area of plane flows has been assumed to be unity. The cylindrical flow has an axial length of unity and the cross-sectional area at radius r is πr^2 . The cross-sectional area of a spherical flow at radius r is taken to be πr^2 . Molecules that leave the flow across either a stream or vacuum boundary are removed from the simulation. This is achieved in the subroutine REMOVE by simply replacing this molecule by molecule NM, where NM is the total number of molecules. NM is then reduced to NM-1.

Advantage is taken of cylindrical or spherical symmetry in that the radius is the only spatial coordinate that must be stored for each molecule, and the results are obtained as a function of the radius. At the same time, the logic associated with the three-dimensional motion of the molecules must be exact. It is assumed that, at the beginning of each time step, the molecule lies in the x -axis. The y -velocity component and, in the case of spherical symmetry, the z -velocity component cause the molecule to move off the axis. However, the new radius may be calculated, and this position coordinate is stored for the molecule at the end of the time step. However, this involves a rotation of the direction of the molecule, and the velocity components of the molecules must be transformed accordingly. Before the transformations, the new position on the x -axis is

$$x' = x_i + u \Delta t, \quad (12.6)$$

where x_i is the initial radius of the molecule, u is the velocity component in the x -direction, and Δt is the time step. The molecule moves off the axis through a distance

$$d_n = v \Delta t$$

in a cylindrical flow, or

$$d_n = \{(v \Delta t)^2 + (w \Delta t)^2\}^{1/2}$$

in a spherical flow. The new radius is given by

$$x = (x'^2 + d_n^2)^{1/2} \quad (12.7)$$

while the sine and cosine of the rotation angle are

$$\sin \theta = d_n / x$$

and

$$\cos \theta = x' / x.$$

The transformed velocity component in the radial (i.e. the x) direction is

$$u' = u \cos\theta + u_c \cos\theta, \quad (12.9)$$

where the circumferential velocity component u_c is v in a cylindrical flow or $(v^2 + w^2)^{1/2}$ in a spherical flow. The transformed value of the circumferential velocity component is

$$u'_c = -u \sin\theta + u_c \cos\theta. \quad (12.10)$$

This becomes the new y -velocity component v in a cylindrical flow while, in a spherical flow, an azimuth angle ϕ may be chosen at random between 0 and 2π to give

$$v' = u_r \sin\phi \quad \text{and} \quad w' = u_r \cos\phi. \quad (12.11)$$

These equations are implemented in the subroutine AIFX. This is called at the end of the trajectory element or when the molecule intersects with a boundary.

The calculation of the point of intersection with a boundary must be based on three-dimensional geometry. Eqns (7.85)–(7.87) may be applied to each boundary in turn to calculate the ratio s_d of the distance along the molecular trajectory to any intersection with the boundary to the distance d that is moved during the time step. The direction cosines are given by

$$l_1 = u \Delta t / d, \quad m_1 = v \Delta t / d, \quad \text{and} \quad n_1 = w \Delta t / d,$$

where

$$d = \{(u \Delta t)^2 + (v \Delta t)^2 + (\epsilon - 1)(w \Delta t)^2\}^{1/2}.$$

The z -direction cosine applies only to spherical flows, and the parameter ϵ is 1 for cylindrical flows and 2 for spherical flows. The coefficients of x^2 , y^2 and, for spherical flows, z^2 are unity, and the coefficient a_{44} is $-r^2$, where r is the radius of the cylinder or sphere. All other coefficients are zero, as are y_i and z_i . The ratio s_d is therefore given by the quadratic

$$\frac{1}{2}s_d^2 + (u \Delta t x_i / d^2) s_d + \frac{1}{2}(x_i^2 - r^2) / d^2 = 0. \quad (12.12)$$

The molecule collides with the surface if there is a real solution between 0 and 1. There can be two real solutions for the inner boundary, and the lesser solution then gives the point of intersection. Note that there can be no intersection with the inner boundary unless the value of x' from eqn (12.6) is less than r . Similarly, there can be no intersection with the outer boundary unless the final radius x is greater than r . The fraction s_d is evaluated in the subroutine RBC.

The surface properties of any diffusely reflecting solid surface are sampled as the reflections occur in the routine REFLECT1. The number flux, pressure, shear stress, and heat transfer to these surfaces are output in the subroutine OUT1. The surface data distinguishes between the contributions that are made by the incident and reflected molecules. The heat transfer also records separately the contributions from the translational and rotational modes.

12.2 The viscosity coefficient of argon

The first application of the program DSMC1.FOR is essentially a numerical experiment for the measurement of the coefficient of viscosity in argon. Plane Couette flow is the flow between two plane surfaces, one of which is stationary and the other is moving with a velocity in the plane of the surface. This is generated here by setting the inner boundary as a stationary diffusely reflecting surface and the outer boundary as a diffusely reflecting surface at the same temperature, but with a finite velocity in the y -direction. The gas is initially set to the same temperature as the walls, but it may be either stationary or have a uniform stream velocity gradient.

The surfaces are maintained at a temperature of 273 K with a spacing of 1 m, and the gas is argon at a number density of 1.4×10^{20} . The VHS molecular model is employed with the molecular diameter as listed in Table A2 and the mean free path λ is, from eqn (5.69), 0.00925 m. The Knudsen number based in the surface spacing is, therefore, 0.00925. The velocity of the outer surface is 300 ms^{-1} , which corresponds to a speed ratio of 0.89. The velocity profile is shown in Fig. 12.1. The velocity gradient is very nearly uniform although there is a barely perceptible decrease in the gradient within about 10 to 20 mean free paths from the surfaces. There is a velocity slip of just over 3 ms^{-1} at each surface and this is, as expected, very close to $\lambda dv/dx$.

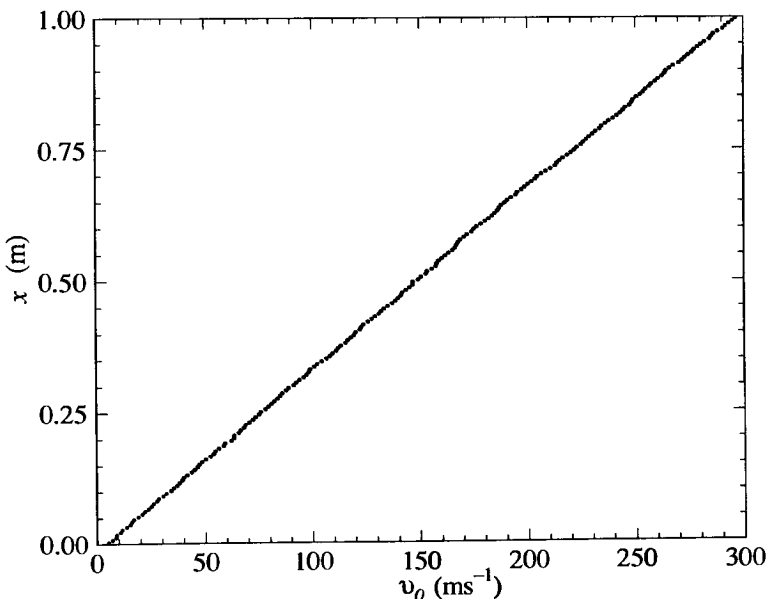


Fig. 12.1 The velocity profile in the Couette flow at (Kn) = 0.00925.

The incompressible continuum solution would be a constant pressure and constant temperature gas with a uniform velocity gradient, and no velocity slip at the surface. The coefficient of viscosity of argon at 273 K (on which the molecular diameter was based) is $2.117 \times 10^{-5} \text{ Nsm}^{-2}$, and the shear stress on the surfaces would be $6.35 \times 10^{-3} \text{ Nm}^{-2}$. The incompressible solution is, however, incompatible with the energy conservation principle. The motion of the wall against the shear stress would generate an energy input to the gas of 1.905 Wm^{-2} , and this would raise the temperature of the gas until the heat that was transferred to the surfaces equalled the energy input. The pressure must be uniform through the gas, and the temperature non-uniformities must lead to density variations that invalidate the incompressibility assumption.

The DSMC solution exhibits the expected compressibility effects. The initial value of the pressure is 0.5277 Nm^{-2} and, because of the heating due to the viscous dissipation, this increases to a steady state value of 0.549 Nm^{-2} . The pressure is uniform across the flow, while the temperature rise in the central portion of the flow is approximately 15 K, or just over 5% of the surface temperature. The DSMC temperature profile is shown in Fig. 12.2. The temperature slip at the surfaces is approximately 0.6 K, and this is close to $\lambda dT/dx$. Because of the uniform pressure, the density change must be the inverse of the temperature change, and the density profile is shown in Fig. 12.3.

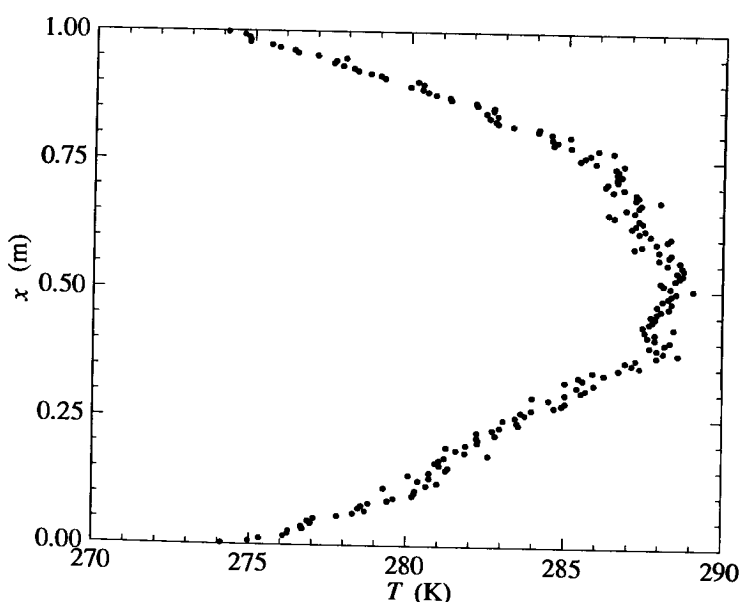


Fig. 12.2 The temperature profile in the Couette flow.

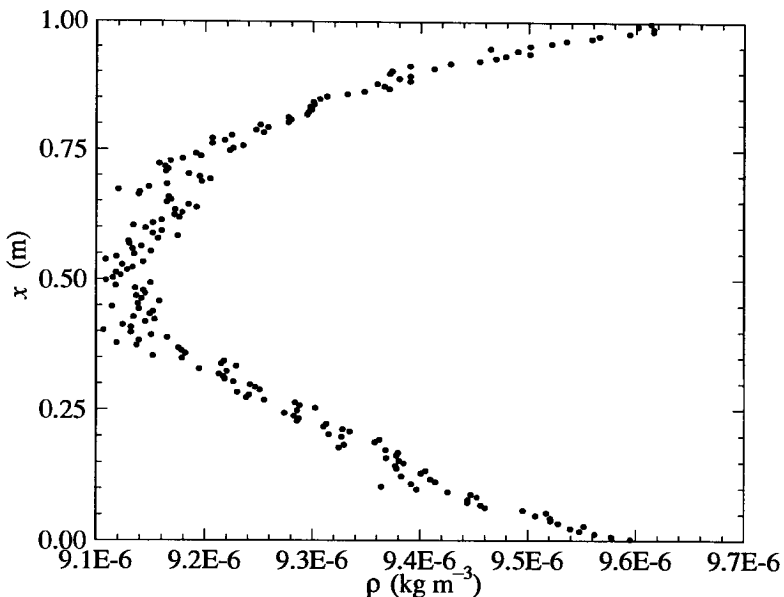


Fig. 12.3 The density profile in the Couette flow.

These results are based on time-averaged sampling over the interval from 0.1 seconds to 0.375 seconds. This run was made with the listed data in the subroutine DATA1, and employs the option that sets a uniform velocity gradient in the initial gas. Runs were also made for a uniform initial gas and steady flow was established at about 0.5 sec. The test case involved the calculation of 7.7×10^6 collision events and 1.5×10^9 molecular moves. Almost 270,000 molecules collided with each surface and the standard deviation associated with the surface pressure is 0.2%. The sample in each cell was more than 1.3×10^6 , and the expected standard deviation in the macroscopic properties is less than 0.1%. However, the flow is subsonic and both the shear stress and heat flux are essentially based on small differences between large numbers. The shear stress is 1.1% of the pressure, and the net heat flux to the surfaces is less than 1% of the incident energy flux. This means that the scatter of a single number can be as high as 10% but, in addition to the sampling of the shear stress as a surface property, it may be sampled as a macroscopic flow property in each cell. The boundary conditions are such that some applications involve a stream velocity component in the x -direction and others a component in the y -direction, but none involve a finite component in each direction. The shear stress for this case can therefore be written from eqn (1.52) as

$$\tau_{xy} = -n \overline{mu v}. \quad (12.13)$$

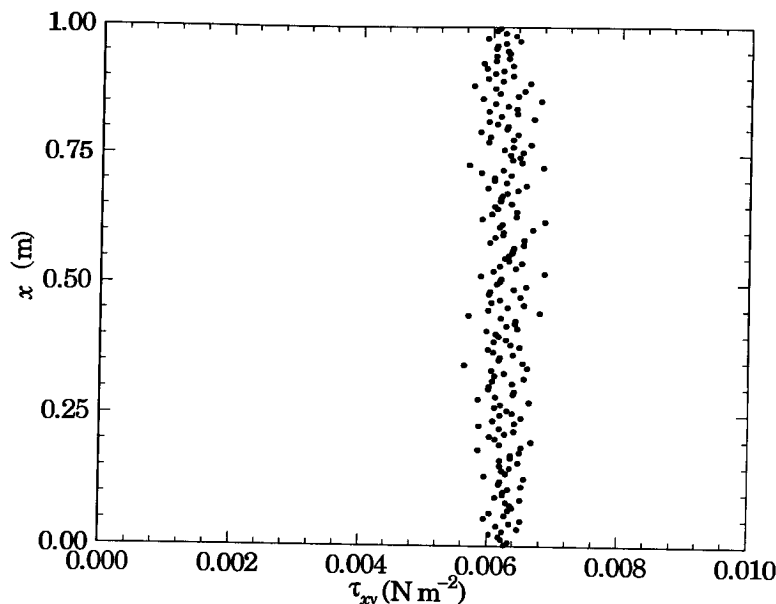


Fig. 12.4 The shear stress profile in the Couette flow.

Similarly, since the stream velocity must consist only of u_0 or v_0 , the heat flux vector in the x -direction can be written from eqn (1.53) as

$$q_x = n(\frac{1}{2}mc^2\bar{u} - \bar{mu}^2u_0 + \bar{mu}_0^3 - \bar{mu}\bar{v}v_0 - \frac{1}{2}\bar{mc}^2u_0 + \bar{\epsilon}u - \bar{\epsilon}u_0). \quad (12.14)$$

The shear stress profile is shown in Fig. 12.4 and, while there is significant statistical scatter, it is constant across the flow. The average value of the stress over the flow was 0.00624 Nm^{-2} and the velocity gradient was 293 (m/s)/m . These values correspond to a coefficient of viscosity of $2.13 \times 10^{-5} \text{ Nsm}^{-2}$, which may be compared with the nominal value of $2.117 \times 10^{-5} \text{ Nsm}^{-2}$ at a temperature of 273 K . The average temperature across the flow is 283 K and, with a temperature-viscosity index of 0.81, the nominal coefficient is $2.18 \times 10^{-5} \text{ Nsm}^{-2}$. Given the scatter associated with the shear stress and the variation of temperature across the flow, the agreement is satisfactory, although the discrepancy is rather larger than would be expected. The mean separation between collision partners was $1.7 \times 10^{-4} \text{ m}$ which is very small in comparison with the mean free path, and the other computational parameters were satisfied by similarly wide margins.

The work done by the moving surface at the average shear stress is 1.87 Wm^{-2} , while the sampled net heat transfer to the inner and outer surfaces is 0.85 Wm^{-2} and 1.03 Wm^{-2} , respectively. The heat flux vector sampled from eqn (12.14) is shown in Fig. 12.5. The scatter in q_x is very high, and better results are obtained here if u_0 is forced to its steady flow value of zero.

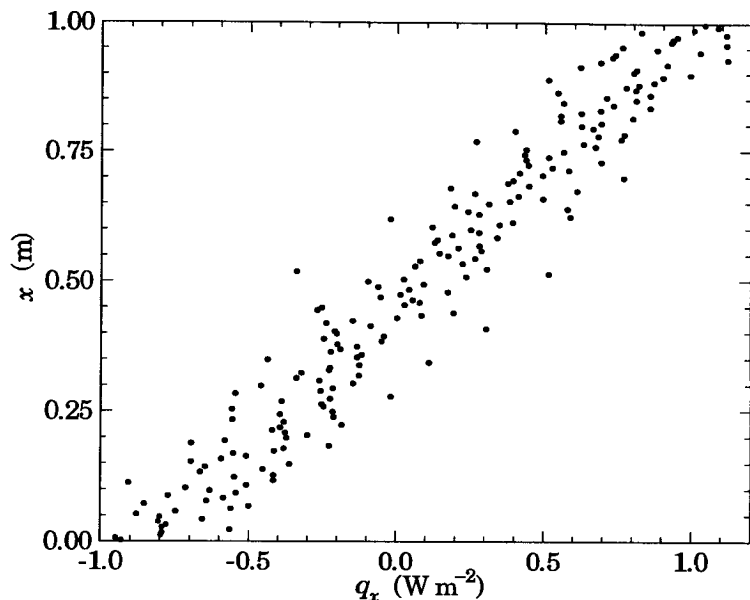


Fig. 12.5 The heat flux vector in the Couette flow.

Because the statistical scatter is a fraction of the undisturbed flow quantities, accurate results are more easily obtained for large disturbance flows than for small disturbance flows. The calculation was therefore repeated for a surface velocity of 1000 m/s, which corresponds to a speed ratio of 2.67. The Mach number based on the wall speed and the temperature of the undisturbed gas is 2.93, and much of the flow is supersonic. The velocity gradient and the shear stress increase by a factor of just over three, but the temperature gradient and heat flux vector increase by a factor of more than ten. The net heat flux to a surface increases from less than one percent of either the incident or reflected flux to more than ten percent of these quantities. The resulting effect on the scatter is quite dramatic, as can be seen from a comparison of Figs. 12.5 and 12.6.

The high speed velocity profile of Fig. 12.7 is qualitatively different from the relatively low speed profile of Fig. 12.1. The velocity gradient in Fig. 12.1 is linear to within the statistical scatter, while the high speed velocity profile is nonlinear over the complete flowfield. This nonlinearity is due to the temperature dependence of the coefficient of viscosity. The temperature profile remains parabolic in form, and the maximum temperature is 438 K. The coefficient of viscosity at the centre of the flow is therefore about 40% higher than that near the surfaces and, in order for the shear stress to remain constant across the flow, the velocity gradient in the cooler gas near the surfaces must be correspondingly larger than that near the centre.

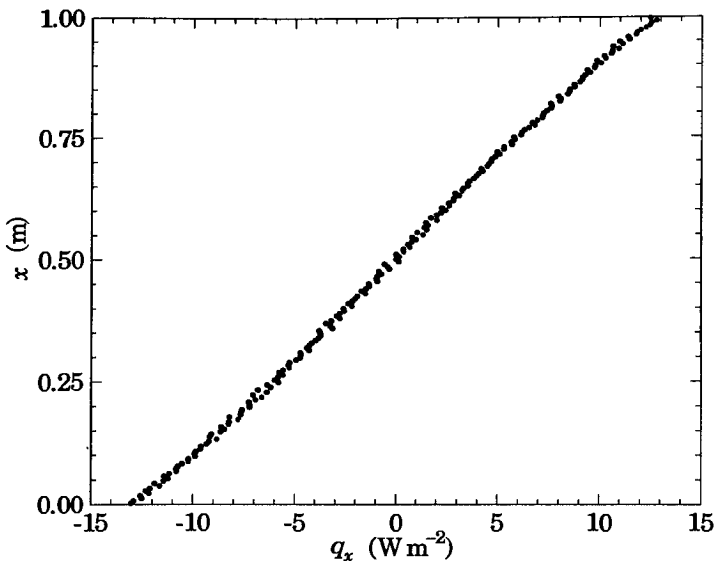


Fig. 12.6 The heat flux in the high-speed Couette flow.

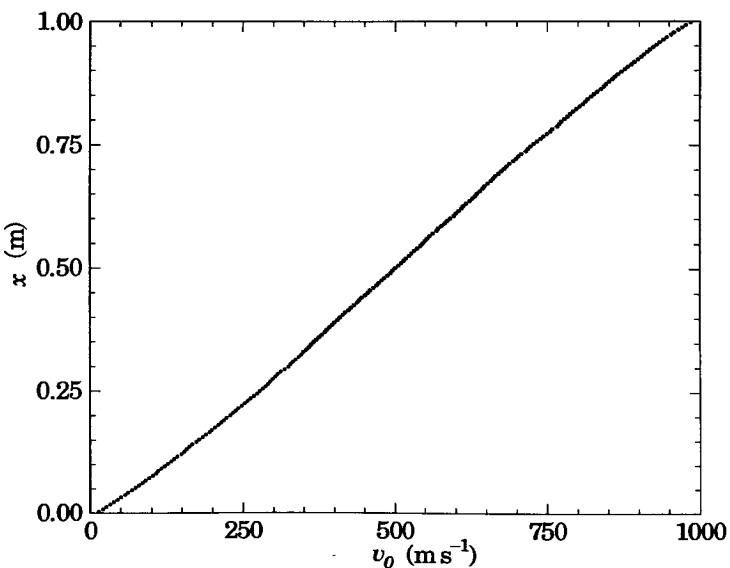


Fig. 12.7 The velocity profile in the high-speed Couette flow.

Rather than use an average velocity gradient and an average temperature as was done for the low-speed case, it is preferable to directly sample the coefficient of viscosity at the reference temperature μ_{ref} from the results in the file DSMC1.OUT. The required equation is

$$\mu_{\text{ref}} = \tau_{xy} (\Delta x / \Delta v_0) (T_{\text{ref}} / T)^{\omega}. \quad (12.15)$$

The quantities τ_{xy} , x , v_0 , and T are output for each cell and the numerical array may be edited out as a separate file and read into a post-processing program for the evaluation of the transport properties. The program that was used here based Δx and Δv_0 for a particular cell on the differences between the values in the two adjacent cells. The coefficient of viscosity was then obtained by averaging over all cells except those in the Knudsen layers very close to the surfaces. The resulting coefficient of viscosity at the reference temperature of 273 K was 2.10×10^{-5} Nsm⁻², and this compares well with the value of 2.117×10^{-5} Nsm⁻² on which the VHS molecular diameter was based.

The velocity and temperature 'slips' at the surfaces were again very close to the product of the local mean free path with the velocity gradient and the temperature gradient, respectively.

The thermal effects in the high-speed case are sufficiently large to allow the determination of the coefficient of heat conduction in addition to the coefficient of viscosity. The equation for the evaluation of the reference value of this coefficient is

$$K_{\text{ref}} = q_x (\Delta x / \Delta T) (T_{\text{ref}} / T)^{\omega}. \quad (12.16)$$

and, since q_y also appears in DSMC1.OUT, values at each cell are readily calculated. The results are hopelessly erratic in the central portion of the flow, but the averaged value in the outer 30% of the flow was 0.0166 Wm⁻¹K⁻¹. This is in reasonable agreement with the measured value of 0.0164 Wm⁻¹K⁻¹ that is quoted by Chapman and Cowling (1970) for argon at 273 K. The resulting Prandtl number is 0.666 which is in excellent agreement with the theoretical value of 2/3 for a monatomic gas.

The temperature correction in the high-speed case is very significant and the calculation was repeated for a surface temperature of 180 K so that the average temperature was much nearer to 273 K. The resulting viscosity coefficient was 2.11 Nsm⁻², and the heat transfer coefficient was 0.0167 Wm⁻¹K⁻¹.

The derivations from and comparisons with theory have been based on the results from the first approximation of the Chapman-Enskog theory, as discussed in §3.5. The second approximation, that is introduced by an additional term in the Sonine polynomial, would increase the theoretical coefficient of viscosity in argon by less than one half of one percent. This is of the order of the statistical scatter in the DSMC results. In addition, the Burnett terms that result from the inclusion of the next term in the Chapman-Enskog expansion itself are probably of the same magnitude. These terms would include the so-called 'thermal stresses' that arise from the contribution of the temperature gradient to the stress tensor.

12.3 The viscosity of an argon-helium mixture

The viscosity of an argon-helium mixture at 293 K has been discussed in detail by Chapman and Cowling (1970). The coefficient of viscosity of argon is 13.6% greater than that of helium but, as long as the percentage of helium is less than about 83%, the coefficient of viscosity of the mixture exceeds that of argon. The maximum viscosity coefficient occurs for about 60% helium and is 4% higher than the coefficient for pure argon. In order to check that the DSMC method reproduces this behaviour, calculations similar to those in the previous section were made for an argon-helium mixture. One difference is that the VHS model is replaced by the VSS model. Also the parameter ISPD has been set to unity, and this requires the effective diameter and viscosity for the argon-helium collisions to be set explicitly in the data rather than being set to the mean values.

The measured values of diffusion coefficient may be used with the VSS scattering parameters that are listed in Appendix A to define the effective diameter $(d_{12})_{\text{ref}}$ of the cross-collisions at a given reference temperature. This procedure is analogous to that used in §4.3 to define a molecular diameter from the coefficient of viscosity, and the result is

$$(d_{12})_{\text{ref}} = \left(\frac{3(\alpha_{12} + 1) \{2kT_{\text{ref}}/(\pi m_r)\}^{1/2}}{8(5 - 2\omega_{12}) n (D_{12})_{\text{ref}}} \right)^{1/2}. \quad (12.17)$$

The diameter is that at the mean value of $c_r^{2\omega-1}$ in an equilibrium gas at the reference temperature. It should again be emphasized that the use of an equilibrium quantity to define the reference diameter is a matter of convenience and has no physical significance. Alternatively, the diameter may be set to the mean diameter of eqn (1.35), and the values of the diffusion coefficient used to calculate the appropriate value of the VSS scattering parameter. This is the preferred approach and is adopted in Appendix A. Both approaches were used here and, although the scattering parameters differ, the viscosity coefficients were indistinguishable.

Since the ‘overshoot’ in the coefficient of viscosity is only 4%, the level of statistical scatter in the DSMC result is of critical importance. The flow is sampled at regular intervals in order to build up a cumulative sample. However, the sample in each cell changes slowly as a consequence of diffusion and it is not easy to choose the minimum time interval that leads to independent samples. In addition, the net shear stress is the small difference between large quantities and the size of the cumulative sample is not a reliable guide to the expected accuracy. The best indication of the accuracy of the DSMC result is given by the time history of the cumulative sample. This history for the coefficient of viscosity in pure argon at 293 K in a gas of VSS molecules is plotted in Fig. 12.8 for more than 3000 individual samples. The sampling started at 0.08 s which was the assumed time for the establishment of steady flow. The sample size at 0.6 s was therefore 25 times larger than that at 0.1 s, and the statistical scatter would be expected to decline by a factor of five over the plotted interval.

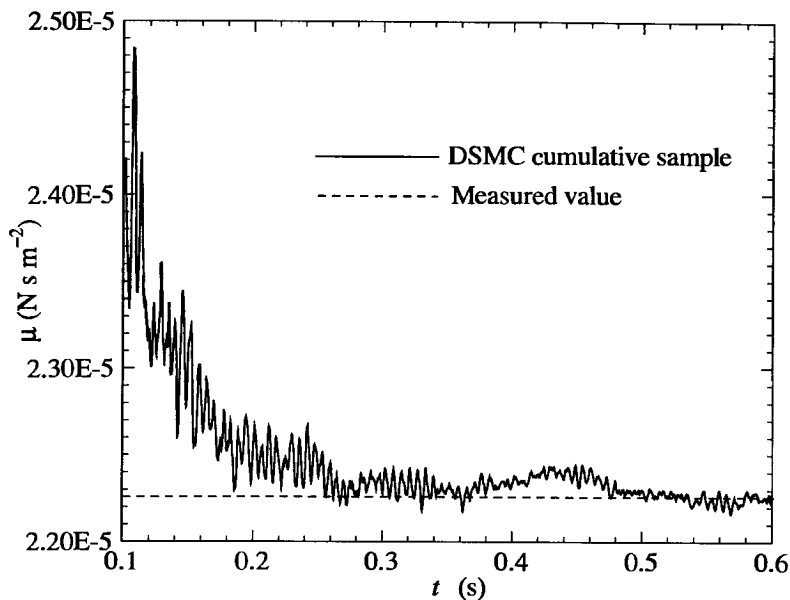


Fig. 12.8 The coefficient of viscosity in argon at 293 K.

The progressive reduction in the level of the statistical scatter is in line with expectations, and the DSMC result is consistent with the measured value. Most of the computations for the gas mixture involved a sample to approximately 0.4 seconds. Fig. 12.8 indicates that the standard deviation of the statistical scatter should be less than 1%. This means that most results should be within 1% of the correct value, but extreme cases could be 2% or more in error. The results from the DSMC calculations with program DSMC1.FOR are shown in Table 12.1. These are in agreement with the measured values to within the expected statistical scatter.

Table 12.1 Viscosity coefficients in He-Ar mixtures at 293 K.

Helium (%)	Measured μ (Nsm^{-2})	Calculated μ (Nsm^{-2})
0.0	2.2275×10^{-5}	2.22×10^{-5}
19.9	2.2707×10^{-5}	2.24×10^{-5}
37.1	2.3095×10^{-5}	2.31×10^{-5}
63.4	2.3161×10^{-5}	2.27×10^{-5}
100.0	1.9604×10^{-5}	1.99×10^{-5}

12.4 The Prandtl number of nitrogen

As shown by eqn (12.14) the internal energy ϵ of the molecules contributes to the heat flux vector. This leads to an increase in the heat flux, but the specific heat also changes, and the degree of departure of the Prandtl number from the monatomic gas value of 2/3 is of interest.

The high speed Couette flow calculation was therefore repeated with the VHS model for nitrogen. The post-processing program was again used to produce averaged values of the viscosity and heat transfer coefficients at 273 K. The viscosity coefficient was found to be 1.645×10^{-5} N s/m², while the VHS diameter was based on the value of 1.656×10^{-5} N s/m² that is quoted by Chapman and Cowling (1970). The corresponding heat transfer coefficient was 0.0232 W/(m K). This may be compared with the measured value of 0.0240 W/(mK) from Chapman and Cowling who note that the estimated error in the experiments that led to these values is not less than one percent. The DSMC and measured values of the Prandtl number are then 0.74 and 0.72, respectively. The Prandtl number of diatomic gases generally approximates 3/4 rather than the 2/3 for monatomic gases.

12.5 The self-diffusion coefficient of argon

Experiments to measure the self-diffusion coefficient generally employ different isotopes in order that the otherwise identical molecules may be distinguished. The fact that the isotopes have slightly different masses adds to the experimental error. The 'numerical experiment' with the DSMC method is facilitated by the fact that identical molecules may be designated as both species 1 and species 2. The VSS model for argon was employed with the molecular properties as listed in Tables A1 and A3. The data for program DSMC1.FOR was set with both boundaries as 'stream boundaries' (IB(1)=IB(2)=4) with a stationary gas as the stream. The stream at the inner boundary at $x=0$ was comprised entirely of species 1 and that at the outer boundary at $x=1$ m was comprised entirely of species 2. In this case, the streams were at a number density of 1.4×10^2 m⁻³ and a temperature of 273 K. The flowfield was plane with the locations of the boundaries, the number of cells, and the number of sub-cells were the same as in the listed data for DSMC1.FOR. The initial composition of the gas was equal parts of the (physically identical) species 1 and species 2.

After the gas had come to a steady state, there was a linear variation of composition across the flowfield, as shown in Fig. 12.9. The molecules that cross the stream boundary from the gas are discarded and there is a 'composition slip' at the boundaries. The gas is macroscopically uniform and stationary but, as shown in Fig. 12.10, the diffusion velocities are quite substantial. It should be noted that the diffusion coefficients are inversely proportional to the number density, so that the diffusion velocities in a gas at standard temperature and pressure would be smaller than those shown here by a factor of approximately 200,000.

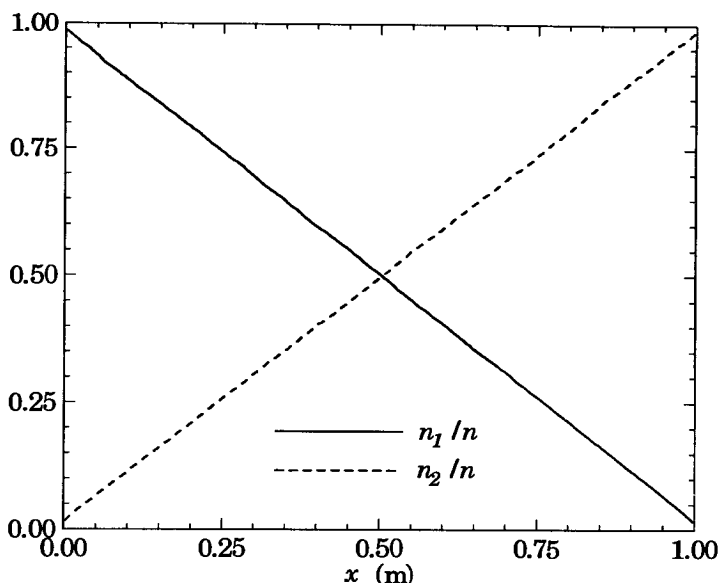


Fig. 12.9 The concentration gradients in the self-diffusion problem.

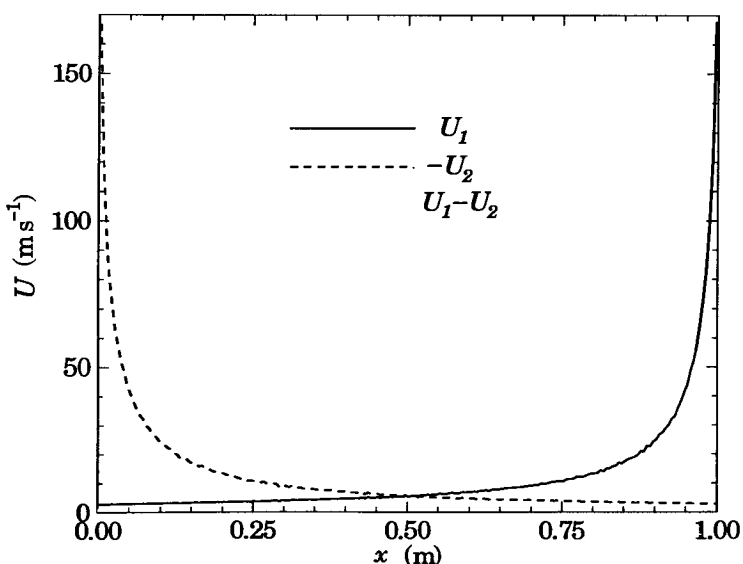


Fig. 12.10 The diffusion velocities in the self-diffusion problem.

For this problem, eqn (3.91) enables the self-diffusion coefficient to be written

$$D_{11} = D_{12} = -(U_1 - U_2) \frac{n_1 n_2}{n^2} \frac{\Delta x}{\Delta(n_1/n)}. \quad (12.18)$$

The concentration gradient is uniform across the flow and the variation of the diffusion velocities is such that, as expected, D_{11} is also constant across the flow to within the expected statistical scatter. The averaged value of D_{11} at a temperature of 273 K and a number density of $1.4 \times 10^{20} \text{ m}^{-3}$ was found to be $2.95 \text{ m}^2 \text{s}^{-1}$. This value corresponds to 1.55×10^{-5} at S.T.P. and is in good agreement with the measured value of $1.57 \times 10^{-5} \text{ m}^2 \text{s}^{-1}$ (Chapman and Cowling 1970).

The calculation was repeated for the VHS model ($\alpha = 1$) and also for the value of $\alpha = 1.67$ proposed by Koura and Matsumoto (1991). The resulting S.T.P. values for D_{11} were $1.26 \times 10^{-5} \text{ m}^2 \text{s}^{-1}$ and $1.72 \times 10^{-5} \text{ m}^2 \text{s}^{-1}$, respectively. As expected from eqn (3.76) D_{11} is proportional to $\alpha + 1$, and the value of α given in Table A3 is the only value that leads to the correct coefficient of self-diffusion.

12.6 Mass diffusion in an argon–helium mixture

In order to test the values of the VSS scattering parameter in Table A3, the ‘diffusion cell’ calculation was repeated with an argon reservoir at the inner boundary and a helium reservoir at the outer boundary. Because of the small molecular diameter of helium, the average mean free path is larger than that in the pure argon calculation. The number densities in the reservoirs was therefore doubled to 2.8×10^{20} in order to keep the local Knudsen numbers well in the range of values for which the Chapman–Enskog theory should be valid.

The species concentration and diffusion velocity profiles are shown in Figs 12.11 and 12.12. These may be compared with Figs 12.9 and 12.10 for the argon self-diffusion problem. The symmetry disappears and the point at which the species concentrations are equal moves from the midpoint of the flow to a location nearer to the argon reservoir. The diffusion velocity in the helium is larger than that in the argon by a factor that approximates the square root of the mass ratio. There is a qualitative difference in the velocity profiles in that there is a shallow minimum in the helium diffusion velocity.

Eqn 12.8 can again be used to determine the diffusion coefficient. Even though there are very large gradients near the boundaries, this was again near uniform across the flow. The averaged S.T.P. value of D_{12} in the central 80% of the flow was $6.39 \times 10^{-5} \text{ m}^2 \text{s}^{-1}$, and that across the complete flow was $6.33 \times 10^{-5} \text{ m}^2 \text{s}^{-1}$. The measured S.T.P. value of D_{12} in an argon–helium mixture is given by Chapman and Cowling as $6.41 \times 10^{-5} \text{ m}^2 \text{s}^{-1}$. The expected error in both the experiments and the DSMC calculation is of the order of 1%.

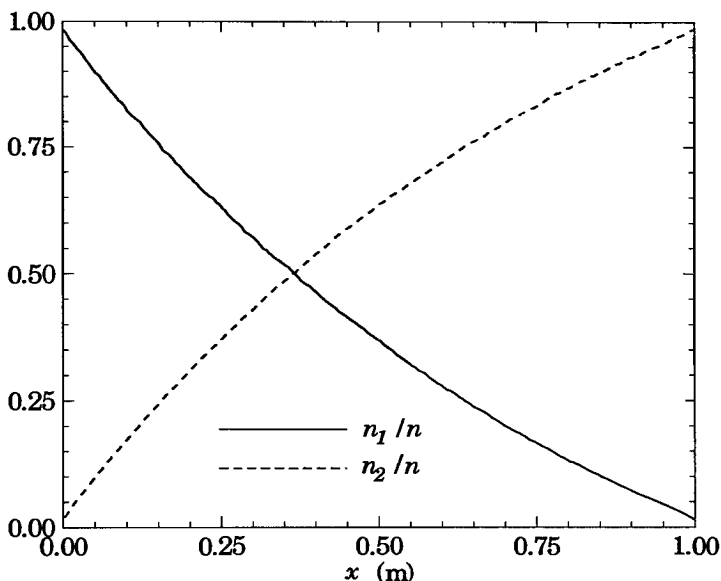


Fig. 12.11 The concentration gradients in Ar-He diffusion.

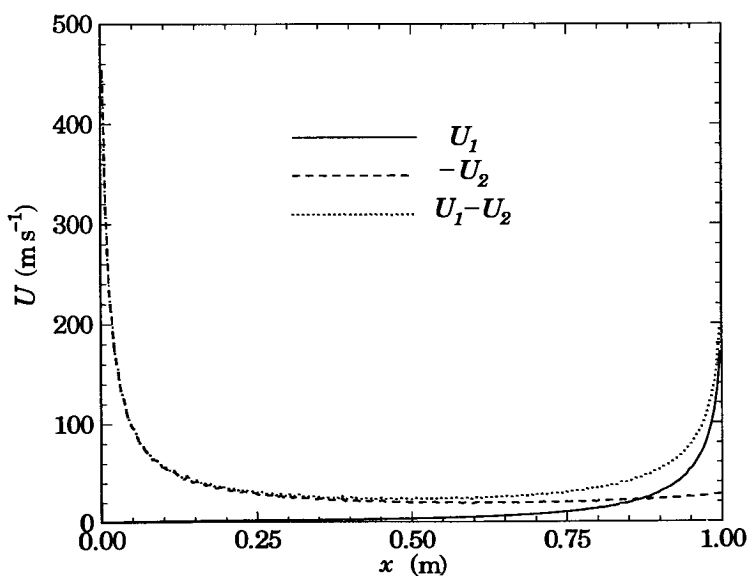


Fig. 12.12 The diffusion velocities in Ar-He diffusion.

12.7 Thermal diffusion

The composition of the gas in the high-speed Couette flow of the 37.1% helium, 62.9% argon mixture is shown in Fig. 12.13. Even though the boundary conditions do not induce mass diffusion, and the flow is at a uniform pressure, there is a partial separation of the two species with a reduction in the concentration of argon at the centre of the flow. This is due to thermal diffusion which, as discussed in §3.5, causes the larger and generally heavier molecules to become concentrated in regions of low temperature.

Thermal diffusion is best studied quantitatively in a simpler flow with no mass velocities. The data in the program DSMC1.FOR may be set such that the inner boundary is a diffusely reflecting boundary at 300 K and the outer surface is a stream boundary with a mixture of equal parts (by number) of helium and argon at a temperature of 2000 K and a number density of 1×10^{20} . The gas is initially set to the stream conditions and, during the unsteady phase of the flow, the gas is cooled at the surface and the consequent increase in the density induces a flow of gas towards the surface. The gas eventually becomes stationary at the stream pressure, but with a strong temperature gradient that produces separation effects due to thermal diffusion.

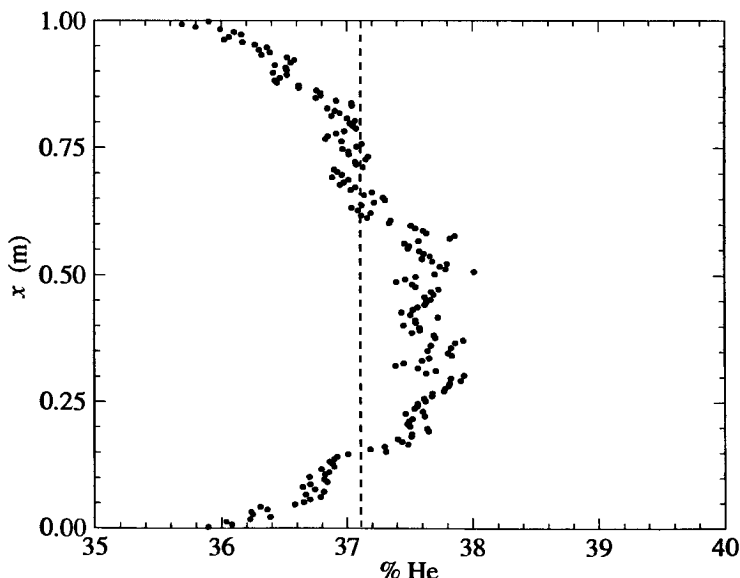


Fig. 12.13 Separation effects in the high-speed Couette flow for a 37.1% He–Ar mixture.

The steady state does not involve any diffusion velocities and eqn (3.91) reduces to

$$\frac{dn_1/n}{dx} = k_T \frac{d\ln(T)}{dx}. \quad (12.19)$$

The thermal diffusion ratio k_T depends strongly on the composition, and it is preferable to quantify the effect through the thermal diffusion factor which is defined by

$$\alpha_T = \{n^2 / (n_1 n_2)\} k_T. \quad (12.20)$$

Eqn (12.19) can then be integrated to give

$$\ln(n_1/n_2) = -\alpha_T \ln(T) + C, \quad (12.21)$$

where C is a constant.

The temperature and species concentration profiles in the steady state are shown in Figs 12.14 and 12.15. The mean free path in the 'stream' at $x = 1$ m is approximately 0.02 m and, since the density is here inversely proportional to the temperature, the mean free path at the surface is less than 0.003 m. The local Knudsen numbers are therefore well within the limits of validity of the Chapman-Enskog theory and the only effects of the rarefaction are the temperature slips at the boundaries. The separation is substantial and extends over the whole simulated region.

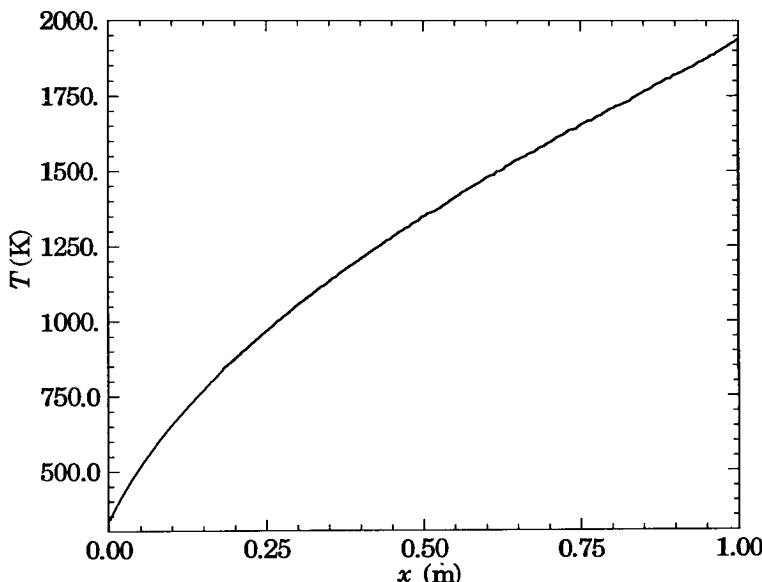


Fig. 12.14 The temperature profile between a surface at 300 K and a stationary gas of equal parts by number of He and Ar at 2000 K.

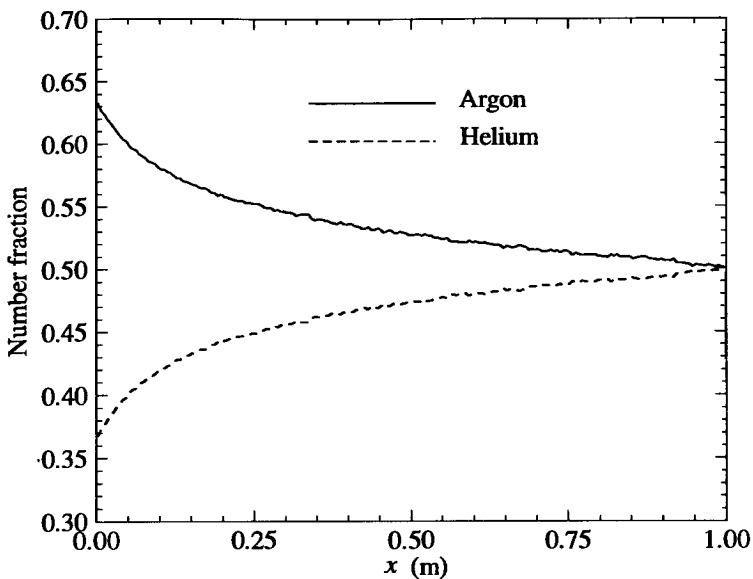


Fig. 12.15 The separation due to thermal diffusion.

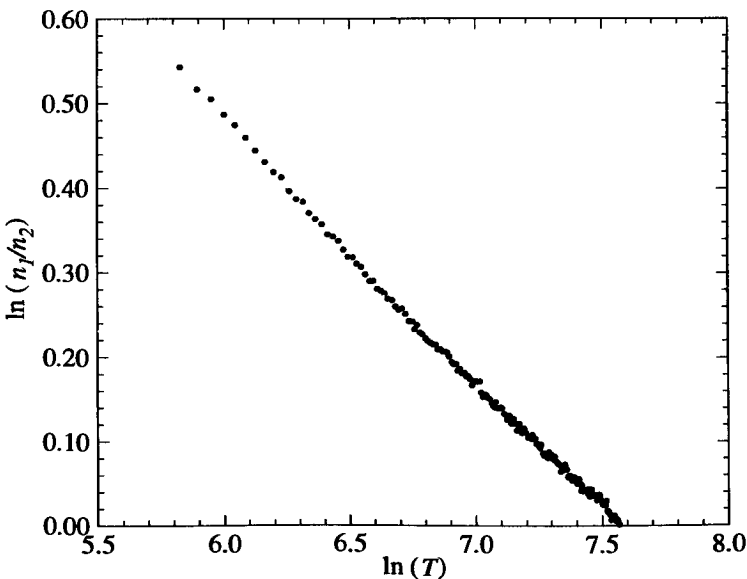


Fig. 12.16 Plot for α_T as the slope (see eqn (12.21)).

Fig. 12.16 plots the logarithmic variables that appear in eqn (12.21) in such a way that the slope should be negative and its absolute value equal to the thermal diffusion factor. There is a slight systematic reduction in the slope at high temperatures, but the slope at the lower temperatures of the order of 300 K gives a value of 0.35 for α_T in a He–Ar mixture. The experimental value of this quantity that is given by Chapman and Cowling (1970) is 0.38.

Thermal diffusion is caused by the variations in size of the molecules. The calculation was repeated with $\omega=1$ for all species and with the reference diameters chosen such that all species had the same collision cross-section. For $\omega=1$, the cross-section is inversely proportional to the relative speed, so that all collision pairs are equally probable. This case is analogous to Maxwell molecules, and it is known that thermal diffusion does not occur in a Maxwell gas. As expected, there was no separation in this case.

12.8 The diffusion thermo-effect

This is the inverse effect to thermal diffusion and is a heat flux in a gas at uniform temperature, but with an inhomogeneity in composition. This effect should have been present in the He–Ar diffusion calculation of §12.6. This was for the mass diffusion between an infinite reservoir of argon at a number density of $2.8 \times 10^{20} \text{ m}^{-3}$ and a temperature of 273 K at $x=0$ and a similar reservoir of helium at $x=1 \text{ m}$. The concentration gradients and the resulting diffusion velocities were discussed in §12.6, and the temperature and number density in the diffusing flow did not depart from the reservoir values. However, the stream velocity and heat flux did exhibit systematic effects.

The stream velocity component is in the direction of the argon diffusion and ranges from 2 to near 20 ms^{-1} . However, as shown in Fig. 12.17, the product of this velocity with the density is uniform across the flow and represents a net mass flux in the positive direction.

Fig. 12.18 shows that the net heat flux q_x is in the negative direction and ranges from 20 to 66 Wm^{-2} . Chapman and Cowling (1970) show that, in the absence of a temperature gradient,

$$q_x = (5/2)kT(n_1U_1 + n_2U_2) + kT(n_1n_2/n)\alpha_T(U_1 - U_2). \quad (12.22)$$

The first term appears because the flux is measured relative to the stream or mass velocity of the gas, rather than the mean velocity of the molecules. This is also plotted in Fig. 12.18 and is in the same direction as q_x , but is slightly larger in magnitude. The small difference is the diffusion thermo-effect that is represented by the third term in eqn (12.22). This is in the direction of the argon diffusion and, as noted by Chapman and Cowling ‘the heat flow is in the direction of diffusion of molecules which, in thermal diffusion, would seek the cold side’. Because the effect is the small difference between large quantities the scatter is high, but the average value of α_T across the flow is 0.44, and this is in reasonable agreement with the measured value of 0.38.

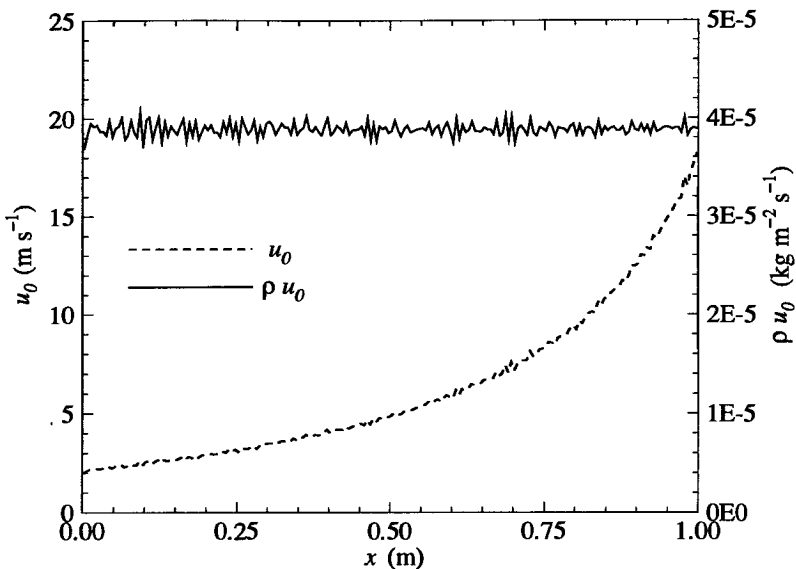


Fig. 12.17 The stream velocity and mass flux in the He–Ar diffusion.

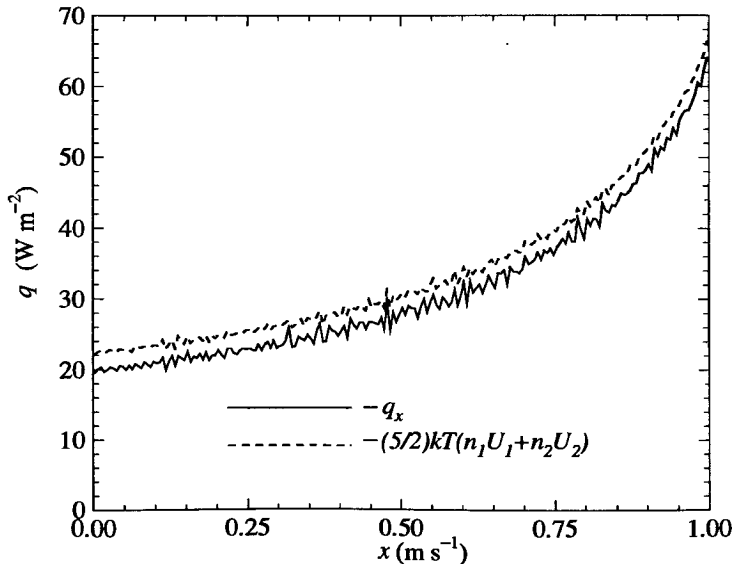


Fig. 12.18 Heat fluxes in the He–Ar diffusion flow.

12.9 Heat transfer in the transition regime

The DSMC calculations in the preceding sections of this chapter were made for sufficiently low Knudsen numbers that the rarefaction effects were confined to the Knudsen layers near the boundaries, and the Chapman-Enskog transport properties were applicable to the rest of the flow. The one-dimensional heat transfer between plane surfaces will now be studied over the full transition regime from continuum to free molecule flow. The free-molecule or collisionless solution was presented, together with the continuum solution, in §7.3. The four-moment solution of Liu and Lees (1961) for this problem in the transition regime was presented in §8.2.

The four-moment solution was for the special case of Maxwell molecules for which the coefficient of heat transfer $K = CT$. Eqns (3.56) and (4.62) show that this relationship can be reproduced by the VHS model if C is given by

$$C = \frac{15k^{3/2}}{8(\pi m T_{\text{ref}})^{1/2} d_{\text{ref}}^2}. \quad (12.23)$$

The comparison between the DSMC and analytical results for the heat flux is most conveniently made if the pressure p on the surfaces is chosen as the independent variable. This pressure in the free-molecule flow is readily shown to be

$$p = n k T_U^{1/2} T_L^{1/2}, \quad (12.24)$$

where T_U and T_L are the temperatures of the upper and lower plates, respectively. Note that the number density n becomes a constant in the collisionless limit. The free molecule solution of eqn (7.24) can then be written

$$q_x = -2^{3/2} p \left(\frac{k}{\pi m} \right)^{1/2} (T_U^{1/2} - T_L^{1/2}). \quad (12.25)$$

The continuum heat flux is independent of the pressure and, since $\omega=1$, it can be written from eqn (7.25) as

$$q_c = -\frac{1}{2} C (T_U^2 - T_L^2) / h, \quad (12.26)$$

where h is the distance between the surfaces. The four-moment solution is, from eqns (8.19) and (8.20),

$$q = \frac{\{(BT_U + AT_L + h/C)^2 - (B^2 - A^2)(T_U^2 - T_L^2)\}^{1/2} - (BT_U + AT_L + h/C)}{B^2 - A^2}, \quad (12.27)$$

where

$$A = \frac{1}{2p} \left(\frac{\pi m T_U}{2k} \right)^{1/2} \quad \text{and} \quad B = \frac{1}{2p} \left(\frac{\pi m T_L}{2k} \right)^{1/2}.$$

This relation reduces to the continuum result when the pressure becomes large, and to the free-molecule value at very small pressures.

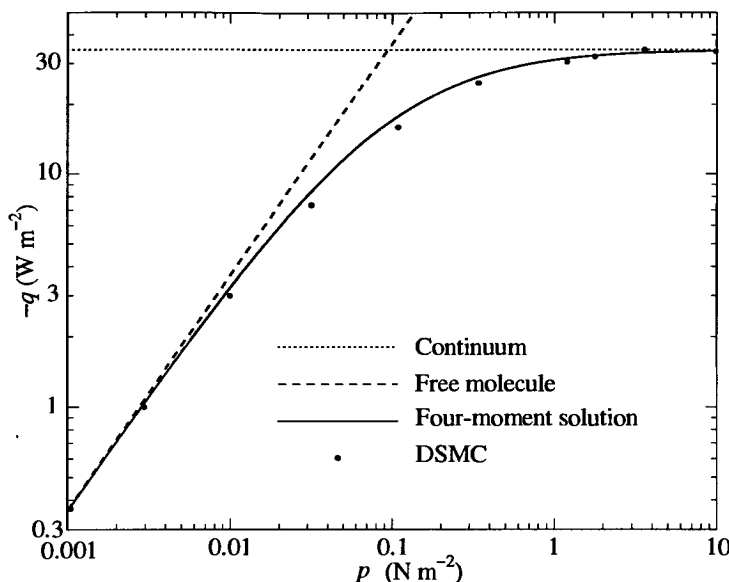


Fig. 12.19 Heat transfer in the transition regime.

Program DSMC1 was applied to this problem with a surface at 250 K as the inner boundary and a surface at 1000 K as the outer boundary. The VHS molecular model was employed with the molecular mass and diameter appropriate to argon, but with $\omega = 1$. The results are compared with the continuum, free molecule, and four-moment solutions in Fig. 12.19. This shows that the four-moment solution is remarkably accurate in predicting the pressure range over which the transition takes place, and the heat transfer values from this solution are about 10% too high over most of the transition region. It might be thought that this difference may be due to the Maxwell collision integral on which the four-moment solution depends not being consistent with the VHS model. However, an earlier DSMC study of this problem (Bird 1976) used the Maxwell molecular model and showed a similar difference. Moreover, this study showed that there is little difference between the results from hard sphere and Maxwell molecules for this problem.

The Knudsen number range may be inferred from a comparison of Fig. 12.19 with Fig. 8.1. This latter figure is misleading in that it suggests that the heat transfer increases with Knudsen number. This is due to the heat transfer being expressed as the ratio to the free-molecule value and, as shown Fig. 12.19, the absolute value decreases with increasing Knudsen number. There is some scatter in the DSMC results at low Knudsen numbers because q_x is then the small difference between large quantities. The scatter at high Knudsen numbers is less by orders of magnitude.

12.10 Breakdown of continuum flow in expansions

A steady isentropic expansion is one of the basic flows of gas dynamics. Exact solutions of the continuum equations are available but, because the flow is isentropic, these do not include any of the transport properties. Therefore, the breakdown in the continuum solution at sufficiently low densities cannot be associated with the breakdown of the Chapman-Enskog theory. It occurs simply because the collision frequency drops below the rate that is required for maintenance of the continual drop in temperature that is predicted by the theory. This form of breakdown was discussed in §1.2, and it was suggested that its onset in a steady flow should correlate with the parameter P that was defined in eqn (1.5) as

$$P = (\pi^{\gamma/2}/2) s (\lambda/\rho) dp/dx.$$

Program DSMC1 has been used to study this form of breakdown in steady spherical and cylindrical expansions. Because the area of these flows increases monotonically with radius, only the supersonic branch of the expansion can be modelled. An overall Knudsen number is most conveniently defined as the ratio of the mean free path under stagnation conditions to the radius at which the flow is sonic, i.e.

$$(Kn) = \lambda_0 / r^*, \quad (12.28)$$

where the subscript $_0$ denotes stagnation conditions and the superscript $*$ denotes sonic conditions. For a flow in which the area is proportional to the distance to the power ϵ , the parameter P can then be written (Bird 1970)

$$P = \frac{(Kn)}{2} \left(\frac{\pi\gamma}{2} \right)^{\gamma/2} \frac{\epsilon (Ma)^{3+1/\epsilon}}{(Ma)^2 - 1} \left(\frac{\gamma+1}{2} \right)^{\frac{\gamma+1}{2\epsilon(\gamma-1)}} \times \left(1 + \frac{\gamma-1}{2} (Ma)^2 \right)^{\frac{\gamma+1}{2(\gamma-1)} \left(\frac{1-\frac{1}{\epsilon}}{\epsilon} \right) - \omega}. \quad (12.29)$$

The singular behaviour of P at the sonic line reflects the fact that the cylindrical and spherical geometries do not satisfy the requirement that dA/dx , and therefore ϵ , should be zero at $(Ma)=1$. P drops to a minimum at a Mach number of the order of 1.4 and then increases. It was found that, if the computation was started at the sonic line, the initial axial and radial temperatures were slightly out of equilibrium. While they rapidly came back into equilibrium, most calculations avoided the singularity by starting the computation at a radius equal to 1.05 times the sonic radius. For a spherical flow, this radius corresponded to a Mach number of just over 1.4.

The first calculation was for the spherical expansion of argon with the overall Knudsen number, as defined in eqn (12.28), equal to 0.001. The flow extended from $x=1.05$ to 10. There were 985 cells, 9,850 sub-cells and approximately 35,000 molecules in the steady state. The inner boundary was a stream that matched the continuum solution, while the outer boundary was a vacuum. The initial state of the flow was also a vacuum.

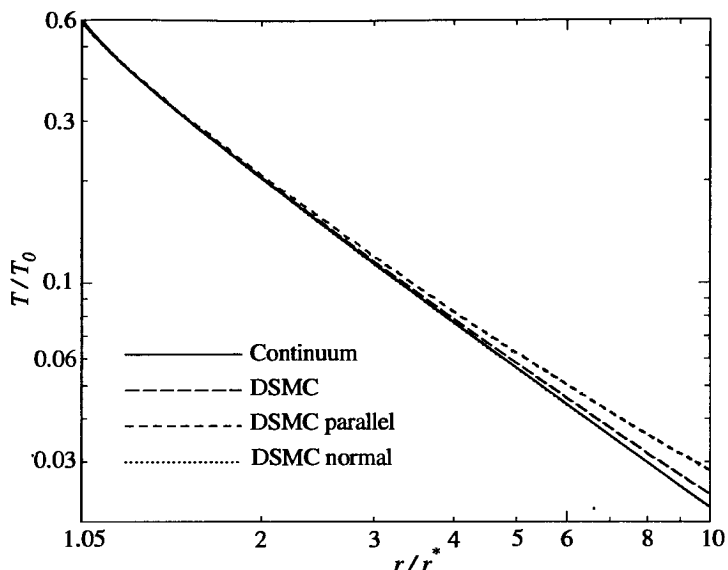


Fig. 12.20 Temperature ratio in a (Kn) = 0.001 expansion of argon.

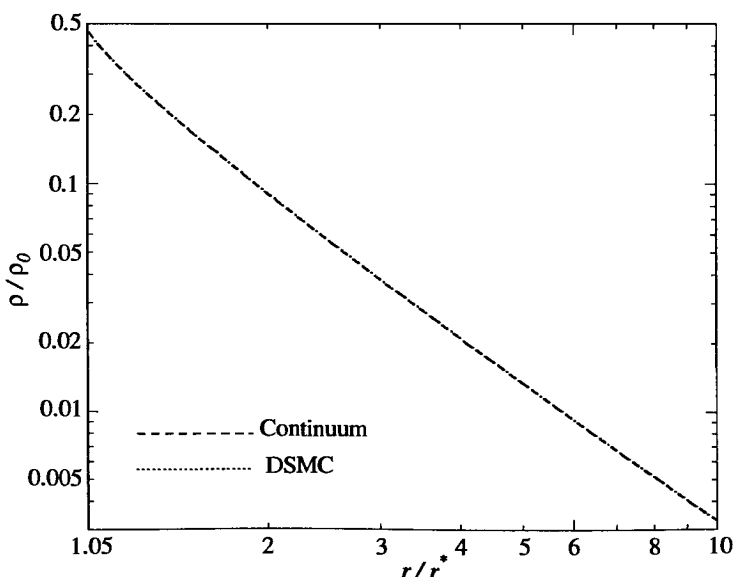


Fig. 12.21 Density ratio in a (Kn) = 0.001 expansion of argon.

The total sample size in this calculation was almost one thousand times larger than that in earlier calculations of this type (Bird 1970), and the statistical scatter was generally a small fraction of one percent. The temperature and density profiles in the expansion are compared with the continuum profiles in Figs 12.20 and 12.21, respectively. The earlier calculations were for hard sphere and Maxwell molecules, and argon with $\omega = 0.81$ is nearer to the Maxwell case. The breakdown shows as a very gradual rise of the temperature above the continuum value. This is associated with a separation of the parallel or axial temperature T_x based on the thermal velocity components in the x -direction and the normal or circumferential temperature T_n that is based on the components normal to this direction. This latter temperature is the mean of the y - and z -components of temperature that are output, along with the x -component, in the output on the 'separate species'. The parallel temperature would eventually become almost constant or 'frozen'. On the other hand, the normal temperature continues to fall, even in a collisionless flow, because of the geometric effect that causes the molecular velocities to become more nearly radial as they move further from the centre. In this case, the normal temperature remains very close to the continuum temperature. The ratio T_x/T_n provides the most convenient measure of the extent of the non-equilibrium, and this is plotted against P in Fig. 12.22.

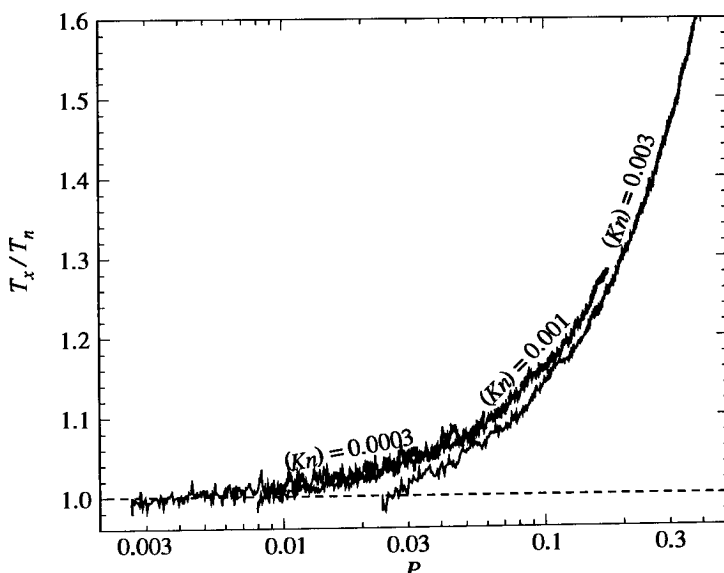


Fig. 12.22 Ratio of the parallel and normal temperatures as a function of the breakdown parameter.

The calculation was repeated for a density one third that of the original case and also for a density three times that of the original case. These are referred to as the $(Kn) = 0.003$ and the $(Kn) = 0.0003$ cases, respectively. The qualitative behaviour was the same for all three cases, and the T_x/T_n ratios are also shown in Fig. 12.22. The results for the $(Kn) = 0.001$ case range from $P = 0.008$ to 0.16. The breakdown for this case commences near $P = 0.01$, which occurs at $r/r^* = 1.28$ where the Mach number is 2.1. The results for the $(Kn) = 0.0003$ case range from $P = 0.0025$ to 0.045, and the breakdown again commences near $P = 0.01$ which occurs here at a Mach number of 4.35. The $(Kn) = 0.003$ case commences at $P = 0.025$ and, for this value, the flow should be out of equilibrium. The boundary condition forces it to be initially in equilibrium and this produces an overall downward displacement of the curve.

The results give very strong support for the use of the parameter P to correlate the breakdown of equilibrium in expansions. The results are in agreement with the early DSMC results (Bird 1970) that led to a proposed breakdown criterion of $P = 0.04$. This comparatively large value was due to the high level of scatter in the original calculations, and the fact that most of these started (like the $(Kn) = 0.003$ case here) at a radius where the flow should already have been out of equilibrium. The temperature ratio at $P = 0.04$ is approximately 1.06, and Fig. 12.20 indicates that the overall temperature is then 2% above the theoretical temperature. In view of the fact that the density and velocity are not affected, this could well remain a suitable criterion, even though the current results indicate that the breakdown starts near $P = 0.01$. Also, the breakdown is so gradual that, if the scatter was reduced further in much larger calculations, some breakdown would be observed at even lower values of P . It is worth noting that the fractional departure of the temperature above the continuum value is approximately equal to $P/2$.

It has sometimes been suggested that the breakdown of equilibrium in a high mass-ratio mixture would lead to pronounced separation effects. The $(Kn) = 0.001$ case was therefore repeated for a mixture of equal parts by mass argon and helium. The results for the temperature, density, and temperature ratio T_x/T_n as a function of the breakdown parameter P were indistinguishable from the results for argon as a simple gas. However, there was a diffusion velocity of approximately -5 ms^{-1} for the argon and a similar positive diffusion velocity for the helium. These are very small in comparison with the final stream velocity of almost 1300 ms^{-1} , and the separation effect was small. The final argon number fraction was found to be about 0.1005, compared with the value of 0.1 that would be obtained in the absence of separation. Moreover, this should not be regarded as a 'breakdown' effect because the diffusion velocities are consistent with the predictions of the diffusion equation (3.91) that is based on the Chapman-Enskog transport properties. The pressure and thermal diffusion terms are much larger than the mass diffusion term. These two effects act in opposite directions in a steady expansion, but the pressure diffusion term is the dominant one.

12.11 The normal shock wave

A shock wave involves the transition from a uniform upstream flow to a uniform downstream flow. In the case of a normal wave, there is no stream speed in the plane of the wave, and the transition is from a supersonic flow to a subsonic flow. The *shock Mach number* (Ma_s) is defined as the ratio of the speed of the wave, relative to the upstream gas, to the speed of sound in this gas. The shock wave is stationary in the steady flow frame of reference, and the shock Mach number may then be identified with the Mach number of the upstream flow. The wave is generally regarded as a discontinuity in a continuum flow and the ratios of the stream speed, density, pressure, and temperature across the wave are given by the Rankine–Hugoniot relations (Liepmann and Roshko 1957). In fact, the shock wave has a finite thickness and the profile depends on the transport properties of the gas.

The Navier–Stokes equations may be applied to the shock structure problem and yield an ordinary differential equation that is amenable to numerical solution (Gilbarg and Paolucci 1953). A shock wave thickness L may be defined as the distance required to span the overall density change by the maximum density gradient within the wave. This thickness is generally expressed as a multiple of the upstream mean free path λ_1 and is a function of the viscosity–temperature index ω and (Ma_s) .

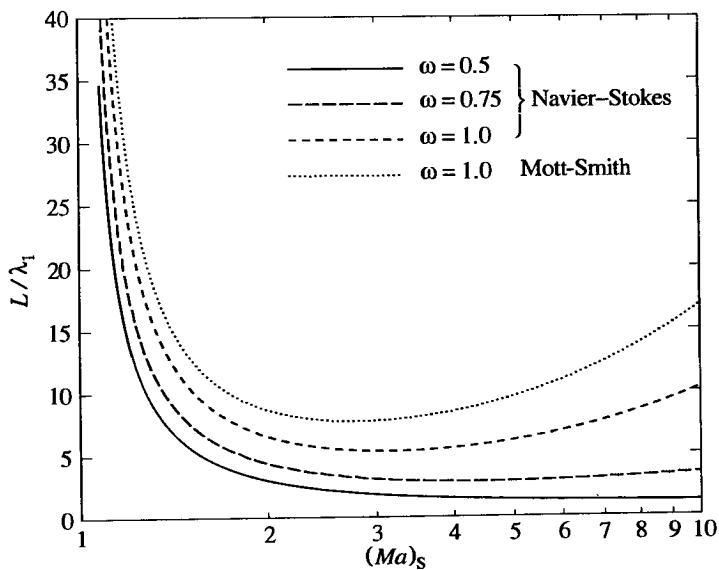


Fig. 12.23 Theoretical shock wave thickness in a monatomic gas.

The predictions of the Navier-Stokes theory for a monatomic gas are shown in Fig. 12.23. These employ the definition of eqn (4.52) for the mean free path and this means that the parameter 'b' in the analysis of Gilbarg and Paolucci becomes

$$\frac{(30\pi)^{1/2}(\alpha+1)(\alpha+2)}{3\alpha(5-2\omega)(7-2\omega)}.$$

For $\alpha = 1$ and $\omega = \frac{1}{2}$, this reduces to the hard sphere value that has been used in most applications of the theory. The calculations that led to Fig. 12.23 set the VSS scattering parameter α to unity. It is the change in the definition of mean free path that is largely responsible for the significant effect of ω on the width of very weak waves that is apparent in Fig. 12.23. The ratio of the 'Maxwell' value to the 'hard sphere' value of L/λ_1 becomes even larger for very strong waves in that the former exhibits a minimum of approximately five at a shock Mach number near three and then increases, while the latter tends to a value near unity. The maximum slope thickness of a gas with a realistic value of ω has a shallow minimum of two to three upstream mean free paths. These thin waves involve such large gradients of the macroscopic gas properties that the Chapman-Enskog theory ceases to be valid and the Navier-Stokes equations fail. Figure 12.23 also shows the result from the Mott-Smith theory of §8.2.

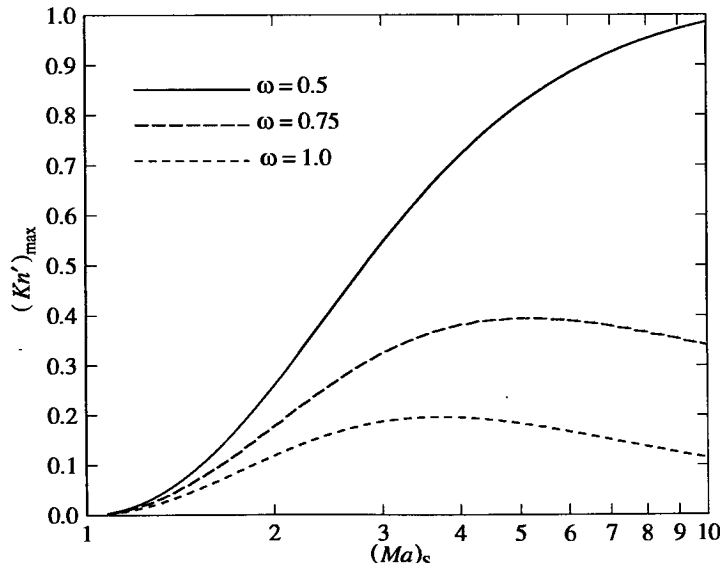


Fig. 12.24 The maximum value of the local Knudsen number in the Navier-Stokes shock profiles.

The onset of significant error in the Chapman-Enskog theory and the Navier-Stokes equations was linked in §1.2 to a value of 0.1 for the local Knudsen number based on eqns (1.1) and (1.2). The maximum values of this local Knudsen number in the Navier-Stokes shock wave profiles was therefore calculated and the results are plotted in Fig. 12.24. This indicates that, for a realistic value of ω , the error in the Navier-Stokes profile becomes significant at a shock Mach number of about 1.6, and very serious at shock Mach numbers greater than two.

High Knudsen numbers that are generally associated with rarefied gas flows therefore occur in strong shock waves at all gas densities. The waves in many flow configurations are well away from the influence of solid surfaces and are not subject to the uncertainties associated with gas-surface interactions. There is a considerable body of well-substantiated experimental data for the structure of normal shock waves, and this flow has provided the most important test case for the verification of numerical methods in molecular gas dynamics.

A number of qualitatively different boundary conditions have been employed in DSMC studies of normal shock waves. One of these could be applied to the general one-dimensional program DSMC1.FOR. This would employ the 'type 3' or stream option at each boundary. The properties of one stream would correspond to the uniform conditions upstream of the wave, while those of the other would correspond to the conditions downstream of the wave. The only modification would be to set half the gas in the initial state to the upstream conditions and the other half to the downstream conditions. There would then be an initial discontinuity or step at the desired location of the centre of mass of the wave. The steady shock profile would develop during the unsteady phase of the calculation. This scheme has led to acceptable results for strong shock waves as long as the number of simulated molecules is large and the sample is relatively small. The problem is that the number of molecules entering the upstream and downstream boundaries fluctuates and the total number of molecules is subject to a random walk effect. Since there is nothing to hold the shock in place, its location is also subject to a random walk and this causes a smearing of the time-averaged profile.

The subsonic downstream boundary at x_d causes the greater part of the problem and it may be replaced by a specularly reflecting solid surface that moves with speed u_s equal to the downstream Rankine-Hugoniot speed. Then, for molecules that move to x beyond x_d , the post-reflection value of the velocity component u is

$$u' = 2u_w - u. \quad (12.30)$$

The post-reflection location of the molecule is readily shown to be

$$x' = 2x_w - x + u' dt, \quad (12.31)$$

where dt is the time step. Should x' remain beyond x_d , the molecule is removed. The boundary condition is essentially a moving piston that, after interacting with the molecule, 'jumps' back to its original position. It has

been implemented in program DSMC1S which is an adoption of the general one-dimensional program DSMC1. This boundary condition has the further advantage that it requires only the downstream speed to be calculated from the Rankine-Hugoniot theory, while the stream boundary condition also employs the theoretical values of the density and temperature. It essentially amounts to the production of a shock wave by a moving piston with the Rankine-Hugoniot velocity ratio used to transform the frame of reference so that the wave is stationary.

The other changes to DSMC1 include the removal of the boundary options that are no longer required, and the tailoring of the input and output to the shock wave problem. In addition, the initial state of the gas is a discontinuous wave at the origin. Even with the piston boundary condition, the total number of molecules is subject to random walk and the time-averaged shock profile can be smeared by the consequent movement of the wave. The subroutine STABIL has been added to prevent this. Should the total number of molecules depart from the initial number by more than a small specified number, all molecules are displaced by the same distance. The molecules that move across one boundary are removed and those that are initially within the displacement distance from the other boundary are duplicated. The displacement distance is calculated on the basis of the upstream and downstream Rankine-Hugoniot densities as that required to restore the number of molecules to the original value.

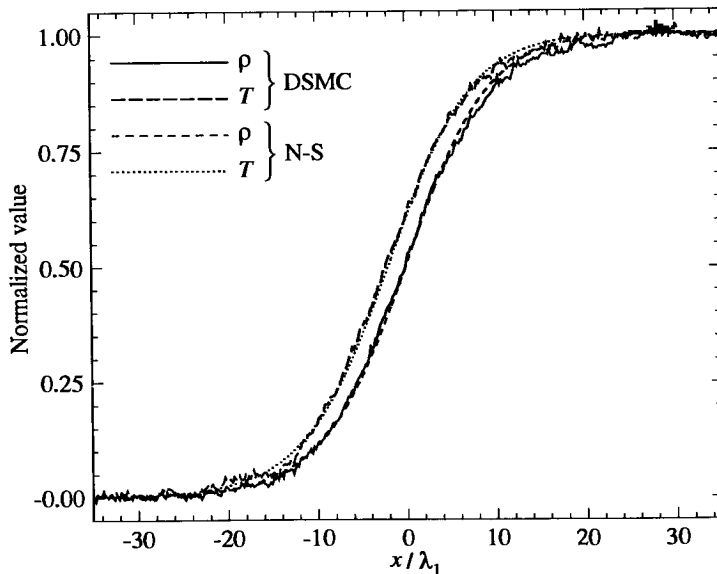


Fig. 12.25 Temperature and density profiles in argon with $(Ma)_S = 1.2$.

A wave with a shock Mach number of 1.2 in argon at 293 K has been chosen as the first test case. The VSS molecular model was used with parameters for argon that are listed in Appendix A. The DSMC calculation employed 27,000 simulated molecules in 400 cells, each divided into six sub-cells. The mean separation between collision pairs was less than one hundredth of the upstream mean free path, and the time step was just over one twentieth of the mean time between collisions. The computational requirements of the DSMC method were therefore satisfied by a very wide margin. Steady flow was assumed after the flow had moved approximately 20 shock widths and the time average was taken over the time for the flow to move several thousand shock widths. This involved the computation of some 43,000,000 collision events.

The results for the density and temperature profiles are compared in Fig. 12.25 with the predictions of the Navier-Stokes equations. The normalized density is defined by

$$\hat{\rho} = \frac{\rho - \rho_1}{\rho_2 - \rho_1}, \quad (12.32)$$

where the subscripts 1 and 2 represent the upstream and downstream Rankine-Hugoniot values, respectively. The normalized values of the other macroscopic flow variables are defined in a similar manner. As expected, the two sets of results are in good agreement for this very weak wave.

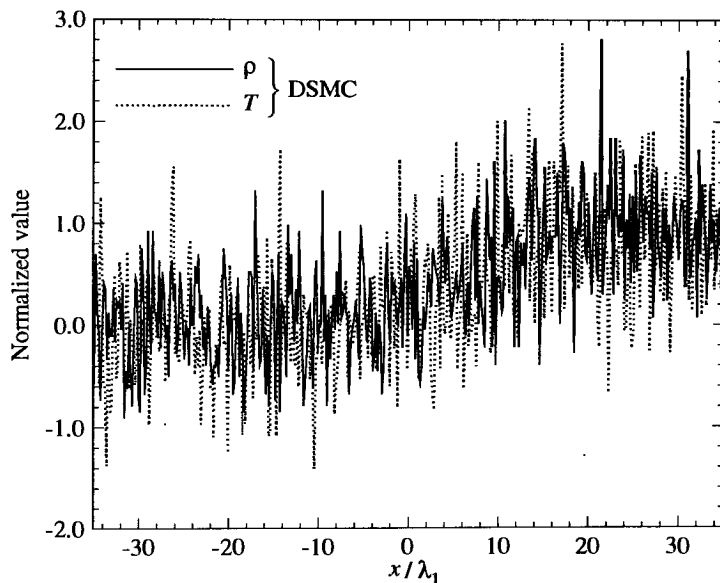


Fig. 12.26 A typical profile based on instantaneous values.

This is a demanding calculation in that it involves relatively small disturbances with the density ratio being only 1.2973. Since the statistical scatter is a fraction of the density, it is a larger fraction of the overall disturbance than is the case with strong shock waves. This is illustrated in Fig. 12.26 which shows the temperature and density profiles from a typical instantaneous sample of the flow. The number of molecules per cell is such that the overall density change across the wave corresponds to about two standard deviations of the statistical scatter. This means that there are a number of cells in which the 'noise' exceeds the 'signal'.

The importance of the stabilization of the shock location through the control of the fluctuation in the total number of molecules in the subroutine STABIL was tested by repeating the calculation with this subroutine disabled. The number of molecules started at 27,022 and executed a random walk. The displacement was generally downward and its magnitude at larger times was typified by the final value of 26,400. This led to a general rearward displacement of the wave and, as shown in Fig. 12.27, the consequent distortion of the time-averaged profiles is very serious. While the net shock displacement was downstream in this case, it could equally likely have been in the upstream direction. Fortunately, the need for direct intervention to control random walks is unique to this flow because the flow configuration is almost always fixed by the geometry of the physical boundaries.

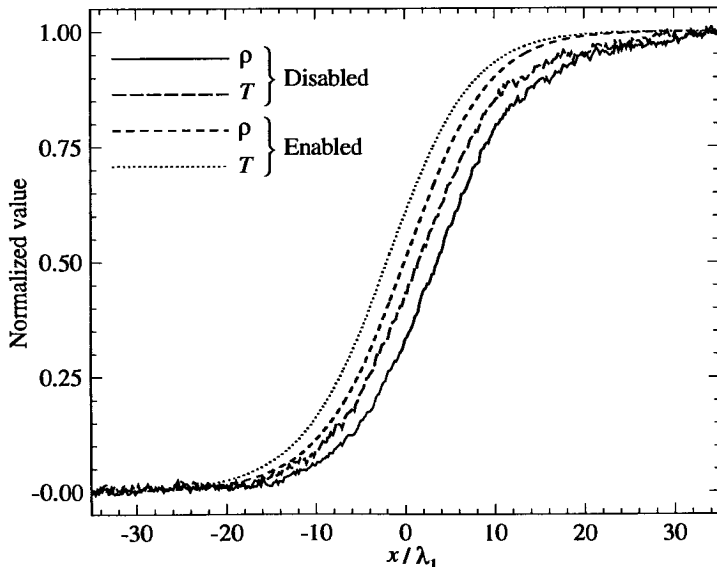


Fig. 12.27 The effect of disabling the subroutine STABIL.

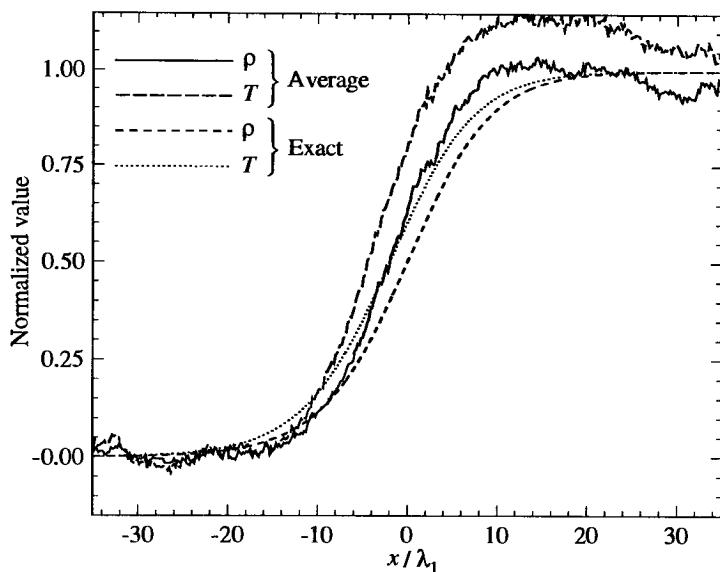


Fig. 12.28 The effect of average rather than exact conservation of momentum and energy in collisions.

As noted in §10.2, some versions of the DSMC method attempt to make the procedures more consistent with the Boltzmann equation by replacing the velocity components of only one of the two molecules in each collision. It was pointed out in §10.4 that, while this conserves momentum and energy on the average, they are not conserved in each collision and this introduces a random walk in the overall momentum and energy of the gas. The program DSMC1S was modified so that the number of collisions was doubled, but only one of the molecules was changed in each collision. If there were no random walks, the results would not be affected. However, as shown in Fig. 12.28, the solution is degraded almost to the point of being rendered useless. It is ironic that a mathematical ‘convergence proof’ has been presented (Babovsky and Illner 1989) for the procedures that include the random walks, but not for the regular procedures. The decline in the statistical scatter with the growth of the time-averaged sample that gradually transforms Fig. 12.26 to Fig. 12.25 is sometimes referred to as ‘convergence’. This is undesirable because the statistical process is quite unrelated to the mathematical concept of convergence. The mathematical model of the simulation did not take into account the possible random walk effects, and these are the real determinant of whether or not an accurate solution is obtained from a probabilistic physical simulation. Note that the velocities of both molecules are changed in the collisions in real gases and, from the physical point of view, the modification is nonsense.

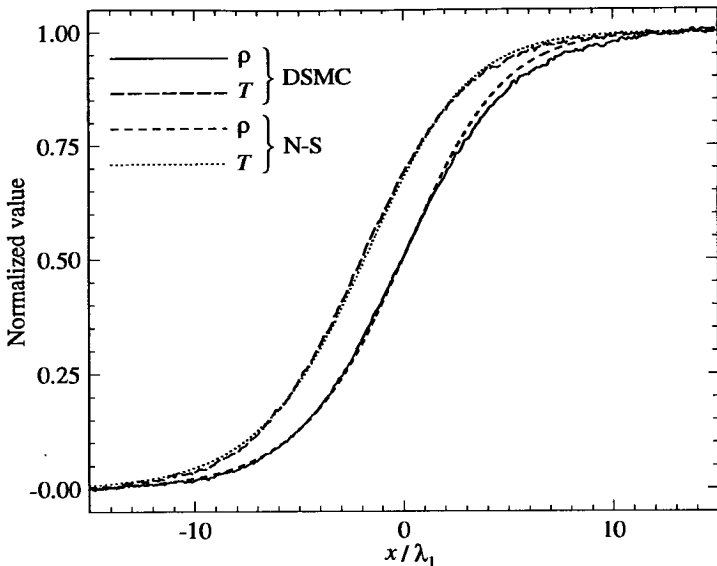


Fig. 12.29 Temperature and density profiles in argon with $(Ma)_S = 1.4$.

The data in the listing of program DSMC1S is for a shock Mach number of 1.4 in argon at 293 K. The density and temperature profiles for this case are shown in Fig. 12.29. This shows the expected reduction in thickness and there is also a significant increase in the separation of the temperature and density profiles. The scatter is reduced as a result of the larger disturbance and, although the shock Mach number is still well within the expected limit on the validity of the Navier-Stokes equations, there is a significant discrepancy in the density profiles for the downstream half of the shock wave. This difference has been observed consistently in studies of weak shock waves and Phan-Van-Diep et al. (1991) showed that it is consistent with the predictions of Simon and Foch (1977) for the differences that are introduced when the Navier-Stokes equations are replaced by the Burnett equations. The maximum slope thickness is clearly inadequate for the quantification of this difference and recourse must be had to the *shape factor* Q_p that was defined by Schmidt (1969) as

$$Q_p = \frac{\int_{-\infty}^0 \hat{\rho} dx}{\int_0^\infty (1-\hat{\rho}) dx}, \quad (12.33)$$

where the origin is at $\hat{\rho} = 0.5$. There is a qualitative difference between the prediction of the Navier-Stokes equation that Q_p should increase monotonically with shock Mach number and that of the Burnett equations

that Q_p should decrease to a minimum near $(Ma)_S = 1.3$. The Navier-Stokes value of Q_p for $(Ma)_S = 1.4$ is 1.09 and the Burnett value of Simon and Foch is 0.95. These values are for $\omega = 1$, and the calculations of Erwin, Muntz, and Pham-Van-Diep indicate that the expected values for a realistic ω would be about 1% lower. The DSMC density profile of Fig. 12.29 is in good agreement with the Burnett value with an estimated maximum error band of $\pm 5\%$. The Burnett equations also predict a separation between the density and temperature profiles at the midpoint of the wave that is about 10% higher than the Navier-Stokes value. The DSMC result is consistent with this, but the difference is of the order of the error band for this quantity.

The corresponding results for a shock Mach number of two are shown in Fig. 12.30. The local Knudsen numbers of Fig. 12.24 indicate that there should be clear errors in the Navier-Stokes profiles for this case, and the DSMC results confirm this. The maximum slope thickness from the Navier-Stokes theory is about 25% smaller than the value of $L/\lambda_1 = 6.2$ from the DSMC calculation. This may appear to be in conflict with the value of 4.8 that was obtained from the experimental study of Alsmeyer (1976). However, the mean free path that is used here is, for $\omega = 0.81$ and $\alpha = 1.6625$, equal to 76% of the hard sphere mean free path that was used by Alsmeyer. Therefore, in terms of the actual thickness, the two results agree to within one or two percent.

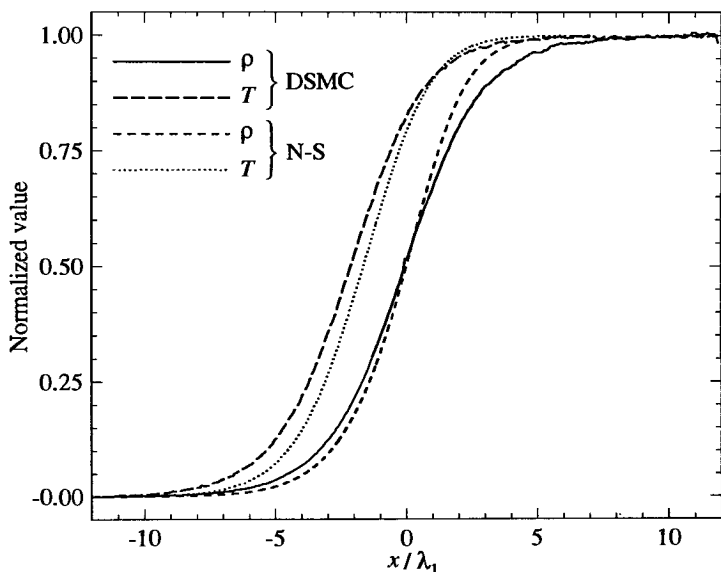


Fig. 12.30 Temperature and density profiles in argon with $(Ma)_S = 2$.

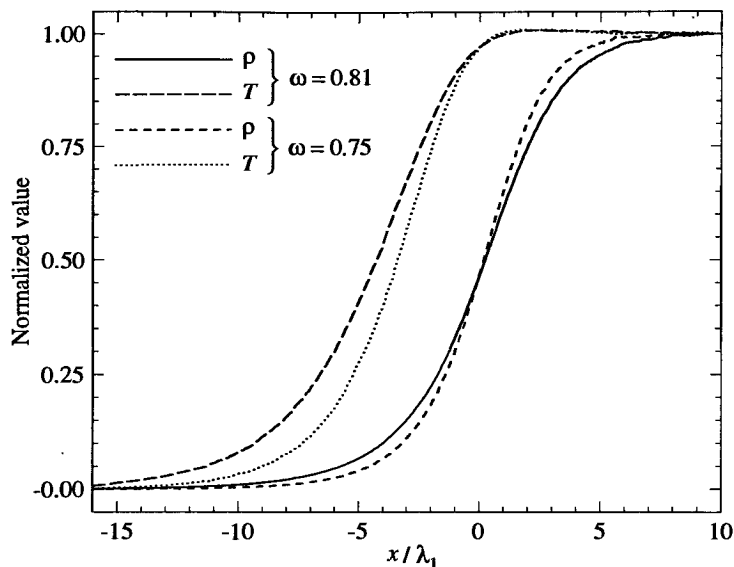


Fig. 12.31 The structure of a strong shock of $(M_s)_S = 8$ in argon.

According to the Burnett theory, the shape factor Q_p should be about unity for $(Ma)_S = 2$, but the value from the integration of the profile in Fig. 12.30 remained at the value of 0.95 that was obtained for the $(Ma)_S = 1.4$ case. This is at the limit of the estimated error bound and the result is inconclusive. On the other hand, the separation between the temperature and density profiles at the higher Mach number now supports the Burnett theory to well within the expected scatter. The Maxwell gas result of Simon and Foch predicts 30% more separation than that given by the Navier-Stokes theory. The separations are less for the more realistic molecular model that is used here, but the percentage increase is consistent with the predicted value.

There are qualitative changes to the profile as the shock becomes stronger. Figure 12.31 is for $(Ma)_S = 8$ and this shows a marked asymmetry in the profiles and also an overshoot of about 1% in the temperature. The asymmetry is accentuated by a region at the front of the wave where the density is essentially equal to the upstream value, but where there is a significant increase in temperature. The relative velocity between the unaffected stream molecules and any affected molecules is so large that a minute proportion of the latter have a noticeable effect on the temperature. The velocity distribution is qualitatively bimodal, but is not the simple mixture of the upstream and downstream Maxwellians that was assumed by Mott-Smith. This has been confirmed by Phan-Van-Diep et al. (1989) who compared the DSMC and Mott-Smith distributions with measured

distributions in helium at $(Ma)_S = 25$. The distributions from the DSMC calculations were in excellent agreement with the experimental values. The distribution near the front of the wave was strongly bimodal, but the Mott-Smith theory provided a poor representation of the merging of these distributions.

The maximum slope thickness for the value of 0.81 for ω that is appropriate at temperatures near the standard temperature is significantly thicker than Alsmeyer's experimental value. Figure 12.31 also shows the profiles for $\omega = 0.75$. When allowance is made for the differing definitions of the mean free path, the thickness is in good agreement with the measured value.

If judged by the results for the shock wave, it might be thought that the use of the VHS or VSS mean free path of eqn (4.52) in place of the hard sphere mean free path of eqn (4.56) is disadvantageous. This is definitely the case for extremely weak waves because it leads to a dependence on ω of the normalized thickness, while both the actual thickness and the thickness based on the upstream hard sphere mean free path do not depend on ω . Furthermore, the profiles for the very strong shock also appear to depend on ω . However, the Knudsen numbers based on the mean free path of eqn (4.52) should employ, in this equation, the collision cross-section at the relative velocity that is most significant for the problem. In the case of a strong shock wave, the most significant collisions occur with a relative velocity of the order of the upstream velocity, and this corresponds to that at a temperature of the order of the downstream temperature. This means that the profiles of strong shock waves should be independent of the molecular model if they are plotted against distance normalized to the downstream rather than the upstream mean free path. The downstream density is a constant in this change, and the difference comes from the change in cross-section. Eqns (3.60) and (3.67) show that the cross-section is inversely proportional to the temperature to the power $\omega - \frac{1}{2}$. Therefore, for the temperature ratio of 20.87 across a $(Ma)_S = 8$ shock in a monatomic gas, the effective ratio of the downstream mean free path at $\omega = 0.75$ to that at $\omega = 0.81$ is 0.833. This would bring the two sets of shock profiles into near coincidence.

Because the velocity difference between the two components of the near bimodal distribution at the front of the wave is along the x -axis, the 'parallel temperature' based on the velocity component in the x -direction is larger than the 'normal temperature' based on the velocity components in the y - and z -directions. This effect is illustrated in Fig 12.32 which shows that extreme nonequilibrium persists over the whole of the region upstream of the centre of the wave, and the gas comes to equilibrium in the downstream half of the wave. The parallel temperature reaches a maximum value that is one third higher than the final downstream temperature. Although these very high values of T_x/T_n are characteristic of strong shocks, this ratio is above unity even in a very weak wave. Its value could be calculated from the Chapman-Enskog distribution functions that accurately describe the transport properties in very weak waves.

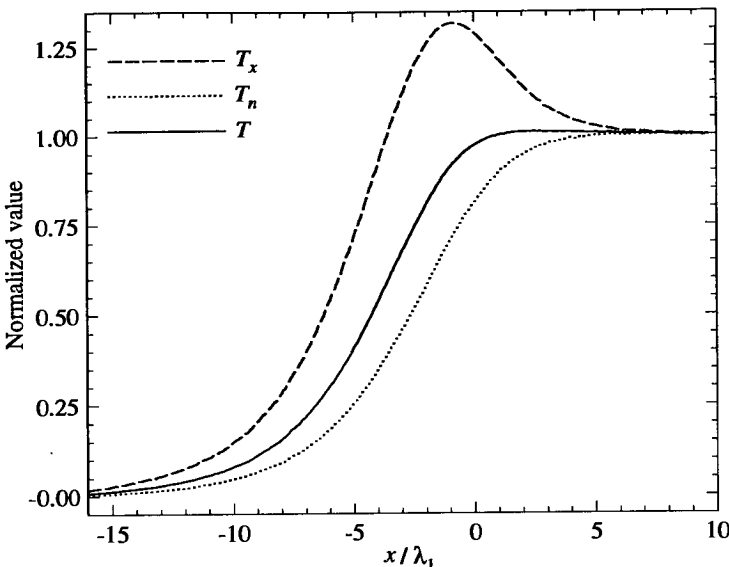


Fig. 12.32 The parallel and normal temperatures in an $(Ma)_S = 8$ shock.

In the case of a diatomic gas with a finite rotational relaxation time, the rotational temperature must lag behind the translational temperature. The program DSMC1S includes the routines that are required for the simulation of molecules with rotational degrees of freedom. A calculation was made for a shock of Mach number 1.71 in nitrogen. The VHS model was used with the parameters for nitrogen that are listed in Appendix A, and the rotational relaxation collision number was set to five. The results for the density and temperature profiles are shown in Fig. 12.33. All the computations in this section are of similar magnitude with regard to CPU time, and the higher level of scatter in calculations for weak shock waves is very noticeable.

The profiles of density and overall temperature are qualitatively similar to those in Figs. 12.25 and 12.29 for weak shocks in a monatomic gas. The significant effects of the internal degrees of freedom relate to the component temperatures and, as expected, the translational temperature profile leads the overall temperature. Also, there is a small overshoot of about one or two percent in the overall temperature. The rotational temperature lags the other temperatures and its profile, in this case, is very close to the density profile. The reason for choosing this case is that measured values of the density and rotational temperature profiles were obtained by Robben and Talbot (1966). They found that the rotational temperature profile lagged slightly behind the density profile, and the DSMC results of Fig. 12.33 are consistent with the experiments.

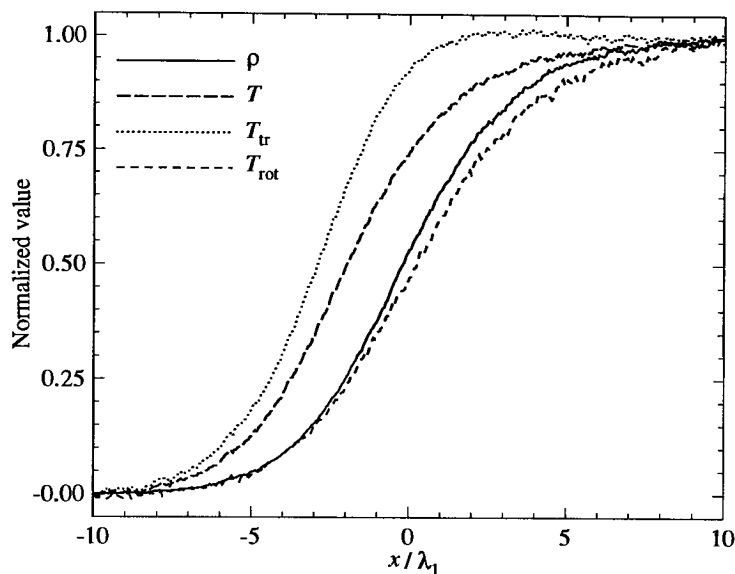


Fig. 12.33 $(Ma)_S = 1.71$ shock in nitrogen with $Z_{\text{rot}} = 5$.

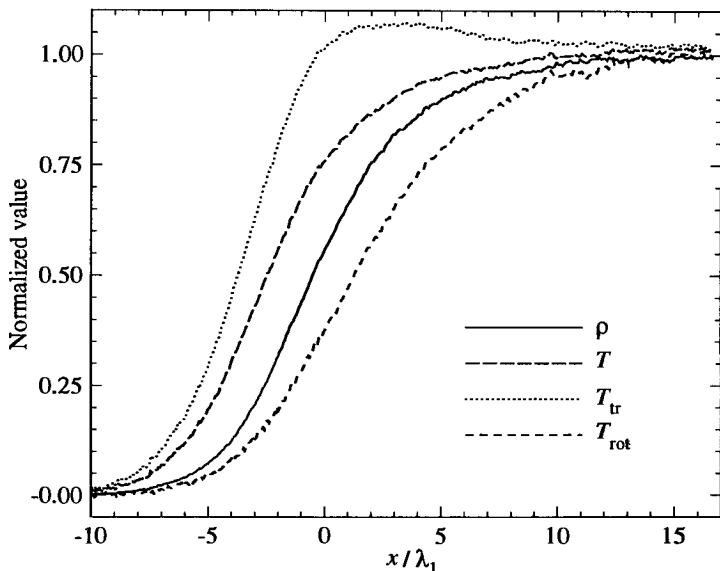


Fig. 12.34 $(Ma)_S = 1.71$ shock in nitrogen with $Z_{\text{rot}} = 10$.

The calculation was repeated with a rotational relaxation collision number Z_{rot} of 10, and the resulting profiles are shown in Fig. 12.34. The separation between the translational and rotational increases, but is significantly less than double the spacing in the $Z_{\text{rot}} = 5$ case. On the other hand, the overshoot in the translational is more than doubled. The rotational temperature profile lags significantly behind the density profile, and the experiments of Robben and Talbot are indicative of a rotational relaxation collision number of approximately five for nitrogen. An interesting and perhaps unexpected result is that the shock wave thickness based on the maximum density slope is directly affected by Z_{rot} . In this case, it increased by approximately 20% as Z_{rot} changed from 5 to 10.

Program DSMC1S.FOR can also be applied to gas mixtures. The most interesting experimental results for shock waves in gas mixtures are those of Gmurczyk et al. (1979) for helium with a small proportion of Xenon. These exhibited the leading of the heavy gas profile by the light gas profile that had long been known from experimental and numerical studies. The novel points were a pronounced and relatively sudden change in the slope of the helium profile and an overshoot in that profile. The former has been confirmed in a number of DSMC studies, but the latter appears to be an artefact of the measurement technique. These findings have been illustrated through a calculation with DSMC1S for a shock of Mach number 3.89 in a mixture of 3% xenon in helium.

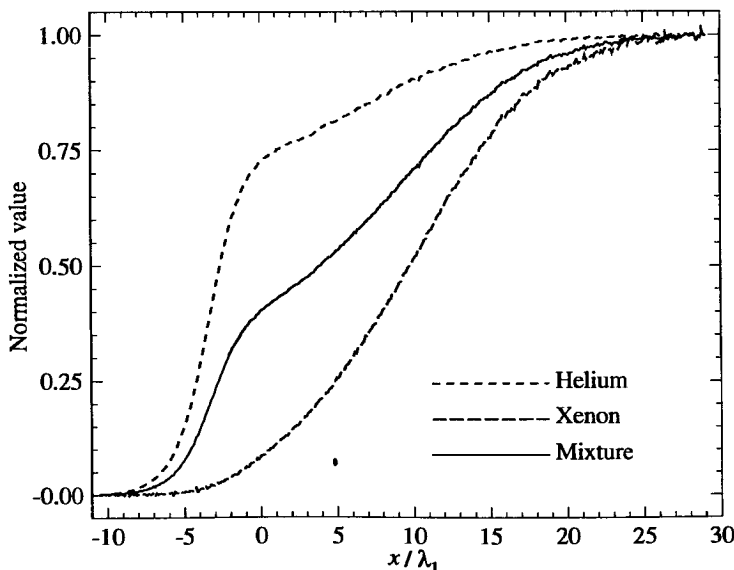


Fig. 12.35 Density profiles in the helium–xenon mixture.

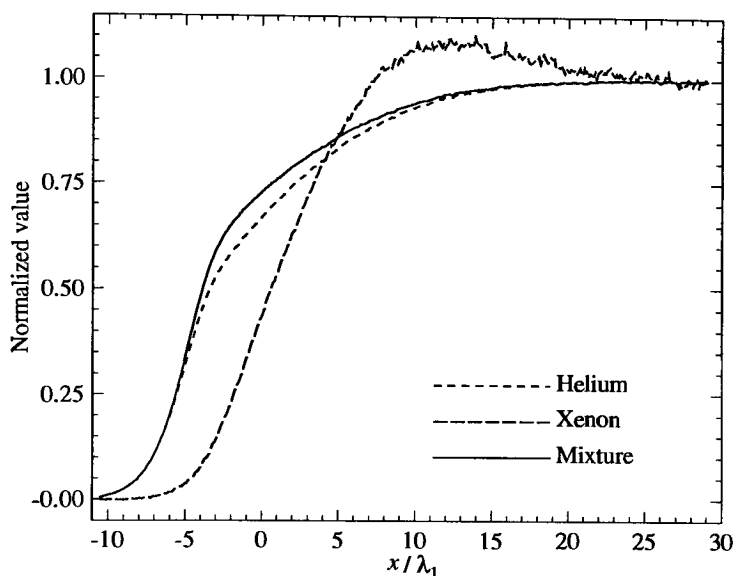


Fig. 12.36 The temperature profiles in the helium–xenon mixture.

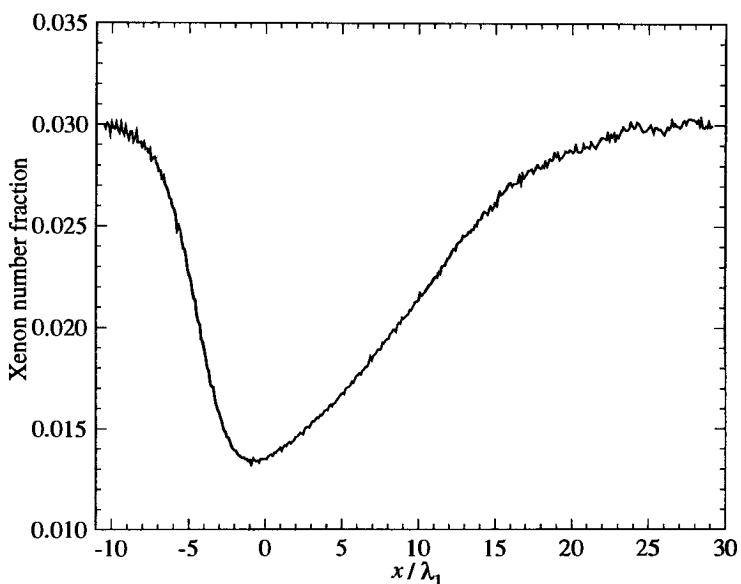


Fig. 12.37 The xenon concentration in the shock wave.

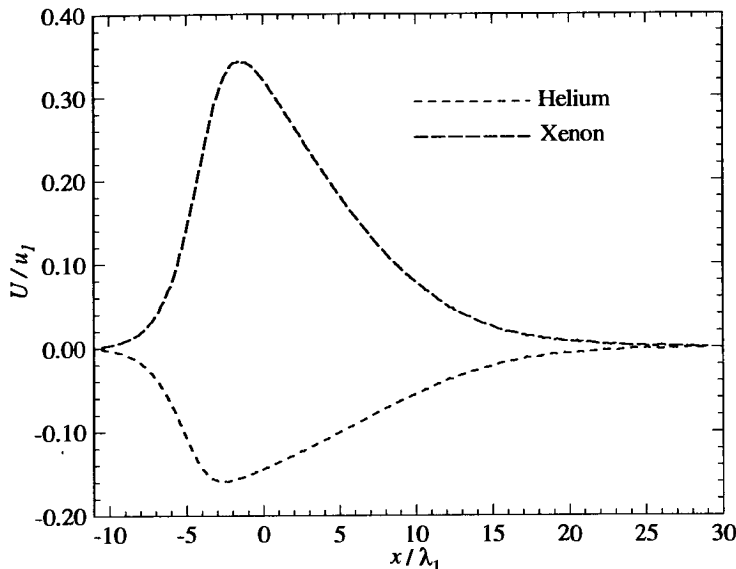


Fig. 12.38 The diffusion velocities in the shock wave.

The VSS model was used with the option that allows separate values of ω and α for all combinations of molecules. The density and temperature profiles are shown in Figs 12.35 and 12.36, respectively. The component densities, like the densities in the simple gas shocks, can be regarded as either number densities or mass densities, while that for the mixture must be a mass density. The origin is at the 'number centre' of the wave. The helium profile exhibits the expected sudden change in slope and there is a suggestion that this is followed by a point of inflection. There is a clear point of inflection in the mixture profile, and this can be said to exhibit a 'bump'. Because of equipartition, the overall temperature is very close to the helium temperature. The temperature profiles lead the density profiles, and the xenon temperature has an overshoot of about 10%. Since the upstream speed would correspond to a shock Mach number of 15.93 in pure xenon, this overshoot is surprisingly small.

Note that all figures that show DSMC results are plotted directly from the output, with the sampled values shown either as points or as line segments between these points. No form of smoothing has been applied to any of the results. The scatter is, of course, much higher in the xenon which is present in a small concentration. Also, as shown in Fig. 12.37, the xenon concentration at the centre of the shock drops to less than half the upstream and downstream values. The diffusion velocities that are associated with this separation effect are shown in Fig. 12.38 as a ratio to the upstream velocity.

The Mott-Smith moment method for the structure of strong shock waves was presented in §8.2 and a solution was obtained for the case of Maxwell molecules. Program DSMC1S has been used to calculate the structure of a shock of Mach number 8 in a monatomic simple gas of Maxwell molecules. The normalized number density profile from the DSMC calculation is compared in Fig. 12.39 with the Mott-Smith profile calculated directly from eqn (8.39). The maximum slope thicknesses based on these profiles are almost identical, but there are significant differences in the structure. The location of the origin is such that

$$\int_{-\infty}^0 (n - n_1) dx = \int_0^\infty (n_2 - n) dx,$$

and, for the symmetrical Mott-Smith profile with $Q_f = 1$, the origin is at a normalized number density of 0.5. The actual profile has a shape factor Q_p well in excess of unity, and this is characteristic of strong shock waves.

Program DSMC1S samples in array SDF the information on the axially symmetric velocity distribution function in a set number of cells. The axial and radial dimensions of the axially symmetric velocity space are divided into 400 and 200 intervals, respectively, and the number of molecules in each of the resulting velocity space cells are output in file DSMCDF.OUT. This defines the velocity distribution function, and this may be partially integrated to give the axial function f_x and the radial or normal function f_n .

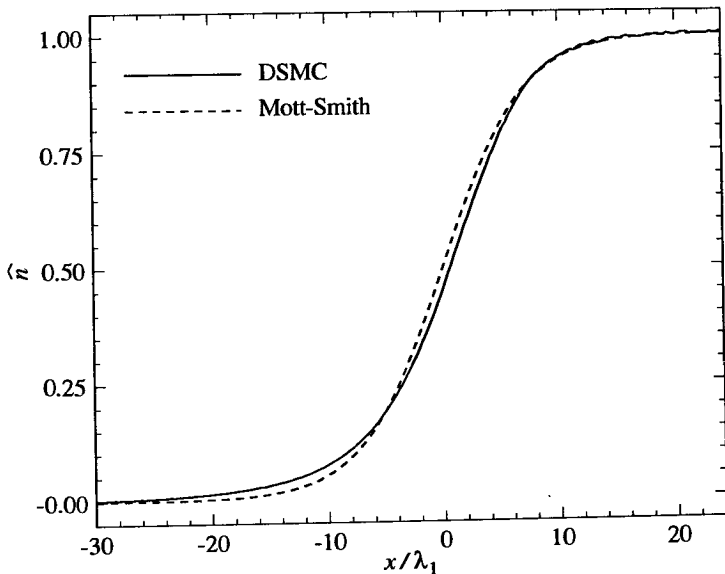


Fig. 12.39 The normalized number density profile for a shock of (Ma)_s = 8 in a simple gas of Maxwell molecules.

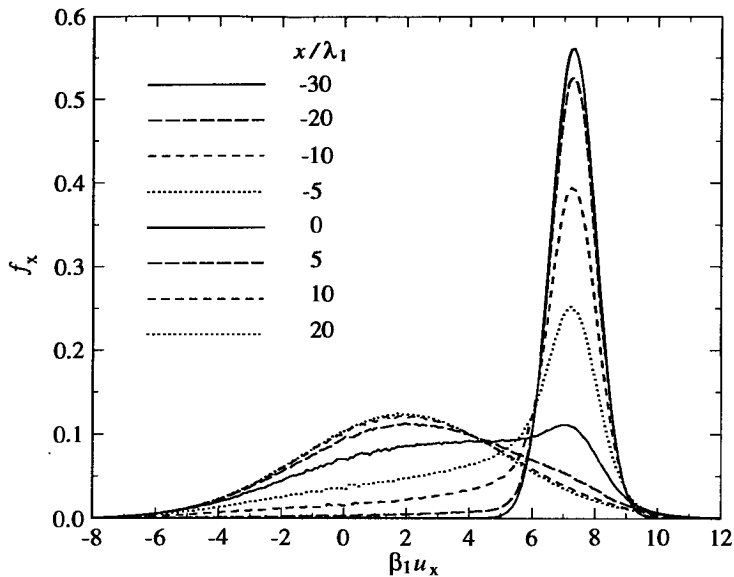


Fig. 12.40 DSMC result for the axial distribution function.

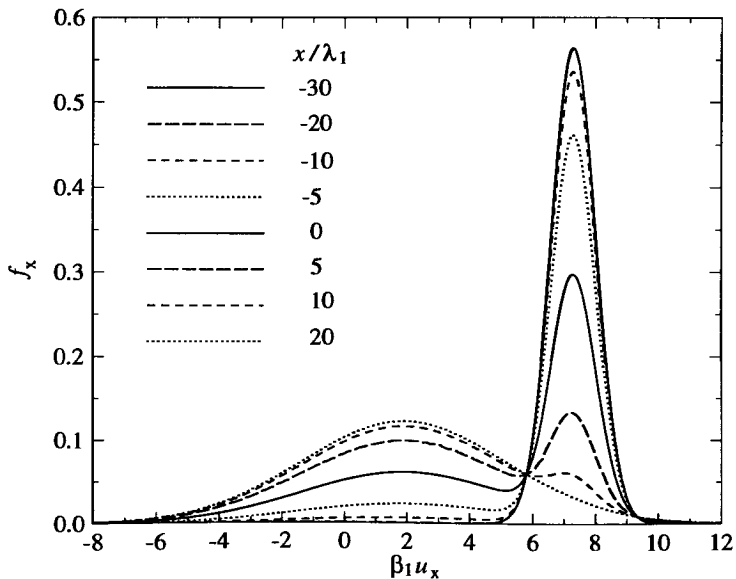


Fig. 12.41 The Mott-Smith prediction of the axial distribution function.

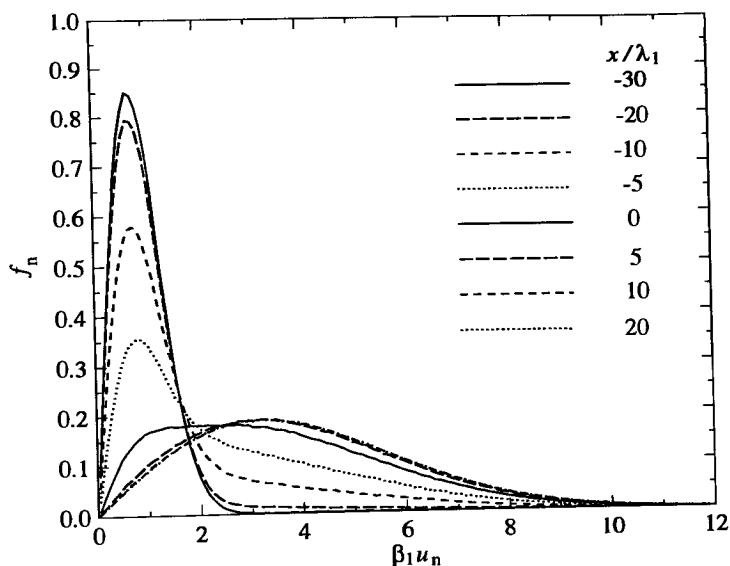


Fig. 12.42 DSMC result for the radial distribution function.

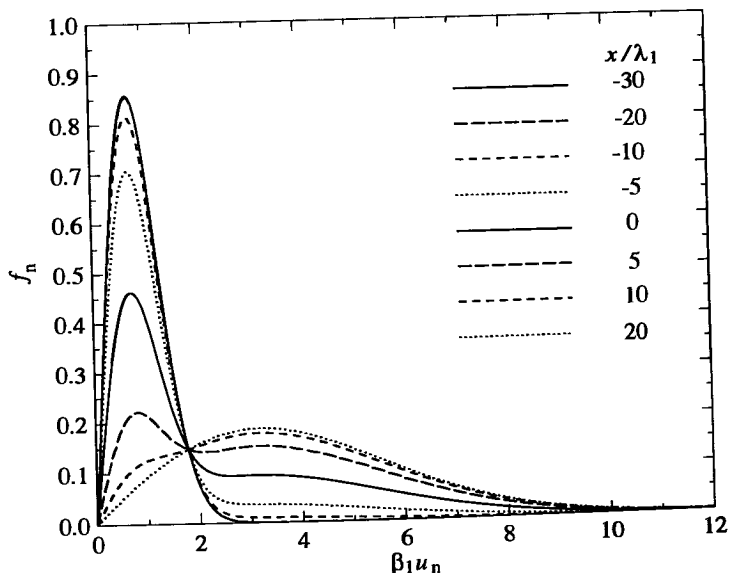


Fig. 12.43 The Mott-Smith prediction of the radial distribution function.

The shortcomings of the Mott-Smith theory are shown most clearly in the details of the velocity distribution functions. The DSMC and Mott-Smith profiles for the distribution function of the axial component of velocity are plotted in Figs 12.40 and 12.41, respectively. The corresponding results for the radial component of velocity are shown in Figs 12.42 and 12.43. The Mott-Smith model overestimates the degree to which the upstream distribution persists to the centre of the wave. This leads to a distribution function with a double peak at the centre of the wave. The actual distribution does not show a double maximum at any location, but has a point of inflection at the centre of the wave. The differences in the radial distribution function are similar, but there is not even a point of inflection in the DSMC profile at the centre of the wave.

The most basic information on the flow is given by the full distribution function and the DSMC result at the centre of the wave is shown in Fig. 12.44. This is defined such that the fraction of molecules with axial component between $\beta_1 u_x$ and $\beta_1 u_x + d(\beta_1 u_x)$ and radial component between $\beta_1 u_n$ and $\beta_1 u_n + d(\beta_1 u_n)$ is equal to $f d(\beta_1 u_x) d(\beta_1 u_n)$. As in the partially integrated distributions, there is a peak in the distribution at the most probable velocity in the upstream gas, but no peak at the downstream most probable velocity. The values in critical regions of the corresponding Mott-Smith distribution would be in error by factors of two or three.

The distribution functions have some resemblance to those for the bimodal distribution but, while the Mott-Smith model is qualitatively useful at the macroscopic level, it is inadequate at the microscopic level. It should also be remembered that the good prediction of the shock thickness by the Mott-Smith theory is dependent on the essentially empirical choice of the macroscopic quantity in the fourth moment equation.

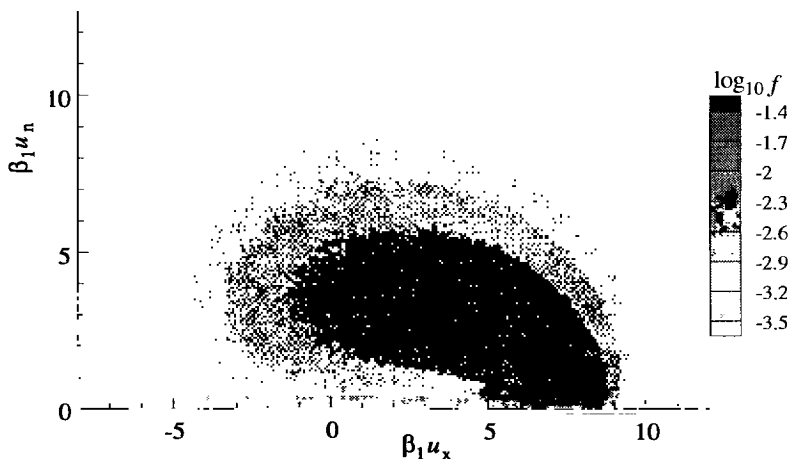


Fig. 12.44 The DSMC distribution function at $x/\lambda_1 = 0$.

12.12 Stagnation streamline flow

Program DSMC1S for the shock wave structure cannot be applied unless the velocity downstream of the wave is known. This is a serious problem for very strong shock waves in diatomic gases that lead to dissociation, because, while the equilibrium downstream conditions can be calculated, the recombination rate can be so slow in a rarefied gas that these conditions are not attained in any distance that can be calculated. The solution is to calculate the one-dimensional equivalent of the streamline in a two- or three-dimensional flow that reaches the stagnation point.

Program DSMC1T.FOR models the stagnation streamline as a constant area flow with a specified supersonic stream entering at one boundary and a diffusely reflecting surface at the other boundary. Initially, the gas has the properties of the undisturbed stream and an unsteady shock wave propagates from the surface into the flow. At some stage, molecules are removed from the sides of a region that extends from the wall to the specified boundary of this 'removal region' which must be downstream of the shock. The removal is such that the outlet flux is equal to the inlet flux and the flow settles down to a steady state with a stationary shock. The problem is to determine the selection rules such that mass, momentum and energy are conserved along the flow. The following analysis follows that of Bird (1986).

The mass conservation must be enforced on the basis of the number flux of each type of atom that comprise the molecules, because the composition of the gas may change across the shock. The streamline is along the x -axis and, if the rate of removal of molecular mass is \dot{m} per unit volume, the equation for the conservation of mass along the streamline is

$$d(\rho u) = -\dot{m} dx. \quad (12.34)$$

Then, if \bar{u} is the mean value of the streamwise velocity components of the removed molecules, the equation of conservation of momentum is

$$dp = -d(\rho u^2) - \bar{u} \dot{m} dx. \quad (12.35)$$

This can be written,

$$dp = -\rho u du - u d(\rho u) - \bar{u} \dot{m} dx$$

and eqn (12.34) shows that the final two terms cancel as long as \bar{u} is equal to u . This means that the continuum momentum equation is satisfied as long as the selection rules for molecular removal are independent of the streamwise velocity component of the molecules.

Finally, the energy conservation equation is

$$d(\rho u h_0) = \dot{m} \bar{e}_0 dx, \quad (12.36)$$

where h_0 is the stagnation enthalpy and \bar{e}_0 is the mean stagnation energy of the removed molecules. This equation can be written

$$\rho u dh_0 + h_0 d(\rho u) = -\dot{m} \bar{e}_0 dx,$$

and, using eqn (12.34), this reduces to the continuum energy equation

$$dh_0 = 0$$

if the molecules are selected such that

$$\bar{e}_0 = h_0. \quad (12.37)$$

Eqn (12.37) shows that the average specific energy of the removed molecules must exceed that averaged over all molecules in the flow by RT . This corresponds to an average energy margin of kT over the average translational value of $3kT/2$. Since the selection must be independent of the streamwise velocity component, the energy increment is best achieved by removing the molecules with probability proportional to the j th power of their velocity component normal to the stream direction. It may be shown that the mean translational energy of the removed molecules in an equilibrium gas is then

$$\bar{e}_{tr} = (3+j)kT/2. \quad (12.38)$$

For $j=0$, this gives the expected value for a stationary gas, and $j=1$ applies to the flux to or across a surface element, as discussed in §4.2. The requirement of eqn (12.37) is satisfied exactly by $j=2$, so that the molecules are removed with probability proportional to the square of the velocity component normal to the stream. It can be shown that eqn (12.38) applies to both removal in one plane, as in a two-dimensional flow, or in the radial direction in an axially symmetric flow.

The distribution of the removed molecules along the streamline must also be specified. If the shock structure is the item of interest, the only requirement on the removal region is that it should be well downstream of the shock. However, if the removal starts at the centre of the shock and is otherwise independent of location, there is evidence (Bird 1986) that the overall flow is a good representation of the stagnation streamline in a real axially symmetric flow. The acceptance-rejection technique is used to impose the 'normal velocity squared' removal rule by comparing this quantity with a maximum value. It is uncertain whether a separate maximum should be kept for each species in a gas mixture. This would affect the species separation effects and this program may not correctly model the pressure diffusion that occurs in a real multi-dimensional flow. Program DSMC1T therefore employs separate maximum values for each species and this point will be examined further in Chapter 14.

Program DSMC1T includes the routines from program DSMC0D that deal with vibrational excitation, dissociation and recombination. The routines for the implementation of the stream and surface boundaries come from program DSMC1. The molecule removal procedures that employs the above logic to model a stagnation streamline is applied in the subroutine STAGR. This is the only subroutine that is unique to this program.

The stagnation streamline approach may be inappropriate for flows with thermal radiation in that electronically excited particles may be removed before spontaneous emission occurs (Moss et al. 1988).

The test case was for a hypersonic flow of nitrogen with the removal region specified such that the complete stagnation streamline was modelled. The surface temperature was small in comparison with the temperature behind the shock and this led to a very large density increase in a narrow region adjacent to the surface. The cell structure of the other programs is inadequate under these circumstances. The flowfield has therefore been divided into a number of regions and each of these has a separate value of DTM and FNUM, although the ratio of these quantities is the same in every region. Because the ratio is the same, the flux of molecules between the regions is matched and there is no need for any removal or duplication of molecules crossing from one region to another. This technique can be used only for flows that become steady, and the flowfield is realistic only when steady flow has been attained. While this example involves a density variation of only two orders of magnitude, the technique makes possible the efficient simulation of flows with density variations of many orders of magnitude.

The stream speed was $-10,000 \text{ ms}^{-1}$ and the freestream number density and temperature were 10^{20} m^{-3} and 180 K, respectively. The molecule removal region extended from the origin at $x=0$ to $x=0.1$, while the boundary of the simulated region was at $x=0.6$. The resulting velocity profile is shown in Fig. 12.45 and it can be seen that the molecule removal commences near the downstream end of the shock wave.

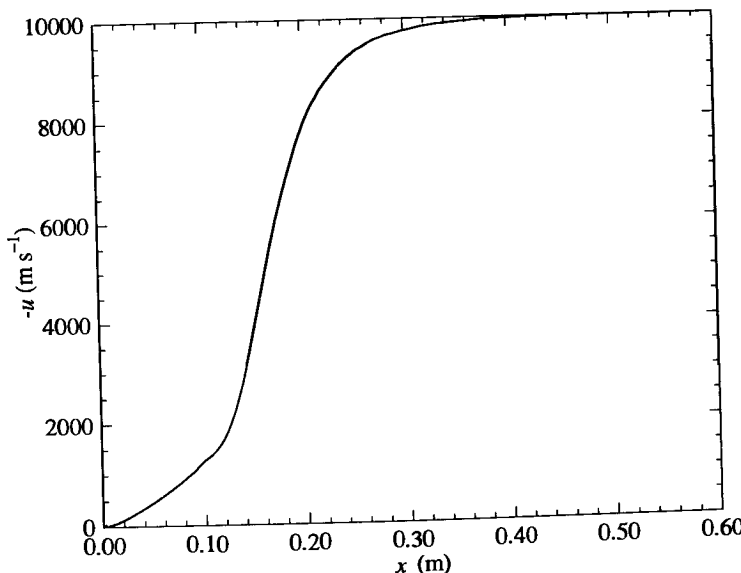


Fig. 12.45 The velocity profile along the stagnation streamline.

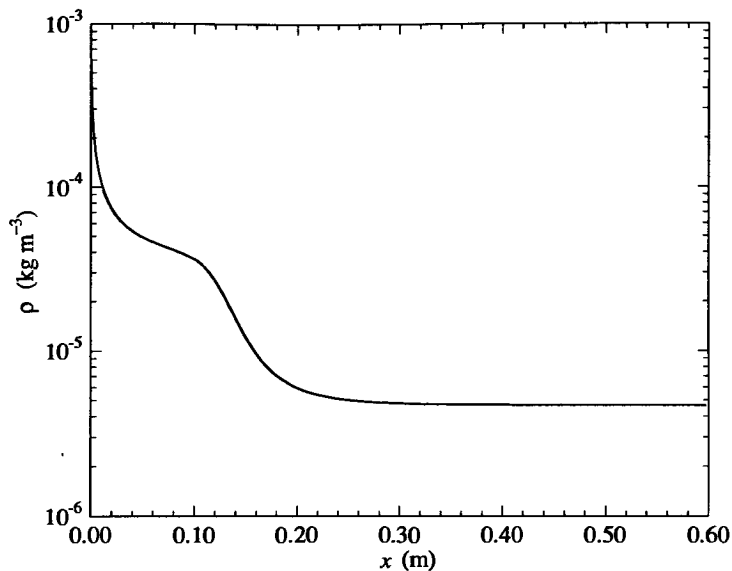


Fig. 12.46 The density rises across the shock and boundary layer.

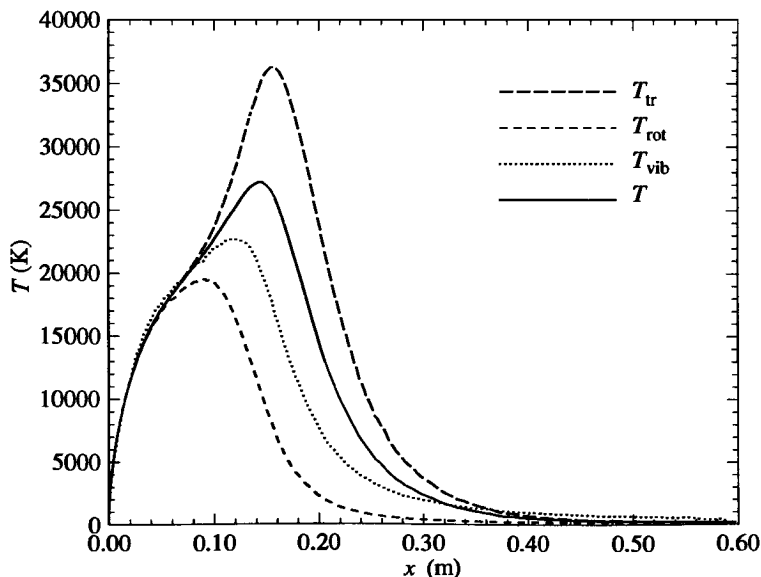


Fig. 12.47 The components of temperature along the streamline.

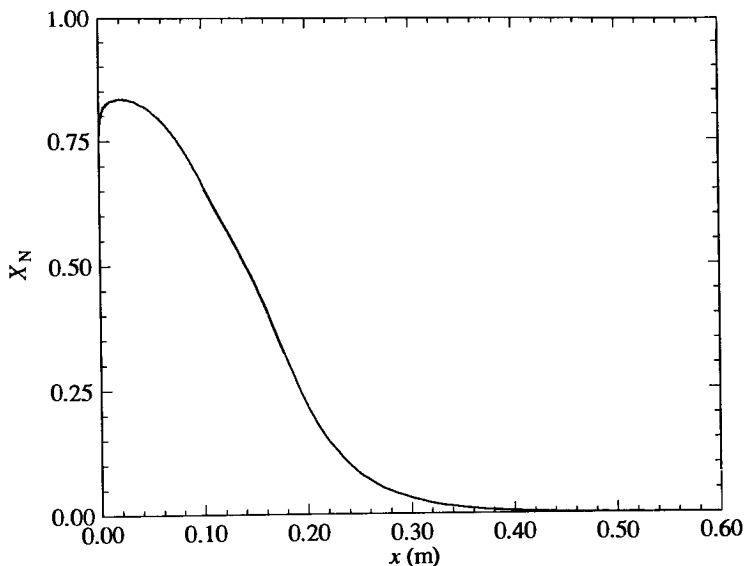


Fig. 12.48 The fraction of atomic nitrogen along the streamline.

There is a factor of ten increase in density across the shock wave and, as shown in Fig. 12.46, a further factor of ten increase across the thermal boundary layer to the surface at 1000 K. The density gradient in the thermal boundary layer is actually higher than that in the shock wave, but Fig. 12.47 shows that the separate rotational, vibrational, and translational temperatures are in equilibrium in the boundary layer. The initial temperature rise occurs well upstream of any significant increase in density, and there is extreme non-equilibrium between the separate components of the temperature in the upstream half of the wave. The temperatures are sufficiently high to cause the dissociation of a significant fraction of the nitrogen, and the number fraction of atomic nitrogen is shown in Fig. 12.48. The fall in the concentration of atomic nitrogen near the surface is a consequence of thermal diffusion.

The near linear decrease in the stream speed in the molecule removal to zero at the stagnation point is similar to that in blunt body flows, and the surface properties are expected to be close to those in axially symmetric or two-dimensional flows that have the same shock standoff distance. The net heat transfer to the surface for the steady state of this flow was 0.28 MW m^{-2} , and this is just over one tenth of the energy flux in the free-stream. The heat transfer due to the translational and internal energies was 0.43 and 0.05 MW m^{-2} , respectively, while that due to the reflected molecules was -0.18 and -0.02 MW m^{-2} . The pressure due to the incident molecules was 246 N m^{-2} and 163 N m^{-2} due to the reflected molecules.

12.13 Adiabatic atmosphere

A gravitational field can be included in applications of program DSMC1 to plane flows. A case was set up with a stationary gas of argon with number density 10^{24} m^{-3} and a temperature of 200 K at the inner boundary at $x=0$. The outer boundary at $x=1 \text{ m}$ was a vacuum and the initial state was a uniform stationary gas at the inner boundary conditions. The continuum solution for a static adiabatic atmosphere predicts a constant temperature lapse rate of

$$\frac{dT}{dx} = \frac{\gamma-1}{\gamma} \frac{mg}{k}. \quad (12.39)$$

The ‘gravitational’ acceleration was set to $-1.25 \times 10^5 \text{ m/s}^2$ and the resulting lapse rate of just over 240 Km^{-1} is such that the ‘atmosphere’ should terminate at about 0.83 m. The unsteady phase of the flow involved strong disturbances as the gas expands into the vacuum while being restrained by the gravitational field. These disturbances are slow to decay, but the eventual establishment of a steady flow is verified in Fig. 12.49 by plotting the time-averaged temperature profile over three separate time intervals. The temperature follows the continuum prediction for a short distance, but then falls at a much slower rate and the atmosphere extends out to the vacuum boundary.

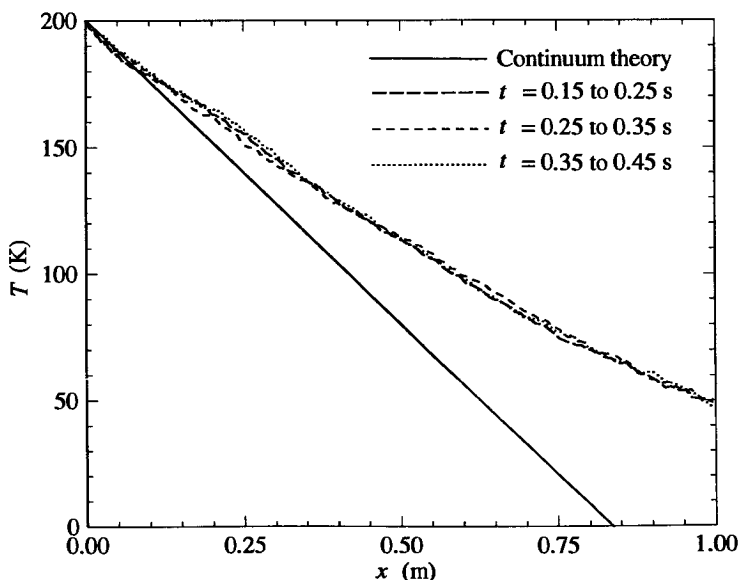


Fig. 12.49 The temperature profile in the adiabatic atmosphere.

The local Knudsen number, based on the density scale length, at the point where the temperature departs from the continuum value is approximately 0.002. The pressure gradient is everywhere consistent with the continuum equation

$$\frac{dp}{dx} = \rho g. \quad (12.40)$$

Note that in both these equations and in program DSMC1 g is positive when it is directed in the positive x -direction. The density at the outer boundary is approximately 1% of the density of the stationary gas that constitutes the inner boundary. The atmosphere is not stationary and the velocity ranges from approximately 0.7 ms^{-1} near $x=0$ to 70 ms^{-1} at the outer boundary.

The calculation was repeated for a mixture of equal parts by number of argon and helium. The gravitational field was adjusted so that the continuum lapse rate was the same as in the simple gas case. As shown in Fig. 12.50 there was no separation of these gases in the atmosphere. This result is perhaps surprising, but it should be noted that the variable \mathbf{F} in both the Boltzmann equation and the diffusion equation is a force per unit mass and does not lead to separation effects in a gas mixture. Any separation would be due to either pressure or thermal diffusion. Thermal diffusion would act to concentrate the argon at the outer boundary and pressure diffusion would tend to concentrate it at the inner boundary. It appears that the cancellation of these effects is almost exact.

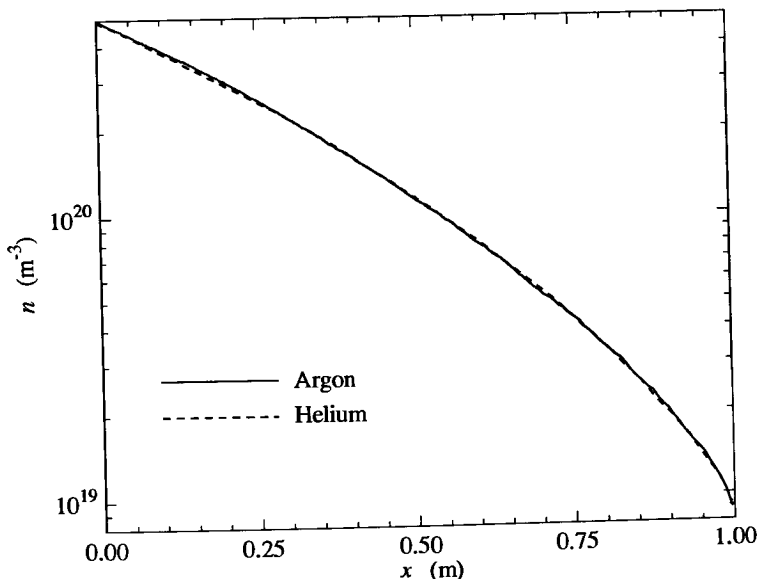


Fig. 12.50 Number density profiles in a mixture of equal parts of argon and helium.

12.14 Gas centrifuge

Consider a cylindrical flow with the axis as the inner boundary and a surface with a circumferential velocity of 1000 m/s as the outer boundary. The gas is initially a mixture of equal parts by number argon and helium that is stationary at a number density of 10^{21} m^{-3} and a temperature of 200 K. The outer moving boundary is diffusely reflecting at a temperature of 200 K. The rotation of the outer boundary effectively starts at zero time and a steady flow is eventually established.

Unlike the preceding case, there is no force acting directly on the molecules but, as shown in Fig. 12.51 for the number density profiles of the separate species, the separation effects are significant. The circumferential velocity and the temperature profiles are shown in Figs. 12.52 and 12.53, respectively. These profiles show that pressure and thermal diffusion act in the same direction in the outer part of the flow, but the pressure diffusion would be dominant. Adjacent to the surface, the argon number density is double the helium number, but the region of enhanced argon extends into the flow only to 0.93 m. There is then a region of enhanced helium that extends to the radius of approximately 0.5 m. The samples are so small near the axis that the apparent separation in this region is probably not significant.

The circumferential velocity declines to near zero near a radius of 0.5 m and the conditions in the inner core of the flow are not significantly different from the initial conditions.

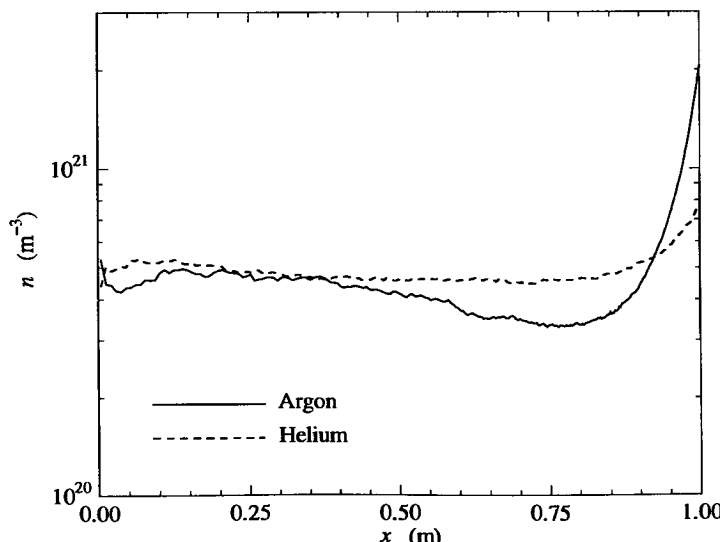


Fig. 12.51 The number density profiles in the gas centrifuge.

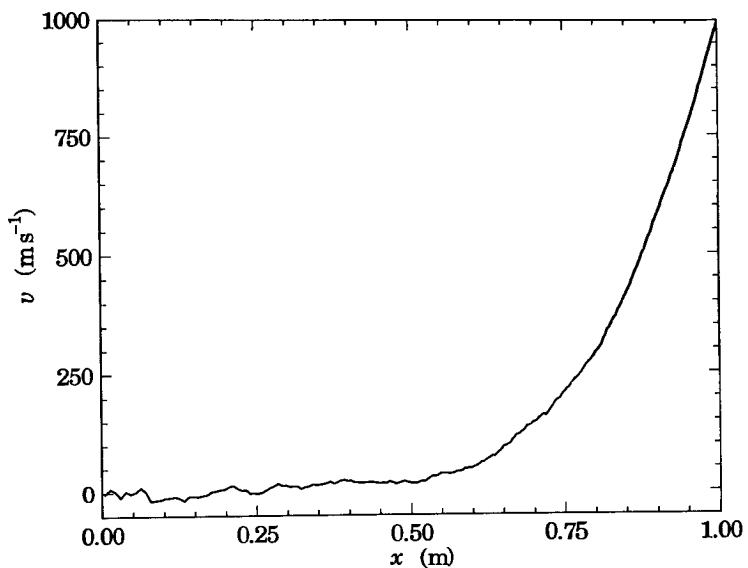


Fig. 12.52 The circumferential velocity profile in the centrifuge.

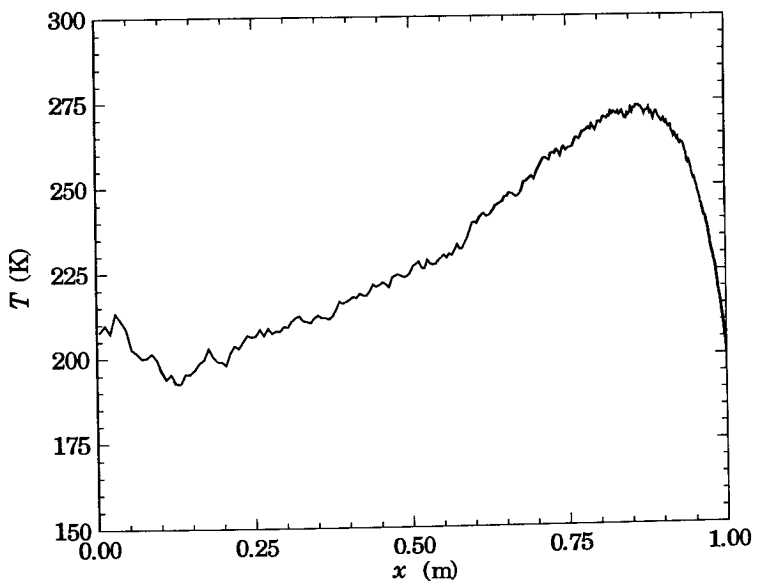


Fig. 12.53 The temperature profile in the centrifuge.

The temperature of the gas adjacent to the surface is only slightly above the surface temperature of 200 K, but it increases to a maximum of just over 270 K at a radius of 0.87 m. This means that there is a net heat transfer to the surface, and this equals the work done against the shear stress by the rotation of the cylinder.

References

- ALSMAYER, H. (1976). Density profiles in argon and nitrogen shock waves measured by the absorption of an electron beam. *J. Fluid Mech.* **74**, 497–513.
- BIRD, G.A. (1970). Breakdown of Translational and Rotational Equilibrium in gaseous expansions. *AIAA Journal* **8**, 1998–2003.
- BIRD, G.A. (1976). *Molecular gas dynamics*, Oxford University Press.
- BIRD, G.A. (1986). Direct simulation of typical AOTV entry flows. *Am. Inst. Aero. Astro. Paper-86-1310*.
- CHAPMAN, S. and COWLING, T.G. (1970). *The mathematical theory of non-uniform gases* (3rd edn). Cambridge University Press.
- GILBARG, D. and PAOLUCCI, D. (1953). The structure of shock waves in the continuum theory of fluids. *J. Rat. Mech. Anal.* **2**, 617–642.
- GMURCZYK, A.S., TARCYNSKI, M., and WALENTA, Z.A. (1979). Shock wave structure in the binary mixtures of gases with disparate molecular masses. In *Rarefied gas dynamics: eleventh symposium* (ed. R. Campargue), Commissariat à l'Energie Atomique, Paris., 333–341.
- KOURA, K. and MATSUMOTO, H. (1991). Variable soft sphere molecular model for inverse-power-law or Lennard-Jones potential. *Phys. Fluids A* **3**, 2459–2465.
- LIEPMANN, H.W. and ROSHKO, A. (1957). *Elements of gasdynamics*, Wiley, New York.
- MOSS, J.N., DOGRA, V. K., and BIRD, G.A. (1988). Nonequilibrium Thermal Radiation for an Aeroassist Flight Experiment Vehicle. *Am. Inst. Aero. and Astro. Paper 88-0081*.
- PHAM-VAN-DIEP, G.C., ERWIN, D.A., and MUNTZ, E.P. (1989). Nonequilibrium molecular motion in a hypersonic shock wave. *Science* **245**, 624–626.
- PHAM-VAN-DIEP, G.C., ERWIN, D.A., and MUNTZ, E.P. (1991). Testing continuum descriptions of low Mach number shock structures. *J. Fluid Mech.* **232**, 403–413.
- ROBBEN, F. and TALBOT, L. (1966). Measurements of rotational temperatures in a low density wind tunnel. *Phys. Fluids* **9**, 633–662.
- SCHMIDT, B. (1969). Electron beam density measurements in shock waves in argon. *J. Fluid Mech.* **39**, 361–373.
- SIMON, C.E. and FOCH, J.D. (1977). Numerical integration of the Burnett equations for shock structure in a Maxwell gas. *Prog. Astro. Aero.* **51**, 493–500.

13

ONE-DIMENSIONAL UNSTEADY FLOWS

13.1 General program for unsteady flows

Program DSMC1U.FOR is a version of DSMC1 that has been adapted to make ensemble averages of repeated runs of an unsteady flow, rather than a time average of a steady flow that is established as the large-time state of a single run of an unsteady flow. As in the preceding programs, the flow is sampled each NIS time steps, but a separate sampling record must be made for each of these sampling events. Excessive memory would be required if the sampling arrays were simply given an extra dimension equal to the total number of sampling events MNOI in each run. The answer is to establish the direct access file DSMC1U.DAT with MNOI records. Note that MNOI is set in the PARAMETER statement and, together with NIS, it controls the length of each run. No more than one record of this file is in memory at any time and, on some occasions that a record of this file is read, most of the variables must be read into dummy arrays so that they do not overwrite the current values of these variables that already exist.

The 'restart' file is not needed because a restart of the program simply adds to the number of runs, and each run starts from the initial conditions specified in the subroutine DATA1U. The output file DSMC1U.OUT now includes the results at each of the sampling times. This amounts to a great deal of information and, if this is to serve as the primary output, the number of sampling times will be restricted to as small a number as possible. On the other hand, if a post-processing program is to be used to automatically construct contours in the distance-time plane, it is desirable to have output at a large number of times. The results in this chapter were obtained through a post-processing program and further details are given in Appendix F.

In order to cope with the desired range of problems, several additions have been made to the range of available boundary conditions. The first is that the uniform initial gas need not extend over the whole of the flowfield, and there may be an initial interface with a vacuum at some location within the flow. The second and more complex new option is that either boundary may be a moving piston. The piston may be plane, cylindrical, or spherical and the molecules are reflected specularly from its face. The number of cells remains constant and, when one or more piston boundary conditions are chosen, the cell boundaries and volumes become a function of time and must be recalculated at each time step.

In the case of a plane flow, the extensions to cope with the moving piston are quite straightforward. The fraction of the trajectory element to the intersection with the piston is

$$s_d = (X_i - x_i) / \{(u - U)\Delta t\}, \quad (13.1)$$

where i denotes the value at the beginning of the time step Δt , x and u are the location and x -velocity component of the molecule, and X and U are the corresponding quantities for the piston. The post-reflection velocity component of the molecule is

$$u' = 2U - u. \quad (13.2)$$

For cylindrical and spherical flows, the extension of eqn (12.12) to include the finite piston velocity gives

$$\frac{1}{2}s_d^2 \{1 - (U\Delta t/d)^2\} + (u\Delta t x_i - U\Delta t r_i)s_d/d^2 + \frac{1}{2}(x_i^2 - r_i^2)/d^2 = 0. \quad (13.3)$$

This equation is evaluated in the subroutine RBCP and, after the collision point velocities have been transformed by subroutine AIFX, eqn (13.2) applies also to these cases. Because there can be multiple reflections with a curved piston during a single time step, the reflected motion is calculated as a separate trajectory element.

13.2 The formation of a strong shock wave

The data in the listing of program DSMC1U is for the formation of a strong plane shock wave by a piston that, at zero time, is impulsively given a constant velocity of 2285.5 ms^{-1} in the x -direction. The gas in front of the piston is the VHS model of argon at a temperature of 273 K and a number density of 10^{20} m^{-3} . The Rankine-Hugoniot theory shows that this leads to a shock of Mach number 10, i.e. $(Ma)_S = 10$. The rate of propagation of this wave is 3078.1 ms^{-1} and the downstream number density and temperature are 3.8835×10^{20} and 8796.6 K , respectively.

A time average was taken over 700 separate runs and the contours, in the distance-time plane, of velocity, number density, temperature, and parallel temperature are shown in Figs 13.1 to 13.4. While the velocity and number density profiles across the fully formed wave are simply the inverse of one another, the formation contours are qualitatively different. The downstream velocity is established immediately, while the density adjacent to the piston increases gradually to the downstream value. The collisionless value of the density adjacent to the piston is given by eqn (7.43) and Fig. 7.5 shows that, for large piston speed ratios, the initial density adjacent to the piston is twice the undisturbed density. Eqn (7.43) also gives the path of the collisionless contours and Fig. 13.2 shows the collisionless contour for $n = 1.2 \times 10^{20}$. The continuum shock path has also been added to Fig. 13.2, and it can be seen that, except for very small times, it very nearly coincides with the contour for $n = 2.4 \times 10^{20}$ which is very close to the mean of the upstream and downstream number densities.

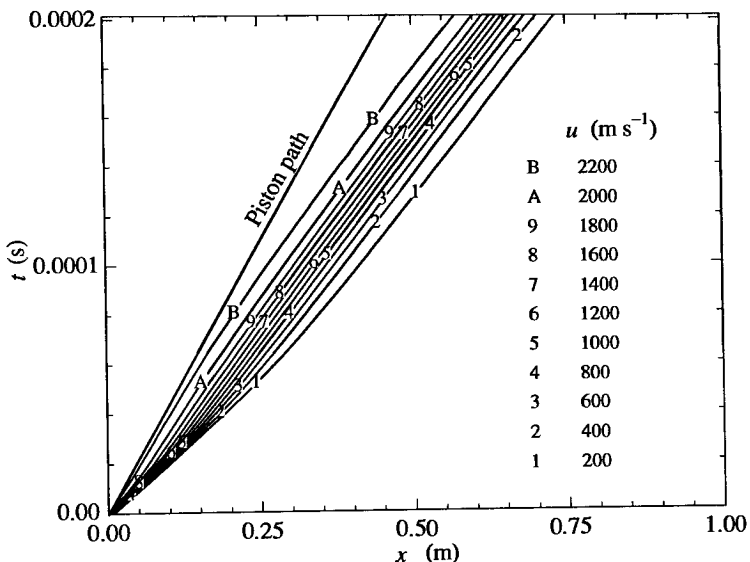


Fig. 13.1 Velocity contours in the distance-time plane.

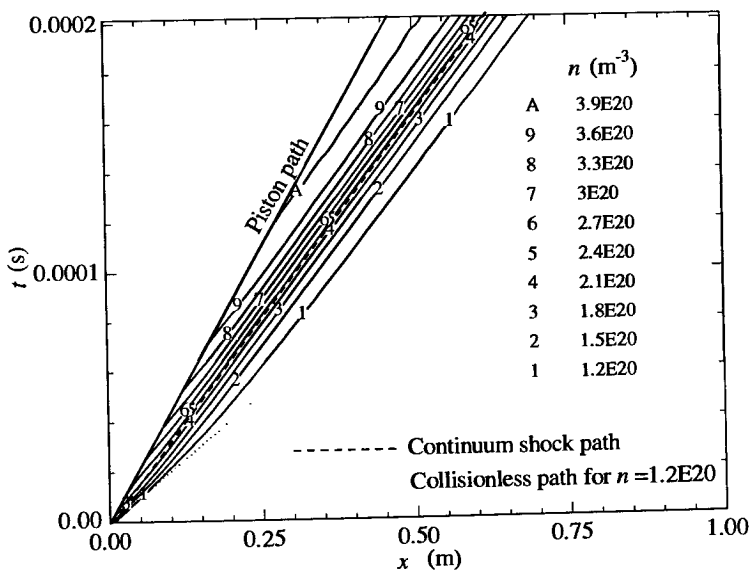


Fig. 13.2 Number density contours in the distance-time plane.

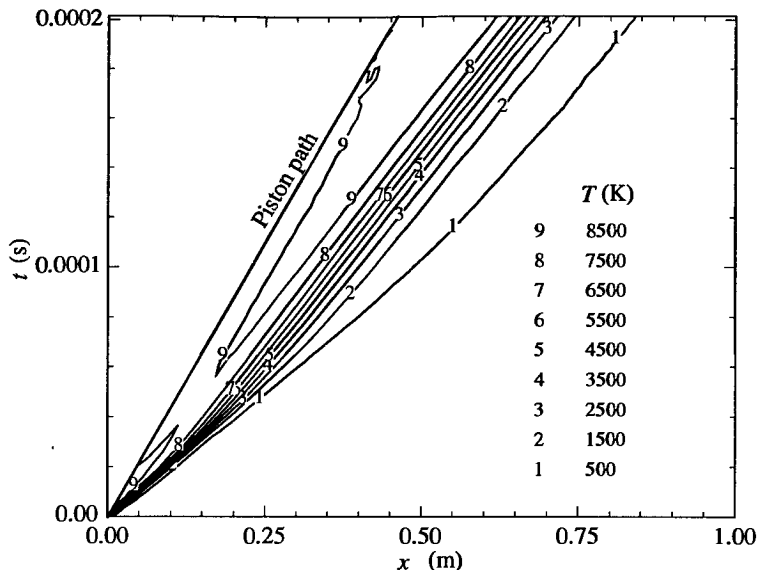


Fig. 13.3 Temperature contours in the distance–time plane.

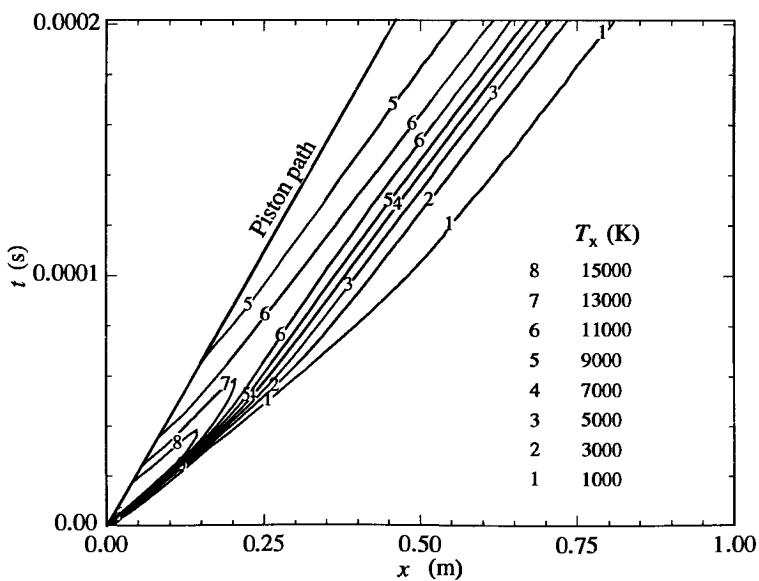


Fig. 13.4 Parallel temperature contours in the distance–time plane.

There is an apparent anomaly in the density contours in that contour A is for a number density of 3.9×10^{20} even though the Rankine-Hugoniot value is only 3.8835×10^{20} . The reason for this is that the partially formed shock involves a greater degree of non-equilibrium than the fully formed shock and the entropy increase across it is greater than that across the fully formed shock. This leads to a lower stagnation temperature in the gas adjacent to the piston than in the gas immediately behind the fully formed shock. This leads in turn to a reduced temperature and therefore an increased density in the gas adjacent to the piston. The 'entropy layer' effect is apparent in the temperature contours of Fig. 13.3. The downstream Rankine-Hugoniot temperature of just under 8,800 K is attained at about 100 μ s. The temperature adjacent to the wall gradually increases as thermal conduction reduces the temperature gradient that is associated with the entropy gradient. The extreme non-equilibrium in the early stages of the shock formation is apparent in the parallel temperature contours of Fig. 13.4. The maximum parallel temperature in the fully formed shock is just over 11,000 K, but a large region has a parallel temperature in excess of 15,000 K.

13.3 The reflection of a strong shock wave

There is a stationary specularly reflecting surface at the outer boundary at $x = 1$ and, if the time span of the run is increased, the shock wave reflects from this surface. The continuum Rankine-Hugoniot theory predicts a reflected shock of Mach number $(Ma)_S = 2.2$. The number density and temperature behind the reflected shock are then 9.593×10^{20} and 20,676 K, respectively.

The DSMC results for the shock reflection process are illustrated in Figs 13.5 to 13.8. The minimum and maximum limits in the velocity are unchanged and the contours are continuous. The number density at the wall increases continuously during the reflection process and the density corresponding to that behind the incident shock occurs very close to the predicted point of impingement of the continuum shock. The velocity gradient normal to the wall is a maximum at this time. Although the shock Mach number of the reflected shock is relatively small, the density upstream of the wave is almost four times that of undisturbed gas and the actual thickness of the reflected wave is less than that of the incident wave.

As with the incident shock, the contour of the mean density in the reflected shock is close to the continuum shock path. The temperature profiles of both the incident and reflected waves show the characteristic shock behaviour of the downstream temperature being almost attained upstream of the centre of the density contour. The temperature contours during the reflection process are qualitatively similar to the number density contours. However, the time at which the incident shock contours change to reflected shock contours is earlier than that for the number density profiles.

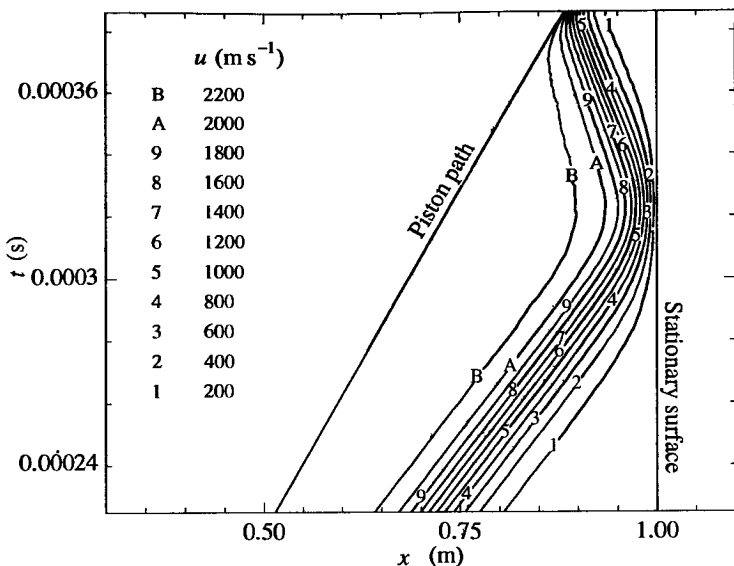


Fig. 13.5 The velocity contours in the shock reflection.

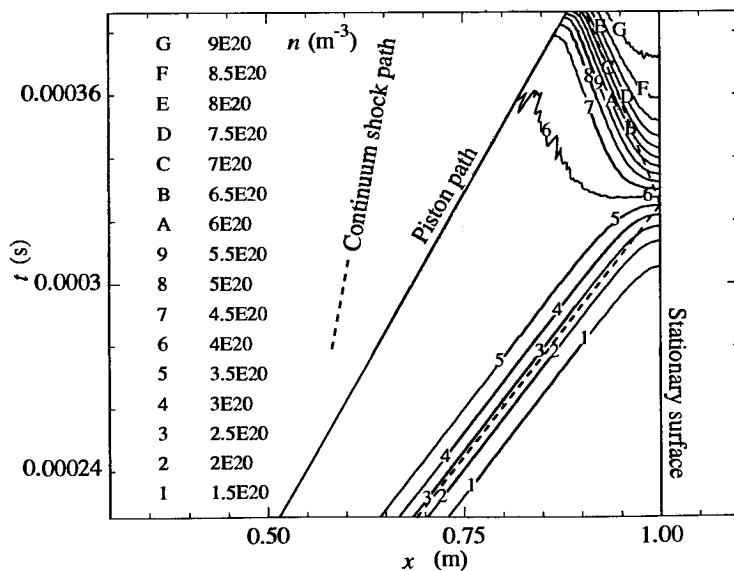


Fig. 13.6 The number density contours in the shock reflection.

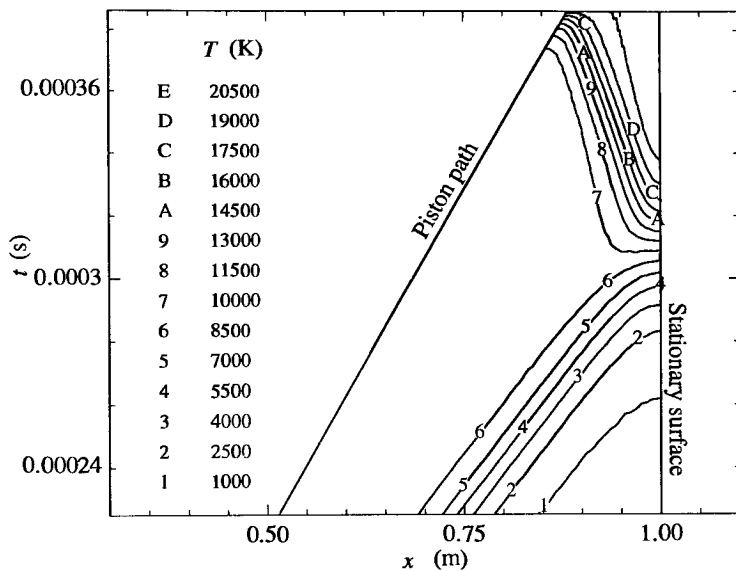


Fig. 13.7 The temperature contours in the shock reflection.

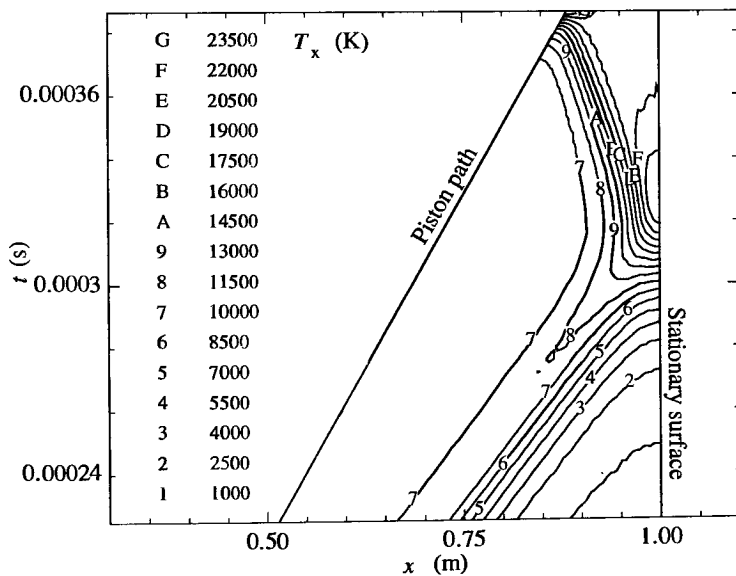


Fig. 13.8 The parallel temperature contours in the shock reflection.

13.4 Formation of a weak shock wave

A calculation similar to that in §13.2 was made for a comparatively weak shock of $(Ma)_S = 1.4$. The required piston speed is 158.3 m/s and the Rankine-Hugoniot values of the number density and temperature are $1.581 \times 10^{20} \text{ m}^{-3}$ and 380.0 K, respectively.

The velocity contours are shown in Fig. 13.9. The downstream contour is for a velocity only 2% less than the piston velocity and the statistical scatter is responsible for the jagged appearance of this and, to a lesser extent, the first contour. The 95 m/s contour is almost coincident with the continuum shock path.

The number density contours in Fig. 13.10 are qualitatively different from those for the strong shock and are generally similar to the velocity contours. The reason is that the collisionless density at the piston face from eqn (7.43) is $1.49 \times 10^{20} \text{ m}^{-3}$, and this is only slightly less than the continuum density ratio. This means that the density rise along the piston is quite small, but there is again a density overshoot near the piston as a result of the entropy layer. As in the strong shock case, the maximum value of this overshoot is about 2%. While the Navier-Stokes equations are valid for the structure of a fully formed shock wave of $(Ma)_S = 1.4$, they are not valid for the stronger gradients that occur in the early stages of the shock formation. Finally, the temperature contours of Fig. 13.11 clearly show the effects of the entropy layer and also show that most of the temperature rise occurs ahead of the continuum shock path.

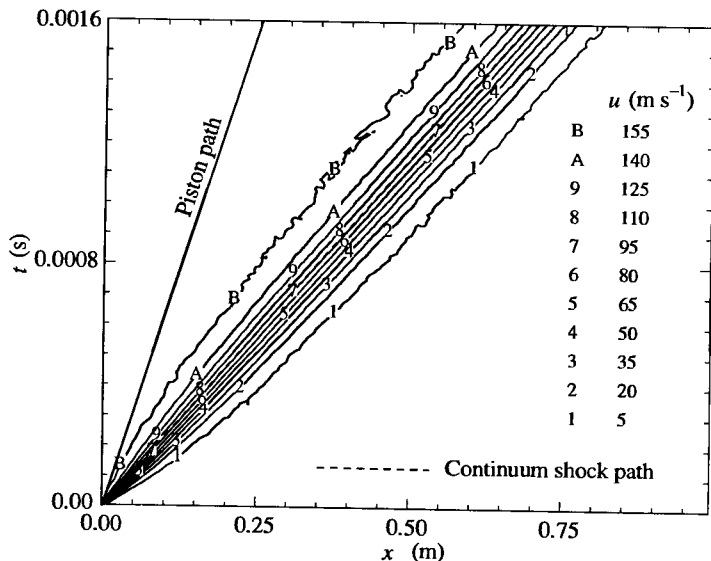


Fig. 13.9 Velocity contours in the formation of a weak shock wave.

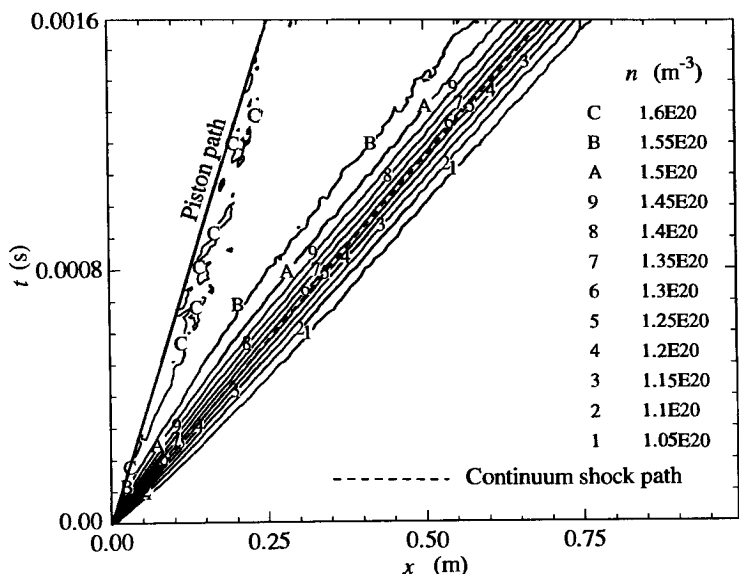


Fig. 13.10 Number density contours in the formation of a weak shock.

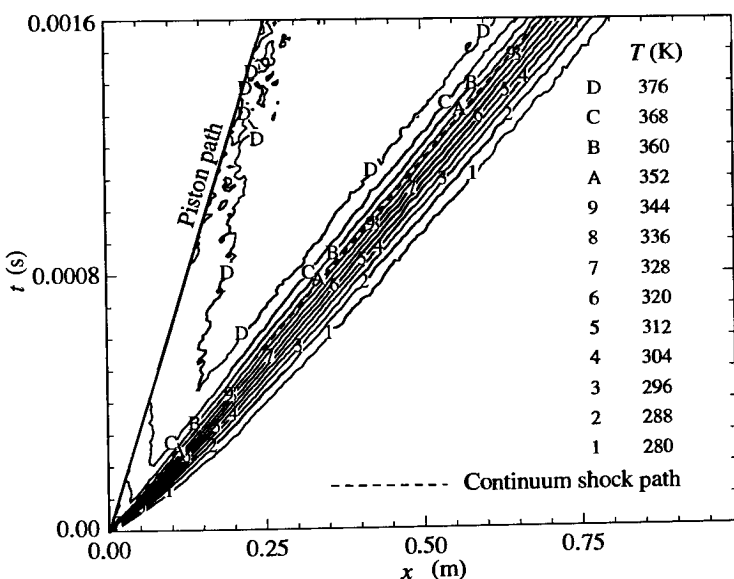


Fig. 13.11 Temperature contours in the formation of a weak shock wave.

13.5 The complete rarefaction wave

A complete rarefaction wave arises at a discontinuous plane interface between a uniform gas and a vacuum. In the continuum solution, the leading edge of the wave advances into the gas at the speed of sound while, within the wave, the gas expands into the vacuum. The speed of the expanding gas becomes sonic at the location of the interface, and the flow Mach number is infinite at the tail of the expansion even though the limiting speed is only $2/(\gamma-1)$ times the undisturbed speed of sound. The continuum theory must break down at the tail of rarefaction wave at all times and, at very small times, it will fail over the whole flow.

An indication of the expected extent of the breakdown of translational equilibrium in the rarefaction wave may be gained from the breakdown parameter P defined by eqn (1.4). This expression has been combined with the continuum equations for the complete rarefaction (Bird 1970), and the initial value of P at the leading edge of the expansion is

$$P_i = \{1/(\gamma-1)\} (\pi\gamma/2)^{1/2} (\lambda_0/x_i). \quad (13.4)$$

Here, λ_0 is the mean free path in the undisturbed gas and x_i is the distance measured from the initial discontinuous interface. The subsequent change in P along the particle paths is given by

$$DP/Dt = (P/t) \{(\gamma-1)(\gamma+1)\} (1-2\omega). \quad (13.5)$$

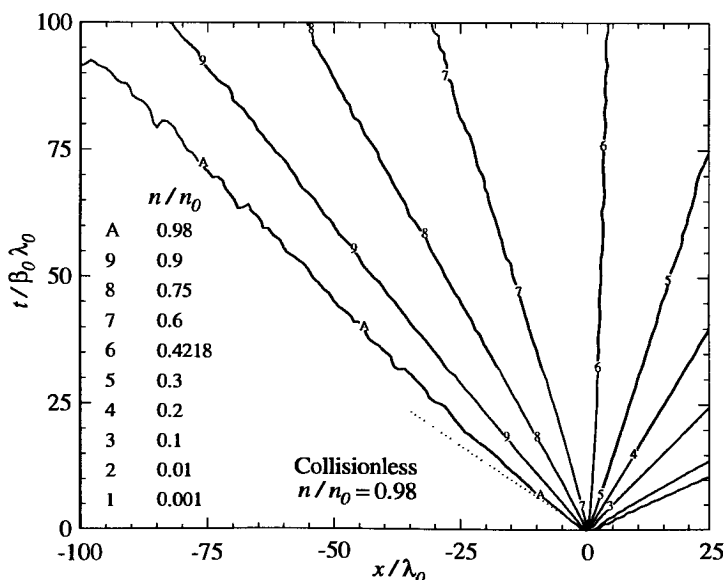


Fig. 13.12 Number density contours in a complete rarefaction wave.

This shows that P remains constant along a particle path in a hard sphere gas but, for more realistic models, there is a gradual reduction in P and a consequent move towards equilibrium. For a monatomic gas, eqn (13.4) reduces to

$$P_i = 0.60676 \lambda_0 / x_i. \quad (13.6)$$

Should the values of P that were found in §12.10 to be necessary for a steady expansion apply also to an unsteady flow, the flow at the leading edge of the rarefaction would not be in equilibrium until it had progressed some hundreds of mean free paths into the gas.

Program DSMC1U was used to calculate the expansion of a monatomic gas with an extent of 100 mean free paths from a plane of symmetry. The initial vacuum extended for 50 initial mean free paths and was terminated by a 'vacuum' boundary. Some typical contours of constant number density are shown in Fig. 13.12. These are normalised to the undisturbed number density n_0 , and the contour for 0.98 is close to the leading edge of the wave. The initial slope of this contour in the distance-time plane is consistent with the collisionless theory of eqn (7.41). The effective speed of the wave then decreases, but it reflects from the plane of symmetry well before the normalised time of 109.5 that is predicted by the continuum theory. This theory predicts a constant number density ratio of 0.4218 at the origin. This contour has a positive slope, but gradually becomes more vertical.

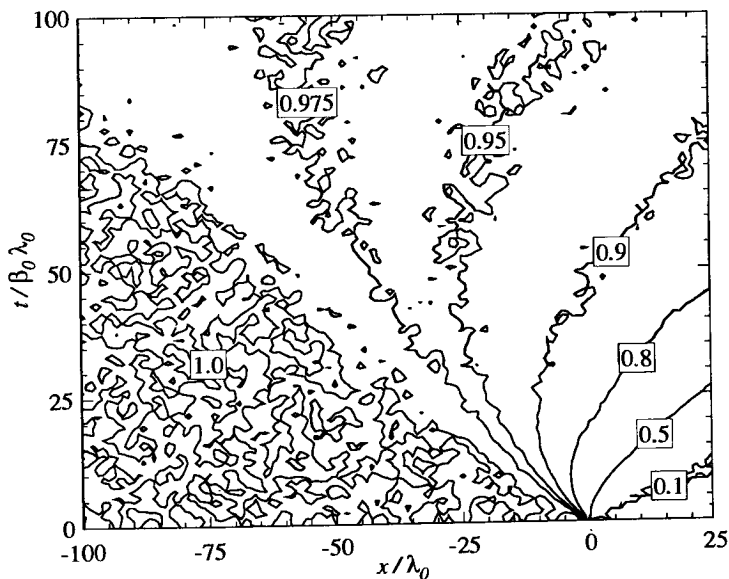


Fig. 13.13 The ratio of the parallel to the normal temperature.

As in the steady expansion, a more precise measure of the degree of nonequilibrium in the expansion is given by the ratio of the parallel temperature T_x to the normal temperature T_n . Contours for this ratio are shown in Fig. 13.13. The ratio is, of course, unity in the undisturbed gas but the statistical scatter produces a random pattern for this contour. Scatter is also present for the values of the ratio near unity, but the figure clearly shows the gradual approach to equilibrium in early part of the expansion together with the extreme nonequilibrium near the tail of the rarefaction wave.

Key contours of velocity normalised to the undisturbed speed of sound a_0 are shown in Fig. 13.14. The contour for 0.02 is consistent with the number density contour of 0.98, except that the reflection of the wave at the plane of symmetry causes an outward rather than inward deflection of the contour. The collisionless theory of eqn (7.42) predicts an initial velocity ratio of 0.618 at $x=0$, but this applies only at extremely small times. The continuum prediction of sonic flow at this location leads in a monatomic gas to a velocity ratio of 0.75. This contour is similar to the density contour for sonic flow. These contours would become vertical at a normalised time of 200 at only five or six mean free paths from $x=0$. Despite the extreme temperature nonequilibrium, the limiting velocity of $3a_0$ is attained at the tail of the rarefaction (or front of the advancing gas).

The results are generally consistent with the theory for the behaviour of the breakdown parameter, with a gas element that is initially out of equilibrium tending to remain out of equilibrium along its particle path.

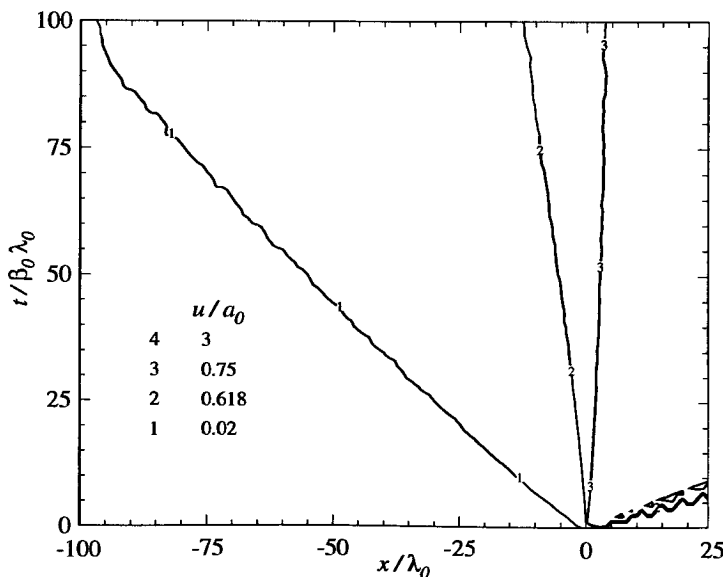


Fig. 13.14 The key velocity contours in the rarefaction wave.

13.5 Spherically imploding shock wave

In the plane flow case, the shock waves are of constant strength and the flow conditions are uniform outside the waves. This ceases to be the case for waves in cylindrically or spherically symmetric flows. The reflection of a spherical wave from the centre or origin has been the subject of many studies because the continuum theory with a discontinuous wave leads to a singularity at the origin. The singularity disappears for real shock waves of finite thickness, and it is necessary to define the problem by the process that produces the wave and the strength of the wave when it is a specified number of mean free paths from the origin. The first case to be considered is a wave in argon that is driven by a hollow spherical piston that is contracting with a uniform velocity of -2285.5 ms^{-1} . The initial gas number density is 10^{20} m^{-3} and the contraction starts impulsively from a radius of 1 m. This corresponds to a shock Mach number of 10 at a radius of approximately 70 mean free paths.

There is a problem in obtaining a good sample near the origin. The calculation was made with 30,000 simulated molecules and the width of the cell at the origin was one hundred times the width of the cell adjacent to the piston. While this led to a reasonably large sample in each cell, the inner tenth of the flow in terms of the radius initially contained only 300 molecules. This caused an unexpected problem that required modifications to the code.

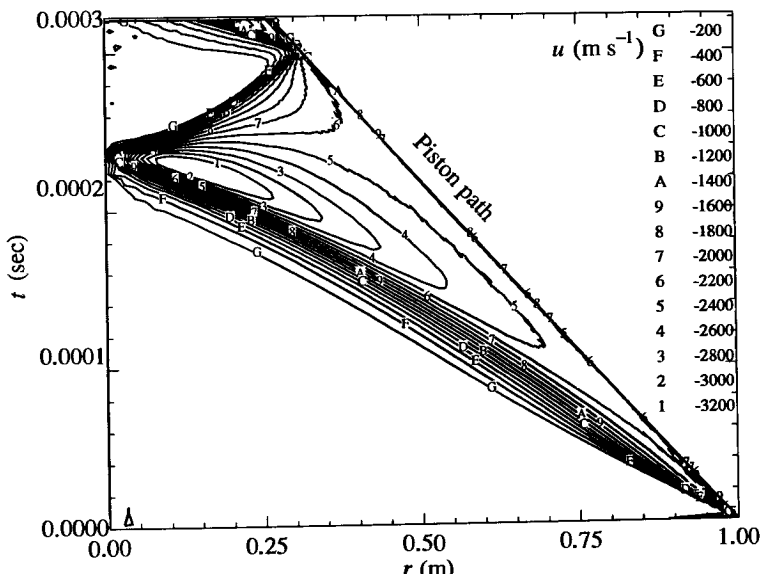


Fig. 13.15 Velocity contours in a spherically imploding shock wave.

In all the preceding programs that involve the generation of an initially uniform gas, each of the molecules in that gas is generated independently. This means that there are always initial non-uniformities in the gas and these lead to extraneous disturbances. These have not been a problem in the earlier applications but, in this case, the disturbances that move towards the axis were amplified to such an extent that the flow near the axis was seriously affected. The disturbances had the characteristics of pressure waves in that both the density and temperature were either increased or decreased, and their timing was such that they came from the inner 300 molecules. The subroutine INIT1U in program DSMC1U was modified such that the initial molecules were generated in pairs rather than as single molecules. The two molecules in each pair had radial velocity components that were equal and opposite, but were otherwise identical. There was therefore no net initial momentum in the radial direction and the problem disappeared. This modification is in the nature of a 'quick fix' and there is a need for procedures that systematically generate initial states that are, as near as possible, unbiased in all respects. This is one aspect of the 'variance reduction' issue that has been discussed in §7.7 and in §10.4. Given the large number of dimensions of phase space, this will probably be best achieved through matched lists rather than through uniform spacing of the molecules in phase space.

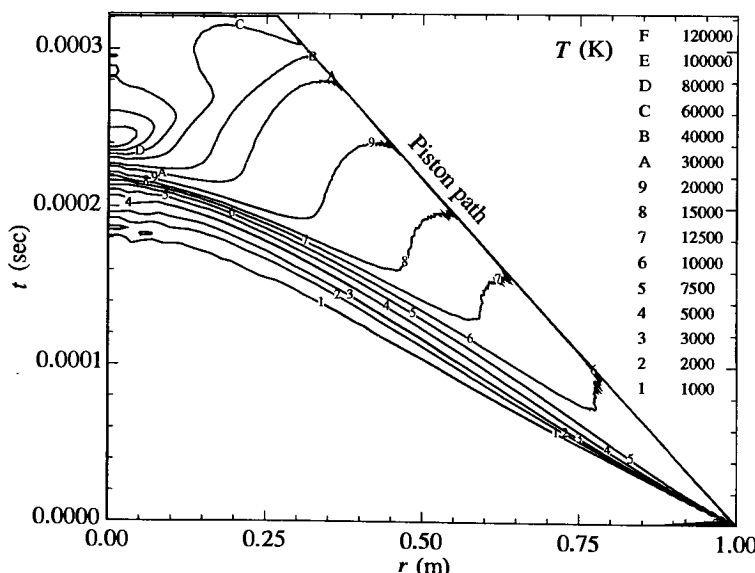


Fig. 13.16 Temperature contours in a spherically imploding shock wave.

The velocity contours of Fig. 13.15 show that, as expected, the speed of the incident shock increases as it moves toward the origin and that of the reflected shock decreases as it moves away from the origin. The velocity of the gas behind the incident shock and ahead of the reflected shock is higher than the piston velocity by a maximum of about 50%. On the other hand, the gas behind the reflected shock is almost stationary.

The magnitude of the maximum temperature at the origin has been the focus of much of the interest in this flow. Figure 13.16 shows that it is just over 150,000 K in this case, but ionization has not been included in the simulation and this would significantly reduce the maximum temperature in the real gas. Also, the simulation procedures force the simulated flow to be spherically symmetric while asymmetries could develop in a real flow. The most interesting feature of the temperature contours is that the maximum temperature occurs after, rather than during, the formation of the reflected shock.

The approximate theory of Whitham (1958) predicts that the shock Mach number of a strong spherical shock wave is inversely proportional to the radius raised to the power $\mu\gamma/(2+\mu)(\mu+\gamma)$, where $\mu^2=2\gamma/(\gamma-1)$. The resulting shock path is included in Fig. 13.17 for the density contours in the distance-time plane. The theory is in reasonable agreement with the DSMC calculation. Note that the maximum density at the centre coincides with the temperature maximum.

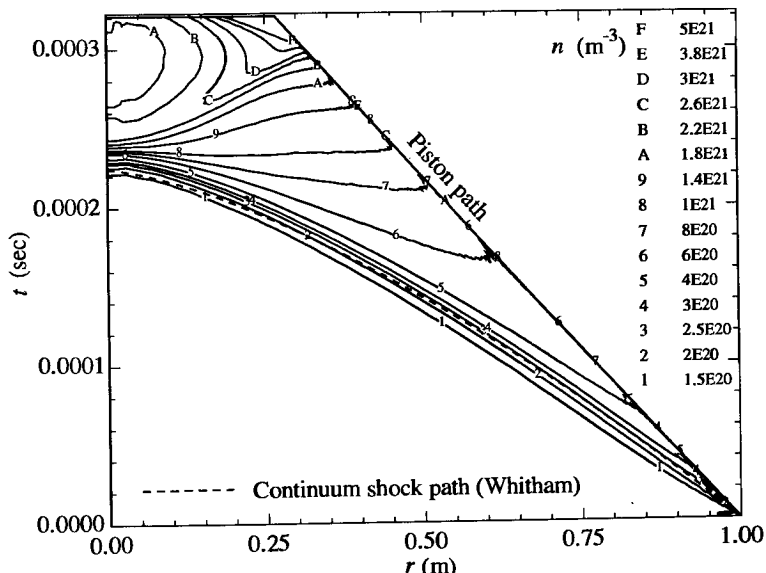


Fig. 13.17 Density contours for the spherically imploding shock wave.

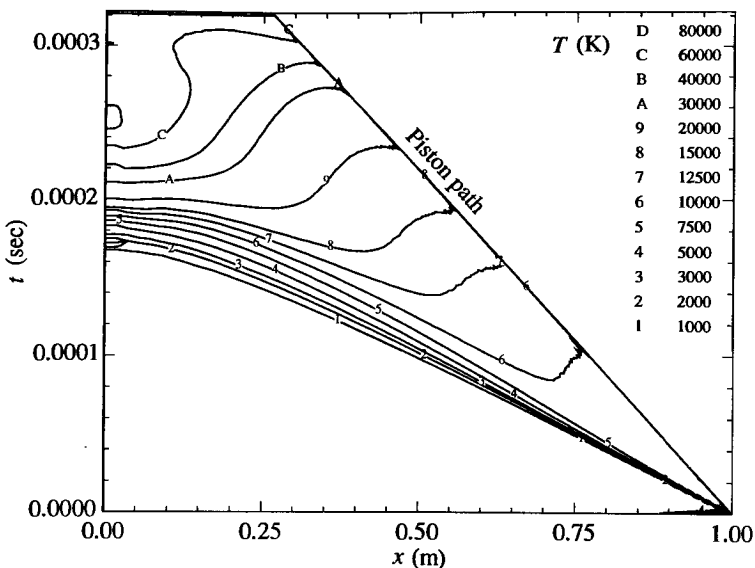


Fig. 13.18 Temperature contours at a density half that of Fig. 13.13.

If the number of mean free paths between a shock of given strength and the origin is increased or decreased, the temperature maximum in the reflection at the origin would be expected to also increase or decrease. In order to investigate this effect, the calculation was repeated for an initial number density of 0.5×10^{20} . The temperature contours in the distance-time plane are shown in Fig. 13.18. The reduction in density by a factor of two causes the maximum temperature to fall by one third.

An interesting point is that the reduction in density causes the shock profile to be sharper at small times. This is because the profile becomes wider with time during shock formation and the reduction in the collision rate slows this process.

13.6 Collapse of a cylindrical cavity

The final example is the flow that is produced when, at zero time, a cylindrical cavity with a radius of 0.5 m exists in argon of number density 10^{20} m^{-3} at temperature 273 K. A full rarefaction wave is initially centred at the boundary between the gas and the vacuum. The edge of this moves at the undisturbed speed of sound, but the cylindrical geometry causes the other characteristics in the distance-time plane to be curved. The high-speed tail of the rarefaction travels towards the axis of the flow and eventually reflects from it. This leads to the compression of the gas near the centre by compression waves that eventually move out from the axis.

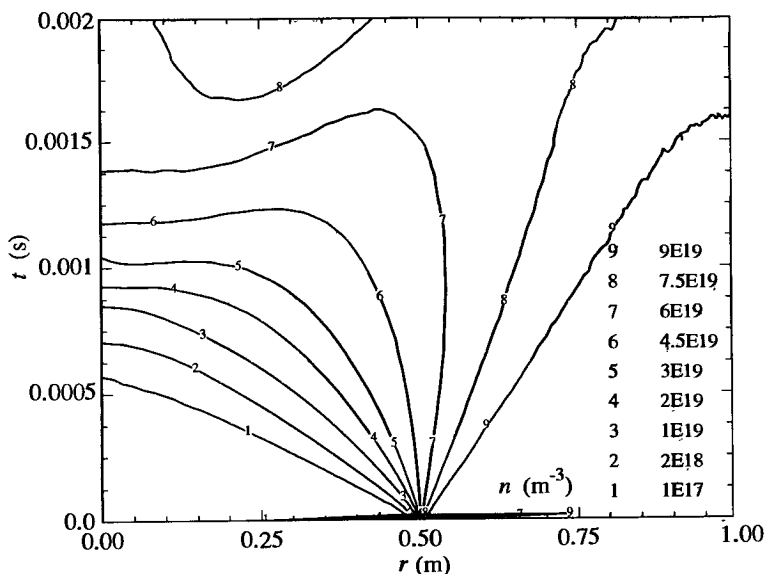


Fig. 13.19 Number densities in the collapse of a cylindrical cavity.

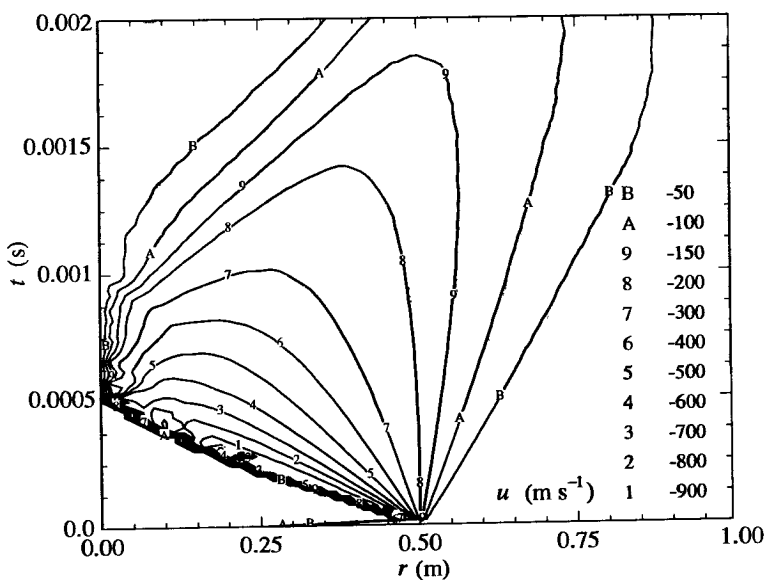


Fig. 13.20 Velocities in the collapse of a cylindrical cavity.

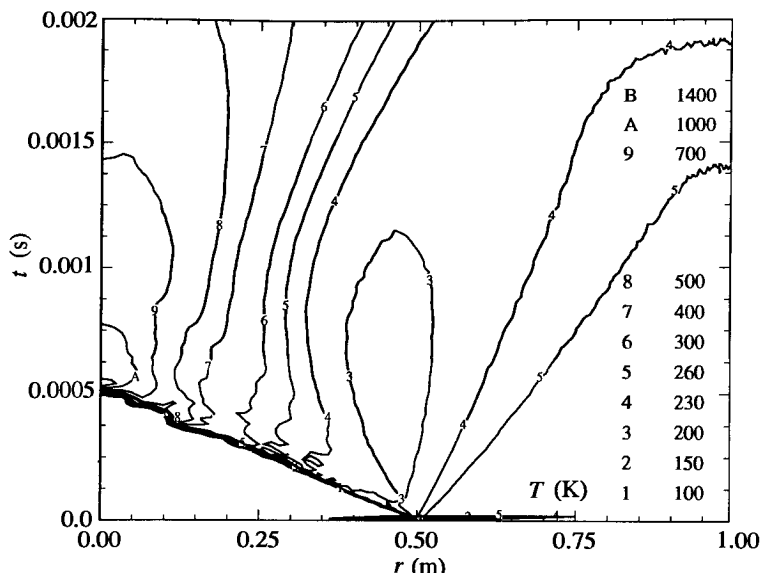


Fig. 13.21 Temperatures in the collapse of a cylindrical cavity.

The number density, velocity, and temperature contours are shown in Figs 13.19 to 13.21, respectively. The effective 'edge' of the gas moves at a speed of about 1000 ms^{-1} , and this is higher than the theoretical limiting velocity of three times the undisturbed speed of sound. This undisturbed speed of sound is 308 ms^{-1} and there is a region in which the flow speed exceeds 900 ms^{-1} . There is an almost stationary region in which the temperature is less than 200 K , but low temperatures are otherwise confined to the 'edge region' which is at a number density less than 1% of the undisturbed number density. The reflected waves that result from the interaction of the rarefaction with the decreasing area are compression waves and, as long as they remain the hypersonic flow near the edge of the expanding gas, these waves also move towards the axis. This causes the 'edge' to acquire some of the characteristics of a shock wave, and the temperature within a radius of one half the initial radius of the cavity is larger than the initial temperature. The maximum temperature at the axis is about 1500 K and occurs shortly after the initial arrival of the gas.

References

- BIRD, G.A. (1970). Breakdown of translational and rotational equilibrium in gaseous expansions. *AIAA Journal* **8**, 1998–2003.
 WHITHAM, G.B. (1958). On the propagation of shock waves through regions of non-uniform area or flow. *J. Fluid Mech.* **4**, 337–360.

14

TWO-DIMENSIONAL FLOWS

14.1 Grids for DSMC computations

The basic simulation procedures that were developed in Chapter 11 for homogeneous gases, and were applied in Chapter 12 to one-dimensional flows, are applicable also to two- and three-dimensional flows. It is the requirement for efficient schemes for the generation and utilization of grid systems that represents the new challenge when the direct simulation Monte Carlo (DSMC) method is applied to multi-dimensional problems. The ideal DSMC grid would:

- (a) have high computational efficiency;
- (b) allow efficient definition of complex flow geometries;
- (c) be 'fitted' to any body and other significant flow boundaries;
- (d) have variable cell sizes related to the local gradients in the flow properties and to the mean free path;
- (e) allow this size to adapt to local conditions as the flow develops; and
- (f) employ sub-cells for effective 'nearest neighbour' collision pair selection.

While some of these criteria are common to the grid generation problem for applications of the finite difference and finite element methods to continuum flows, there are basic differences in the requirements of the DSMC method. Continuum methods generally require a near orthogonal grid structure with no discontinuities in the lines that define this structure. The DSMC method uses the grid or cell system only for the sampling of the macroscopic properties and for the selection of possible collision partners. The cell structure can therefore be irregular with regard to the shape of the cells and there can be discontinuities in the grid lines that define the cells. However, if flow contours are to be constructed, it is generally desirable for the grid to be continuous.

The sampled density is used in the DSMC procedures for establishing the collision rate and, in order for this rate to be realistic, it is desirable to have the number of molecules as large as possible, the desirable minimum being about ten to twenty. On the other hand, in the selection of possible collision partners, it is desirable to have this number as small as possible in order to reduce the mean spacing of collision pairs and thereby minimize the smearing of gradients. As in the one-dimensional programs, these conflicting requirements can be reconciled by dividing the sampling cell structure into a set of sub-cells for the selection of collision pairs.

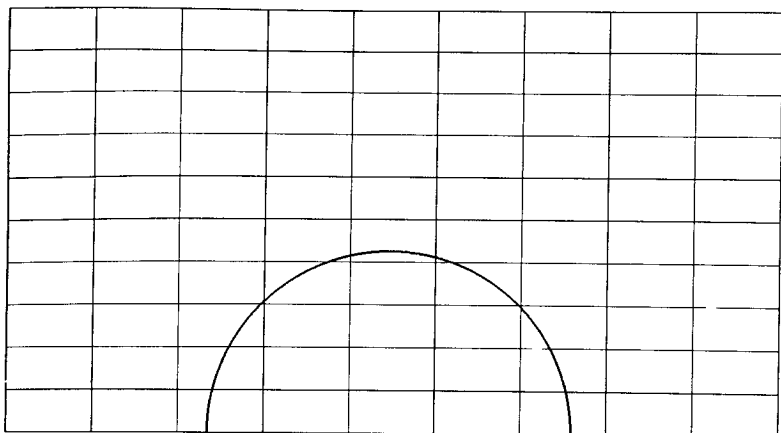


Fig. 14.1 Simple rectangular grid for the flow past a cylinder.

The existing cell schemes may be summarized as follows:

(i) *Simple constant area cells defined by a rectangular grid.*

These are almost always used in the first set of simulation programs by any group because of the ease of implementation. The scheme is very efficient computationally but has severe disadvantages. For flows with large density variations, some cells will contain far more than the optimum number of simulated molecules, while others will contain far fewer than the optimum number. More seriously, if surface boundaries are not rectangular as in the example in Fig. 14.1, the effective cells near the boundaries are irregular and the scheme is not adequate for serious calculations at low Knudsen numbers. Also, because the cell structure is unrelated to the surface geometry, each different surface requires special coding within the program.

(ii) *Multi-level rectangular grid.*

This feature is illustrated in Fig. 14.2 and alleviates some of the disadvantages of the simple scheme in which all cells are of the same size. The blocks of subdivided cells must be rectangular and it is not easy to define them efficiently when the flow geometry is complex. Changes in the flow geometry still require modifications to the program, and the scheme is not suited to general programs that accommodate new geometries through changes to the data alone.

(iii) *Adaptive rectangular cells.*

Instead of a whole block of cells being subdivided as in scheme (ii), individual cells may be subdivided when the density exceeds a set value. The grid can therefore be made to adapt to the flow and the scheme has been implemented by Babovsky et al. (1989).

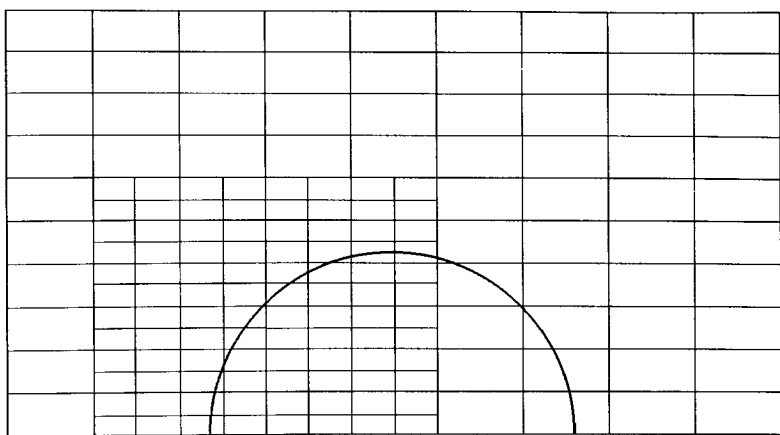


Fig. 14.2 Subdivided cells in a region of higher density.

(iv) '*Point reference*' scheme.

This scheme (Bird 1976) indexes the simulated molecules to a series of points rather than volumetric cells. The molecule is 'in a cell' when it is nearest to the point that defines that cell. This procedure was used in the first 'general' program to cope with arbitrary flow geometry in both two and three dimensions. However, there was an effective distortion of the flow boundaries for non-rectangular geometries and the cell volume could not be precisely defined. This led to serious difficulties with some flows and the method is largely of historical interest.

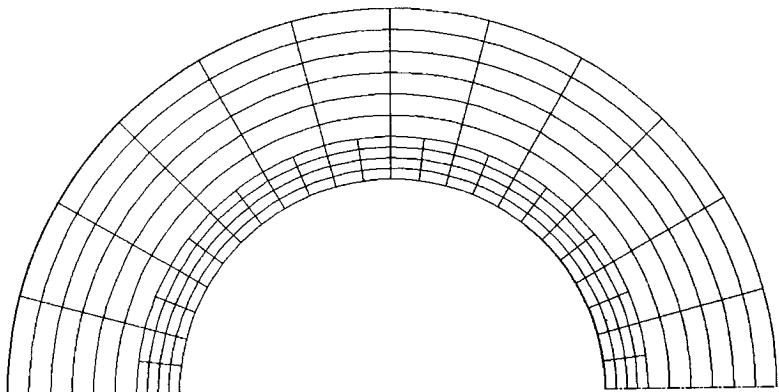


Fig. 14.3 Body fitted cells for a cylinder.

(v) *Body-fitted 'analytical' cells.*

This option is illustrated in Fig. 14.3 for the flow past a cylinder. One set of cell boundaries is geometrically similar to one of the boundaries (generally a body surface) that primarily defines the flow. The method can be used only when all the boundaries can be described analytically. Quadric surface geometries are particularly amenable to this approach because of the existence of the theorem of eqns (7.85)–(7.87). Given a specified initial location and direction cosines, this provides a simple quadratic expression for the distances to any intersections with the surface. New programs are generally required when there is a significant change in the geometry, and the programs are much less efficient than those with rectangular cells. On the other hand, the computational requirements for accuracy at low Knudsen numbers are readily satisfied by this scheme.

(vi) *'General' scheme.*

The flowfield is divided into an arbitrary number of four-sided regions. Two opposite sides are curved and the other two are straight. The curved sides are specified by two sets of points that may be specified individually or may lie on segments of straight lines and conic sections. Corresponding points are joined by straight lines and these are, in turn, divided into segments and the ends of these segments are joined to form the system of quadrilateral cells. Each of the four sides can be an axis, a plane of symmetry, an interface with a specified uniform or non-uniform flow, a solid surface which may be absorbing or outgassing, a vacuum, or an interface with another side. Virtually any flow can be constructed from these regions. The current implementation of this scheme by the author is called the 'G2' set of programs.

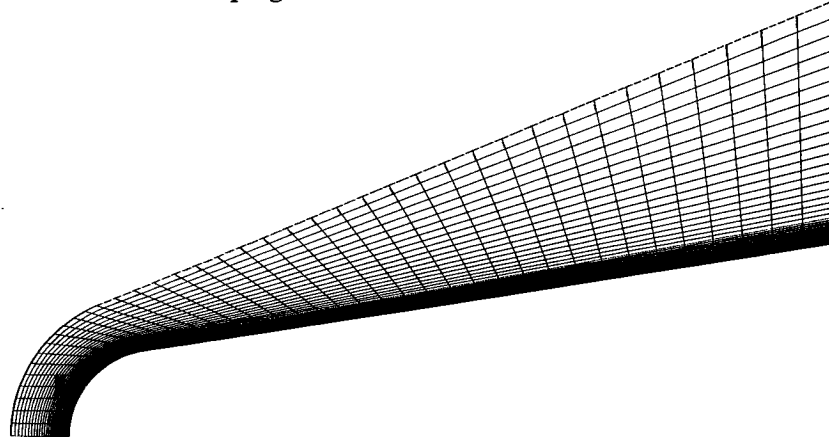


Fig. 14.4 Cells for blunt cone generated by the G2 program system.

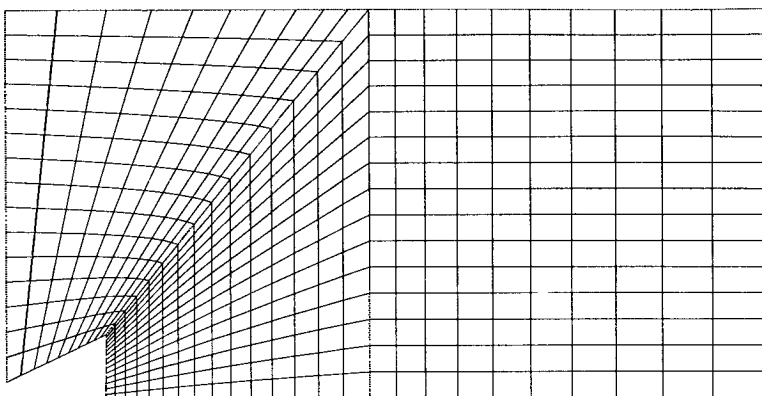


Fig. 14.5 Cells generated for a plume backflow calculation.

As shown in Figs 14.4 and 14.5, diverse problems can be accommodated without any changes being made to the code, but this is at the cost of computational efficiency. The molecules are traced through the grid by computing the intersections with all the cell boundaries. The computation time for the 'molecule movement' section of the programs is an order of magnitude larger than for a simple rectangular grid. The overall performance penalty depends on the Knudsen number and the consequent balance between the computation time spent in the move and collision routines, but there is typically a factor of five increase in the CPU time. As noted earlier, sub-cells are used to control the maximum separation of the collision partners and are highly desirable in regions of high vorticity. They are incorporated into the G2 programs but the smaller the sub-cells, the larger the computation time penalty.

(vii) *Orthogonal transformations to rectangular grids.*

This approach permits a rectangular grid to be used for flows that have curved boundaries in physical space. There are some restrictions on the geometries that allow transformation, and the necessity of moving the molecules along curved paths in the transformed space may cost more efficiency than is gained by the rectangular grid.

(viii) *Rectangular multi-level sub-cells with adaptive body-fitted cells.*

This is based on a fixed rectangular grid of very small sub-cells. The body intersects these and is specified by the lines joining its points of intersection with the sub-cell boundaries. The sub-cells that contain a surface intersection are regarded as zero level cells. Those within the flow that touch these are 'level 1' cells and so on throughout the flow. These sub-cell levels provide an easy determination of whether possible surface interactions need be considered when molecules are moved. When these need not be considered, the procedures are as fast as in the programs

described in scheme (i). The initial cells are simple rectangular cells as shown in Fig. 14.1. Once a steady flow has been established, an automatic adaptive re-gridding can take place. The resulting grid structure for the two-dimensional flow past a circular cylinder is shown in Fig. 14.6.

The cells in Fig. 14.6 may look bizarre in comparison with those for continuum calculations, but the DSMC method uses the grid or cell system only for the sampling of the macroscopic properties and for the establishment of the collision rate, with collision partners selected from the sub-cells. The cell structure can therefore be irregular with regard to the shape of the cells and there can be discontinuities in the grid lines that define the cells. The sub-cells may be sub-divided in the vicinity of the surface so that the separation of the collision partners is reduced to the values that are required for accurate results at low Knudsen numbers. The time step and the number of real molecules represented by each simulated molecule may be reduced in cells near the surface in order to establish a reasonable average number of molecules in the very small sub-cells. While the boundaries of the sub-cell region is rectangular, the boundary of the simulation region may be inset from these boundaries in order to avoid the computation of unnecessarily large regions of uniform flow.

There is generally a trade-off between the ease of setting up a case with complex boundaries and the computational efficiency of the programs. The ideal program would take care of all the computational details and would require the user to specify only the geometry and the undisturbed flow conditions.

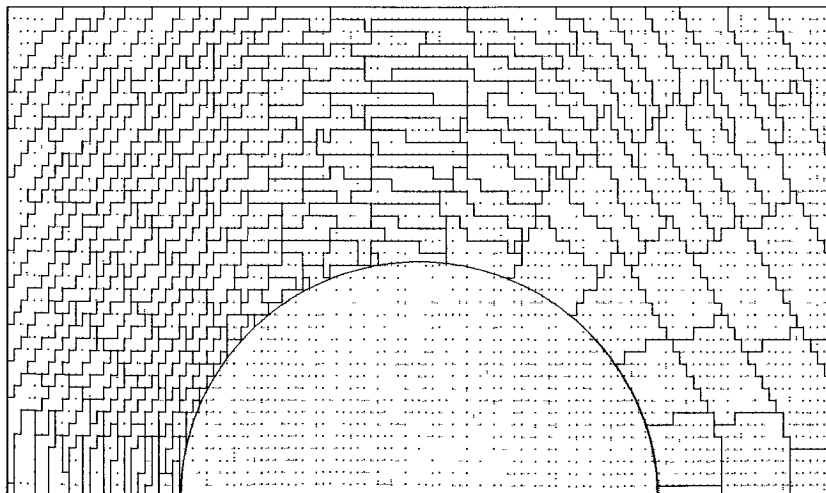


Fig. 14.6 An automatically generated adaptive grid for the flow past a circular cylinder.

14.2 DSMC program for two-dimensional flows

The demonstration program DSMC2.FOR deals only with problems involving flat surfaces that can lie along the cell boundaries of a simple rectangular grid. The flowfield is rectangular and is aligned such that the sides are parallel to the x -and y -axes. Each of the four sides may be a boundary with a uniform stream, a plane of symmetry, or a vacuum. The stream is specified by the velocity components in the x -and y -directions, the number density, the temperature, and the composition. The flowfield is divided into a grid of rectangular cells. As with program DSMC1, the cell spacing may be either uniform or in a geometric progression. There may be one or two single-sided surfaces that must be parallel to either the x - or y -axis, lie along a cell boundary, and terminate at one of the grid points. The size and locations of the surfaces are specified through these cell boundaries and grid points. The two single-sided surfaces may be placed back-to-back to form a double-sided surface. The surface temperatures are assumed to be uniform and it is assumed that the reflection is diffuse with complete thermal accommodation. In addition to the surfaces, the flow may include a jet. The plane of the jet efflux is specified in a similar manner to a surface and the initial direction of the jet must be aligned with one of the axes. The efflux is uniform and is specified by its number density, temperature, and composition. The specification of the gas is similar to that in program DSMC1.

14.3 The supersonic leading-edge problem

The 'leading-edge' or 'horizontal flat plate' problem relates to the two-dimensional flow past a semi-infinite thin flat plate that is aligned with the stream. It is of fundamental interest in gas dynamics and has been the subject of many theoretical and experimental studies. While continuum theory is frequently applied to this problem, as in the Blasius theory for the incompressible laminar boundary layer, the solutions are invalid very close to the edge of the plate. The unresolvable leading-edge singularity in continuum gas dynamics becomes a well-defined problem in molecular gas dynamics.

In the case of a supersonic external flow, the displacement effect of the boundary layer produces a weak oblique shock wave in the external flow. At a distance of some tens of mean free paths from the leading edge, the shock wave structure overlaps with that of the boundary layer and, as the leading edge is approached, the shock and boundary layer gradually merge and lose their separate identities. Even in a hypersonic stream, the disturbance extends a few mean free paths upstream of the leading edge and, contrary to some descriptions, the conditions at the leading edge do not correspond to those of free molecule flow. However, the velocity slip at the leading edge is a large fraction of the freestream velocity. This slip velocity gradually decreases along the plate but, again contrary to the continuum assumption, it does not disappear completely.

The supersonic leading-edge problem has provided one of the most useful test cases for the verification of the DSMC method through comparison with experiment (e.g. Harvey 1986). One of its advantages as a test case is that the pressure disturbance is generated indirectly rather than through direct impact of the stream. In addition, the shear stress is of the same order as the pressure and this, together with the heat transfer, is particularly sensitive to any failure to meet the computational requirements of the DSMC method. This flow is therefore employed in §14.5 for a study of the effects of the cell size and time step in a DSMC computation.

The listed data in DSMC2.FOR is for the flow of nitrogen at a Mach number of four past a flat plate with a length of approximately 70 times the mean free path in the undisturbed gas. The temperature of the plate is 1.6 times the undisturbed gas temperature. The stream is in the positive x -direction and the plate lies along the lower y -boundary. The leading edge is 5.4 mean free paths from the upstream boundary and the plate extends to the downstream boundary. The plane in which the plate lies is specified as a plane of symmetry and the leading edge is effectively a transition from specular reflection to diffuse reflection. The downstream boundary is specified as a stream boundary but, at a Mach number of four, there is no practical difference between a stream boundary and a vacuum boundary. This means there is an interaction between the flow and the downstream boundary. Calculations were made for several plate lengths in order to determine the extent of the interference region from this unrealistic boundary condition. The grid is 100×60 and the cell widths and heights are both in geometric progression with an increase by a factor of two in both directions. There are two sub-cells per cell in each direction so that the computational requirements are satisfied by a narrow margin.

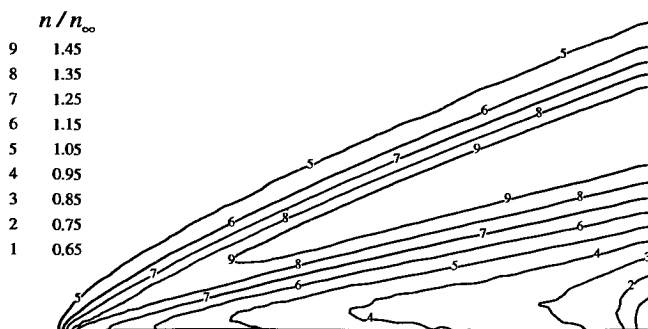


Fig. 14.7 Number density contours at $(Ma) = 4$ and $(Kn) = 0.0143$.

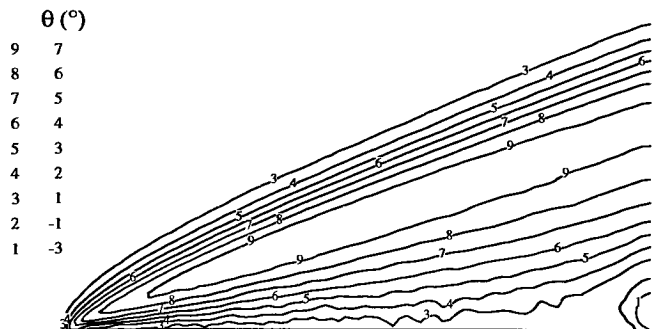


Fig. 14.8 Contours of constant flow angle.

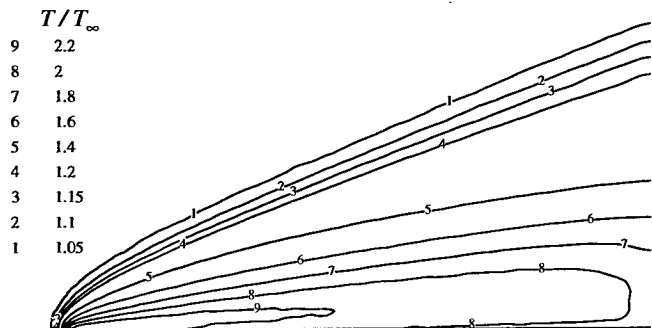


Fig. 14.9 Temperature contours at $(Ma) = 4$ and $(Kn) = 0.0143$.

The contours of constant number density are shown in Fig. 14.7. These show that the oblique shock wave and the boundary layer emerge as distinct identities at about 20 mean free paths from the leading edge. The flow angle contours of Fig. 14.8 indicate that the displacement effect of the boundary layer is equivalent to a wedge angle of just over seven degrees, and the strength of the oblique shock wave is consistent with this deflection angle. The number density increases across the shock, but it then decreases to a value near the surface that is less than the stream density. Fig. 14.9 shows that this low density is associated with temperatures that are higher than both the temperature at the rear of the shock and the surface temperature.

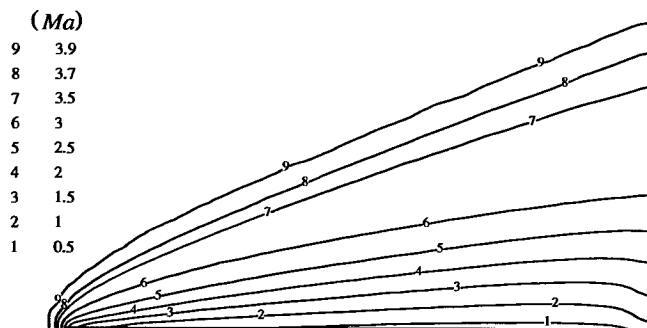


Fig. 14.10 Contours of constant value of the local Mach number.

The temperature contours show most clearly the extent of the flow disturbance upstream of the leading edge. The upstream temperature rise is approximately equal to that rise across the oblique shock. On the other hand, the upstream density increase is small compared with that across the shock. The final set of contours in Fig. 14.10 are for the local Mach number. These show the magnitude of the velocity slip at the surface in that Mach numbers less than 0.5 are confined to a thin region over the latter half of the plate. The ratio of the surface temperature to the stream temperature is 1.66 and the temperature contours show that the temperature slip is also substantial.

The unrealistic downstream boundary condition has a noticeable effect on the flow near the surface for at least ten to fifteen mean free paths upstream of this boundary. The vacuum boundary has a negligible effect when the Mach number based on the velocity component normal to the boundary is greater than about two. This means that the effect is most pronounced near the surface. There is a sharp fall in the density near the downstream end of the plate and the flow acquires a negative flow angle that reaches six degrees at the end of the plate. In addition, the region of subsonic flow becomes very narrow at the downstream boundary. The extent of the upstream influence from this boundary is more precisely defined by the surface properties that are plotted in Figs 14.11 to 14.14.

The number flux to the surface is compared to the free-molecule value in Fig. 14.11. The flux at the leading edge is substantially above the free-molecule value, but there is then a sharp increase in the ratio which reaches a maximum at about four or five mean free paths from the leading edge. This is followed by a gradual decline in the flux towards the free-molecule value, but this is concluded by a sharp decrease due to the downstream boundary condition.

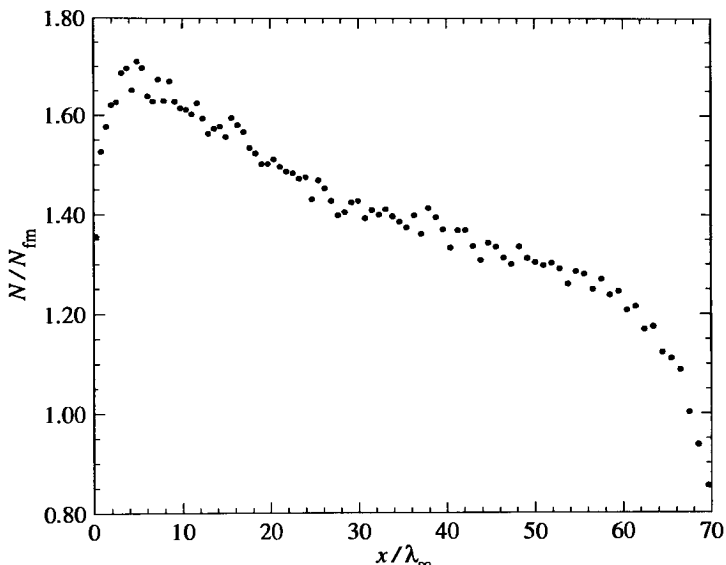


Fig. 14.11 The number flux as a ratio to the free-molecule value.

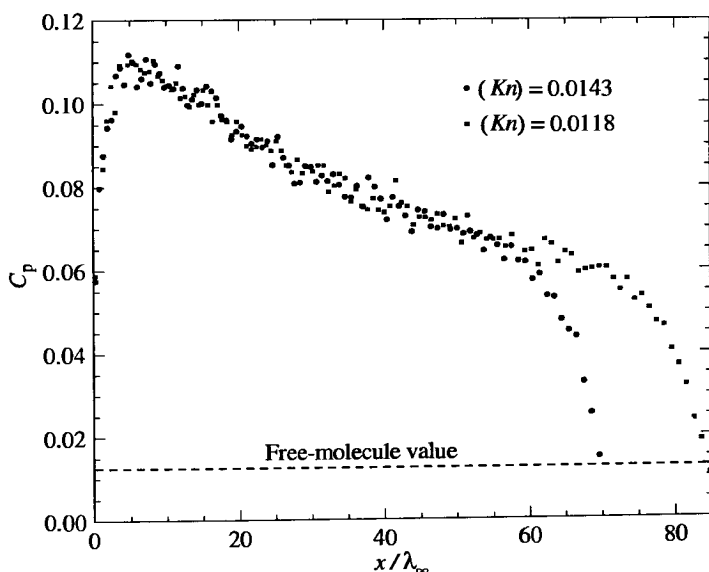


Fig. 14.12 The pressure distribution along the plate.

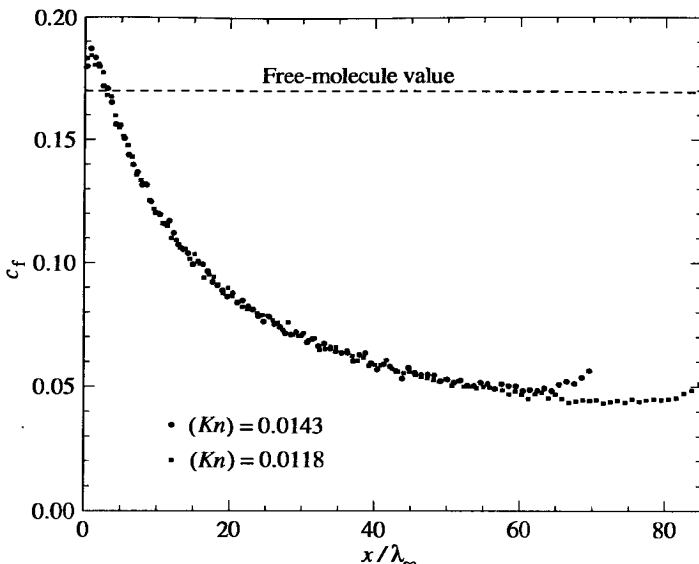


Fig. 14.13 The skin friction coefficient along the plate.

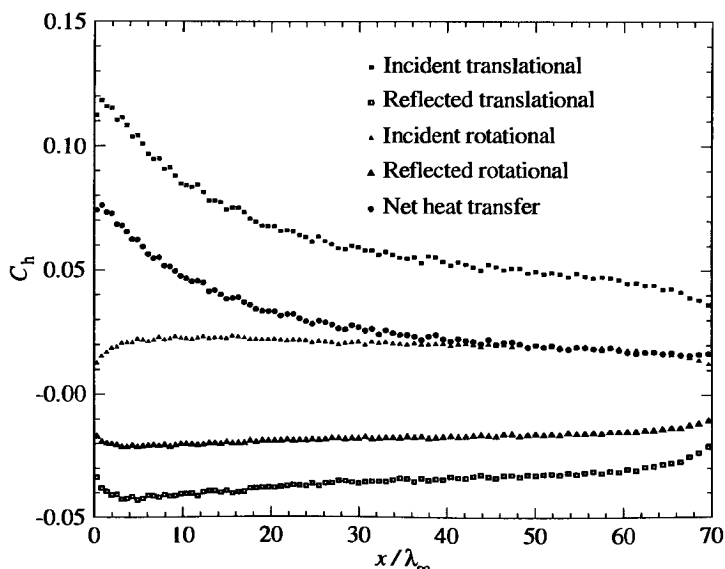


Fig. 14.14 The heat transfer coefficients along the plate.

In order to clearly define this influence, a similar run was made for a plate length of 85 freestream mean free paths. The pressure and shear stress distributions are shown for both calculations and it is clear that the upstream influence of the downstream boundary is largely confined to about 15 freestream mean free paths.

As expected, the pressure coefficient at the leading edge is well above the free-molecule value. The general shape of the pressure profile is similar to that for the number flux. The skin friction distribution is qualitatively different, in that the maximum occurs at the leading edge and is only slightly higher than the free-molecule value. The skin friction coefficient then falls well below the free-molecule value. Although the large pressure effect is inconsistent with laminar boundary layer theory, the shear stress is generally consistent with this theory in that the skin friction coefficient is very nearly inversely proportional to the square root of the distance from the leading edge. The acceleration of the flow near the surface to the downstream vacuum boundary causes an increase in the skin friction.

The heat transfer coefficient C_h is defined as the ratio of the heat flux per unit area to $\frac{1}{2}\rho u_\infty^3$. Separate results are shown in Fig. 14.14 for the translational and rotational contributions from both the incident and reflected molecules. The distribution of the incident translational heat flux is generally similar to the skin friction profile except that the boundary disturbance is a decrease rather than an increase. The surface temperature is uniform, so that the reflected distributions of both the rotational and translational components are similar to the number flux distribution. The incident and reflected components for the rotational energy are very nearly in balance and the internal mode has very little effect on the net heat flux. The net heat transfer coefficient is of the order of half the skin friction coefficient

14.4 Effect of cell size

The calculations in §14.3 were made with a cell grid that met the general requirements that were discussed in §10.5, although not by a large margin. The time step does not affect the results unless it is outside the recommended range by an unrealistically large amount. The cell size is most critical in the direction with the highest gradients and, for the flat-plate flow, this is the direction normal to the plate. The calculation in the previous section was repeated for a shorter plate of approximately 40 freestream mean free paths and with a uniform cell spacing. Runs were made for a number of cell and sub-cell arrangements in the normal (y) direction, while the cell size in the streamwise (x) direction remained fixed.

The first case with 40 cells and 80 sub-cells in the y -direction was expected to have an accuracy similar to the previous calculations. The resulting distributions of pressure coefficient and skin friction coefficient are shown in Figs 14.15 and 14.16, respectively. A comparison of these results with Figs 14.12 and 14.13 shows that, allowing for the effects due to the downstream boundary condition, the results are equivalent.

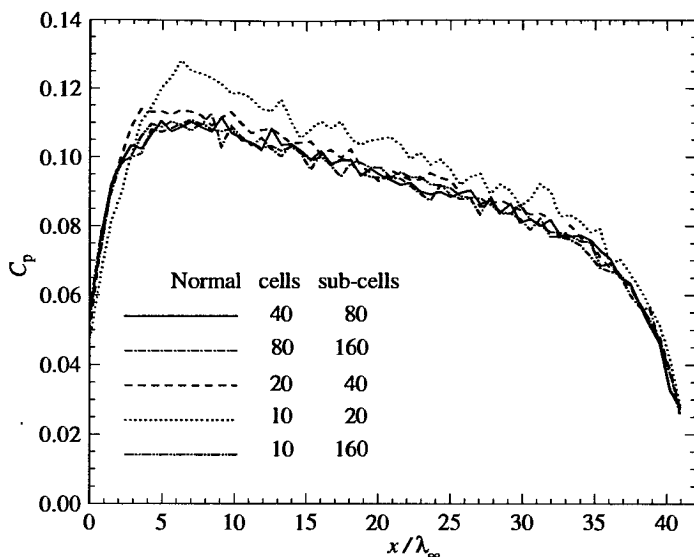


Fig. 14.15 The effect of cell size on the pressure distribution.

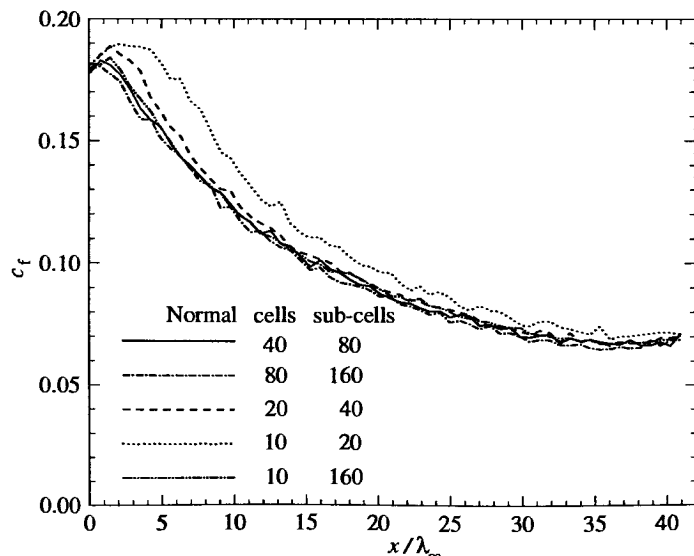


Fig. 14.16 The effect of cell size on the skin friction coefficient.

The second case employed twice as many cells and sub-cells as in the 'standard' case, but there was no significant change in the results. This verified that the original choice of cell size was adequate. The calculation was then repeated for half as many cells as in the standard case and there was then a three or four percent increase in both the pressure and skin friction coefficients. A further halving of the cell size led to errors of the order of ten to fifteen percent. The error decreases along the plate as the gradients decrease. The sub-cell height in this worst case is well over two local mean free paths and the errors are surprisingly small.

In order to test the effectiveness of the sub cells, the case with only 10 cells in the y -direction was repeated with eight sub-cells per cell in that direction. This meant that the only deleterious effect of the large cells was a lack of discrimination in the collision rate. The mean spacing between collision partners, which is included in the output, was restored to the value in the standard case. As expected, the results are consistent with those for the standard case to within the statistical scatter. With regard to the sub-cells, it should be noted that the SELECT subroutine is unchanged from the one-dimensional programs. This means that, if there is only one molecule in a given sub-cell, the potential collision partner is chosen from the nearest sub-cell in numerical order. However, the sub-cells in DSMC2 are in columns and rows within each cell, and the nearest occupied sub-cell in numerical order is not necessarily the physically nearest sub-cell. This did not affect this calculation because there were only two sub-cells per cell in the other direction. Should both NSCX and NSCY be large with few molecules per sub-cell, the selection process for the collision partner should be modified to take account of the arrangement of sub-cells within the cell.

14.5 The formation of vortices

In a free-molecule flow, all particles follow straight trajectories and, for simple boundary conditions such as a vertical plate in a uniform stream, there can be no vortices. There is little information on the Knudsen number range over which circulation develops behind such a plate. Program DSMC2 has therefore been used to study the flow of argon at a speed of $u = 172 \text{ ms}^{-1}$ past a vertical flat plate. The stream temperature is 300 K, and this corresponds to a Mach number of 0.53. The vertical plate is at $x = 0$ and is assumed to be specularly reflecting. A plane of symmetry is imposed at $y = 0$. If the semi-height of the plate is denoted by h , the upstream boundary is at $x = -1.33h$, the outer boundary is at $y = 2h$, and the downstream boundary is at $x = 2h$. These boundaries are assumed to be 'stream' boundaries such that the outgoing molecules are discarded, while the incoming molecules are characteristic of the undisturbed stream. Boundary interference effects are unavoidable in a subsonic flow such as this and, as in the preceding calculation, these can be assessed only by placing the boundaries in alternate positions. Calculations were made for a range of freestream densities and typical streamlines in the resulting flows are shown in Figs 14.17 to 14.22.

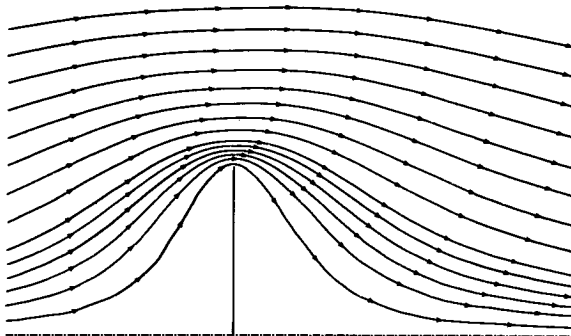


Fig. 14.17 Streamlines for $n = 5 \times 10^{17}$, $(Kn) = 8.8$.

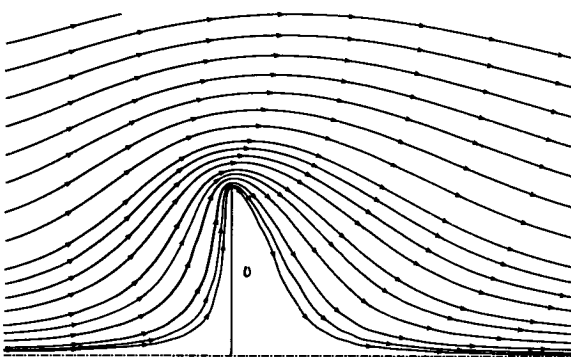


Fig. 14.18 Streamlines for $n = 5 \times 10^{18}$, $(Kn) = 0.88$.

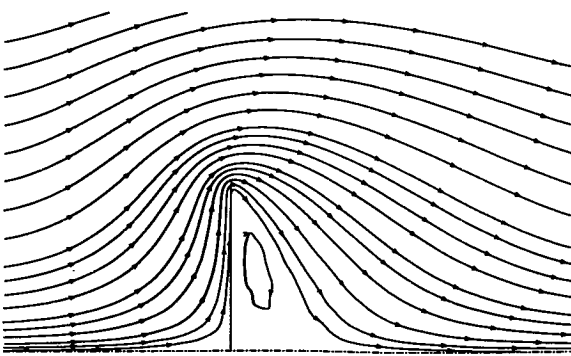


Fig. 14.19 Streamlines for $n = 1.5 \times 10^{19}$, $(Kn) = 0.293$.

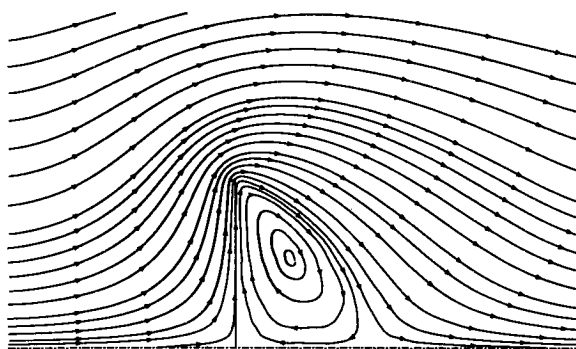


Fig. 14.20 Streamlines for $n = 3 \times 10^{19}$, $(Kn) = 0.147$.

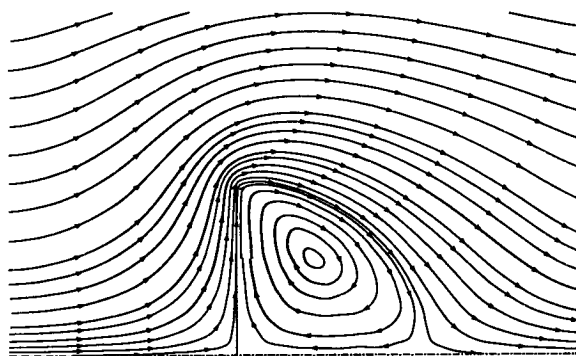


Fig. 14.21 Streamlines for $n = 5 \times 10^{19}$, $(Kn) = 0.088$.

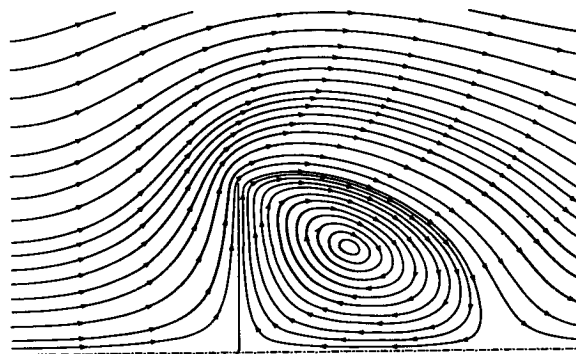


Fig. 14.22 Streamlines for $n = 1 \times 10^{20}$, $(Kn) = 0.044$.

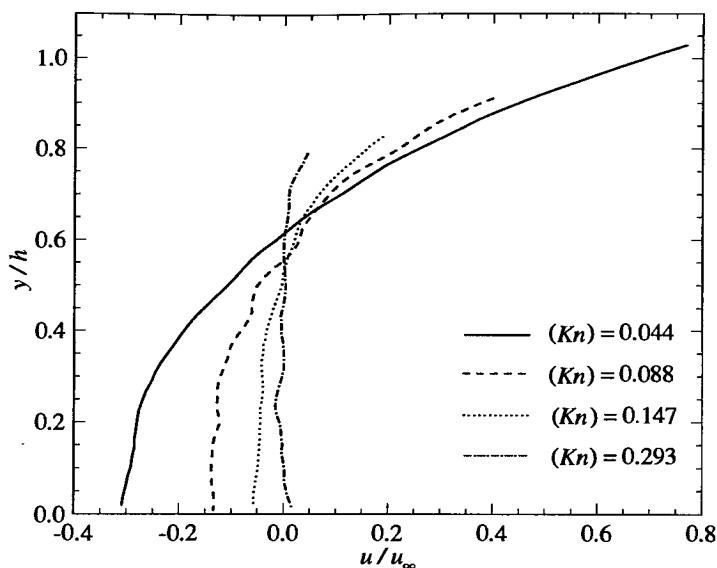


Fig. 14.23 The profile of the u velocity component along a vertical line through the centre of the vortex.

The Knudsen number is defined by the ratio of the freestream mean free path to the semi-height h of the plate. The first case in Fig. 14.17 is for $(Kn)=8.8$, and the flow can be classified as ‘near free-molecule’. The molecules travel in straight lines for distances that are large compared with h and, while it is possible to base streamlines on the mean values of their velocity components, these streamlines do not have the same physical significance as in continuum flows. The reduction in the mean free path by a factor of ten to Fig. 14.18 leads to qualitative changes in that the streamlines are no longer nearly symmetric about the plate. However, the magnitude of velocities in the ‘separated flow region’ downstream of the plate is of the same order as the statistical scatter and there is virtually no evidence of an organized vortex. There is definite evidence of a vortex after a further reduction in mean free path by a factor of three to the $(Kn)=0.293$ case of Fig. 14.19. However, as shown in Fig. 14.23, the velocities in the vortex are less than 5% of the freestream velocity. The final three cases show that the vortex continually increases in size and strength with further increases in the density. In fact, the velocity profiles of Fig. 14.23 show that the velocities in the vortex increase very nearly linearly with density over this range of Knudsen number. However, the velocity at the outer edge of the vortex in the $(Kn)=0.044$ case is almost equal to the freestream velocity and this rate of increase in the vortex strength could not be sustained much further.

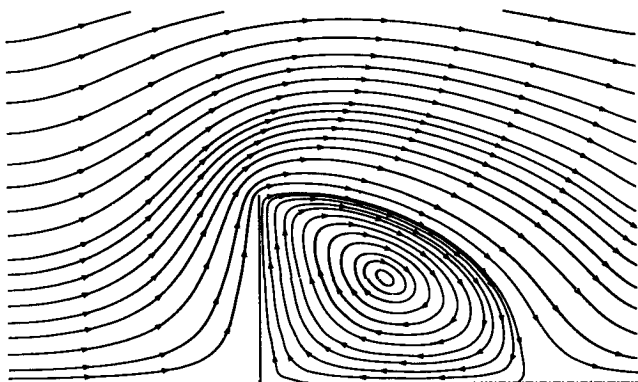


Fig. 14.24 The streamlines for $(Kn) = 0.044$ when there is diffuse reflection from the surface of the plate.

In order to assess the effect of a boundary layer on the vortex, the $(Kn) = 0.044$ case was repeated with diffuse rather than specular reflection from the surface. The streamlines are shown in Fig. 14.24, and the number and location of these corresponds with those in Fig. 14.22. The effect of the boundary layer on the front surface of the plate is to displace the inner streamlines from the plate. The streamlines in the vortex behind the plate are at fixed locations along the normal to the surface that passes through the centre of the vortex. The reduced mass flow in the boundary layer causes the lower portion of these streamlines to be displaced towards the centreline. The magnitude of the velocity on the outer streamline of the vortex at a point directly above the centre of the vortex is 98 ms^{-1} compared with 130 ms^{-1} in the specular reflection case.

This problem involves boundaries across which the flow is subsonic and, as was noted in §14.3, the effects due to these boundaries can only be determined by alterations in their location. Additional DSMC calculations by Dogra (private communication) have shown that the downstream boundary should be located at least $5h$ downstream of the plate. The vortex in the $(Kn) = 0.044$ case is then more elongated by a factor of approximately two, but the flow is qualitatively unchanged. The Reynolds number associated with this case is approximately 150. Existing incompressible flow data indicates that the two vortices behind a full plate would be expected to be stable, and the calculations by Dogra have confirmed that this prediction remains valid at the higher speed ratio of these calculations. Higher Reynolds numbers are required for the formation of a vortex street behind a vertical plate.

An apparent property of all the vortices is that the centre of the vortex lies on the line joining the upper edge of the plate to the stagnation point on the centreline.

14.6 The supersonic blunt-body problem

Program DSMC2 can be used to study this problem using the same boundary conditions as in the preceding section. The first calculations employed a stream of argon at a temperature of 200 K, a number density of 10^{20} , and a velocity of 1317.3 ms^{-1} past a vertical flat plate with a semi-height of 0.15 m. This corresponds to a stream Mach number of 5 and a Knudsen number, based on the full height of the plate, of 0.043. The surface is diffusely reflecting with the front at the stream stagnation temperature of 1866.7 K and the rear at the static temperature of 200 K.

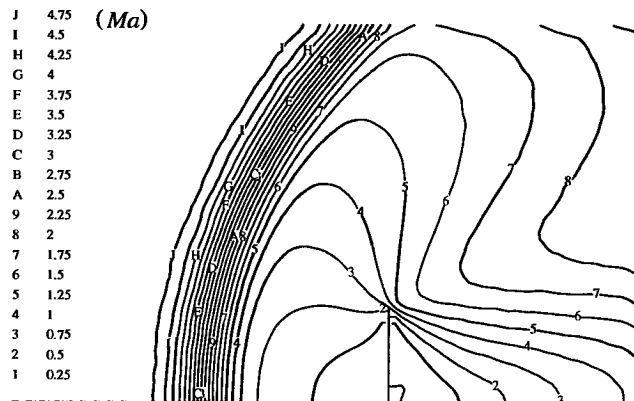


Fig. 14.25 Local Mach number contours for $(Ma)_\infty = 5$ and $(Kn) = 0.043$.

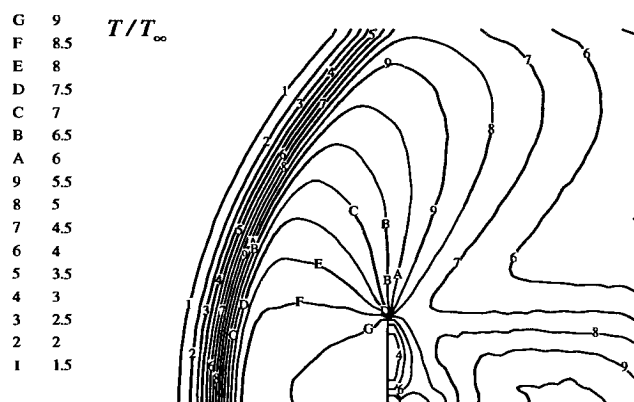


Fig. 14.26 Contours of constant temperature.

The contours of local Mach number and temperature in Figs 14.25 and 14.26 show the expected detached shock wave with a large subsonic region that extends well beyond the tip of the plate. The streamlines are shown in Fig. 14.27 and, from these, it is clear that the density must be very small in the inner wake region. There is no sign of any circulation in the wake in this case, even though there would have been a vortex if the flow had been subsonic. There is a region of enhanced temperature where the wake flow impinges on the plane of symmetry.

The ratio of the upstream surface temperature to the stream temperature is 9.33 and there is a large region in which the temperature ratio exceeds 9.0, but is less than 9.5. The heat flux to the surface at the stagnation point due to the incident molecules is 5040 Wm^{-2} and that carried by the reflected molecules is 5020 Wm^{-2} . These values may be compared with the stream kinetic energy flux $\frac{1}{2}\rho u^3 = 7577.7 \text{ Wm}^{-3}$. This difference is barely significant and the adiabatic surface temperature is very nearly equal to the stagnation temperature at the stagnation point. Both the incident and reflected energy fluxes decrease along the plate, but the decrease for the reflected flux is the greater and there is a net flux to the surface of about 300 Wm^{-2} near the tip of the plate. This corresponds to a heat transfer coefficient of 0.04. The pressure coefficient at the stagnation point is 1.80, while that near the tip of the plate is 1.56. The skin friction coefficient is zero at the stagnation point, but it increases to 0.08 at a point half-way to the tip and is approximately 0.3 at the tip.

The average pressure coefficient on the rear surface is only 0.007. The shear stress is positive but the skin friction coefficients of the order of only 0.0005. The temperature adjacent to the rear of the plate averages about 700 K but, even though the surface temperature is only 200 K, and the average heat transfer coefficient is only 0.0015.

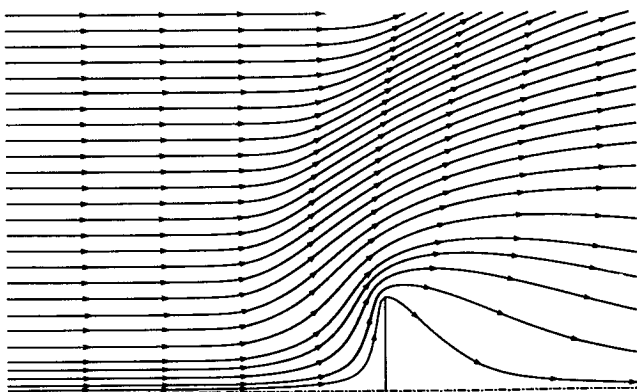


Fig. 14.27 Streamlines in the flow at $(Ma)=5$ and $(Kn)=0.043$.

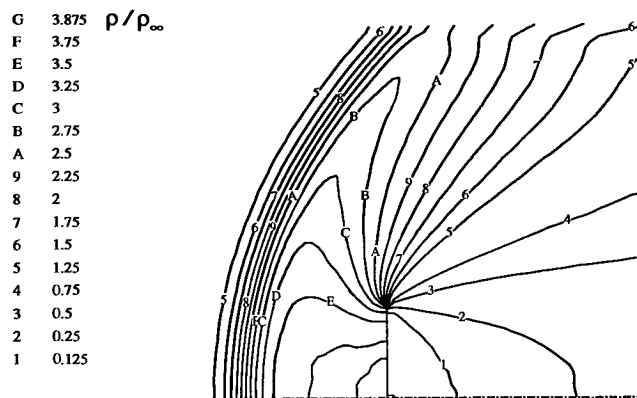


Fig. 14.28 Contours of constant density at $(Kn) = 0.043$.

The density contours are shown in Fig. 14.28 and, as expected, much of the density increase in the shock wave occurs after the temperature has reached its post-shock value. The compression wave produced by the outer boundary condition is shown more clearly in the density contours than in the temperature contours. Because of the high Mach number, this wave affects only the outer edge of the flow.

A reduction in density by a factor of two causes the shock thickness to double, as shown in Fig. 14.29. However, the location of the contour at the centre of the density profile hardly changes, and this is the location of the shock wave in the corresponding continuum flow.

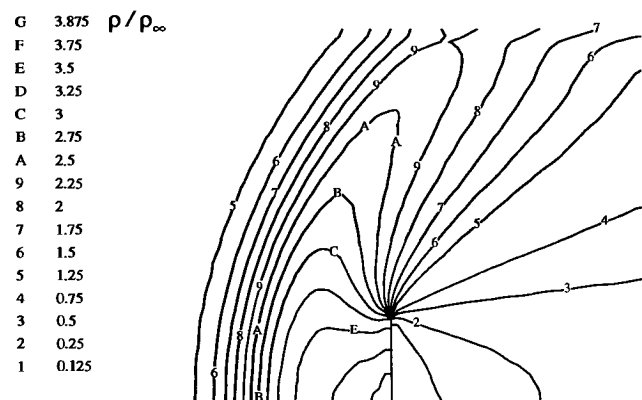


Fig. 14.29 Contours of constant density at $(Kn) = 0.086$.

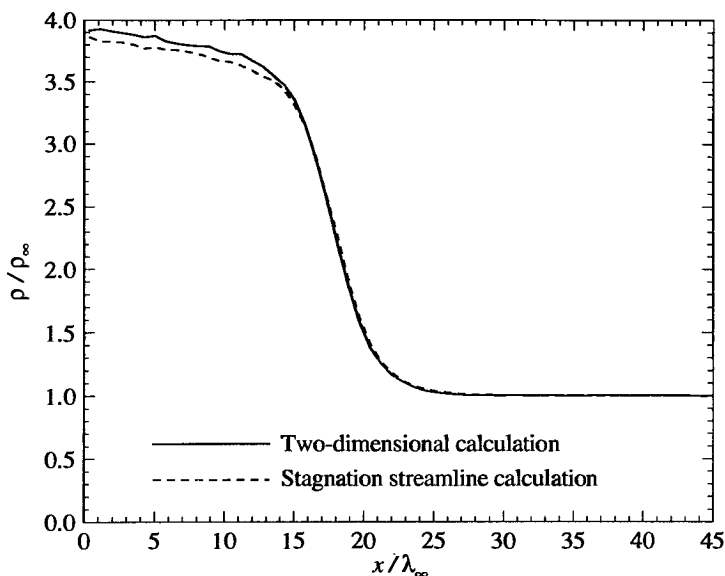


Fig. 14.30 The density profile along the centreline for $(Ma)=5$ and $(Kn)=0.043$.

The main test case has also been calculated by the stagnation streamline program DSMC1T that was discussed in §12.12. The Rankine-Hugoniot density ratio across the wave is 3.57, and the centre of the shock is defined by the mean density ratio of 2.285. The location of the centre of the wave was obtained from the two-dimensional calculation as 0.23 m from the surface. The molecule removal in program DSMC1T was between this location and the surface. The total number of molecules in the flow was adjusted so that a density of 2.285 times the freestream density was attained at this location. The resulting density profile along the stagnation streamline from program DSMC1T is compared in Fig. 14.30 with the corresponding result from the full two-dimensional program DSMC2. Both calculations employed identical values of the computational parameters such as the cell size. There is excellent agreement for almost all of the shock wave profile, and agreement to within a few percent over the compression region behind the shock wave.

The number flux to the surface in the stagnation streamline calculation was $9.74 \times 10^{22} \text{ m}^{-2}$, and this agrees with that at the stagnation point in the two-dimensional calculation to within the statistical scatter. The pressure coefficient at the surface was 1.77, and this is between one and two percent lower than the two-dimensional value. Finally, the heat fluxes due to the incident and reflected molecules were 5070 and 5020 W m^{-2} , respectively. These values also agree with the two-dimensional results to within the statistical scatter.

14.7 Diffusion in blunt-body flows

As was noted in §3.5, the conventional formulation of the Navier-Stokes equations include the diffusion terms that tend to reduce concentration gradients in the flow, but neglect the terms for pressure diffusion and thermal diffusion that act to set up concentration gradients. The blunt-body problem provides a convenient test case for the investigation of the species separation effects that occur in real gases.

The main test case of the preceding section (freestream number density of 1×10^{20}) was repeated for a mixture of 71.78% by number helium and the remainder xenon. This mixture has a mean molecular weight equal to that of argon so that the Mach number is unchanged. The first run was made with the cross-sections of both components equal to that of argon so that the Knudsen number was also unchanged. The second run repeated the calculation with the VSS parameters for helium and xenon that are listed in Appendix A.

The species separation effects are illustrated in Fig. 14.31 by contours of the helium to xenon ratio normalized by the freestream value of this ratio. These are from the second calculation that employed the appropriate cross-sections. The separations in the shock wave due to the pressure and thermal diffusion are consistent with those obtained for the normal shock wave in §12.11. The helium density rise occurs ahead of the xenon rise and the interior of the shock wave is a region of enhanced helium. The sharp curvature of the streamlines near the stagnation point leads to pressure diffusion that concentrates the xenon in this region. If the surface temperature had been cold rather than hot, the thermal diffusion would have acted to further concentrate the xenon in the stagnation region. By far the largest separations are in the wake and the gas immediately behind the plate is composed almost entirely of helium.

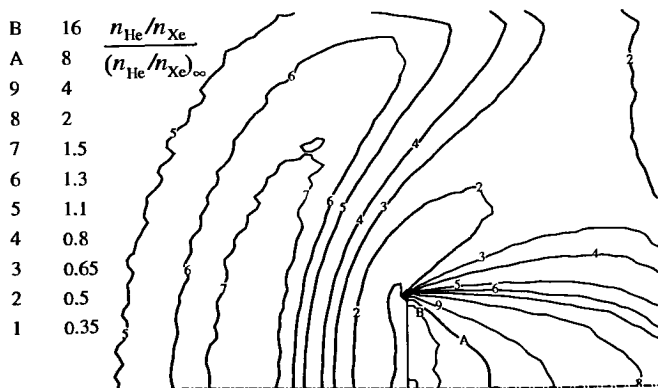


Fig. 14.31 Species separation effects in a helium-xenon mixture.

The density and temperature contours for the gas mixture are plotted in Figs 14.32 and 14.33, respectively. These are based on the first calculation that employed the argon cross-sections, so that the results are directly comparable with those in Figs 14.28 and 14.26. As expected from the shock wave studies, the waves in the mixture are much more diffuse than those in the simple gas. The most striking difference is that the density in the stagnation region is almost twice as high as in the simple gas case. The reason for this is that the pressure is not greatly affected by the change from a simple gas to a gas mixture, and the temperature is set largely by the temperature of the surface. Then, since $p = nkT$, the number density is similarly unaffected. This means that the enhanced xenon concentration must lead to an increase in the density in this region.

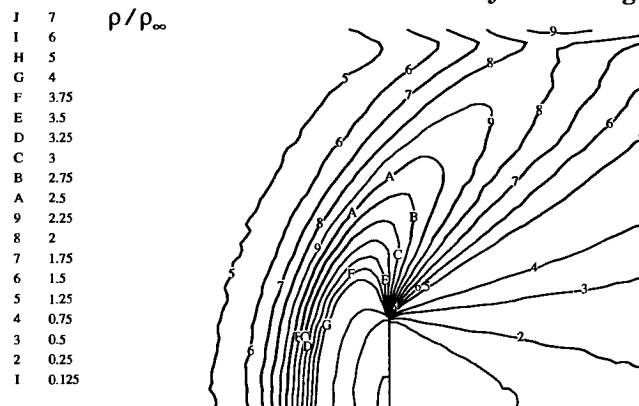


Fig. 14.32 Contours of constant density in the helium-xenon mixture.

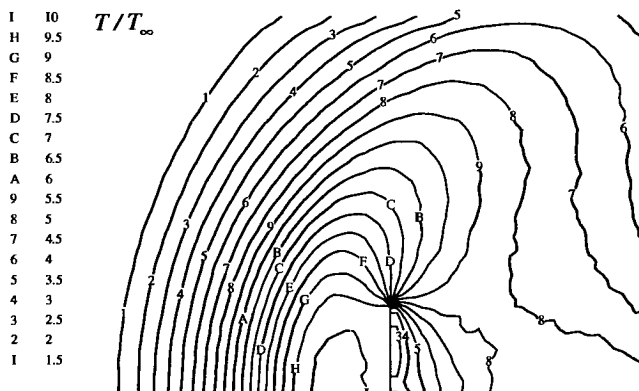


Fig. 14.33 Temperature contours in the helium-xenon mixture.

The very high concentration of helium at the rear of the plate also leads to densities that are higher than in the continuum case. The average pressure coefficient over the rear surface of the plate is 0.035 and this is five times higher than in the simple gas case. Less than three in a thousand of the molecules that strike the rear of the plate are xenon. This is in contrast to the front of the plate where the pressure coefficient is not significantly affected.

The stagnation streamline program DSMC1T was modified slightly to cope with two independent gases rather than a dissociating diatomic gas and was applied to this problem. The composition profile along the stagnation streamline is shown in Fig. 14.34. The pressure diffusion cannot be expected to be accurately modelled because it depends on the shape of the body, and this does not enter the data for DSMC1T. However, there is some enhancement of the heavy gas near the stagnation point and this would probably be quite realistic for a cylindrical or spherical body. It does not appear necessary to enhance the separation by using a single maximum value of the square of the normal velocity, as was suggested in §12.12. The program was temporarily modified to employ a single maximum and this was found to lead to grossly excessive separation.

While this is an extreme case with regard to mass ratio and low density, the results are indicative of the errors that can be introduced by the inadequate representation of diffusion in the Navier-Stokes equations.

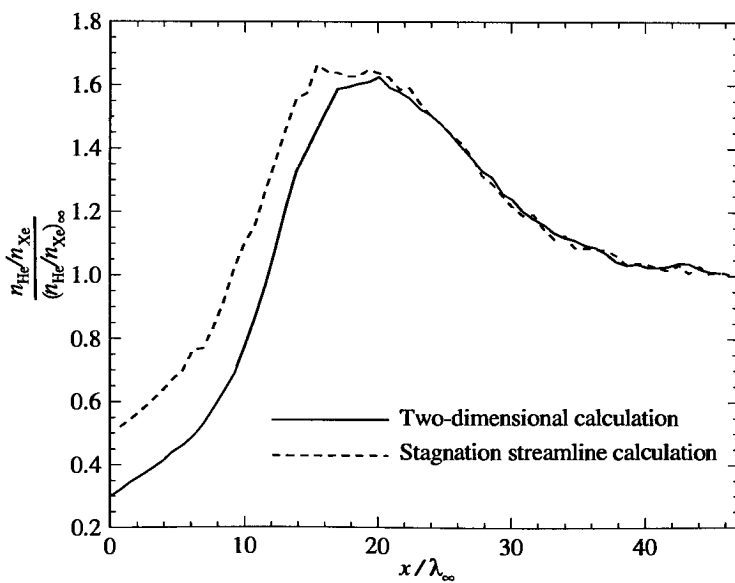


Fig. 14.34 The normalized helium to xenon number ratio along the stagnation streamline.

14.8 The flat plate at incidence

Although the surfaces in program DSMC2 must be coincident with the boundaries of the rectangular cells, freestream velocity components may be specified in both directions and the program may be used to study the flow past a flat plate at any incidence. The main test case is the flow of argon at a Mach number of 5.0 past a flat plate at an incidence of 30° . The plate length is 30.9 times the freestream mean free path, so that the overall Knudsen number is 0.0324. The temperatures of the lower and upper surfaces of the plate are equal to the stagnation and static temperatures, respectively.

In any engineering study that involves solid surfaces, there may be uncertainty due to the lack of reliable data for gas-surface interactions. For low speed flows and surfaces that have not been exposed to the 'cleaning' effects of high temperature and high vacuum, it is reasonable to assume diffuse reflection with complete thermal accommodation. The effects of non-diffuse reflection are generally studied through calculations with a mixture of diffuse and specular reflection. Complete specular reflection is not realistic, but is a useful option in that an 'inviscid' calculation can be made with no boundary layer. The flow is calculated for both the diffuse and specular limits but, rather than rely on a mixture of these for the intermediate case, program DSMC2 has been extended to include Lord's implementation of the Cercignani-Lampis model. This model was outlined in §5.8 and the translational interaction is specified by the normal and tangential accommodation coefficients a_n and a_t , which are denoted in the data by ALPN and ALPT.

As in §5.8, the inward normal component of the incident velocity is u_i and the parallel components are v_i and w_i . These velocity components have been normalized by the most probable speed at the surface temperature. Without loss of generality, the axes are chosen such that v_i lies in the *interaction plane* that contains the incident molecular path and the normal to the surface, so that w_i is zero. In the Cercignani-Lampis-Lord (CLL) option in the subroutine REFLECT2, u_i and v_i are denoted by VNI and VPI, respectively. The reflected components are calculated relative to the interaction plane and the orientation of this plane relative to the axes is given here by the angle ANG.

The distributions of θ and r^2/α in eqn (5.75) are similar to those of θ and $\beta^2 r^2$ in eqns (C10) and (C11) so that

$$\theta = 2\pi R_f \quad (14.1)$$

and

$$r = \{-\alpha \ln(R_f)\}. \quad (14.2)$$

These equations are applied in turn to the normal component with $\alpha=a_n$ and the tangential component with $\alpha=a_t(2-a_t)$. The outward normal reflected velocity component follows from Fig. 5.2 as

$$u = \{r^2 + (1-\alpha)u_i^2 + 2r(1-\alpha)^{1/2}u_i \cos\theta\}^{1/2}. \quad (14.3)$$

The reflected tangential component in the interaction plane follows similarly as

$$v = (1 - \alpha)v_i + r\cos\theta, \quad (14.4)$$

and

$$w = r\sin\theta. \quad (14.5)$$

Note that there are separate definitions of α for the normal and tangential components, and that separate random values of r and θ must be used for these components. The reflected components must be transformed back to the original coordinate system.

As noted in §5.8, the distribution of an angular velocity component ω is similar to that for the normal velocity component u . A rotational energy accommodation coefficient α_r is introduced and, with an appropriate change in the normalization, the equations for diatomic molecules are analogous to those for the normal velocity component. The polyatomic case with three internal degrees of freedom is special and Lord (1991) has shown that the distribution function for the parameter r is given by

$$f(r) \propto r^2 \exp(-r^2/\alpha_r), \quad (14.6)$$

while the cosine of θ is uniformly distributed. The acceptance-rejection method is employed for the selection of r .

The CLL model reduces to specular or diffuse reflection when all the accommodation coefficients are zero or unity, respectively. However, the CLL code is inefficient in each of these limits and it is preferable to retain separate code for each option. Another change to the code is that the shear stress due to the reflected molecules has been sampled. This is not necessary for diffuse reflection where it is zero, or for specular reflection where it is equal and opposite to the shear stress due to the incident molecules.

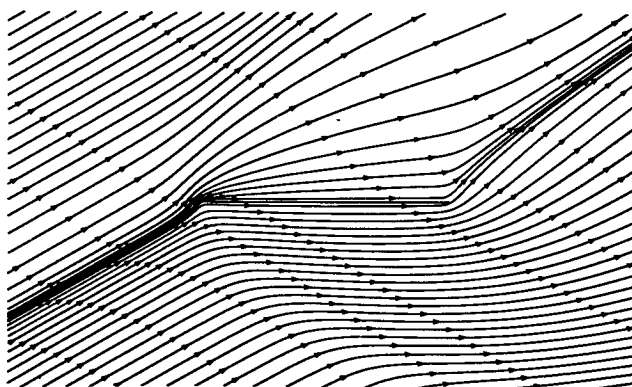


Fig. 14.35 Flow at $\alpha = 30^\circ$, $(Ma) = 5$, $(Kn) = 0.043$, and $\gamma = 5/3$ for diffuse reflection.

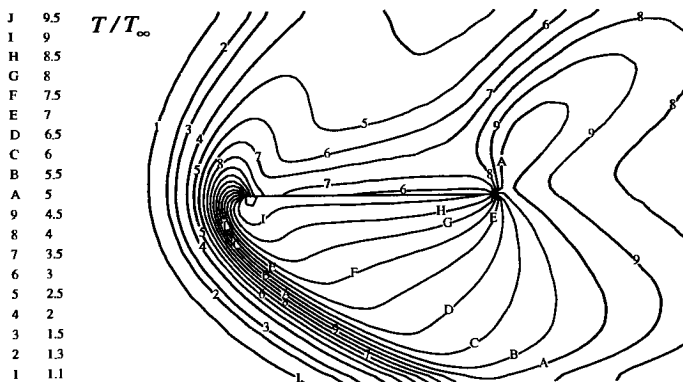


Fig. 14.36 Temperature contours for the diffuse reflection case.

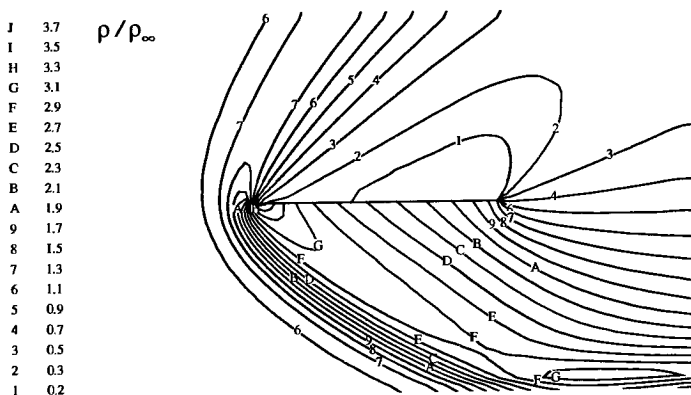


Fig. 14.37 Density contours for the diffuse reflection case.

The streamlines, temperature contours, and density contours for the diffuse reflection case are shown in Figs 14.35 to 14.37, respectively. The maximum deflection angle for an attached shock wave for this case is given by continuum inviscid theory as 33.5° . Although the incidence is less than the critical value, the displacement effect of the boundary layer has evidently led to a detached shock. The curvature of the stagnation streamline at the leading edge of the plate occurs in the subsonic region of the flow. This causes the flow near the leading edge to be inclined at an angle of slightly over 50° to the plate, which is more than 20° higher than the incidence of the stream. The shock wave extends into the region above the plate, but is rapidly weakened by the expansion above the leading edge and becomes very diffuse.

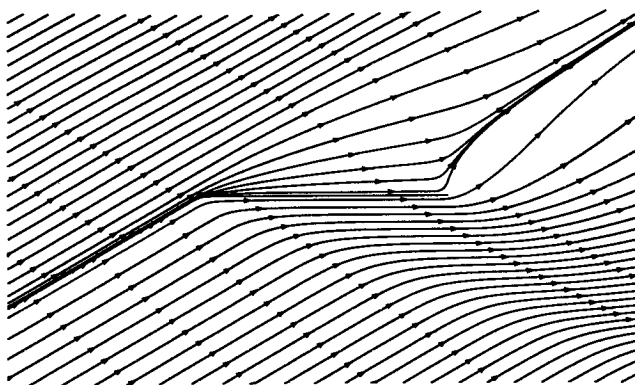


Fig. 14.38 Flow at $\alpha = 30^\circ$, $(Ma) = 5$, $(Kn) = 0.043$, and $\gamma = 5/3$ for specular reflection.

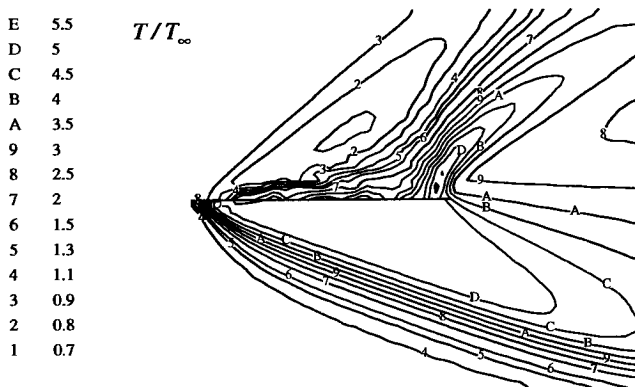


Fig. 14.39 Temperature contours for the specular reflection case.

The corresponding information for the specular reflection case is shown in Figs 14.38 to 14.40. At the leading edge, the oblique shock wave is attached to the lower surface and the expansion over the upper surface is directly from the freestream conditions. Unlike the diffuse reflection case, there is a region in which the temperature falls below the freestream value. The shock wave is much weaker and the maximum temperature is not much more than half that in the diffuse case. The compression above the trailing edge is much sharper than in the diffuse case, and the maximum temperature in this region is almost as high as the maximum temperature under the leading edge.

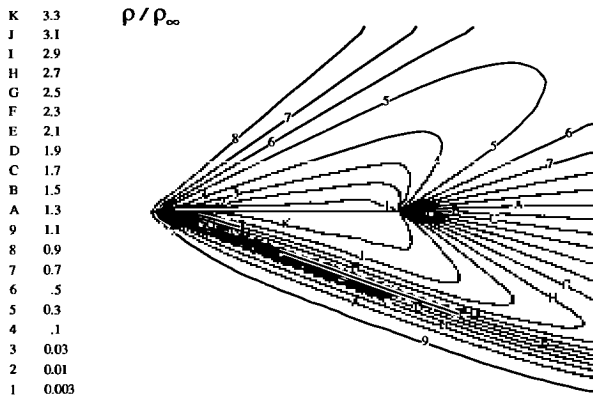


Fig. 14.40 Density contours in the specular reflection case.

In order to confirm that the major difference between the diffuse and specular cases is due to the shock being attached in the specular case and detached in the diffuse case, the specular case was repeated for incidences of 40° and 60° . The streamlines for these cases are shown in Figs 14.41 and 14.42. The curvature of the stagnation streamline gradually increases and this may be identified with the transition to the vertical flat plate case that was studied in §4.6 and for which the streamlines are shown in Fig. 14.27. The contour plots for these cases are qualitatively similar to those for the diffuse reflection case. For example, a density and therefore a pressure gradient develops along the lower surface.

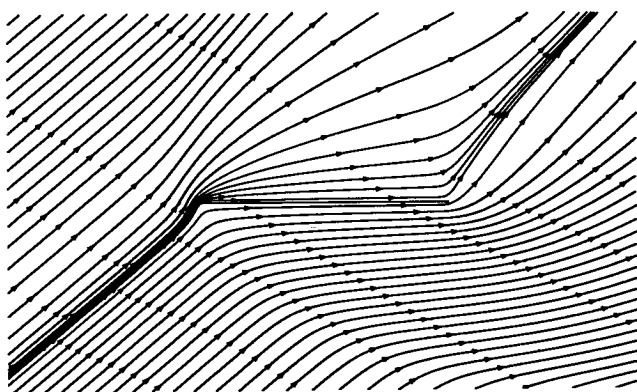


Fig. 14.41 Streamlines for the specularly reflecting plate at $\alpha = 40^\circ$.

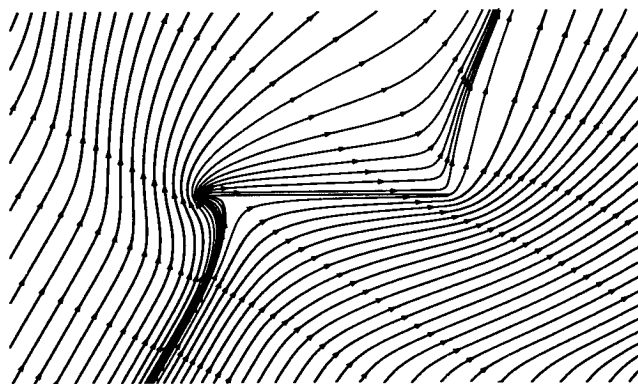


Fig. 14.42 Streamlines for the specularly reflecting plate at $\alpha = 60^\circ$.

The pressure and shear stress distributions in the $\alpha = 30^\circ$ case are shown in Figs 14.43 and 14.44, respectively. In addition to the full diffuse and specular reflection cases, results were obtained for the Cercignani–Lampis–Lord model with both the normal and parallel momentum coefficients equal to one half, and also for 50% diffuse and 50% specular reflection.

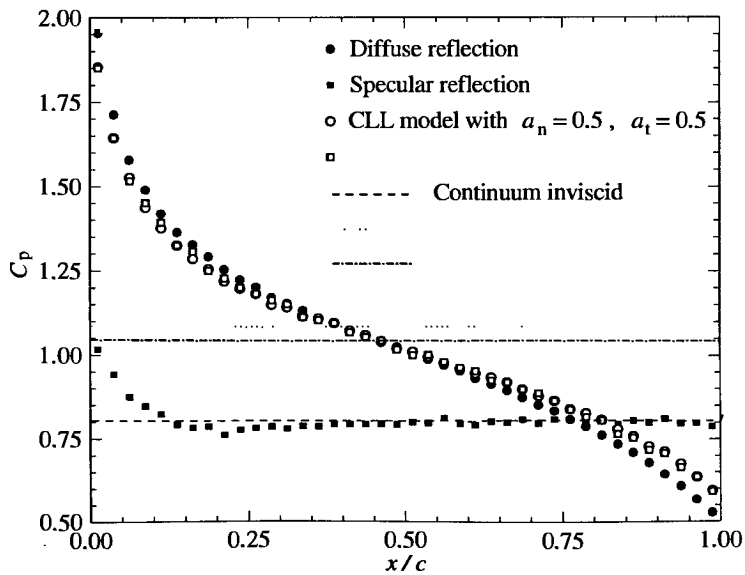


Fig. 14.43 The pressure coefficient along the lower surface at $\alpha = 30^\circ$.

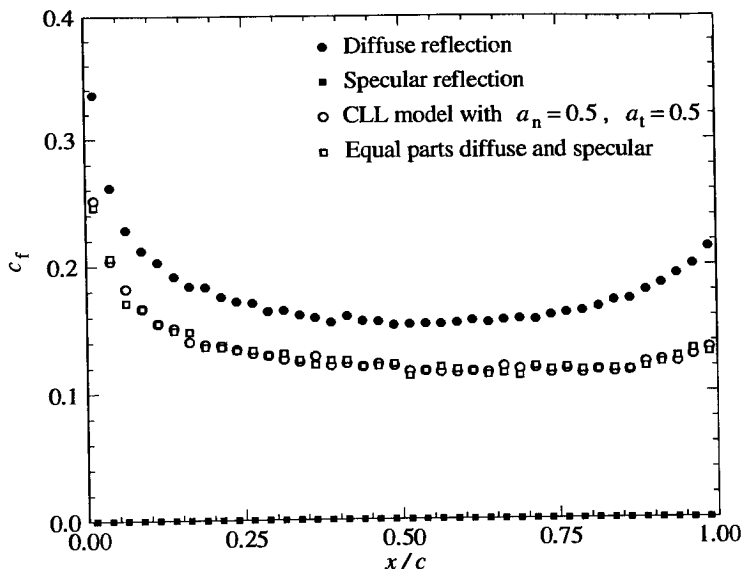


Fig. 14.44 The skin friction coefficient along the lower surface at $\alpha = 30^\circ$.

The pressure at the leading edge in the specular case is equal to the free-molecule value. This is because there is virtually no upstream influence with specular reflection. The pressure falls to the oblique shock value of continuum inviscid theory over about 15 local mean free paths and then remains constant. In the absence of a boundary layer, there is also no upstream influence from the expansion at the trailing edge.

The pressure distribution for diffuse reflection also has a maximum at the leading edge and the pressure coefficient of 2 at the leading edge is characteristic of that at the stagnation point of a blunt body. The pressure then falls and, in the region affected by the trailing edge expansion, falls below the specular value. The shear stress also has a maximum at the leading edge and then falls, but the acceleration of the flow as it approaches the trailing edge causes it to increase.

Both the CLL model and the part specular reflection have little effect on the pressure, but lead to a significant decrease in the skin friction. There is no significant difference in this case between these options. This is reassuring in that it indicates that the simple combination of specular and diffuse reflection can provide a useful representation of non-diffuse effects. However, this is a single-parameter model which depends only on the fraction of specular reflection. The CLL model is far more general in that it permits the specification of independent values of the accommodation coefficients for the normal momentum, the tangential momentum, and each of the internal energy modes.

14.9 The Prandtl-Meyer expansion

If the continuum equations for the expansion of a uniform sonic or super-sonic stream around a sharp corner are expressed in cylindrical coordinates r, θ with the origin at the corner, they reduce to an ordinary differential equation with the angle θ as the independent variable. If this angle is measured from the sonic line, the Mach number is given by the standard result

$$(Ma)^2 = \{(\gamma+1)/(\gamma-1)\} \tan^2[\{(\gamma-1)/(\gamma+1)\}^{1/2} \theta] + 1. \quad (14.7)$$

The Mach number becomes infinity at $\theta = \{(\gamma+1)/(\gamma-1)\}^{1/2}\pi/2$ and the continuum theory predicts a vacuum beyond this angle. The Mach angle is zero and the streamlines are normal to $\gamma=0$, so that the maximum flow deflection angle is 90° less than this angle.

The continuum breakdown parameter P that was defined in eqn (1.5) may be expressed in a closed form (Bird 1981) as

$$P = \left(\frac{\gamma\pi}{2}\right)^{1/2} \frac{\{(Ma)^2 - 1\}^{1/2}}{\gamma + 1} \left(\frac{1 + \{(\gamma-1)/2\}(Ma)^2}{(\gamma+1)/2}\right)^{1/(\gamma-1)-\omega+1/2} \frac{\lambda^*}{r}, \quad (14.8)$$

where λ^* is the mean free path at the sonic line.

Program DSMC has been used to compute the expansion of oxygen at a temperature of 300 K, a number density of 2×10^{20} , and a Mach number of 2.151 to a vacuum. This Mach number was chosen because the continuum predicts a vacuum at a flow deflection angle of 90° . The jet option was used to generate the flow between a specularly reflecting surface at $y = 0.155$ m and the lower boundary at $y = 0$ which is specified as a plane of symmetry. The other boundaries employ the vacuum option. The calculated streamlines are shown in Fig. 14.45 and it can be seen that the rarefaction effects cause the flow to expand beyond 90° .

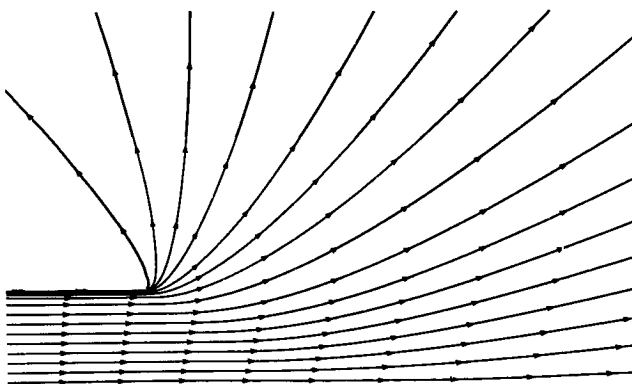


Fig. 14.45 The expansion of a diatomic gas at $(Ma) = 2.151$ to a vacuum.

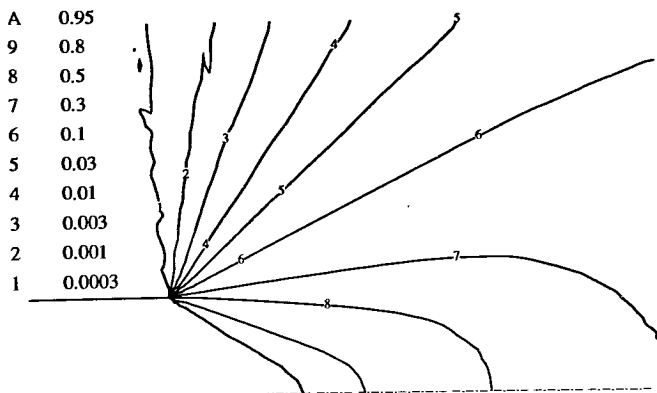


Fig. 14.46 Contours of constant density in the expansion.

All contours in a Prandtl-Meyer expansion are straight radial lines and the curvature of the DSMC number density contours in Fig. 14.46 is largely due to the reflection of the expansion from the plane of symmetry. The value of the breakdown parameter P at the leading edge of the expansion is $0.0078/r$, and this edge intersects with $y=0$ at $r=0.334$. The flow near the corner is immediately out of equilibrium and that near the plane of symmetry, where P is approximately 0.023, is in marginal equilibrium. The extent of the departure from translational and rotational equilibrium is conveniently assessed through the parameter $(T/T_\infty)/(\rho_\infty/\rho)^{\gamma-1}$ which would remain unity in an isentropic expansion.

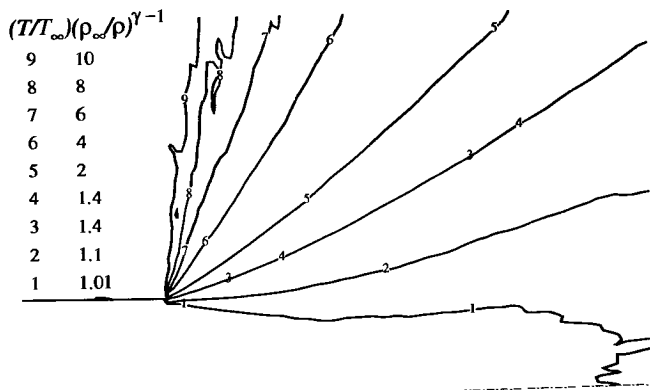


Fig. 14.47 The departure from isentropic conditions in the expansion.

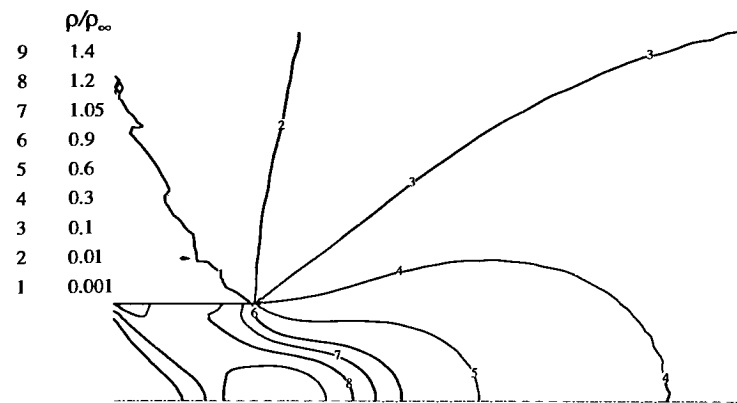


Fig. 14.48 Density contours with diffuse reflection along the plate.

The contours for this 'isentropic parameter' are shown in Fig. 14.47 and, while the flow is close to equilibrium in the early stages of the expansion, the low-density region where the density exceeds the continuum predictions is in a highly non-equilibrium state.

The calculation was repeated with diffuse rather than specular reflection from the plate and the contours of constant density are shown in Fig. 14.48. This led to a boundary layer along the plate, to a weak shock from the front of plate, and to the reflection of this shock from the plane of symmetry. However, it is the reduction in the flow Mach number in the region immediately upstream of the corner that has the greatest influence on the expansion. The density at a deflection angle of 90° is an order of magnitude higher than in the specular reflection case and the density in the 'backflow' regions is enhanced by even larger factors.

References

- BABOVSKY, H., GROPENGREISSER, F., NEUNZERT, H., STRUCKMEIER, J., and WIESEN, B. (1989). Low-discrepancy method for the Boltzmann equation. *Prog. Astro. Aero.* **118**, 85–99.
- BIRD, G.A. (1976). *Molecular gas dynamics*, Oxford University Press.
- BIRD, G.A. (1981). Breakdown of continuum flow in freejets and rocket plumes. *Prog. Astro. and Aero.* **74**, 681–694.
- HARVEY, J.K. (1986). Direct simulation Monte Carlo method and comparison with experiment. *Prog. Astro. Aero.* **103**, 25–42.
- LORD, R.G. (1991). Application of the Cercignani-Lampis scattering kernel to direct simulation Monte Carlo calculations. In *Rarefied gas dynamics* (ed A.E. Beylich), pp 1427–1433, VCH Verlagsgesellschaft mbH, Weinheim, Germany.

15

AXIALLY SYMMETRIC FLOWS

15.1 Procedures for axially symmetric flows

An axially symmetric flow is similar to the two-dimensional flow in that it has two independent spatial variables and the discussion of grids in §14.1 applies also to these flows. Program DSMC2A is a version of DSMC2 for application to axially symmetric flows. Instead of modelling unit width of the two-dimensional flow, it models the full azimuth of 2π about the axis which is chosen to lie along the x -axis. The y -coordinate becomes the radius and there are obvious consequences with regard to the cell volumes and surface areas. However, it is no longer sufficient to simply ignore the motion in the z -direction and the three-dimensional character of the molecular trajectories must be taken into account.

Advantage is taken of the symmetry to transform, at each time step, the initial point of each trajectory element to the zero azimuth plane. These transformations are similar to those for the one-dimensional flows with cylindrical or spherical symmetry. Consider a molecule at radius y_1 with velocity components in the radial and circumferential directions of v_1 and w_1 , respectively. If the molecule moves for time Δt , the new radius is

$$y = \{(y_1 + v_1 \Delta t)^2 + (w_1 \Delta t)^2\}^{1/2}. \quad (15.1)$$

Also, the velocity components must be rotated so that v remains the radial component. The new values of the radial and circumferential components are

$$v = \{v_1(y_1 + v_1 \Delta t) + w_1^2 \Delta t\} / y$$

and

$$w = \{w_1(y_1 + v_1 \Delta t) - v_1 w_1 \Delta t\} / y. \quad (15.2)$$

These equations are implemented in the subroutine AIFR. Program DSMC2A is restricted to surfaces that lie along the cell boundaries, so that they are either parallel to or normal to the axis. Molecular collisions with a normal surface are due to the axial velocity component and the two-dimensional logic remains valid. The parallel surfaces are cylindrical and the three-dimensional logic that led to eqn (12.12) applies also to this flow. This leads to complex code and more general surfaces would involve intersections with conical elements for which the parameters could change at each cell. The logic then becomes even more complex and there is an increase in the computation time. Cell systems such as those used in the G2 codes require this logic for all interactions with cell boundaries and the computation time is prohibitive if the three-dimensional logic is employed.

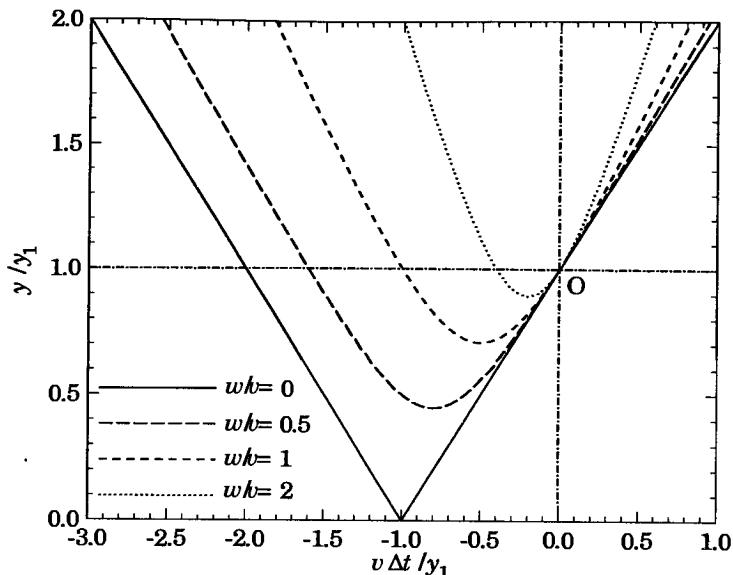


Fig. 15.1 The projection of typical trajectories on the normal plane.

The alternative to the exact three-dimensional logic is to subdivide the basic time step into a sufficiently large number of intervals that two-dimensional logic can be applied at each of the resulting sub-steps. Note that this is in regard to possible intersections with surfaces during the sub-step and that the transformations of eqns (15.1) and (15.2) are still applied at the end of each sub-step. The problem is to determine the necessary degree of subdivision.

Eqn (15.1) may be rearranged to give the following expression for the ratio of the radius y after time Δt to the initial radius y_1 as

$$y/y_1 = [1 + 2vt/y_1 + \{1 + (w/v)^2\}(vt/y_1)^2]^{1/2}. \quad (15.3)$$

This result is illustrated in Fig. 15.1. For negative values of v , the radius ratio has a minimum value of

$$y_m/y_1 = |w/v|/[1 + (w/v)^2]^{1/2}$$

after a time interval of

$$v\Delta t/y_1 = -\{1 + (w/v)^2\}^{-1}.$$

It seems reasonable to restrict the size of the time sub-step to one fourth the time interval to this minimum with some restriction on the minimum sub-step when v is very small. Also, for both positive and negative values of v , the time sub-step may be restricted to one sixth the value of $y_1/|w|$. This set of criteria has been employed in the axially symmetric version of the G2 program system and has been found to give satisfactory results.

15.2 Radial weighting factors

The most severe practical problem associated with DSMC calculations for axially symmetric flows is the small fraction of the molecules that are located near to the axis. For example, if there are 50 equally spaced cells in the radial direction in uniform flow, the sample size in the outermost cell will be 100 times greater than that in the cell at the axis. This has led to the introduction of *radial weighting factors* such that a molecule located far from the axis represents more real molecules than one near the axis. This can even up the number of molecules per cell but, since the weighting factor will change along the molecular trajectories, there is the probability that each molecule will have to be either discarded or duplicated at every time step. Weighting factors will obviously lead to fewer problems if the flow is primarily directed away from the axis and the predominant effect of the factors is that molecules are discarded rather than duplicated.

The weighting factors may be based either on the radius of the cell in which the molecule lies or on the radius of the molecule itself. The former case leads to errors when a molecule that is moving parallel to the axis moves to a cell with a different height and therefore a different weighting factor. In addition, this procedure has been found to lead to general difficulties in maintaining smooth flow gradients normal to the axis. Cell-based factors are not recommended. The alternative molecule-based factors would appear to require inefficient and complex collision coding in that the model molecules in the cell represent different numbers of real molecules. However, it has been found that there is a negligible effect on the flow if all the molecules in a cell are regarded as having an average weighting factor in the collision routines. The average weighting factor then multiplies the number of molecular choices, but each collision counts as a number of identical collisions equal to this factor, and the collision procedures need not be changed.

Program DSMC2A employs weighting factors that are equal to the ratio of the molecule radius to a reference radius RWF that is set in the data. This reference radius may be set to a small fraction of the height of the inner cell and all cells in the above hypothetical case would then contain the same number of simulated molecules. For very small values of RWF, a molecule that moves very close to the axis would be multiply duplicated and the logic in the subroutine WEIGHT allows for this. The possibility of having identical molecules in a cell forced several modifications to the subroutine SELECT that has been common to almost all the programs. The undesirable impact of the molecule duplication may be lessened in a steady flow by the imposition of a time delay on the appearance of the duplicate molecule. This has been implemented in this program through the 'molecule duplication buffer' which contains MNB molecules. Each duplicated molecule is first generated at a random address in this buffer. The molecule that was previously at this address is then placed into the flow, but this is after a random delay with an average value that depends on the size of the buffer.

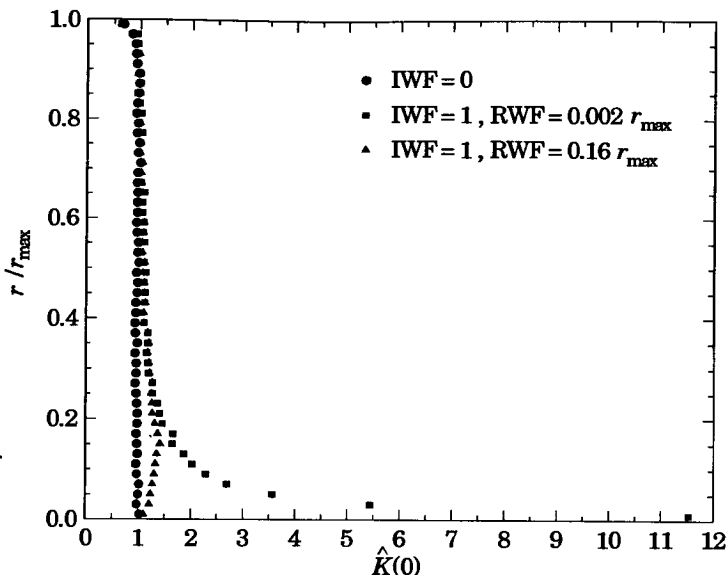


Fig. 15.2 The normalized mean square density fluctuation.

Radial weighting factors have been widely used in applications of the DSMC method to axially symmetric flows. However, the results have frequently exhibited a greater degree of scatter than would be expected from the usual criteria based on sample size or from experience with two-dimensional calculations with similar geometry. Program DSMC2A has therefore been used to determine typical normalized mean square density fluctuations in a uniform stationary gas with and without weighting factors and for various values of the reference radius RWF.

The test cases employ 50 cells of uniform height in the radial direction. The axial length of the flowfield is equal to the radius, but the mean square fluctuation has been averaged in the axial direction. Calculations were made without weighting factors, for weighting factors with a reference radius of 0.002, and for weighting factors with a reference radius of 0.16. The results from the three cases are shown in Fig. 15.2. For no weighting factors ($IWF = 0$), the normalized mean square density fluctuation has the expected value of unity, although there is some reduction in the scatter near the outer stream boundary. The second case employs weighting factors and a reference radius of one tenth the cell height. The number of molecules in the innermost cell then increases by a factor of 50 and, if the normalized mean square fluctuation remained unity, the scatter would be reduced by a factor of about seven. However, Fig. 15.2 shows that the normalized mean square fluctuation in the cell nearest the axis increases by more than a factor of ten. This shows that the use of radial weighting factors can actually lead to an increase in the scatter at the axis.

The third test case with a reference radius of 0.15 improves the sample in the innermost cell by a factor of just over three. There is only a slight increase in the normalized mean square density fluctuation in this cell so that there is a clear gain. There is an increase in the scatter of approximately 50% at the reference radius. However, there is a factor of four increase in the sample at this radius over the no-weighting-factor case and there is a net gain at this radius also.

The use of the very small reference radius in order to obtain similar samples in each cell was not only counterproductive in terms of the scatter, but led to a systematic reduction of the order of 10 to 20% in the density at the axis. The calculation was repeated with an axial velocity corresponding to a Mach number of three and, while the excess scatter was reduced by about 40%, the systematic error in the density was not improved. If radial weighting factors are used, the reference radius should be very large in comparison with the radius of the innermost cell. Even then, there may be a slight anomaly in the flow properties at the reference radius.

15.3 Flow past a flat-nosed cylinder

The listed data in the program DSMC2A is for the flow of argon at a number density of 10^{21} m^{-3} and a temperature of 100 K at a velocity of 1000 ms^{-1} past a flat-nosed cylinder. The radius r_c of the cylinder is 0.01 m so that the overall Knudsen number based on the diameter of the cylinder is 0.0474. The Mach number of the flow is 5.37 and the conditions are similar to those for the two-dimensional vertical plate that was the subject of §14.6. The temperature of the flat face is 1000 K which is close to the continuum stagnation temperature of 1060.5 K and this case will be referred to as the 'adiabatic case'. The temperature of the cylindrical surface is 300 K and the diffuse reflection model is assumed.

The centre of the flat face is located at the origin and the extent of the simulated flowfield in the axial direction is from -0.02 m to 0.02 m, while it extends to a radius of 0.03 m. The cell grid is 80×60 with equal spacing in each direction. The cell width and height is approximately equal to one-half a mean free path and there are four sub-cells per cell. The maximum density is just over four times the freestream density and this occurs at a temperature of approximately ten times the freestream density where the mean cross-section for argon is half that at the stream temperature. This means that the mean free path in the stagnation region is approximately equal to the cell dimension. The grid dimensions are marginal but, given that the sub-cell dimension is then one-half a mean free path, this should not lead to any error. A 'cold surface' calculation was also made with the temperature of the flat surface equal to 300 K. The cell size was excessive for this calculation and flows with large density increases in the stagnation region require a more sophisticated grid. Weighting factors were employed for these calculations with the reference radius RWF set to 0.004. This is eight times the cell height and this choice corresponds to the value that led to satisfactory results in the preceding section.

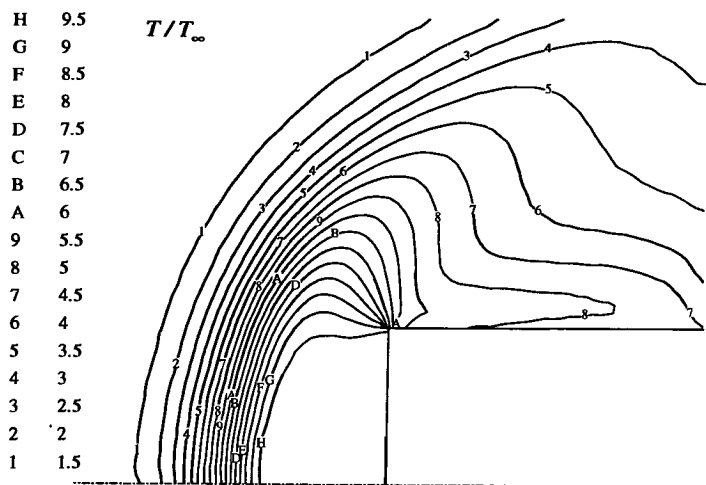


Fig. 15.3 Temperature contours in the adiabatic surface case.

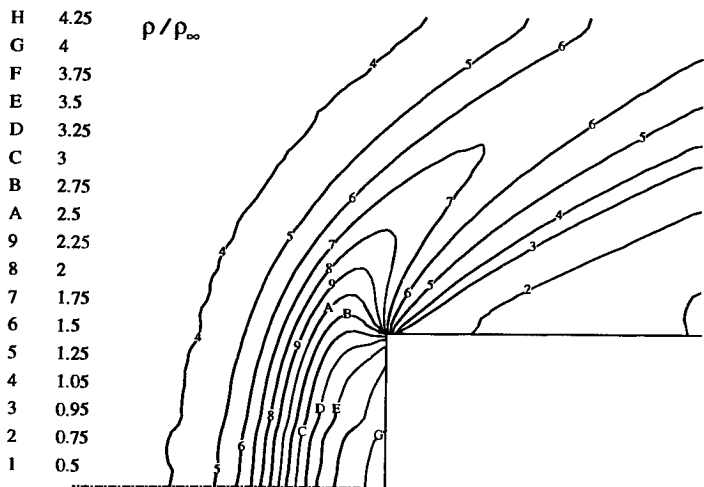


Fig. 15.4 Contours of constant density in the adiabatic surface case.

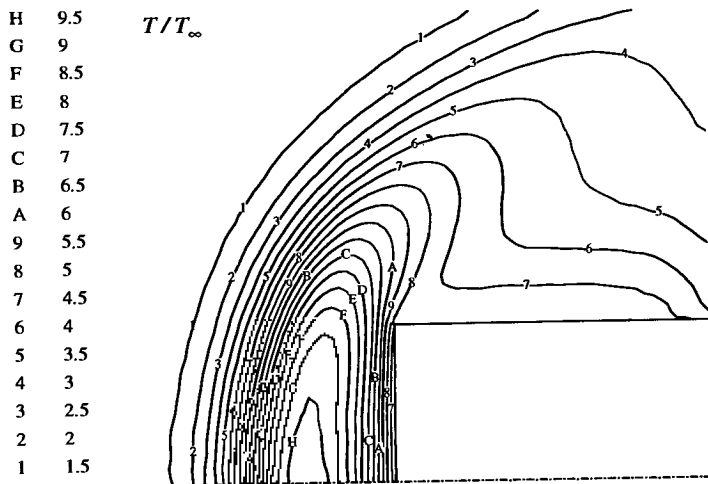


Fig. 15.5 Temperature contours in the cold-surface case.

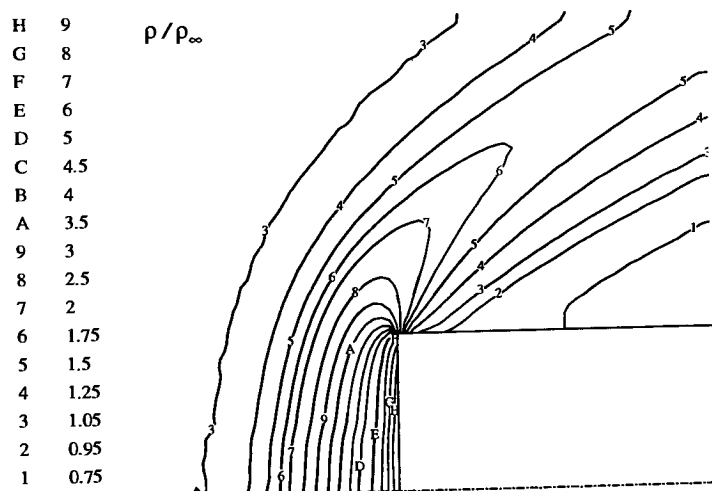


Fig. 15.6 Contours of constant density in the cold-surface case.

The temperature and density contours for the adiabatic case are shown in Figs. 15.3 and 15.4, respectively. These are generally similar to Figs 14.26 and 14.28 for the two-dimensional flow past a vertical flat plate. The shock stand-off distance may be defined by the intersection with the axis of the contour $\rho/\rho_\infty = 2.43$ that lies at the centre of the normal shock wave. This occurs in the adiabatic case at 0.34 times the diameter of the cylinder. This may be compared with the figure of 0.78 that is obtained from Fig. 14.28 for the two-dimensional flow.

The corresponding contours for the cold-surface case are shown in Figs 15.5 and 15.6. There is a significant increase in the density and a decrease in the temperature in the thermal boundary layer adjacent to the surface. The shock stand-off distance drops to 0.31 times the diameter of the cylinder. The cooling effect extends around the shoulder of the body, but the flow properties well away from the stagnation region are not greatly affected.

The pressure distribution along the flat surface is shown in Fig. 15.7 through the ratio of the pressure coefficient to the continuum stagnation pressure ratio ($C_p)_0$ as a function of the radius ratio. The pressure near to the axis is slightly above the continuum pressure, but the area represented by this region is small and the pressure is significantly below the continuum stagnation pressure over most of the face. The average pressure is three to four percent below the stagnation pressure. This result is consistent with the observed pressures (Potter and Bailey 1963).

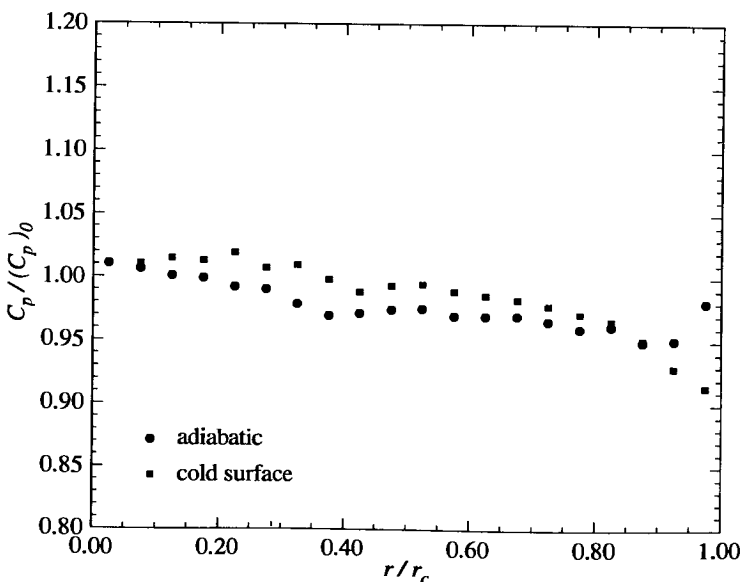


Fig. 15.7 The pressure distribution along the flat face.

15.4 The Taylor-Couette flow

A Couette flow with one stationary surface and one moving parallel surface can be generated by program DSMC2A in five distinct ways. Two coaxial cylinders could have a relative velocity in the axial direction with either the inner or outer cylinder moving. Alternatively, either the inner or outer cylinder could rotate about the axis with a fixed angular velocity and give its surface a circumferential velocity. Finally, one of two plates normal to the axis could rotate about the axis. The Taylor-Couette flow is concerned with the case in which the inner cylinder has a circumferential velocity. Taylor found that, at some critical angular velocity, the flow becomes unstable and develops annular vortices. Stefanov and Cercignani (1993) have shown that the DSMC method can be used to study these vortices and program DSMC2A has been used to re-calculate one of their cases.

This case employs an outer cylinder with a radius r_2 that is double the radius r_1 of the inner cylinder. The gas is a simple monatomic gas of hard sphere molecules. The gas is initially stationary and uniform with a density such the mean free path is $(r_2 - r_1)/50$. At zero time, the inner cylinder instantaneously acquires a constant angular velocity such that its circumferential velocity is equal to three times the most probable molecular speed. The flow is therefore characterized as having a Knudsen number (Kn) of 0.02 and a speed ratio s of 3.0. The Taylor number is defined by

$$(Ta) = \frac{4 \rho^2 \omega^2 r_1^4}{\mu^2 \{1 - (r_1/r_2)^2\}^2}, \quad (15.4)$$

where ω is the angular velocity of the rotating cylinder. Stefanov and Cercignani quote a Taylor number of 521,600 for this case and this is well above the critical number of 33,110. However, for the 'supersonic' surface speed that is employed here, large density and temperature variations develop within the flow and the effective or local values of the dimensionless parameters may be quite different from their nominal values.

For the purposes of the computation, the flow must have a limited length in the axial direction. This was chosen to be equal to the diameter of the outer cylinder so that, as shown in Fig. 15.8, the computational region has an aspect ratio of four. The cylindrical surfaces are specified as being diffusely reflecting with an accommodation coefficient of unity, while the end-planes are specularly reflecting and can be regarded as planes of symmetry. The cells were of a uniform size with a grid of 200 in the axial direction and 50 in the radial direction, with two sub-cells per cell in each direction. There were a total of 120,000 simulated molecules in the calculation. These numbers are larger than those that have been employed in previous examples and there was a problem in keeping within the 8 Mb limit that has been set for the examples. The program has therefore been modified so that memory is not wasted on the storage of the molecular species in a simple gas or on the rotational energy for a monatomic gas. The changes are quite straightforward, but extra care must be taken in setting the variables in the PARAMETER statements.

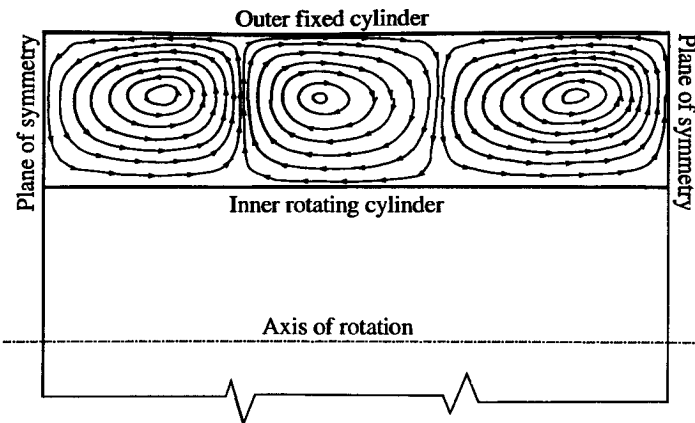


Fig. 15.8 Configuration of Taylor vortices for $s = 3$, $(Kn) = 0.02$.

Fig. 15.8 shows the projection of the streamlines onto the ‘normal’ plane that contains the axis and is normal to the rotating surface. This is a time average over the 21st to the 30th revolution of the inner cylinder. The apparently stable configuration of three counter-rotating annular vortices evolved through an unsteady process that is illustrated in Fig. 15.9.

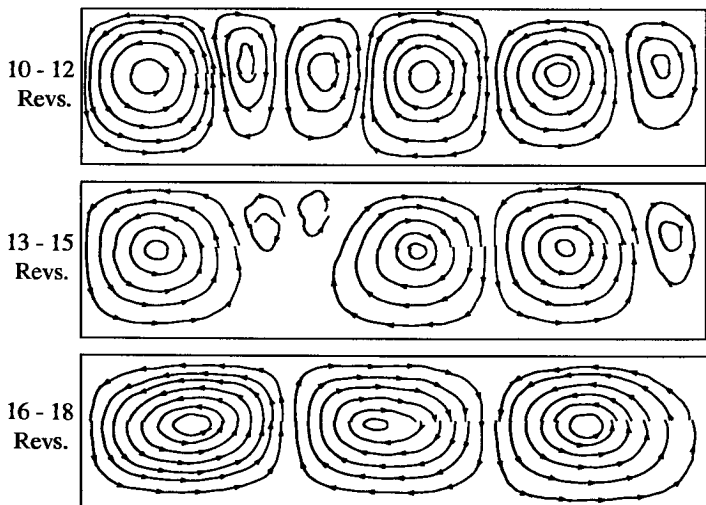


Fig. 15.9 Evolution with time of the Taylor-Couette flow.

The initial state was a uniform gas of density ρ_i in equilibrium with stationary cylinders at the temperature T_w . The rotation of the inner cylinder started impulsively at zero time. A downward moving jet of gas was apparent during the first few revolutions and this developed into the vortex at the left. The other vortices devolved subsequently and, over the time interval corresponding to 10 to 12 revolutions, there were six vortices in three ordered pairs of one large and one small vortex. The three small vortices decayed over the next three revolutions and, after 17 revolutions, there were only three vortices of approximately equal size. The right-hand vortex became larger than the other two by 20 revolutions and it appeared that a single vortex could eventually develop. However, the relative sizes remained constant over the nine revolutions that led to Fig. 15.8 and this indicates that the three-vortex structure could well be stable for this configuration. The results of Stefanov and Cercignani show five vortices for this case, but they did not report the time interval over which the flow was sampled.

As in the one-dimensional high-speed Couette flow of §12.2, the high surface speed of the cylinder leads to a significant heating of the gas. The gas temperature increases until the heat transfer to the surfaces equals the work done in moving the surface. The highest temperatures are near the rotating surface and Fig. 15.10, for the centre vortex, shows that the vortices lead to significant axial gradients in the temperature.

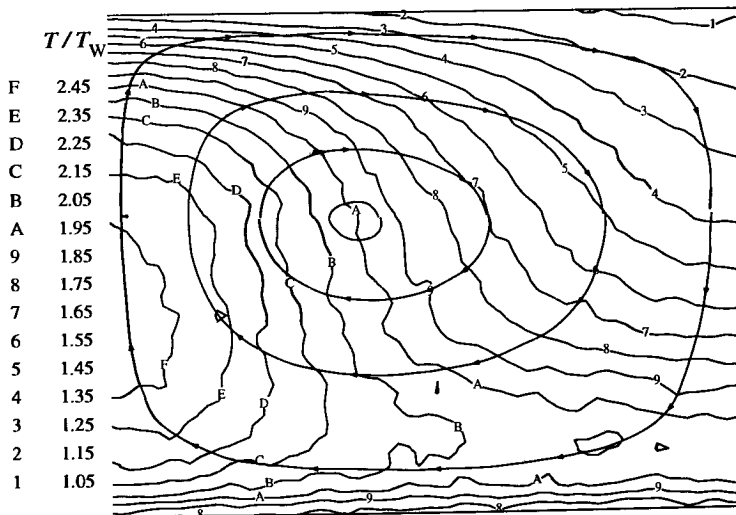


Fig. 15.10 The temperature contours in the centre vortex.

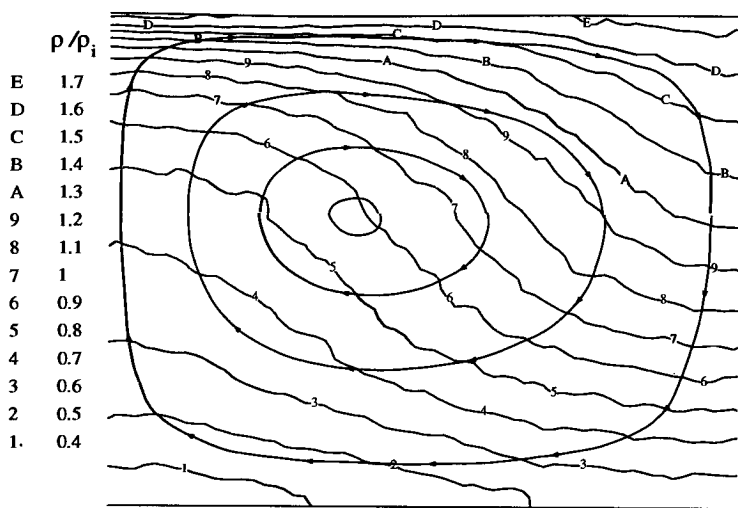


Fig. 15.11 The density contours in the centre vortex.

The density contours of Fig. 15.11 show that the high temperatures correspond to low densities, but the variation in the product of density and temperature shows that there are significant pressure gradients within the flowfield. Sufficient streamlines are shown in these figures to enable the flow features to be related to the vortex. These streamlines are generated as upper and lower segments and the accuracy with which the segments meet indicates that the flow was very nearly steady over the sampling time interval. The results are similar for all three vortices.

The distribution of the circumferential velocity component is shown in Fig. 15.12, and that of the 'vortex' speed in the normal plane is shown in Fig. 15.13. Both of these have been normalized by the most probable molecular speed in the gas at temperature T_w . Note that this is a fixed value and, while these quantities are expressed as speed ratios, they are different from the local speed ratio that takes the temperature variation into account. The speed ratio of the inner cylinder is three and there is significant velocity and temperature slips at this surface. The slips are much less at the fixed upper surface. The speed ratio of the rotational motion in the annular vortices ranges from 0.05 to 0.35. These values are consistent with those reported by Stefanov and Cercignani. The higher speeds in the vortex occur in the lower-density regions of the flow.

While the sampling procedures in the programs are intended primarily for the study of a large time steady flow, the calculation is always unsteady with a physically significant time parameter. Figure 15.9 shows that the programs can be used to obtain information on unsteady processes.

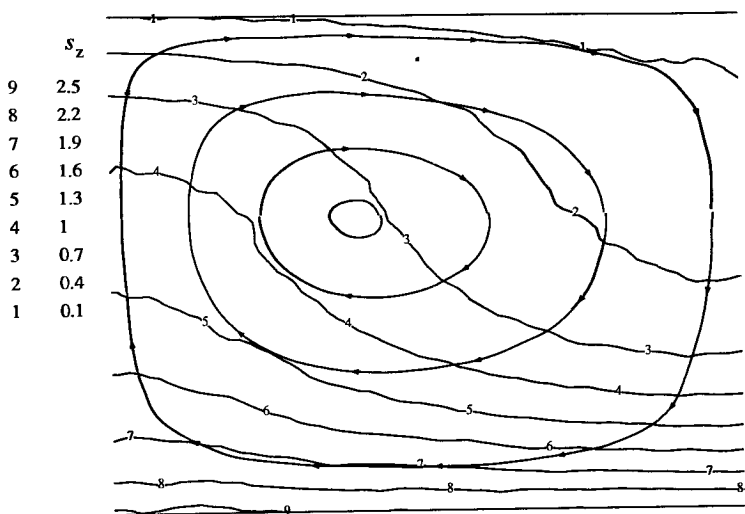


Fig. 15.12 Contours of the circumferential velocity component.

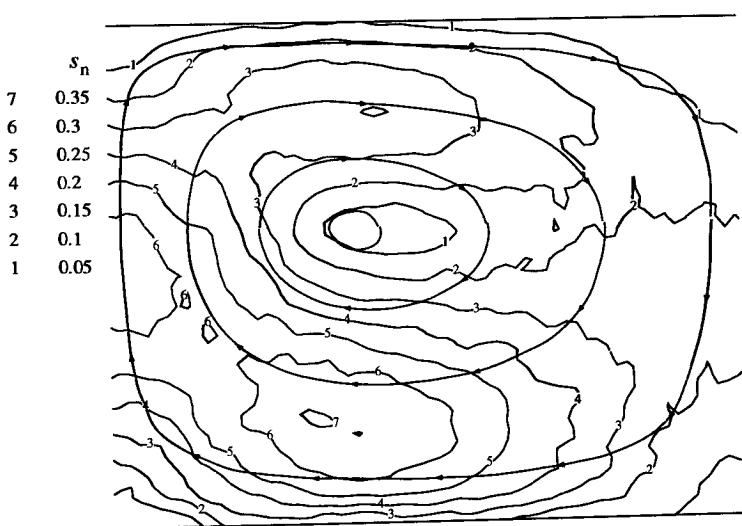


Fig. 15.13 Contours of the rotational speed in the vortex.

The Taylor number that is defined in eqn (15.4) is the square of the Reynolds number

$$(Re) = \frac{\rho u_w \hat{r}}{\mu}. \quad (15.5)$$

Here, $u_w \equiv r_1 \omega$ is the surface speed of the rotating cylinder and the characteristic radius is defined by

$$\hat{r} = \frac{2r_1}{1 - (r_1/r_2)^2} = \frac{2r_2(1 - \Delta r/r_2)}{2\Delta r/r_2 - (\Delta r/r_2)^2}, \quad (15.6)$$

where Δr is the distance $r_2 - r_1$ between the cylinders. The value of this Reynolds number for the computed case is 722.

Eqns (1.1), (4.23), (4.62), and (4.65) enable the Reynolds number in a gas of VHS molecules to be written in terms of the speed ratio and Knudsen number as

$$(Re) = \frac{2(5 - 2\omega)(7 - 2\omega)}{15\pi^{1/2}} \frac{s}{(Kn)}. \quad (15.7)$$

For the hard sphere gas that has been used in this calculation, eqn (15.7) becomes

$$(Re) = \frac{16}{5\pi^{1/2}} \frac{s}{(Kn)} = \frac{1.8054 s}{(Kn)}.$$

In the application of this equation to a rarefied gas, there is a case for basing the Knudsen and Reynolds numbers on Δr rather than \hat{r} . The values of these numbers for this case are then 0.02 and 271, respectively.

Additional calculations were made to investigate the upper limits of the Knudsen and the lower limits on the speed ratio at which Taylor vortices form. It was found that, at the speed ratio of 3, the Knudsen number could not be increased much above 0.025. However, the width of the flow could be decreased significantly and most calculations were made with just 30 initial mean free paths between the planes of symmetry. This permitted the speed ratio to be increased while still maintaining a reasonable sample near the rotating cylinder. It was found that the single vortex split into two (with the dividing plane normal to the axis) at a speed ratio of about 10. The density was increased and it was found that there was a similar splitting of the vortex at a Knudsen number of approximately 0.003.

Reichelmann and Nanbu (1993) have also applied the DSMC method to the Taylor-Couette flow in air. They employed a rotational speed such that the surface speed ratio was just below 0.5, and calculations were made for Knudsen numbers that ranged from 0.037 to 0.00435. These conditions were chosen to match the experiments of Kuhlthau (1960). The establishment of the Taylor vortices was detected through the behaviour of the torque coefficient on the fixed cylinder. The predictions of the DSMC calculations were in excellent agreement with the measurements.

15.4 Normal impact of a supersonic jet

This application involves the impact of an axially symmetric supersonic jet on a plane normal to the axis. A uniform Mach 5 jet of oxygen with a radius of 0.2 m is directed at a disk of radius 0.6 m that is normal to the axis and is located at 1 m from the exit plane of the jet. The number density of the jet is 10^{20} and its temperature is 300 K, while the disk is diffusely reflecting at a temperature of 1000 K. The mean free path in the jet is 0.01294 m, so that the jet radius is approximately 15.5 mean free paths.

The jet and disk were located at opposite ends of the flowfield which extended to a radius of 0.8 m. The grid was 100 cells in the axial direction and 80 in the radial direction with two sub-cells per cell in each direction. Weighting factors were employed with a reference radius of 0.1 m. The boundaries were specified as vacuum boundaries.

The streamlines of the resulting flow are shown in Fig. 15.14. A normal shock wave forms just upstream of the stagnation point and the sharp 90° deflection of the streamlines occurs in the subsonic region behind this wave. However, the most striking feature of the flow is the very large deflections of the streamlines from near the outer edge of the jet. The Mach number contours in Fig. 15.15 show that these deflections occur in a subsonic region that extends back to near the lip of the jet.

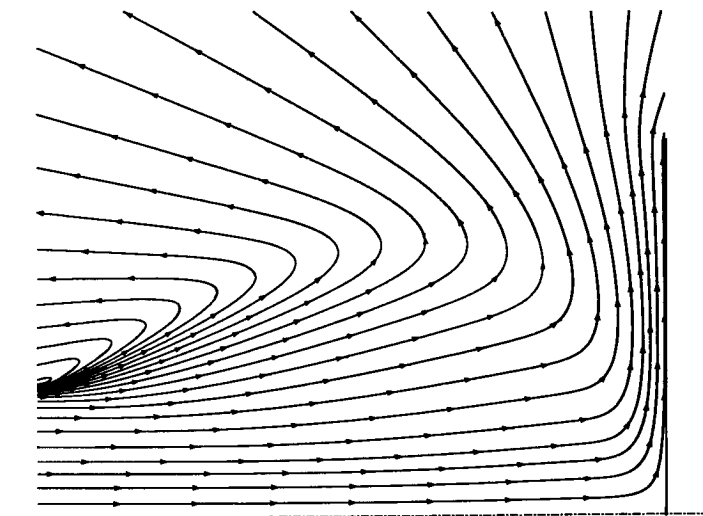


Fig. 15.14 Streamlines in the impact of a (Ma) = 5 jet on a disk.

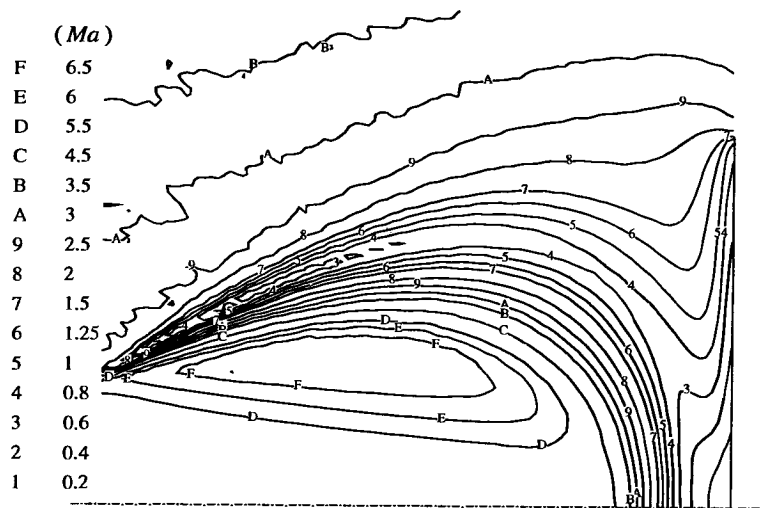


Fig. 15.15 Contours of constant Mach number

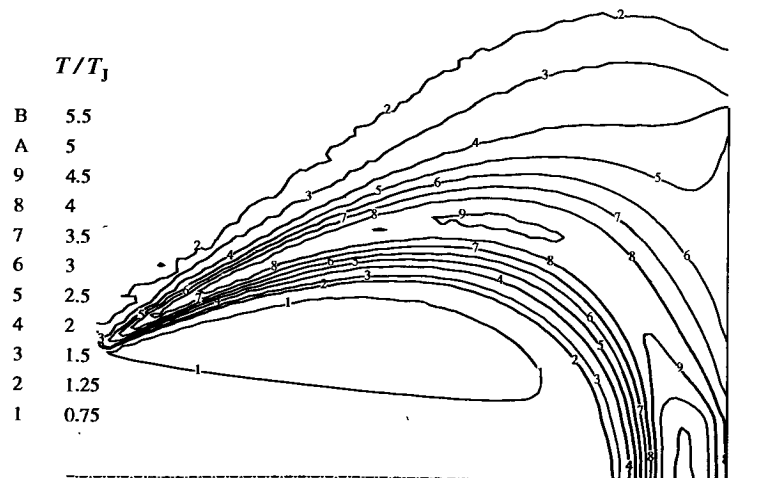


Fig. 15.16 Contours of constant temperature.

The temperature contours are shown in Fig. 15.16 and these are generally similar to the Mach number contour. The subsonic turning region is preceded by an oblique shock wave and is followed by expansion waves. The density contours of Fig. 15.17 are qualitatively different. They are influenced primarily by the expansion from the edge of the jet. There is a large density increase in the stagnation region, but the density increase associated with the oblique shock is relatively small. The subsonic turning region is associated with a 'turning back' of the density contours as the flow subsequently expands supersonically.

The Mach number increases to approximately seven in the outer part of the jet, but the normal shock wave precedes the arrival of the expansion at the axis. The degree of initial expansion of the jet would increase as the disk was moved further from the exit plane.

The extraordinary feature of the subsonic turning region is that it is actually thinner than the shock wave that precedes it. Consider this region at its maximum radius. The density is 0.03 times the initial density ρ_J in the jet and the temperature is about four times the jet temperature. The mean free path is therefore more than ten times larger than the width of the subsonic region. The process is therefore one of *molecular scattering* rather than the quasi-continuum process that is implied by the use of streamlines to describe the flow. The collisions that cause a flow deflection in a highly rarefied gas can occur well away from the site of the deflection.

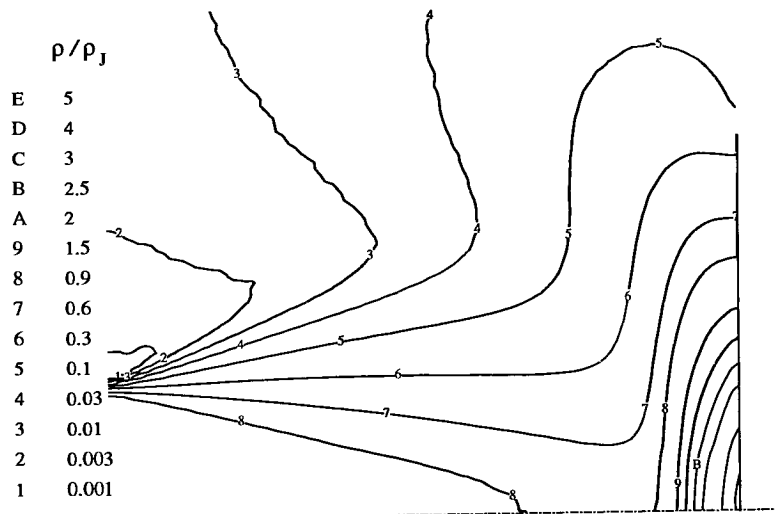


Fig. 15.17 Contours of constant density.

The calculation was repeated for a density three times higher than in the above case. The shock wave thickness decreased proportionally, but the size and shape of the subsonic region was barely affected. However, the density is still far too low for any reliable predictions to be made about the configuration of the eventual continuum flow.

15.5 The satellite contamination problem

The final application of program DSMC2A deals with the partial return of molecules that are outgassed from a circular disk to the disk as a result of collisions with a supersonic ambient stream. Outgassing is simulated by the superimposition of a zero (macroscopic) velocity jet onto the surface of the disk. For cases that involve realistic outgassing rates from satellites in orbit, the densities in this jet are so low that the 'self-scattered return flux' due to collisions between outgassed molecules is completely absent.

Bird (1981) presented DSMC calculations and an approximate theory for this problem. The theory suggested that the 'return ratio' should follow an equation of the form

$$\frac{N_r}{N_b} \propto \frac{\sigma_{bf}}{\sigma_{ff}} \left(\frac{m_b}{m_f} \right)^{1/2} \frac{s_f}{(Kn)_f} \left(\frac{T_f}{T_b} \right)^{1/2}. \quad (15.8)$$

The subscript _b denotes the outgassed molecules and _r the outgassed molecules that return to the surface, while _f denotes the freestream molecules. The effect of the molecular model enters through the ratio of the cross-section for collisions between a freestream and outgassed molecule and the cross-section for collisions between freestream molecules. The results were generally in accordance with eqn (15.8), although the effect of mass ratio was closer to a $\frac{1}{4}$ power law.

These previous calculations were severely restricted by the limitations of the computer that was used, and were made for Knudsen numbers in the range 1 to 10. These are relevant to re-entry vehicles, but are orders of magnitude less than the Knudsen numbers that apply under orbital conditions. It is therefore desirable to make similar calculations for representative orbital conditions.

The orbital altitude is taken as 360 km and the atmosphere may be assumed to be atomic oxygen at a number density of $3 \times 10^{14} \text{ m}^{-3}$ and a temperature of 1000 K. The outgassing rate at the surface is specified as $5 \times 10^{-10} \text{ kg m}^{-2} \text{ s}^{-1}$ of heavy polymer molecules with a molecular weight of 500 and an assumed diameter of $8 \times 10^{-10} \text{ m}$. For simplicity, the satellite is represented by a disk of diameter 1 m normal to the stream and a surface temperature of 300 K. The reference diameter of atomic oxygen is assumed to be $3 \times 10^{-10} \text{ m}$, with $\omega = 0.75$. This leads to a freestream mean free path of 11,600 m. Eqn (4.24) shows that the outgassing rate is equivalent to molecular effusion from a number density of 2.14×10^{13} . This is less than one tenth the freestream density and, since the flowfield dimensions must be large in comparison with the diameter of the disk, there is extreme difficulty in attaining a sufficient sample of outgassed molecules.

This situation calls for weighting factors to be applied to the species but, as discussed in §10.4, these have not been included in the programs in order to avoid random walk effects. Random walks are not a danger in a near free-molecule flow such as this, and weighting factors can be effectively introduced through the following computational artifice. The freestream number density is reduced by, in this case, a factor of 10,000 while the diameter of the freestream molecules is increased by a factor of 100. The increase in cross-section exactly matches the reduction in density so that an outgassed molecule has the correct probability of collision with a freestream molecule. The molecular mass is unchanged so that the collision mechanics are not affected. However, the velocity components of the freestream molecule should only be changed in one in every 10,000 collisions with an outgassed molecule. This is readily achieved through temporary modifications to the subroutine ELASTIC. Collisions between freestream molecules are realistic because the modifications have no net effect on the freestream collision rate. With these changes, there were approximately equal numbers of outgassed and freestream molecules in the flowfield and the calculation became easy. The flowfield extended to a radius of 6.25 m and to 12.5 m upstream of the disk with a 50×100 cell grid.

It was found that 565 out of 3,282,508 outgassed molecules returned to the surface. The return ratio is therefore 1 in 5,800 and, when substituted into eqn (15.8) this leads to a constant of proportionality $c = 0.075$. This is consistent with the $c = 0.092$ that was obtained from the earlier study for a sphere. This indicates that eqn (15.5) might be useful for the satellite as well as the low altitude case. A similar calculation for outgassed molecules with an atomic weight of 50, rather than 500, verified that the mass ratio power law of $\frac{1}{2}$, rather than $\frac{1}{4}$, is applicable in this case. Additional calculations with higher and lower freestream densities also verified the inverse linear dependence on the Knudsen number.

References

- BIRD, G.A. (1981). Spacecraft outgas ambient flow interaction, *J. Spacecraft and Rockets*, **18**, 31–35.
- KUHLTHAU, A.R. (1960). Recent low-density experiments using rotating cylinder techniques, In *Proceedings of the first international symposium on rarefied gas dynamics*, (ed. F.M. Devienne), pp. 192–200, Pergamon, London.
- POTTER, J.L. and BAILEY, A.B. (1963). Pressures in the stagnation regions of blunt bodies in the viscous-layer to merged-layer regimes of rarefied flow, Report AEDC-TDR-63-168, Arnold Engineering Development Center, USAF.
- REICHELmann, D. and NANBU, K. (1993). Monte Carlo direct simulation of the Taylor instability in rarefied gas, *Phys. Fluids A*, **5**, 2585–2587.
- STEFANOV, S. and CERCIGNANI, C. (1993). Monte Carlo simulation of the Taylor-Couette flow of a rarefied gas, *J. Fluid Mech.* to be published

16

THREE-DIMENSIONAL FLOWS

16.1 General considerations

Homogeneous (or zero-dimensional), one-dimensional, two-dimensional, and axially symmetric flows are idealizations and all real gas flows are three-dimensional. In DSMC computations of the idealized flows with restricted dimensions, the other dimension or dimensions may be regarded as being so small that the statistical fluctuations correspond with those in the real gas. This is not possible in a three-dimensional flow and the number of real molecules that are represented by each simulated molecule (the parameter FNUM in the DSMC programs) must be regarded as a computational approximation. While this poses an ideological difficulty, it is the sheer magnitude of the computational task that is the most serious problem associated with DSMC computations of three-dimensional flows.

The various classes of grid that were discussed in §14.1 in the context of two-dimensional flows may be extended to three dimensions. The simplest possible grid consists of uniform rectangular parallelepipeds defined by three sets of equally spaced planes. The moving molecules are readily indexed to such a grid and, while three-dimensional quadric surfaces may be embedded in it, the cells can be ‘fitted’ only to flat surfaces that lie in one of the planes that define the cell boundaries. The demonstration program DSMC3 is an extension of the two-dimensional program DSMC2 and is an implementation of this simplest possible case. While some of the problems that can be studied through this program are of engineering interest, more sophisticated programs are required for most applications.

The two-dimensional ‘general scheme’ that was discussed as item (vi) of §14.1 has been extended to cover three-dimensional flows. The multiple four-sided regions that were the building blocks for that scheme become regions with six faces as illustrated in Fig. 16.1. The upper and lower faces are defined by a set of points that are specified by their x - y - and z -coordinates and are arranged in a rectangular array of rows and columns. There are an equal number of points in the rows and columns on each of these faces and the corresponding points are joined by straight lines. Each of these lines is divided into an equal number of points, and the corresponding points on each line are joined in order to define a regular three-dimensional array of six-faced cells. These cells may be referred to as ‘deformed hexahedra’, but they differ from a hexahedron in that the faces are, in general, not plane. This means that they cannot be used in tracing the progression of the molecules through the flow and they must be subdivided into tetrahedra.

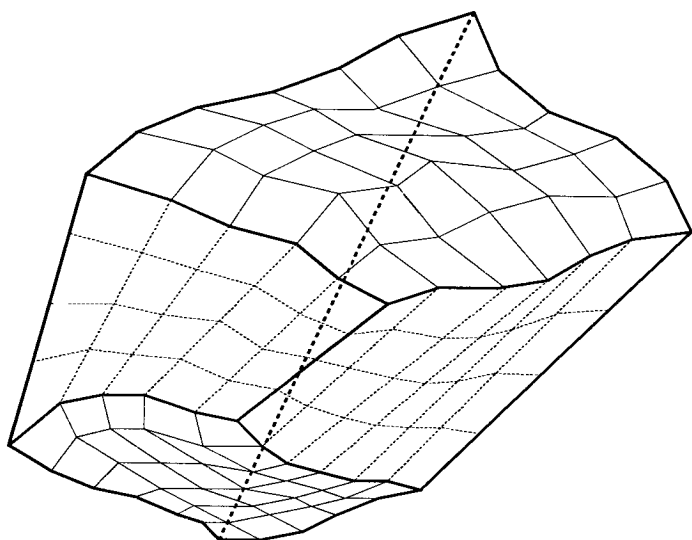


Fig. 16.1 An irregularly shaped six-faced region with an ordered array of cell columns, rows and slices.

Two of the faces of each region (the upper and lower in Fig. 16.1) may have double curvature because there is no restriction on the locations of the array of points that define it. The points on the other faces must lie along a series of straight lines and the geometry of these faces is effectively limited to single curvature. Each face may be a solid surface, a plane of symmetry, an interface with a uniform or non-uniform flow, a vacuum, or an interface with other regions. Despite the restriction on the degree of curvature of four of the sides, the spatial domain of almost all problems can be divided into regions of this type. The molecules are traced through the flow by calculating the successive collisions of the molecules with the faces of the tetrahedra.

After the division into tetrahedra, the region boundaries become a set of triangular plane elements. Each of the deformed hexahedra may be divided into one 'central' and four 'corner' tetrahedra as shown in Fig. 16.2. Alternatively, each hexahedron may be divided across one of the 'diagonal planes' into two solid elements with three four-sided and two triangular faces. Each of these elements may then be divided into three tetrahedra, as shown in Fig. 16.3 for the right-hand-side element. The 'six-tetrahedron scheme' is to be preferred over the 'five-tetrahedron scheme' which can break down for the very thin hexahedra that are often required in regions with high flow gradients. The breakdown occurs when the tetrahedron edges that join the opposite corners of one face intersect with the opposite face. In addition, the tetrahedra serve as sub-cells and there is less average separation of the collision pairs in the alternative scheme.

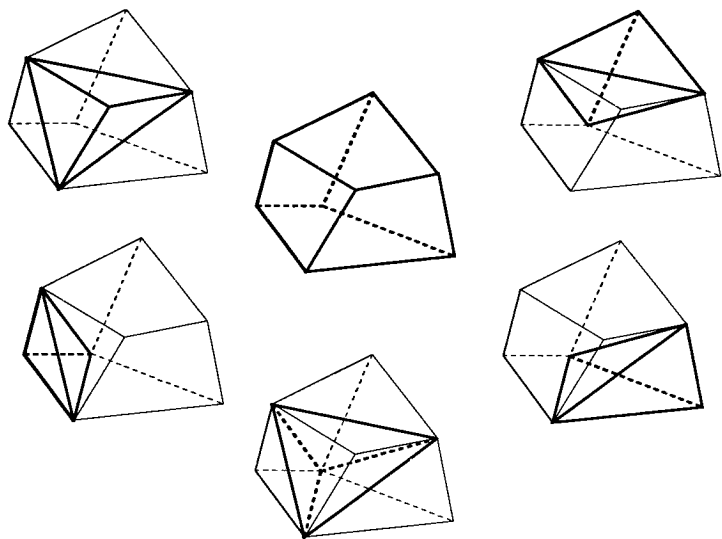


Fig. 16.2 The subdivision of a 'deformed hexahedral' cell into five tetrahedral sub-cells.

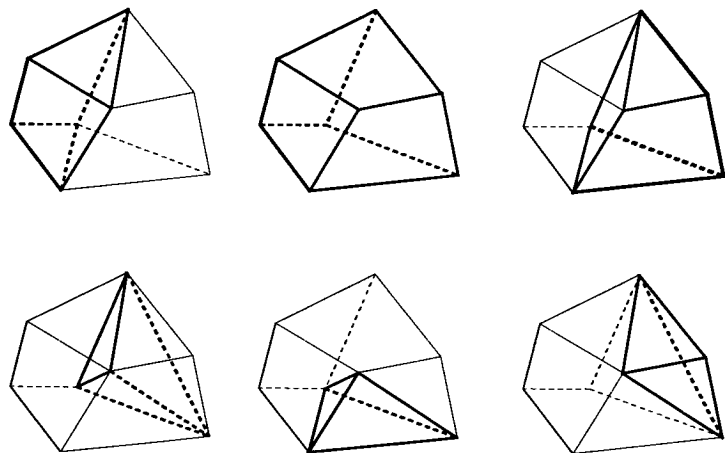


Fig. 16.3 The subdivision of a 'deformed hexahedral' cell into six tetrahedral sub-cells.

As noted earlier, the indexing of each molecule to the cells requires the calculation of the intersection point of its trajectory with each tetrahedral face through which it passes. This is not only expensive in terms of computation time, but round-off error is a serious problem. It can be seen from Fig. 16.3 that up to 24 tetrahedra can meet at a single node of the grid. When a molecule passes extremely close to a node, the round off error may place it into the wrong tetrahedron and it then becomes 'lost'. It has been found that, if lost molecules are simply discarded from the calculation, the resulting error can be unacceptable unless double precision arithmetic is employed. It may be necessary to introduce 'recovery' procedures to deal with these lost molecules and to also cope with the gaps that can develop in the flowfield if there is a change in grid spacing at an interface between regions.

This scheme has been employed in a number of studies (e.g. Celenligil and Moss 1992), but the labour that is necessary for the generation of the mass of data that is required for the specification of a complex application can pose a problem that is even more serious than the computation time. Some form of automatic grid generation is necessary in practice and the protocols that must be followed in the specification of multiple regions leads to difficulties with the logic. The objective is to develop a code that requires only the specification of the boundaries, either as sets of coordinates or analytical expressions, and the flow conditions. The program should itself generate the grid and, ideally, it should adapt the grid to its optimal form as the flow develops.

One possible solution is to replace the structured tetrahedral grid by an unstructured tetrahedral grid of the type that has been widely used in applications of the finite element method. Each triangular face within the grid either lies on a boundary or is an interface between two adjacent tetrahedra. The molecules are again followed through their intersections with these triangular faces. The challenge is to develop procedures that efficiently generate a near-optimal grid and to minimize the amount of information that must be stored for each tetrahedral element.

Another option is to extend to three-dimensions the scheme that was described under heading (viii) in §14.1. That scheme employed cells that were aggregated from small sub-cells, with the surface being described by small straight line segments in the appropriate sub-cells. However, it is difficult to extend this to three dimensions because of the complexity of the possible interaction of surfaces with three-dimensional sub-cells. An alternative is to subdivide the sub-cells through which the surfaces pass into much smaller rectangular elements and to define the surface by marking some of these elements as 'surface elements'. While this causes the surface to have a stepped structure, the correct direction cosines of the surface normal may be stored for each element, and the approximation that is introduced through this process then becomes one of resolution rather than of shape. This scheme should lead to satisfactory results as long as the surface elements are smaller than the local mean free path in the flow.

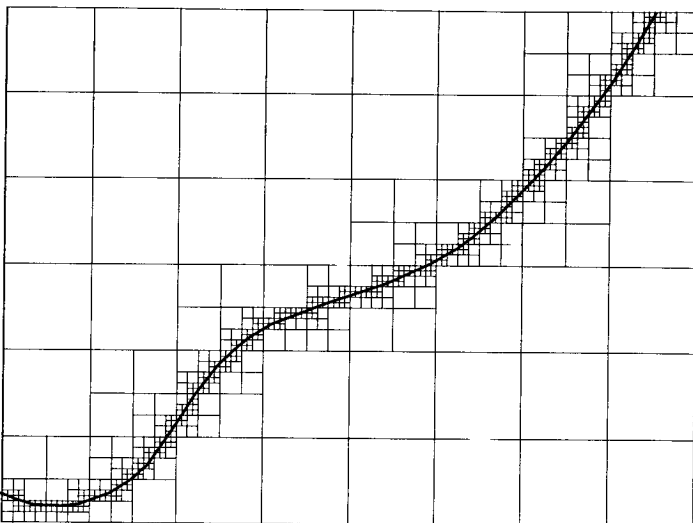


Fig. 16.4 The division of sub-cells to a depth of four for the definition of surface elements.

This scheme has been implemented (Bird 1990) for the Shuttle orbiter geometry. The sub-cell array was $60 \times 48 \times 42$ and the sub-cells containing surface elements were divided $8 \times 8 \times 8$. The linear dimension of a surface element was approximately 10 cm and, as expected, the error became significant at about 120 km altitude where the mean free path falls to 10 cm. This surface definition required only 2 Mb of memory but, to reduce the linear dimension of a surface element by a factor of ten to maintain accuracy to 15 km lower altitude, requires the number of surface elements to increase by a factor of 1000. The solution is to divide a cell into eight equal parts, then divide only those parts that include the surface into eight further parts, and so on. This procedure is illustrated in two dimensions in Fig 16.4. This scheme has been implemented to a depth of eight divisions such that the linear dimension of the element is reduced by a factor of 256. It was verified that the storage requirements for this scheme increase as the inverse square, rather than the inverse cube, of the element size. Only one integer is required for each of the elements at any depth of subdivision and, at the surface element level, the direction cosines and surface temperature are packed into this integer. Sub-cells and elements that do not include surface elements are also divided where necessary to produce smaller cells. The disadvantage of this scheme is that it is very complex and, while it permits much smaller elements, they retain a finite size and there are unavoidable side effects associated with this. For example, the edge of a surface cannot be thinner than the linear dimension of a surface element. The optimal grid scheme for engineering studies of complex three-dimensional flows of rarefied gases has yet to be determined.

16.2 Supersonic corner flow

The data in the disk listing of program DSMC3 is for the flow in the 'corner' between two flat plates that are perpendicular to one another and parallel to the stream. It is a basic three-dimensional flow that is related to the two-dimensional leading edge or flat plate problem that was the main test case for program DSMC2 in §14.3.

As noted above, program DSMC3 is a straightforward extension of program DSMC2 to three dimensions. The cell 'columns' in the x -direction and 'rows' in the y -direction are supplemented by cell 'slices' in the z -direction. The flowfield is a rectangular parallelepiped and each of its six faces may be either a plane of symmetry, an interface with a uniform stream, or a vacuum. The program does not have the option of a geometric progression for the cell size, and the cells must have a uniform width, height, and depth in the x -, y -, and z -directions, respectively. The surfaces must be plane and lie along an interface between cell rows, columns, or slices. They must be rectangular in shape and must terminate at cell boundaries. The surfaces may lie along a flowfield boundary as long as the boundary is otherwise a plane of symmetry. A uniform jet may be present in addition to the external stream, but its dimensions are no longer tied to the cell boundaries and it must be circular in cross-section.

The two-dimensional calculation in §14.3 employed a 100×60 cell grid with four sub-cells per cell. The three-dimensional calculation is of a similar computational magnitude if the cell grid is $30 \times 18 \times 18$ with no sub-cells. The stream is argon at a temperature of 300 K and a number density of 10^{20} m^{-3} at a Mach number of 6, and is parallel to the x -axis. The width, height, and depth of the cells is 0.01 m and the 30 cells are along the x -axis. The leading edge of the plates is five cells from the upstream face of the flowfield at $x=0$ and the surfaces cover the remainder of the $y=0$ and $z=0$ planes. Diffuse reflection is assumed and the surfaces are at a uniform temperature of 1000 K. The freestream mean free path is 0.0129 m and the cell size is greater than the recommended value for DSMC computations.

Program DSMC2 was used to make calculations for the corresponding two-dimensional flow to which the three-dimensional flow can be expected to tend at large distances from the corner. Because of the marginal cell size in the three-dimensional calculation, the two-dimensional calculation was first made for a 30×18 grid with no sub-cells that corresponds to the three-dimensional grid. It was then repeated for a 60×36 grid with two sub-cells per cell in each direction. The latter grid easily meets the requirements of the DSMC method.

The distribution of the pressure coefficient over the plates is shown in Fig. 16.5. The flow is symmetrical about a plane that includes the x -axis and bisects the angle between the plates. This means that the contours on each plate should ideally be identical and they are, in fact, very similar. The results from the corresponding two-dimensional calculations for the distribution of the pressure coefficient are shown in Fig. 16.6.

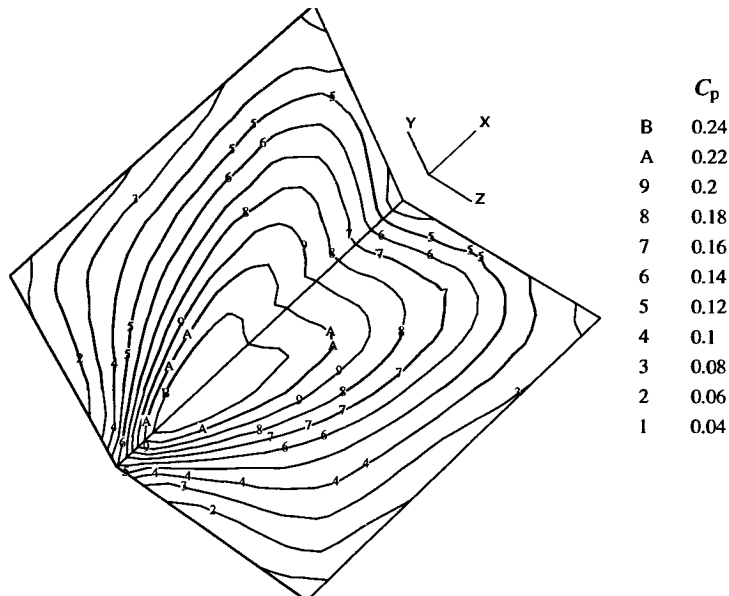


Fig. 16.5 Contours of pressure coefficient over the surfaces.

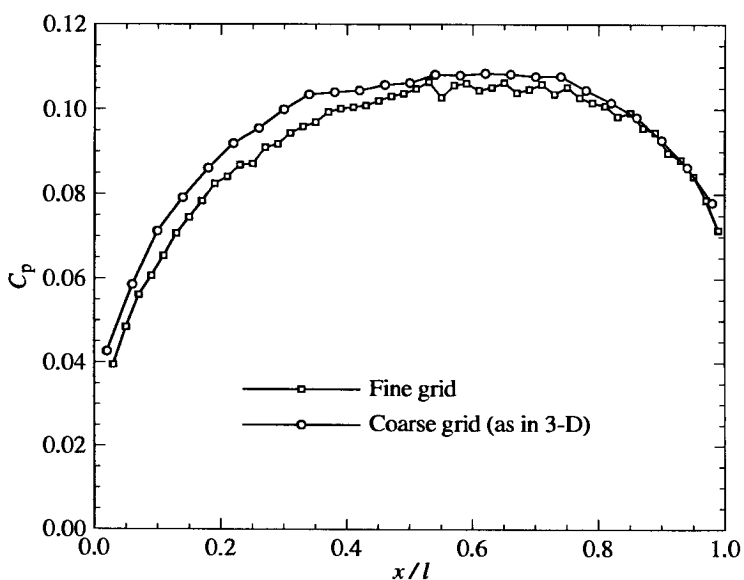


Fig. 16.6 The distribution of pressure coefficient over the corresponding two-dimensional flat plate.

The length l of the plate is 23.26 freestream mean free paths so that the overall Knudsen number is 0.043. The two-dimensional pressure distribution has a maximum at about 15 freestream mean free paths from the leading edge. A comparison with Fig. 14.12, which is for a diatomic gas at $(Ma)=4$ and $(Kn)=0.0143$, shows that the pressure maximum is now further from the leading edge. As expected from the study of cell size in §14.4, the coarse grid that is used in the three-dimensional calculations causes the pressure over the forward half of the plate to be up to 8% too high. This systematic error should be kept in mind when interpreting the three-dimensional results. The boundary condition at the outer planes that are defined by $y=0.18$ and $z=0.18$ is an undisturbed freestream rather than a plane of symmetry, and this would be expected to lead to some reduction in the pressure near these boundaries. The pressure distribution along these outer boundaries is about 20% less than the two-dimensional pressures.

The pressure coefficient along the junction between the plates has a maximum at about $x/l=0.3$. This maximum is also the maximum pressure on the plates and its value is just twice the maximum pressure in the two-dimensional case. The pressure at the trailing edge of the junction is less than 50% greater than the trailing edge pressure in the two-dimensional case. The downstream boundary is specified as a stream boundary and, at this Mach number, there is effectively no difference between this and a vacuum boundary. It is possible that the effects of this boundary condition extend further upstream in the corner than in the outer part of the flow or in the two-dimensional case.

The corresponding three-dimensional and two-dimensional results for the net heat transfer coefficient are shown in Figs 16.7 and 16.8. The effect of cell size is similar to that for the pressure coefficient. The heat transfer coefficient at the outer edge is only about 10% less than in the two-dimensional case. It increases towards the junction between the plates, but there is a reduction very close to the junction and the maximum heat transfer occurs in two lobes that are some mean free paths from the junction. The maximum heat transfer is less than 50% higher than the maximum two-dimensional heat transfer, so that the proportional increase is less than that for the pressure. The reduction close to the junction becomes more pronounced towards the trailing edge and the heat transfer at the trailing edge of the junction is only one third of the minimum heat transfer to the two-dimensional plate.

The results for the skin friction coefficient based on the component of shear stress in the x -direction are shown in Figs 16.9 and 16.10. The effect of cell size is similar to that in the other cases, but the skin friction at the outer edge shows almost no reduction on the two-dimensional distribution. The general form of the contours is remarkably similar to that for the net heat transfer coefficient. The values of the skin friction coefficient are of the order of twice the net heat transfer coefficient. This indicates that the 'Reynolds analogy' between heat transfer and skin friction may sometimes be a useful approximation for rarefied gas flows.

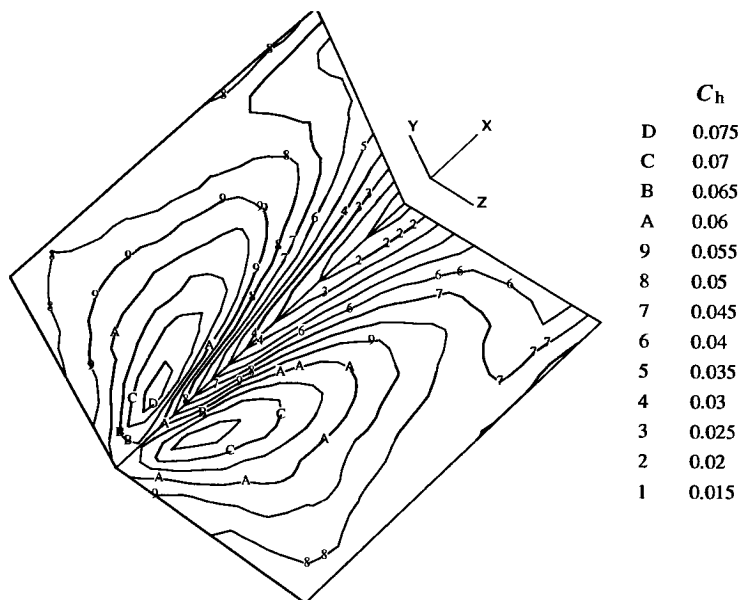


Fig. 16.7 Contours of constant value of the heat transfer coefficient in the three-dimensional case.

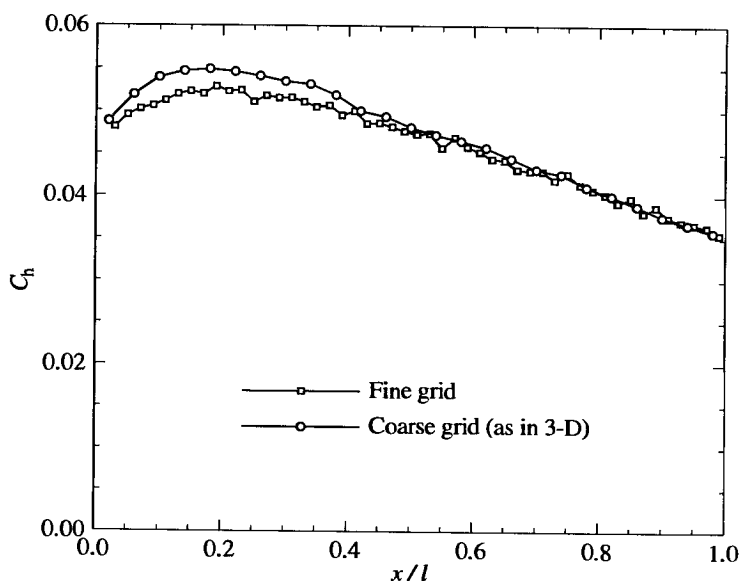


Fig. 16.8 The heat transfer distribution in the two-dimensional case.

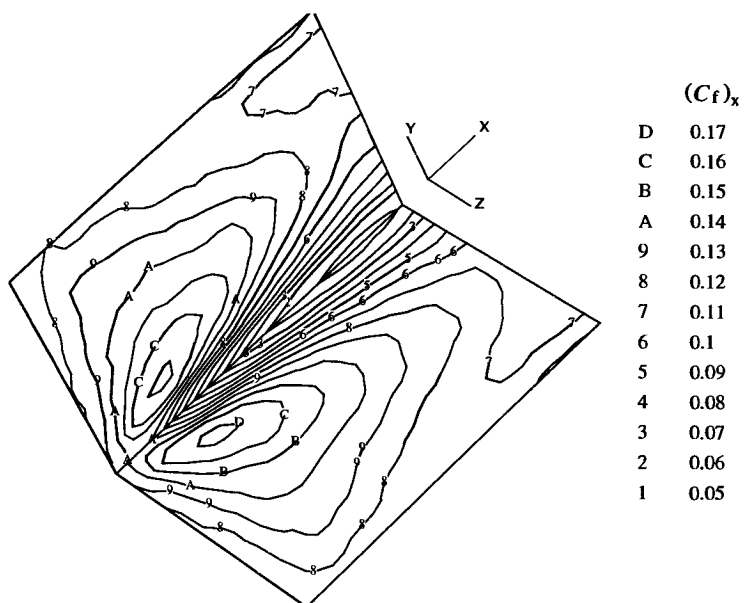


Fig. 16.9 The streamwise skin friction coefficient in the corner flow.

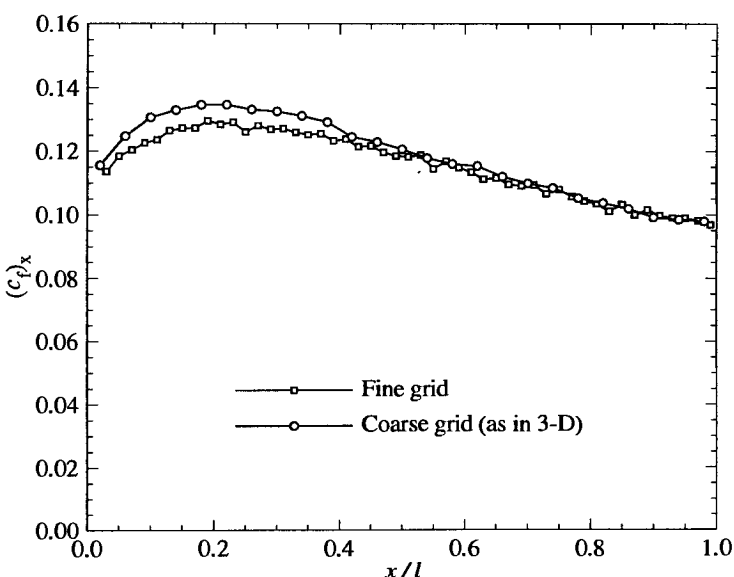


Fig. 16.10 The distribution of the streamwise skin friction coefficient in the two-dimensional case.

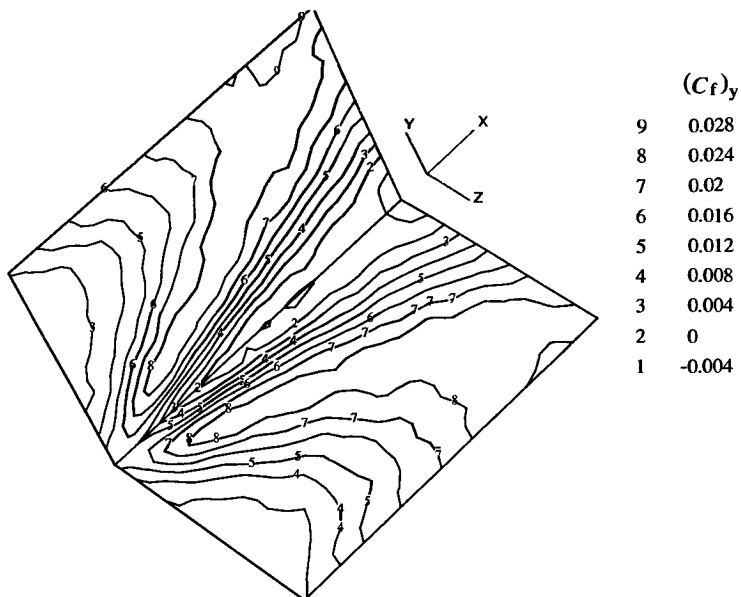


Fig. 16.11 The normal skin friction coefficient in the corner flow.

The skin friction coefficient in the direction normal to the streamwise direction is denoted by $(c_f)_y$ and the contours of constant value of this coefficient are shown in Fig. 16.11. As would be expected, this coefficient increases towards the trailing edge and toward the outer part of the plate. The flow near the junction of the plates appears to be directed toward the junction over most of the span, but the negative skin friction coefficients are very small in magnitude. The magnitude of the normal coefficient is generally small in comparison with that of the streamwise skin friction coefficient.

Finally, Figs 16.12 to 16.14 show, respectively, contours of constant value of temperature, density, and Mach number in a number of planes normal to the streamwise direction. The density contours are qualitatively different from the temperature and Mach number contours, and the most interesting feature of these contours is the isolated region of high density that develops on the plane of symmetry. The contours in the plane nearest the leading edge approach the expected two-dimensional configuration in the outer region of the flow, but those near the trailing edge show that the computational grid would have to be very much larger if the transition to a two-dimensional flow was to be adequately covered. The gas in the vicinity of the corner has a high temperature and density, but a very small velocity. The slip velocity increases at the outer edge of the plate and this is associated with the 'stream' boundary condition. Low subsonic velocities occur only in a small region near the corner.

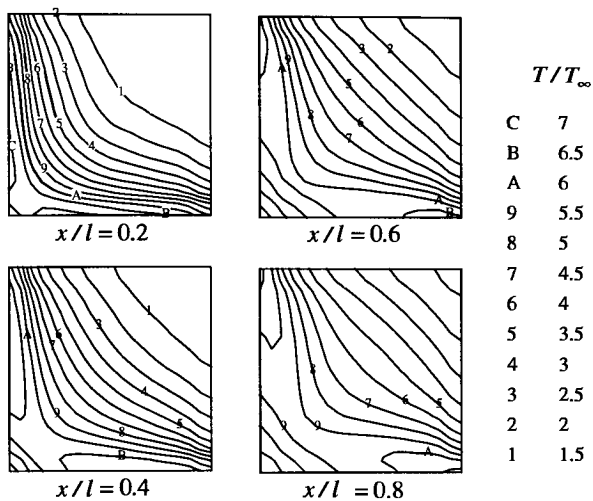


Fig. 16.12 Temperature contours in planes normal to the plates.

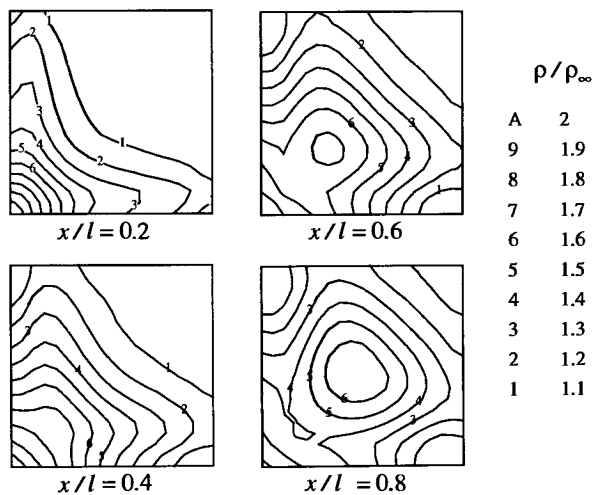


Fig. 16.13 Density contours in planes normal to the plates.

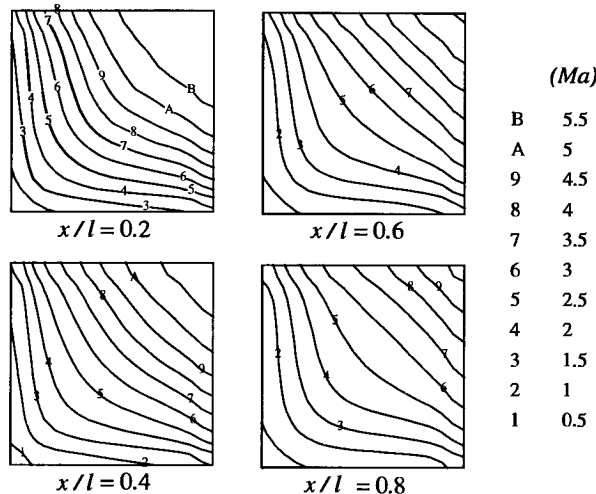


Fig. 16.14 Mach number contours in planes normal to the plates.

16.3 Finite span flat plate at incidence

The flow of argon at a Mach number of 5 about a two-dimensional flat plate was studied in §14.8. The main test case was for an incidence of 30° and an overall Knudsen number of 0.043. This Knudsen number is too low for a three-dimensional calculation of the magnitude to which these test cases are limited. However, the $30 \times 18 \times 18$ grid that was used in the previous application of program DSMC3 allows calculations for a three-dimensional plate with an aspect ratio of two at an overall Knudsen number of 0.108. The stream direction is normal to the z -axis and the $z=0$ plane is a plane of symmetry. The other boundaries are interfaces with the uniform stream. The double-sided surface that forms the flat plate lies along the lower boundary of the ninth cell row. It extends from the start of cell column 10 to the end of column 21 in the x -direction and from the plane of symmetry to the end of slice 12 in the z -direction. The half of the plate that is in the computational region therefore has a square planform. As in the two-dimensional case, the temperature of the upstream or lower side of the plate is equal to the stream stagnation temperature, and the downstream or upper side is at the stream static temperature. The surface reflection is diffuse with complete thermal accommodation. The high temperature of the lower surface minimizes the density increase, but the cell size is again larger than is recommended for DSMC computations.

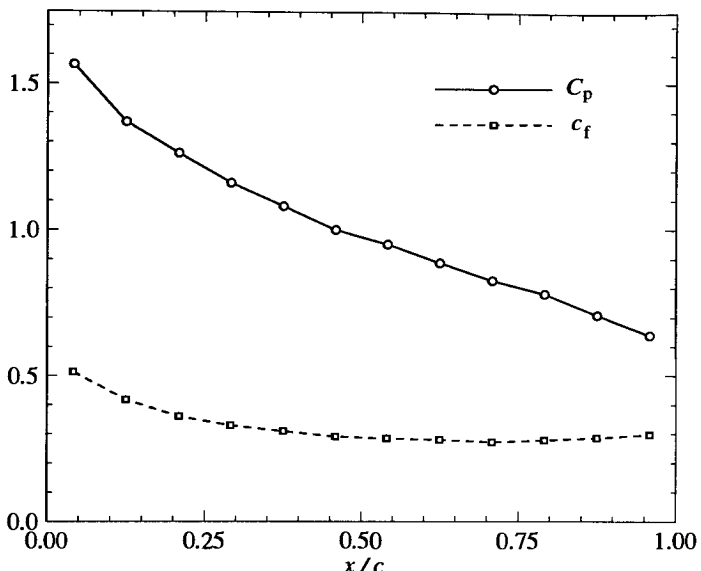


Fig. 16.15 Contours of the pressure coefficient over the lower surface.

The pressure distribution over the lower surface is shown in Fig. 16.15. The corresponding results for the streamwise and spanwise skin friction coefficients are shown in Figs 16.16 and 16.17, respectively. The distributions of pressure and skin friction that are obtained from program DSMC2 for the corresponding two-dimensional flow are shown in Fig 16.18. The two-dimensional calculation employs a grid with the same resolution, so that the errors due to the coarser than recommended grid should be similar. There is good agreement between the three-dimensional results at the plane of symmetry and the two-dimensional results. The increase in the skin friction coefficient near the trailing edge is due to the acceleration of the flow in this region, but it is less pronounced than in Fig. 14.44 for a lower Knudsen number.

The effects due to the finite span show primarily as gradients in the spanwise direction, and these increase with proximity to the tip. However, at the trailing edge, there appears to be a small reduction in pressure and the development of a spanwise shear stress component that persists almost to the plane of symmetry. The major effect on the pressure distribution is a reduction in the pressure near the leading edge and towards the tip. The relative change in the streamwise shear stress is slightly larger than that for the pressure. The spanwise skin friction coefficient becomes significant near the tip, but it is small in comparison with the streamwise coefficient.

Finally, Fig. 16.19 shows some contours of constant Mach number in planes over the plate that are normal to the stream direction.

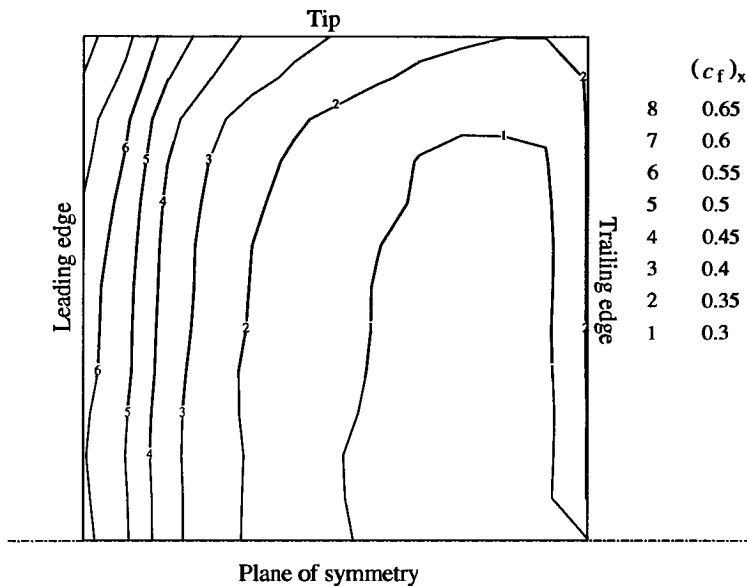


Fig. 16.16 The streamwise skin friction coefficient on the lower surface.

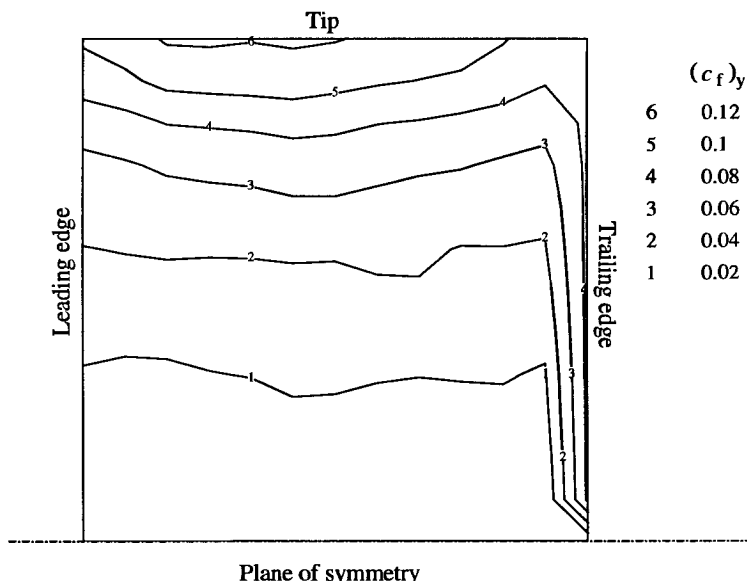


Fig. 16.17 The spanwise skin friction coefficient on the lower surface.

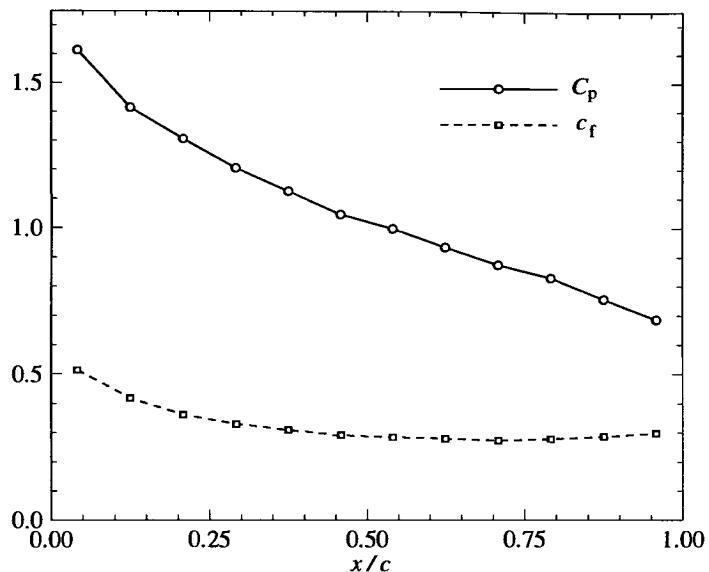


Fig. 16.18 The pressure and skin friction distribution along the lower surface of the corresponding two-dimensional flow.

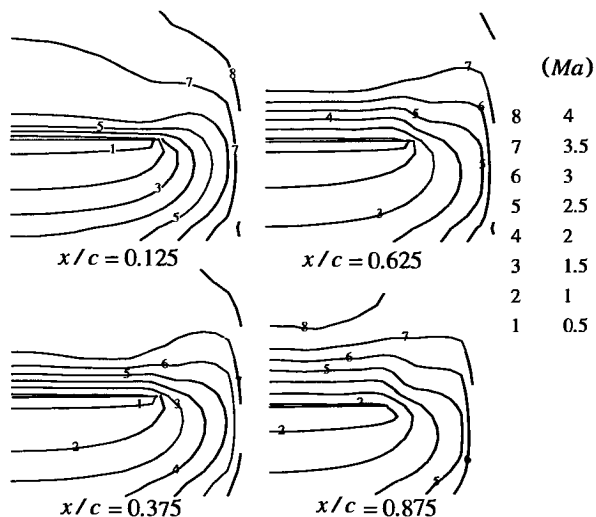


Fig. 16.19 Mach number contours in planes normal to the stream.

16.4 Corner flow with normal jet plume

The final demonstration flow takes advantage of the jet option in program DSMC3 to add a jet plume to the supersonic corner flow of §16.2. The constraints on the data force the exit plane of the jet to lie in the $y=0$ plane and the exit flow must be in the positive y -direction. The radius of the jet is 0.03 m and its centre is at $x=0.15$, $z=0.09$. This location is at 40% of the length of the surface and midway between the junction between the surfaces and the outer boundary. The exit plane density is three times the stream density, while its composition, temperature, and speed are equal to the corresponding stream values. No other changes were made to the data that led to the results in §16.2 for the supersonic corner flow.

The addition of the plume causes the corner flow to lose its symmetry about the plane that bisects the angle between the horizontal and vertical surfaces. The contours of constant value of the pressure coefficient, the resultant (rather than the components of the) skin friction coefficient, and the heat transfer coefficient are shown in Figs 16.20 to 16.22. The extent to which the jet modifies the flow may be seen from a comparison of these figures with Figs 16.5 to 16.11. The most striking feature is the region of high pressure, shear stress, and heat transfer that develops on the vertical surface. The distribution of heat transfer is again similar to that for the shear stress.

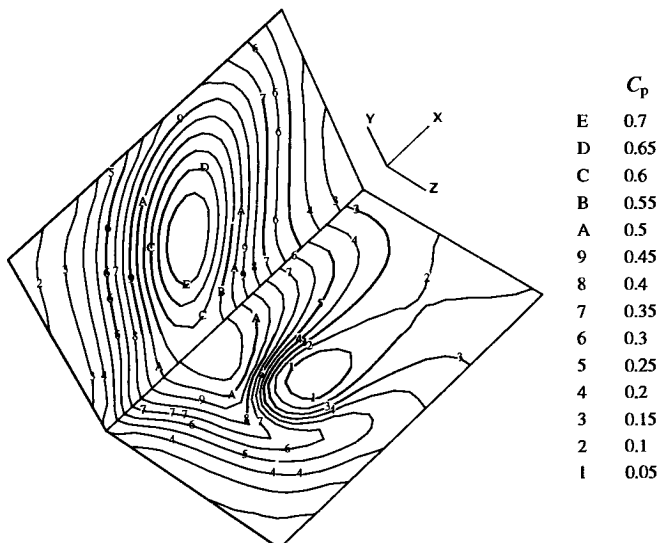


Fig. 16.20 The corner flow pressure distribution in the presence of a jet with its efflux plane in the xz -plane.

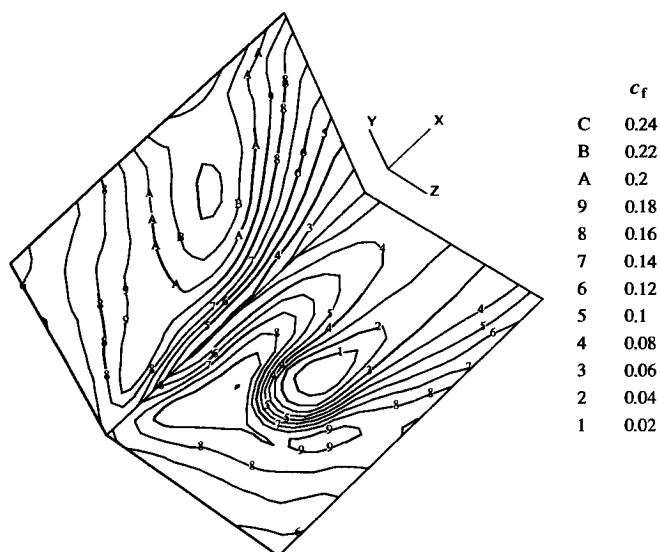


Fig. 16.21 The distribution of the skin friction coefficient.

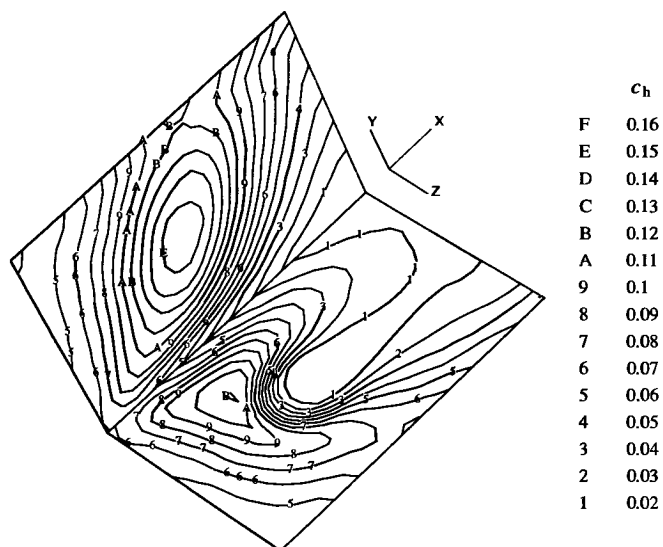


Fig. 16.22 The distribution of the heat transfer coefficient.

16.5 Concluding remarks

The applications of the demonstration programs have been limited to cases that require no more than 24 hours of computation time on a contemporary 'top of the line' personal computer. This has been taken to be an 'IBM compatible' machine equipped with an Intel i486 running at 66 Mhz. In addition, the problems have been restricted to a memory requirement of 6 Mb. By the time that this book is published, the speed and memory capacity of personal computers will have doubled. This doubling of capability has, over the past fifteen years, occurred at intervals of about two years and this rate of progress can be expected to continue.

The computational limits were not a significant factor in the choice of problems for homogeneous and one-dimensional flow problems. These flows can be calculated with a sufficiently high sample size that the statistical scatter is reduced to less than one per cent. Moreover, test calculations can be made for conditions that fall within the range of validity of the continuum equations.

Two-dimensional calculations at 'continuum Knudsen numbers' require computer resources that exceed the limits that have been applied here to the demonstration cases.

Three-dimensional calculations are much more difficult and it is not yet possible to make three-dimensional calculations for non-trivial applications in the continuum regime. The degree of difficulty that is now associated with these calculations is, however, comparable to that which applied to two-dimensional flows twenty years ago.

References

- BIRD, G.A. (1990). Application of the direct simulation Monte Carlo method to the full Shuttle geometry, Am. Inst. Aero. Astro., Paper AIAA-90-1692.
- CELENLIGIL, M.C. and MOSS, J.N. (1992). Hypersonic rarefied flow about a delta wing – direct simulation and comparison with experiment, *AIAA Journal*, **30**, 2017–2023.

APPENDIX A

Representative gas properties

Representative gas properties have been used to illustrate the theory and, more importantly, they are necessary for the application of the DSMC demonstration programs. The relationship between the molecular models and the real gas is based primarily on the coefficient of viscosity, together with the power law of the variation of this coefficient with temperature. Table A1 is based on the data in Chapman and Cowling (1970).

Table A1 Properties under standard conditions (101,325 Pa and 0°C).

Gas	Symbol	Degrees of freedom ξ	Molecular mass $m \times 10^{27} \text{ kg}$	Viscosity coefficient $\mu \times 10^5 \text{ Nsm}^{-2}$	Viscosity index ω
Hydrogen	H ₂	5	3.34	0.845	0.67
Helium	He	3	6.65	1.865	0.66
Methane	CH ₄	6.4	26.63	1.024	0.84
Ammonia	NH ₃	6.25	28.27	0.923	1.1
Neon	Ne	3	33.5	2.975	0.66
Carbon monoxide	CO	5	46.5	1.635	0.73
Nitrogen	N ₂	5	46.5	1.656	0.74
Nitric oxide	NO	5	49.88	1.774	0.79
Sea level air		5	48.1	1.719	0.77
Oxygen	O ₂	5	53.12	1.919	0.77
Hydr'n chloride	HCl	5	61.4	1.328	1.0
Argon	Ar	3	66.3	2.117	0.81
Carbon dioxide	CO ₂	6.7	73.1	1.380	0.93
Nitrous oxide	N ₂ O		73.1	1.351	0.94
Sulphur dioxide	SO ₂		106.3	1.164	1.05
Chlorine	Cl ₂	6.1	117.7	1.233	1.01
Krypton	Kr	3	139.1	2.328	0.8
Xenon	Xe	3	218.	2.107	0.85

Eqn (4.62) with $\alpha = 1$ then gives the following reference diameters for the VHS molecular model.

Table A2 VHS molecular diameters at 273 K.

Gas	Diameter ($d \times 10^{10}$ m)	Gas	Diameter ($d \times 10^{10}$ m)	Gas	Diameter ($d \times 10^{10}$ m)
H ₂	2.92	N ₂	4.17	CO ₂	5.62
He	2.33	NO	4.20	N ₂ O	5.71
CH ₄	4.83	Air	4.19	SO ₂	7.16
NH ₃	5.94	O ₂	4.07	Cl ₂	6.98
Ne	2.77	HCl	5.76	Kr	4.76
CO	4.19	Ar	4.17	Xe	5.74

The VSS molecular model can reproduce the measured values of the coefficient of diffusion as well as the coefficient of viscosity. With regard to diffusion between unlike molecules, and noting that the diameter for the cross-collisions is not necessarily equal to the mean of the diameters of the individual species, the matching of diffusion and viscosity coefficients does not lead to a unique set of parameters. In fact, a cross-collision diameter could be chosen to achieve this match even for the VHS molecule. However, the requirement for consistency between the viscosity and self-diffusion coefficients in a simple gas does lead to a uniquely defined value of α for simple gases.

Eqn (3.76) can be used to write the diameter of a VSS molecule in terms of the self-diffusion coefficient D_{11} as

$$d = \left(\frac{3(\alpha+1)(kT_{\text{ref}})^{\omega}}{8\Gamma(7/2-\omega)(\pi m)^{1/2} n(D_{11})_{\text{ref}} E_t^{\omega-1/2}} \right)^{1/2}. \quad (\text{A1})$$

This may be combined with eqn (3.74) to relate α directly to the Schmidt number (Sc), i.e.

$$(Sc) \equiv \frac{\mu_{\text{ref}}}{\rho(D_{11})_{\text{ref}}} = \frac{2+\alpha}{(3/5)(7-2\omega)\alpha}. \quad (\text{A2})$$

For a hard sphere gas (Sc) reduces to $5/6$, and this is the subject of much discussion in Chapman and Cowling (1970). Reliable data for the self-diffusion coefficient is available for many gases from experiments with isotopes. The values of α from this data are presented in Table A3. The change in α from the VHS value of unity also leads to a small change in the reference diameter from eqn (4.62), and this is also tabulated.

Table A3 VSS molecular parameters

Gas	$\rho D_{11}/\mu$	α	d (at 273 K) $\times 10^{10} \text{ m}$
H ₂	1.37	1.35	2.88
He	1.32	1.26	2.30
CH ₄	1.42	1.60	4.78
Ne	1.35	1.81	2.72
CO	1.42	1.49	4.12
N ₂	1.34	1.86	4.11
O ₂	1.35	1.40	4.01
HCl	1.33	1.59	5.59
Ar	1.33	1.40	4.11
CO ₂	1.375	1.61	5.54
Kr	1.29	1.32	4.70
Xe	1.33	1.44	5.65

The above values of α are for temperatures of the order of the standard temperature. Chapman and Cowling (1970) report data on Kr at 473 K and Xe at 378 K, and the corresponding values for α are 1.29 and 1.40, respectively. Data is also given for Ne, N₂, and O₂ at 78 K. The value of α for Ne is unchanged, but those for N₂ and O₂ increase to 1.52 and 1.45, respectively. Given the restricted temperature range and the uncertain accuracy of the data, it is not clear whether α can reasonably be regarded as a constant in applications that involve large changes in temperature.

Data is also available in Chapman and Cowling (1970) for the coefficient of diffusion D_{12} between a large number of gas pairs and, for some of these, the temperature exponent ω_{12} is also available. This data defines the reference values of these quantities, and the reference diameter $(d_{12})_{\text{ref}}$ will be assumed to be given by the mean value, as in eqn (1.35). Eqns (3.75) and (4.61) may then be combined to give the appropriate value of the VSS scattering parameter α_{12} as

$$\alpha_{12} = \frac{8(5-2\omega_{12})n(D_{12})_{\text{ref}}\pi(d_{12})_{\text{ref}}^2}{3(2\pi k T_{\text{ref}}/m_r)^{1/2}} - 1. \quad (\text{A3})$$

The resulting values of the VSS scattering parameter are presented in Table A4. For the cases in which a value of ω_{12} is not available, this parameter may be set to the mean value of ω for the two species. It should be noted that these are not the only sets of parameters that reproduce the transport properties.

Table A4 VSS parameters for cross-collisions.

Pair	α_{12}	ω_{12}	S_C	Pair	α_{12}	ω_{12}
H ₂ -He	1.20		0.234	Ne-CO ₂	1.97	0.83
H ₂ -CH ₄	1.54		0.694	Ne-Kr	1.59	
H ₂ -CO	1.33		0.715	Ne-Xe	1.84	
H ₂ -N ₂	1.41		0.74	CO-N ₂	1.54	
H ₂ -O ₂	1.32	0.78		CO-O ₂	1.54	0.71
H ₂ -Ar	1.47			CO-CO ₂	1.61	
H ₂ -CO ₂	1.69	0.84		N ₂ -O ₂	1.38	
He-Ne	1.28			N ₂ -Ar	1.33	
He-N ₂	1.50	0.69		N ₂ -CO ₂	1.87	0.75
He-O ₂	1.49			N ₂ -Xe	1.42	
He-Ar	1.64	0.725		O ₂ -Ar	1.33	
He-CO ₂	2.13	0.84		O ₂ -CO ₂	1.72	
He-Kr	1.81			O ₂ -Xe	1.34	
He-Xe	2.20			Ar-CO ₂	1.63	0.805
CH ₄ -O ₂	1.47	0.79		Ar-Kr	1.41	
CH ₄ -CO ₂	1.67			Ar-Xe	1.47	
CH ₄ -Ar	1.46			Kr-Xe	1.44	

The DSMC calculations that are presented in §12.2 to §12.7 verify that the reference values of the VHS and VSS parameters that are listed in Tables A1–A4 reproduce the transport properties of real gases at normal temperatures. The situation is less satisfactory for problems that involve very high temperatures in that reliable experimental values are not available.

Semi-empirical values of the viscosity of the components of air at high temperature have been given by Gupta et al. (1990). Their expression for molecular nitrogen is

$$\mu = 0.1 \exp(-11.8153) T^{0.0203 \ln(T) + 0.4329} \quad (A4)$$

This result is compared in Fig. A1 with that of Table A1. While the latter result is based on experiments at temperatures of the order of the standard temperature, its extrapolation to very high temperatures yields results that agree with eqn (A4) to within the uncertainty that is associated with this equation. The high-temperature calculations in this book have employed the low-temperature values, but the possible errors in these values at high temperatures should be kept in mind.

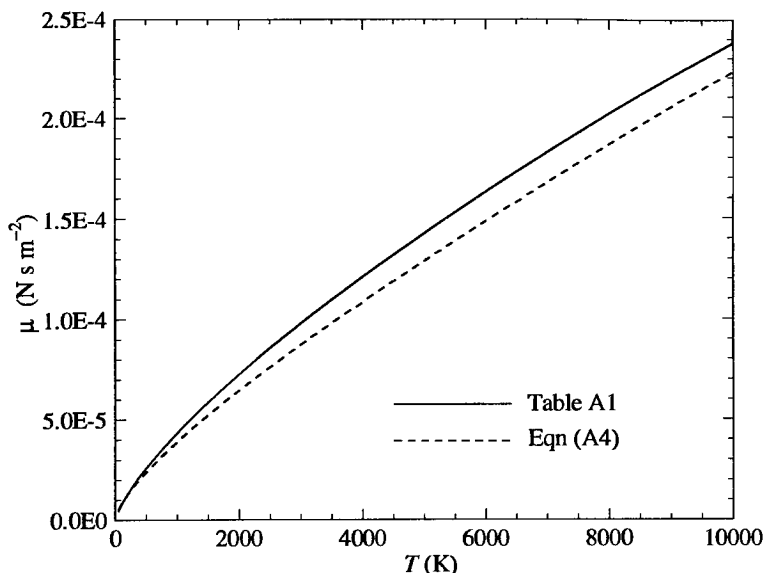


Fig. A1 Alternative values for the viscosity coefficient of molecular nitrogen at high temperatures.

The characteristic temperatures of rotation, vibration, dissociation, and ionization of typical diatomic molecules are listed in Table A5.

Table A5 Characteristic temperatures of diatomic molecules

Gas	Rotation Θ_r (K)	Vibration Θ_v (K)	Dissociation Θ_d (K)	Ionization Θ_i (K)
CH	20.4	4,102	40,300	129,000
Cl ₂	0.35	801	28,700	
CO	2.77	3,103	29,700	162,000
H ₂	85.4	6,159	52,000	179,000
N ₂	2.88	3,371	113,500	181,000
NO	2.44	2,719	75,500	108,000
O ₂	2.07	2,256	59,500	142,000
OH	26.6	5,360	50,900	,

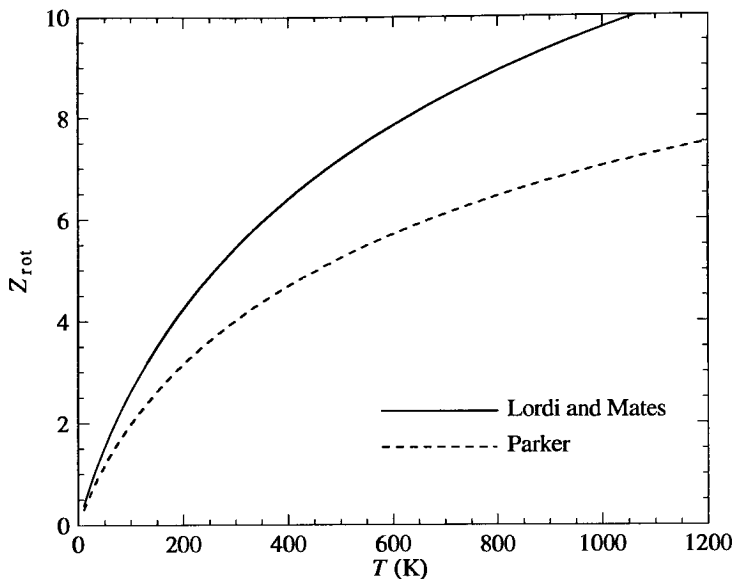


Fig. A2 Rotational relaxation collision number for air.

As noted in §1.7, rotation can generally be regarded as being fully excited, but data is needed for the rotational relaxation collision number Z_{rot} . Values have been inferred from a variety of experiments and, while these are subject to a considerable degree of scatter (Lumpkin et al. 1989), they are generally consistent with predictions based on the Landau-Teller model. Parker (1959) employed the equation

$$Z_{\text{rot}} = \frac{Z_{\text{rot}}^{\infty}}{1 + (\pi^{1/2}/2)(T^*/T_{\text{tr}})^{1/2} + (\pi + \pi^2/4)(T^*/T_{\text{tr}})} \quad (\text{A5})$$

with $Z_{\text{rot}}^{\infty} = 15.7$ and $T^* = 80.0$. When the data of Lordi and Mates (1970) is fitted to this equation the values are $Z_{\text{rot}}^{\infty} = 23.0$ and $T^* = 91.5$. The results from the two sets of coefficients are plotted in Fig. A2 for temperatures up to 1200 K. Little experimental data is available at higher temperatures, but Lumpkin et al. have proposed a model for nitrogen that predicts a reduction in Z_{rot} at higher temperatures. The values in this model depend on the ratio of the rotational to translational temperature as well as the overall temperature. The demonstration programs make provision for Z_{rot} to be specified as a second-order polynomial in the overall temperature. This is adequate for the approximation of eqn (A5) over a restricted temperature range, but would not cope with the more complex model in the context of a hypersonic flow calculation. Modified coding would be required and, since Z_{rot} is used in the collision subroutine, a table look-up would be preferable to repeated evaluation of the equation.

The vibrational relaxation rate is discussed in §6.7 where it was shown that the Millikan and White (1963) expression for the vibrational collision number can be put into the form

$$Z_v = (C_1/T^\omega) \exp(C_2 T^{-1/3}), \quad (A6)$$

where C_1 and C_2 are constants. Table A6 presents tentative values of these constants based on the data of Millikan and White. The values are for molecule 1 in a collision with 'molecule' 2. Note that values of C_1 and C_2 that are individually very different can lead to similar results for Z_v as a function of temperature.

Table A6 Constants for the evaluation of the vibrational collision number.

Molecule 1	Molecule 2	C_1	C_2
N_2		9.1	220.0
O_2		56.5	153.5
F_2		1007.0	65.0
CO		37.7	175.0
CO	Ar	7.27	221.
CO	He	1200.0	97.0
CO	H_2	2100.0	68.7
O_2	Ar	50.6	163.0
O_2	He	1950.0	65.8
O_2	H_2	4070.0	40.4
Cl_2		924.0	57.9
I_2		1750.0	29.0

The vibrational excitation program DSMC0V employs the levels that are given by the harmonic oscillator model and the characteristic vibrational temperature is the only data that is required. On the other hand, program DSMC0D employs anharmonic levels and the test case made use of the comprehensive data that has been assembled by Herzberg (1950). This is semi-empirical and the levels for nitrogen were expressed as eqn (11.35). The first coefficient is the characteristic temperature and the value of this is slightly different from that in Table A5. Variations of this order are generally present in data from different sources. The distribution of vibrational levels in other molecules are readily obtained from the data of Herzberg.

The chemical reaction rate theory of §6.6 and the comparisons of the dissociation-recombination results from program DSMC0D with the equilibrium composition required data on the partition function that are defined in eqns (6.31) – (6.34). The translational function depends only on the temperature, while the rotational and vibrational functions require the characteristic temperatures that are listed in Table A5. This electronic function of eqn (6.34) requires additional data and values for the degeneracies and characteristic temperatures are implicit in the following expressions that have been listed by Hansen (1976). Additional terms become progressively significant as the temperature increases, and these values are recommended for temperatures below 20,000 K in the case of atoms and for temperatures below 10,000 K for molecules.

$$Q_{\text{el}}(\text{H}) = 2$$

$$Q_{\text{el}}(\text{N}) = 4 + 10 \exp(-27658/T) + 6 \exp(-41495/T)$$

$$\begin{aligned} Q_{\text{el}}(\text{O}) = & 5 + 3 \exp(-228.9/T) + \exp(-325.9/T) \\ & + 5 \exp(-22830/T) + \exp(-48621/T) \end{aligned}$$

$$Q_{\text{el}}(\text{N}_2) = 1$$

$$Q_{\text{el}}(\text{O}_2) = 3 + 2 \exp(-11393/T) + \exp(-18985/T)$$

$$Q_{\text{el}}(\text{NO}) = 2 + 2 \exp(-174.2/T)$$

$$Q_{\text{el}}(\text{H}_2) = 1$$

$$Q_{\text{el}}(\text{Cl}_2) = 1 + 6 \exp(-26345/T)$$

This Appendix is not intended to be a handbook for the best available data on the fullest possible range of gases. It merely provides reasonable values, for some common gases, of the physical quantities that are required for the application of the DSMC method. Alternative DSMC procedures would require different data. For example, the ‘equilibrium collision theory’ of §6.5 would require data on the chemical rate constants.

The values of the physical constants are included in the list of symbols.

References

- CHAPMAN, S. and COWLING, T.G. (1970). *The mathematical theory of non-uniform gases* (3rd edn), Cambridge University Press.
 GUPTA, R.N., YOS, J.M., THOMPSON, R.A., and LEE, K-P (1990). A review of reaction rates and thermodynamic and transport properties for an 11-species air model for chemical and thermal nonequilibrium calculations to 30 000 K, NASA Reference Publication 1232.

- HANSEN, C.F. (1976). *Molecular physics of equilibrium gases, a handbook for engineers*, NASA SP-3096.
- HERZBERG, G. (1950). *Spectra of Diatomic Molecules*, Van Nostrand, New York.
- LORDI, J.A. and MATES, R.E. (1970). Rotational relaxation in nonpolar diatomic gases, *Phys. Fluids* **13**, 291-308.
- LUMPKIN, F.E., CHAPMAN, D.R., and PARK C. (1989). A new rotational relaxation model for use in hypersonic computational fluid mechanics, Am. Inst. Aero. Astro., Paper AIAA-89-1737.
- MILLIKAN, R.C. and WHITE, D.R. (1963). Systematics of vibrational relaxation. *J. Chem. Phys.* **39**, 3209-3213.
- PARK, CHUL (1990). *Nonequilibrium hypersonic aerothermodynamics*, Wiley, New York.
- PARKER, J.G. (1959). Rotational and vibrational relaxation in diatomic gases, *Phys. Fluids* **2**, 449-462.

APPENDIX B

Probability functions and related integrals

B.1 The gamma function

The taking of moments of the distribution function leads to definite integrals of the form

$$\int_a^{\infty} v^n \exp(-\beta^2 v^2) dv. \quad (\text{B1})$$

For zero a , this integral is related to the gamma function and, in the general case, to the incomplete gamma function. The gamma function of argument j is defined by

$$\Gamma(j) = \int_0^{\infty} x^{j-1} \exp(-x) dx, \quad (\text{B2})$$

and, for j equal to zero or a positive integer,

$$\Gamma(j+1) = j!. \quad (\text{B3})$$

More generally, the reduction formula is

$$\Gamma(j+1) = j \Gamma(j). \quad (\text{B4})$$

The incomplete gamma function is required for finite values of a , and this is defined by

$$\Gamma(j, \alpha) = \int_{\alpha}^{\infty} x^{j-1} \exp(-x) dx, \quad (\text{B5})$$

and the reduction formula is

$$\Gamma(j, \alpha) = (j-1) \Gamma(j-1, \alpha) + \alpha^{j-1} \exp(-\alpha). \quad (\text{B6})$$

Note that

$$\Gamma(0, \alpha) = E_1(\alpha),$$

where $E_1(\alpha)$ is the exponential integral. Also,

$$\Gamma(\frac{1}{2}, \alpha) = \pi^{1/2} \operatorname{erfc}(\alpha^{1/2}),$$

where erfc is the complementary error function.

Alternative forms of the incomplete gamma function for $j > 0$ are

$$P(j, \alpha) \equiv \frac{\gamma(j, \alpha)}{\Gamma(j)} \equiv \frac{1}{\Gamma(j)} \int_0^\alpha x^{j-1} \exp(-x) dx, \quad (\text{B7})$$

and

$$Q(j, \alpha) \equiv 1 - P(j, \alpha) \equiv \frac{\Gamma(j, \alpha)}{\Gamma(j)} \equiv \frac{1}{\Gamma(j)} \int_\alpha^\infty x^{j-1} \exp(-x) dx. \quad (\text{B8})$$

Equation (B1) is integrable for the special case in which n is an integer. It is desirable to distinguish between odd and even values of n and between positive and negative values of a . We then have

$$\begin{aligned} \int_{\pm a}^{\infty} v^{2n} \exp(-\beta^2 v^2) dv &= \frac{(2n-1)(2n-3)\dots 1}{2^{n+1} b^{2n+1}} \pi^{\frac{1}{2}} \{1 \mp \operatorname{erf}(\beta a)\} \pm \\ &\pm \frac{(\beta a) \exp(-\beta^2 a^2)}{\beta^{2n+1}} \sum_{m=1}^n \left(\frac{1}{2^m} \frac{(2n-1)(2n-3)\dots 1}{\{2(n+1-m)-1\}\{2(n+1-m)-3\}\dots 1} (\beta a)^{2(n-m)} \right) \end{aligned} \quad (\text{B9})$$

and, noting that $0! = 1$,

$$\int_{\pm a}^{\infty} v^{2n+1} \exp(-\beta^2 v^2) dv = \frac{\exp(-\beta^2 a^2)}{2\beta^{2n+2}} \sum_{m=1}^{n+1} \left(\frac{n!}{(n+1-m)!} (\beta a)^{2(n+1-m)} \right). \quad (\text{B10})$$

For $n = 0, 1$, and 2 , these equations give:

$$\int_{\pm a}^{\infty} \exp(-\beta^2 v^2) dv = \frac{\pi^{\frac{1}{2}}}{2\beta} \{1 \mp \operatorname{erf}(\beta a)\} \quad (\text{B11})$$

$$\int_{\pm a}^{\infty} v \exp(-\beta^2 v^2) dv = \frac{\exp(-\beta^2 a^2)}{2\beta^2} \quad (\text{B12})$$

$$\int_{\pm a}^{\infty} v^2 \exp(-\beta^2 v^2) dv = \frac{\pi^{\frac{1}{2}}}{4\beta^3} \{1 \mp \operatorname{erf}(\beta a)\} \pm \frac{\beta a \exp(-\beta^2 a^2)}{2\beta^3} \quad (\text{B13})$$

$$\int_{\pm a}^{\infty} v^3 \exp(-\beta^2 v^2) dv = \frac{\exp(-\beta^2 a^2)}{2\beta^4} (1 + \beta^2 a^2) \quad (\text{B14})$$

$$\int_{\pm a}^{\infty} v^4 \exp(-\beta^2 v^2) dv = \frac{3\pi^{\frac{1}{2}}}{8\beta^5} \{1 \mp \operatorname{erf}(\beta a)\} \pm \frac{\beta a \exp(-\beta^2 a^2)}{2\beta^5} \left(\frac{3}{2} + \beta^2 a^2 \right) \quad (\text{B15})$$

$$\int_{\pm a}^{\infty} v^5 \exp(-\beta^2 v^2) dv = \frac{\exp(-\beta^2 a^2)}{2\beta^6} (2 + 2\beta^2 a^2 + \beta^4 a^4). \quad (\text{B16})$$

For the special case in which a is $-\infty$, eqns (B7) and (B8) show that

$$\int_{-\infty}^{\infty} v^{2n} \exp(-\beta^2 v^2) dv = 2 \int_0^{\infty} v^{2n} \exp(-\beta^2 v^2) dv \quad (\text{B17})$$

and

$$\int_{-\infty}^{\infty} v^{2n+1} \exp(-\beta^2 v^2) dv = 0. \quad (\text{B18})$$

For $a = 0$, the results are related to the gamma function and eqns (B7) and (B8) become

$$\int_0^{\infty} v^{2n} \exp(-\beta^2 v^2) dv = \frac{(2n-1)(2n-3)\dots 1}{2^{n+1} b^{2n+1}} \pi^{1/2}, \quad (\text{B19})$$

and, noting that $0! = 1$,

$$\int_0^{\infty} v^{2n+1} \exp(-\beta^2 v^2) dv = \frac{n!}{2\beta^{2n+2}}. \quad (\text{B20})$$

The results for $n = 0$ to 3 may be listed for quick reference as follows:

$$\int_0^{\infty} \exp(-\beta^2 v^2) dv = \frac{\pi^{1/2}}{2\beta} \quad (\text{B21})$$

$$\int_0^{\infty} v \exp(-\beta^2 v^2) dv = \frac{1}{2\beta^2} \quad (\text{B22})$$

$$\int_0^{\infty} v^2 \exp(-\beta^2 v^2) dv = \frac{\pi^{1/2}}{4\beta^3} \quad (\text{B23})$$

$$\int_0^{\infty} v^3 \exp(-\beta^2 v^2) dv = \frac{1}{2\beta^4} \quad (\text{B24})$$

$$\int_0^{\infty} v^4 \exp(-\beta^2 v^2) dv = \frac{3\pi^{1/2}}{8\beta^5} \quad (\text{B25})$$

$$\int_0^{\infty} v^5 \exp(-\beta^2 v^2) dv = \frac{1}{\beta^6} \quad (\text{B26})$$

$$\int_0^\infty v^6 \exp(-\beta^2 v^2) dv = \frac{15\pi^{1/2}}{16\beta^7} \quad (\text{B27})$$

$$\int_0^\infty v^7 \exp(-\beta^2 v^2) dv = \frac{3}{\beta^8}. \quad (\text{B28})$$

B.2 The error function

The error function of the argument a is

$$\text{erf}(a) = (2/\pi^{1/2}) \int_0^a \exp(-x^2) dx \quad (\text{B29})$$

and the complementary error function is

$$\text{erfc}(a) = 1 - \text{erf}(a). \quad (\text{B30})$$

Note that

$$\text{erf}(-a) = -\text{erf}(a), \quad (\text{B31})$$

$$\text{erf}(0) = 0, \quad (\text{B32})$$

and

$$\text{erf}(\infty) = 1. \quad (\text{B33})$$

The following asymptotic series is useful for large positive arguments

$$\text{erf}(a) = 1 - \frac{1}{\pi^{1/2}} \exp(-a^2) \left(\frac{1}{a} - \frac{1}{2a^3} + \frac{1 \cdot 2}{2^2 a^5} - \dots \right). \quad (\text{B34})$$

The most useful series for the computation of the error function is

$$\text{erf}(a) = \frac{2}{\pi^{1/2}} \exp(-a^2) \sum_{n=0}^{\infty} \frac{2^n}{1 \cdot 3 \cdots (2n+1)} a^{2n+1}. \quad (\text{B35})$$

Since the ratio of the n th term to the $(n-1)$ th term is simply $2a^2/(2n+1)$, eqn (B35) is readily programmed as a computer subroutine. Alternatively, the error function may be computed from the following rational approximation which is based on one of those listed by Abramowitz and Stegun (1965).

$$\begin{aligned} \text{erf}(a) = & 1 - b(0.254829592 + b(-0.284496736 + b(1.421413741 \\ & + b(-1.453152027 + b \times 1.061405429)))) \exp(-a^2), \end{aligned}$$

where

$$b = 1/(1 + 0.3275911 a). \quad (\text{B36})$$

Some typical values of the error function are listed in Table B1.

TABLE B1 Representative values of the error function.

a	$\text{erf}(a)$	a	$\text{erf}(a)$	a	$\text{erf}(a)$
0.001	0.00112838	0.42	0.447468	1.15	0.896124
0.002	0.00225676	0.44	0.466225	1.2	0.910314
0.003	0.00338516	0.46	0.484655	1.25	0.922900
0.004	0.00451349	0.48	0.502750	1.3	0.934008
0.005	0.00564185	0.5	0.520500	1.35	0.943762
0.006	0.00677019	0.52	0.537899	1.4	0.952285
0.007	0.00789853	0.54	0.554939	1.45	0.959695
0.008	0.00902684	0.56	0.571616	1.5	0.966105
0.009	0.0101551	0.58	0.587923	1.55	0.971623
0.01	0.0112834	0.6	0.603856	1.6	0.976348
0.012	0.0135399	0.62	0.619411	1.65	0.980376
0.014	0.0157963	0.64	0.634586	1.7	0.983790
0.016	0.0180525	0.66	0.649377	1.8	0.986672
0.018	0.0203086	0.68	0.663782	1.9	0.9927904
0.02	0.0225646	0.7	0.677801	2.0	0.9953222
0.03	0.0338412	0.72	0.691433	2.1	0.9970205
0.04	0.0451111	0.74	0.704678	2.2	0.9981371
0.06	0.0676216	0.76	0.717537	2.3	0.9988568
0.08	0.0900781	0.78	0.730010	2.4	0.99931149
0.1	0.112463	0.8	0.742101	2.5	0.99959305
0.12	0.134758	0.82	0.753811	2.6	0.99976397
0.14	0.156947	0.84	0.765143	2.7	0.99986567
0.16	0.179012	0.86	0.776100	2.8	0.999924987
0.18	0.200936	0.88	0.786687	2.9	0.999958902
0.2	0.222703	0.9	0.796908	3.0	0.999977910
0.22	0.244296	0.92	0.806768	3.2	0.9999939742
0.24	0.265700	0.94	0.816271	3.4	0.9999984780
0.26	0.286900	0.96	0.825427	3.6	0.99999964414
0.28	0.307880	0.98	0.834232	3.8	0.999999922996
0.3	0.328627	1.0	0.842701	4.0	0.999999984583
0.32	0.349126	1.02	0.850838	4.2	0.9999999971445
0.34	0.369365	1.04	0.858650	4.4	0.99999999951083
0.36	0.389330	1.06	0.866144	4.6	0.9999999999922504
0.38	0.409009	1.08	0.873326	4.8	0.9999999999988648
0.4	0.428392	1.1	0.880205	5.0	0.999999999998462

B.3 The beta function

The beta function appears in the Larsen–Borgnakke distribution functions for the internal energy modes. It is defined by

$$B(z, w) = \int_0^1 t^{z-1} (1-t)^{w-1} dt \quad (\text{B37})$$

and is related to the gamma function by

$$B(z, w) = \frac{\Gamma(z)\Gamma(w)}{\Gamma(z+w)} = B(w, z). \quad (\text{B38})$$

The most common forms of the incomplete beta function are

$$B_x(a, b) = \int_0^x t^{a-1} (1-t)^{b-1} dt, \quad (\text{B39})$$

and

$$I_x(a, b) = B_x(a, b)/B(a, b). \quad (\text{B40})$$

A useful symmetry relation for the latter form is

$$I_x(a, b) = 1 - I_{1-x}(b, a). \quad (\text{B41})$$

The second argument may be reduced through the recurrence relation

$$I_x(a, b) = \frac{\Gamma(a+b)}{\Gamma(a+1)\Gamma(b)} x^a (1-x)^{b-1} + I_x(a+1, b-1), \quad (\text{B42})$$

and

$$I_x(a, 1) = x^a. \quad (\text{B43})$$

FORTRAN program subroutines for the evaluation of all functions that have been discussed in this appendix have been listed by Press et al. (1986).

References

- ABRAMOWITZ, M. and STEGUN, I.A. (1965). *Handbook of mathematical functions*, Dover, New York.
 PRESS, W.H., FLANNERY, B.P., TEUKOLSKY, S.A., and VETTERLING, W.T. (1986). *Numerical recipes*, Cambridge University Press.

APPENDIX C

Sampling from a prescribed distribution

Probabilistic modelling of physical processes requires the generation of representative values of variables that are distributed in a prescribed manner. This is done through random numbers and is a key step in direct simulation Monte Carlo procedures. We will assume the availability of a set of successive random fractions R_f that are uniformly distributed between 0 and 1.

The distribution of the variate x may be described by a normalized distribution function such that the probability of a value of x lying between x and $x + dx$ is given by

$$f_x dx. \quad (\text{C1})$$

If the range of x is from a to b , the total probability is

$$\int_a^b f_x dx = 1. \quad (\text{C2})$$

Now define the *cumulative distribution function* as

$$F_x = \int_a^x f_x dx. \quad (\text{C3})$$

We may now generate a random fraction R_f and set this equal to F_x . The representative value of x is therefore given by

$$F_x = R_f. \quad (\text{C4})$$

First consider the trivial example in which the variate x is uniformly distributed between a and b . For this case f_x is a constant and the normalization condition of eqn (C2) requires that

$$f_x = 1/(b-a).$$

Therefore, from eqn (C3),

$$F_x = \int_a^x 1/(b-a) dx = (x-a)/(b-a),$$

and eqn (C4) gives

$$(x-a)/(b-a) = R_f,$$

or, as is otherwise obvious,

$$x = a + R_f(b-a). \quad (\text{C5})$$

Now consider the variate r distributed between a and b such that the probability of r is proportional to r . This distribution is encountered when setting a random radius in an axially symmetric flow. Now

$$f_r = \text{const} \times r$$

and, again evaluating the constant by eqn (C2),

$$f_r = 2r/(b^2 - a^2).$$

Therefore, from eqn (C3),

$$F_r = (r^2 - a^2)/(b^2 - a^2)$$

and eqn (C4) now gives

$$r = \{a^2 + (b^2 - a^2)R_f\}^{1/2}. \quad (\text{C6})$$

The similar distribution when r is proportional to r^2 in a spherical flow is

$$r = \{a^3 + (b^3 - a^3)R_f\}^{1/3}. \quad (\text{C6a})$$

Further examples from the *inverse-cumulative method* are given in eqns (C12), (C16), and (C18). The operation of the method is illustrated graphically in Fig. C1.

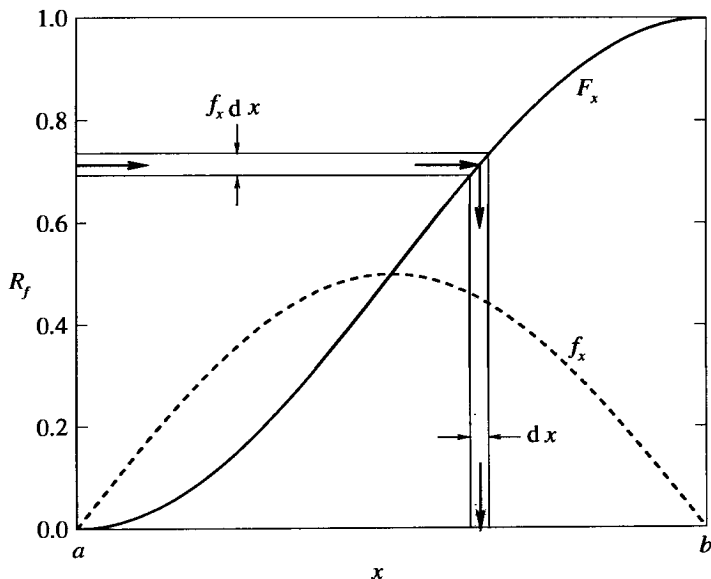


Fig. C1 Typical normalized and cumulative distribution functions.

Unfortunately, the inverse-cumulative method can be used only when it is possible to invert eqn (C4) to obtain an explicit function for x . Consider the distribution function $f_{u'}$ for a thermal velocity component in an equilibrium gas. This is given by eqn (4.13) as

$$f_{u'} = (\beta/\pi^{1/2}) \exp(-\beta^2 u'^2). \quad (\text{C7})$$

Therefore

$$F_{u'} = (\beta/\pi^{1/2}) \int_{-\infty}^{u'} \exp(-\beta^2 u'^2) du'$$

or

$$F_{u'} = 1/2 \{1 + \operatorname{erf}(\beta u')\}.$$

This expression cannot be inverted to give u' in terms of R_f , and the method fails.

The general alternative is to apply the *acceptance-rejection method*. In order to make direct use of the random fraction, the distribution function is normalized by dividing it by its maximum value f_{\max} to give

$$f_x' = f_{u'} / f_{\max}. \quad (\text{C8})$$

A value of x is then chosen at random on the basis of x being uniformly distributed between its limits (i.e. from eqn (C5)). The function f_x' is then calculated for this value of x and a second random fraction R_f is generated. The value of x is then either accepted or rejected according to whether f_x' is greater or less than this R_f . The procedure is repeated until a value of x is accepted. Since R_f is uniformly distributed between 0 and 1, the probability of a particular value of x being accepted is obviously proportional to f_x' and the accepted values conform to this distribution.

As an example, consider the function defined by eqn (C7). It has a maximum value of $\beta/\pi^{1/2}$ at $u'=0$, so that

$$f_{u'} = \exp(-\beta^2 u'^2).$$

The uniformly distributed value of u' is given by eqn (C5) with a and b set as arbitrary finite cut-off values in place of the real limits of $-\infty$ to ∞ . If a and b are set at $-3/\beta$ and $+3/\beta$ respectively, the fraction of values lying outside these limits as $1 - \operatorname{erf}(3)$ or 0.000022. Therefore,

$$u' = (-3 + 6R_f)/\beta$$

and

$$f_{u'} = \exp\{-(-3 + 6R_f)^2\}.$$

The *next* value of R_f is then generated and, if $f_{u'} > R_f$, u' is accepted. If $f_{u'} < R_f$, the value of u' is rejected and the process is repeated until a value is accepted.

While the acceptance-rejection method involves a repetitive process which may require the evaluation of a large number of functions and random fractions, it can be used with almost any distribution function and is readily incorporated into computer programs.

Additional methods are available for special cases. One of these provides a direct method of sampling pairs of values from the normal distribution of eqn (C7). These values may be denoted by u' and v' and, from eqn (C7),

$$\begin{aligned} f_{u'} du' f_{v'} dv' &= (\beta/\pi^{1/2}) \exp(-\beta^2 u'^2) du' (\beta/\pi^{1/2}) \exp(-\beta^2 v'^2) dv' \\ &= (\beta^2/\pi) \exp\{-\beta^2(u'^2 + v'^2)\} du' dv'. \end{aligned}$$

Now set

$$u' = r \cos \theta$$

and

$$v' = r \sin \theta. \quad (C9)$$

Then, since the Jacobian

$$\frac{\partial(u', v')}{\partial(r, \theta)} = \begin{vmatrix} \frac{\partial u'}{\partial r} & \frac{\partial u'}{\partial \theta} \\ \frac{\partial v'}{\partial r} & \frac{\partial v'}{\partial \theta} \end{vmatrix} = \begin{vmatrix} \cos \theta & -r \sin \theta \\ \sin \theta & r \cos \theta \end{vmatrix} = r,$$

$$\begin{aligned} f_{u'} du' f_{v'} dv' &= (\beta^2/\pi) \exp(-\beta^2 r^2) r dr d\theta \\ &= \exp(-\beta^2 r^2) d(\beta^2 r^2) d\theta/(2\pi). \end{aligned}$$

Now θ is uniformly distributed between 0 and 2π so that, from eqn (C5),

$$\theta = 2\pi R_f. \quad (C10)$$

The variable $\beta^2 r^2$ is distributed between 0 and ∞ and its distribution function

$$f_{\beta^2 r^2} = \exp(-\beta^2 r^2) \quad (C11)$$

is already in a normalized form. The cumulative distribution function is

$$F_{\beta^2 r^2} = 1 - \exp(-\beta^2 r^2)$$

and, noting that R_f and $1-R_f$ are equivalent functions, eqn (C4) gives,

$$r = \{-\ln(R_f)\}^{1/2}/\beta. \quad (C12)$$

A pair of values of r and θ may be sampled from eqns (C10) and (C12) using successive random fractions. The normally distributed values of u' and v' follow from eqn (C9) and provide typical values for a thermal velocity component in an equilibrium gas.

There is also a requirement to sample the internal energy of molecules in an equilibrium gas. Eqn (5.6) may be normalized to show that the distribution function for the ratio of the internal energy ϵ_i of a single molecule to kT is

$$f_{\epsilon_i/(kT)} = \frac{\{\epsilon_i/(kT)\}^{\zeta_i/2-1}}{\Gamma(\zeta_i/2)} \exp\{-\epsilon_i/(kT)\}, \quad (\text{C13})$$

where ζ_i is the number of fully excited internal degrees of freedom.

For the special case of two internal degrees of freedom, this function becomes

$$f_{\epsilon_i/(kT)} = \exp\{-\epsilon_i/(kT)\}. \quad (\text{C14})$$

This is the same distribution as that in eqn (C11) and the cumulative distribution function is

$$F_{\epsilon_i/(kT)} = 1 - \exp\{-\epsilon_i/(kT)\}. \quad (\text{C15})$$

The required representative value of the internal energy is, therefore,

$$\epsilon_i = -\ln(R_f) kT. \quad (\text{C16})$$

Recourse must be had to the acceptance-rejection method when ζ_i is not equal to two.

The Larsen-Borgnakke distribution of collision energy into a single energy mode with two internal degrees of freedom may also be sampled from the cumulative distribution function. The distribution function is, from eqn (5.45),

$$f\left(\frac{E_a}{E_a + E_b}\right) = \Xi_b \left(1 - \frac{E_a}{E_a + E_b}\right)^{\Xi_b-1}.$$

The range of the variable is from 0 to 1, and the cumulative distribution function is

$$F\left(\frac{E_a}{E_a + E_b}\right) = 1 - \left(1 - \frac{E_a}{E_a + E_b}\right)^{\Xi_b}. \quad (\text{C17})$$

Again making use of the equivalence of R_f and $1-R_f$, the representative value that corresponds to the random fraction R_f is

$$\frac{E_a}{E_a + E_b} = 1 - R_f^{1/\Xi_b}. \quad (\text{C18})$$

Special methods have been developed to avoid the calculation of transcendental functions in the selection of random directions. The method of Marsaglia (1972) for the selection of uniformly distributed points on a sphere provides a good example in the context of hard sphere collisions.

Consider a hard sphere collision between similar molecules such that the magnitude of the relative velocity is c_r . The problem is to generate the three components of the post-collision relative velocity \mathbf{c}_r^* , and the following procedure implements Marsaglia's scheme.

- (i) Generate $a = 2R_f - 1$ and $b = 2R_f - 1$.
- (ii) Calculate $c = a^2 + b^2$.
- (iii) If $c < 1$, return to step (i).
- (iv) Calculate $d = 2(1-c)^{1/2}$.
- (v) Then (C19)

$$u_r^*/c_r = 1 - 2c$$

$$v_r^*/c_r = ad \quad .$$

$$w_r^*/c_r = bd$$

The speed of this scheme relative to the direct coding in terms of random elevation and azimuth angles that has been employed in the demonstration programs will depend on the characteristics of the computer that is being used. This application appears in the collision subroutine and, in some cases, there could be significant gains in execution speed if the above procedure is adopted in place of the direct coding.

The preceding discussion has implicitly assumed that a single selection is being made from the distribution. Should a number of simultaneous selections be required, the representative values should not be chosen independently, but should reflect the overall distribution. For example, if a total of m choices of a linear variate are to be made from a uniform distribution between a and b , eqn (C5) should not be applied m times. The n th of the m values should be generated from

$$x = a + \{(n-R_f)/m\}(b-a). \quad (C20)$$

Similarly, if m selections of radius are to be made from a uniform distribution between a and b , the n th value is

$$r = [a^2 + (b^2 - a^2)\{(n-R_f)/m\}]^{1/2}. \quad (C21)$$

This is one aspect of the variance reduction techniques that are discussed in §7.7 and §10.4.

Reference

MARSAGLIA, G. (1972). Choosing a point from the surface of a sphere. *Ann. Math. Stat.* **43**, 645–6.

APPENDIX D

Listing of program FMF.FOR

The following FORTRAN 77 program relates to the collisionless flow cylindrical tube flux problem that was discussed in §7.7.

```
PROGRAM FMF
* calculates the fraction of molecules that pass through a diffusely
* reflecting cylindrical tube under free-molecule conditions
  WRITE (*,*) ' INPUT THE LENGTH TO RADIUS RATIO '
  READ (*,*) TL
  WRITE (*,*) ' INPUT THE TOTAL NUMBER OF TRAJECTORIES '
  READ (*,*) NTR
  ND=0
* ND is the number that pass through without any surface collision
  NT=0
* NT is the total number that pass through the cylinder
  DO 100 N=1,NTR
    RM=SQRT(RND())
* RM is the initial radius (eqn (7.79) with cylinder radius = 1.)
* RND() generates a random fraction between 0. and 1.
    CALL DCS(AL,AM,AN)
    X=AL*(RM*AM+SQRT(AM*AM+(1.-RM*RM)*AN*AN))/(AM*AM+AN*AN)
* X is the x coordinate of the first surface interaction (eqn (7.88))
    IF (X.GT.TL) THEN
      ND=ND+1
      NT=NT+1
      GO TO 100
    END IF
50   CALL DCS(AM,AL,AN)
    X=X+2.*AL*AM/(AM*AM+AN*AN)
* X is now the x coordinate of a subsequent interaction (eqn (7.89))
    IF (X.LT.0.) GO TO 100
    IF (X.GT.TL) THEN
      NT=NT+1
      GO TO 100
    END IF
    GO TO 50
100  CONTINUE
    WRITE (*,*) ' DIRECT FRACTION = ',FLOAT(ND)/NTR
    WRITE (*,*) ' TOTAL FRACTION = ',FLOAT(NT)/NTR
    STOP
    END
*
* SUBROUTINE DCS(DC1,DC2,DC3)'
* DC1 is the direction cosine with the effusion direction
* DC2 and DC3 are the direction cosines with the other directions
* (the code is based on eqns (7.82) to (7.84))
  DC1=SQRT(RND())
  A=SQRT(1.-DC1*DC1)
  B=6.28318531*RND()
  DC2=A*COS(B)
  DC3=A*SIN(B)
  RETURN
  END
```

APPENDIX E

Numerical artefacts

Computers represent numbers by a finite number of binary bits and this limited word length places restrictions on the precision of computer arithmetic. All computational methods are affected by the 'round-off' error that is a consequence of these restrictions. The probabilistic simulation methods, such as the DSMC method, are also affected by the fact that computer generated random numbers do not follow the ideal distribution.

E.1 Effect of word length

The chosen word length represents a compromise between cost and precision. Some early computers employed 48 bit words and this is arguably the best compromise. Early minicomputers employed 16 bit words, but this is insufficient for most computations and the software, through the use of double word operations, effectively converted them to 32 bit precision. Almost all modern computers employ either 32 or 64 bit words. The so-called 'supercomputers' such as the CRAY family employ the longer word length and round-off error is minimal. However, most DSMC calculations employ either a 'workstation' or a 'Personal Computer' (PC) and, although several of the newer workstations are 64 bit, these are 32 bit machines. However, it is necessary to distinguish between machines that employ 32 bits throughout and those that employ a longer wordlength in the central processing unit (CPU). In particular, the Intel family of CPU chips in 'IBM compatible' PCs employ a number of 80 bit floating point registers in the CPU and a good compiler will calculate almost all expressions to this accuracy. Also, the compilers can use 'double precision' arithmetic but, if the registers are 32 bit, there will be a speed penalty. The 32 bit word offers sufficient precision for the stored quantities in DSMC calculations.

Some consequences of the finite word length may be illustrated through the following FORTRAN program:

```
*--precision test program
A=0.
N=0
100 DO 200 M=1,100000
      A=A+1.
      N=N+1
200 CONTINUE
      WRITE (*,99001) A,N
99001 FORMAT (F12.1,I14)
      GO TO 100
      END
```

This program contains an infinite loop that advances the floating point variable A and the integer variable N by unity in each cycle. The sum is printed each 100000 cycles. On a 32 bit machine that has the standard floating point format with a 24 bit mantissa, the variable A will increase to 16777216, but will then remain constant. Although, the maximum floating point number is usually 3.4×10^{38} , the *precision* is such that adding 1 to a mantissa that is already 2^{24} (or 16777216) has no effect. This case is reasonably predictable and the behaviour is even more dangerous if A is incremented by 10 rather than 1. This causes the maximum count to increase to 268435456, but the error commences at 33500000 where the advance at each printing interval becomes 90888 rather than 100000. If single precision is used for a sampling variable in a DSMC calculation, the error due to the maximum count should be obvious, but that due to the second effect would be quite insidious. Double precision variables are employed for the sampling variables in the demonstration programs. The double precision format generally employs a mantissa of 53 bits and the precision increases from the order of one part in 10^7 to one part in 10^{16} .

The integer variable N increases to 2147483647 (or $2^{31}-1$). It then jumps to -2147483648 and subsequently cycles between these limits. This avoids the setting of the separate sign bit that is used in the floating point format.

The upper and lower limits of the single precision (32 bit) floating point numbers may have a direct impact on the coding. For example, the square of a molecular mass generally falls below the lower limit and the reduced mass must be calculated from $\{m_1/(m_1+m_2)\}m_2$ rather than $m_1m_2/(m_1+m_2)$.

Because of the limited precision of computer arithmetic, it is often necessary to add or subtract a very small number from a point of impact of a molecule with a surface in order that the subsequent steps identify the molecule as being off the surface and on the appropriate side of it. It is important that these 'round-off' numbers be a multiple of, say, the cell size rather than being specified as an absolute number. This ensures that the program functions properly if the dimensions of the flow are extremely small. In order to check this aspect of the demonstration programs, the data in the listed test case in program DSMC2A was altered such that all linear dimensions were reduced by a factor of 10^6 . In order to retain the Knudsen number, the freestream density was increased by a factor of 10^6 . The time step was reduced by the factor of 10^6 , while the parameter FNUM was increased by a factor of 10^{12} to be very close to unity. This illustrates that, in a problem with very small dimensions, there can be a one-to-one correspondence between the real and simulated molecules. The radius of the cylinder was only 5×10^{-9} m, but there were no problems with the calculation. The non-dimensional parameters such as the pressure and heat transfer coefficients on the surface and the temperature and density ratios in the stream were identical to those in the original calculation. The dimensioned output followed the changes in the size and density. For example, the pressures, shear stress, and heat transfer scale with the density and increased by a factor of 10^6 .

E.2 Random number generators

Just as the finite length representations of numbers in a computer do not have all the properties of real numbers, the numbers from a random number generator on a computer do not conform to the properties of an ideal set of random numbers. Such a set is necessarily hypothetical in that an ideal random number generator does not exist, and computer generated numbers are sometimes called *pseudo-random* numbers. The compilers for the various computer operating systems generally have a random number generator as a subroutine with a name like 'RAN'. Press et al. (1986) have stated; 'If all scientific papers whose results are in doubt because of bad RAN's were to disappear from library shelves, there would be a gap on each shelf about as big as your fist.' The DSMC method is one of those that are most dependent on random numbers and it is essential to check the adequacy of the generator that is used. Most random number generators present their results as random fractions between zero and unity rather than as integer numbers.

The literature on random number generators and the statistical tests that have been applied to them is extensive. The most common of these tests check the uniformity of the distribution of successive sets of N numbers in N -dimensional space. This checks the uniformity of the set and determines whether there are any obvious low-order correlations. The following program tests 10^8 pairs of random fractions in a two-dimensional space.

```

PROGRAM RANDIST
---check the distribution of pairs of random fractions in a plane
---the fractions are generated from successive calls of RANF(0)
DIMENSION NDIST(100,100),NDEV(5)
---DIST counts the numbers in a 100 x 100 array
DO 100 L=1,100
    DO 50 M=1,100
        NDIST(L,M)=0
50    CONTINUE
100   CONTINUE
      DO 200 N=1,100000000
          L=100.*RANF(0)+1
          M=100.*RANF(0)+1
          NDIST(L,M)=NDIST(L,M)+1
200   CONTINUE
      DO 300 N=1,5
          NDEV(N)=0
300   CONTINUE
      DO 400 L=1,100
          DO 350 M=1,100
              DO 320 N=1,5
                  IF (NDIST(L,M).GT.10000+N*100.OR.NDIST(L,M).LT.10000-N*100)
&                    NDEV(N)=NDEV(N)+1
320   CONTINUE
350   CONTINUE
400   CONTINUE
      WRITE (*,*) ' NUMBER OUTSIDE 1 TO 5 STANDARD DEVIATIONS '
      WRITE (*,*) NDEV
      WRITE (*,*) ' NORMAL DISTN. IS 3173, 455, 27.0, 0.63, 0.0057 '
      STOP
END

```

The two-dimensional space is divided into 10,000 uniform elements and each should contain an average of 10,000 pairs. Statistical scatter is present and the output lists the number of elements with samples that are outside 1, 2, 3, 4, and 5 standard deviations.

Most of the system supplied routines satisfy this test. For example, an i486 PC using the random number function RND that is supplied with the Lahey F77L-EM/32A FORTRAN compiler gives the following results: 3131 439 33 0 0. These numbers are consistent with the predictions from the normal distribution of eqn (1.15) that are quoted in the third last line of the test program. When this program is applied to the FORTRAN compiler for the Silicon Graphics Iris Indigo, the corresponding results are: 3062 378 20 0 0. This distribution exhibits less than the expected deviation and the reason for this is given by the second test program that is listed below. This program determines the total number of distinct random fractions that can be generated, as long as this number is less than 100,000. Given sufficient computer memory, the program could readily be modified to deal with larger totals, although the documentation of the better generators quote the relevant number.

```

PROGRAM RANTEST
---test for the number of distinct values from the function
---RANF(0) which generates successive random fractions (0 to 1)
  PARAMETER (M=100000)
  DIMENSION I(M)
  DO 1 N=1,M
    I(N)=1
1   CONTINUE
---all elements of the array I have been set to 1
  DO 2 N=1,100
    DO 3 L=1,10000
      K=RANF(0)*(FLOAT(M)-0.00001)+1
      I(K)=0
    ---a random element is set to zero
3   CONTINUE
  J=0
  DO 4 L=1,M
    ---count the unselected elements
    J=J+I(L)
4   CONTINUE
    A=FLOAT(J)/FLOAT(M)
---A is the unselected fraction
    B=(FLOAT(M-1)/FLOAT(M))**(10000*N)
    WRITE (*,*) ' SAMPLES ',10000*N,' UNSELECTED FRACTION ',A,
    & ' THEORY ',B
2   CONTINUE
  STOP
END

```

Each random fraction is used to select one element of the array I(M) and, if it has not already been selected, it is changed from 1 to 0. If the array contains a total of m numbers, the theoretical result for the unselected fraction after n selections is $\{(m-1)/m\}^n$.

If the number of distinct random fractions exceeds 100,000, the result for the unselected fraction will progressively decrease and will agree with the theoretical fraction to within the statistical scatter. This is the case for most generators, but the FORTRAN compiler for the Silicon Graphics Iris Indigo generates only 32,768 distinct fractions. The Iris Indigo is a UNIX based system and the random number generators supplied with FORTRAN compilers under UNIX are generally unsatisfactory. For example, the random number generator in a version of the GreenHills FORTRAN that has been supplied for a number of UNIX systems was found to be better, but the number of distinct fractions only doubled.

A random number generator is best tested in the context of the application that employs it. A typical DSMC application involves the generation of hundreds of millions of random fractions so that generators with very short periods are suspect. However, the numbers are used in many procedures and the number of calls of the random number routine within each procedure is also subject to random variations. This means that most DSMC calculations are very tolerant of imperfections in the random number generator. Program DSMC0R.FOR is an exception in that it involves 100,000 simulated molecules in a single cell so that, during the execution of the collision routine, a very large number of random fractions are employed in an ordered sequence. The quoted results for the listed test case of this program in §11.3 were that the translational and rotational temperatures came into equilibrium to within 0.03 K at a temperature of approximately 300 K. This was approximately one standard deviation for the sample size of approximately 10^8 and the random number generator was evidently satisfactory. That calculation was made on an i486 PC using the random number function RND (with a claimed period of 2.7×10^{11} numbers) that is supplied with the Lahey F77L-EM/32A FORTRAN compiler. A similar calculation with the Silicon Graphics random number generator yielded a translational temperature of 434.17 K and a rotational temperature of 98.25. While the short period is the obvious source of such a large error, equilibrium is also affected by the more subtle properties of the various generators. The Silicon Graphics generator was also employed in a test run of program DSMC2A for the supersonic flow past a flat-nosed cylinder and there were no anomalies in the flow. This confirms that most DSMC programs are generally tolerant of poor random number generators.

The inadequacy of many system supplied generators introduces a need for 'portable' generators coded in FORTRAN that can be used to obtain consistent results on any computer. The DSMC calculations that have been reported in the preceding chapters were made on either the i486-F77L-EM combination or on the Iris Indigo with the INTEGER*4 version of the Wichmann and Hill (1982) random number generator. This is the most compact generator in terms of code length but, on the i486 (66 Mhz DX2 version), each call of the routine requires 10.8 μ s compared with only 2.1 μ s for the Lahey RND routine. Hash (personal communication) has pointed out that the RAN3 routine of Press et al. (1986), which is based on an algorithm due to Knuth (1981), is three times faster at 3.5 μ s per call.

The RAN3 routine, with several minor modifications, is included in all the DSMC demonstration programs as the function subroutine RF(0), including the program DSMC0S in Appendix G. The SAVE statement has been added at the head of the program so that its correct functioning is less dependent on the correct choice of compiler options. A redundant resetting of the argument in the initialization section of the program has been removed because it caused the Iris Indigo to hang. The most important modification is the addition of the conditions to the RETURN statement. These conditions prevent the return of random fractions that are exactly zero or unity. Both of these limits would have zero probability of return in an ideal generator with infinite precision but, if they do occur, a zero in an expression such as eqn (C12) causes the computer to hang. Test runs were made to list the numbers that would be excluded by these conditions when applied to the various generators. The very small numbers retain eight digits precision in the Lahey system routine RND(), and exact zero or unity are effectively absent. There would be no need for the exclusion conditions in the portable FORTRAN generators if the numbers that they returned were as good as those from RND(). However the precision of the very small numbers from RF(0) is only single digit and exact zero is returned about once in every 10^8 calls. The Wichmann and Hill generator returns fewer zeros but, for both this and RF(0) the incidence of zeros on the RISC based workstation was much higher than on the PC.

The results from program RANDIST for the generator RF(0) when run on the Iris Indigo were: 3271 454 29 1 0 and, when run on the i486 PC: 3173 459 35 0 0. The corresponding numbers for the Wichmann and Hill generator were 3151 451 24 0 0 and 3091 449 23 0 0.

When either RF(0) or the Wichmann and Hill generator was employed in program DSMC0R, the translational and rotational temperatures came to equilibrium to within the expected statistical scatter, although Hash found a temperature separation of several degrees from the Wichmann and Hill generator on a Sun workstation. One version of the well-known generator of Lewis et al. (1969) and the RAN1 generator of Press et al. led to temperatures that were out of equilibrium by as much as 10 K. For example, the Lewis, Goodman, and Miller generator led to a translational temperature of 296.81 K and a rotational temperature of 305.27 K. The RANDIST result for this generator was: 2680 266 7 0 0. This scatter is much less than the normal scatter and it is something of a paradox that this generator led to a poor result for the temperature equilibrium.

Both poor simulation algorithms and poor random number generators can lead to non-equilibrium between the various components of the overall temperature. While it is desirable for RF(0) to be replaced by a faster system routine, it is essential to make sure that the system routine is adequate. Particular care should be taken when using 32 bit RISC-based workstations operating under UNIX. The generators on mainframes are generally satisfactory and the system random number on a CRAY mainframe led, as expected, to equilibrium within the expected statistical scatter.

References

- KNUTH, D.E. (1981). *Seminumerical algorithms*, Vol 2 of *The art of computer programming*, Addison-Wesley, Reading, Mass.
- LEWIS, P.A.W., GOODMAN, A.S., and MILLER, J.M. (1969). A pseudo-random number generator for the System 360, *IBM Syst. J.*, **2**, 136–146.
- PRESS, W.H., FLANNERY, B.P., TEUKOLSKY, S.A., and VETTERLING, W.T. (1986). *Numerical recipes*, Cambridge University Press.
- WICHMANN, B.A. and HILL, I.D. (1982). An efficient and portable pseudo-random number generator, *Appl. Statist.*, **31**, 188–190.

APPENDIX F

Summary of the DSMC demonstration programs

F.1 Implementation notes

The background theory of, the data for, and the results from the thirteen DSMC demonstration programs have been discussed in the text. All the programs are included as FORTRAN source code on the enclosed disk. To list all the programs would require more than 300 pages, and only the shortest program has been listed as Appendix G. This listing of program DSMC0S.FOR illustrates the general structure of the programs.

The main program controls the calculation in that it advances the time parameter but, otherwise, it merely calls the subroutines that contain the data, initialize the flow, move the molecules, calculate the collisions, output the results, and so on. The variables are grouped into a number of related COMMON blocks and these, rather than argument lists, are used to share the information between the main program and subroutines. The pattern of the subroutines is common to all the programs and, as far as possible, the subroutines are unchanged from program to program.

The programs are in standard FORTRAN 77 and are self-contained in that all the necessary subroutines are included in each program file. The procedures in the programs are related to the theory in the appropriate chapters by comment statements that quote the equation numbers of the relevant theory. The program names are all in the form DSMCNX where the integer N is 0 for homogeneous (zero-dimensional) cases, 1 for one-dimensional flows, 2 for two-dimensional (including axially symmetric) flows, and 3 for three-dimensional flows. The final character X is absent from the basic programs of each class and is used to distinguish between the variations of each basic program. The corresponding subroutines, where they differ, are also distinguished by the N and X. The extension .FOR is attached to each file and some systems may require this to be changed. For example, UNIX systems generally require the .F extension for FORTRAN source files

The programs are made restartable through the periodic writing of the current information to the unformatted 'restart' file which has the program name with the extension .RES. The data of the 'listed' demonstration case for each program is included in the subroutine DATANX. For most of the programs, there is more than one demonstration case and the data for the other cases is briefly described in the appropriate section.

The primary output is to the formatted files DSMCNX.OUT. Some of the programs produce additional output or .OUT files for special purposes. The output is extensive and these files can become large for multi-dimensional flows, particularly if they involve gas mixtures.

F.2 Catalogue of programs

- DSMC0** This program tests the NTC collision sampling procedures in a homogeneous gas mixture of monatomic molecules. Although the gas is uniform and is macroscopically stationary, the 'flow' is divided into cells and the molecules are moved in a one-dimensional spatial region between specular boundaries. These conditions reproduce the changing cell population that is characteristic of more general flows so that the basic DSMC procedures can be properly tested.
- DSMC0S** A version of program DSMC0 that implements all the simplifications that can be made if the gas mixture is replaced by a simple gas. The procedures in all the other programs are for a multi-component gas mixture.
- DSMC0R** Tests the Larsen–Borgnakke procedures for the rotational degrees of freedom of diatomic and polyatomic molecules.
- DSMC0V** Implements the quantum version of the Larsen–Borgnakke procedures for vibrational excitation. This assumes the equally spaced levels of the harmonic oscillator model.
- DSMC0D** Extends the vibrational procedures to the anharmonic case and to the dissociation that occurs when the vibration reaches the dissociation limit. The recombination reaction is also included so that the equilibrium state can be examined.
- DSMC0F** A version of DSMC0 with additional sampling to investigate the properties of the statistical fluctuations.
- DSMC1** A general program for flows with a single spatial variable. The geometry may be plane, cylindrical, or spherical. This program includes the procedures for molecular rotation, but not vibration. The boundaries may be an axis, a vacuum, a solid surface, or an interface with a stream. The solid surfaces may have a parallel velocity, and there may be a gravitational field along the spatial coordinate.
- DSMC1S** A version of DSMC1 that is restricted to plane flows, but has the initialization, boundary conditions, and sampling routines modified expressly for the study of normal shock waves.
- DSMC1T** This program models a stagnation streamline flow as a constant area flow with molecule removal at the sides. The upstream and downstream boundaries are a supersonic stream and a solid surface, respectively. Vibration and dissociation are included.

DSMC1U This is a version of DSMC1 in which the sampling has been altered so that an ensemble average is made of an unsteady flow instead of a time average of a large-time steady flow.

DSMC2 A general program for two-dimensional flows that is restricted to a rectangular flowfield and flat surfaces. The boundaries may be interfaces with a uniform stream, a vacuum, or a plane of symmetry. There may be two single-sided surfaces that must lie along a boundary or one of the planes defined by the simple rectangular cell system. These may be placed back-to-back to form a single double-sided surface. In addition, there may be a uniform plane jet with a flat exit plane.

DSMC2A A version of DSMC2 for axially symmetric flows. The axis must lie along the x -axis and y becomes the radius. The surfaces may have axial or circumferential velocities.

DSMC3 An extension of DSMC2 to three-dimensional flows. The flow-field must be a rectangular parallelepiped and there may again be two flat surfaces. There may be a jet, but this must have an exit plane with a circular cross-section.

F.3 Computing environment

The programs were developed on an i486 (66 Mhz DX2) PC with 8 Mb memory using the Lahey F77L-EM/32 FORTRAN compiler. The extensions to the FORTRAN 77 standard were avoided. The readability of the working programs was enhanced by processing them through the SPAG program from Polyhedron Software Ltd.

The applications of the demonstration programs were executed either on the PC or on a Silicon Graphics Iris Indigo. The latter was slightly faster than the PC and had 16 Mb memory. However, the applications were restricted to problems that allowed each case to be run on the PC in less than 24 hours of computing time.

No attempt has been made to optimize the coding for vector processors such as the CRAY 2. This means that the CRAY is only about three times faster than the 66Mhz i486 for these DSMC programs. The CRAY speed could be enhanced by a factor of about five through suitable modifications to the code but, since a single user cannot expect to have more than 5% of the time on such a machine, it is generally faster as well as incomparably less expensive to make the calculations on a PC or workstation.

The x - y diagrams, contour plots, and streamline representations have been made with the TECPLLOT program from Amtec Engineering Inc.

The purpose of the programs is to demonstrate the DSMC method. They are not guaranteed to be free of error and should not be relied on for solving problems where an error could result in injury or loss. If the programs or routines are used for such solutions, it is entirely at the user's risk and the author and publisher disclaim all liability.

APPENDIX G

Listing of program DSMC0S.FOR

```
*   DSMC0S.FOR
*
      PROGRAM DSMC0S
*
*--test of collision procedures in a uniform simple gas
*
*--SI units are used throughout
*
      PARAMETER (MNM=1000,MNC=50,MNSC=400)
*
*--MNM  is the maximum number of molecules
*--MNC  is the maximum number of sub-cells
*--MNSC is the maximum number of sub-cells
*
      DOUBLE PRECISION MOVT,NCOL,SELT,SEPT
*
*--NCOL is the total number of collisions
*--MOVT the total number of molecular moves
*--SELT the total number of pair selections
*--SEPT the sum of collision pair separations
*
      COMMON /MOLSS / NM,PP(MNM),PV(3,MNM),IP(MNM),IR(MNM)
*
*--NM is the number of molecules
*--PP(M)  is the x coordinate molecule M
*--PV(1 to 3,M) u,v,w velocity components of molecule M
*--IP(M)  sub-cell number of molecule M
*--IR(M)  cross-reference array (molecule numbers in order of sub-cells)
*
      COMMON /CELLSS/ CC(MNC),CG(3,MNC),IC(2,MNC),ISC(MNSC),CCG(2,MNC),
      &           ISCG(2,MNSC)
*
*--CC(M) is the cell volume
*--CG(N,M) is for collisions in cell M
*---N=1 is the maximum value of (relative speed)*(coll. cross-section)
*---N=2 is the remainder when the selection number is rounded
*--CG(N,M) is the geometry related information on cell M
*---N=1 the minimum x coordinate
*---N=2 the maximum x coordinate
*---N=3 the cell width
*--IC(N,M) information on the molecules in cell M
*---N=1 (start address -1) of the molecule numbers in the array IR
*---N=2 the number of molecules in the cell
*--ISC(M) the cell in which the sub-cell lies
*--ISCG(N,M) is the indexing information on sub-cell M
*---N=1 (start address -1) of the molecule numbers in the array IR
*---N=2 the number of molecules in the sub-cell
*
      COMMON /GASS  / SP(2),SPM(5)
*
*--SP(N) information on species
*---N=1 the molecular mass
*---N=2 the reference diameter of the molecule
*--SPM(N) information on the interaction
*---N=1 the reference value of the collision cross-section
*---N=2 the reference temperature
*---N=3 the viscosity-temperature power law
```

```

*----N=4 the reciprocal of the VSS scattering parameter
*----N=5 the Gamma function of (5/2 - viscosity-temperature power law)
*
      COMMON /SAMPS / NCOL,MOVT,SELT,SEPT,CS(5,MNC),TIME,NPR,NSMP,FND,
      &           FTMP
*
*--CS(N,M) sampled information on cell M
*--N=1 the number in the sample
*--N=2,3,4 the sum of u,v,w
*--N=5 the sum of u*u+v*v+w*w
*--TIME time
*--NPR the number of output/restart file update cycles
*--NSMP the total number of samples
*--FND the stream number density
*--FTMP the stream temperature
*
      COMMON /COMP / FNUM,DTM,NIS,NSP,NPT
*
*--FNUM is the number of real molecules represented by a simulated mol.
*--DTM is the time step
*--NIS is the number of time steps between samples
*--NSP is the number of samples between restart and output file updates
*--NPT is the estimated number of samples to steady flow
*--NPT is the number of file updates to STOP
*
      COMMON /GEOM / CW,NSC,XF,XR
*
*--CW is the cell width
*--NSC is the number of sub-cells per cell
*--XF is the minimum x coordinate
*--XR is the maximum x coordinate
*
      COMMON /CONST / PI,SPI,BOLTZ
*
*--PI is pi and SPI is the square root of pi
*--BOLTZ is the Boltzmann constant
*
      WRITE (*,*) ' INPUT 0,1 FOR CONTINUING, NEW CALCULATION:- '
      READ (*,*) NQL
*
      IF (NQL.EQ.1) THEN
*
         CALL INIT0S
*
      ELSE
*
         WRITE (*,*) ' READ THE RESTART FILE'
         OPEN (4,FILE='DSMC0S.RES',STATUS='OLD',FORM='UNFORMATTED')
         READ (4) BOLTZ,CC,CCG,CG,COL,CS,CW,DTM,FND,FNUM,FTMP,IC,IP,IR,
         &           ISC,ISCG,MOVT,NCOL,NIS,NM,NSC,NSMP,NPR,NPT,NSP,PI,PP,
         &           PV,SELT,SEPT,SP,SPI,SPM,TIME,XF,XR
         CLOSE (4)
*
         END IF
*
         IF (NQL.EQ.1) CALL SAMPOS
*
100    NPR=NPR+1
*
         DO 200 JJJ=1,NSP
            DO 150 III=1,NIS
               TIME=TIME+DTM
*
               WRITE (*,99001) III,JJJ,NIS,NSP,IFIX(NCOL)
99001   FORMAT (' DSMC0S:- Move ',2I5,' of ',2I5,I14,' Collisions')
*
            CALL MOVE0S

```

```
*          CALL INDEXS
*
*          CALL COLLS
*
150      CONTINUE
*
*          CALL SAMPLE0S
*
200      CONTINUE
*
WRITE (*,*) ' WRITING RESTART AND OUTPUT FILES',NPR,' OF ',NPT
OPEN (4,FILE='DSMCOS.RES',FORM='UNFORMATTED')
WRITE (4) BOLTZ,CC,CCG,CG,COL,CS,CW,DTM,FND,FNUM,FTMP,IC,IP,IR,
&           ISC,ISCGR,MOVT,NCOL,NIS,NM,NSC,NSMP,NPR,NPT,NSP,PI,PP,PV,
&           SELT,SEPT,SP,SPI,SPM,TIME,XF,XR
CLOSE (4)
*
CALL OUT0S
*
IF (NPR.LT.NPT) GO TO 100
STOP
END
* INIT0S.FOR
*
*--initialize the variables and the flow at zero time
*
SUBROUTINE INIT0S
*
PARAMETER (MNM=1000,MNC=50,MNSC=400)
*
DOUBLE PRECISION MOVT,NCOL,SELT,SEPT
*
COMMON /MOLSS / NM,PP(MNM),PV(3,MNM),IP(MNM),IR(MNM)
COMMON /CELLSS/ CC(MNC),CG(3,MNC),IC(2,MNC),ISC(MNSC),CCG(2,MNC),
&           ISCG(2,MNSC)
COMMON /GASS  / SP(2),SPM(5)
COMMON /SAMPS / NCOL,MOVT,SELT,SEPT,CS(5,MNC),TIME,NPR,NSMP,FND,
&           FTMP
COMMON /COMP   / FNUM,DTM,NIS,NSP,NPT
COMMON /GEOM   / CW,NSC,XF,XR
COMMON /CONST  / PI,SPI,BOLTZ
*
*--set constants
*
PI=3.141592654
SPI=SQRT(PI)
BOLTZ=1.3806E-23
*
CALL DATA0S
*
*--set additional data on the gas
*
SPM(1)=PI*SP(2)**2
*--the collision cross section is given by eqn (1.8)
SPM(5)=GAM(2.5-SPM(3))
*
*--initialise variables
*
TIME=0.
NM=0
*
CG(1,1)=XF
CW=(XR-XF)/MNC
DO 100 M=1,MNC
    IF (M.GT.1) CG(1,M)=CG(2,M-1)
    CG(2,M)=CG(1,M)+CW
100
```

```

CG(3,M)=CW
CC(M)=CW
CCG(2,M)=RF(0)
CCG(1,M)=SPM(1)*300.*SQRT(FTMP/300.)
*--the maximum value of the (rel. speed)*(cross-section) is set to a
*--reasonable, but low, initial value and will be increased as necessary
100    CONTINUE
*
*--set sub-cells
*
      DO 200 N=1,MNC
         DO 150 M=1,NSC
            L=(N-1)*NSC+M
            ISC(L)=N
150    CONTINUE
200    CONTINUE
*
*--generate initial gas in equilibrium at temperature FTMP
*
      REM=0
      VMP=SQRT(2.*BOLTZ*FTMP/SP(1))
*--VMP is the most probable molecular speed, see eqns (4.1) and (4.7)
*--A is the number of simulated molecules in cell N
      DO 300 N=1,MNC
         A=FND*CG(3,N)/FNUM+REM
      IF (N.LT.MNC) THEN
         MM=A
         REM=(A-MM)
      ELSE
         MM=NINT(A)
      END IF
      DO 250 M=1,MM
         IF (NM.LE.MNM) THEN
*--round-off error could have taken NM to MNM+1
         NM=NM+1
         PP(NM)=CG(1,N)+RF(0)*(CG(2,N)-CG(1,N))
         IP(NM)=(PP(NM)-CG(1,N))*(NSC-.001)/CG(3,N)+1+NSC*(N-1)
*--species, position, and sub-cell number have been set
         DO 210 K=1,3
            CALL RVELC(PV(K,NM),A,VMP)
210    CONTINUE
*--velocity components have been set
         END IF
250    CONTINUE
300    CONTINUE
      WRITE (*,99001) NM
99001 FORMAT (' ',I6,' MOLECULES')
*
      RETURN
      END
*   SAMPIOS.FOR
*
      SUBROUTINE SAMPIOS
*
*--initialises all the sampling variables
*
      PARAMETER (MNM=1000,MNC=50,MNSC=400)
*
      DOUBLE PRECISION MOVT,NCOL,SELT,SEPT
*
      COMMON /SAMPS / NCOL,MOVT,SELT,SEPT,CS(5,MNC),TIME,NPR,NSMP,FND,
      &                   FTMP
      COMMON /COMP  / FNUM,DTM,NIS,NSP,NPT
*
      NPR=0
      NCOL=0

```

```

NSMP=0
MOVLT=0.
SELT=0.
SEPT=0.
DO 100 N=1,MNC
    CS(1,N)=1.E-6
    DO 50 M=2,5
        CS(M,N)=0.
50      CONTINUE
100     CONTINUE
      RETURN
      END
*   MOVE0S.FOR
*
*   SUBROUTINE MOVE0S
*
*--the NM molecules are moved over the time interval DTM
*
*   PARAMETER (MNM=1000,MNC=50,MNSC=400)
*
*   DOUBLE PRECISION MOVLT,NCOL,SELT,SEPT
*
COMMON /MOLSS / NM,PP(MNM),PV(3,MNM),IP(MNM),IR(MNM)
COMMON /CELLSS/ CC(MNC),CG(3,MNC),IC(2,MNC),ISC(MNSC),CCG(2,MNC),
&               ISCG(2,MNSC)
COMMON /SAMPS / NCOL,MOVLT,SELT,SEPT,CS(5,MNC),TIME,NPR,NSMP,FND,
&               FTMP
COMMON /COMP  / FNUM,DTM,NIS,NSP,NPT
COMMON /GEOM  / CW,NSC,XF,XR
*
DO 100 N=1,NM
    MOVLT=MOVLT+1
    MSC=IP(N)
    MC=ISC(MSC)
*--MC is the initial cell number
    XI=PP(N)
    DX=PV(1,N)*DTM
    X=XI+DX
*--molecule N at XI is moved by DX to X
    IF (X.LT.XF) THEN
*--specular reflection from the minimum x boundary at x=XF (eqn (11.7))
    X=2.*XF-X
    PV(1,N)=-PV(1,N)
    END IF
    IF (X.GT.XR) THEN
*--specular reflection from the maximum x boundary at x=XR (eqn (11.7))
    X=2.*XR-X
    PV(1,N)=-PV(1,N)
    END IF
    IF (X.LT.CG(1,MC).OR.X.GT.CG(2,MC)) THEN
*--the molecule has moved from the initial cell
    MC=(X-XF)/CW+0.99999
    IF (MC.EQ.0) MC=1
*--MC is the new cell number (note avoidance of round-off error)
    END IF
    MSC=((X-CG(1,MC))/CG(3,MC))*(NSC-.001)+1+NSC*(MC-1)
*--MSC is the new sub-cell number
    IP(N)=MSC
    PP(N)=X
100    CONTINUE
      RETURN
      END
*   INDEXS.FOR
*
*   SUBROUTINE INDEXS
*
*--the NM molecule numbers are arranged in order of the cells and,

```

```

*--within the cells, in order of the sub-cells
*
      PARAMETER (MNM=1000,MNC=50,MNSC=400)
*
      COMMON /MOLSS / NM,PP(MNM),PV(3,MNM),IP(MNM),IR(MNM)
      COMMON /CELLSS/ CC(MNC),CG(3,MNC),IC(2,MNC),ISC(MNSC),CCG(2,MNC),
      &           ISCG(2,MNSC)
      COMMON /GASS  / SP(2),SPM(5)
*
      DO 100 NN=1,MNC
         IC(2,NN)=0
100    CONTINUE
      DO 200 NN=1,MNSC
         ISCG(2,NN)=0
200    CONTINUE
      DO 300 N=1,NM
         MSC=IP(N)
         ISCG(2,MSC)=ISCG(2,MS)+1
         MC=ISC(MSC)
         IC(2,MC)=IC(2,MC)+1
300    CONTINUE
*--numbers in the cells and sub-cells have been counted
      M=0
      DO 400 N=1,MNC
         IC(1,N)=M
         M=M+IC(2,N)
400    CONTINUE
*--the (start address -1) has been set for the cells
      M=0
      DO 500 N=1,MNSC
         ISCG(1,N)=M
         M=M+ISCG(2,N)
         ISCG(2,N)=0
500    CONTINUE
*--the (start address -1) has been set for the sub-cells
      DO 600 N=1,NM
         MSC=IP(N)
         ISCG(2,MS)=ISCG(2,MS)+1
         K=ISCG(1,MS)+ISCG(2,MS)
         IR(K)=N
600    CONTINUE
*--the molecule number N has been set in the cross-reference array
600    CONTINUE
      RETURN
      END
*
      COLLS.FOR
*
      SUBROUTINE COLLS
*
*--calculates collisions appropriate to DTM in a monatomic gas
*
      PARAMETER (MNM=1000,MNC=50,MNSC=400)
*
      DOUBLE PRECISION MOVT,NCOL,SELT,SEPT
*
      COMMON /MOLSS / NM,PP(MNM),PV(3,MNM),IP(MNM),IR(MNM)
      COMMON /CELLSS/ CC(MNC),CG(3,MNC),IC(2,MNC),ISC(MNSC),CCG(2,MNC),
      &           ISCG(2,MNSC)
      COMMON /GASS  / SP(2),SPM(5)
      COMMON /SAMPs / NCOL,MOVT,SELT,SEPT,CS(5,MNC),TIME,NPR,NSMP,FND,
      &           FTMP
      COMMON /COMP   / FNUM,DTM,NIS,NSP,NPT
      COMMON /GEOM   / CW,NSC,XF,XR
      COMMON /CONST  / PI,SPI,BOLTZ
*
      DIMENSION VRC(3),VRCP(3),VCCM(3)
*--VRC(3) are the pre-collision components of the relative velocity
*--VRP(3) are the post-collision components of the relative velocity

```

```

*--VCCM(3) are the components of the centre of mass velocity
*
      DO 100 N=1,MNC
*--consider collisions in cell N
      SN=CS(1,N)
      IF (SN.GT.1.) THEN
         AVN=SN/FLOAT(NSMP)
      ELSE
         AVN=IC(2,N)
      END IF
*--AVN is the average number of group MM molecules in the cell
      ASEL=0.5*IC(2,N)*AVN*FNUM*CCG(1,N)*DTM/CC(N)+CCG(2,N)
*--ASEL is the number of pairs to be selected, see eqn (11.3)
      NSEL=ASEL
      CCG(2,N)=ASEL-NSEL
      IF (NSEL.GT.0) THEN
         IF (IC(2,N).LT.2) THEN
            CCG(2,N)=CCG(2,N)+NSEL
*--if there are insufficient molecules to calculate collisions,
*--the number NSEL is added to the remainder CCG(2,N)
         ELSE
            CVM=CCG(1,N)
            SELT=SELT+NSEL
            DO 20 ISEL=1,NSEL
               K=INT(RF(0)*(IC(2,N)-0.0001))+IC(1,N)+1
               L=IR(K)
*--the first mol. L has been chosen at random from group NN in cell N
5            MSC=IP(L)
            IF (ISCG(2,MSD).EQ.1) THEN
*--if MSC has only the chosen mol., find the nearest sub-cell with one
               NST=1
               NSG=1
               INC=NSG*NST
               NSG=-NSG
               NST=NST+1
               MSC=MSC+INC
               IF (MSC.LT.1.OR.MSC.GT.MNSC) GO TO 6
               IF (ISC(MSC).NE.N.OR.ISCG(2,MSD).LT.1) GO TO 6
            END IF
*--the second molecule M is now chosen at random from the
*--molecules that are in the sub-cell MSC
            K=INT(RF(0)*(ISCG(2,MSD)-0.0001))+ISCG(1,MSD)+1
            M=IR(K)
            IF (L.EQ.M) GO TO 5
*--choose a new second molecule if the first is again chosen
*
            DO 10 K=1,3
               VRC(K)=PV(K,L)-PV(K,M)
10          CONTINUE
*--VRC(1 to 3) are the components of the relative velocity
            VRR=VRC(1)**2+VRC(2)**2+VRC(3)**2
            VR=SQRT(VRR)
*--VR is the relative speed
            CVR=VR*SPM(1)
            &           *((2.*BOLTZ*SPM(2)/(0.5*SP(1)*VRR))***(SPM(3)-0.5))
            &           /SPM(5)
*--the collision cross-section is based on eqn (4.63)
            IF (CVR.GT.CVM) CVM=CVR
*--if necessary, the maximum product in CVM is upgraded
            IF (RF(0).LT.CVR/CCG(1,N)) THEN
*--the collision is accepted with the probability of eqn (11.4)
            DO 12 K=1,3
               VCCM(K)=0.5*(PV(K,L)+PV(K,M))
12          CONTINUE
*--VCCM defines the components of the centre-of-mass velocity (eqn 2.1)
            NCOL=NCOL+1
            SEPT=SEPT+ABS(PP(L)-PP(M))

```

```

      IF (ABS(SPM(4)-1.) .LT. 1.E-3) THEN
*--use the VHS logic
      B=2.*RF(0)-1.
*--B is the cosine of a random elevation angle
      A=SQRT(1.-B*B)
      VRCP(1)=B*VR
      C=2.*PI*RF(0)
*--C is a random azimuth angle
      VRCP(2)=A*COS(C)*VR
      VRCP(3)=A*SIN(C)*VR
      ELSE
*--use the VSS logic
      B=2.*(RF(0)**SPM(4))-1.
*--B is the cosine of the deflection angle for the VSS model (eqn (11.8))
      A=SQRT(1.-B*B)
      C=2.*PI*RF(0)
      OC=COS(C)
      SC=SIN(C)
      D=SQRT(VRC(2)**2+VRC(3)**2)
      IF (D.GT.1.E-6) THEN
          VRCP(1)=B*VRC(1)+A*SC*D
          VRCP(2)=B*VRC(2)+A*(VR*VRC(3)*OC-VRC(1)*VRC(2)*SC)/D
          VRCP(3)=B*VRC(3)-A*(VR*VRC(2)*OC+VRC(1)*VRC(3)*SC)/D
      ELSE
          VRCP(1)=B*VRC(1)
          VRCP(2)=A*OC*VRC(1)
          VRCP(3)=A*SC*VRC(1)
      END IF
*--the post-collision rel. velocity components are based on eqn (2.22)
      END IF
*--VRCP(1 to 3) are the components of the post-collision relative vel.
      DO 14 K=1,3
          PV(K,L)=VCCM(K)+0.5*VRCP(K)
          PV(K,M)=VCCM(K)-0.5*VRCP(K)
14      CONTINUE
      END IF
20      CONTINUE
      CCG(1,N)=CVM
      END IF
      END IF
100     CONTINUE
      RETURN
      END
* SAMPLE0S.FOR
*
*
      SUBROUTINE SAMPLE0S
*
*--sample the molecules in the flow.
*
      PARAMETER (MNMM=1000,MNC=50,MNSC=400)
*
      DOUBLE PRECISION MOVT,NCOL,SELT,SEPT
*
      COMMON /MOLSS / NM,PP(MNM),PV(3,MNM),IP(MNM),IR(MNM)
      COMMON /CELLSS/ CC(MNC),CG(3,MNC),IC(2,MNC),ISC(MNSC),CCG(2,MNC),
      &                ISCG(2,MNSC)
      COMMON /SAMPS / NCOL,MOVT,SELT,SEPT,CS(5,MNC),TIME,NPR,NSMP,FND,
      &                FTMP
      COMMON /COMP  / FNUM,DTM,NIS,NSP,NPT
*
      NSMP=NSMP+1
      DO 100 N=1,MNC
          L=IC(2,N)
          IF (L.GT.0) THEN
              DO 20 J=1,L
                  K=IC(1,N)+J

```

```

M=IR(K)
CS(1,N)=CS(1,N)+1
DO 10 LL=1,3
    CS(LL+1,N)=CS(LL+1,N)+PV(LL,M)
    CS(5,N)=CS(5,N)+PV(LL,M)**2
10      CONTINUE
20      CONTINUE
       END IF
100     CONTINUE
       RETURN
       END
*   OUTOS.FOR
*
      SUBROUTINE OUTOS
*
*--output a progressive set of results to file DSMC0S.OUT.
*
      PARAMETER (MN=1000,MNC=50,MNSC=400)
*
      DOUBLE PRECISION MOVT,NCOL,SELT,SEPT,FND2
*
      COMMON /MOLSS / NM,PP(MN),PV(3,MN),IP(MN),IR(MN)
      COMMON /CELLSS/ CC(MNC),CG(3,MNC),IC(2,MNC),ISC(MNSC),CCG(2,MNC),
      &           ISCG(2,MNSC)
      COMMON /GASS  / SP(2),SPM(5)
      COMMON /SAMPs / NCOL,MOVT,SELT,SEPT,CS(5,MNC),TIME,NPR,NSMP,FND,
      &           FTMF
      COMMON /GEOM  / CW,NSC,XF,XR
      COMMON /COMP  / FNUM,DTM,NIS,NSP,NPT
      COMMON /CONST / PI,SPI,BOLTZ
      DIMENSION VEL(3)
*
      OPEN (4,FILE='DSMC0S.OUT',FORM='FORMATTED')
*
      WRITE (4,*) ' FROM ZERO TIME TO TIME',TIME
      WRITE (4,*) ' COLLISIONS =',NCOL
      WRITE (4,*) ' TOTAL NUMBER OF SAMPLES ',NSMP
      WRITE (4,*) NM,' MOLECULES'
      WRITE (4,*) MOVT,' TOTAL MOLECULAR MOVES'
      WRITE (4,*) INT(SELT),' SELECTIONS ',INT(NCOL),
      &           ' COLLISIONS, RATIO ',REAL(NCOL/SELT)
      IF (NCOL.GT.0) WRITE (4,*) ' MEAN COLLISION SEPARATION ',
      &           REAL(SEPT/NCOL)
*
      WRITE (4,*) ' FLOWFIELD PROPERTIES'
      WRITE (4,*) ' CELL X COORD SAMPLE N DENS.          U          V W
      &TEMP'
      TOT=0.
      DO 100 N=1,MNC
        A=FNUM/(CG(3,N)*NSMP)
        DENN=CS(1,N)*A
*--DENN is the number density
        IF (CS(1,N).GT.0.5) THEN
          DO 20 K=1,3
            VEL(K)=CS(K+1,N)/CS(1,N)
20      CONTINUE
*--VEL is the stream velocity components, see eqn (1.21)
        UU=VEL(1)**2+VEL(2)**2+VEL(3)**2
        TT=SP(1)*(CS(5,N)/CS(1,N)-UU)/(3.*BOLTZ)
*--TT is the temperature, see eqn (1.29a)
        TOT=TOT+TT
        XC=0.5*(CG(1,N)+CG(2,N))
*--XC is the x coordinate of the midpoint of the cell
        WRITE (4,99001) N,XC,INT(CS(1,N)),DENN,VEL(1),VEL(2),VEL(3),TT
      END IF

```

LISTING OF PROGRAM DSMC0\$FOR

449

```

99001  FORMAT (' ',I5,F10.4,I9,1P,E12.4,0P,4F10.4)
100  CONTINUE
*
*
C--compare with theoretical collision number (actual temperarure)
    AVTMP=TOT/MNC
    WRITE (4,*) ' AVERAGE TEMPERATURE ',AVTMP
    WRITE (4,*) ' '
    WRITE (4,*) ' RATIO OF COLLISION NUMBER TO THEORETICAL VALUE'
    WRITE (4,*) ' '
    FND2=FND
    TCOL=2.*TIME*FND2*FND2*(XR-XF)*SPM(1)
    &      *((AVTMP/SPM(2))**(.1.-SPM(3)))*SQRT(BOLTZ*SPM(2)/(PI*SP(1)))
    &      /FNUM
*---TCOL is the equilibrium collision rate, see eqn (4.64)
    WRITE (4,*) NCOL/TCOL
*
        CLOSE (4)
*
        RETURN
        END
*
        RVELC.FOR
*
        SUBROUTINE RVELC(U,V,VMP)
*
*--generates two random velocity components U an V in an equilibrium
*--gas with most probable speed VMP (based on eqns (C10) and (C12))
*
        A=SQRT(-LOG(RF(0)))
        B=6.283185308*RF(0)
        U=A*SIN(B)*VMP
        V=A*COS(B)*VMP
        RETURN
        END
*
        GAM.FOR
*
        FUNCTION GAM(X)
*
*--calculates the Gamma function of X.
*
        A=1.
        Y=X
        IF (Y.LT.1.) THEN
            A=A/Y
        ELSE
50      Y=Y-1
            IF (Y.GE.1.) THEN
                A=A*Y
                GO TO 50
            END IF
        END IF
        GAM=A*(1.-0.5748646*Y+0.9512363*Y**2-0.6998588*Y**3+
&          0.4245549*Y**4-0.1010678*Y**5)
        RETURN
        END
*
        RF.FOR
*
        FUNCTION RF(IDUM)
*--generates a uniformly distributed random fraction between 0 and 1
*----IDUM will generally be 0, but negative values may be used to
*-----re-initialize the seed
        SAVE MA,INEXT,INEXTP
        PARAMETER (MBIG=1000000000,MSEED=161803398,MZ=0,FAC=1.E-9)
        DIMENSION MA(55)
        DATA IFF/0/
        IF (IDUM.LT.0.OR.IFF.EQ.0) THEN
            IFF=1

```

```

MJ=MSEED-IABS(IDUM)
MJ=MOD(MJ,MBIG)
MA(55)=MJ
MK=1
DO 50 I=1,54
    II=MOD(21*I,55)
    MA(II)=MK
    MK=MJ-MK
    IF (MK.LT.MZ) MK=MK+MBIG
    MJ=MA(II)
50      CONTINUE
DO 100 K=1,4
    DO 60 I=1,55
        MA(I)=MA(I)-MA(1+MOD(I+30,55))
        IF (MA(I).LT.MZ) MA(I)=MA(I)+MBIG
60      CONTINUE
100     CONTINUE
INEXT=0
INEXTP=31
END IF
200     INEXT=INEXT+1
IF (INEXT.EQ.56) INEXT=1
INEXTP=INEXTP+1
IF (INEXTP.EQ.56) INEXTP=1
MJ=MA(INEXT)-MA(INEXTP)
IF (MJ.LT.MZ) MJ=MJ+MBIG
MA(INEXT)=MJ
RF=MJ*FAC
IF (RF.GT.1.E-8.AND.RF.LT.0.99999999) RETURN
GO TO 200
END
*   DATA0S.FOR
*
*       SUBROUTINE DATA0S
*
*--defines the data for a particular run of DSMC0S.FOR
*
PARAMETER (MNM=1000,MNC=50,MNSC=400)
*
DOUBLE PRECISION MOVT,NCOL,SELT,SEPT
*
COMMON /GASS   / SP(2),SPM(5)
COMMON /SAMPS  / NCOL,MOVT,SELT,SEPT,CS(5,MNC),TIME,NPR,NSMP,FND,
&                 FTMP
COMMON /COMP   / FNUM,DTM,NIS,NSP,NPT
COMMON /GEOM   / CW,NSC,XF,XR
*
*--set data (must be consistent with PARAMETER variables)
*
FND=1.E20
*--FND is the number density
FTMP=300.
*--FTMP is the temperature
FNUM=1.0E17
*--FNUM is the number of real molecules represented by a simulated mol.
DTM=.25E-4
*--DTM is the time step
NSC=8
*--NSC is the number of sub-cells in each cell
XF=0.
XR=1.
*--the simulated region is from x=XF to x=XR
SP(1)=5.E-26
SP(2)=3.5E-10
*--SP(1) is the molecular mass
*--SP(2) is the molecular diameter
SPM(2)=273.

```

```
SPM(3)=0.75
SPM(4)=1.
---SPM(2) is the reference temperature
---SPM(3) is the viscosity-temperature power law
---SPM(4) is the reciprocal of the VSS scattering parameter
    NIS=4
---NIS is the number of time steps between samples
    NSP=40
---NSP is the number of samples between restart and output file updates
    NPT=500
---NPT is the number of file updates to STOP
*
      RETURN
      END
```



SUBJECT INDEX

- acceptance-rejection method 105, 424
accommodation coefficient 118–121
activation energy 124
adiabatic atmosphere 311–312
surface temperature 169, 354
apse line 33, 35, 39, 95
Arrhenius equation 124
atomic mass constant 5
average *see* mean
averages ensemble 11
instantaneous 10
time 10
Avogadro's number 5, 19, 124
axially symmetric flows 370–388
DSMC procedures 370–371

BBGKY equations 50
beta function 112, 422
BGK equation 195
bimodal distribution 148–150, 156, 191–196, 295, 305
bimolecular reaction 124–125, 129–133
binary collision 7, 27, 30–36, 88, 129, 137
blunt-body problem two-dimensional 353–359
axially symmetric 374–377
Boltzmann CFD 200
Boltzmann constant 14, 25, 211, 243
Boltzmann distribution 114, 116, 146, 239–240, 245
Boltzmann equation 1, 50–53, 61, 183–186, 199, 202, 209, 292
Chapman–Enskog solution of 64
collision term 54, 196
collisionless 156, 160
derivation of 50–53
direct CFD for 200
for gas mixture 54
generalized 54, 64
moment of 55

normal solution of 65
relationship to simulation 208–210
Borgnakke–Larsen *see* Larsen–Borgnakke
breakdown parameter 4
DSMC determination of 282–285
bridging formulae 189
Burnett equations 70, 293

cellular automata 204
Cercignani–Lampis–Lord (CLL) surface reflection model 120–121, 360–361, 366
Chapman–Enskog theory 3, 20, 64–75
distribution function 3, 73–74, 91, 173
second approximation to 74
characteristic temperature of rotation 25, 412
vibration 25, 113, 241, 412
dissociation 25, 245, 412
ionization 412
chemical reactions 123–144, 245–251
coefficient of diffusion *see* diffusion
coefficient of heat conduction *see* heat conduction
coefficient of viscosity *see* viscosity
collapse of cylindrical cavity 331
collision cross-section differential 33
relative speed dependence 20, 38
total 5, 34–39, 67
in mixture 16
reference 67, 72
collision cut-off 20, 37
collision integral 56–57
evaluation of 60, 68
collision lifetime 129

- collisional invariants 58
 collisionless
 Boltzmann equation 156
 flow 2
 unsteady flows
 free expansion 157–160
 piston problem 160–162
 see also free-molecule
 complete rarefaction wave 325–327
 computational grids *see* grids
 conservation equations 58–60
 of energy 59
 of mass 58
 of momentum 58
 continuum breakdown parameter
 see breakdown parameter
 Couette flow 154, 212, 262, 271, 275
 Taylor *see* Taylor–Couette
 cumulative distribution function 110, 239, 423–427
 cross-section *see* collision cross-section
 Coulomb molecules 26
 cylindrical symmetry 260
 de Broglie wavelength 24
 Debye length 204
 deflection angle 36
 degree of dissociation 130
 degrees of freedom 25, 408
 internal 83
 density 9
 of mixture 17
 diffuse reflection 97
 diffusion
 coefficient
 Chapman–Enskog result 69
 for GHS molecules 73
 for VHS molecules 69
 for VSS molecules 70
 DSMC result for 273
 cross-section 38
 equation 75
 forced 75
 pressure 75
 thermal 75, 275–278
 thermo-effect 278–279
 velocity 18
 relative 75
- dilute gas 7, 12
 direct Boltzmann CFD 200
 direct simulation Monte Carlo (or DSMC) method 203–407
 collision sampling 217–227
 discrete ordinate method 205
 discrete velocity method 205
 dissipation function 59
 dissociation 25
 dissociation–recombination reaction 133–140
 DSMC simulation of 245–251
- distribution functions
 see bimodal
 Boltzmann
 Chapman–Enskog
 cumulative
 equilibrium
 Larsen–Borgnakke
 normal
 Poisson
 velocity
- effusion 151
 Einstein coefficients 29, 145
 elastic collisions 30
 electric dipole moment 145
 electric field 204
 ensemble average 11
 equation of change 56
 equilibrium 8
 air composition 27
 collision rate 90
 in mixtures 96
 DSMC result 224–227
 collisional energy 93–5
 constant 130
 distribution function 64, 77–98
 in cylindrical coordinates 80
 in polar coordinates 77
 of internal energy 104
 rotational from DSMC 234–237
 vibrational from DSMC 240
- flux
 energy
 translational 83
 internal 83
 total 84
- momentum
 normal

- parallel 82
- number 82
- mean free path 91, 93
 - in mixtures 96
- relative speeds in collisions 89
- ergodic 11
- error function 79, 420–421
- Euler equations 60, 186
- exchange reactions 140
- field molecules 7, 16, 52
- flat plate
 - free-molecule 169–172
 - supersonic 360–366
 - three-dimensional 401–404
- flux vector 12
- forced diffusion 75
- four moment method 187–194
- free expansion problem 157
- free-molecule
 - aerodynamics 162–172
 - flat plate 169–172
 - heat transfer coefficient 167
 - number flux 164
 - pressure coefficient 165
 - skin friction coefficient 165
 - internal flow 175–181
 - one-dimensional heat transfer 154–156
 - piston problem 160
 - test particle method for 176
 - see also* collisionless
- frozen flow 28
- gamma function 94, 112, 126, 417
- gas
 - constants 14
 - centrifuge 313–315
 - dilute 7, 12
 - equilibrium 8
 - properties 19–29, 408–416
 - simple 5
- gas-surface interactions 97, 118–121, 360–361
- Gaussian *see* normal distribution
- generalized hard sphere (GHS) model 44
- Grad's thirteen moment equations 186
- gravitational field 258, 311
- grids
 - three-dimensional 389–393
 - two-dimensional 335–339
 - effect of cell-size 346–348
 - sub-cells 216
- H*-theorem 61–63
- hard sphere 5, 39–40
- harmonic oscillator *see* vibrational excitation
- heat conduction
 - coefficient
 - Chapman–Enskog result for 66
 - heat flux vector 15, 74
- Heisenburg uncertainty principle 24
- hypersonic limit 84–86
- impact parameters 33
- information theory 124
- intermolecular
 - force field 6, 35
 - potential 35
- inverse collision 33
- inverse–cumulative method 424
- ionization 26, 140–142
- ionized gas 204
- isentropic 9
- Knudsen number 2
 - local 2
 - overall 2
- Knudsen layer 191
- Kronecker delta 14
- lapse rate 311–312
- Larsen–Borgnakke model 104–107
 - distribution functions
 - general
 - internal energy 107
 - translational energy 106
 - DSMC implementation
 - general 109–112
 - rotation 228–237
 - vibration 238–245
 - method 100, 104–116
 - for simple gas 104–107
 - for vibration 112–116
 - quantum version 114–115
 - in a mixture 108–109

- serial application 111
 lattice gas method 204
 leading-edge problem 340–346
 Lennard–Jones model 43
 Liouville equation 50, 156
 list of symbols xiii
 local thermodynamic equilibrium 9,
 146
 Loschmidt's number 19
- Mach number 165
 macroscopic model 1
 mass velocity 13
 mass average velocity 17
 maximum entropy principle 124
 Maxwell model 43
 Maxwellian distribution *see*
 equilibrium distribution
 mean
 collision frequency 7
 collision rate 7
 in gas mixture 16
 collision time 7
 free path 2, 8
 in mixture 17
 in equilibrium gas 90
 molecular spacing 5
 radiative lifetime 145
 square molecular speed 20
 translational energy in collisions
 93, 97
 velocity 17
 values in collisions 92
- microscopic model 1
 model equation *see* BGK
 molecular
 angular velocity 101, 145
 chaos 49–50, 88, 204, 209
 cross-section *see* collision cross-
 section
 diameter
 hard sphere 5
 reference value 92, 409
 VHS 68, 93, 97
 in mixture 69
 VSS 70
- dynamics (MD) method 202, 209
 effusion 151
 elastic models 39–44
 GHS 44
- hard sphere 5, 39–40
 Lennard–Jones 43
 Maxwell 43
 square-well 43
 Sutherland 43
 VHS 20, 40–41
 VSS 41–42
 scattering parameter 42, 410
- force field 6
 inelastic models
 rough-sphere 99, 101–103
 sphero-cylinder 99
 two centres of repulsion 99
 see also Larsen–Borgnakke
 inverse power law 37
 mass 5, 408
 reduced 31
 mean spacing 5
 speed ratio 82
 reflection at surfaces
 diffuse 97
 specular 97
 transpiration 151
 weight 5
 moment equation 55
 moment methods 184
 momentum cross-section 38–42
 Monte Carlo
 direct simulation *see* direct simul-
 ation Monte Carlo method
 test particle method
 free-molecule 176
 transition regime 203
 Morse potential 245–246
 most probable thermal speed 78
 Mott-Smith solution 191–194
- Navier–Stokes equations 1–2, 74,
 186
- nomenclature xiii–xvii
 normal distribution 9
 normal shock wave *see* shock wave
 NTC method 219
 number density 5
 in gas mixture 16
 standard 19
- one-dimensional heat transfer
 four moment method 187–191
 DSMC result for 280–281

- ordinary gas constant 14
- partition functions 131, 415
- peculiar velocity 13
- photophoresis 174
- piston problem 317–324
 collisionless 160–162
 spherical 328–331
- Planck's constant 24
- plasma 204
- Poisson distribution 9
- Poisson equation 204
- phase space 1
- phenomenological models 100
- physical space 46
- Prandtl number 66
 DSMC result for 271
- Prandtl-Meyer expansion 367–369
- pressure
 diffusion 75
 scalar 14
 tensor 13
- quantum vibration model 114
- radiation *see* thermal radiation
- random numbers 203, 432, 435
- random velocity 13
- random walk 211
- rarefaction wave 325–327
- rate coefficient 28, 115, 124
- rate equation 124
- reaction cross-section 125, 133
- recombination 26
- reciprocity condition 97
- reduced mass 31
- relaxation collision number 104,
 117, 138
- relaxation time 28
- relaxation rates 116–117
 DSMC result for rotation 232–
 237
 DSMC result for vibration 242–
 245
- Reynolds number 383
- rotational radiation 144–145
- rotational collision number 228
 see also relaxation collision
 number
- root mean square speed 21
- satellite contamination 387–388
- Schmidt number 409
- self-diffusion coefficient 271
- shock Mach number 286
- shock wave
 Burnett solution 293–295
 BGK solution 197
 DSMC results for 288–305
 in mixture 299–301
 with rotational energy 297
- formation of strong 317–320
- formation of weak 323–324
- local Knudsen number in 287
- Mott-Smith solution 191–194,
 302–305
- Navier–Stokes solution 286–287
- oblique 340, 363, 386
- reflection of strong 320–322
- shape factor 293
- spherically imploding 328–321
- thickness 286
- simple gas 5
- slip boundary condition 190, 190
- slip velocity 150
- specific heat 25
 ratio 25, 83
- specular reflection 97
- speed ratio 82
- sphere drag 172
- spherical symmetry 260
- square terms 127
- stagnation streamline flow 306–311
- standard conditions 19
- standard deviation 9
- statistical fluctuations 9, 179, 214
 in DSMC calculations 211–214,
 251–256
 spatial correlations 256
 temporal correlations 254
- steric factor 125
- stream velocity 13
- sub-cells 216
- substantial derivative 58
- summational invariants 58
- supersonic
 blunt body *see* blunt body
 corner flow 394–401
 leading edge *see* leading edge
 jet
 impact on wall 384–387

- in corner flow 405–406
- surface
 - density at 150
 - gas interaction *see* gas–surface interaction
 - slip at 150, 190
- symbols xiii–xvii

- Taylor number 378
- Taylor–Couette flow 378–383
- temperature 15
 - characteristic
 - of dissociation 25, 412
 - of rotation 25, 412
 - of vibration 25, 412
 - in mixture 18
 - internal 15
 - jump 150, 190
 - kinetic 14
 - overall 15
 - thermodynamic 14
 - translational 14
- termolecular reactions 128–129
- test molecule 7, 16, 52, 176, 203
- test particle Monte Carlo method for
 - collisionless flows 176
 - transition regime flows 203
- thermal
 - backflow limit 84–86
 - diffusion 75
 - DSMC result for 275–278
 - equilibrium *see* equilibrium
 - radiation 28
 - bound–bound 29, 145–146
 - bound–free 29
 - free–free 29
 - speed in equilibrium gas
 - average 78
 - most probable 78
 - transpiration
 - velocity 13
 - single species 18
- thermophoresis 173–174
- time counter (TC) method 218
- transfer equation 56
- transition regime 183

- transport properties *see* viscosity coefficient etc.

- uncertainty principle 24
- universal gas constant 14

- variable hard sphere (VHS) 20, 40–41
- variable soft sphere (VSS) 41–42
- variance reduction 181, 212, 428
- velocity distribution functions
 - Chapman–Enskog 3
 - equilibrium 3, 64
 - full range 148
 - half range 150
 - Maxwellian 3, 64
 - N particle 49
 - single particle in velocity space 46
 - single particle in phase space 48
- velocity space 46
- VHS *see* variable hard sphere
- vibrational excitation
 - anharmonic 245–246
 - collision number 138, 141, 413
 - energy levels 114, 245–246
 - harmonic oscillator 113
 - DSMC result for 241
- viscosity
 - coefficient
 - Chapman–Enskog result 66
 - for power-law molecules 67
 - for VHS molecules 67
 - for VSS molecules 70
 - DSMC result for 262–270
 - in mixture 269–270
 - measured 408
 - cross-section 38
 - temperature index 20, 408
- viscous stress tensor 14, 74
- vortices
 - behind vertical plate 348–352
 - Taylor–Couette 378–383
- VSS *see* variable soft sphere

- weighting factors 213, 372–374, 388